CAMK2 and RHEB1 Mutations Associated with Intellectual Disability and Epilepsy

Martina Proietti Onori

ISBN 978-94-6332-619-3

Cover design and layout: Martina Manna
Book layout: Martina Proietti Onori
Printed by: GVO drukkers & vormgevers B.V. | Ponsen & Looijen

CAMK2 and RHEB1 Mutations Associated with Intellectual Disability and Epilepsy

CAMK2 en RHEB1 mutaties geassocieerd met verstandelijke beperking en epilepsie

Proefschrift

ter verkrijging van de graad van doctor aan de
Erasmus Universiteit Rotterdam
op gezag van de rector magnificus

Prof.dr. R.C.M.E. Engels

en volgens het besluit van het College voor Promoties.

De openbare verdediging zal plaatsvinden op

woensdag 9 september 2020 om 9.30 uur

door

Martina Proietti Onori

geboren te Subiaco, Italië

Erasmus University Rotterdam

Promotiecommissie:

Promotor:	Prof.dr. Y. Elgersma
Overige leden:	Prof.dr. F.E. Hoebeek Prof.dr. J.G.G. Borst Prof.dr. S.A. Kushner
Copromotor:	Dr. G.M. van Woerden

TABLE OF CONTENTS

"We especially need imagination in science.
It is not all mathematics, nor all logic,
but it is somewhat beauty and poetry."

Maria Mitchell (1818-1889)
Astronomer, librarian, naturalist, educator

Chapter I

GENERAL INTRODUCTION

PART I: NEURODEVELOPMENTAL DISORDERS

Neurodevelopmental disorders (NDDs) are disorders that result from an abnormal brain development. This broad definition includes syndromic disorders, caused by a known (genetic) cause, such as Rett syndrome or fragile X syndrome, and disorders with an unidentified cause with an often early onset during development (Sherr, 2016). The phenotypical spectrum of these disorders is highly variable. NDDs can be characterized by impairments in cognition, social and motor skills and sensory processing. Therefore, based on some of their clinical features, autism spectrum disorder (ASD), attention-deficit/hyperactivity disorder (ADHD), intellectual disability (ID) and stereotypic movement and tic disorders (such as Tourette's disorder) can all fall under this category (American Psychiatric Association, 2013).

Genetic investigations show that there are often **genetic risk factors** responsible for neurodevelopmental pathologies (van Loo and Martens, 2009). Originally, many of the identified causative genes for NDDs were those inherited in an X-linked pattern [see for example the identification of the *FMR1* gene as cause of fragile X syndrome (Kremer *et al*., 1991)]. However, over the past few years, many different genetic causes, ranging from chromosomal deletions to single-nucleotide polymorphisms (SNPs), have been identified and associated with NDDs, and more are being discovered thanks to the technical advancement in sequencing methodologies (Gilissen *et al*., 2011; Vissers *et al*., 2016). **Next-generation sequencing** (NGS), compared to previous technologies, allows the high-throughput sequencing of the DNA with a low cost and now often complements or replaces the Sanger sequencing method originally used to identify genetic variants in the DNA [for a review on the technological evolution of DNA sequencing methodologies see (Shendure *et al*., 2017)]. NGS potentially makes the identification possible of all genetic variations at single base pair resolution in the entire genome within one single experiment and this explains the high number of genetic variants identified associated with NDDs (Behjati and Tarpey, 2013).

The unbiased approaches most commonly used to detect genetic variations in an individual are **whole-exome sequencing** (WES) (Gilissen *et al*., 2011) and **whole-genome sequencing** (WGS), the latter also providing the tool to access non-coding regions of the genome (Coe *et al*., 2019; Turner and Eichler, 2019). Recently, the use of WES in parent-child trios suggested that *de novo* and rare inherited variants in coding parts of the genome can play a role in the development of NDDs (O'Roak *et al*., 2011; O'Roak *et al*., 2012a; Sanders *et al*., 2012; Iossifov *et al*., 2014; McRae *et al*., 2017; Wilfert *et al*., 2017; Wang *et al*., 2019). The importance of *de novo* variants in NDDs was first shown in a large-scale genomic study including children with severe ID where truncating or *de novo* variants were considered candidate variants causative for the disorder (de Ligt *et al*., 2012). Afterwards, candidate *de novo* variants were also demonstrated for ASD, studying cohorts of families where one child was affected with ASD (Iossifov *et al*., 2014; Turner *et al*., 2017a).

The **clinical heterogeneity** of NDDs would imply that the underlying molecular and cellular mechanisms responsible for their occurrence are the most diverse. However, genome-wide association studies (GWAS) show that there is substantial overlap in genetic risk factors identified in clinically unrelated NDDs (Plummer *et al*., 2016; Thapar *et al*., 2017). GWAS studies make use of NGS technologies to search for common genetic variants in the genome of a defined population of patients with similar clinical features that reach a certain statistical threshold to be associated with the disease as risk factors (Mullin *et al*., 2013; Tam *et al*., 2019). Despite the clinical diversity, shared molecular cascades and pathways often appear to be affected in different neurodevelopmental pathologies (Plummer *et al*., 2016). For example,

one group of genes identified as risk factors for several NDDs, encode for postsynaptic density (PSD) proteins (Verpelli *et al*., 2013; Kaizuka and Takumi, 2018). The PSD is the core structure at the basis of the anatomical and electrical connection that neurons form with each other. It contains thousands of different proteins, including neurotransmitter receptors and channels, scaffolding and cytoskeleton proteins, cell adhesion molecules and signaling enzymes (Ziff, 1997; Cheng *et al*., 2006; Trinidad *et al*., 2008). Therefore, it is not surprising that mutations in many of its components have been associated with human neurological disorders with different phenotypical outcome (Laumonnier *et al*., 2007; Bayés *et al*., 2011; Grant, 2012; Kaizuka and Takumi, 2018; Roy *et al*., 2018; Zhu *et al*., 2018).

A comparative analysis of high confidence risk genes compiled for different disorders (Plummer *et al*., 2016) shows that the majority of the selected high risk genes is often associated with **ID**. It is not surprising, since ID can occur in isolation but is most often a common comorbidity of other NDDs, including ASD and epilepsy (Hannah and Brodie, 1998; Bowley and Kerr, 2000; Srivastava and Schwartz, 2014). ID is also one of the most common early onset developmental disorders with a prevalence in the general population of 1-3%, characterized by a general limitation in intellectual functioning (IQ<70) (Maulik *et al*., 2011; McKenzie *et al*., 2016). Its severity is highly variable and this is reflected by an extreme genetic heterogeneity (Mefford *et al*., 2012). Trio-based exome sequencing became the primary method to identify new *de novo* variants as possible causes for sporadic ID, after the very first pilot study in 2010 (Vissers *et al*., 2010). In 2012, two exome studies with large cohorts of patients showed that *de novo* variants in known ID genes can explain between 13 and 35% of the most severe ID cases (de Ligt *et al*., 2012; Rauch *et al*., 2012). In 2014, the de Ligt study was further expanded applying WGS in 50 of the 100 ID patients included in the previous study and the percentage of severe ID cases explained by *de novo* variants increased to 60% (Gilissen *et al*., 2014). Overall, now more than 700 genes (including X-linked, autosomal dominant and recessive genes) have been linked to ID and ID-associated disorders (Vissers *et al*., 2016). With the identification of these genes, several common molecular pathways are starting to emerge for being involved in ID, including for example the RAS/MAPK (mitogen-activated protein kinase) and mTOR (mammalian target of rapamycin) signaling pathways (Borrie *et al*., 2017), the Rho-GTPase pathway (Nadif Kasri and Van Aelst, 2008; Zamboni *et al*., 2018) and members of transcription regulation and chromatin remodeling (Izumi, 2016; Iwase *et al*., 2017).

In a large number of cases [estimated between 4 and 8 out of 1000 children suffering from ID, (Steffenburg *et al*., 1995)], early childhood **epilepsy** is also present in association with ASD and ID (Caplan and Austin, 2000; Reilly *et al*., 2014; Nickels *et al*., 2016). Epilepsy is a neurological disorder characterized by frequent and recurrent seizures, defined as rhythmic firings of interconnected neuronal populations (Devinsky *et al*., 2018). In most cases (between 30 and 40% of patients), epilepsy is intractable and anti-epileptic drugs are only symptomatic (Ben-Menachem, 2014). A preventive cure has not been identified so far (Mula, 2015). Understanding the intrinsic mechanisms that drive a normal brain to become epileptic (defined as epileptogenesis) is therefore pivotal in the identification of new therapeutic strategies aimed at preventing the occurrence of seizures (Pitkänen and Lukasiuk, 2011; Goldberg and Coulter, 2013; Pitkänen *et al*., 2015). Epilepsy can be caused by many different factors and it is not considered necessarily a neurodevelopmental disorder [for an historical overview on the etiology of epilepsy see (Shorvon, 2011)]. For example, structural lesions, brain tumors or trauma caused by accidents can lead to the occurrence of epilepsy (Lucke-Wold *et al*., 2015; Englot *et al*., 2016). However, several developmental factors are a frequent cause

of epilepsy. For example, perturbation of genetic pathways underlying the proper shaping of neuronal circuitry during critical period of embryonic life can lead to brain malformations and subsequent epilepsy (Leventer *et al*., 2008; Bozzi *et al*., 2012; Parrini *et al*., 2016). So far, several genes have been linked to the emergence of epilepsy, within those, not surprisingly, many belong to the ion channel class, such as subunits of voltage gated potassium and sodium channels and ligand activated GABA and acetylcholine channels (Steinlein, 2001; Lerche *et al*., 2013; Bomben *et al*., 2016; Lehman *et al*., 2017). In addition to genes already known to cause epilepsy, many more *de novo* candidate variants in new and known genes associated with epilepsy are being discovered thanks to NGS (Heyne *et al*., 2018).

The main challenge that still remains in human genetic studies is the **biological validation** of the contribution of the candidate variant to the pathogenesis of the disorder under investigation (Vissers *et al*., 2016; Willsey *et al*., 2018). Indeed, as was already mentioned in the editorial for the New England Journal of Medicine in 2013: "….*A major challenge of interpreting genetic sequence is the determination of whether any given variant is pathogenic*" (Jacob, 2013). For this purpose, we are now entering a new era where **functional assays** to assess the pathogenicity are a crucial next step in this endeavor. Before embarking in the use of any functional assay however, strong genetic evidence supporting the pathogenicity of a given variant in a certain disorder is a necessary requirement. Although a description of the genetic prerequisites to evaluate pathogenicity falls beyond the scope of this thesis, I refer the reader to a comprehensive review that summarizes in detail the major guidelines and recommendations in the analysis of candidate genetic variants (MacArthur *et al*., 2014). After establishing a clear statistically relevant association of the genetic variant to the disease under investigation (Mullin *et al*., 2013), to be able to assess its pathogenicity, the understanding of the biological processes affected by the gene within a cell and the functional relevance of this within the cellular network is pivotal. To date, several functional assays investigating how risk genes can alter protein structure, function and the general network in relation to the surrounding environment are in use but these are often laborious and require high investment of time and resources (Kircher *et al*., 2014; Starita *et al*., 2017). With the increased number of new candidate genes thought to be involved in NDDs being identified, the need for low cost and **high-throughput** functional assays is becoming more and more demanding.

The first step in a functional screening to characterize the pathogenicity of a variant, besides using *in silico* prediction models, would be to characterize the molecular and physiological contribution of the gene under investigation in an *in vitro* setting. Relevant structural and molecular changes caused by the variant can be first rapidly detected in several cell types, like human embryonic kidney cells, Neuro2a cells and primary neuronal cultures, which are physiologically relevant for the study of the disease. The human induced pluripotent stem cell approach (hIPSCs) also is a very attractive tool to study the mechanisms of pathogenesis of NDDs, since it would allow the reprogramming of somatic cells of the patient into a variety of neuronal cell types (Telias and Ben-Yosef, 2014; Muotri, 2016; Ardhanareeswaran *et al*., 2017; Taoufik *et al*., 2018; Vitrac and Cloët-Tayarani, 2018; Shen *et al*., 2019). But this technique is still under development and cannot be used yet in a standardized manner. As a second step, still *in vitro*, a higher-level cell-cell interaction would have to be investigated to understand the effects of the risk gene at a circuit level. New exciting technologies, such as Multi-electrode arrays (MEAs), are being developed to get insight in the development of neuronal circuitry and activity to assess the pathogenic effect of a candidate genetic variant (Gullo *et al*., 2014; Bart Martens *et al*., 2016; Frega *et al*., 2019, 2020).

All these *in vitro* models can provide a detailed understanding of the cell intrinsic

processes that are disrupted but they lack the system-level physiological context, thus the next step would be to go to multicellular *in vivo* models. The Zebrafish is a very powerful animal model that is currently being used to identify behavioral phenotypes caused by NDDs candidate genes (Sakai *et al*., 2018; Vaz *et al*., 2019). As an alternative *in vivo* system, *Drosophila melanogaster*, the fruit fly, represents a relatively simple model to investigate disease associated genes (Gatto and Broadie, 2011; Coll-Tane *et al*., 2019). A third model is represented by the *Xenopus*, a frog which is evolutionary closer to humans than Zebrafish and possesses the basic features of the vertebrate brain development (Pratt and Khakhalin, 2013). Besides all the previous models, the nematode *Caenorhabditis elegans* represents a good compromise to study NDDs: the well described anatomy and neuronal interconnectivity, the existence of transgenic lines and specific behavioral repertoires make it a suitable model to study in a large scale the genetic contribution to NDDs (Bessa *et al*., 2013). However, at the moment, the golden standard *in vivo* model to study NDDs is *Mus musculus*, although the time and costs to study one single gene limit the use of mouse models and mammalian systems in general (Willsey *et al*., 2018). More recently, the development of 3D cell cultures and organoids, that closely resemble the human brain, generated new possibilities to study (although again *in vitro*) the cellular processes that take place in a pathogenic context (Di Lullo and Kriegstein, 2017; Hartlaub *et al*., 2019; Pollen *et al*., 2019). All these models have been proven in the past to be extremely valuable in studying the underlying mechanisms of genes causing diseases, but not all are suitable for high-throughput screening of many candidate variants to identify the truly pathogenic variants from the non-pathogenic variants.

In recent years, we set up a functional screen in the laboratory, called **PR*i*SM** (Pipeline for Rapid Screening of novel Mutations) to test the pathogenicity of candidate variants identified in individuals with a neurodevelopmental disorder. After a first *in silico* prediction model analysis, the screening consists of a series of standardized assays *in vitro* and *in vivo* to investigate the effect of the variant. The *in vitro* assays investigate the stability of the mutated protein in HEK cells and the effect of the mutated protein in primary neuronal cultures, where we quantify basic morphological parameters (soma size and neurite arborization). For the *in vivo* assay, we make use of *in utero* electroporation (IUE) where we overexpress the mutated protein at an early time point during brain development (E14.5) to assess if this interferes with the normal migration of newly born neurons through the cortical layers. As will be described in part III of this introduction, cortical development is a very tightly regulated biological process and small perturbations of the molecular balance in progenitor cells can result in an improper cortical migration. Thereby, IUE represents a very sensitive assay to assess if a specific variant has any effect on the protein function. In all of these assays, the effect of the mutated protein is compared to the effect of an empty vector control and to the overexpression of the wild type protein as well as to the knock-down of the gene of interest. In this way, we can conclude if the mutation is acting as a pure loss-of-function or dominant negative mutation or as a gain-of-function mutation.

Several variants in different genes have been tested using the PR*i*SM screen (some are listed in https://functionalgenomics.nl/tested-genes/) and many of those were selected from list of candidate genes for ID published in WES studies. Making use of the PR*i*SM screen and other assays, the results presented in this dissertation represent our contribution to the field in trying to disentangle the biological neurological effects of *de novo* missense variants identified in *CAMK2* and *RHEB1* in patients with ID and epilepsy.

PART II: CAMK2 AND INTELLECTUAL DISABILITY

Structure and regulation of the CAMK2 holoenzyme

Calcium/calmodulin dependent protein kinase II (**CAMK2**) is a multimeric holoenzyme composed of different subunits encoded by four distinct genes, known as *CAMK2A*, *CAMK2B*, *CAMK2D* and *CAMK2G* [referring to the ortholog genes from *Homo Sapiens* (for an evolutionary perspective see Tombes *et al*., 2003)].

CAMK2 was initially discovered in the central nervous system as a kinase being activated by calcium (Ca^{2+}) and calmodulin (CaM) (Schulman and Greengard, 1978a, 1978b). The kinase was later purified from rat brain homogenate and the major brain isoforms were characterized (Kennedy and Greengard, 1981; Bennett *et al*., 1983; Kennedy *et al*., 1983a; Lin *et al*., 1987). The high abundance in the brain, especially in the dendritic spines, of CAMK2 isoforms led to the assumption that this kinase might play a substantial role in neuronal activity and synaptic transmission (Griffith, 2004). And indeed, one of the first identified targets of CAMK2 phosphorylation was Synapsin I (CAMK2 was originally named calmodulin-dependent Synapsin I kinase), a protein located primarily in the neuronal presynaptic terminals where it binds to the cytoplasmic surface of synaptic vesicles and to the actin cytoskeleton (Kennedy and Greengard, 1981; Cesca *et al*., 2010).

Each **CAMK2 subunit** is composed of an N-terminal catalytic domain, a C-terminal association domain and an autoregulatory domain in the middle (**Figure 1A**). While all these domains are highly homologous between the different isoforms, most of the variability lies in the linker region connecting the autoregulatory domain to the association domain (also called the variable domain) (Bennett and Kennedy, 1987; Hanley *et al*., 1987; Lin *et al*., 1987; Bulleit *et al*., 1988). The arrangement of single subunits to form a holoenzyme structure is ensured by the combination of the C-terminal association domains of 12-14 subunits to constitute the central core in a double ring shape, while the N-terminal catalytic domains extend towards the outside in a "hub-and-spoke" fashion (Kanaseki *et al*., 1991; Braun and Schulman, 1995; Kolodziej *et al*., 2000; Morris and Török, 2001) (**Figure 1B**). A recent study using 3D electron microscopy (EM) revealed that the holoenzymes in their basal state are very dynamic structures with highly flexible kinase domains (Myers *et al*., 2017). This flexibility enables a reversible exchange of subunits in the holoenzyme, potentially giving rise to transition states of tetradecamers (14 subunits) which have been recently modeled *in silico* and experimentally observed (Stratton *et al*., 2014; Bhattacharyya *et al*., 2016; Myers *et al*., 2017; Singh and Bhalla, 2018).

It's the **functional regulation** of the holoenzyme, through this fascinating unique structure, that drew the attention of the scientific community all over the years. A plethora of studies showed that CAMK2 functions as a Ca^{2+} detector in the cell (Hanson *et al*., 1994; Soderling, 1999; Hudmon and Schulman, 2002a; Chang *et al*., 2017; Ardestani *et al*., 2019). In the basal state, the auto-inhibitory segment in each CAMK2 subunit is bound to the kinase domain thereby keeping the enzyme catalytically inactive (Stratton *et al*., 2013) (**Figure 1C**). When the level of intracellular Ca^{2+} rises, it binds to CaM upon which the Ca^{2+}/CaM complex can bind the C-terminal end of the autoregulatory domain disrupting the position of the auto-inhibitory segment (Lisman *et al*., 2002). This has, as a consequence, the exposure of a critical phosphorylation site, a Threonine (Thr) in position 286 for CAMK2A (and 287 for CAMK2B), which can now be phosphorylated by the neighboring activated subunit in the holoenzyme (Kuret and Schulman, 1985; Lai *et al*., 1986; Hanson *et al*., 1989, 1994; Molloy and Kennedy, 1991). The autophosphorylation of this site increases by 1000-fold the affinity of the enzyme

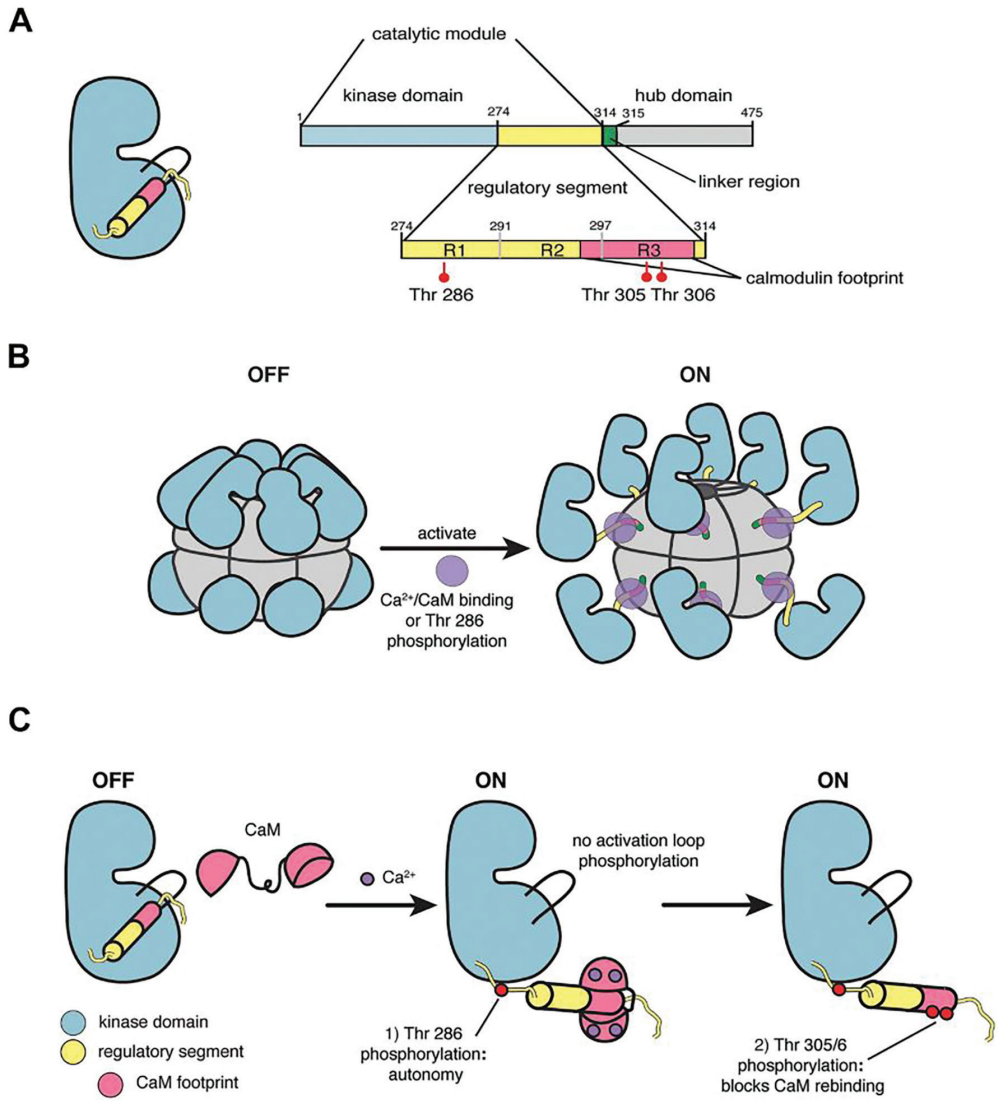

Figure 1. CAMK2 domain structure and organization. (A) One single subunit of CAMK2 and relative domains. All isoforms contain a kinase domain (in light blue), a regulatory domain (in yellow) containing the Ca^{2+}/CaM binding site (in pink) and the major phosphorylation sites (Thr286 and Thr/Thr305/6 in CAMK2A) and an association domain or hub domain (in gray). Most of the isoforms' variability lies in the variable domain or linker region (in green) **(B)** Architecture of the dodecameric CAMK2 holoenzyme in its inactive conformation (OFF) and active conformation (ON) upon binding of Ca^{2+}/CaM (in purple) **(C)** Regulation of CAMK2 activity by phosphorylation. Normally the autoinhibitory segment of the regulatory domain blocks the substrate binding (OFF); upon Ca^{2+}/CaM binding phosphorylation in *trans* of the Thr286 takes place and the autoinhibitory segment is displaced from its position, ensuring autonomous activity; after CaM dissociates from the subunit the Thr/Thr305/6 is phosphorylated which prevents further binding of Ca^{2+}/CaM. Adapted from **Stratton *et al.*, eLife, 2014**

for Ca^{2+}/CaM resulting in the trapping of CaM itself to the enzyme (Meyer *et al*., 1992). Even when Ca^{2+} drops in the cell, the complex Ca^{2+}/CaM remains trapped for several seconds, ensuring full catalytic activity. After Ca^{2+}/CaM dissociates from the kinase, the presence of a phosphate group on the Thr286/287 makes sure that the kinase can maintain partial activity (**autonomous state**) until dephosphorylation (Shields *et al*., 1985; Lou *et al*., 1986; Miller and Kennedy, 1986; Schworer *et al*., 1986). When Ca^{2+}/CaM dissociates, other sites within the CaM-binding domain can be phosphorylated [Threonines 305/306 (306/307 for CAMK2B)], and this phosphorylation prevents Ca^{2+}/CaM from further binding and induces insensitivity to intracellular changes in Ca^{2+} level (Colbran and Soderling, 1990; Patton *et al*., 1990; Hanson and Schulman, 1992; Mukherji and Soderling, 1994) (**Figure 1C**). This regulatory mechanism makes the CAMK2 enzyme the perfect detector for high frequency oscillations of Ca^{2+} in the cell and has major implications for neuronal function (Hanson *et al*., 1994; Bayer *et al*., 2002; Hudmon and Schulman, 2002b; Coultrap and Bayer, 2012).

So far, I mentioned two critical sites present in the auto-inhibitory domain that are important for CAMK2 autoregulation. One is the Thr286 (Thr287 in CAMK2B), whose phosphorylation is essential for autonomous activity (Miller *et al*., 1988; Hanson *et al*., 1989), and the second is the Thr305/306 (Thr306/307 in CAMK2B) that, when phosphorylated, causes a decreased affinity of the kinase for Ca^{2+}/CaM (Colbran and Soderling, 1990; Patton *et al*., 1990). Mutation of the Thr286 into an Aspartate introduces a negatively charged amino acid that mimics the phosphate group and results in an autonomously active kinase (Fong *et al*., 1989). On the contrary, an Alanine in place of the Threonine generates a kinase that is fully dependent on Ca^{2+}/CaM for activation (Fong *et al*., 1989; Neal Waxham *et al*., 1990). The inhibitory role of the Thr305/306 sites was revealed by double site-directed mutagenesis of the Threonine into Alanine. In this state, the residues are no longer available for autophosphorylation and the kinase can be fully activated by Ca^{2+}/CaM without inhibition (Hanson and Schulman, 1992).

Once the kinase is activated, the catalytic function is ensured by a Lysine in position 42 (43 for CAMK2B) of the catalytic domain, a conserved residue near the ATP binding site. If the Lysine is mutated into an Alanine, Arginine or Methionine the kinase becomes kinetically inactive (Hanson *et al*., 1994; Mukherji and Soderling, 1994; Shen and Meyer, 1999). Another mutation in the CaM binding site where an Alanine is mutated into an Arginine (Ala303Arg) completely blocks Ca^{2+}/CaM binding, preventing any activation of the kinase (Shen *et al*., 2000).

Besides the main and most studied residues described above that are critical for CAMK2 regulation and functioning (shortly summarized in **Table 1**), several other residues in both catalytic and auto-inhibitory domain have been shown to modulate the activation of the kinase. Yang and Schulman used site-directed mutagenesis to substitute most of the residues in the auto-inhibitory domain and catalytic domain to show which residues are critical for the autoregulation of the kinase (Yang and Schulman, 1999). They showed that the N-terminal region of the pseudosubstrate is the most critical in the auto-inhibition and mutations in many of the residues belonging to this sequence result in constitutive activity of the kinase. A summary on the most relevant mutations for this dissertation and their general effects on Ca^{2+}/CaM affinity and autonomous kinase activity are reported in **Table 2**.

Table 1. Functional role of critical residues in CAMK2

RESIDUE POSITION (CAMK2A/CAMK2B)	MUTATION	LOCATION	EFFECT
42/43	Lys>Arg	Catalytic domain	No kinase activity
286/287	Thr>Ala	Auto-inhibitory domain	Phospho-dead, no autonomous activity
	Thr>Asp		Phospho-mimic, autonomously active
303	Ala>Arg	Auto-inhibitory domain, Calmodulin binding domain	No calmodulin binding, no activation
305-306/306-307	Thr>Asp	Auto-inhibitory domain, Calmodulin binding domain	No calmodulin binding, constantly inhibited
	Thr>Val Thr>Ala		Can still bind calmodulin, no inhibition

Functional specialization and redundancy of the CAMK2 major brain isoforms

Most of the neuroscience and biochemistry research in the last 40 years has focused on CAMK2A and, to a lesser extent, CAMK2B, since these are the most highly expressed isoforms in the adult brain (0.3% of total brain protein and 1-2% of the hippocampal protein for CAMK2A in the rodent brain) (Bennett *et al*., 1983; Erondu and Kennedy, 1985). The high structural homology between the major brain isoforms suggests that there might be redundancy in function. However, specific and unique functions for each isoform can emerge from differences in localization, time of expression and substrate specificity. The scope of this part of the introduction is to summarize both similarities, which might underlie functional redundancy, and specificities of the two isoforms in the context of brain distribution and their role in learning and plasticity. In fact, synaptic plasticity, when disrupted, can account for symptoms that are shared between several neurological diseases including epilepsy and ID (Grant, 2012), which are the main focus of this dissertation.

In terms of general broad **brain distribution** of the CAMK2 isoforms, only CAMK2A is strictly brain specific, being found primarily in the forebrain and hippocampus in the rodent adult brain (Bennett *et al*., 1983; Erondu and Kennedy, 1985). Its expression is thought to start around P1 in the rodent brain, when the first transcripts are being detected (Bayer *et al*., 1999). CAMK2B, on the contrary, is enriched in the cerebellum but it is also expressed in the skeletal muscle, intestines and endocrine system and it is present already in the embryonic rodent brain, starting from E12 (Tobimatsu and Fujisawa, 1989; Brocke *et al*., 1995; Bayer *et al*., 1999; Tombes *et al*., 2003). This diversity in developmental, tissue and cellular expression of the different isoforms is ensured by several (up to seven) variable domain exons that are alternatively spliced to generate multiple unique isozymes (summarized in Tombes *et al*., 2003). At the **cellular level**, CAMK2A, in cortex and hippocampus, is expressed only in excitatory neurons (Benson *et al*., 1992; Jones *et al*., 1994; Liu and Jones, 1996; Sík *et al*., 1998; Tighilet *et al*., 1998a; Wang *et al*., 2013) while CAMK2B is present in both excitatory and inhibitory neurons and in oligodendrocytes (Waggener *et al*., 2013). In addition to homomers composed of CAMK2A subunits, mixed holoenzymes consisting of both *alpha* and *beta* subunits (with an average ratio of 3:1 in favor of the *alpha* subunit in the forebrain) have been purified from rat brain (Miller and Kennedy, 1985; Bulleit *et al*., 1988; Vallano, 1989; Brocke *et al*., 1999). The differences in time of expression and location of the CAMK2 isoforms, despite high homology, would suggest different functions in both prenatal and postnatal brain, which were investigated by making use of several different mouse models, especially for CAMK2A, summarized in (Elgersma *et al*., 2004).

Table 2. Effect on calmodulin affinity and/or autonomous kinase activity of CAMK2A upon single mutations into basic or acid residues in the catalytic or autoinhibitory domains

MUTATED RESIDUE	LOCATION	CALMODULIN AFFINITY/KINASE ACTIVITY
Glu96Lys	Catalytic domain	Enhanced calmodulin affinity
Phe98Lys	Catalytic domain	Constitutive active
Glu105Lys	Catalytic domain	Enhanced calmodulin affinity
Lys148Glu	Catalytic domain	Constitutive active
Ile205Lys	Catalytic domain	Enhanced calmodulin affinity
Glu236Lys	Catalytic domain	Enhanced calmodulin affinity
Asp238Arg	Catalytic domain	Constitutive active
Glu243Arg	Catalytic domain	Constitutive active
Arg296Glu	Pseudosubstrate region	Decreased calmodulin affinity
Arg297Glu	Pseudosubstrate region	No change in calmodulin affinity
Lys298Glu	Pseudosubstrate region	Decreased calmodulin affinity
Lys300Glu	Pseudosubstrate region	Decreased calmodulin affinity
Arg274Glu	Autoinhibitory domain	Constitutive active
His282Lys	Autoinhibitory domain	Constitutive active
Arg283Glu	Autoinhibitory domain	Constitutive active
Thr286Asp	Autoinhibitory domain	Constitutive active
Arg287Glu	Autoinhibitory domain	Constitutive active
Lys291Glu	Autoinhibitory domain	Enhanced calmodulin affinity
Asn294Asp	Autoinhibitory domain	Constitutive active

Kinase activity was determined using a kinase assay with AC-2 or AC-3 as substrate and the result for each mutant was compared to the wild type; calmodulin affinity was determined in order to identify the important residues for kinase auto-inhibition when no constitutive activity was detected. Adapted from Yang and Schulman, J. Biol. Chem, 1999

The very first transgenic mouse line generated in the field of learning and memory was the *Camk2a*$^{-/-}$ mouse model in the early 90s (Silva *et al*., 1992a, 1992b). CAMK2A was previously shown to be present both pre- and postsynaptic and to be particularly enriched in the PSD (Kennedy and Greengard, 1981; Kennedy *et al*., 1983a, 1983b; Kelly *et al*., 1984). Already in the 80s, it was hypothesized that CAMK2A may function in the brain as a 'memory' kinase that, in its activated state, can lead to long-term strengthening of the synapse (Lisman, 1985). In accordance with the Hebbian rule (Hebb, 1949), this synaptic strengthening of the postsynaptic synapse can occur upon synchronous firing of converging presynaptic inputs onto the postsynaptic cell (Bliss and Lømo, 1973). This mechanism is now known as long-term potentiation (LTP) (Nicoll, 2017). The *Camk2a*$^{-/-}$ mouse lines generated show reduced hippocampal NMDA-dependent LTP and impaired spatial learning in the Morris water maze, with the lack of abnormal gross brain morphology (Silva *et al*., 1992a, 1992b; Elgersma *et al*., 2002). These deficits are not due to a developmental role for CAMK2A, since deletion of *Camk2a* in adulthood can recapitulate the defects observed in the global germline deletion line, indicating the requirement for CAMK2A to be present at the time of learning (Achterberg *et al*., 2014). The importance of CAMK2A in LTP was further highlighted by the generation of knock-in mouse models where biochemical changes were made in crucial sites for CAMK2A functioning (described earlier in this introduction). When the Threonine 286 is mutated into an Alanine (phospho-dead mutant with no autonomous activity), mice show defective LTP, more severe than the full knock-out, and impaired spatial learning (Giese *et al*., 1998). On the contrary, a mouse model that constitutively mimics the Threonine 286 phosphorylation (Thr286Asp) shows normal LTP (Mayford *et al*., 1995). Similarly to the Thr286Ala mice, the substitution of the Threonine 305 into an Aspartate to generate a mouse model where CAMK2A can no longer bind Ca^{2+}/CaM and is constantly inactive, causes learning deficits and complete loss of LTP (Elgersma *et al*., 2002).

For a long time, no specific mouse models for CAMK2B were generated because it was thought that the *Camk2b*$^{-/-}$ mouse would be embryonically lethal (Karls *et al*., 1992). Only in 2009 the very first knockout mouse model for CAMK2B was generated and its role in cerebellar synaptic plasticity was investigated (van Woerden *et al*., 2009). In the cerebellum, the plasticity rules are reversed compared to the hippocampus: activation of kinases at high influx of Ca^{2+} at the parallel fiber-Purkinje cell synapses will lead to long term depression (LTD) instead of LTP (Malenka and Bear, 2004; Hirano, 2013). Interestingly, while deleting CAMK2A in the cerebellum impairs the induction of LTD (Hansel *et al*., 2006), loss of CAMK2B results in a reversal of plasticity at the parallel fiber-Purkinje cell synapses and causes cerebellar learning deficits (van Woerden *et al*., 2009). This effect was partially explained by the **kinase function** of CAMK2B (the balance between activity of the phosphatases and kinases in the cell), and partially by a specific and unique **structural role** for CAMK2B: regulating the location of CAMK2A through its actin-binding domain (Shen *et al*., 1998). Indeed, it was previously shown that when overexpressing one of the two CAMK2 isoforms *in vitro*, at the postsynaptic site the *alpha* isoform is mainly found in the cytosol while the *beta* isoform is observed to colocalize with PSD95, a major scaffolding protein in the PSD, and actin (Shen *et al*., 1998; Shen and Meyer, 1999). This differential distribution is due to the fact that CAMK2B contains a unique actin-binding domain in the variable domain that is not present in CAMK2A (Shen *et al*., 1998; Fink *et al*., 2003; O'Leary *et al*., 2006; Okamoto *et al*., 2007; Lin and Redmond, 2008). Furthermore, co-expression of the two isoforms together changes the CAMK2A distribution to a similar pattern observed for CAMK2B (Shen *et al*., 1998).

These results demonstrate a critical role for CAMK2B in the cerebellum, where

it is abundantly expressed, but does the presence of a unique domain ensuring binding to the cytoskeleton confer specific functions to CAMK2B also in other brain regions? In the hippocampus this has indeed been shown. The *Camk2b*$^{-/-}$ mice, like the *Camk2a*$^{-/-}$ mouse model, exhibit impaired hippocampal LTP as well as hippocampus-dependent learning deficits (Borgesius *et al*., 2011). To understand whether this was because of the kinase function or due to a structural role for CAMK2B (Kim *et al*., 2016), a knock-in mouse model was used carrying a point mutation in the Ca^{2+}/Calmodulim binding site (Ala303Arg) that prevents enzymatic activation but preserves the actin-binding (Borgesius *et al*., 2011). This Ala303Arg mouse model did not show deficits in hippocampal LTP, nor in hippocampus-dependent learning, indicating that presence of CAMK2B is sufficient for proper hippocampal functioning. In contrast to the global knock-out, the Ala303Arg mouse model can still target CAMK2A to the spines, thereby showing normal hippocampal plasticity, suggesting that the deficit in LTP observed in the *Camk2b*$^{-/-}$ is still due to CAMK2A enzymatic function. But there are some clues that CAMK2B might still have an enzymatic role in the hippocampus also, which mainly comes from the *Camk2a*$^{-/-}$ mouse model. This model still has some residual hippocampal LTP, which could be due to the potential compensation by CAMK2B for the absence of CAMK2A, given the high structural homology. This hypothesis would suggest some level of redundancy between the two kinases.

The use of specific mouse models for either CAMK2A or CAMK2B can unravel some specific functions for each isoform but it also shows that there is potentially some redundancy between the two isoforms. The *CAMK2* gene is much conserved across the animal kingdom, spanning from small invertebrates such as fruit flies, worms and sponges to vertebrates such as mammals (Tombes *et al*., 2003). However, while lower species only have one single *Camk2* gene, mammals present multiple copies that probably arouse from gene duplication of a common ancestral gene (Tombes *et al*., 2003). This specialization argues for the acquisition of specific functions for the CAMK2 isoforms in higher organisms that remain so far uncovered. The simultaneous deletion of CAMK2A and CAMK2B can unravel new roles for the CAMK2 family that were previously masked by their redundancy, which is the topic of **chapter II.**

The functional role of the CAMK2 holoenzyme in the **presynaptic side** is one of the examples where the specific function of CAMK2 still remains to be fully disclosed. Studies using *Camk2a* mutant mice show that CAMK2 is involved in neurotransmitter release and short-term synaptic plasticity in the CA3-CA1 area in the hippocampus (Lin *et al*., 1990; Nichols *et al*., 1990; Chapman *et al*., 1995; Hojjati *et al*., 2007; Wang, 2008; Pang *et al*., 2010). Other studies, using a pharmacological approach, suggest a presynaptic role for CAMK2 in the induction of LTP, though not consistently (Ninan and Arancio, 2004). However, the use of CAMK2 inhibitors does not allow a distinction between CAMK2A and CAMK2B and does not take into account the structural role that CAMK2A has been shown to play in the presynapse (Hojjati *et al*., 2007). In light of the absence of clear evidence for a presynaptic role of CAMK2 in LTP, in **chapter II**, we used a genetic approach deleting at the same time CAMK2A and CAMK2B to investigate the presynaptic function of CAMK2 in the CA3 synapse in inducing hippocampal LTP.

From mice to men

As summarized above, CAMK2 has for a long time been studied in the context of hippocampal learning and memory using *in vitro* experiments and *in vivo* mouse models [reviewed in (Lisman and McIntyre, 2001; Lisman *et al*., 2002, 2012; Elgersma *et al*., 2004; Hell, 2014; Bayer and Schulman, 2019)]. Only in the past few years, CAMK2 dysfunction has been indirectly

linked to brain disorders. So far, alterations of CAMK2 expression and/or activity were found in animal models of drug addiction, depression, schizophrenia, epilepsy and neurodevelopmental disorders (for an extensive review on the subject see Robison, 2014). However, while several human genetic studies linked mutations in components of the PSD to psychiatric diseases and neurodevelopmental disorders (Wu *et al*., 2007; Endele *et al*., 2010; Hamdan *et al*., 2011; Ting *et al*., 2012; Carvill *et al*., 2013; Lesca *et al*., 2013; Lemke *et al*., 2014; Philips *et al*., 2014; Li *et al*., 2016), CAMK2 was never directly linked to neurological disorders.

Only in 2014, the first evidence of a contribution of CAMK2A to ID was shown in a genetic study where a large chromosomal deletion encompassing the *CAMK2A* gene was identified in patients with Treacher Collins syndrome (Vincent *et al*., 2014). However, no functional studies were performed to directly link the ID to the *CAMK2A* gene deletion.

A *de novo* missense mutation in CAMK2A (Glu183Val) was later identified in a large human study including children with ASD, where, for the first time, a direct connection between CAMK2A and a neurodevelopmental disorder was established (Iossifov *et al*., 2014). The functional effect of this mutant was later characterized *in vitro* and *in vivo* showing a dominant negative effect, decreased interaction with PSD proteins and alteration of dendritic arborization and spine density. Furthermore, knock-in mice bearing the mutation display aberrant behavioral phenotypes in tasks commonly used to assess neuropsychiatric symptoms in mice (Stephenson *et al*., 2017).

Recently we identified 19 new rare variants in both the *CAMK2A* and *CAMK2B* genes associated with ID. This represents the very first study with a large number of point mutations that provides evidence of a direct involvement of the *CAMK2* gene in neurological disorders and it will be the topic of **chapter III**. Together with other recent studies that highlight the importance of CAMK2 for cognitive function (Akita *et al*., 2018; Chia *et al*., 2018) we are now starting to bridge the gap between mice and men, expanding the current knowledge on a protein whose role in learning and memory has been studied for more than 25 years.

Novel players in the field: CAMK2D and CAMK2G

When it comes to CAMK2D and CAMK2G, much less is known on how they might play a role in the brain, compared to CAMK2A and CAMK2B. Several splicing variants exist for the *Camk2g* and *Camk2d* genes, most of which are ubiquitously distributed and differentially expressed in various parts of the body, including the cardiac system (*Camk2d*), immune and endocrine systems (*Camk2g*) and the brain, though in the adult brain at lower levels compared to *Camk2a* and *Camk2b* (Mayer *et al*., 1993; Nghiem *et al*., 1993; Bayer *et al*., 1999). Interestingly, *Camk2g* and *Camk2d* transcripts are already present in the embryonic mouse brain as early as E11.5, representing the most abundant *Camk2* isoforms in the developing brain (Sakagami and Kondo, 1993; Bayer *et al*., 1999). The high expression and broad distribution in the embryonic rodent central nervous system of the *Camk2g* and *Camk2d* isoforms transcripts suggests a specific role during development for the minor isoforms of the CAMK2 family (Bayer *et al*., 1999).

With the recent discovery of likely pathogenic variants in CAMK2D and CAMK2G in patients with ID, a role in the human brain for the less well-known isoforms of the CAMK2 family is starting to emerge (**this thesis** and data not published). For the purpose of this dissertation, the next section will give an overview of what is known about CAMK2D and CAMK2G in the brain.

CAMK2D is the predominant isoform in the cardiac system and its physiological and pathological role in the heart has been extensively investigated (for a review see Gray and

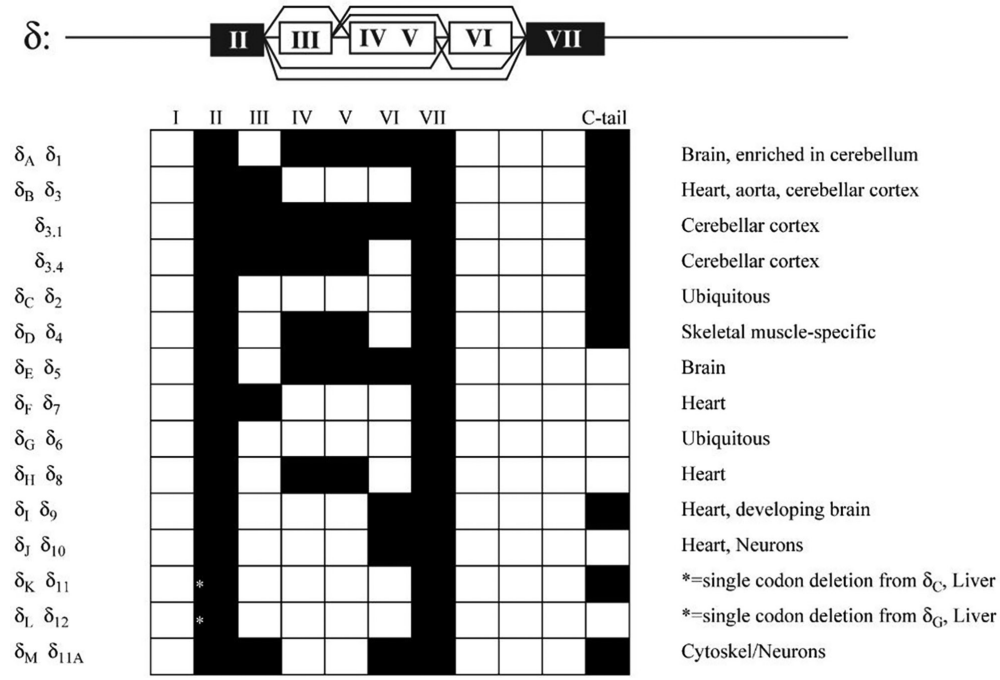

Figure 2. Alternative CAMK2D isoforms and their tissue distribution. Roman numbers in the boxes indicate the different variable domain exons connected by lines crossing the intron regions, whose differential combination gives rise to the isoforms listed in the table. Compared to all the other isoforms, CAMK2D contains a unique second variable domain at the C-terminal end used by some isoforms enriched in the brain (d_1 and d_3). Modified from **Tombes *et al.*, Gene, 2003**

Brown, 2014). Multiple alternatively spliced variants have been described that are expressed in different tissues (Schworer *et al*., 1993; Edman and Schulman, 1994) (**Figure 2**). The neuronal CAMK2D isoform exists primarily as the full length d_1 (or d_A) variant (60 kDa) (Tobimatsu and Fujisawa, 1989; Schworer *et al*., 1993). Some *delta* isoforms (d_1 to d_4) possess a unique second variable domain region at the C-terminal end of the association domain, which is not present in any other isoform of the CAMK2 family (Mayer *et al*., 1993, 1994). Furthermore, a few variants contain a nuclear localization signal (NLS) (Edman and Schulman, 1994; Srinivasan *et al*., 1994), whose role in the brain will be further addressed in the next section.

Not much is known regarding the distribution of CAMK2D in the central nervous system. At the anatomical level, most of the neuroscience research on CAMK2D has been focusing on the analysis of the *Camk2d* distribution in the brain at the mRNA level (Sakagami and Kondo, 1993) and the only few rodent studies that characterized the regional protein expression focused on the cerebellum, where CAMK2D is most highly expressed (Takeuchi *et al*., 1999). In the adult rodent brain, we can indeed find CAMK2D to be mostly enriched in the granular layer of the cerebellum (Sakagami and Kondo, 1993; Bayer *et al*., 1999; Takeuchi *et al*., 1999). In this compartment, at the cellular level, not only CAMK2D is present in neuronal cells, but it has been shown that expression of CAMK2D (in its d_2 variant) is also observed in cerebellar cultured astrocytes, where no CAMK2A or CAMK2B is detected (Vallano *et al*., 2000). This would suggest a specific role for the CAMK2D isoform in the cerebellum, although this function *in vivo* has not yet been investigated. Furthermore, presence of CAMK2D has also been identified in the cerebrum and specifically in the rat substantia nigra (Kamata *et al*., 2006), mouse hippocampus (Zalcman *et al*., 2019) and monkey visual cortex (Tighilet *et al*.,

1998b), expanding the possibile roles for this isoform in the brain.

So far, the only brain specific function attributed to CAMK2D has been investigated in developing neurons, where a role in axonal differentiation, neurite outgrowth and stability of the axon has been suggested (Omar Faison *et al*., 2002; Easley *et al*., 2006; Johnson *et al*., 2008), although some other studies report CAMK1 and not CAMK2D as the one responsible for regulation of axonal extension (Wayman, 2004; Ageta-Ishihara *et al*., 2009). Only recently, a first attempt to show a role *in vivo* for CAMK2D in the brain has been made. In a 2018 work, Zalcman and colleagues proposed a role for CAMK2D in memory persistence and maintenance. They employed an antisense oligonucleotide strategy to knock down *Camk2d* in the hippocampus and test the mice in a novel object recognition task where they showed impairments in retention of long-lasting memories. Unfortunately, from this study the contribution of the other main isoforms to the phenotype cannot be ruled out, since the specificity of the knock down was not assessed (Zalcman *et al*., 2019).

Given the discrepancies in some of the results obtained so far and the lack of convincing experiments, it is still unclear what the neuronal role of CAMK2D is. Recently, the discovery of new ID patients with possibly pathogenic variants in the *CAMK2D* gene opened up new avenues for the study of the functional role of CAMK2D in the brain.

Together with CAMK2D, **CAMK2G** represents the most abundant CAMK2 isoform in the developing murine nervous system (Bayer *et al*., 1999). *Camk2g*$^{-/-}$ mice are viable, however female *Camk2g*$^{-/-}$ mice are infertile (Backs *et al*., 2010). This is because the *Camk2g* transcript represents the major isoform in mouse oocytes and its absence in fertilized oocytes triggers an arrest of the activation in metaphase II halting embryo development (Backs *et al*., 2010). In behavioral tests, *Camk2g*$^{-/-}$ mice display deficits in long-term memory assessed in spatial learning tasks (morris water maze, radial arm maze and inhibitory avoidance task), in combination with reduced late hippocampal LTP compared to wild-type mice (Cohen *et al*., 2018).

In a more direct relation to human studies, *CAMK2G* was also described for being an important gene for human memory function, together with NMDA, PKAa and metabotropic glutamate receptors. This was shown by correlating the genetic variability of this cluster of genes together with episodic memory performance (de Quervain and Papassotiropoulos, 2006). *Camk2g* has also been reported to be the target of a miRNA, miR-219, which is involved in neurological and psychiatric disorders (Lukiw, 2007; Kocerha *et al*., 2009; Saus *et al*., 2010). Targeting of *Camk2g* by miR-219 modulates central sensitization in chronic pain and mediates NMDA dependent behavioral dysfunctions associated with psychiatric disorders (Kocerha *et al*., 2009; Pan *et al*., 2014; Zhang *et al*., 2015). Other than a function in memory, a role for CAMK2G in promoting neuronal survival through upregulation of the NF-kB signaling pathway after ischemic insult has been shown (Ye *et al*., 2019), although this mechanism is not specific for CAMK2G, since also CAMK2D appears to be upregulated upon ischemia.

So far, most of the rodent studies concerning a neuronal function for CAMK2G have been focusing on the role that the brain specific *gamma* isoform (g_a, containing an NLS) plays in modulating long-term plasticity through control of gene expression. For the purpose of this thesis, this topic will be extensively discussed in the next section.

Beyond catalytic activity: regulation of gene expression

It has been suggested that some CAMK2 isoforms can contain, within the variable region, a short sequence after a Lysine (KRKSSSSVQLM) that represents the canonical NLS: KKRK (Braun and

Schulman, 1995; Hudmon and Schulman, 2002b; Tombes *et al*., 2003). The phosphorylation of the Serine just after the NLS (Ser332 in *delta* and *alpha* isoforms, Ser334 in *gamma*) determines whether the NLS is functional, since when phosphorylated it prevents entering into the nucleus (Heist *et al*., 1998) (**Figure 3A**). Mutations of the nuclear targeting sequence can prevent the nuclear translocation of the holoenzyme and cloning the NLS sequence in CAMK2 isoforms which normally do not contain any NLS favors nuclear translocation (Edman and Schulman, 1994; Srinivasan *et al*., 1994). Therefore, the presence of an NLS led to the hypothesis that CAMK2 can also play a critical role in the regulation of gene expression.

Splicing variants containing an NLS have been identified in all the isoform families, except *beta* (Srinivasan *et al*., 1994; Brocke *et al*., 1995). The a_b isoform with nuclear target signal is found primarily in the midbrain and hypothalamus and has been proposed to play a role in regulating brain derived neurotrophic factor (BDNF) expression in NG108-15 cells (Brocke *et al*., 1995; Takeuchi *et al*., 2000). Interestingly, the *gamma* isoform containing the NLS (g_a) has been detected only in the brain (Tombes *et al*., 2003) while the *delta* isoforms with NLS (d_3 and d_7) are expressed widely in the body but are also enriched in the cerebellum (Takeuchi *et al*., 1999; Gray and Brown, 2014). So far, the functional role that these isoforms can play in regulating gene expression have remained elusive, also considering that the critical number of subunits containing the NLS needed to drive the holoenzyme in the nucleus is not known. However, some recent studies tried to elucidate the role that the nuclear targeted isoforms can play in the brain, especially concerning the less well studied CAMK2D and CAMK2G.

Neuronal activity can initiate a long range signaling cascade that ultimately leads to gene regulation, in a process called "**excitation-transcription coupling**", which is thought to be critical for numerous forms of long-term plasticity (Bading, 2013). Various stimuli and several signaling pathways can have an effect on gene expression regulation (West and Greenberg, 2011).

For example, a link between dopaminergic activated signaling pathway leading to BDNF expression and the nuclear isoform of CAMK2D (d_3) has been proposed (Shioda and Fukunaga, 2018). The d_3 isoform is highly expressed in the rat substantia nigra and it was previously demonstrated that upon activation of the dopamine receptor D2 the transcription of the *Bdnf* gene is promoted *in vitro* (Takeuchi *et al*., 2002; Kamata *et al*., 2006). Shioda and colleagues showed that in dopaminergic neurons the translocation in the nucleus of the isoform d_3 occurs upon dephosphorylation of the Ser332 in the NLS by the protein phosphatase-1 (PP1) and that stimulation of the D2 receptors enhances the nuclear translocation of CAMK2D *in vivo*. Furthermore, the activation of CAMK2D leads to increased BDNF production and promotes survival and neurite extension in dopaminergic neurons (Shioda *et al*., 2015) (**Figure 3B, left**).

Another example of the excitation-transcription coupling mechanism is the regulation of the transcription factor cAMP-response element binding protein (CREB), mediated by Ca^{2+} entrance through voltage-gated L-type Ca^{2+} channels (Cav1), which induces the transcription of several early immediate genes implicated in synaptic plasticity and memory (Cohen *et al*., 2015). CAMK2A, together with CAMK2B, participates in this process by interacting with Cav1 channels in nanodomains on the membrane to initiate a long-range signaling to the nucleus (Wheeler *et al*., 2008, 2012; Wang *et al*., 2017). However, how this interaction in the cell membrane can lead to transcription regulation in the nucleus is not yet fully understood.

It has been proposed that CAMK2G might be the mediator of the activity dependent CREB activation through translocation, together with Ca^{2+}/CaM, from the membrane to the nucleus upon influx of Ca^{2+} through the Cav channels (Ma *et al*., 2014). This is thought to occur only when a Serine in position 334, localized in the NLS, is dephosphorylated by calcineurin

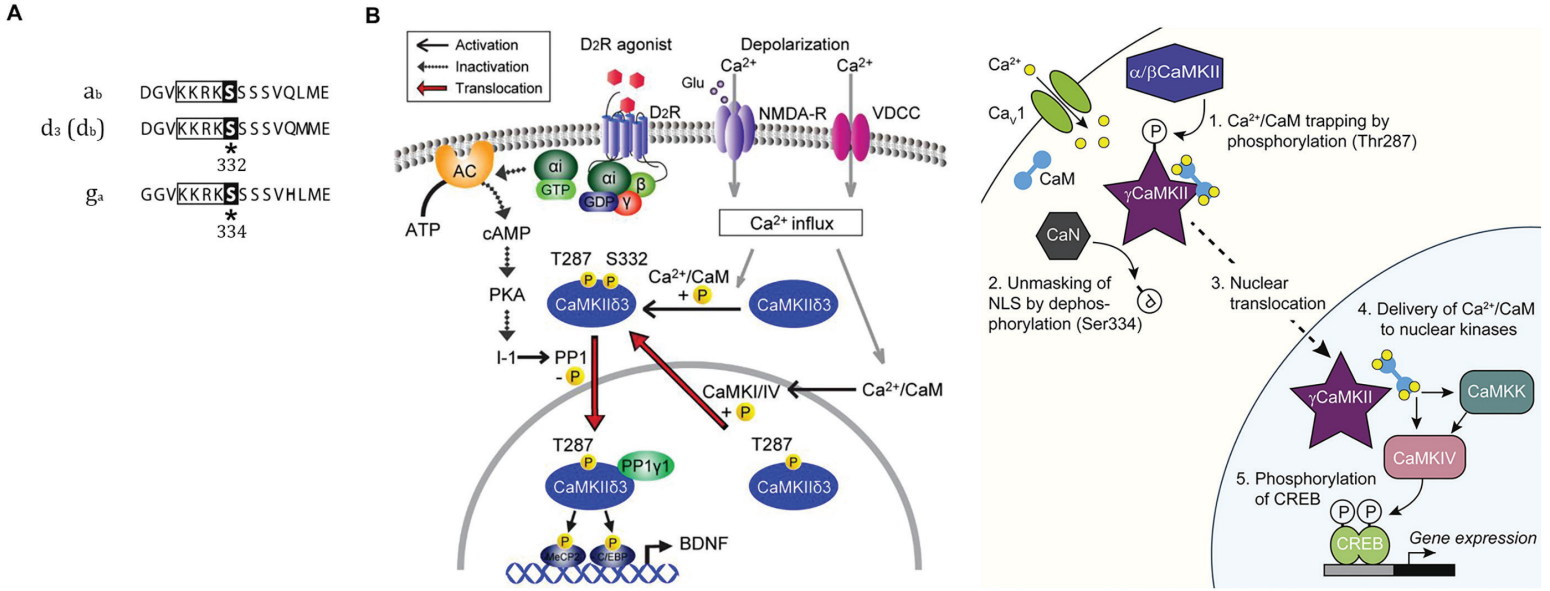

Figure 3. Models of excitation-transcription coupling proposed for CAMK2D and CAMK2G. (A) Comparison of amino acid sequences of the CAMK2 isoforms containing an NLS (KKRK, in the box). The asterisk denotes the Ser that needs to be dephosphorylated (Ser332 in *alpha* and *delta*, Ser334 in *gamma*) to allow translocation into the nucleus. **(B) left**: model for CAMK2/PP1 signaling in cytoplasmic-nuclear transport in dopaminergic neurons: D2R-mediated PP1 activation ensures CAMK2D dephosphorylation at Ser332 enabling its nuclear translocation. Nuclear CAMK2D phosphorylates transcription factors and transcription regulators, including CREB and MeCP2, increasing BDNF expression; **right**: activity-dependent nuclear translocation of CAMK2G. After phosphorylation at the Thr287 by CAMK2B and dephosphorylation of the Ser334 by calcineurin CAMK2G can translocate to the nucleus to shuttle Ca^{2+}/CaM; this leads to the phosphorylation of CREB transcription factor which is associated with enhanced transcription. (A) and (B) left: adapted from **Shioda *et al.*, J Biol Chem, 2015** (B) right: adapted from **Ma *et al.*, Cell, 2014**

and the Thr287 on CAMK2G is phosphorylated by CAMK2B at the surface membrane. This ensures proper binding and co-transport of Ca^{2+}/CaM to the nucleus, which is necessary for CREB activation (Ma *et al*., 2014) (**Figure 3B, right**).

Although this is an interesting mechanism to explain the involvement of CAMK2 in mediating the excitation-transcription coupling, it might not be the only process in place to link neuronal activity and transcriptional regulation. For example, interneurons seem to use a different mechanism that couples activity with gene transcription that does not involve CAMK2G (Cohen *et al*., 2016). Furthermore, control of gene expression might not be the only mechanism through which CAMK2G exerts its function in the brain. In **chapter IV** we studied the putative pathogenic role of a *de novo* point mutation in CAMK2G (Arg292Pro) previously identified in a patient with severe ID (de Ligt *et al*., 2012). Here we show a new emerging role for CAMK2G in neurodevelopmental disorders that can occur independently from its nuclear function.

PART III: RHEB1, CORTICAL MALFORMATIONS AND EPILEPSY

General features of cortical malformations

Within the many different causes for NDDs, including developmental delay and epilepsy, we can classify a group of heterogeneous disorders generally referred as **malformations of cortical development** (MCDs) (Pang *et al*., 2008). MCDs are characterized by micro- and macroscopic brain abnormalities seen in the cortex which arise from problems during the early embryological cortical development (Barkovich *et al*., 1996, 2012; Sisodiya, 2004). The first description of MCDs cases can be dated back to almost 200 years ago, with the identification of hemisphere enlargement and presence of alterations in the brain structure (Sims, 1835; Bourneville, 1880). MCDs were originally classified based on a combination of genetic, embryological, histopathological and morphological features. The development of magnetic resonance imaging (MRI) allowed a first definition of three subgroups of MCDs based on the structural characteristics of the cortical defect: generalized, lateralized and focal (Barkovich *et al*., 1987, 1996; Palmini *et al*., 1991; Kuzniecky, 1994; Leventer *et al*., 1999). **Generalized** developmental disorders include *lissencephaly* (absence of sulci in the brain), band or subependymal *heterotopia* (with a band of grey matter or clusters of neurons underneath the white matter or lining the lateral ventricles, respectively); **lateralized** malformations comprise unilateral *megalencephaly* (*hemimegalencephaly*), with an enlargement of a cerebral hemisphere; **focal** disorders are probably the most common and include *focal cortical dysplasia* (consisting of cortical dyslamination and in some cases enlarged cells), *polymicrogyria* (many small *gyri*) and focal subcortical heterotopias. For an extensive overview on MCDs, I refer to several reviews describing the general features and the latest genetic discoveries for each disorder (Leventer *et al*., 2008; Barkovich *et al*., 2012, 2015; Desikan and Barkovich, 2016; Lee, 2017; Juric-Sekhar and Hevner, 2019).

Cerebral cortical development

The definition of MCDs is constantly evolving and a recent comprehensive classification takes into account also the genetic pathways underlying the disorders and the developmental processes affected by their dysfunction (Barkovich *et al*., 2012). Based on this, MCDs have been categorized as (1) disorders of neuronal and glial proliferation or apoptosis; (2) disorders

of differentiation or migration; (3) malformations occurring during the post-migrational development (which includes also disorders of axon pathway formation) (Barkovich *et al.*, 2012; Desikan and Barkovich, 2016; Lee, 2017; Juric-Sekhar and Hevner, 2019). To be able to fully comprehend the rationale behind the classification of MCDs, I will summarize in the next section how normal cortical development occurs.

The correct positioning of neuronal populations in the neocortex is a prerequisite for proper formation of brain circuitry and complex behavioral functioning (Sun and Hevner, 2014). The neocortex is organized in layers, parallel to the pial surface. Within each layer, cells with similar morphology, molecular characteristics and connections are found. Local variations between columns of neurons receiving the same inputs and with similar electrophysiological properties are responsible for the formation of distinct functional areas which make up the cytoarchitectonic map of the cortex (Broadmann, 1909; O'Leary and Nakagawa, 2002; Rakic, 2009; Jabaudon, 2017).

According to the revised classical model of neocortical development, originally described by the Boulder Committee in 1970, cortical neurons are generated in the ventricular zone (VZ), the germinal epithelium lining the cerebral ventricles (Angevine *et al.*, 1970; Bystron *et al.*, 2008). The VZ contains progenitor cells dividing symmetrically to increase the pool of multipotent progenitors and the surface and thickness of the area. When neurogenesis starts (around E10 in mice), progenitor cells begin an asymmetric mode of division, with one daughter cell that remains progenitor and the other that becomes a postmitotic cell (Kwan *et al.*, 2012). A second group of intermediate progenitor cells appears later during neurogenesis (around E13.5 in the mouse) and forms a second germinal layer, the subventricular zone

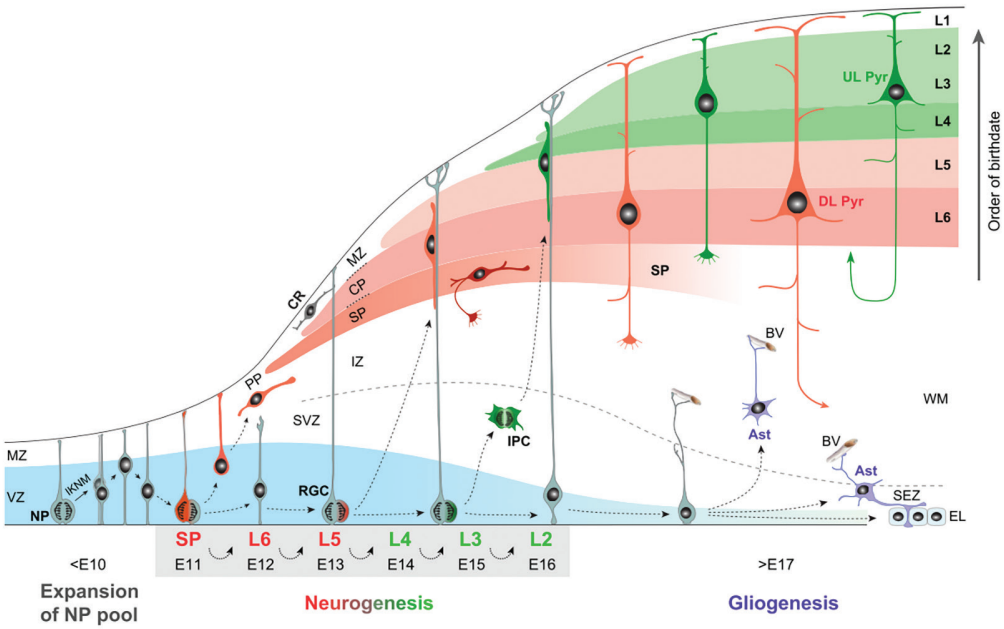

Figure 4. Schematic of neurogenesis and radial migration of pyramidal projection neurons in the mouse neocortex. The tangential migration and laminar positioning of interneurons are not illustrated. Refer to the text for the description of the steps of normal cortical development. VZ ventricular zone; MZ marginal zone; NP neural progenitor; IKNM interkinetic nuclear migration; SP subplate; RGC radial glia cell; PP preplate; SVZ subventricular zone; IZ intermediate zone; CP cortical plate; IPC intermediate progenitor cell; Ast astrocyte; BV blood vessel; CR Cajal-Retzius neuron; DL Pyr deep-layer pyramidal neuron; UL Pyr upper-layer pyramidal neuron; WM white matter.; SEZ subependymal zone; EL ependymal layer. Adapted from **Kwan *et al.*, Development, 2012**

(SVZ), above the VZ (Bystron *et al*., 2008; Paridaen and Huttner, 2014). Newly born neurons migrate from the germinal areas through the intermediate zone (IZ) to reach the outer wall of the primordial cortex, called preplate (PP). The PP is a transient layer occupied by various cell types destined to die, including the Cajal-Retzius cells which express Reelin, a molecule that terminates neuronal migration (Barber and Pierani, 2016; Hirota and Nakajima, 2017). The PP is later split into the subplate (SP), a transient deeper structure, and the most superficial marginal zone (MZ), by the arrival of the first postmitotic neurons into the cortical plate (CP), which will constitute the adult cortex. The migration is ensured by the presence of radial glia progenitor cells which span the entire developing cortex and form a scaffold for migrating neurons (Rakic, 1990; Nadarajah, 2003; Ostrem *et al*., 2017). The mammalian cortex is formed in an "inside-out" pattern: newly born neurons migrate radially from the VZ, past the cells born before them, until they reach their position in the cortex where they start to differentiate (Cooper, 2008; Sakakibara and Hatanaka, 2015; Takano *et al*., 2015). This means that earliest-born neurons (starting from E11.5 in the mouse) are destined to become the future layer 6 and the latest-born (E17.5) will form layer 2 (**Figure 4**).

Genetic causes for cortical malformations: mTORopathies

Each cortical neuron appears to be committed to its laminar positioning already before the migration begins and its fate is determined by the time and place of origin (Greig *et al*., 2013; Costa and Müller, 2015). During the past years, a considerable progress in the identification of genes involved in the specification of the different cortical neuronal subtypes has been made (Molyneaux *et al*., 2007; Ohtaka-Maruyama and Okado, 2015). Specific transcription factors are expressed in progenitors early during development and define the class of projection neurons being generated (MacDonald *et al*., 2013). For example, the zinc-finger FEZF2 transcription factor and COUP-TF-interacting protein 2 (CTIP2) are crucial for the specification of subcerebral projection neurons (Chen *et al*., 2005a, 2005b; Molyneaux *et al*., 2005; Greig *et al*., 2016; Woodworth *et al*., 2016); on the contrary, the activation of the transcription factor SATB2 (Special AT-rich sequence-binding protein 2) is necessary to favor the axonal crossing of commissural neurons (Alcamo *et al*., 2008).

It is not surprising that alterations in genes that regulate proliferation and migration during development can have an impact on cortical growth and organization (Sun and Hevner, 2014). In addition to environmental insults *in utero*, the majority of MCDs are now thought to be caused by genetic mutations in molecular pathways that regulate both early and later stages of cortical development, with a more or less severe phenotype (Pang *et al*., 2008; Juric-Sekhar and Hevner, 2019). Several variants in genes regulating cell cycle, apoptosis, cytoskeletal function, migration and metabolic activities have been identified in different types of MCD pathologies [reviewed in (Pang *et al*., 2008; Moffat *et al*., 2015; Stouffer *et al*., 2015; Desikan and Barkovich, 2016; Parrini *et al*., 2016; Lee, 2017; Juric-Sekhar and Hevner, 2019)].

Over the recent years, thanks to the advances in neuropathology and NGS, hyperactivation of the mTOR signaling pathway has been associated with some types of MCDs, providing a common molecular pathogenic link between these disorders (Crino, 2005, 2011; Lim and Crino, 2013; Majolo *et al*., 2018). For example, variants in genes encoding for proteins belonging to, or regulating, the mTOR cascade (*AKT1*, *PIK3CA*, *DEPDC*5, *PTEN* and *MTOR* itself) have now been identified and linked to FCD and hemimegalencephaly (HME) (Crino, 2007; Baek *et al*., 2015; Mirzaa *et al*., 2016; Patil *et al*., 2016; D'Gama *et al*., 2017; Hanai *et al*., 2017; Hu *et al*., 2018; Salinas *et al*., 2019; Zhao *et al*., 2019) (summarized in **Table 3**). The presence of increased mTOR signaling in histopathological specimens, brain abnormalities,

Table 3. mTOR-related genes linked to cortical malformations disorders

Gene	Typical mutation	Syndromes	Brain malformations
AKT1	Postzygotic mosaic GOF	Proteus	HME
AKT3	De novo germline, postzygotic mosaic, GOF, Chromosomal microduplication	MPPH	DMEG, HME, FCD-Ib, periventricular or subcortical heterotopia
CCND2	De novo germline	MPPH	DMEG
DEPDC5	Heterozygous germline, postzygotic mosaic LOF	BPP*	HME, FCD-I, FCD-IIa/b
FGFR3	De novo constitutional GOF	TD	Occipitotemporal hypergyration
MTOR	Mosaic, GOF	ND	MEG, HME, FCD-IIa/b
NPRL2	Heterozygous germline, LOF	ND*	FCD-I, FCD-IIa
NPRL3	Familial, heterozygous germline, LOF	ND*	FCD-IIa
PIK3CA	Mosaic GOF	CLOVES (severe), MCAP (moderate)	DMEG, HME, FCD-IIa
PIK3R2	De novo constitutional, postzygotic mosaic, GOF	MPPH, BPP	DMEG, HME
PTEN	Germline with postzygotic mosaic LOF	Cowden, PTENHTSe	DMEG, HME, FCD-IIb
RHEB	De novo constitutional GOF, postzygotic mosaic GOF#	ND*	HME, MEG, FCD-IIb
STRADA	De novo constitutional GOF	PMSE	MEG
TSC1	Germline with postzygotic mosaic LOF	TSC	Tubers, subependymal nodules, SEGA, FCD-IIa/b
TSC2	Germline with postzygotic mosaic LOF	TSC	Tubers, subependymal nodules, SEGA, HME, FCD-IIa

Abbreviations: BPP, bilateral perisylvian polymicrogyria; CLOVES, congenital lipomatous overgrowth, vascular malformations, epidermal nevi and scoliosis/skeletal/spinal anomalies; DMEG, dysplastic hemimegalencephaly; FCD-I/-IIa/-IIb, focal cortical dysplasia type I/type IIa/type IIb; GOF, gain of function; HME, hemimegalencephaly; LOF, loss of function; MCAP, megalencephaly-capillary malformation; MEG, megalencephaly; MPPH, megalencephaly-polymicrogyria-polydactyly-hydrocephalus; ND, not detected; PMSE, polyhydramnios, megalencephaly, and symptomatic epilepsy; PTEN-HTS, PTEN-hamartoma tumor syndrome; SEGA, subependymal giant cell astrocytoma; TD, thanatophoric dysplasia; TSC, tuberous sclerosis. **DEPDC5*, *NPRL2*, *NPRL3* and *RHEB* mutations are also associated with temporal lobe epilepsy, febrile seizures, and frontal lobe epilepsy. #refer to Zhao S. *et al*., Exp Mol Med 2019 and Salinas V. *et al*., Eur J Med Genet for the postzygotic mosaic mutations in *RHEB*. For the specific references of each gene see Juric-Sekhar G. and Hevner R.F., Annu Rev Pathol 2019 from which this table is adapted.

developmental delay and epilepsy is what defines "mTORopathies" as a clinical subgroup of MCDs (Crino, 2007).

In this thesis we describe for the first time the identification of patients with *de novo* mutations in the *RHEB1* gene, the main direct activator of the mTOR pathway, associated with ID, megalencephaly and epilepsy.

Ras Homologue Enriched in Brain (RHEB)

The discovery of new variants in genes potentially causing FCD or other types of MCDs, allows the study of the biological mechanisms leading to cortical malformations. In this part of the introduction I will focus on what is known on Ras Homologue Enriched in Brain (*RHEB*), whose role in MCDs has recently been described (**this thesis**, Salinas *et al*., 2019; Zhao *et al*., 2019).

RHEB was first identified in the early 90s as a novel member of the Ras family of small GTP-binding proteins whose expression is rapidly induced upon NMDA-dependent neuronal activation and seizures in the rat brain (Yamagata *et al*., 1994). The human RHEB is a small monomeric protein of 183-184 amino acids (**Figure 5A**) with partial homology with members of the Ras family GTPases (Rap2, RAS1 Ha-Ras) and comparable GTP hydrolysis rate to HA-Ras (Neal *et al*., 1988; Bos, 1997; Wennerberg *et al*., 2005; Heard and Tamanoi, 2018). Compared to other proteins of the Ras family though, RHEB retains specific and unique biochemical and structural aspects (Yu *et al*., 2005). The N-terminal contains the GTPase domain while the C-terminal region is a variable region ending with the CAAX motif required for farnesylation and subsequent post-translational modifications that allow the localization of RHEB in the endomembranes (Aspuria and Tamanoi, 2004; Hanker *et al*., 2010) (**Figure 5A**). Most of the structural variability between the GTP- and GDP-bound RHEB complexes lies in the regions of the switch I (residue 33-41 in the human RHEB) and switch II (residue 63-79) segments that are involved in the interaction with the GTPase activating proteins (GAPs), GTP exchange factors (GEFs) and targets. The switch I segment, which determines the specificity of small GTP binding proteins towards their substrate, is subjected to major conformational changes upon transition from the GTP-bound to the GDP-bound state while the switch II maintains a unique conformation and stable structure compared to other Ras proteins (Yu *et al*., 2005; Marshall *et al*., 2009; Heard *et al*., 2014; Schöpel *et al*., 2017). While many Ras proteins utilize a Glutamine (Gln) in position 61 (in Ras) to promote the GTP hydrolysis, the homologous Gln in RHEB (Gln^{64}) is unlikely to be involved in it due to a conformational displacement (Yu *et al*., 2005).

It has been suggested that the presence of an Arginine in position 15 (instead of a Glycine, present in the homologous residue in position 12 in the Ras protein) might confer a high basal activation state and low GTPase intrinsic activity, which is further inhibited by the presence of a Tyrosine in position 35 (Im *et al*., 2002; Li *et al*., 2004; Mazhab-Jafari *et al*., 2012). In fact, in mammalian cells, the ratio of GTP-bound RHEB over the GDP-bound is higher compared to other Ras proteins and it accounts for 25% of all the RHEB proteins present in the cell (Im *et al*., 2002).

Mutagenesis studies led to the identification of critical sites for RHEB function to produce activating mutants, such as the Gln64Leu and Ser16His, and loss of function mutants, such as Asp36Ala, Pro37Ala and Thr38Ala (Li *et al*., 2004; Urano *et al*., 2005; Yan *et al*., 2006; Long *et al*., 2007; Sato *et al*., 2008; Heard *et al*., 2014; Mazhab-Jafari *et al*., 2014).

RHEB is expressed in several tissues in the body and, in the rodent brain, basal mRNA

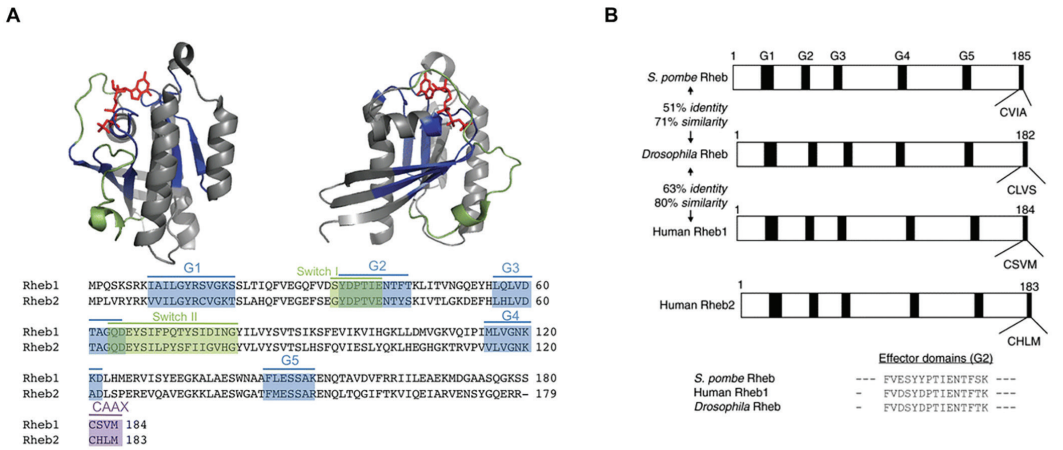

Figure 5. GTP-RHEB crystal structure and sequence alignment of the RHEB family. (A) Crystal structure of RHEB bound to GTP (in red). The effector switch regions where G proteins interact with downstream signaling proteins are shown in green, the five GTP-binding boxes are highlighted in blue and the CAAX motif in purple. Mammals contain two different *Rheb* genes, *Rheb1* and *Rheb2* that share 54% identity and 74% similarity. **(B)** Structure of RHEB proteins from human, *Drosophila*, and fission yeast are shown. G1–G5 boxes are indicated and the sequence of the effector domain (G2) is shown. Identity and similarity among different RHEB proteins are shown. Adapted from **Heard and Tamanoi, En Sign Mol, 2018** and from **Parmar and Tamanoi, The Enzymes, 2010**

levels appear to be high in hippocampus and cortex and they tend to transiently increase upon LTP stimulation and induction of seizures *in vivo* (Yamagata *et al*., 1994; Tian *et al*., 2016). Also *in vitro*, the addition of growth factors induces an increase in the expression of mRNA levels (Yamagata *et al*., 1994). The *Rheb* gene is conserved across species, being found, other than mammals, also in fungi, yeast, zebrafish, fruit fly and sea squirt (Aspuria and Tamanoi, 2004; Parmar and Tamanoi, 2010) (**Figure 5B**). While most of the species contain one *Rheb* gene, two different genes have been identified in mammals: *Rheb1* which is ubiquitously expressed, and *Rheb2* (or *RhebL1*) whose expression is more restricted (Patel *et al*., 2003; Aspuria and Tamanoi, 2004). In mammals, the RHEB1 protein is already detectable at very early embryonic stages in mice (starting from E3.5) and it is highly expressed in the developing central nervous system and in the postnatal brain (Tian *et al*., 2016). RHEB1 expression is critical for early murine embryonic development, since *Rheb*$^{-/-}$ embryos die already between E10.5 and E11.5, probably due to circulatory problems (Goorden *et al*., 2011; Zou *et al*., 2011). On the contrary, *Rheb1* heterozygous embryos develop normally with no significant cognitive deficits (Goorden *et al*., 2015). Deletion of *Rheb1* from neural progenitor cells induces a decrease in cortical thickness and hypomyelination *in vivo* due to lack of mature oligodendrocytes (Zou *et al*., 2011, 2014). RHEB1 appears to be crucial also for adult survival, since adult inducible deletion of *Rheb1* leads to death within 2-3 weeks from gene deletion (Goorden *et al*., 2015).

RHEB functioning in the mTOR pathway

Original studies in *Drosophila* identified RHEB as a member of the mTOR signaling pathway (Saucedo *et al*., 2003; Stocker *et al*., 2003; Zhang *et al*., 2003). These studies were the first to suggest that a complex formed by the proteins hamartin and tuberin, encoded respectively by the genes *TSC1* and *TSC2*, acts upstream of RHEB, catalyzing the conversion of the GTP bound RHEB to the GDP form, thereby inactivating RHEB. TSC1 binds to TSC2 to prevent its ubiquitination while TSC2 acts as a GTPase-activating protein (GAP) towards RHEB (van

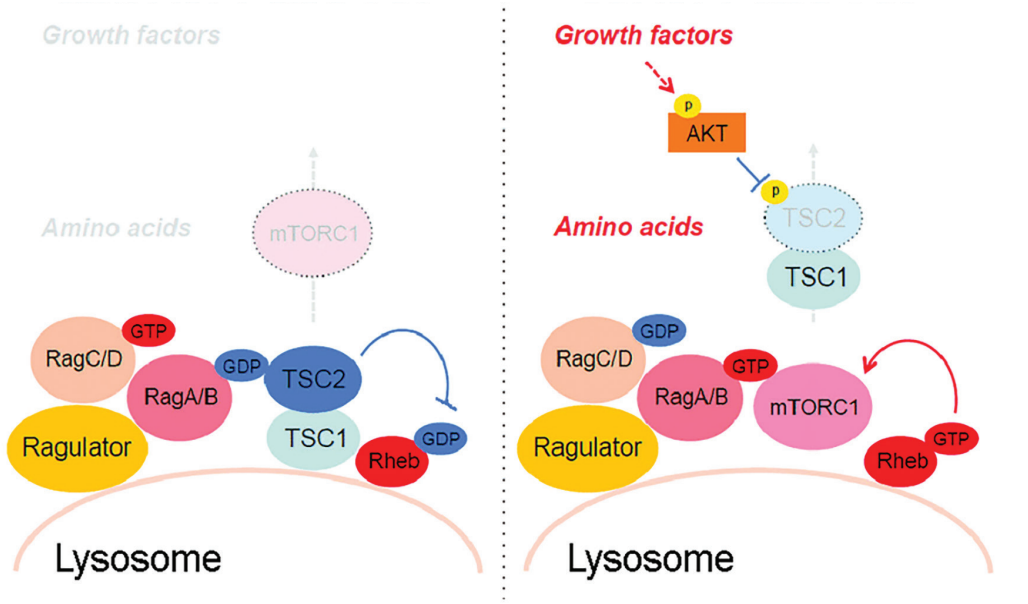

Figure 6. mTORC1 regulation by TSC1:TSC2 complex and RHEB. In the absence of amino acids and growth factor the TSC complex preferentially interacts with both GDP-bound RAGA and RHEB on the lysosomal membrane to inhibit the mTOR signaling cascade (left). Upon growth factor and amino acid stimulation, TSC2 is phosphorylated by AKT and dissociates from the lysosomal membrane leading to the activation of RHEB and mTOR pathway (right). Modified from **Yao *et al*., Biomolecules, 2017**

Slegtenhorst *et al*., 1998; Harris and Lawrence, 2003). In response to nutrients, growth factors or amino acids that can inhibit the TSC1:TSC2 complex (Ma and Blenis, 2009; Sengupta *et al*., 2010; Mendoza *et al*., 2011), mTOR translocates to the lysosomes where it can get activated by RHEB once released from the TSC1:TSC2 complex inhibition (Castro *et al*., 2003; Long *et al*., 2005; Groenewoud and Zwartkruis, 2013; Demetriades *et al*., 2014; Menon *et al*., 2014; Yao *et al*., 2017; Deng *et al*., 2019) (**Figure 6**). Studies in mice showed that RHEB1 protein level represents the rate-limiting step for mTOR activation in the brain, since RHEB1 deletion results in a significant reduction of mTOR pathway activation (Zou *et al*., 2011; Goorden *et al*., 2015) and overexpression of RHEB1 wild type protein is sufficient to cause hyperactivation of the mTOR pathway with functional consequences (**chapter V** and Sokolov *et al*., 2018).

mTOR is a ubiquitous and highly conserved serine/threonine kinase (Harris and Lawrence, 2003). It was first identified in yeast and later in mammals as the target of a potent antifungal agent, called rapamycin, isolated from the bacterium *Streptomyces hygroscopicus* (Brown *et al*., 1994; Chen *et al*., 1994; Sabatini *et al*., 1994; Sabers *et al*., 1995). It can function in two distinct heteromeric complexes, mTORC1 and mTORC2 (Sabatini, 2017). Each complex is characterized by different binding partners: mTORC1 is composed of mTOR, raptor, DEPTOR and mLST8 while mTORC2 contains mTOR, rictor, Sin1, mLST8, DEPTOR and protor (Bhaskar and Hay, 2007). Raptor in mTORC1 is the rapamycin sensitive partner of mTOR (Kim *et al*., 2002; Oshiro *et al*., 2004). RHEB is thought to specifically activate mTOR in complex 1 but the exact mechanism for this preferential activation is still unknown (Yang *et al*., 2006, 2017; Sato *et al*., 2009). mTORC1 mainly controls cell growth, metabolism and differentiation while mTORC2 regulates survival and cytoskeletal organization (Shiota *et al*., 2006; Laplante and Sabatini, 2012a, 2012b; Wahane *et al*., 2014) (**Figure 7**).

Active mTORC1 can regulate components of the translation machinery, mainly through

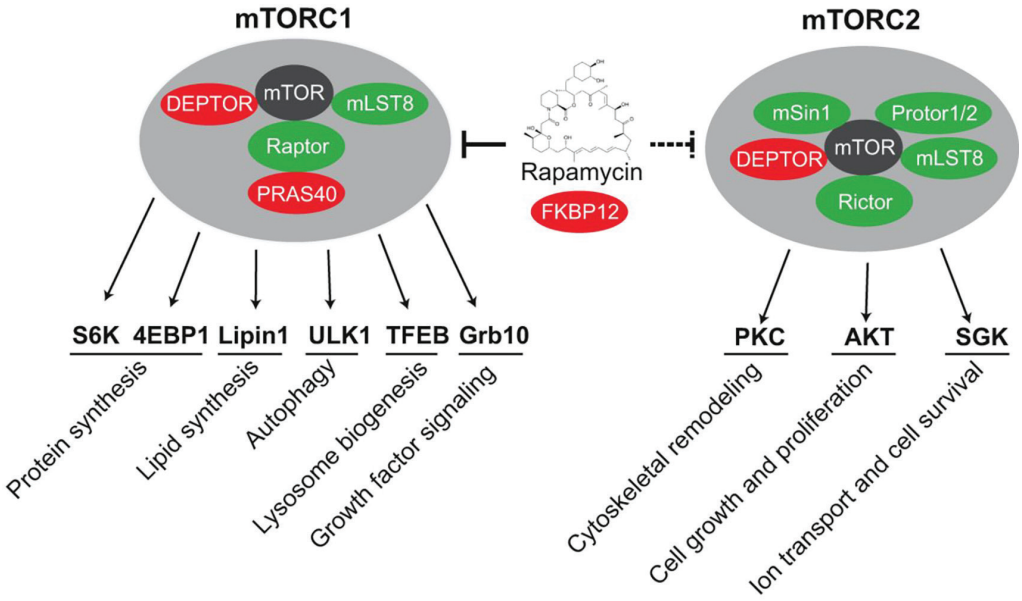

Figure 7. Physiological processes regulated by the components of mTORC1 and mTORC2 complexes. (Left) mTORC1 regulates protein synthesis, lipid synthesis, autophagy, lysosome biogenesis and growth factor signaling by phosphorylating its substrates S6K, 4EBP1, LPIN1, ULK1, TFEB and GRB10. (Right) mTORC2 regulates cytoskeletal remodeling, cell growth and proliferation, ion transport, and cell survival through its downstream substrates PKC, AKT and SGK. mTORC1 is inhibited by acute rapamycin treatment (indicated by a solid inhibitory line), whereas mTORC2 is not inhibited by acute rapamycin treatment but is inhibited by prolonged rapamycin treatment (indicated by broken inhibitory line). Positive regulators in each complex are shown in green and negative regulators in red. Abbreviations: 4EBP1, eIF4E-binding protein; AKT,RAC-α serine/threonine-protein kinase; DEPTOR, DEP-domain-containing mTOR-interacting protein; mLST8, mammalian lethal with Sec13 protein 8; mSin1, mammalian stress-activated MAPK-interacting protein 1; mTOR, mammalian target of rapamycin or mechanistic target of rapamycin; mTORC1, mTOR complex 1; mTORC2, mTOR complex 2; PKC, protein kinase C; PRAS40, proline-rich AKT substrate 40 kDa; Protor1/2, protein observed with Rictor 1 and 2; Raptor, regulatory-associated protein of mTOR; Rictor, rapamycin-insensitive companion of mTOR; S6K, ribosomal S6 kinase; SGK, serum/glucocorticoid-regulated kinase; TFEB, transcription factor EB; ULK1, Unc-51-like kinase 1. Adapted from **Meng *et al.*, Development, 2018**

eukaryotic initiation factor 4E-binding protein (4E-BP1) and p70S6Kinase (p70S6K) (Hay and Sonenberg, 2004) (**Figure 7, left**). Beyond protein synthesis, mTOR also plays a role in transcription and RNA processing, protein degradation and actin dynamics, which highlights the critical contribution of this pathway to proper nervous system functioning (Switon *et al.*, 2017).

mTOR pathway in brain development and disease

As summarized above, RHEB is the primary activator of the mTOR pathway. mTOR signaling is not only a pivotal cellular cascade that regulates proliferation, growth and migration during early developmental stages but it's also functionally relevant during adulthood in modulating cellular metabolism, autophagy and, in neurons, differentiation and synaptic organization (Han *et al.*, 2008; Fishwick *et al.*, 2010; Paliouras *et al.*, 2012; Takei and Nawa, 2014; Kim, 2015; Lee, 2015; Garza-Lombó and Gonsebatt, 2016; Ka *et al.*, 2017). Therefore, it is not surprising that mTOR dysfunction has been associated with several neurological diseases such as epilepsy, mental retardation, autism and brain tumors [for reviews see (Swiech *et al.*, 2008; Garelick and Kennedy, 2011; Lipton and Sahin, 2014; Bockaert and Marin, 2015; Switon *et al.*, 2017)].

The importance of mTOR in early phases of neurogenesis and embryonic development

is shown by several *in vitro* and *in vivo* studies. Mice with a loss of function mutation in the *mTOR* gene develop patterning defects, especially in the telencephalon, and null mutant mice for *mTOR* die during early development before differentiation into neurons can occur (Hentges *et al*., 2001; Murakami *et al*., 2004; Cloëtta *et al*., 2013; Ka *et al*., 2014). Also, decreasing mTOR activity in neural stem cells (NSCs) in the SVZ reduces the progenitor lineage expansion and the differentiation into neurons (Sato *et al*., 2010; Hartman *et al*., 2013). mTOR seems to also have a role in later stages of neurogenesis, since hyperactivation of mTOR during early embryonic stages leads to an aberrant neuronal migration (Lafourcade *et al*., 2013; Kassai *et al*., 2014). Increased mTOR activity was also shown to induce an increase in dendritic arborization and an elongation of the axon *in vivo* and *in vitro* (Choi *et al*., 2008; Nie *et al*., 2010; Goto *et al*., 2011; Amiri *et al*., 2012; Feliciano *et al*., 2012; Gong *et al*., 2015; Sokolov *et al*., 2018).

Probably the most well-known genetic disease directly related to mTOR dysfunction is tuberous sclerosis complex (TSC) (Gómez, 1995). The TSC disorder is caused by loss of function mutations in either the *TSC1* or *TSC2* genes. TSC patients suffer from intellectual disability and often intractable epilepsy (in 80-85% of the cases) (Curatolo *et al*., 2015; Islam and Roach, 2015). Clinical and basic research into TSC provided a detailed insight into mTOR signaling regulation and paved the way for a better understanding of mTORopathies. Neuropathological manifestations of TSC are cortical tubers, subependymal nodules (SENs) and subependymal giant cell astrocytomas (SEGAs) (Grajkowska *et al*., 2010). Tubers in TSC are focal disruption of the cytoarchitecture of the cortex and they present histopathological similarity with the lesions observed in FCD (Becker *et al*., 2002; Baybis *et al*., 2004; Fassunke *et al*., 2004; Crino, 2005). Interestingly, somatic mutations in *TSC1* and *TSC2* were recently identified in patients with FCDII, indicating a relation between TSC and some forms of FCD (Wong and Crino, 2010; Lim *et al*., 2017).

The majority of TSC patients (80%) present epilepsy as one of the major neurological manifestations and TSC was the first epilepsy syndrome where mTOR hyperactivity in the tubers was directly associated with epilepsy (Crino, 2015). Nowadays, several other disorders showing brain malformations and epilepsy have been linked to aberrant mTOR signaling (Sisodiya, 2004; Crino, 2011; Barkovich *et al*., 2015; Represa, 2019). FCD represents the most common cause of intractable pediatric epilepsy and often requires surgery as a treatment (Sisodiya, 2000; Bast *et al*., 2006). It is estimated that up to 40% of drug resistant childhood epilepsies are MCDs related and at least 75% of MCDs patients develop epilepsy (Leventer *et al*., 1999, 2008). However, the exact pathophysiological mechanisms of epilepsy in MCDs still remain unclear. Although the phenotypic variability of MCDs does not provide clear indications on the epileptogenic processes involved, the analysis of new causative genes and their cellular effects can shed light on this aspect.

One of the main challenging questions is to what extend seizures associated with MCDs result from aberrant developmental processes causing brain malformations or from mTOR hyperactivation as an effect of genetic mutations. A few recent studies proposed that hyperactivation of the mTOR pathway can lead to neuronal and synaptic dysfunctions, and ultimately epilepsy, independently of brain alterations. In a RHEB mouse model generated using *in utero* electroporation, when mTOR hyperactivity was induced after corticogenesis without cell misplacement, mice still developed spontaneous seizures (Hsieh *et al*., 2016 and **chapter VI**); in agreement with this, heterozygote *Tsc1-ko* mice show spontaneous epilepsy only during the first month of life without the presence of cortical defects (Lozovaya *et al*., 2014).

Another interesting finding emerges from electroencephalography (EEG) and imaging

studies in patients with MCDs which show that interictal and ictal events are not only detectable in the focal malformations but can be identified also in distant cortical areas (Tyvaert *et al*., 2008; Valton *et al*., 2008; Shafi *et al*., 2015; Pizzo *et al*., 2017). This would lead to the hypothesis that supposedly healthy areas of the brain can be affected by the cortical malformations and can contribute to the epileptic phenotype. However, how exactly cell autonomous (emerging from the mutated ectopic neurons) and cell non-autonomous mechanisms (cells not directly affected by the mutation) can contribute to the epileptogenesis process is still a matter of debate (Lim and Crino, 2013; Represa, 2019).

SCOPE OF THIS THESIS

This dissertation focuses on two different evolutionary conserved "old genes", *CAMK2* and *RHEB1*, both well known to play an important role in proper brain function, as summarized in the introduction of this thesis, but only recently implemented in human NDDs with the discovery of *de novo* mutations (**this thesis**). The common denominator between these two genes is that they cause an NDD, with ID as one of the main characteristics. Besides ID, the clinical features within *CAMK2*-related disorders are very variable (**chapter III and IV)**, and they are different from the *RHEB1* NDD, where epilepsy is an important clinical outcome (**chapter V and VI**).

The first part of this thesis focuses on *CAMK2*. Although several mouse models were generated over the years, contributing to further understanding of the role that CAMK2 plays in the brain, in **Chapter II**, using an inducible double knock-out approach in mice, we uncover previously unknown roles for CAMK2A and CAMK2B, showing their critical function in survival.

Moving from mice to men, **Chapter III** describes the very first identification of *de novo* variants in *CAMK2A* and *CAMK2B* found in patients with ID. Using the vast basic knowledge acquired over the years on CAMK2, we could functionally assess the pathogenicity of these variants and show that tightly regulated CAMK2 functioning plays a critical role in neuronal development and function.

Surprisingly, the first CAMK2 isoform to be found associated with ID was CAMK2G (de Ligt *et al*., 2012), a much less abundant protein in the brain compared to CAMK2A and CAMK2B. In **Chapter IV** we describe a second unrelated patient with ID with the same mutation in CAMK2G identified in the de Ligt study and using a genomic functional screening we reveal that CAMK2G can play an indispensable previously unknown function in neurodevelopment.

The second part of this thesis focuses on *RHEB1*. Although we have an extensive knowledge of the mTOR pathway and mTOR related epilepsy, mainly through TSC mouse models, RHEB1, the main activator of mTOR, was never directly linked to human disorders. In **Chapter V** we report a whole set of *de novo* variants in both known and novel mTOR-related genes associated with brain growth and ID and highlight the contribution of *RHEB1* as a causative gene, when hyperactive, for ID with megalencephaly and epilepsy.

Finally, in **Chapter VI** we expand on the findings of **Chapter V** to explore the mechanisms through which cortical defects caused by hyperactivating mutations in RHEB1 can contribute to epilepsy.

Chapter II

CAMK2-dependent signaling in neurons is essential for survival

Martijn J. Kool,* Martina Proietti Onori,* Nils Z. Borgesius, Jolet E. van de Bree, Minetta Elgersma-Hooisma, Enzo Nio, Karel Bezstarosti, Gabriëlle H.S. Buitendijk, Mehrnoush Aghadavoud Jolfaei, Jeroen A.A. Demmers, Ype Elgersma, and Geeske M. van Woerden

*These authors contributed equally

Published in J Neurosci. 2019 Jul 10;39(28):5424-5439

ABSTRACT

Ca^{2+}/CaM-dependent protein kinase II (CAMK2) is a key player in synaptic plasticity and memory formation. Mutations in *Camk2a* or *Camk2b* cause intellectual disability in humans, and severe plasticity and learning deficits in mice, indicating unique functions for each isoform. However, considering the high homology between CAMK2A and CAMK2B, it is conceivable that for critical functions, one isoform compensates for the absence of the other, and that the full functional spectrum of neuronal CAMK2 remains to be revealed. Here we show that germline as well as adult deletion of both CAMK2 isoforms in male or female mice is lethal. Moreover, Ca^{2+}-dependent activity as well as autonomous activity of CAMK2 is essential for survival. Loss of both CAMK2 isoforms abolished LTP, whereas synaptic transmission remained intact. The double-mutants showed no gross morphological changes of the brain, and in contrast to the long-considered role for CAMK2 in the structural organization of the postsynaptic density (PSD), deletion of both CAMK2 isoforms did not affect the biochemical composition of the PSD. Together, these results reveal an essential role for CAMK2 signaling in early postnatal development as well as the mature brain, and indicate that the full spectrum of CAMK2 requirements cannot be revealed in the single mutants because of partial overlapping functions of CAMK2A and CAMK2B.

Keywords: CAMK2; hippocampus; survival; synaptic plasticity

SIGNIFICANCE STATEMENT

CAMK2A and CAMK2B have been studied for over 30 years for their role in neuronal functioning. However, most studies were performed using single knock-out mice. Because the two isoforms show high homology with respect to structure and function, it is likely that some redundancy exists between the two isoforms, meaning that for critical functions CAMK2B compensates for the absence of CAMK2A and vice versa, leaving these functions to uncover. In this study, we generated *Camk2a/Camk2b* double-mutant mice, and observed that loss of CAMK2, as well as the loss of Ca^{2+}-dependent and Ca^{2+}-independent activity of CAMK2 is lethal. These results indicate that despite 30 years of research the full spectrum of CAMK2 functioning in neurons remains to be unraveled.

INTRODUCTION

Since the discovery of the Ca^{2+}/CaM-dependent protein kinase II (CAMK2) protein family in the 1970s, >2000 papers have been published in which the function of CAMK2A or CAMK2B, the most abundant CAMK2 isoforms in the brain, has been studied. The generation of different *Camk2a* mutants [of which the knock-out was already published >25 years ago (Silva *et al*., 1992a,b)] and *Camk2b* mutants, greatly contributed to the understanding of the role of these two isoforms in neuronal functioning, learning, and plasticity in mice (Mayford *et al*., 1995; Giese *et al*., 1998; Elgersma *et al*., 2002; Borgesius *et al*., 2011; Achterberg *et al*., 2014; Kool *et al*., 2016). Very recently, the importance of CAMK2A and CAMK2B for normal human neurodevelopment was shown (Kury *et al*., 2017b; Stephenson *et al*., 2017; Akita *et al*., 2018; Chia *et al*., 2018).

CAMK2A and CAMK2B are estimated to have evolved from a common ancestral *CAMK2* gene ~1 billion years ago (Ryan and Grant, 2009) and are highly homologous, consisting both of a catalytic, regulatory, variable, and association domain. The catalytic and regulatory domain show an 89–93% sequence homology in rats (Tobimatsu and Fujisawa, 1989), whereas the

differences lie within the variable domain, where CAMK2B but not CAMK2A contains an F-actin binding domain.

CAMK2 forms a holoenzyme of ~12 subunits, which can consist of both CAMK2A and CAMK2B subunits. This CAMK2 holoenzyme is able to convert a short high-frequency signal into a long-term change in synaptic strength (for review, see Lisman *et al*., 2002; Hell, 2014). With the difference in binding affinity for CaM, which is ~8-fold higher for CAMK2B homomers than for CAMK2A homomers (half-maximum autophosphorylation of CAMK2 is achieved at 15 vs 130 nM CaM, respectively; Brocke *et al*., 1999), the subunit composition of the CAMK2 holoenzyme determines the sensitivity for fluctuating calcium levels (Thiagarajan *et al*., 2002). Upon calcium influx Ca^{2+}/CaM binds CAMK2 in the regulatory domain (Vallano, 1989), allowing the release of a pseudosubstrate region of the protein from the catalytic domain. When two adjacent subunits within the holoenzyme are activated by Ca^{2+}/CaM, one subunit can phosphorylate the neighboring subunit on Thr286 (CAMK2A) or Thr287 (CAMK2B) leaving this subunit autonomously active (Ca^{2+}-independent activity) when calcium levels drop to baseline (Miller and Kennedy, 1986; Hanson *et al*., 1994). However, upon detachment of Ca^{2+}/CaM from CAMK2, Thr305/Thr306 (CAMK2A) or Thr306/Thr307 (CAMK2B) within the CaM binding region can be phosphorylated thereby preventing future binding of Ca^{2+}/CaM (thus Ca^{2+}-dependent activity). The importance of the autophosphorylation events for CAMK2 function, was shown by generating *Camk2a* point mutants, in which the Thr286 or Thr305/Thr306 were mutated to either phosphomimic residues (*e.g.*, Thr305Asp), or phosphodead residues (*e.g.*, Thr286Ala). All of these mutations resulted in learning and plasticity phenotypes (Mayford *et al*., 1995; Giese *et al*., 1998; Elgersma *et al*., 2002).

In addition to an important enzymatic function, there are also studies showing that CAMK2A and CAMK2B play important and unique structural roles, using either *Camk2a* or *Camk2b* knock-out mice. For example, CAMK2A has been shown to play an important structural role in the presynapse in short-term plasticity (Hojjati *et al*., 2007) and CAMK2B plays an important structural role in determining the localization of CAMK2A during hippocampal plasticity, through its F-actin binding domain (Borgesius *et al*., 2011). Thus, the unique functions of CAMK2A and CAMK2B in neuronal functioning are well established. However, CAMK2A and CAMK2B are highly homologous, thus it is conceivable that there is substantial redundancy in function, and that these functions of CAMK2 are missed when studying the *Camk2a* or *Camk2b* single mutants.

In this study we aimed to reveal novel CAMK2 functions by studying different *Camk2a*/*Camk2b* double-mutants, showing that despite the enormous wealth of literature on CAMK2 functions, its full spectrum is still not uncovered and that the role of CAMK2 signaling in neurons is much more important than what was previously thought.

MATERIALS AND METHODS

Animals. In this study the following mice were used: *Camk2a*$^{-/-}$ (Camk2a^{tm3Sva}, MGI:2389262) and *Camk2b*$^{-/-}$ mice to generate *Camk2a*$^{+/+}$;*Camk2b*$^{+/+}$ (WT mice); *Camk2a*$^{+/-}$;*Camk2b*$^{-/-}$ (mice heterozygous for *Camk2a* and knock-out for *Camk2b*); *Camk2a*$^{-/-}$;*Camk2b*$^{+/-}$ (mice knock-out for *Camk2a* and heterozygous for *Camk2b*); *Camk2a*$^{-/-}$;*Camk2b*$^{-/-}$ (*Camk2a* and *Camk2b* double knock-out mice); *Camk2a*$^{T286A/T286A}$ (Camk2a^{tm2Sva}, MGI:2158733) and *Camk2b*$^{T287A/T287A}$ mice to generate *Camk2a*$^{+/T286A}$;*Camk2b*$^{T287A/T287A}$ (mice heterozygous for a T286A knock-in mutation in *Camk2a* and homozygous for a T287A knock-in mutation in *Camk2b*); *Camk2a*$^{T286A/T286A}$;*Camk2b*$^{+/T287A}$ (mice homozygous for a T286A knock-in mutation in *Camk2a* and heterozygous for a T287A knock-in mutation in *Camk2b*); *Camk2a*$^{T286A/T286A}$;*Camk2b*$^{T287A/T287A}$ (homozygous for

T286A and T287A knock-in mutations in *Camk2a* and *Camk2b*, respectively); *Camk2a*$^{T305D/T305D}$ (Camk2a^{tm5Sva}, MGI: 2389272) and *Camk2b*$^{A303R/A303R}$ (Camk2b$^{tm2.1Yelg}$, MGI:5285573) mice to generate *Camk2a*$^{+/T305D}$; *Camk2b*$^{A303R/A303R}$ (mice heterozygous for a T305D knock-in mutation in *Camk2a* and homozygous for a A303R knock-in mutation in *Camk2b*); *Camk2a*$^{T305D/T305D}$;*Camk2b*$^{+/A303R}$ (mice homozygous for a T305D knock-in mutation in *Camk2a* and heterozygous for a A303R knock-in mutation in *Camk2b*); *Camk2a*$^{T305D/T305D}$;*Camk2b*$^{A303R/A303R}$ (homozygous for T305D and A303R knock-in mutations in *Camk2a* and *Camk2b*, respectively); *Camk2a*$^{f/f}$;*Camk2b*$^{f/f}$ (homozygous floxed *Camk2a* (Camk2a$^{tm1.1Yelg}$, MGI:5662417) and *Camk2b* mice with no *Cre* expression; controls); *Camk2a*$^{f/f}$;*Camk2b*$^{f/f}$;*CAG-Cre*^{ESR} (homozygous floxed *Camk2a* and *Camk2b* mice with transgenic *Cre* expression throughout the body after injection with tamoxifen (Tg(CAG-cre/Esr1*)5Amc; MGI:2182767), and *Camk2a*$^{f/f}$;*Camk2b*$^{f/f}$;*CA3-Cre* (knock-out mutants for *Camk2a* and *Camk2b* specifically in the CA3 region of the hippocampus (Grik4$^{tm1.1(cre)Slab}$; MGI:4398684, kindly provided by Ralf Schoepfer, Laboratory for Molecular Pharmacology, NPP, University College London, and York Rudhard, In Vitro Pharmacology, Evotec AG, Manfred Eigen Campus; Filosa *et al*., 2009). All mice were back-crossed >16 times in a C57BL/6J background and were group-housed in IVC cages (Sealsafe 1145 T, Tecniplast) with bedding material (Lignocel BK 8/15, Rettenmayer) on a 12 h light/dark cycle in 21°C (±1°C), humidity at 40–70% and with chow (No. 1 maintenance autoclave pellets, Special Diets Services) and water available *ad libitum*. Experimenters were blind to all genotypes throughout experiments and data analysis. Mice (males and females) were genotyped when they were 7-d-old, and re-genotyped after the mice were killed. Genotyping records were obtained and kept by a technician not involved in the experimental design, performance, and analysis. All experiments were done during the light phase, with animals between 2 and 4 months of age. All experiments were done with approval of the local Dutch Animal Ethical Committee for animal research and were in accordance with the European Communities Council Directive (86/609/EEC).

Generation of mouse mutants. The generation of both the floxed and knock-out *Camk2a* (Elgersma *et al*., 2002; Achterberg *et al*., 2014) and *Camk2b* (Borgesius *et al*., 2011; Kool *et al*., 2016) mouse mutants have been described previously. All knock-in mutants used in this study have been published before as well: *Camk2a*^{T286A} (Giese *et al*., 1998); *Camk2a*^{T305D} (Elgersma *et al*., 2002); *Camk2b*^{T287A} (Kool *et al*., 2016); and *Camk2a*^{A303R} (Borgesius *et al*., 2011). To generate a CA3-specific deletion of the *Camk2a* and *Camk2b* genes we crossed *Camk2a*$^{f/f}$;*Camk2b*$^{f/f}$ mice with *Grik4-Cre-Neo* (in this study referred to as *CA3-Cre* mice). *CA3-Cre* expression starts as early as P5 and is predominantly restricted to the CA3 area of the hippocampus. To make sure that full deletion of the gene-of-interest had taken place, experiments were started at a minimum age of 8 weeks.

Tamoxifen injections. Adult *Camk2a*$^{f/f}$;*Camk2b*$^{f/f}$ and *Camk2a*$^{f/f}$;*Camk2b*$^{f/f}$;*CAG-Cre*^{ESR} mice (8–10 weeks of age) were injected intraperitoneally with tamoxifen (Sigma-Aldrich; 0.1 mg/g bodyweight) for 8 consecutive days. To keep the levels of tamoxifen constant throughout injection days we kept a tight injection scheme, injecting mice 24 +/- 1h after the previous injection. Tamoxifen was dissolved in sunflower oil (20 mg/ml). For electrophysiological experiments we killed adult mice (12–16 weeks old) 25 d after the first tamoxifen injection. Though tamoxifen is not known to have an effect on emotional reactivity, neurological functioning, or learning (Vogt *et al*., 2008) we injected both *Camk2a*$^{f/f}$;*Camk2b*$^{f/f}$ and *Camk2a*$^{f/f}$;*Camk2b*$^{f/f}$;*CAG-Cre*^{ESR} mice to control for any possible effects of tamoxifen.

Mass spectrometry. Cortical tissue was isolated from adult *Camk2a*$^{f/f}$;*Camk2b*$^{f/f}$ and *Camk2a*$^{f/}$

f;Camk2b$^{f/f}$;CAG-Cre^{ESR} mice 21 d after tamoxifen injection. Cell lysis was performed in 50 mM Tris-HCl, pH 8.2, with 0.5% sodium deoxycholate. Briefly, cells were incubated with the buffer and then boiled and sonicated for 10 min using a Bioruptor (Diagenode). Protein quantitation was performed using the colorimetric absorbance BCA protein assay kit (ThermoFisher Scientific). Proteins were reduced using 5 mM 1,4-dithiothreitol for 30 min at 50°C and subsequently alkylated using 10 mM iodoacetamide for 15 min in the dark. Proteins were first digested for 4 h with Lys-C (Wako Pure Chemicals; 1:200 enzyme– substrate ratio) and then overnight with trypsin (ThermoFisher Scientific; 1:50 enzyme–substrate ratio) at 30°C. The detergent was then removed by adding trifluoroacetic acid to 0.5% and precipitated detergent was spun down at 10,000 X *g* for 10 min. Extracted proteolytic peptides were labeled with TMT 6-plex labeling reagents (ThermoFisher Scientific) allowing for peptide quantitation. Peptides were mixed at the 6-plex level and further fractionated into six fractions by HILIC chromatography. Fractions were collected and analyzed by nanoflow LC-MS/ MS. nLC-MS/MS was performed on EASYnLC 1000 coupled to an Orbitrap Fusion Tribid mass spectrometer (ThermoFisher Scientific) operating in positive mode and equipped with a nanospray source. Peptides were separated on a ReproSil C18 reversed phase column (Dr. Maisch GmbH; column dimensions 15 cm X 50 µm, packed in-house) using a linear gradient from 0 to 80% B [A = 0.1% formic acid; B = 80% (v/v) acetonitrile, 0.1% formic acid] in 70 min and at a constant flow rate of 200 nl/min using a splitter. The column eluent was directly sprayed into the electrospray ionization source of the mass spectrometer. Mass spectra were acquired in continuum mode; fragmentation of the peptides was performed in data-dependent mode using the multinotch SPS MS3 reporter ion-based quantification method.

PSD fraction isolation. Cortical tissue was isolated from adult *Camk2a$^{f/f}$;Camk2b$^{f/f}$* and *Camk2a$^{f/f}$;Camk2b$^{f/f}$;CAG-Cre^{ESR}* mice 21 d after tamoxifen injection (Group 1) or in the days preceding death (4–5 weeks after the first tamoxifen injection; Group 2), and placed on ice until further processing. The lysates were prepared in homogenization buffer containing 0.32 M Sucrose, 1 mM $NaHCO_3$, 1 mM $MgCl_2$, 10 mM HEPES, pH 7.4, and protease and phosphatase inhibitors cocktails (P8340, P5726, and P0044, Sigma-Aldrich). This extract was immediately processed for the isolation of synaptosomes as described by Carlin *et al*., 1980. Protein concentration of the synaptosome fraction was determined using the BCA protein assay kit (Pierce) and adjusted to 1 mg/ml. Postsynaptic densities (PSD) were obtained from 100 µg of synaptosomes by adding 1% (v/v) Triton X-100 and HEPES, standing on ice for 15 min and centrifugation for 30 min. The pellet (PSD fraction) was dissolved in Laemmli sample buffer (1X). Samples were then used for subsequent Western blotting.

Western blot. Mice were anesthetized using isoflurane and killed by decapitation. Brain samples (or acute hippocampal slices in the case of the Western blots after the electrophysiology experiments) were taken out quickly and stored in liquid nitrogen. Lysates were then first prepared and brain samples were homogenized in lysis buffer (10 mM Tris-HCl 6.8, 2.5% SDS, 2 mM EDTA). Protein concentration in the samples was determined and lysate concentrations were adjusted to 1 mg/ml. Western blots were probed with primary antibodies against either CAMK2A (clone 6G9, 1:20,000; Millipore, catalog #MAB8699; RRID: AB_2067919), CAMK2B (clone CB-β1, 1:10,000; ThermoFisher Scientific, catalog #13-9800; RRID:AB_2533045), PSD95 (1:1000; Proteintech Group, catalog #20665-1-AP; RRID:AB_2687961), GRIA2 (1:1000; Proteintech Group, catalog #11994-1-AP; RRID:AB_2113725), GRIN2B (1: 2000; Proteintech Group, catalog #21920-1-AP; RRID:AB_11232223), and actin (1:20,000; Millipore, catalog #MAB1501R; RRID:AB_2223041) and secondary antibodies (goat anti-mouse and/ or goat anti-rabbit, both 1:3000; Jackson ImmunoResearch, catalog #115-007-003; RRID:

AB_2338476; and catalog #111-007-003; RRID:AB_2337925). Blots were stained either with Enhanced Chemiluminescence (ECL; 32106, Pierce) or stained and quantified using LI-COR Odyssey Scanner and Odyssey 3.0 software (Odyssey CLx; RRID:SCR_014579). Quantification of Western blot in ECL was done using ImageJ (Fiji; RRID:SCR_002285).

Immunohistochemistry and immunofluorescence. Mice were anesthetized with pentobarbital and perfused transcardially with PBS followed by freshly prepared 4% paraformaldehyde (PFA) solution (Sigma-Aldrich). Brains were taken out after perfusion, postfixed for 1.5 h in PFA, and afterward kept in 30% sucrose solution overnight. Free-floating 40-µm-thick frozen sections were made and for immunohistochemistry, a standard avidin-biotin-immunoperoxidase complex method (ABC, Vector Laboratories) with CAMK2A (clone 6G9, 1:10,000; Millipore, catalog #MAB8699; RRID:AB_2067919) as the primary antibody and diaminobenzidine (0.05%) as the chromogen was used. For immunofluorescence, free-floating 40-µm-thick sections were washed in PBS once and afterward primary antibody was added (anti-CAMK2B, 1:1000; Abcam, catalog #ab34703; RRID:AB_2275072) diluted in PBS containing 2% NHS, 0.5% Triton X-100, and 150 mM bovine serum albumin (BSA) and kept at 4°C for 48 h. Two days later sections were washed three times with PBS and secondary antibodies were added (Cy3 rabbit, 1:200 for immunofluorescence; Jackson ImmunoResearch, catalog #711-165-152; RRID:AB_2307443) diluted in PBS containing 2% NHS, 0.5% Triton X-100, and 150 mM BSA. After 1–2 h incubation of the secondary antibody at room temperature sections were washed four times in PB (0.05 M) and mounted on slides using chromium (III) potassium sulfatedodecahydrate and left to dry. Finally, for immunofluorescence, sections were covered using Mowiol (Sigma-Aldrich). For immunohistochemistry, the slices were, after drying, dehydrated in alcohol, cleared with xylene and covered using Permount (Fisher Scientific).

Half-life calculations. For the protein degradation curves, mice received tamoxifen injections and were killed 4, 8, 10, 12, 15, 18, 21, and 24 d after the start of the experiment (n = 2 for each time point). *Camk2a*$^{f/f}$*;Camk2b*$^{f/f}$ mice without Cre were taken along for baseline levels. Protein levels were measured using Western blot and data were plotted using Prism data analysis software (GraphPad Prism; RRID: SCR_002798).

Local field potential surgery. Mice were anesthetized with a mixture of isoflurane and oxygen (5% for induction and <2% for maintenance) and body temperature was kept constant at 37° during the entire surgical procedure. Temgesic (0.3 mg/ml) and lidocaine (Xylocaine, 100 mg/ml) were used for general and local analgesia. After fixation in a custom-designed stereotaxic apparatus, the scalp was opened to expose the skull. The membranous tissue underneath was cleared and the bone was surgically prepared with Optibond prime and adhesive (Kerr). The placement of the recording electrodes (Bear Lab Chronic Microelectrodes, 30070, FHC) was determined using a digital *x-y* manipulator according to the following coordinates: for the somatosensory cortex from the bregma AP: -1.94 mm, DL: -3.00 mm, DV: 0.6 mm; for the motor cortex from the bregma AP: +1.42, DL: + 1.75, DV: 0.5 mm. A reference electrode (silver wire) was placed on top of the vermis in the cerebellum. A small brass pedestal was attached to the skull with Charisma (Heraeus Kulzer) to ensure the fixation of the mice to the head bar during recording.

Local field potential recordings. Two days after the surgical procedure, mice were head-fixed to a brass bar suspended over a cylindrical treadmill to allow anesthesia-free recording sessions and placed in a light-isolated Faraday cage. Mice were allowed to habituate to the setup before proceeding to the recording. Local field potential (LFP) signals were acquired every 2 d in

sessions of 20 min each until the days preceding death, using the Open Ephys platform with a sampling rate of 3 kS/s and a bandpass filter between 0.1 and 200 Hz. Mice were observed daily and humanely killed when showing signs of behavioral discomfort (not before day 32 post-injection).

Electrophysiology. Mice were killed after being anesthetized with isoflurane (Nicholas Piramal) and the brain was taken out quickly and submerged in ice-cold oxygenated (95%) and carbonated (5%) artificial CSF (ACSF; <4.0°) containing the following (in mM): 120 NaCl, 3.5 KCl, 2.5 $CaCl_2$, 1.3 $MgSO_4$, 1.25 NaH_2PO_4, 26 $NaHCO_3$, and 10 D-glucose. Using a vibratome 400-µm-thick sagittal slices were made for CA3–CA1 experiments and 400-µm-thick coronal slices for CA3–CA3 experiments. Hippocampal sections were dissected out afterward and maintained at room temperature for at least 1.5 h in an oxygenated and carbonated bath to recover before experiments were initiated. At the onset of experiments hippocampal slices were placed in a submerged recording chamber and perfused continuously at a rate of 2 ml/min with ACSF equilibrated with 95% O_2, 5% CO_2 at 30°C. Extracellular recording of field EPSPs (fEPSPs) and stimulation were done using bipolar platinum (Pt)/iridium (Ir) electrodes (Frederick Haer). Stimulus duration of 100 µs for all experiments was used. In CA3–CA1 measurements, the stimulating electrode and recording electrode were placed on the CA3–CA1 Schaffer collateral afferents and apical dendrites of CA1 pyramidal cells (both 150–200 µm from *stratum pyramidale*), respectively. In CA3–CA3 measurements both the stimulating electrode and recording electrode were placed on the *stratum radiatum* of the CA3 area. The *stratum lucidum* was carefully avoided. Upon placement of the electrodes slices were given 20–30 min to rest before continuing measurements. All paired-pulse facilitation (PPF) experiments were stimulated at one-third of slice maximum. Varying intervals were used in PPF: 10, 25, 50, 100, 200, and 400 ms. CAMK2-dependent LTP was evoked using four different tetani: (1) 100 Hz (1 train of 1 s at 100 Hz, stimulated at one-third of slice maximum), (2) 200 Hz (4 trains of 0.5 s at 200 Hz, spaced by 5 s, stimulated at one-third of slice maximum), (3) theta burst (2 trains of 4 stimuli at 100 Hz, 200 ms apart, stimulated at two-thirds of slice maximum), and (4) CA3–CA3 LTP (2 trains of 1 s at 100 Hz 10 s apart, stimulated at one-third of slice maximum). A possible caveat in fEPSP measurements in the CA3 area is distinguishing between the mossy fiber pathway and the commissural (CA3–CA3) pathway. Therefore, we took several measures to make sure we recorded from the commissural pathway. First, with respect to the mossy fibers we used antidromic stimulation in the CA3 area. Second, we made use of the electrophysiological parameters PPF and 1 Hz frequency facilitation that differ between these two pathways. Mossy fiber transmission shows very strong facilitation (± 215% for PPF and ± 250% for 1 Hz; Scanziani *et al*., 1997), hence, we chose an upper limit of 180% for PPF and 130% for 1 Hz, and excluded all slices exceeding those limits. Finally, at the end of all experiments we used a pharmacological approach using DCG-IV (3 µM) to distinguish between both pathways. DCG-IV (3 µM) is known to reduce mossy fiber transmission by 80% (Kirschstein *et al*., 2004). This way, we felt confident that we only included data from experiments where we specifically stimulated CA3–CA3 synapses. Chemical LTD was induced using a 5 min wash-in of DHPG (100 µM; Tocris Biosciences) 20 min after establishing a stable baseline. For PKA-dependent LTP a similar baseline was established before chemical induction. We added picrotoxin (50 µM) to the ACSF throughout the experiment and LTP was induced chemically (cLTP) by bath application of picrotoxin (50 µM), forskolin (50 µM), and rolipram (0.1 µM) for 15 min, after which bath circulation was returned to ACSF with only picrotoxin (50 µM). During LTP slices were stimulated once per minute. Potentiation was measured as the normalized increase of the mean fEPSP slope for the duration of the baseline. During induction

of chemical LTP slices were stimulated at half of slice maximum. Only stable recordings were included and this judgment was made blind to genotype. Average LTP was defined as the mean last 10 min of the normalized fEPSP slope.

Data analysis and statistics. Statistical tests were performed using a two-way repeated-measures ANOVA or Student's *t* test to determine the effect of genotype in the experiments. In LTP experiments, the last 10 data points were used for comparison. The mass spectrometry data were analyzed with Proteome Discoverer 2.1 (RRID:SCR_014477). Peak lists were automatically created from raw data files using the Mascot Distiller software v2.3; Matrix Science; RRID:SCR_000307). The Mascot search algorithm (version 2.3.2, Matrix Science; RRID:SCR_000307) was used for searching against the UniProt database (taxonomy: *Mus musculus*, version December 2015; RRID:SCR_002380). The peptide tolerance was typically set to 10 ppm and the fragment ion tolerance was set to 0.8 Da. The reporter ion tolerance was set to 0.003 Da. A maximum number of 2 missed cleavages by trypsin were allowed and carbamidomethylated cysteine and oxidized methionine were set as fixed and variable modifications, respectively. Typical contaminants were omitted from the output tables. Protein ratios were calculated from the scaled normalized abundances of the reporter ions over the six quantitation channels. Gene ontology analysis was performed on the statistically different proteins with >20% difference in abundance ratio identified through mass spectrometry using the PANTHER Overrepresentation Test (GO Ontology database, Release date 2019-01-01, PANTHER; RRID:SCR_004869). The full list of proteins identified in the mass spectrometry analysis was used as reference dataset. A binomial test with Bonferroni correction was used for the statistical analysis. Statistical difference of PSD-associated proteins was assessed using a two-tailed Student's *t* test. For the analysis of the Western blots for the PSD associated protein levels, unpaired one-tailed or two-tailed Student's *t* test was used. For the LFP analysis, the average power density spectrum of the last 3 d of recording was obtained using MATLAB software (MathWorks; RRID:SCR_001622). The mean relative power was calculated over four frequency bands relative to the total power: delta (2–4 Hz), theta (5–8 Hz), beta (13–30 Hz), and gamma (30–50 Hz). After determining normality of the distribution using the Wilk–Shapiro test, we determined statistical significance using an unpaired two-tailed Student's *t* test to assess the effect of genotype across each band frequency. For all statistical analyses α was set at 0.05. Values are represented as average ± SEM. Group sizes can be found in the figure legends. All values are based on number of slices measured. Each experimental group contained at minimum three different mice. All statistical tests were performed either using GraphPad Prism (RRID: SCR_002798) or SPSS Statistics v22.0 (RRID:SCR_002865).

RESULTS

Loss of both CAMK2A and CAMK2B results in neonatal death

To unravel the full spectrum of CAMK2 functions, the *Camk2a*/*Camk2b* double-heterozygous mice (*Camk2a*$^{-/+}$;*Camk2b*$^{-/+}$) were intercrossed to obtain F2 *Camk2a*/*Camk2b* double knock-out mice (*Camk2a*$^{-/-}$;*Camk2b*$^{-/-}$; see Materials and Methods). Genotyping performed at day 7 on 222 pups, revealed 0 *Camk2a*$^{-/-}$;*Camk2b*$^{-/-}$ double-mutants, whereas 14 pups were expected based on a Mendelian distribution (Fig. 1*a*), indicating that the double-mutant might be lethal. Moreover, all of the *Camk2a*$^{+/-}$;*Camk2b*$^{-/-}$ mice died within 36 d after birth, whereas only 28% of the *Camk2a*$^{-/-}$;*Camk2b*$^{+/-}$ died within the same period, indicating that complete loss of CAMK2B is less tolerated than complete loss of CAMK2A. Importantly, other genotypes obtained by this breeding (such as *Camk2a*$^{+/-}$;*Camk2b*$^{+/-}$ mice, data not shown) appeared just as vital as wild-type mice. To understand whether the lethality of *Camk2a*$^{-/-}$;*Camk2b*$^{-/-}$ mice

was prenatal or postnatal, mice were monitored immediately from birth on. We observed that a small number of the born pups died within the first day after birth, which all appeared to be *Camk2a*$^{-/-}$;*Camk2b*$^{-/-}$ upon genotyping. Taken these pups into account, we found that 6 of 100 pups were *Camk2a*$^{-/-}$;*Camk2b*$^{-/-}$ double-mutants, which is the expected number of double-mutants, indicating that the *Camk2a*$^{-/-}$;*Camk2b*$^{-/-}$ mutants are born at normal frequency (X^2: 9.4, p = 0.31), but die within 1 d after birth. When observing the pups directly after birth it was not possible to predict which pup would die, because the *Camk2a*$^{-/-}$;*Camk2b*$^{-/-}$ pups did not show notable growth retardation or morphological changes, and a milk spot was visible in the abdomen, indicating that it was not lack of food intake that killed the pups. Additionally, immunohistochemistry showed no gross morphological changes in brains of pups on P0 (data not shown). Together, this shows that simultaneous loss of both CAMK2A and CAMK2B results in neonatal death, indicating a critical role of CAMK2 during this period, which cannot be revealed by studying the CAMK2 isoforms in isolation.

Loss of Ca^{2+}-independent and Ca^{2+}-dependent activity of CAMK2 results in neonatal death

Activity of CAMK2 is governed by multiple phosphorylation sites, of which the Thr286 (Thr287 in CAMK2B) is important for Ca^{2+}-independent activity (Fig. 1*d*, bottom) and Thr305/Thr306 (Thr306/Thr307 in CAMK2B) for the Ca^{2+}-dependent activity (Fig. 1*d*, middle), because they are located within the Ca^{2+}/CaM binding site on CAMK2. Considering the phenotypes of the *Camk2a* and *Camk2b* single-mutants, we know that the CAMK2A phosphomimic mutation at Thr305 (CAMK2A-T305D), which blocks Ca^{2+}/CaM binding and keeps CAMK2 in its inactivated state, is more detrimental than not having CAMK2A at all (Elgersma *et al*., 2002). This is also the case for a similar mutation in CAMK2B (CAMK2B-A303R) with respect to locomotion (Kool *et al*., 2016), although this is not the case for hippocampal learning (Borgesius *et al*., 2011). Hence, we expected that a double-mutant of CAMK2A-T305D and CAMK2B-A303R might be lethal as well. Indeed, when inter-crossing *Camk2a*$^{+/T305D}$;*Camk2b*$^{+/A303R}$ double-mutant mice we found that upon P7, only two *Camk2a*$^{T305D/T305D}$;*Camk2b*$^{A303R/A303R}$ mutants were found in a total of 126 pups (number expected was 8). The two pups that survived until P7 still died a premature death within 16–23 d after birth (Fig. 1*b*). Similar to the *Camk2a*/*Camk2b* double-mutants, homozygous mutations in the Ca^{2+}/CaM binding of CAMK2B were less tolerated than comparable mutations in CAMK2A (Fig. 1*b*).

We then tested whether Ca^{2+}-independent activity (also known as autonomous activity) was essential for life. To that end, we intercrossed *Camk2a*$^{+/T286A}$;*Camk2b*$^{+/T287A}$ double-mutant mice, such that autophosphorylation of both CAMK2A and CAMK2B at the Thr286/287 site is prevented (Giese *et al*., 1998; Kool *et al*., 2016). Surprisingly, despite the fact that these mice still have Ca^{2+}-dependent activity, we found that the *Camk2a*$^{T286A/T286A}$;*Camk2b*$^{T287A/T287A}$ mice started dying from P11 onward and that all had died by P27 (Fig. 1*c*). Again, homozygous mutations in CAMK2B were less tolerated than comparable mutations in CAMK2A. This indicates that CAMK2 autonomous activity is essential for survival.

Adult deletion of CAMK2A and CAMK2B is lethal

The premature death observed in the various *Camk2a*/*Camk2b* double-mutants described in the previous section, indicate a crucial role for CAMK2-dependent signaling during development. Using inducible *Camk2a* and *Camk2b* knock-out mice, we have recently shown that CAMK2-dependent signaling is also important after brain development (Achterberg *et al*., 2014; Kool *et al*., 2016). Notably, the phenotypes observed when deleting the *Camk2a* gene in adult mice are as severe as when deleting the gene at germline (Achterberg *et al*., 2014).

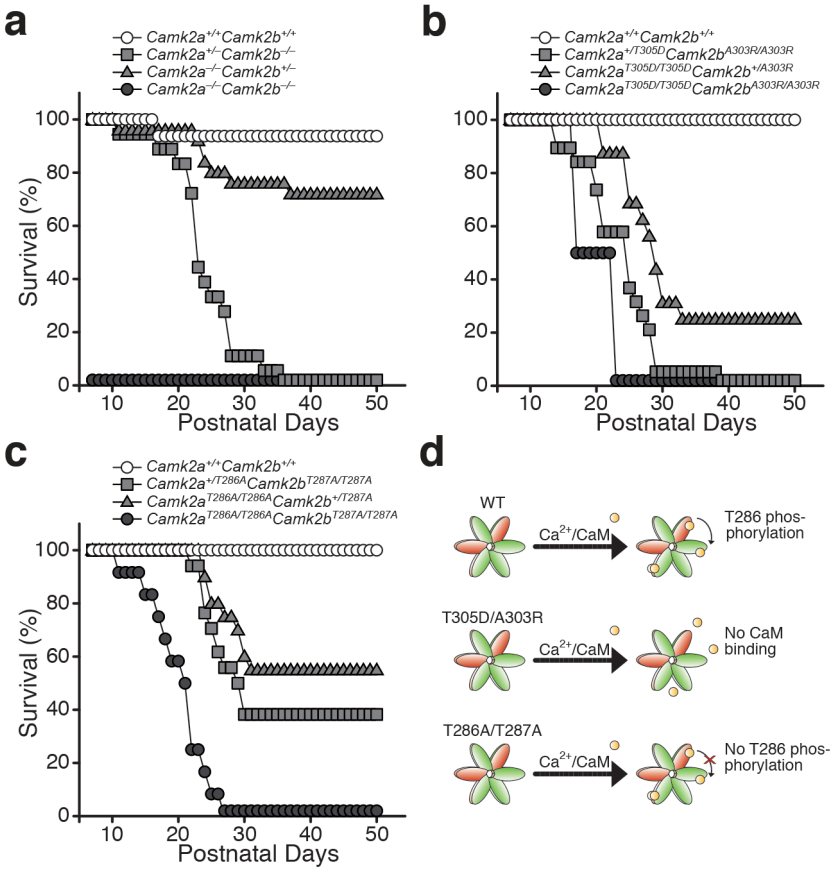

Figure 1. Multiple *Camk2a* mutants crossed with *Camk2b* mutants and their survival in percentage of their total group size. ***a***, Double knock-out mice for both *Camk2a* and *Camk2b* (*Camk2a*$^{-/-}$;*Camk2b*$^{-/-}$) die on P0. Homozygosity for *Camk2b* (with 1 functioning allele of *Camk2a*: *Camk2a*$^{+/-}$;*Camk2b*$^{-/-}$, *n* = 18) has a more severe impact on survival than homozygosity for *Camk2a* (and 1 functioning allele of *Camk2b*: *Camk2a*$^{-/-}$;*Camk2b*$^{+/-}$, *n* = 25). *Camk2a*$^{+/+}$;*Camk2b*$^{+/+}$ were used as controls (*n* = 16). ***b***, Homozygous loss of Ca^{2+}-dependent activity of both CAMK2A and CAMK2B (*Camk2a*$^{T305D/T305D}$;*Camk2b*;$^{A303R/A303R}$, *n* = 2) results in early death. Homozygosity for a A303R knock-in mutation in *Camk2b* and a heterozygous T305D knock-in mutation for *Camk2a* (*Camk2a*$^{+/T305D}$;*Camk2b*$^{A303R/A303R}$, *n* = 18) has a more severe impact on survival than a homozygous knock-in mutation for *Camk2a* and a heterozygous A303R knock-in mutation for *Camk2b* (*Camk2a*$^{T305D/T305D}$;*Camk2b*$^{+/A303R}$, *n* = 15). *Camk2a*$^{+/+}$;*Camk2b*$^{+/+}$ were used as controls (*n* = 4). ***c***, Homozygous loss of autonomous activity of both CAMK2A and CAMK2B (*Camk2a*$^{T286A/T286A}$;*Camk2b*$^{T287A/T287A}$, *n* = 12) results in early death. Again, homozygosity for a T287A knock-in mutation in *Camk2b* (and a heterozygous T286A knock-in mutation for *Camk2a*: *Camk2a*$^{+/T286A}$;*Camk2b*$^{T287A/T287A}$, *n* = 34) has a more severe impact on survival than a homozygous knock-in mutation for *Camk2a* (and a heterozygous T287A knock-in mutation for *Camk2b*: *Camk2a*$^{T286A/T286A}$;*Camk2b*$^{+/T287A}$, *n* = 20). *Camk2a*$^{+/+}$;*Camk2b*$^{+/+}$ were used as controls (*n* = 14). With the exception of one mouse in the first experiment (***a***), all *Camk2a*$^{+/+}$;*Camk2b*$^{+/+}$ mice survived a minimum of up to 50 d postnatally. ***d***, Model showing the effect of the different mutations used on the activity of the holoenzyme for the survival experiments. Green, CAMK2A; red, CAMK2B; yellow, calcium/calmodulin.

Therefore, we postulated that deletion of both CAMK2A and CAMK2B could potentially also be lethal in adult mice. We generated inducible *Camk2a*$^{f/f}$;*Camk2b*$^{f/f}$;*CAG-Cre*^{ESR} mice, which were injected daily for 4 consecutive days with tamoxifen at 8 weeks of age to induce deletion of both *Camk2a* and *Camk2b*. Up until 4 d after the onset of gene deletion (first tamoxifen injection), the protein levels remained the same, but after that time point the levels reduced exponentially. Both CAMK2A and CAMK2B showed similar half-lives and decay constants in

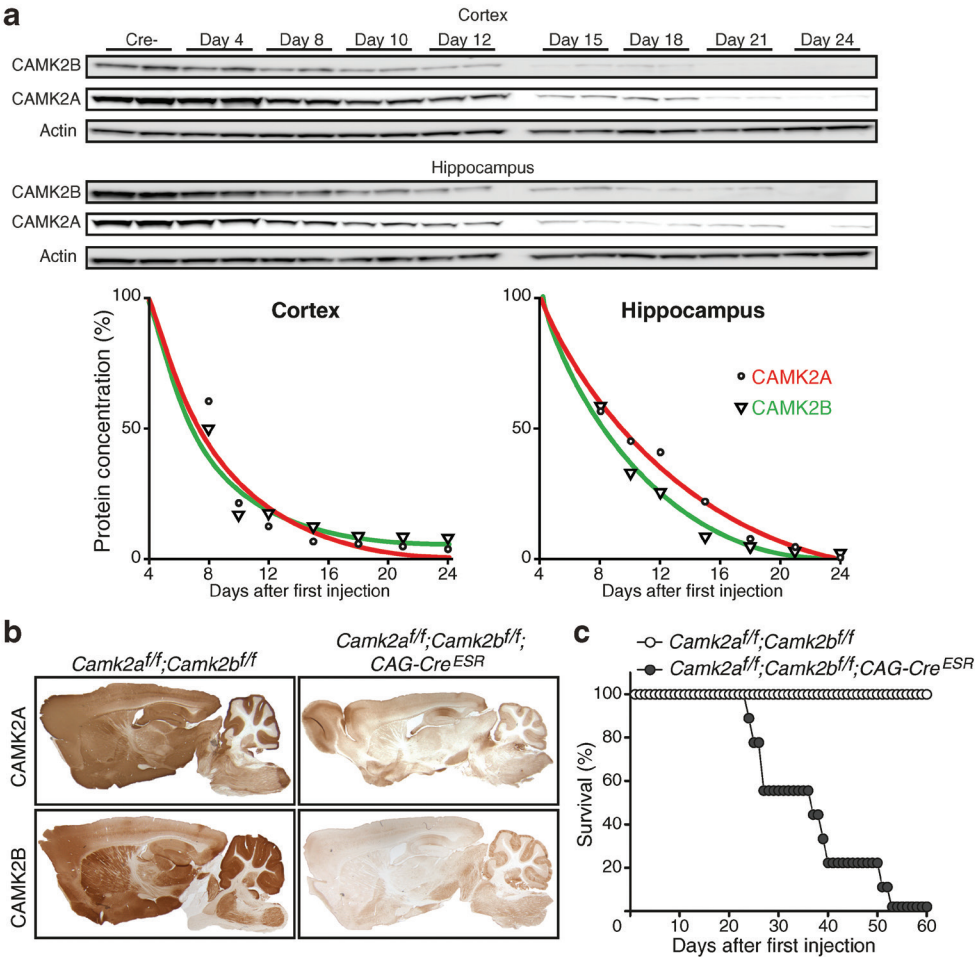

Figure 2. Adult loss of CAMK2Aand CAMK2B is lethal. ***a***, Western blot of cortical (top) and hippocampal (bottom) lysates using antibodies targeted against CAMK2A and CAMK2B. Actin was used as loading control. Days after first injection are indicated above the blots. Cre- mice were killed 4 d after the first tamoxifen injection. Bottom left graph, Nonlinear regression curve showing protein degradation in cortex, showing no difference in protein degradation rate of both CAMK2A and CAMK2B (n = 2 for each time point). Bottom right graph, Nonlinear regression curve showing protein degradation in hippocampus, where CAMK2B degradation is faster than CAMK2A degradation. Comparing both graphs, protein degradation of both CAMK2Aand CAMK2Bis faster in the cortex than in the hippocampus. ***b***, Immunohistological stainings showing effective loss after tamoxifen injections of CAMK2A (top) and CAMK2B (bottom) in *Camk2a$^{f/f}$;Camk2b$^{f/f}$;CAG-Cre^{ESR}* mice 21 d after onset of gene deletion. ***c***, Loss of both CAMK2A and CAMK2B (*Camk2a$^{f/f}$;Camk2b$^{f/f}$;CAG-Cre^{ESR}*) in adulthood is lethal. Both groups of mice [*Camk2a$^{f/f}$;Camk2b$^{f/f}$;CAG-Cre^{ESR}* (n = 9) and *Camk2a$^{f/f}$; Camk2b$^{f/f}$* (n = 8)] received tamoxifen injections (see Materials and Methods).

the cortex (CAMK2A, half-life: 3.5 d; CAMK2B, half-life: 2.8 d) as well as in the hippocampus (CAMK2A, half-life: 5.3 d; CAMK2B, half-life: 4.4 d; Fig. 2*a*). Immunohistochemical stainings at 21 d after onset of gene deletion showed that despite a few CAMK2A- or CAMK2B-positive cells, most brain areas were devoid of CAMK2 staining (Fig. 2*b*). Around 15–19 d (depending on the brain region) after onset of gene deletion, the levels of CAMK2A and CAMK2B dropped <10%, after which the *Camk2a$^{f/f}$;Camk2b$^{f/f}$;CAG-Cre^{ESR}* mice started to die. All injected *Camk2a$^{f/}$*

Table1. Protein ratio abundances of key PSD enriched proteins

Protein name	Gene	Uniprot ID	No. of Peptides	Abundance ratio: (wt)/(mut)	*p*
Calcium/calmodulin-dependent protein kinase type II subunit alpha	*Camk2a*	P11798	20	8.1	**<0.0001**
Calcium/calmodulin-dependent protein kinase type II subunit beta	*Camk2b*	Q5SVJ0	23	5.2	**<0.0001**
Glutamate receptor interacting protein 2	*Grip2*	G3XA20	2	1.3	0.394
SH3 and multiple ankyrin repeat domains protein 2	*Shank2*	Q80Z38-3	31	1.3	0.317
SH3 and multiple ankyrin repeat domains protein 3	*Shank3*	Q4ACU6-9	19	1.1	0.599
Synaptic functional regulator FMR1	*Fmr1*	P35922	13	1.1	0.267
Septin-7	*Sept7*	E9Q1G8	25	1.1	0.234
alpha-actinin 4	*Actn4*	P57780	41	1.0	0.085
MAGUK p55 subfamily member 5	*Mpp5*	B2RRY4	3	1.0	0.674
Cadherin-2	*Cdh2*	P15116	11	1.0	0.255
alpha-actinin 1a	*Actn1*	A1BN54	42	1.0	0.273
Src substrate cortactin	*Cttn*	Q60598	18	1.0	**0.026**
Cortactin-binding protein 2	*Cttnbp2*	B9EJA2	20	1.0	0.161
Catenin beta-1	*Ctnnb1*	Q02248	28	1.0	0.463
PRKCA-binding protein	*Pick1*	E9PUZ5	7	1.0	0.691
Homer protein homolog 1	*Homer1*	Q9ZZY3	20	1.0	0.401
MAGUK p55 subfamily member 3	*Mpp3*	Q6XE40	6	1.0	0.88
Neuroligin-3	*Nlgn3*	A2AGI2	6	1.0	0.878
Metabotropic glutamate receptor 3	*Grm3*	Q9QYS2	15	1.0	0.879
Neuroligin-4 like	*Nlgn-4l*	B0F2B4	7	1.0	0.961
Neuroligin-2	*Nlgn2*	Q69ZK9	10	1.0	0.916
Metabotropic glutamate receptor 5	*Grm5*	Q3UVX5	16	1.0	0.907
MAGUK p55 subfamily member 2	*Mpp2*	Q9WV34-2	23	1.0	0.739
Cytoplasmic FMR1-interacting protein 2	*Cyfip2*	Q5SQX6	36	1.0	0.802
Glutamate receptor 3	*Gria3*	Q9Z2W9	22	1.0	0.868
MAGUK p55 subfamily member 6	*Mpp6*	Q9JLB0-2	20	1.0	0.486
SH3 and multiple ankyrin repeat domains protein 3	*Shank3*	A0A0A0MQD5	32	1.0	0.663
Homer protein homolog 2	*Homer2*	Q9QWW1	4	1.0	0.807
SH3 and multiple ankyrin repeat domains protein 1	*Shank1*	D3YZU1	36	1.0	0.604
SH3 and multiple ankyrin repeat domains protein 2	*Shank2*	D3Z5K8	33	1.0	0.527
Cytoplasmic FMR1-interacting protein 1	*Cyfip1*	Q7TMB8	23	1.0	0.633
alpha-actinin 2	*Actn2*	Q9JI91	27	1.0	0.613
Kalirin	*Kalrn*	A2CG49-7	29	1.0	0.228
Glutamate receptor ionotropic, NMDA 2B	*Grin2b*	G3X9V4	11	1.0	0.099
Glutamate receptor 2	*Gria2*	P23819-4	30	0.9	**0.046**
Glutamate receptor 3	*Gria3*	B0QZW1	22	0.9	0.267
Metabotropic glutamate receptor 2	*Grm2*	Q14BI2	16	0.9	0.336
Metabotropic glutamate receptor 1	*Grm1*	P97772	4	0.9	0.134
Glutamate receptor 1	*Gria1*	P23818	17	0.9	0.128
Glutamate receptor-interacting protein 1	*Grip1*	Q925T6	4	0.9	**0.043**
Glutamate receptor ionotropic, NMDA 1	*Grin1*	A2AI21	15	0.9	**0.009**
Glutamate receptor ionotropic, NMDA 2A	*Grin2a*	P35436	13	0.9	**0.022**
Neuroligin-1	*Nlgn1*	Q99K10	7	0.9	0.229
Ras/Rap GTPase-activating protein SynGAP	*Syngap1*	F6SEU4	36	0.9	**<0.001**
Glutamate receptor 4	*Gria4*	Q9Z2W8	8	0.8	0.465
Glutamate receptor ionotropic, NMDA 2D	*Grin2d*	Q03391	1	0.8	**0.0059**

Table 1: Selection of PSD-enriched proteins detected with mass spectrometry performed on *Camk2a*$^{f/f}$;*Camk2b*$^{f/f}$;*CAG-CreESR* (n = 3) and *Camk2a*$^{f/f}$;*Camk2b*$^{f/f}$ control mice (n = 3) killed 21 d after onset of gene deletion. Protein ratios were calculated from the scaled normalized abundances of the reporter ions over the six quantitation channels. A Student's t test analysis was performed over the scaled normalized abundances to evaluate significance. For the full list of proteins analysed using mass spectrometry, see Table 1-1, available at https://doi.org/10.1523/JNEUROSCI.1341-18.2019.t1-1. p-values lower than 0.05 are put in bold.

^{f};*Camk2b*$^{f/f}$;*CAG-Cre*^{ESR} mice died within 24–53 d, with a median survival of 37 d (Fig. 2*c*). These mice did not show any obvious alterations in behavior until their last 24 h, during which they would stop moving, eating, and drinking. Importantly, *Camk2a*$^{f/f}$;*Camk2b*$^{f/f}$ mice without *CAG-Cre*^{ESR} (control group) all survived.

CAMK2A and CAMK2B deletion does not result in overt changes in PSD composition

Analysis of the double-mutant brains did not reveal any gross morphology changes (Fig. 2*b*, and data not shown). Because both CAMK2A and CAMK2B have been shown to play an important structural role during plasticity and, upon activation, CAMK2 becomes highly

enriched in PSD (Shen and Meyer, 1999), we hypothesized that the acute loss of both isoforms might interfere with the PSD protein composition and/or its stability. To evaluate this, we performed a proteomics analysis on cortical tissue from *Camk2a*$^{f/f}$;*Camk2b*$^{f/f}$;*CAG-Cre*^{ESR} mice compared with *Camk2a*$^{f/f}$;*Camk2b*$^{f/f}$ controls 21 d after onset of gene deletion. Surprisingly, in addition to a reduction of CAMK2A and CAMK2B, we found little changes in the key PSD-associated proteins (Sheng and Kim, 2011) in the *Camk2a*$^{f/f}$;*Camk2b*$^{f/f}$;*CAG-Cre*^{ESR} samples. Only SynGAP, GRIP1, the NMDA receptor subunits and the GRIA2 subunit of the AMPA receptor revealed a small (<10–20%) but significant increase in expression level in the *Camk2a*$^{f/f}$;*Camk2b*$^{f/f}$;*CAG-Cre*^{ESR} compared with *Camk2a*$^{f/f}$; *Camk2b*$^{f/f}$ control samples (Table 1; *p* values are two-tailed unpaired Student's *t* tests; for the raw values, see Table 1-1, available at https://doi.org/10.1523/JNEUROSCI.1341-18.2019.t1-1). The full list of proteins revealed some more proteins showing a significant difference of 20% or more in abundance ratio (up-regulated or downregulated) between the *Camk2a*$^{f/f}$;*Camk2b*$^{f/f}$; *CAG-Cre*^{ESR} and *Camk2a*$^{f/f}$;*Camk2b*$^{f/f}$ control samples (Table 1-1, available at https://doi.org/10.1523/JNEUROSCI.1341-18.2019.t1-1). Subsequent GO-analysis did not reveal any overrepresented or underrepresented GO term in this dataset (PANTHER GO-analysis; Thomas *et al*., 2003).

To zoom in further on the PSD itself, we isolated the synaptosomes from cortical tissue of *Camk2a*$^{f/f}$;*Camk2b*$^{f/f}$;*CAG-Cre*^{ESR} mice and *Camk2a*$^{f/f}$;*Camk2b*$^{f/f}$ control mice. Group 1 was killed 21 d after onset of gene deletion and the Group 2 was killed 1 d before they would die (assessed by observation, between 35 and 42 d after onset of gene deletion). We focused on the major PSD proteins PSD95, the NR2B subunit of the NMDA receptor (the subunit to which CAMK2A binds), and the GluA2 subunit of the AMPA receptor. Because the proteomics results showed only minor changes in the expression of PSD-related proteins from total lysates, equal amounts of synaptosomes were used as a starting point for the PSD fraction enrichment for both groups as shown in Figure 3, *b* and *d* (Group 1: PSD95, $t_{(10)} = 0.4$, $p = 0.7$; NR2B, $t_{(10)} = 0.11$, $p = 0.91$; GluR2, $t_{(10)} = 0.03$, $p = 0.98$; Group 2: PSD95, $t_{(14)} = 0.68$, $p = 0.51$; NR2B, $t_{(14)} = 0.32$, $p = 0.75$; GluR2, $t_{(14)} = 0.35$, $p = 0.74$; two-tailed unpaired *t* test). Despite the successful deletion of both CAMK2 isoforms as seen in the synaptosome fraction and in the PSD-enriched fraction (synaptosome fraction Group 1: CAMK2A, $t_{(10)} = 13.55$, $p < 0.0001$; CAMK2B, $t_{(10)} = 7.45$, $p < 0.0001$; PSD fraction Group 1: CAMK2A, $t_{(10)} = 10.82$, $p < 0.0001$; CAMK2B, $t_{(10)} = 3.79$, $p < 0.005$; synaptosome fraction Group 2: CAMK2A, $t_{(14)} = 7.69$, $p < 0.0001$; CAMK2B, $t_{(14)} = 7.40$, $p < 0.0001$; PSD fraction Group 2: CAMK2A, $t_{(13)} = 8.37$, $p < 0.0001$; CAMK2B, $t_{(13)} = 3.59$, $p < 0.005$; one-tailed unpaired *t* test; Fig. 3*b*,*d*), no significant differences in the protein levels of any of the PSD associated proteins were found, neither at 21 d after onset of gene deletion (PSD95: $t_{(10)} = 1.58$, $p = 0.15$; NR2B: $t_{(10)} = 1.93$, $p = 0.08$; GluR2: $t_{(10)} = 0.33$, $p = 0.75$; two-tailed unpaired *t* test) nor close to death (PSD95: $t_{(13)} = 0.83$, $p = 0.42$; NR2B: $t_{(12)} = 0.37$, $p = 0.72$; GluR2: $t_{(10)} = 0.003$, $p = 0.1$; two-tailed unpaired *t* test) in the *Camk2a*$^{f/f}$;*Camk2b*$^{f/f}$;*CAG-Cre*^{ESR} group compared with the *Camk2a*$^{f/f}$;*Camk2b*$^{f/f}$ control group. Together, this suggests that, in contrast to what could be expected, acute deletion of both CAMK2 isoforms does not lead to major alterations of the PSD composition.

Adult loss of CAMK2A and CAMK2B does not cause changes in brain activity

Because it is known that downregulation of CAMK2A results in increased neuronal excitability and seizures (Butler *et al*., 1995), we assessed whether epilepsy could be the cause of death in these mice. Even though we did not observe any seizures in the *Camk2a*$^{f/f}$;*Camk2b*$^{f/f}$;*CAG-Cre*^{ESR} mice, we performed continuous EEG recordings on a subset of the mice, to monitor epileptic activity more carefully. None of the tested mice showed epileptic activity in their EEG recordings (data not shown).

To assess whether there is any decline of brain activity upon simultaneous deletion of CAMK2A and CAMK2B, the LFP was measured starting from 23 d after onset of gene deletion until 35 d after onset of gene deletion and detailed analysis of the power spectrum was performed. Power spectrum analysis on the last days of recording revealed no difference in the total power between *Camk2a*$^{f/f}$;*Camk2b*$^{f/f}$;*CAG-Cre*^{ESR} and *Camk2a*$^{f/f}$; *Camk2b*$^{f/f}$ control mice in [Somatosensory cortex (SScx), Total power: $t_{(11)} = 0.25$, $p = 0.81$; Motor cortex (M1), Total power: $t_{(11)} = 0.01$, $p = 0.99$; Fig. 4]. Also the contribution of specific frequency bands to the total power (normalized against the total power), did not reveal any differences (SScx: delta, $t_{(5.5)} = 0.59$, $p = 0.58$; theta, $t_{(11)} = 1.81$, $p = 0.10$; beta, $t_{(4.19)} = 1.66$, $p = 0.17$; gamma, $t_{(4.12)} = 1.46$, $p = 0.22$; M1: delta, $t_{(11)} = 0.60$, p =0.56; theta, $t_{(11)} = 0.24$, $p = 0.82$; beta, $t_{(11)} = 0.13$, $p = 0.90$; gamma, $t_{(11)} = 0.38$, $p = 0.71$; Fig. 4*a*,*b*). These results indicate that there is no decline in brain activity upon simultaneous deletion of CAMK2A and CAMK2B.

Loss of CAMK2A and CAMK2B completely abolishes LTP

We next tested the effect of the combined loss of CAMK2A and CAMK2B on basal synaptic transmission and LTP. Thus far, previous reports on conventional and inducible *Camk2a* and *Camk2b* single knock-out mice showed an impairment of LTP upon *Camk2* gene deletion with ~50% of residual LTP left compared with wild-type levels (Hinds *et al*., 1998; Elgersma *et al*., 2002; Borgesius *et al*., 2011; Achterberg *et al*., 2014). It is likely that the remaining fraction of LTP present in these mutant mice is provided by the remaining isoform present (CAMK2B in the case of *Camk2a* mutant mice and vice versa). To test this, we injected 8-week-old mice and chose 25 d after onset of gene deletion as the moment of kill and electrophysiological testing, corresponding to the moment when CAMK2 levels have dropped to a minimum but well before most of these mice start dying, to keep confounding effects of dying on the LTP measurements to a minimum (Fig. 5*a*). We measured basal synaptic transmission, PPF, LTP, and DHPG-induced LTD in the well-studied CA3–CA1 Schaffer collateral pathway in acute hippocampal slices. In agreement with the lack of gross brain morphology changes, *Camk2a*$^{f/f}$;*Camk2b*$^{f/f}$;*CAG-Cre*^{ESR} mice still showed normal basal synaptic transmission as fiber volley amplitude, fEPSP slope, and their ratio did not differ significantly between both *Camk2a*$^{f/f}$; *Camk2b*$^{f/f}$;*CAG-Cre*^{ESR} and *Camk2a*$^{f/f}$;*Camk2b*$^{f/f}$ mice (effect of genotype: fiber volley: $F_{(1,57)} = 0{,}53$, $p = 0.47$; fEPSP slope: $F_{(1,90)} = 0.74$, $p = 0.39$; repeated-measures ANOVA; Fig. 5*b*). Subsequently PPF was not impaired in *Camk2a*$^{f/f}$;*Camk2b*$^{f/f}$; *CAG-Cre*^{ESR} mice (effect of genotype: PPF: $F_{(1,89)} = 0.34$, $p = 0.56$; repeated-measures ANOVA; Fig. 5*c*). We then tested LTP by giving a 100 Hz tetanus and found a complete abolishment of LTP 50 min after induction in *Camk2a*$^{f/f}$;*Camk2b*$^{f/f}$;*CAG-Cre*^{ESR} mice (effect of genotype: 100 Hz LTP: $F_{(1,35)} = 19.86$, $p < 0.001$; repeated-measures ANOVA; Fig. 5*d*). We then tested a much stronger LTP induction protocol (4 trains of 200 Hz for 0.5 s, spaced 5 s apart) known to activate different pools of CAMK2 in the spines (Lee *et al*., 2009). This LTP induction protocol yields normal LTP in *Camk2b*$^{-/-}$ mice and only partially reduces LTP in *Camk2a*$^{-/-}$ mice (Borgesius *et al*., 2011). However, like in the 100 Hz LTP protocol, *Camk2a*$^{f/f}$;*Camk2b*$^{f/f}$;*CAG-Cre*^{ESR} mutants showed complete absence of LTP in the 4 X 200 Hz protocol (effect of genotype: 200 Hz LTP: $F_{(1,18)} = 27.19$, $p < 0.001$; repeated-measures ANOVA; Fig. 5*e*). To investigate whether other LTP inducing pathways were similarly affected, we tested PKA-dependent plasticity, using a 15 min wash-in of forskolin (50 µM) and rolipram (0.1 µM) in the presence of picrotoxin (50 µM) to induce cLTP. We found that also this LTP pathway was affected in the *Camk2a*$^{f/f}$;*Camk2b*$^{f/f}$;*CAG-Cre*^{ESR} mice, although considerable potentiation was still observed (effect of genotype: PKA LTP: $F_{(1,55)} = 9.75$, $p < 0.01$; repeated-measures ANOVA; Fig. 5*f*). Finally, we found no involvement of CAMK2A and CAMK2B in DHPG-induced LTD (effect of genotype: DHPG LTD: $F_{(1,20)} = 1.05$, $p = 0.32$; repeated-measures ANOVA; Fig. 5*g*). As

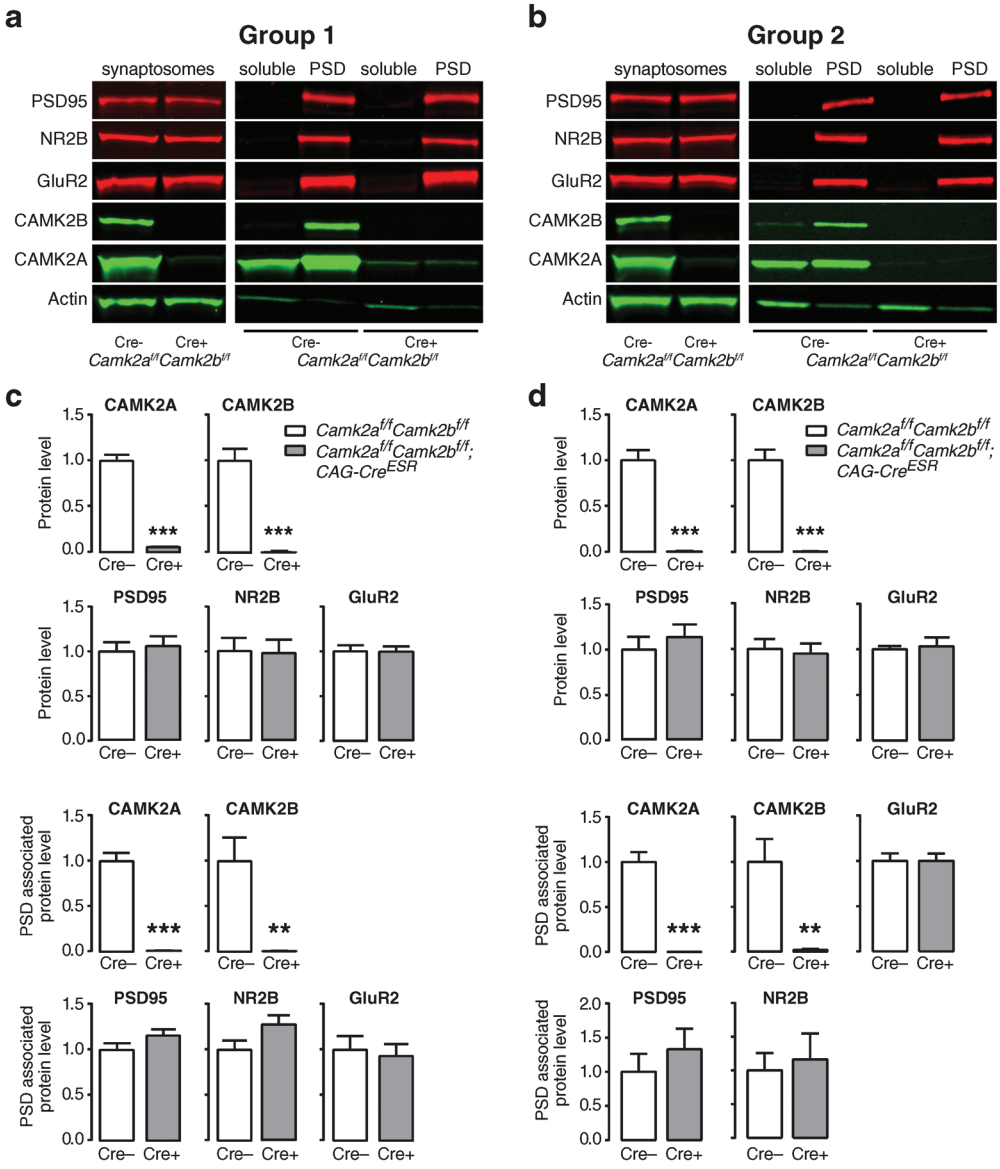

Figure 3. Adult loss of both CAMK2A and CAMK2B does not cause alterations of the postsynaptic density. ***a***, ***b***, Western blot examples of synaptosomes, soluble fraction and PSD-enriched fraction probed with common PSD proteins antibodies (PSD95, NR2B, and GluR2) of cortical lysates from *Camk2a$^{f/f}$;Camk2b$^{f/f}$;CAG-Cre^{ESR}* (***a***, $n = 6$; ***b***, $n = 6$) and *Camk2a$^{f/f}$;Camk2b$^{f/f}$* control mice (***a***, $n = 6$; ***b***, $n = 8$) killed at 21 d after gene deletion (Group 1; ***a***) or just before death (Group 2; ***b***). Actin was used as a control to show efficient enrichment in the PSD fraction of solely PSD proteins. ***c***, ***d***, Quantification of protein levels in the synaptosomes fraction (top) and in the PSD fraction (bottom). Synaptosomes show equal starting levels for both *Camk2a$^{f/f}$;Camk2b$^{f/f}$;CAG-Cre^{ESR}* and control mice for all PSD proteins. Quantification of the PSD associated fraction of PSD95, NR2B, GluR2 shows no difference between the control mice and *Camk2a$^{f/f}$;Camk2b$^{f/f}$;CAG-Cre^{ESR}* mice at either time points of analysis. Error bars indicate SEM. $^{**}p < 0.005$; $^{***}p < 0.0001$.

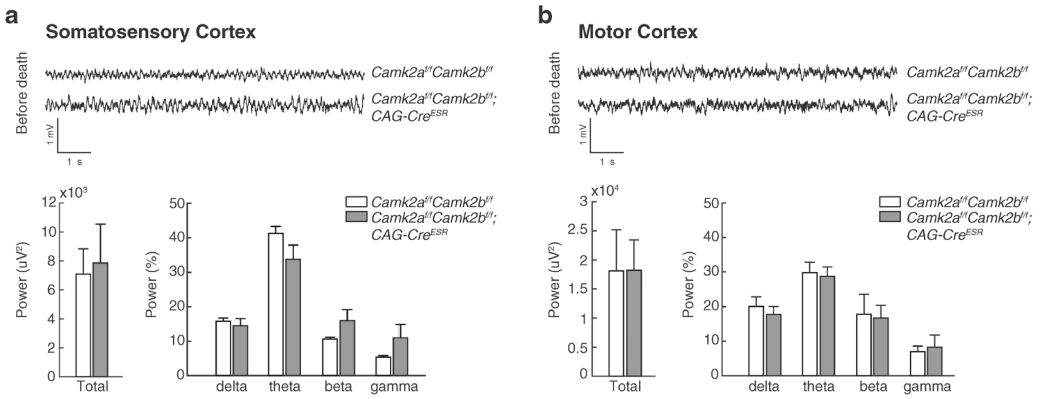

Figure 4. Power spectra analysis reveal no changes in brain activity upon deletion of both CAMK2A and CAMK2B. ***a***, Example traces of LFP recordings obtained from somatosensory cortex of *Camk2a*$^{f/f}$;*Camk2b*$^{f/f}$ control mice (top trace; n = 8) and *Camk2a*$^{f/f}$;*Camk2b*$^{f/f}$;*CAG-Cre*^{ESR} (bottom trace; n = 5) during the last day of recording (35 d after onset of gene deletion). Bar graphs depict calculated total power across the last 3d of recording (bottom left) and percentage of relative power normalized against the total power across four different frequency bands: delta (2–4 Hz), theta (5–10 Hz), beta (13–30 Hz), and gamma (30–50 Hz) (bottom right). ***b***, Example traces of LFP recordings obtained from motor cortex of *Camk2a*$^{f/f}$;*Camk2b*$^{f/f}$ control mice (top trace; n = 8) and *Camk2a*$^{f/f}$;*Camk2b*$^{f/f}$;*CAG-Cre*^{ESR} (bottom trace; n = 5) during the last day of recording (35 d after gene deletion). Bar graphs depict averaged total power across the last 3d of recording (bottom left) and percentage of relative power normalized against the total power across four different frequency bands: delta (2–4 Hz), theta (5–10 Hz), beta (13–30 Hz), and gamma (30–50 Hz) (bottom right). No differences were observed in the days preceding death in either total power or specific frequency bands. Error bars depict the SEM.

a control for the efficiency of gene deletion, we performed Western blot analysis on the acute hippocampal slices used in these experiments. As expected, the slices of *Camk2a*$^{f/f}$;*Camk2b*$^{f/f}$;*CAG-Cre*^{ESR} mice showed a clear absence of CAMK2A and CAMK2B (Fig. 5*h*).

Presynaptic CAMK2 is indispensable for CA3–CA1 LTP

CAMK2 was originally found as a presynaptic protein, involved in the phosphorylation of Synapsin I (DeLorenzo *et al*., 1979; Kennedy and Greengard, 1981; Kennedy *et al*., 1983a). Additionally, more recent literature shows involvement of CAMK2A in vesicle release and short-term presynaptic plasticity as well as a role for presynaptic CAMK2 in LTP in culture conditions (Llinás *et al*., 1985; Nichols *et al*., 1990; Chapman *et al*., 1995; Hinds *et al*., 2003; Ninan and Arancio, 2004; Lu and Hawkins, 2006; Hojjati *et al*., 2007; Jiang *et al*., 2008; Pang *et al*., 2010; Achterberg *et al*., 2014). Therefore, it is likely that loss of both presynaptic as well as postsynaptic CAMK2 contributes to the LTP deficits described above. To investigate the requirement of presynaptic CAMK2 for LTP induction, we deleted *Camk2* in the CA3 region of the hippocampus, without affecting CAMK2 expression in the other hippocampal regions, by crossing *Camk2a*$^{f/f}$;*Camk2b*$^{f/f}$ mice with a *Cre*-line in which Cre is under the control of the GRIK4 promotor (glutamate ionotropic receptor kainate type subunit 4). This gene is highly expressed in CA3 neurons, but absent in CA1 neurons (Filosa *et al*., 2009). We confirmed the specificity of this cre-line in *Camk2a*$^{f/f}$;*CA3-Cre* and *Camk2b*$^{f/f}$;*CA3-Cre* mice. These mice showed specific deletion of CAMK2A and CAMK2B in the pyramidal cells of the CA3 region of the hippocampus at the age of 8 weeks, with no deletion in other parts of the hippocampus (Fig. 6*a*). Note that the mossy fibers coming from the dentate gyrus still express CAMK2A and can now be readily observed crossing through the CA3 area. We used immunofluorescence to confirm the deletion of CAMK2B in these mice. Although confirmation of the deletion of CAMK2B is complicated by the residual expression of CAMK2B in oligodendrocytes (Waggener

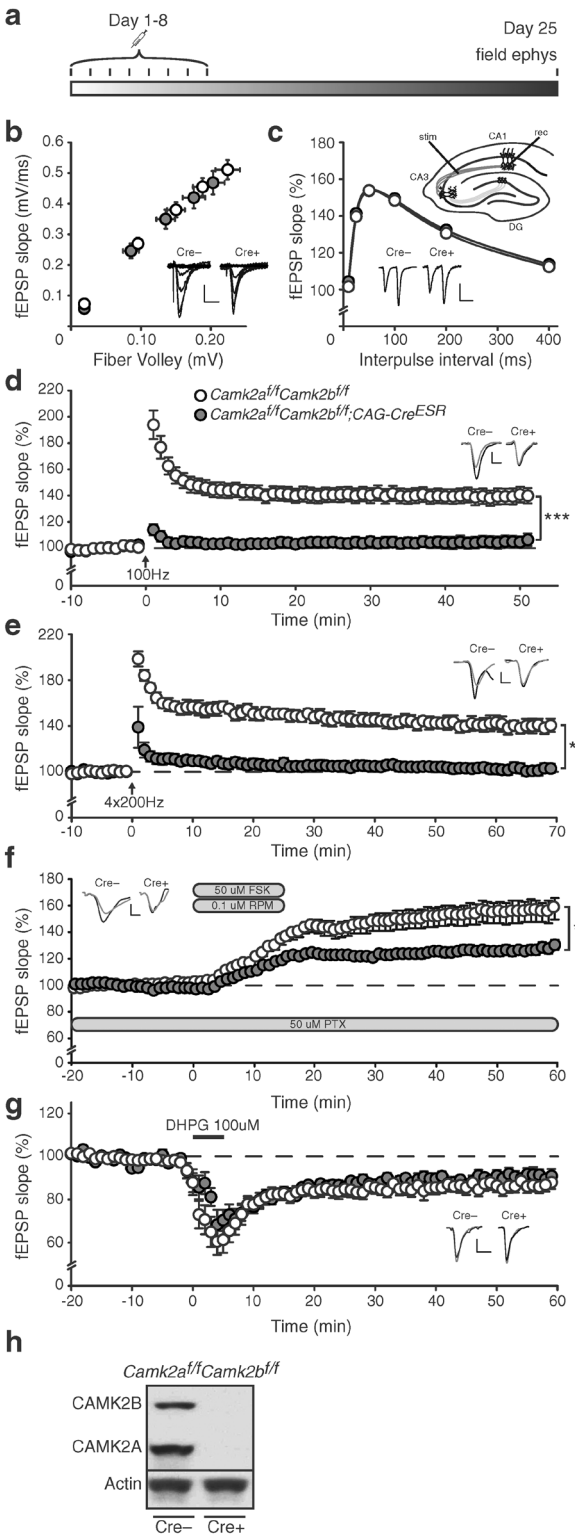

Figure 5. CAMK2Aand CAMK2B are essential for CA3–CA1 LTP. ***a***, Timeline showing the loss of CAMK2A and CAMK2B upon induction of genomic deletion with Tamoxifen injections (see Materials and Methods). Mice were killed 25 d after the first injection to conduct electrophysiological experiments. ***b***, *Camk2a$^{f/f}$;Camk2b$^{f/f}$;CAG-Cre^{ESR}* mice [fiber volley: (n = 30 from 11 mice), fEPSP slope: (n = 42 from 11 mice)] show normal basal synaptic transmission compared with *Camk2a$^{f/f}$;Camk2b$^{f/f}$* mice [fiber volley: (n = 29 from 15 mice), fEPSP slope: (n = 50 from 15 mice)]. ***c***, Inset, Schematic overview of LTP induction in the CA3–CA1 pathway (see Materials and Methods). stim, Stimulating electrode; rec, recording electrode; DG, dentate gyrus. *Camk2a$^{f/f}$;Camk2b$^{f/f}$;CAG-Cre^{ESR}* mice (n = 40 from 11 mice) show normal PPF compared with *Camk2a$^{f/f}$;Camk2b$^{f/f}$* mice (n = 51 from 15 mice). ***d***, *Camk2a$^{f/f}$;Camk2b$^{f/f}$;CAG-Cre^{ESR}* mice (n = 16 from 6 mice) show a complete loss of 100 Hz LTP compared with *Camk2a$^{f/f}$;Camk2b$^{f/f}$* mice (n = 21 from 9 mice). ***e***, *Camk2a$^{f/f}$;Camk2b$^{f/f}$;CAG-Cre^{ESR}* mice (n = 11 from 4 mice) show a complete loss of 200 Hz LTP compared with *Camk2a$^{f/f}$;Camk2b$^{f/f}$* mice (n = 9 from 5 mice). ***f***, *Camk2a$^{f/f}$;Camk2b$^{f/f}$;CAG-Cre^{ESR}* mice (n = 28 from 7 mice) show impaired forskolin/rolipram-induced (50 μM/0.1 μM) LTP compared with *Camk2a$^{f/f}$;Camk2b$^{f/f}$* mice (n = 29 from 7 mice). FSK, Forskolin; RPM, rolipram; PTX, picrotoxin. ***g***, *Camk2a$^{f/f}$;Camk2b$^{f/f}$;CAG-Cre^{ESR}* mice (n = 9 from 5 mice) show normal DHPG-induced (100 μM) LTD compared with *Camk2a$^{f/f}$;Camk2b$^{f/f}$* mice (n = 13 from 6 mice). ***h***, Western blot showing efficient loss of both CAMK2A and CAMK2B in the acute hippocampal slices of *Camk2a$^{f/f}$;Camk2b$^{f/f}$;CAG-Cre^{ESR}* mice with normal CAMK2A and CAMK2B expression in *Camk2a$^{f/f}$;Camk2b$^{f/f}$* mice. Actin levels are shown as loading control. Error bars indicate SEM. Electrophysiological example traces can be found within the figures. Scale bars: y, 0.2 mV; x, 10 ms. $^{**}p < 0.005$; $^{***}p < 0.0001$.

et al., 2013) and interneurons (Lamsa *et al*., 2007), we could still observe a decrease in fluorescence in the stratum pyramidale of the CA3 region of the hippocampus (Fig. 6*a*).

As we observed in the *Camk2a*$^{f/f}$;*Camk2b*$^{f/f}$;*CAG-Cre*^{ESR} mice, synaptic transmission and PPF were not affected in the absence of presynaptic CAMK2A and CAMK2B (effect of genotype: fiber volley: $F_{(1,39)} = 0.15$, $p = 0.70$; fEPSP: $F_{(1,39)} = 0.89$, $p = 0.35$; PPF: $F_{(1,83)} = 0.89$, $p = 0.35$; repeated-measures ANOVA; Fig. 6*b*,*c*). As different LTP induction protocols rely on different molecular pathways (Grover and Teyler, 1990; Cavus¸ and Teyler, 1996; Raymond and Redman, 2002) and are reported to differ in their dependence on presynaptic CAMK2A (Lu and Hawkins, 2006), we tested 100 Hz as well as theta burst (2 Theta; see Materials and Methods) LTP-induction protocols. Surprisingly, both the 100 Hz and theta burst LTP-inducing protocols resulted in normal LTP in *Camk2a*$^{f/f}$;*Camk2b*$^{f/f}$;*CA3-Cre* mice (effect of genotype: 100 Hz LTP: $F_{(1,32)} = 0.002$, $p = 0.96$; Theta burst LTP: $F_{(1,17)} = 0.001$, $p = 0.98$; repeated-measures ANOVA; Fig. 6*d*,*e*), indicating that presynaptic CAMK2A and CAMK2B are not required for LTP at the CA3–CA1 synapse of the hippocampus. Thus the complete loss of high-frequency stimulation (HFS) induced LTP in *Camk2a*$^{f/f}$;*Camk2b*$^{f/f}$;*CAG-Cre*^{ESR} mice is completely caused by loss of postsynaptic CAMK2.

Role of CAMK2A and CAMK2B in plasticity at the CA3–CA3 synapse

Control over gene deletion in the CA3 area of the hippocampus does not only provide a great tool for investigating a presynaptic role in the well-studied CA3–CA1 synapse, it can also be used to investigate the role of CAMK2A and CAMK2B both presynaptically and postsynaptically in the associational/commissural pathway (CA3–CA3 synapse). The CA3–CA3 synapse in the hippocampus has been widely proposed to play a pivotal role in spatial processing and previous studies have shown that LTP at this synapse is NMDA dependent (Debanne *et al*., 1998). Therefore, we examined the role of CAMK2A and CAMK2B in the properties of the CA3–CA3 synapse in our *Camk2a*$^{f/f}$;*Camk2b*$^{f/f}$;*CA3-Cre* mutant (Fig. 7*a*).

Although CA3–CA3 basal synaptic transmission and PPF were not affected in the *Camk2a*$^{f/f}$;*Camk2b*$^{f/f}$;*CA3-Cre* mice (effect of genotype: fiber volley: $F_{(1,45)} = 0.18$, $p = 0.68$; fEPSP slope: $F_{(1,49)} = 0.03$, $p = 0.87$; PPF: $F_{(1,36)} = 0.92$, $p = 0.34$, repeated-measures ANOVA; Fig. 7*b*,*c*), deletion of both CAMK2A and CAMK2B in the CA3 region of the hippocampus resulted in a significant impairment of LTP at the CA3–CA3 synapse (effect of genotype: $F_{(1,32)} = 6.89$, $p = 0.01$; repeated-measures ANOVA; Fig. 7*d*). Pyramidal neurons in the CA3 region of the hippocampus receive inputs from different pathways. The major source of inputs originates from the CA3 itself through the commissural pathway (CA3–CA3 synapse), but also the mossy fibers coming from the dentate gyrus (DG–CA3 synapse) form an important source. To distinguish between these different pathways, we used three different approaches: (1) antidromic stimulation, (2) differences in physiological characteristics of 1 Hz facilitation and PPF, and (3) differences in sensitivity to DCG-IV (see Materials and Methods). Importantly, 1 Hz stimulation did not show any facilitation [1 Hz facilitation (10th stimulus): *Camk2a*$^{f/f}$; *Camk2b*$^{f/f}$;*CA3-Cre* 106.8 ± 2.1 vs *Camk2a*$^{f/f}$;*Camk2b*$^{f/f}$ 103.8 ± 2.3; 1 Hz Facilitation (10 stimuli, data not shown): effect of genotype: $F_{(1,40)} = 1.56$, $p = 0.22$, repeated-measures ANOVA]. Furthermore, 3 μM DCG-IV reduced transmission by <20% in our experiments (81.9 ± 2.7% and 78.1 ± 3.3% transmission in the last 10 min for *Camk2a*$^{f/f}$;*Camk2b*$^{f/f}$ and *Camk2a*$^{f/f}$;*Camk2b*$^{f/f}$;*CA3-Cre*, respectively; DCG-IV: $t = 1.12$, $p = 0.27$; unpaired two tailed *t* test; Fig. 7*e*). Therefore, we are confident that we selectively stimulated CA3–CA3 connections.

Notably, the phenotype observed in the *Camk2a*$^{f/f}$;*Camk2b*$^{f/f}$;*CA3-Cre* mice appeared to be the result of the combined deletion of CAMK2A and CAMK2B and not because of absence of CAMK2A or CAMK2B alone, as the same parameters were not affected in the *Camk2a*$^{f/f}$;*CA3-Cre*

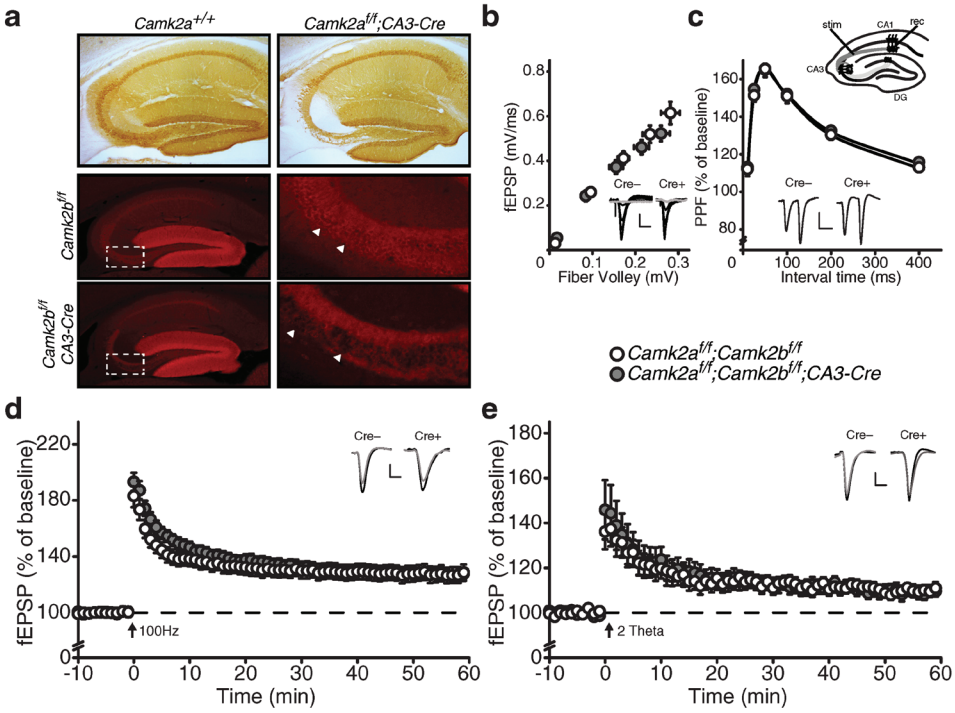

Figure 6. Presynaptic CAMK2A and CAMK2B are not necessary for CA3–CA1 LTP. ***a***, Specific deletion of CAMK2A (*Top*) and CAMK2B (middle and bottom) in the CA3 area of the hippocampus. Immunohistochemical stainings showing deletion of CAMK2A in the CA3 area in *Camk2a$^{f/f}$;CA3-Cre* mice (top right). Note the absence of CAMK2A staining in all layers of the CA3 area except for mossy fibers coming from the dentate gyrus that still express CAMK2A. Immunofluorescent images showing deletion of CAMK2B in the CA3 area in *Camk2b$^{f/f}$;CA3-Cre* mice (bottom right). Note that interneurons, oligodendrocytes, and mossy fibers coming from the dentate gyrus still express CAMK2B. The middle and bottom right pictures are enlarged images of boxed areas. Arrowheads show CA3 pyramidal cell somas in *Camk2b$^{f/f}$* mice (middle right) and absence of fluorescence in cell somas in *Camk2b$^{f/f}$;CA3-Cre* mice (bottom right). ***b***, *Camk2a$^{f/f}$;Camk2b$^{f/f}$;CA3-Cre* mice [fiber volley: (n = 19 from 6 mice), fEPSP slope: (n = 19 from 6 mice)] show normal basal synaptic transmission compared with *Camk2a$^{f/f}$;Camk2b$^{f/f}$* mice [fiber volley: (n = 22 from 6 mice), fEPSP slope: (n = 22 from 6 mice)]. ***c***, Inset, Schematic overview of LTP induction in the CA3–CA1 pathway (see Materials and Methods). stim, Stimulating electrode; rec, recording electrode; DG, dentate gyrus. *Camk2a$^{f/f}$;Camk2b$^{f/f}$;CA3-Cre* mice(n = 41 from 6 mice) show normal PPF compared with *Camk2a$^{f/f}$;Camk2b$^{f/f}$* mice(n = 44 from 6 mice). ***d***, *Camk2a$^{f/f}$;Camk2b$^{f/f}$;CA3-Cre* mice(n = 20 from 6 mice) show normal 100 Hz LTP compared with *Camk2a$^{f/f}$;Camk2b$^{f/f}$* mice (n = 14 from 6 mice). ***e***, *Camk2a$^{f/f}$;Camk2b$^{f/f}$;CA3-Cre* mice (n = 9 from 4 mice) show normal theta burst LTP compared with *Camk2a$^{f/f}$;Camk2b$^{f/f}$* mice (n = 10 from 4 mice). Error bars indicate SEM. Electrophysiological example traces can be found within the figures. Scale bars: y, 0.2 mV; x, 10 ms.

or *Camk2b$^{f/f}$;CA3-Cre* mice, in which only CAMK2A or CAMK2B is deleted from the CA3 region of the hippocampus (effect of genotype: *Camk2a$^{f/f}$;CA3-Cre* LTP: $F_{(1,43)} = 0.43$, $p = 0.52$; *Camk2b$^{f/f}$;CA3-Cre* LTP: $F_{(1,50)} = 0.004$, $p = 0.95$, repeated-measures ANOVA; Fig. 7*f*,*g*). Because we did not observe an effect in the expression level of CAMK2A in *Camk2a$^{f/f}$* animals without Cre in comparison with wild-type mice (data not shown), we used the wild-type littermate *Camk2a$^{+/+}$* mice as the control group for one of these experiments (Fig. 7*f*). Importantly, basal synaptic transmission and PPF were both not significantly different and the control experiments for mossy fiber stimulation 1 Hz facilitation and DCG-IV wash-in were all within normal range and not significantly different for both *Camk2a$^{f/f}$;CA3-Cre* and *Camk2b$^{f/f}$;CA3-Cre* mice (data not shown). Together, these data show that either CAMK2A or CAMK2B needs to be expressed

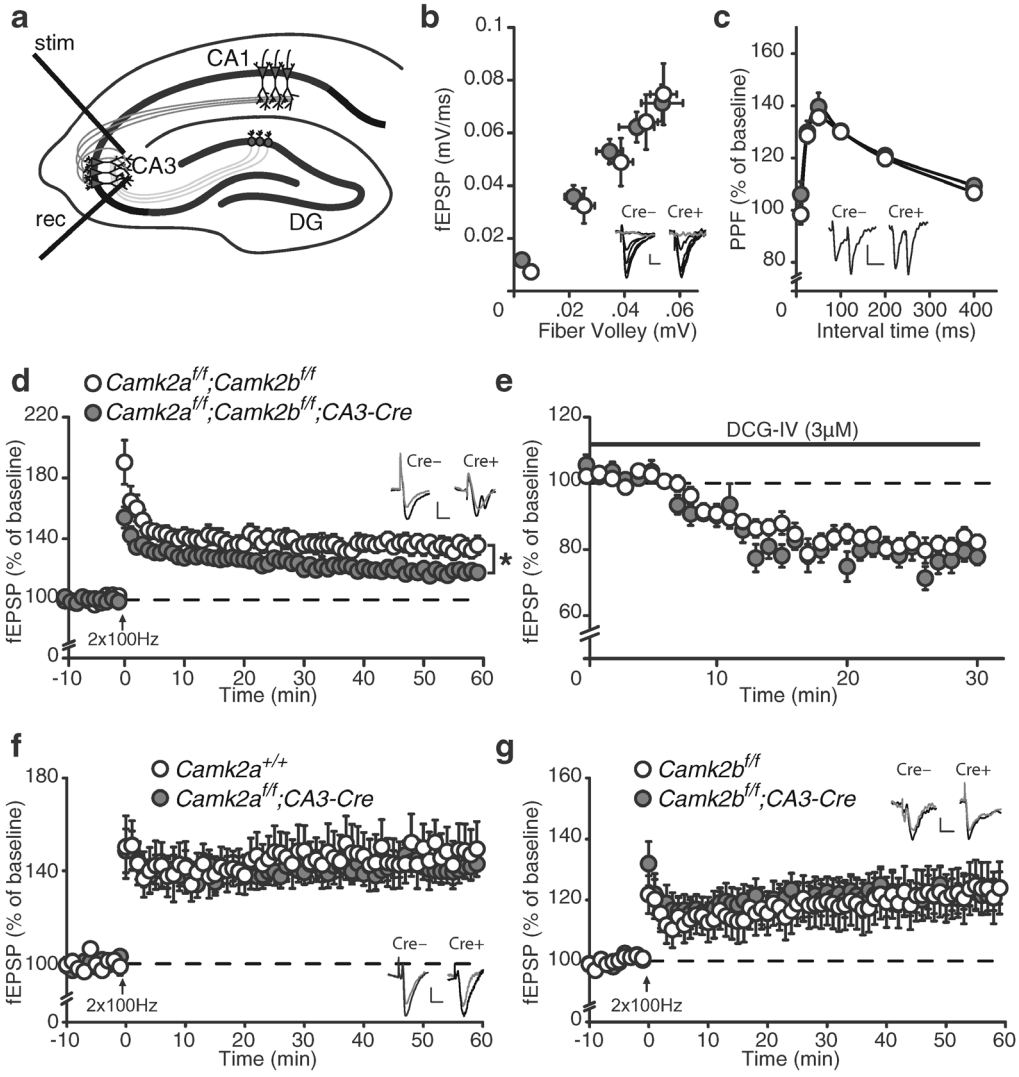

Figure 7. Redundancy of CAMK2A and CAMK2B in CA3–CA3 LTP. ***a***, Schematic overview of LTP induction in the CA3–CA3 pathway (see Materials and Methods). stim, Stimulating electrode; rec, recording electrode; DG, dentate gyrus. ***b***, *Camk2a$^{f/f}$;Camk2b$^{f/f}$;CA3-Cre* mice [fiber volley: (*n* = 27 from 4 mice), fEPSP slope: (*n* = 23 from 4 mice)] mice show normal basal synaptic transmission compared with *Camk2a$^{f/f}$;Camk2b$^{f/f}$* mice [fiber volley: (*n* = 24 from 4 mice) fEPSP slope: (*n* = 24 from 4 mice)]. ***c***, *Camk2a$^{f/f}$;Camk2b$^{f/f}$;CA3-Cre* (*n* = 17 from 4 mice) mice show normal PPF compared with *Camk2a$^{f/f}$;Camk2b$^{f/f}$* (*n* = 21 from 4 mice) mice. ***d***, *Camk2a$^{f/f}$;Camk2b$^{f/f}$;CA3-Cre* (*n* = 16 from 4 mice) show reduced 100 Hz LTP compared with *Camk2a$^{f/f}$;Camk2b$^{f/f}$* (*n* = 18 from 4 mice) mice. ***e***, DCG-IV only minimally blocks the fEPSP signal in both *Camk2a$^{f/f}$;Camk2b$^{f/f}$;CA3-Cre* (*n* = 21 from 4 mice) and *Camk2a$^{f/f}$;Camk2b$^{f/f}$* (*n* = 21 from 4 mice) mice. ***f***, *Camk2a$^{f/f}$;CA3-Cre* (*n* = 29 from 8 mice) show normal 100 Hz LTP compared with *Camk2a$^{+/+}$* (*n* = 16 from 5 mice) mice. ***g***, *Camk2b$^{f/f}$;CA3-Cre* (*n* = 28 from 8 mice) show normal 100 Hz LTP compared with *Camk2b$^{f/f}$* (*n* = 24 from 8 mice) mice. Error bars indicate SEM. Electrophysiological example traces can be found within the figures. Scale bars: *y*, 0.1 mV; *x*, 10 ms. *p = 0.01

at the CA3–CA3 synapse for normal CA3–CA3 LTP. Hence, this confirms the notion that some functions of CAMK2 cannot be uncovered using *Camk2a* or *Camk2b* single-mutants.

DISCUSSION

CAMK2A and CAMK2B are the most abundant proteins in the brain and are shown to be crucial for learning, memory, and plasticity in mice and for normal neurodevelopment in humans (Silva *et al*., 1992a, 1992b; van Woerden *et al*., 2009; Borgesius *et al*., 2011; Li *et al*., 2013; Küry *et al*., 2017b; Stephenson *et al*., 2017). Because of the high homology in their structure, we contemplated that the full spectrum of CAMK2 functions has yet to be revealed, because crucial functions can potentially be masked due to compensation by the non-deleted isoform. In this study we confirm this hypothesis with the following findings. (1) Loss of CAMK2A and CAMK2B simultaneously is lethal both during development as well as in adult mice. (2) Loss of the combined CAMK2A and CAMK2B Ca^{2+}-dependent or Ca^{2+}-independent activity is lethal. (3) Simultaneous loss of CAMK2A and CAMK2B results in complete absence of LTP at the CA3–CA1 synapse in the hippocampus. (4) Simultaneous loss of CAMK2A and CAMK2B but not of CAMK2A or CAMK2B alone results in LTP deficits at the CA3–CA3 synapse. Together these results show that there is quite some redundancy in the CAMK2A and CAMK2B isoform function, and that crucial functions of CAMK2 remain to be uncovered.

It remains to be investigated why absence or dysregulation of CAMK2 function results in lethality. CAMK2 is critical for NMDA receptor-dependent signaling, and it is known that absence of the NR1 subunit of the NMDA receptor results in neonatal death due to respiratory failure in these mice (Forrest *et al*., 1994). CAMK2 activity mediates the emergence and maintenance of synchronous activity in the pre-Bötzinger complex, a center in the brainstem important for respiratory motor output (Mironov, 2013). Thus respiratory distress could underlie the lethality seen in the $Camk2a^{-/-}$;$Camk2b^{-/-}$ mutants. Also NR2B-null mutants are not viable (Kutsuwada *et al*., 1996), which is because of a defect in the suckling response. Indeed lethality was rescued when the pups were hand-fed (Kutsuwada *et al*., 1996). We do not think that a similar mechanism underlies the lethality seen in our mice, because all pups had milk in their stomach just before they died. Moreover, when looking at the catalytically and autonomously inactive mutants ($Camk2a^{T305D/T305D}$;$Camk2b^{A303R/A303R}$ and $Camk2a^{T286A/T286A}$;$Camk2b^{T287A/T287A}$, respectively) it seems unlikely that either feeding or breathing deficits are the cause of death, because some of these mice survive until P17 or later. These findings also indicate that enzymatic activity of CAMK2 is dispensable in the first 2 weeks after birth and that the survival of these mice depends solely on the presence of CAMK2, pointing out an essential structural role of CAMK2. Interestingly, during the early postnatal period, LTP is dependent on PKA, but not on CAMK2 and this switches ~P9 (Yasuda *et al*., 2003), further supporting the lack of need of the enzymatic activity of CAMK2 during this early postnatal period. Our results further indicate that loss of CAMK2B is less tolerated than loss of CAMK2A, because the mice that were heterozygous for CAMK2A (knock-out or point mutant) and homozygous for CAMK2B died earlier than mice carrying a homozygous CAMK2A mutation and heterozygous CAMK2B mutation. This could be caused by the earlier onset of expression of CAMK2B, ~E12.5, compared with CAMK2A, which starts to be expressed ~P1 (Bayer *et al*., 1999).

Although homozygous loss of CAMK2A and CAMK2B resulted in death, it is surprising how little biochemical, morphological and electrophysiological phenotypes we observed in these double-mutants: (1) we observed no gross brain morphology differences. This is similar to the NR1- or the NR2B-null mutants (Forrest *et al*., 1994; Kutsuwada *et al*., 1996), and is

consistent with the finding that the anatomical development of the brain does not need CAMK2-NMDA receptor-dependent plasticity or functional synapses (Sando *et al*., 2017; Sigler *et al*., 2017). (2) Although proteomic analysis indicated that simultaneous deletion of CAMK2A and CAMK2B did result in the upregulation or downregulation of a few PSD-associated proteins, we did not observe significant changes in the biochemical composition of the PSD. These findings indicate that presence of CAMK2 is not necessary for maintaining the PSD composition, which is a surprising finding given that it is generally believed that CAMK2 plays a critical role in the structural organization of the PSD (for review, see Hell, 2014). Future experiments are needed to investigate the structural integrity of the PSD in these mutants. (3) Total brain activity as measured with LFP recordings, remained unchanged, even close to death. This indicates that CAMK2 does not play a role in the background oscillatory activity present in the brain. (4) We did not observe changes in basal synaptic transmission, which we will discuss further.

The complete loss of HFS-induced LTP upon deletion of both CAMK2A and CAMK2B is not surprising considering the impairments both *Camk2a*$^{-/-}$ (Hinds *et al*., 1998; Elgersma *et al*., 2002) and *Camk2b*$^{-/-}$ (Borgesius *et al*., 2011) mice show in this kind of LTP. The complete loss of LTP in *Camk2a*$^{f/f}$*;Camk2b*$^{f/f}$*;CAG-Cre*^{ESR} mice suggests that the residual LTP left in the single knock-out mice is mediated by the remaining isoform. Indeed a recent study confirms the lack of a CAMK2-independent form of NMDA receptor-dependent LTP (Incontro *et al*., 2018). This is further strengthened by the observation that single amino acid mutations in *Camk2a* mutant mice such as *Camk2a*^{T286A} (Giese *et al*., 1998) and *Camk2a*^{T305D} (Elgersma *et al*., 2002) have more detrimental effects on LTP than the loss of the *Camk2a* isoform as a whole. This could well be explained by the dominant-negative effects of these *Camk2a* point mutations on the proper functioning of the heteromeric CAMK2A-CAMK2B holoenzyme.

In contrast to impaired LTP, basal synaptic transmission and PPF in the CA3–CA1 area were unaffected in absence of both CAMK2A and CAMK2B. Given the abundance of CAMK2 in synapses both presynaptically and postsynaptically and its major role in AMPA phosphorylation, GluN2B binding and AMPA insertion (for review, see Lisman *et al*., 2012), these findings were unexpected. However, these findings are in line with the observation that the PSD composition seems to be largely unaffected by the absence of CAMK2. Hence, synaptic strength in the CA3–CA1 synapse can be maintained independently of the presence of CAMK2A and CAMK2B. These findings are in contrast to a recent study that found a role for CAMK2A, but not CAMK2B, in basal synaptic strength in a subset of neurons (Incontro *et al*., 2018). Using CRISPR/Cas9 in slices and *in utero* electroporation to induce sparse deletion of CAMK2, these authors found that basal AMPA receptor- and NMDA receptor-dependent synaptic transmission requires CAMK2A, but not CAMK2B, that CAMK2A signaling is critically dependent on its binding to the NMDA receptor. Possibly, the discrepancy between our findings and theirs is explained by the different approaches. Targeting a subset of neurons, as done by Incontro *et al*. (2018), could induce a transcellular competitive process, which is absent in our global knock-out mutants.

Forskolin-induced LTP has been shown to be primarily PKA-dependent (Sokolova *et al*., 2006), but also NMDA-dependent components have been described (Otmakhov *et al*., 2004). Thus the impairment seen in cLTP in our *Camk2a*$^{f/f}$*;Camk2b*$^{f/f}$*;CAG-Cre*^{ESR} could be caused by the selective loss of the NMDA (CAMK2)-dependent pathway while leaving the PKA-dependent pathway intact.

The finding that presynaptic CAMK2 is dispensable for LTP at the CA3–CA1 synapse is surprising, considering that CAMK2 was first discovered as a presynaptic protein (DeLorenzo *et al*., 1979; Kennedy and Greengard, 1981; Kennedy *et al*., 1983a). Indeed, CAMK2A has long been shown to play a role in presynaptic plasticity and regulation of neurotransmitter release

at the CA3–CA1 synapse in brain slices (Llinás *et al*., 1985; Nichols *et al*., 1990; Chapman *et al*., 1995; Hinds *et al*., 2003; Hojjati *et al*., 2007; Jiang *et al*., 2008; Pang *et al*., 2010; Achterberg *et al*., 2014). Additionally, a previous study reported a role for presynaptic CAMK2 in LTP in dissociated hippocampal neurons (Ninan and Arancio, 2004). In this study, the role of presynaptic CAMK2 was assessed using different CAMK2 inhibitors, which when applied resulted in reduced LTP. Thus, in light of these studies, we expected to find a requirement for presynaptic CAMK2A and CAMK2B in synaptic transmission and LTP at the CA3–CA1 synapse. However, we found that presynaptic CAMK2 is completely indispensable for LTP at the Schaffer collateral pathway. There are a few reasons to explain the discordance between literature and our findings. First, in our model CAMK2 is already absent from as early as P5. We cannot exclude that the lack of effect in our experiments is because of presynaptic compensatory mechanisms during this phase of development. Second, to study the role of presynaptic CAMK2 in LTP in hippocampal cultures, CAMK2 inhibitors were used to block presynaptic CAMK2 activity. These are general CAMK2 blockers, blocking not only CAMK2A or CAMK2B, but also CAMK2D and CAMK2G. It could be that in our experiments CAMK2D and CAMK2G are compensating for the absence of CAMK2A and CAMK2B. Indeed, evidence for a neuronal role for CAMK2G is emerging (Ma *et al*., 2014; Cohen *et al*., 2018; Proietti Onori *et al*., 2018). Together, it is clear that complete understanding of the precise role of presynaptic CAMK2 at the CA3–CA1 Schaffer collateral syn- apse is still lacking.

CA3–CA3 LTP shares many characteristics with Schaffer collateral (CA3–CA1) LTP. Most notably, both CA3–CA3 and CA3–CA1 LTP depend on NMDA receptor activation and a postsynaptic rise in Ca^{2+} (Bradler and Barrionuevo, 1990; Zalutsky and Nicoll, 1990; Debanne *et al*., 1998, 1999; Bains *et al*., 1999; Smith and Swann, 1999; Pavlidis *et al*., 2000; Kakegawa *et al*., 2004). We show here that CA3–CA3 LTP is impaired when deleting both CAMK2A and CAMK2B, but not upon deletion of either CAMK2A or CAMK2B, indicating that one of the two CAMK2 isoforms needs to be present to support normal LTP. These results are in agreement with a previous study using a pharmacological approach, which described a presynaptic and postsynaptic role for CAMK2 in LTP at the CA3–CA3 synapse (Lu and Hawkins, 2006). Using a CAMK2 synthetic peptide (281–309) CAMK2 inhibitor, on organotypic slice cultures the authors saw a decrease of 50% in theta burst LTP when CAMK2 was blocked presynaptically or postsynaptically. This inhibitor does not distinguish between the four different CAMK2 isoforms, leaving open the question which CAMK2 isoform is responsible for the LTP deficit. Here we showed that the loss of either CAMK2A or CAMK2B isoform does not affect LTP, but that only the simultaneous absence of both CAMK2A and CAMK2B causes a CA3–CA3 LTP deficit. Interestingly, whereas CA3–CA1 LTP is completely abolished in absence of CAMK2, CA3–CA3 LTP is only reduced indicating that there are some fundamental differences underlying CA3–CA1 LTP compared with CA3–CA3 LTP.

Together, our results show that despite our vast knowledge about CAMK2, there are many aspects of CAMK2 function that remain to be uncovered.

"The most beautiful protein in the world"
Geeske van Woerden

Chapter III

De novo mutations in protein kinase genes *CAMK2A* and *CAMK2B* cause intellectual disability

Sébastien Küry,* Geeske M. van Woerden,* Thomas Besnard,* Martina Proietti Onori, ..., Stéphane Bézieau, Sylvie Odent, Ype Elgersma, and Sandra Mercier

*These authors contributed equally

(for the full list of authors see **page 82)**

Published in Am J Hum Genet. 2017 Nov 2;101(5):768-788

ABSTRACT

Calcium/calmodulin-dependent protein kinase II (CAMK2) is one of the first proteins shown to be essential for normal learning and synaptic plasticity in mice, but its requirement for human brain development has not yet been established. Through a multi-center collaborative study based on a whole-exome sequencing approach, we identified 19 exceedingly rare *de novo CAMK2A* or *CAMK2B* variants in 24 unrelated individuals with intellectual disability. Variants were assessed for their effect on CAMK2 function and on neuronal migration. For both *CAMK2A* and *CAMK2B*, we identified mutations that decreased or increased CAMK2 auto-phosphorylation at Thr286/Thr287. We further found that all mutations affecting auto-phosphorylation also affected neuronal migration, highlighting the importance of tightly regulated CAMK2 auto-phosphorylation in neuronal function and neurodevelopment. Our data establish the importance of *CAMK2A* and *CAMK2B* and their auto-phosphorylation in human brain function and expand the phenotypic spectrum of the disorders caused by variants in key players of the glutamatergic signaling pathway.

INTRODUCTION

Modification of synaptic strength, i.e., synaptic plasticity, is a cornerstone in human capacity to adapt to environmental change. The ability of synapses to modulate their strength is critical for learning and memory processes (Grant and Silva, 1994). Both strengthening (known as long-term potentiation [LTP]) and weakening (known as long-term depression [LTD]) of synaptic transmission have been shown to contribute to distinct types of learning and long-term memory (Malenka and Bear, 2004; Lisman *et al*., 2012; Buffington *et al*., 2014; Fan *et al*., 2014). Abnormal synaptic plasticity is a well-recognized cause of numerous neurological and psychiatric disorders (Bliss *et al*., 2013), as exemplified by dysfunctional ionotropic glutamate receptor signaling, notably a-amino-3-hydroxy-5-methyl-4-isoxazole propionic acid receptors (AMPAR) and N-methyl-D-aspartate receptor (NMDAR) signaling (Lau and Zukin, 2007; Mony *et al*., 2009; Traynelis *et al*., 2010; Zhang and Abdullah, 2013; Barkus *et al*., 2014). For example, pathogenic variants in AMPAR genes *GRIA3* (MIM: 305915) (GluA3, associated with mental retardation, X-linked 94 [MIM: 305915]) (Wu *et al*., 2007; Philips *et al*., 2014) and *CACNG2* (MIM: 602911) (stargazin, associated with mental retardation, autosomal-dominant 10 [MIM: 614256]) (Hamdan *et al*., 2011), and in genes of NMDAR subunits *GRIN1* (MIM: 138249) (GluN1, associated with mental retardation, autosomal-dominant 8 [MIM: 614254]), *GRIN2A* (MIM: 138253) (GluN2A, associated with focal epilepsy, with speech disorder, and with or without mental retardation [MIM: 245570]), *GRIN2B* (MIM: 138252) (GluN2B, associated with early infantile epileptic encephalopathy, 27 [MIM: 616139] and mental retardation, autosomal-dominant 6 [MIM: 613970]), and *GRIN2D* (MIM: 602717) (GluN2D, associated with epileptic encephalopathy, early infantile, 46 [MIM: 617162]) (Hamdan *et al*., 2011; Carvill *et al*., 2013; Lemke *et al*., 2013; Lesca *et al*., 2013; Endele *et al*., 2014; Li *et al*., 2016) are a cause of neurodevelopmental disorders.

Another major regulator of synaptic plasticity is the calcium/calmodulin (Ca^{2+}/CaM)-dependent serine/threonine protein kinase CAMK2, whose activation is necessary and sufficient for hippocampal LTP induction (Lisman *et al*., 2002). In the hippocampus, CAMK2 forms a dodecameric holoenzyme that is mainly composed of its two predominant subunits, alpha (CAMK2A) and beta (CAMK2B), which together represent 2% of the total hippocampal protein content (Erondu and Kennedy, 1985). The CAMK2A and CAMK2B subunits share a very high degree of homology and consist of four distinct domains: a catalytic domain

containing the active site required for CAMK2 kinase activity, a regulatory domain comprising the Ca^{2+}-CaM binding site (including the auto-inhibitory sub-domain of the Thr286/Thr287 phosphorylation site required for autonomous [Ca^{2+}-independent] activity), a variable domain, i.e., the domain in which CAMK2A and CAMK2B show the largest difference, and an association domain necessary for assembly of the (mixed) holoenzyme with 10–12 CAMK2 subunits (Lisman *et al*., 2002; Colbran, 2004; Kim *et al*., 2016). Subunits combine mainly to form CAMK2A homomers or CAMK2A-CAMK2B heteromers (Lisman *et al*., 2012).

CAMK2 contributes in various ways to synaptic plasticity, but most critical is its regulation of ionotropic glutamate receptors. In particular, CAMK2 binding to the NMDAR and its ability to regulate the membrane insertion and activity of AMPAR are crucial for regulating synaptic strength (Lisman *et al*., 2012; Hoffman *et al*., 2013; Paoletti *et al*., 2013; Kim *et al*., 2016). This process is triggered by Ca^{2+} entry through the NMDAR, resulting in Ca^{2+}/CaM binding to the CAMK2 regulatory domain (Kim *et al*., 2016). Subsequent auto-phosphorylation of amino acid residue Thr286 in the inhibitory domain of the α-subunit isoform (or Thr287 in the β-subunit isoform) of CAMK2 allows the enzyme to maintain its activated conformation, thereby effectively converting a very brief Ca^{2+} signal into a long-lasting enzymatic change. Activated CAMK2 translocates from the dendritic shaft to post synaptic densities (PSDs) of dendritic spines, where it binds to NMDAR (GluN1, 2A and 2B) and enhances the insertion and function of AMPAR GluA1 (*GRIA1* [MIM: 138248]), stargazin, and SAP97 (*DLG1* [MIM: 601014]) (Kim *et al*., 2016) in the PSD. The importance of these events is highlighted by the observation that *Camk2* knock-in mice with mutations interfering with CaM binding, or silencing the autonomous or kinetic activity of the protein, result in profound learning and plasticity deficits (Giese *et al*., 1998; Elgersma *et al*., 2002; Yamagata *et al*., 2009).

Paradoxically, although the *Camk2a* knock-out was the first murine knock-out in the field of neuroscience to establish a critical role for NMDA receptor-mediated Ca^{2+} signaling in learning and synaptic plasticity (Silva *et al*., 1992a, 1992b), the importance of *CAMK2A* (MIM: 114078) for cognitive function has not yet been established. Similarly, *Camk2b* has been shown to be important for learning and synaptic plasticity in mice (van Woerden *et al*., 2009; Borgesius *et al*., 2011) but mutations in *CAMK2B* (MIM: 607707) have not yet been described. In the present study, we report 19 rare variants in *CAMK2A* or *CAMK2B* in 24 unrelated individuals with intellectual disability (ID), with 23 individuals shown to have *de novo* occurrence of the variants. We also provide evidence that most of these alterations of CAMK2 are likely to affect protein and neuronal function.

METHODS

Inclusion of the Individuals and Connection between the Participating Studies

The 24 affected individuals selected in the present study were enrolled together with their healthy parents in 14 different programs or centers investigating the molecular basis of developmental disorders in a research or clinical setting: (1) the Baylor Genetics (BG) Laboratories (Houston, TX, USA; individuals 1 and 16), (2) the Western France consortium HUGODIMS (Projet inter-régional Français des Hôpitaux Universitaires du Grand Ouest pour l'exploration par approche exomique des causes moléculaires de Déficience Intellectuelle isolée ou syndromique Modérée à Sévère; individuals 2 and 7), (3) the Wellcome Trust Sanger Institute British program Deciphering Developmental Disorders (DDD, UK; individuals 3, 14, 18, and 21), (4) the University Medical Center Utrecht (the Netherlands; individuals 4 and 12), (5) the Simons Simplex Collection (SSC) (USA; individuals 5 and 6), (6) the University Hospital Center (CHU) of Lyon (France; individual 8), (7) Leiden University Medical Center

(the Netherlands; individual 9), (8) the Children's Hospital of Philadelphia (USA; individual 10), (9) the Institute of Human Genetics, University Hospital Heidelberg (Germany; individual 11), (10) the Arkansas Children's Hospital, St. Louis Children's Hospital, and Seattle Children's Hospital via GeneDx laboratory (USA; individuals 13, 15, 19, and 22), (10) the Boston Children's Hospital (USA; individual 17), (11) the Undiagnosed Diseases Network (UDN) through the Boston Children's Hospital and Harvard Clinical Site and BG laboratories sequencing site (USA; individual 20), (13) the University of Illinois College of Medicine at Peoria via Ambry Genetics (USA; individual 23), and (14) the Telemark Hospital Trust in Skien (Norway; individual 24). Connecting the 14 centers was facilitated by the web-based tools GeneMatcher (Sobreira *et al*., 2015) and DECIPHER (Firth *et al*., 2009).

In each participating center, clinical assessment was performed by at least one expert clinical geneticist. Routine clinical genetic and metabolic screenings performed during initial workup was negative in each case, which warranted further investigation on a research basis. All families gave written informed consent for inclusion in the study and consent for the publication of photographs was obtained for individuals 3, 7, 15, 16, 17, 22, and 23. The study has been approved by the CHU de Nantes-ethics committee (number CCTIRS: 14.556).

Whole-Exome Sequencing Strategy

Except BG Laboratories, which performed clinical singleton exome sequencing as a first-tier molecular test in individuals 1 and 16, all other centers followed a trio-based approach. Most of the methods used by the centers were detailed previously: HUGODIMS program focused on intellectual disabilities (ID) in 76 trios from simplex families (Isidor *et al*., 2016), DDD analyzed more than 4,293 children with severe developmental disorders and their parents (Deciphering Developmental Disorders, 2017), SSC parsed data from 2,508 trios with an autism spectrum disorder (Iossifov *et al*., 2014), GeneDx laboratory analyzed 11,388 case subjects with ID or developmental disorder (DD) with 8,897 of them being sequenced with both parents and following the method described previously (Retterer *et al*., 2016), the Boston Children's Hospital analyzed more than 300 trios including 50 trios with developmental disabilities (Brownstein *et al*., 2016), the Children's Hospital of Philadelphia sequenced 400 whole exomes (323 trios) including 138 trios with developmental delay that were analyzed according to the method described previously (Nesbitt *et al*., 2015), Ambry Genetics sequenced 2,583 parent-proband trios where the child had childhood-onset neurological disorder applying the strategy described earlier (Farwell *et al*., 2015), the University Medical Center Utrecht analyzed the exomes of more than 500 parent-proband trios that were negative after analyzing the gene panel for intellectual disability (~800 known ID genes) (Hempel *et al*., 2015), the Telemark Hospital Trust in Skien analyzed 531 exomes including 99 trios (Holla *et al*., 2015), Leiden University Medical Center tested 825 exomes including 579 trios with a child presenting ID following a strategy described previously (Santen *et al*., 2012), BG Laboratories queried its internal database of ~5,900 clinical exomes including about 100 trios regarding *CAMK2A* and ~6,400 clinical exomes including about 200 trios regarding *CAMK2B*, which comprised UDN exomes and had been analyzed following clinical diagnostics protocol defined previously (Bainbridge *et al*., 2011; Yang *et al*., 2013), and the Institute of Human Genetics, Heidelberg, analyzed trios from 57 families with 63 probands with (neuro) developmental disorders as previously described (Evers *et al*., 2017).

The CHU of Lyon included individual 8 in a cohort of children with typical or atypical Rolandic epilepsy. This last one is among the most common epileptic syndromes in childhood and may be associated with cognitive impairment or autistic features in a subset of affected children. Individual 8 was recruited in the Department of Epilepsy, Sleep and Pediatric

Neurophysiology, at the Lyon University Hospital. The IRB approval number was 05/78, CPP Strasbourg Alsace 1. Exome sequencing was performed with a trio design (in blood DNA from the affected individual and his parents) using in-solution exome capture kits (Sure Select Human All exome 50MB kit, Agilent Technology, or Illumina TruSeq exome Enrichment, Illumina) and Illumina HiSeq sequencing platforms (Illumina) to generate paired end reads sequences (Centre National de Genotypage [CNG], Évry, France).

Following their respective analysis pipelines, participating centers generated a list of candidate variants filtered against public database variants and according to modes of inheritance. Save for families from BG in which *de novo* events in *CAMK2A* and *CAMK2B* were sought post hoc, all other variants reported in the present study were determined independently by participating centers. Candidate variants were confirmed by Sanger capillary sequencing for all but individuals 4, 9, 18, and 21.

Transfection Constructs

The cDNA sequences from human *CAMK2A*^{WT} (GenBank: NM_015981.3) and *CAMK2B*^{WT} (GenBank: NM_001220.4) were obtained from a human brain cDNA library by PCR (Phusion high fidelity, Thermo Fisher) using the following primers: for *CAMK2A* Fw 5′-GAATCCGGCGCGCCACCATGGCCACCATCACCTGCAC-3′ and Rev 5′-GGATTCTTAATTAATCAGTGGGGCAGGACGGAGG-3′; for *CAMK2B* Fw 5′-GAATCCGGCGCGCCACCATGGCCACCACGGTGACCTG-3′ and Rev 5′-GGATTCTTAATTAATCACTGCAGCGGGGCCACAG-3′ and they were cloned into our dual promoter expression vector (Figure S5). The dual promoter expression vector was generated from the pCMV-*tdTomato* vector (Clontech), where the *CMV* promoter was replaced with a *CAGG* promoter followed by a multiple cloning site (MCS) and transcription terminator sequence. To assure expression of the tdTOMATO independent from the gene of interest, a PGK promoter was inserted in front of the *tdTomato* sequence. For all the *in vivo* and *in vitro* experiments, the vector without a gene inserted in the MCS was taken along as control (control vector). The different point mutations were introduced with site-directed Mutagenesis (Invitrogen for *CAMK2A*-c.327G>C, *CAMK2A*-c.845A>G, *CAMK2B*-c.328G>A and NEB Q5 Site-Directed Mutagenesis Kit for others) using the following primers: *CAMK2A*-c.293T>C (p.Phe98Ser), Fw 5'-GGGGAACTGTcTGAA GATATCG-3' and Rev 5'-ACCAGTGACCAGGTCGAA-3'; *CAM K2A*-c.327G>C (p.Glu109Asp), Fw 5'-GGAGTATTACAGTGACGCGGATGCCAGTCAC-3' and Rev 5'-GTGACTGGCATCCGCGTCACTGTAATACTCC-3'; *CAMK2A*-c.412C>G (p.Pro138Ala), Fw 5'-GGACCTGAAGgCTGAGAATCTGTTG-3' and Rev 5'-CGGTGCACCACCCCCATC-3'; *CAMK2A*-c.548A>T (p.Glu183Val), Fw 5'-CTCTCCCCAGtAGTGCTGCGG-3' and Rev 5'-ATATCCAGGAGTCCCTGCAAAC-3'; *CAMK2A*-c.635C>T (p.Pro212Leu), Fw 5'-GGGTACCCCCtGTTCTGGGAT-3' and Rev 5'-AACCAGCAGGATGTACAGG-3'; *CAMK2A*-c.704C>T (p.Pro235Leu), Fw 5' TTCCCATCGCtGGAATGGGAC-3' and Rev 5'-ATCATAGGCGCCGGCTTT-3'; *CAMK2A*-c.845A>G (p.His282Arg), Fw 5'-GG CATCCTGCATGCGCAGACAGGAGACCG-3' and Rev 5'-CGGTCTCCTGTCTGCGCATGCAGGATGCC-3'; *CAMK2A*-c.856A>C (p.Thr286Pro), Fw 5'-CAGACAGGAGcCCGTGGACTG-3' and Rev 5'-TGCATGCAGGATGCCACG-3'; *CAMK2B*-c.328G>A (p.Glu110Lys), Fw 5'-GAGAGAGTACTACAGCAAGGCTGATGCCAGTCA-3' and Rev 5'-TGACTGGCATCAGCCTTGCTGTAGTACTCTCTC-3'; *CAMK2B*-c.416C>T (p.Pro139Leu), Fw 5'-GACCTCAAGCtGGAGAACCTG-3' and Rev 5'-TCTGTGGACGACCCCCAT-3'; *CAMK2B*-c.709G>A (p.Glu237Lys), Fw 5'-CCCGTCCCCTaAGTGGGACAC-3' and Rev 5'-AAGTCATAGGCACCAGCC-3'; *CAMK2B*-c.901A>G (p.Lys301Glu), Fw 5'-GAGAAAGCTCgAGGGAGCCATC-3' and Rev 5'-CTGGCATTGAACTTTTTCAGAC-3'. For the control mutations of *CAMK2A*, the different point mutations were introduced with site-

directed Mutagenesis (Invitrogen) using the following primers: *CAMK2A*-c.125,126AG>GA (p.Lys42Arg), Fw 5'-GGCCAGGAGTATGCTGCCAGAATCATCAACACAAAGAAGC-3' and Rev 5'-GCTTCTTTGTGTTGATGATTCTGGCAGCATACTCCTGGCC-3'; *CAMK2A*-c.856-858ACC>GCT (p.Thr286Ala),Fw5'-ATCGCTATGATGCATAGACAGGAGGCTGTGGACTGCCTGAAGAAGTTCAAT-3' and Rev 5'-AGTGTGATGCATGCAGGATGCCACGGTGGAGCGGTGCGAGAT-3'; *CAMK2A*-c.856,857AC>GA (p.Thr286Asp), Fw 5'-ATCGCTATGATGCATAGACAGGAGGACGTGGACTGCCTGAAGAAGTTCAAT-3' and Rev 5'-AGTGTGATGCATGCAGGATGCCACGGTGGAGCGGTGCGA-3'.

shRNA constructs were obtained from the MISSION shRNA library for mouse genomes of Sigma Life Sciences and The RNAi Consortium (TRC). For knockdown of CAMK2A we had five different shRNA plasmids, each with a different target sequence: (1) GCGTTCAGTTAATGGAATCTT, (2) CCTGGACTTTCATCGATTCTA, (3) CGCAAACAGGAAATTATCAAA, (4) GCTGATCGAAGCCATAAGCAA, and (5) GTGTTGCTAACCCTCTACTTT. For knockdown of CAMK2B, we had five different shRNA plasmids, each with a different target sequence: (1) CCACCTTGTTATCTCCACAAA, (2) GTACCATCTATACGAGGATAT, (3) CCTGCTGAAGCATTCCAACAT, (4) GACTGTGGAATGTCTGAAGAA, and (5) CTGACCTCATTTGAGCCTGAA. The control shRNA plasmid is the MISSION non-target shRNA control vector: CAACAAGATGAAGAGCACCAA.

Mice

For the neuronal cultures, FvB/NHsD females were crossed with FvB/NHsD males (both ordered at 8–10 weeks old from Envigo). For the *in utero* electroporation, FvB/NHsD (Envigo) females were crossed with C57Bl6/J males (ordered at 8–10 weeks old from Charles River). All mice were kept group-housed in IVC cages (Sealsafe 1145T, Tecniplast) with bedding material (Lignocel BK 8/15 from Rettenmayer) on a 12/12 hr light/dark cycle in 21˚C (51˚C), humidity at 40%–70% and with food pellets (801727CRM(P) from Special Dietary Service) and water available *ad libitum*. All animal experiments were approved by the Local Animal Experimentation Ethical Committee, in accordance with Institutional Animal Care and Use Committee guidelines.

Cell Culture and Analysis of Protein Stability in Transfected Cells

HEK293T Cell Transfections

We used Thr286/Thr287 auto-phosphorylation as a readout of kinase function. To test the expression vector with the *CAMK2* constructs and to measure the phosphorylation levels of CAMK2, we used a cell line that is easy to transfect and culture, so we chose HEK293T cells. These cells were mycoplasma-free and authenticated (293T-ATCC CRL-3216). HEK293T cells were cultured in DMEM/10% Fetal Calf Serum (FCS)/1% penicillin/streptomycin in 6-well plates and transfected when 50% confluent with the following DNA constructs: control vector, $CAMK2A^{WT}$, $CAMK2A^{p.(Phe98Ser)}$, $CAMK2A^{p.(Glu109Asp)}$, $CAMK2A^{p.(Pro138Ala)}$, $CAMK2A^{p.(Glu183Val)}$, $CAMK2A^{p.(Pro212Leu)}$, $CAMK2A^{p.(Pro235Leu)}$, $CAMK2A^{p.(His282Arg)}$, $CAMK2A^{p.(Thr286Pro)}$ and $CAMK2B^{WT}$, $CAMK2B^{p.(Glu110Lys)}$, $CAMK2B^{p.(Pro139Leu)}$ and $CAMK2B^{p.(Glu237Lys)}$, and $CAMK2B^{p.(Lys301Glu)}$ (all 3 mg per coverslip). Transfection of the plasmids was done using polyethylenimine (PEI) according to the manufacturer instructions (Sigma). 6–12 hr after transfection, the medium was changed to reduce toxicity. Transfected cells were then used for western blot.

Western Blot

2–3 days after transfection, HEK cells were harvested and homogenized in lysis buffer (10 mM Tris-HCl [pH 6.8], 2.5% SDS, 2 mM EDTA), containing protease inhibitor cocktail (#P8340,

Sigma), phosphatase inhibitor cocktail 2 (#P5726, Sigma), and phosphatase inhibitor cocktail 3 (#P0044, Sigma). Protein concentration in the samples was determined using the BCA protein assay kit (Pierce) and then lysate concentrations were adjusted to 1 mg/mL. Western blots were probed with the following primary antibodies: CAMK2A (6G9, 1:40,000, Abcam; validated in Elgersma *et al*., 2002), CAMK2B (CB-b1, 1:10,000, Invitrogen; validated in van Woerden *et al*., 2007), ph-Thr286/Thr287 (autophosphorylated CAMK2 antibody; #06-881; 1:1,000; Upstate Cell Signaling Solutions; validated in Elgersma *et al*., 2002), and RFP (#600401379, 1:2,000, Rockland, validated in this study by overexpression experiments). Secondary antibodies used were goat anti-mouse (#926-32210) and goat anti-rabbit (#926-68021) (all 1:15,000, LI-COR). Blots were quantified using LI-COR Odyssey Scanner and Odyssey 3.0 software. Analysis was done by an experimenter blinded for the transfection conditions.

Testing the Efficiency and Specificity of the shRNA Constructs

Primary Hippocampal Cultures

Primary hippocampal neuronal cultures were prepared from FvB/NHsD wild-type mice according to the procedure described in Banker and Goslin, 1991. Briefly, hippocampi were isolated from brains of E16.5 embryos and collected altogether in 10 mL of neurobasal medium (NB, GIBCO) on ice. After two washings with NB, the samples were incubated in pre-warmed trypsin/EDTA solution (Invitrogen) at 37˚C for 20 minutes. After 2 times washing in pre-warmed NB, the cells were resuspended in 1.5 mL NB medium supplemented with 2% B27, 1% penicillin/streptomycin, and 1% glutamax (Invitrogen), and dissociated using a 5 mL pipette. After dissociation, neurons were plated in a small drop on poly-D-lysine (25 mg/mL, Sigma)-coated 15 mm glass coverslips at a density of 1 x 10^6 cells per coverslip in 12-well plates containing 1 mL of supplemented NB for each coverslip. The plates were stored at 37˚/5% CO_2 until the day of the transfection.

Neuronal Transfection and Immunocytochemistry

Neurons were transfected after 3 days *in vitro* (DIV) with a pool of either the *CAMK2A* shRNAs or CAMK2B shRNAs with an RFP plasmid (Addgene) or the control shRNA with an RFP plasmid (all in total 4 mg per coverslip). Lipofectamine 2000 was used to transfect neurons, according to the manufacturer instructions (Invitrogen). To measure level of knockdown of CAMK2A and CAMK2B, neurons were fixed 5 days post-transfection with 4% paraformaldehyde (PFA)/4% sucrose and stained for CAMK2A or CAMK2B. The following primary antibodies were used: MAP2 (1:500, #188004, Synaptic System, validation can be found on the manufacturer's website), CAMK2A (6G9, 1:200, Abcam), and CAMK2B (CB-b1, 1:100, Invitrogen). For secondary antibodies, anti-mouse-Alexa488 (#715-545-150) and anti-guinea-pig-Alexa647 (#706-605-148) conjugated antibodies (all 1:200, Jackson ImmunoResearch) were used. Slides were mounted using mowiol-DABCO (Sigma) mounting medium. Confocal images were acquired using a LSM700 confocal microscope (Zeiss).

For the analysis of the protein levels upon shRNA transfection, the ''Measure RGB'' plugin for ImageJ software was used to measure the intensity of the fluorescent signal of the transfected cell, which was normalized against non-transfected cells on the same coverslip and then normalized against the mean value of control shRNA transfected cells. Analysis was done by an experimenter blinded for the transfection conditions.

Analysis of Neuronal Migration

In Utero *Electroporation*

The procedure was performed in pregnant FvB/NHsD mice at E14.5 of gestation to target mainly the progenitor cells giving rise to pyramidal cells of the layer 2/3. The DNA construct (1.5–3 mg/mL) was diluted in fast green (0.05%) and injected in the lateral ventricle of the embryos while still *in utero*, using a glass pipette controlled by a Picospritzer III device. To ensure the proper electroporation of the injected DNA constructs (1–2 mL) into the progenitor cells, five electrical square pulses of 45V with a duration of 50 ms per pulse and 150 ms inter-pulse interval were delivered using tweezer-type electrodes connected to a pulse generator (ECM 830, BTX Harvard Appartus). The electrodes were placed in such a way that the positive pole was targeting the developing somatosensory cortex. The following plasmids were injected: control vector, *CAMK2A*^{WT}, *CAMK2A*$^{p.(Phe98Ser)}$, *CAMK2A*$^{p.(Glu109Asp)}$, *CAMK2A*$^{p.(Pro138Ala)}$, *CAMK2A*$^{p.(Glu183Val)}$, *CAMK2A*$^{p.(Pro212Leu)}$, *CAMK2A*$^{p.(Pro235Leu)}$, *CAMK2A*$^{p.(His282Arg)}$, *CAMK2A*$^{p.(Thr286Pro)}$, *CAMK2A*$^{p.(Thr286Ala)}$, *CAMK2A*$^{p.(Thr286Asp)}$, *CAMK2A*$^{p.(Thr286Pro/p.(Lys42Arg)}$ and *CAMK2B*^{WT}, *CAMK2B*$^{p.(Glu110Lys)}$, *CAMK2B*$^{p.(Pro139Leu)}$, *CAMK2B*$^{p.(Glu237Lys)}$, *CAMK2B*$^{p.(Lys301Glu)}$ or for knockdown experiments with a pool of the *CAMK2A* shRNAs with an RFP plasmid (Addgene) or *CAMK2B* shRNAs with an RFP plasmid, or the control shRNA with an RFP plasmid. After birth, pups (M/F) were sacrificed at P0 for histochemical processing.

Immunohistochemistry

Mice were deeply anesthetized with an overdose of Nembutal and transcardially perfused with 4% paraformaldehyde (PFA). Brains were extracted and post-fixed in 4% PFA. Brains were then embedded in gelatin and cryoprotected in 30% sucrose in 0.1 M phosphate buffer (PB), frozen on dry ice, and sectioned using a freezing microtome (40/50 mm thick). Free-floating coronal sections were washed in 0.1 M PB and a few selected sections were counterstained with 4',6-diamidino-2-phenylindole solution (DAPI, 1:10,000, Invitrogen) before being mounted with mowiol on glass.

For the migration analysis, at least 9 confocal images (10x objective, 0.5 zoom, 1,024 x 1,024 pixels) were taken from 2–3 non-consecutive sections from at least 3 successfully targeted animals per plasmid. Images were rotated to correctly position the cortical layers, and the number of cells in different layers was counted using ImageJ (Analyze particles option), and the results were exported to a spreadsheet for further analysis. Cortical areas from the pia to the ventricle were divided in 10 equal-sized bins and the percentage of tdTOMATO-positive cells per bin was calculated. To calculate the total percentage of cells that reached the outer layers of the cortex, the sum of the percentage of targeted cells of bin 1 to 4 was calculated, based on the observation that in the control vectors, the sum of these first four bins corresponded to the outer layers of the cortex. Analysis was done by an experimenter blinded for the transfection conditions.

Structural Modeling

Homology modeling of the CAMK2B was performed using the I-TASSER protein structure prediction server (Zhang, 2008). The protein sequence of the CAMK2B (GenBank: NP_001211.3) without the F-actin binding domain (amino acids 316–504) was submitted as input for structure prediction. The model with the highest confidence (C-score) and topological similarity (Tm-score) was used for structural representation.

Statistical Analysis

All data were assumed to be normally distributed. Statistical difference between each single mutant and its wild-type control for the western blot analyses (stability and phosphorylation)

was determined using the two-tailed unpaired t test (dual comparison), since each mutation was tested against its own wild-type control. For the *in vitro* knock-down experiments, statistical difference was assessed using one-way ANOVA followed by Dunnet's multiple comparison test.

For the *in vivo* experiments on neuronal migration, the analysis was performed on the amount of targeted cells (measured as area under the curve) of the first four bins, considered to correspond to the layers 2/3 of the somatosensory cortex. Statistical analysis was performed using one-way ANOVA, followed by Bonferroni's multiple comparison tests. Based on previous experiments performed in our lab, we considered that for the knock-down experiments *in vitro*, at least 10 neurons were necessary. For the western blot analysis, we considered at least 3 replicates, and for the IUE experiments, previous experiments in our laboratory showed that at least 3 targeted pups and a minimum of 2 pictures from different brain slices per pup were necessary to draw any conclusion about the migration. Data are represented as box and whisker plots with the minimum and maximum of all the data and p values less than 0.05 are considered significant. All the data were analyzed using the graphpad prism 6.0 software.

RESULTS

Distribution of the Variants in *CAMK2A* and *CAMK2B*

Nineteen different heterozygous variants in *CAMK2A* or *CAMK2B* were identified in 24 unrelated individuals with ID (Table 1). The *de novo* status of these was confirmed for 18 of the 19 variants; it could not be confirmed in individual 1, whose paternal DNA sample was unavailable. The vast majority of the distinct variants—eight in *CAMK2A* and four in *CAMK2B* (Figure 1 and Table 1)—are missense substitutions; eight of the missense variants are predicted to affect the catalytic domain of the protein and the remainder to affect the regulatory domain (Figure 1). Two variants, one in *CAMK2A* and the other in *CAMK2B*, induce the production of mRNA transcripts with a premature stop codon. These transcripts are either eliminated by nonsense-mediated mRNA decay (NMD) or result in a severely truncated and non-functional protein (Figure 1 and Table 1). According to ExAC, the probability of being loss-of-function (LoF) intolerant (pLI) is high for *CAMK2A* (pLI = 1) but lower for *CAMK2B* (pLI = 0.47). However, when one takes into account only the LoF variants observed in the most abundant transcript in brain, GenBank: NM_172079.2 (Ensembl: ENST00000457475), pLI increases to 1 (Figure S9). In the context of a neurodevelopmental disorder, it suggests that *CAMK2B* is also intolerant to LoF variants. The five remaining variants affect canonical splice sites (Table 1), according to bioinformatic predictions and *in vitro* assessment by mini-gene system: three of them would induce skipping of in-frame exons encoding a part of the CAMK2A kinase domain or the entire CAMK2B regulatory domain, while the fourth variant would entail loss of most of the CAMK2 association domain by out-of-frame skipping of exon 17 (Figure S3).

Except variants c.635C>T (p.Pro212Leu) and c.704C>T (p.Pro235Leu), which were deposited in dbSNP, all variants are absent in available public databases (Table S4) and represent the only confirmed *de novo* events in *CAMK2* genes in more than 68,123 in-house exomes, including 19,980 complete trios whose proband had developmental delay of unknown etiology. Individual 10's variant c.704C>T (p.Pro235Leu) was assigned dbSNP accession number rs864309606 (with no frequency) after its submission to ClinVar under accession number SCV000258098; to our knowledge it was reported in no other study than the present one. With respect to variant rs926027867 (p.Pro212Leu) (not validated; no frequency in dbSNP), it was batch-submitted from the large project HUMAN_ LONGEVITY|HLI-5-150251808-G-A. Because the phenotype of the individuals from this cohort is not documented, it is possible that the

Table 1. *CAMK2A* and *CAMK2B* mutations identified in individuals 1-24.

Individual	Geographical origin	Gene [a]	Chromosomal position [a]	HGVSc [b]	HGVSp [b]	CADD (score) [c]	PolyPhen-2 (score) [d]	Functional effect [e/f]	Mutation origin
1	USA	*CAMK2A*	5:g.149652720del	c.65del	p.(Gly22Glufs*10)	-	-	LoF [f]	Uncertain [g]
2	France	*CAMK2A*	5:g.149636374A>G	c.293T>C	p.(Phe98Ser)	17.01	D (1.0)	LoF	*De novo*
3	UK	*CAMK2A*	5:g.149636340C>G	c.327G>C	p.(Glu109Asp)	19.53	D (0.988)	GoF	*De novo*
4	Netherlands	*CAMK2A*	5:g.149636332G>A	c.335C>T	p.(Ala112Val)	32	D (0.999)	ND	*De novo*
5	USA	*CAMK2A*	5:g.149631595T>A	c.548A>T	p.(Glu183Val)	32	D (1.0)	LoF	*De novo*
6	USA	*CAMK2A*	5:g.149631543dup	c.598+2dup	p.?	-	-	ND	*De novo*
7	France	*CAMK2A*	5:g.149631371G>A	c.635C>T	p.(Pro212Leu)	35	D (1.0)	uncertain	*De novo*
8	France	*CAMK2A*	5:g.149631371G>A	c.635C>T	p.(Pro212Leu)	35	D (1.0)	uncertain	*De novo*
9	Netherlands	*CAMK2A*	5:g.149631371G>A	c.635C>T	p.(Pro212Leu)	35	D (1.0)	uncertain	*De novo*
10	USA	*CAMK2A*	5:g.149630363G>A	c.704C>T	p.(Pro235Leu)	15.91	D (1.0)	uncertain	*De novo*
11	Germany	*CAMK2A*	5:g.149629873C>T	c.817-1G>A	p.?	-	-	ND	*De novo*
12	Netherlands	*CAMK2A*	5:g.149629844T>C	c.845A>G	p.(His282Arg)	27.0	D (1.0)	GoF	*De novo*
13	USA	*CAMK2A*	5:g.149629833T>G	c.856A>C	p.(Thr286Pro)	29.0	D (0.999)	GoF	*De novo*
14	UK	*CAMK2A*	5:g.149607754C>T	c.1204+1G>A	p.?	-	-	LoF	*De novo*
15	USA	*CAMK2B*	7:g.44323805G>A	c.85C>T	p.(Arg29*)	35	-	LoF [f]	*De novo*
16	USA	*CAMK2B*	7:g.44294154C>T	c.328G>A	p.(Glu110Lys)	26.3	D (1.0)	GoF	*De novo*
17	USA	*CAMK2B*	7:g.44283125G>A	c.416C>T	p.(Pro139Leu)	20.6	D (1.0)	GoF	*De novo*
18	UK	*CAMK2B*	7:g.44283125G>A	c.416C>T	p.(Pro139Leu)	20.6	D (1.0)	GoF	*De novo*
19	USA	*CAMK2B*	7:g.44283125G>A	c.416C>T	p.(Pro139Leu)	20.6	D (1.0)	GoF	*De novo*
20	USA	*CAMK2B*	7:g.44283125G>A	c.416C>T	p.(Pro139Leu)	20.6	D (1.0)	GoF	*De novo*
21	UK	*CAMK2B*	7:g.44281927C>T	c.709G>A	p.(Glu237Lys)	25.9	D (1.0)	GoF	*De novo*
22	USA	*CAMK2B*	7:g.44281383C>T	c.820-1G>A	p.?	-	-	ND	*De novo*
23	USA	*CAMK2B*	7:g.44281301T>C	c.901A>G	p.(Lys301Glu)	22.6	D (0.996)	LoF	*De novo*
24	Norway	*CAMK2B*	7:g.44281298C>T	c.903+1G>A	p.?	-	-	ND	*De novo*

[a] The reference genome used for bioinformatic predictions is GRCh37/hg19.
[b] HGVSc/HGVSp: coding DNA/protein variant described according to the nomenclature HGVS V2.0 established by the Human Genome Variation Society: NM_171825.2/NP_741960.1 for *CAMK2A* and NM_172079.2/NP_742076.1 for *CAMK2B*; nucleotide numbering uses +1 as the A of the ATG translation initiation codon in the reference sequence, with the initiation codon as codon 1.
[c] CADD v1.3 (Phred score): Combined Annotation Dependent Depletion; higher scores are more deleterious.
[d] PolyPhen-2 HumDiv: PolyPhen-2 Human Diversity; D: Probably damaging (>=0.957).
[e] Effect inferred from *in vitro* experiments; LoF: loss of function, GoF: gain of function, ND: not determined.
[f] Putative effect.
[g] Paternal sample was unavailable.

individual carrying variant p.Pro212Leu has intellectual disability.

The variants identified affect amino acids that are highly conserved across CAMK2 paralogs (Figure S4) and species, and are predicted to be likely pathogenic by the majority of bioinformatic programs tested (Table S4); for instance, all variants are predicted to belong to the 5% to 0.05% most deleterious substitutions in the human genome (CADD PHRED score between 16 and 35; Table S4).

Recurrence is noted for two variants located at CpG sites: *CAMK2A* c.635C>T (p.Pro212Leu; n = 3 unrelated individuals) and *CAMK2B* c.416C>T (p.Pro139Leu; n = 4 unrelated individuals) (Table S4). Strikingly, homologous amino acid residues Glu109 in CAMK2A and Glu110 in CAMK2B are altered in two individuals (c.327G>C [p.Glu109Asp] in individual 3 and c.328G>A [p.Glu110Lys] in individual 16). The two *CAMK2B* splice site variants c.820-1G>A and c.903+1G>A affect the canonical splice sequence and are predicted to lead to in-frame skipping of exon 11 according to bioinformatic predictions and *in vitro* studies (Figure S3). Their homologous counterpart in *CAMK2A*, c.817-1G>A, is predicted to have a similar consequence on CAMK2A exon 11 (Figure S3).

We used denovolyzeR (Ware *et al*., 2015) to determine whether the 23 *de novo* variants found among our case subjects could have been found by chance given the number of case-ascertained trios studied. Based on the collection of 19,980 trios, and accounting for a gene's underlying mutability, the probability of seeing 13 non-synonymous *CAMK2A de novo* variants by chance is $p = 1.7 \times 10^{-11}$ and $p = 3.9 \times 10^{-8}$ for observing 10 *CAMK2B* non-synonymous *de novo* variants by chance. Both these signals are genome-wide significant after correction for the ~19,000 protein-coding genes where an enrichment could have been found (adjusted $\alpha = 2.6 \times 10^{-6}$). Furthermore, we found that the case missense *de novo* variants within our series were preferentially affecting the most missense intolerant sequence of these two genes. We compared the missense tolerance ratio (MTR) scores (Traynelis *et al*., 2017) of the 17 *CAMK2A* and *CAMK2B de novo* missense variants to 39 rare *CAMK2A* and *CAMK2B* missense variants found among the DiscovEHR cohort of approximately 50,000 control individuals that do not overlap with the gnomAD dataset. Remarkably, 16/17 (94%) of our case missense *de novo* variant events and 12/39 (31%) of the novel control missense variants affect the 50% most missense intolerant sequence of these two genes, as defined by the MTR (Figure S10; Fisher's exact test $p = 1.8 \times 10^{-5}$; OR 33.7 [95% CI 4.3–1,549.4]).

In addition to the 19 distinct *de novo* variants, we extended our functional investigations to *CAMK2A* c.412C>G (p.Pro138Ala), reported as a *de novo* event in an individual showing severe global developmental delay with seizures (S.E. Holder, personal communication) from a large cohort study (Deciphering Developmental Disorders Study, 2015). Interestingly, this variant lies in the region encoding the kinase domain, within the most missense-depleted sequence of *CAMK2A* (Figure S10). It is predicted as pathogenic by bioinformatic programs (Table S4) and affects amino acid P138, which is homologous to CAMK2B residue Pro139 altered by variant p.Pro139Leu found in individuals 17–20.

Phenotypic Characterization of Individuals with *CAMK2A* and *CAMK2B* Variants

CAMK2A/B variants cause a neurodevelopmental disorder associated with ID. The main clinical features of affected individuals are summarized in Table 2 using Human Phenotype Ontology terms. More detailed observations are described in Supplemental Note: Case Reports and Tables S1 and S2. Key features are ID, language impairment, and behavioral anomalies. All individuals (24/24) have mild to severe ID. Impaired language development is frequently associated (23/24) with severe delayed speech (first words after age of 3 in 13/21 and no speech or few words after 5 years in 12/15). Epilepsy is reported in 7/23 (absence, febrile,

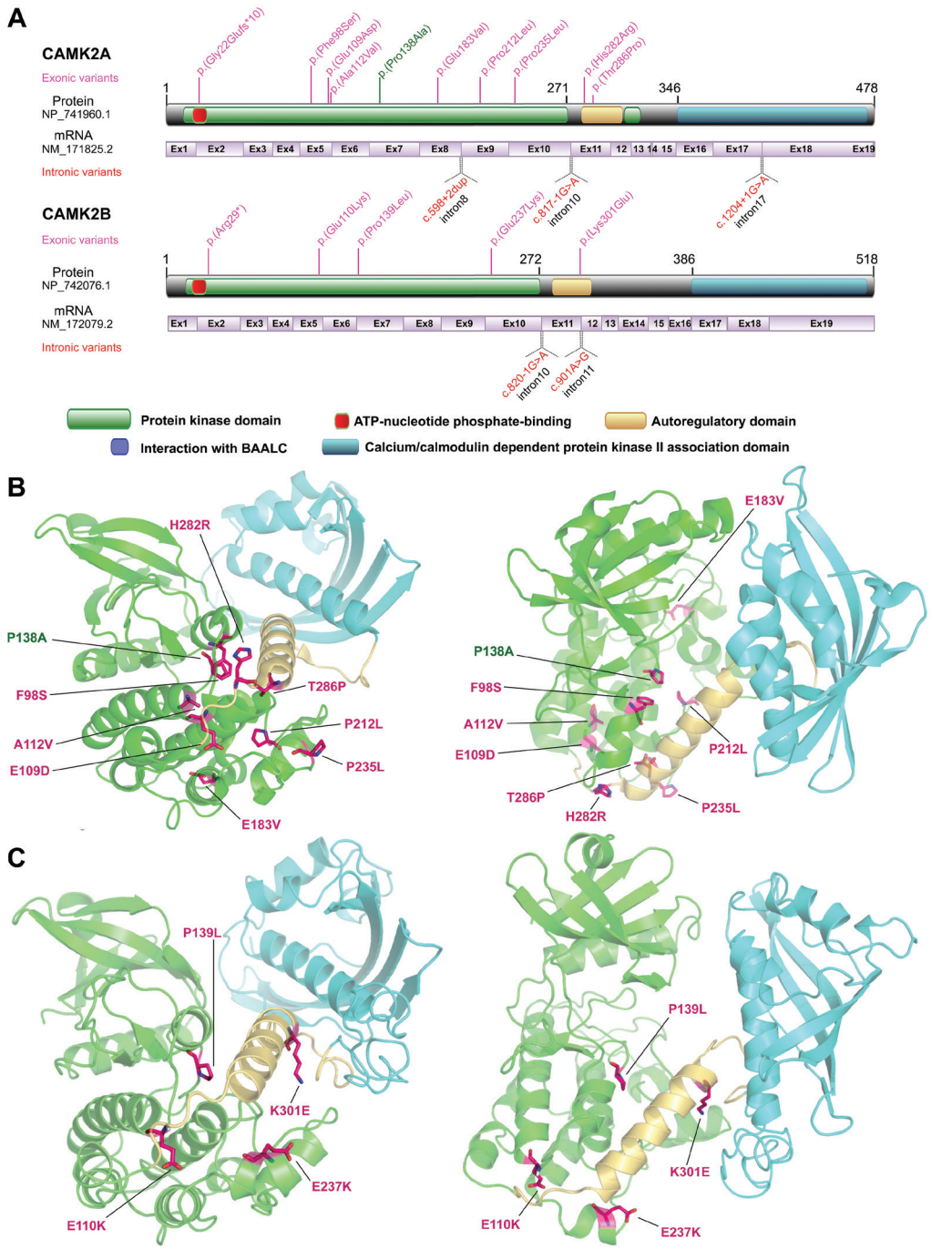

Figure 1. Molecular Genetic Findings in Individuals with *CAMK2A* and *CAMK2B* Variants (A) Schematic of CAMK2A and CAMK2B protein domain organizations and corresponding mRNA structure (derived from PDB features for Q9UQM7 and Q13554) indicating the positions of 12 missense variants, 1 stop-gain variant, 1 frameshift deletion, and 5 splice site variants found in affected individuals, together with the variant CAMK2A p.Pro138Ala reported in the literature as *de novo* (Iossifov *et al.*, 2014; Deciphering Developmental Disorders Study, 2015). (B and C) Representation of the structure of a single human CAMK2A subunit obtained from the corresponding full-length holoenzyme structure

present in the protein data bank (PDB ID: 3SOA) (B) and homology model of a single human CAMK2B subunit without the F-actin binding domain (C). For both structures, the catalytic domain is represented in green, the autoregulatory domain in yellow, and the association domain in cyan. The location of each single point variant (in magenta) in CAMK2A and CAMK2B, respectively, is indicated in the 3D structure (two different orientations), showing that for CAMK2A seven of the missense variants are located in the catalytic domain, and two variants in the autoregulatory domain. No variants were found in the association domain (B). For CAMK2B, three of the missense variants are located in the catalytic domain and one in the autoregulatory domain. No variant was found in the association domain (C). Structure representations were made with PyMol. Correspondence between the nomenclatures of amino acid changes: F98S, p.Phe98Ser; G109D, p.Glu109Asp; A112V, p.Ala112Val; P138A, p.Pro138Ala; E183V, p.Glu183Val; P212L, p.Pro212Leu; P235L, p.Pro235Leu; H282R, p.His282Arg; T286P, p.Thr286Pro; E110K, p.Glu110Lys; P139L, p.Pro139Leu; E237K, p.Glu237Lys; K301E, p.Lys301Glu.

Rolandic, or tonic-clonic seizures). Behavioral issues (19/24) include irritability, low tolerance to frustration, hyperactivity, anxiety, aggressiveness, or autistic traits. Brain imaging was generally normal (mild corpus callosum anomalies in 3/21). The recurrent extra-neurological anomalies include facial dysmorphism (11/24; e.g., hypotelorism, down-slanting palpebral fissures, and epicanthus), visual problems (9/24, including 7/10 in subjects found with a *CAMK2B* variant; e.g., strabismus [4/24], visual impairment, and visual tracking difficulty), gastro-intestinal issues (8/21; e.g., feeding difficulties, reflux, and constipation; 7/9 related to *CAMK2B* variants versus 1/12 related to *CAMK2A*), breathing irregularities (2/24), and scoliosis (2/24). A few features tend to differ between the *CAMK2A*- and the *CAMK2B*-associated groups, although the robustness of the comparison is based on a relatively small sample size (Table S2). Cognitive impairment seems more severe when caused by *CAMK2B* variants, with severe or mild-to-moderate ID present in 8 of 10 individuals with *CAMK2B* variants and 8 of 14 individuals with *CAMK2A* variants. Similarly, hypotonia is more predominant in the *CAMK2B* subgroup (9/10, 90%) than in the *CAMK2A* subgroup (7/14, 50%). When CAMK2A and CAMK2B variants are taken together, ID appears to be more severe when variants affect the autoregulatory domain (6/6) compared to the kinase domain (10/17).

CAMK2A and *CAMK2B* Mutations Can Affect Protein Expression

Missense variants were tested using *in vitro* and *in vivo* assays to understand their possible effect on protein stability and function (Figure 2A).

Confirming a recent study showing that the $CAMK2A^{p.(Glu183Val)}$ variant renders CAMK2A unstable both *in vitro* and *in vivo* (Stephenson *et al*., 2017), transfection of HEK293T cells with the $CAMK2A^{p.(Glu183Val)}$ mutant construct showed a significant reduction of CAMK2A protein level compared to $CAMK2A^{WT}$ (for all statistics, see Table 3) (Figure 2B). Of the additional seven variants tested, the $CAMK2A^{p.(His282Arg)}$ variant also resulted in reduced CAMK2A protein levels after transfection in HEK293T cells, whereas $CAMK2A^{p.(Phe98Ser)}$, $CAMK2A^{p.(Glu109Asp)}$, $CAMK2A^{p.(Pro138Ala)}$, $CAMK2A^{p.(Pro212Leu)}$, $CAMK2A^{p.(Pro235Leu)}$, and $CAMK2A^{p.(Thr286Pro)}$ did not affect CAMK2A protein levels (Table 3 and Figure 2C). Variants $CAMK2B^{p.(Glu110Lys)}$ and $CAMK2B^{p.(Pro139Leu)}$ showed reduced CAMK2B protein levels (Table 3 and Figure 2C).

Mutations in *CAMK2* Have Heterogeneous Effects on CAMK2 Auto-phosphorylation

CAMK2A auto-phosphorylation at Thr286 is critical for autonomous (Ca^{2+}-independent) function (Giese *et al*., 1998). We therefore investigated how the variants affect Thr286 (CAMK2A) and Thr287 (CAMK2B) auto-phosphorylation. We found that $CAMK2A^{p.(Glu109Asp)}$ as well as $CAMK2A^{p.(His282Arg)}$ despite reduced protein levels, showed a significant increase in phosphorylation at Thr286 when compared to $CAMK2A^{WT}$. In contrast, $CAMK2A^{p.(Phe98Ser)}$ and $CAMK2A^{p.(Glu183Val)}$ showed a significant reduction of Thr286 phosphorylation (Table 3 and Figure 2D), the latter being again consistent with a recent study of $Camk2a^{p.(Glu183Val)}$ knock-in mice (Stephenson *et al*., 2017). As expected, we found no phosphorylation at Thr286

Table 2. Main clinical features of the individuals with *CAMK2A* and *CAMK2B* mutations summarized using Human Phenotype Ontology (HPO) terms.

Individual	1	2	3	4	5	6	7	8	9	10	11	12	13	14
Clinical feature:														
Intellectual Disability (HP:0001249)	+ mod.	+ mod.	+ sev.	+ sev.	+ mild	+ sev.	+ sev.	+ mild/ sev.	+ mod.	+ mild	+ sev.	+ sev.	+ sev.	+ mild
Delayed speech and language development (HP:0000750)	+	+	+	+	+	+	+	+	+	+	+	+	+	-
Abnormal emotion/affect behavior (HP:0100851)	+	+	+	+	+	+	-	+	+	+	+	+	-	+
Global Developmental Delay (HP:0001263)	+	+	+	+	+	+	+	+	+	-	+	+	+	-
Delayed gross motor development (HP:0002194)	+	+	+	+	+	+	+	+	+	-	+	+	+	-
Hypotonia (HP:0001252)	-	+	+	+	-	-	+	+	-	-	+	-	+	-
Abnormal facial shape (HP:0001999)	+	+	+	-	-	-	+	-	-	+	-	-	-	-
Abnormality of the digestive system (HP:0025031)	-	-	-	-	-	-	-	-	-	-	+	ND	-	+
Growth abnormality (HP:0001507)	-	-	-	-	-	-	+	-	-	+	-	-	-	-
Visual impairment (HP:0000505)	-	-	-	-	-	-	-	-	-	-	+	-	-	+
Seizures (HP:0001250)	-	-	+	-	-	-	+	+	-	-	+	-	-	-
EEG abnormality (HP:0002353)	ND	ND	-	-	ND	-	-	+	-	ND	+	-	ND	ND
Microcephaly (HP:0000256)	-	-	-	-	-	-	-	-	-	-	+	-	-	-

Abbreviations: mod, moderate; sev, severe; ND, not determined

when overexpressing CAMK2A$^{p.(Thr286Pro)}$ in HEK293T cells underscoring the specificity of the antibody. *CAMK2A*$^{p.(Pro138Ala)}$, *CAMK2A*$^{p.(Pro212Leu)}$, and *CAMK2A*$^{p.(Pro235Leu)}$ showed similar levels of Thr286 phosphorylation compared to *CAMK2A*^{WT} (Table 3 and Figure 2D). We observed nearly abolished Thr287 phosphorylation of the CAMK2B$^{p.(Lys301Glu)}$ protein, whereas the CAMK2B$^{p.(Glu110Lys)}$, CAMK2B$^{p.(Pro139Leu)}$, and CAMK2B$^{p.(Glu237Lys)}$ proteins showed a significant increase in phosphorylation at Thr287 (Table 3 and Figure 2E).

Taken together, these results indicate that the identified *CAMK2A* and *CAMK2B* variants can exert very diverse effects on CAMK2 auto-phosphorylation.

CAMK2A and *CAMK2B* Mutations that Affect Auto-phosphorylation also Affect Neuronal Function

Neuronal migration is a key aspect of cortical development. The ability of neurons to migrate from the subventricular zone to layer 2/3 of the somatosensory cortex is highly sensitive to changes that perturb normal neuronal function, resulting in migration deficits (Saito and Nakatsuji, 2001; Tabata and Nakajima, 2001; Taniguchi *et al*., 2012). Hence, we used *in utero* electroporation of E14.5 mouse embryos to transfect neurons in the subventricular zone to study the functional effects of variants in *CAMK2A* and *CAMK2B*.

We first assessed whether reduced or increased levels of (wild-type) CAMK2A and CAMK2B affect neuronal function. Neither increasing nor reducing CAMK2A expression levels affected neuronal migration, whereas changing the protein level of CAMK2B in either direction resulted in clear migration deficits (Tables 4 and 5 and Figures 3A–3C). For efficiency and specificity of the shRNAs used, see Figure S6. These differences may reflect the presence of a unique F-actin binding domain in CAMK2B, which is required to target the entire CAMK2 holoenzyme to the F-actin cytoskeleton (Shen *et al*., 1998). Moreover, CAMK2B is the predominant CAMK2 isoform of the developing brain (Bayer *et al*., 1999).

We next electroporated the different mutant *CAMK2* constructs and analyzed their

Table 2. (continued)

Individual	15	16	17	18	19	20	21	22	23	24	
Clinical feature:											**Occurrence**
Intellectual Disability (HP:0001249)	+ mild	+ mild	+ sev.	+ sev.	+ sev.	+ severe	+ sev.	+ sev.	+ sev.	+ mild/sev.	24/24 (100%)
Delayed speech and language development (HP:0000750)	+	+	+	+	+	+	+	+	+	+	23/24 (95.8%)
Abnormal emotion/affect behavior (HP:0100851)	-	+	+	+	+	-	+	-	+	+	19/24 (79.2%)
Global Developmental Delay (HP:0001263)	-	-	+	+	+	+	+	+	-	+	19/24 (79.2%)
Delayed gross motor development (HP:0002194)	-	-	+	+	+	+	+	+	-	+	19/24 (79.2%)
Hypotonia (HP:0001252)	-	+	+	+	+	+	+	+	+	+	16/24 (66.7%)
Abnormal facial shape (HP:0001999)	-	-	+	+	+	+	+	-	+	-	11/24 (45.8%)
Abnormality of the digestive system (HP:0025031)	-	+	+	+	+	+	+	+	-	+	10/23 (43.5%)
Growth abnormality (HP:0001507)	-	-	+	+	+	+	+	-	+	+	9/24 (37.5%)
Visual impairment (HP:0000505)	-	+	+	+	+	+	-	+	-	+	9/24 (37.5%)
Seizures (HP:0001250)	+	-	-	-	-	-	+	-	+	+	8/24 (33.3%)
EEG abnormality (HP:0002353)	ND	+	-	-	ND	ND	+	-	+	+	6/15 (40.0%)
Microcephaly (HP:0000256)	-	-	+	-	+	+	-	-	+	+	6/24 (25.0%)

effects on neuronal migration. Even though overexpression or knockdown of CAMK2A did not affect migration, overexpression of CAMK2A mutants with reduced (CAMK2A$^{p.(Phe98Ser)}$ and CAMK2A$^{p.(Glu183Val)}$) or increased (CAMK2A$^{p.(Glu109Asp)}$ and CAMK2A$^{p.(His282Arg)}$) Thr286 phosphorylation systematically showed reduced migration when compared to overexpression of CAMK2A^{WT} (Tables 4 and 5 and Figures 4A, 4C, and 4D). These results strongly suggest that these variants exert a dominant change of function on the CAMK2 holoenzyme. Conversely, overexpression of the mutant CAMK2A proteins that did not show any effect on Thr286 phosphorylation (CAMK2A$^{p.(Pro138Ala)}$, CAMK2A$^{p.(Pro212Leu)}$, and CAMK2A$^{p.(Pro235Leu)}$) (Figure 2C) also did not affect migration (Tables 4 and 5 and Figures 4A and 4B).

Notably, overexpression of the CAMK2A$^{p.(Thr286Pro)}$ mutant completely blocked neuronal migration (Figures 5A and 5B). Since this variant destroys the Thr286 phosphorylation site, it is conceivable that this dramatic effect on migration is caused by severely reduced CAMK2A activity. However, when testing CAMK2A$^{p.(Thr286Ala)}$ (phospho-dead CAMK2A mutant) (Elgersma *et al*., 2002; Giese *et al*., 1998) and CAMK2A$^{p.(Thr286Asp)}$ (phosphomimetic CAMK2A mutant) (Mayford *et al*., 1995; Mayford *et al*., 1996), only the latter mimicked the migration pattern found in the CAMK2A$^{p.(Thr286Pro)}$ mutant (Figures 5A and 5C). These results indicate that, even though the CAMK2A$^{p.(Thr286Pro)}$ cannot be auto-phosphorylated at the Thr286 site, the variant likely functions as a phosphomimetic mutation, resulting in a gain of function. To further test this hypothesis, we introduced a second variant in the CAMK2A$^{p.(Thr286Pro)}$ mutant, the p.Lys42Arg variant, which blocks all kinase activity (Yamagata *et al*., 2009). We found that overexpression of the CAMK2A$^{p.(Thr286Pro)/p.(Lys42Arg)}$ protein no longer caused a major delay in migration (Figures 5A and 5D), further confirming that the CAMK2A$^{p.(Thr286Pro)}$ variant acts as gain-of-function variant. Taken together, these results highlight the importance of tightly controlled CAMK2A-Thr286 auto-phosphorylation for normal neuronal function and are consistent with the observation that Thr286 mutations that either abolish auto-phosphorylation or mimic auto-phosphorylation impair synaptic plasticity and learning (Mayford *et al*., 1995; Giese *et al*.,

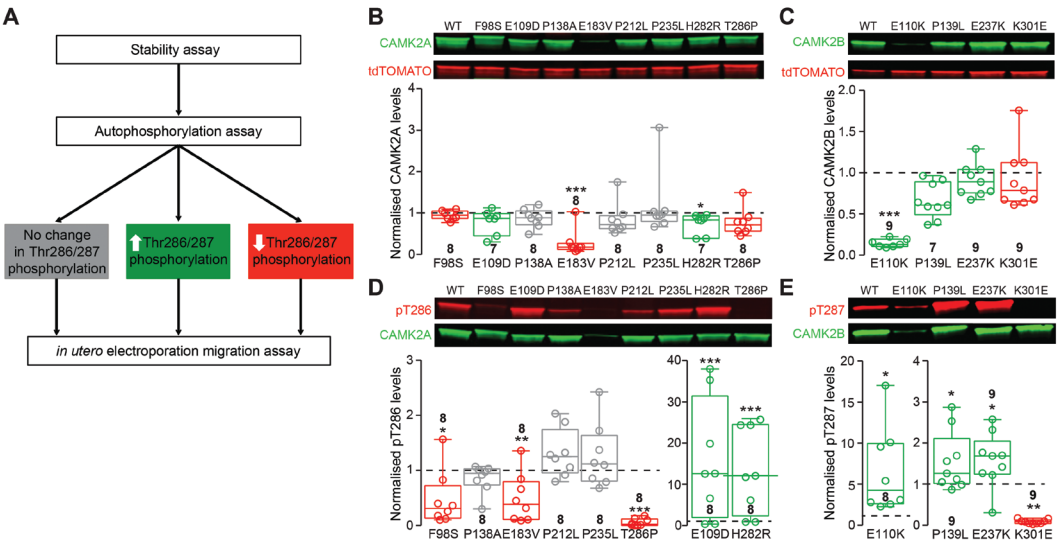

Figure 2. Transfection of HEK293T Cells with the Different CAMK2 Mutants Shows Changes in Stability as well as Phosphorylation at Thr286/287 (A) Schematic overview of the *in vitro* and *in vivo* assays. (B and C) Top, Representative western blots of HEK293T cells transfected with either *CAMK2A* or *CAMK2B* constructs, probed with an antibody against CAMK2A, CAMK2B, and RFP. Below, quantification of the normalized protein levels of CAMK2A or CAMK2B, showing instability for CAMK2A$^{p.(Glu183Val)}$, CAMK2A$^{p.(His282Arg)}$, CAMK2B$^{p.(Glu110Lys)}$, and CAMK2B$^{p.(Pro139Leu)}$ proteins. (D and E) Top, Representative western blots of HEK293T cells transfected with either *CAMK2A* or *CAMK2B* constructs, probed with a specific antibody against the phosphorylation site Thr286/287 and an antibody against CAMK2A and CAMK2B, respectively. Below, quantification of the normalized levels of CAMK2A-Thr286 phosphorylation and normalized levels of CAMK2B-Thr287 phosphorylation. Number in the box and whisker plot graphs indicates the n per construct. Error bars indicate the minimum and maximum of all data. Individual data points are shown in the box and whisker plots. Correspondence between the nomenclatures of amino acid changes: F98S, p.Phe98Ser; G109D, p.Glu109Asp; A112V, p.Ala112Val; P138A, p.Pro138Ala; E183V, p.Glu183Val; P212L, p.Pro212Leu; P235L, p.Pro235Leu; H282R, p.His282Arg; T286P, p.Thr286Pro; E110K, p.Glu110Lys; P139L, p.Pro139Leu; E237K, p.Glu237Lys; K301E, p.Lys301Glu.

1998).

Although overexpression of CAMK2B^{WT} affects neuronal migration, we found that overexpression of CAMK2B$^{p.(Glu110Lys)}$, CAMK2B$^{p.(Pro139Leu)}$, or CAMK2B$^{p.(Glu237Lys)}$ disrupted migration even more severely (Tables 4 and 5 and Figures 6A–6C). This is entirely in line with the finding that these three variants result in increased activity as judged by Thr287 auto-phosphorylation (Figure 2E). Overexpression of CAMK2B$^{p.(Lys301Glu)}$, which displays reduced CAMK2 activity (Figure 2E), showed a less severe migration deficit compared to overexpression of CAMK2B^{WT} (Tables 4 and 5 and Figures 5A–5C), indicating that this variant alleviates the deleterious effect of CAMK2B overexpression. Hence, similarly to *CAMK2A* mutations, these results indicate that all *CAMK2B* missense mutations that affect Thr287 auto-phosphorylation exert a dominant effect, regardless of whether phosphorylation is increased or decreased.

DISCUSSION

The first mouse mutant with impaired learning and memory was reported 25 years ago when the *Camk2a* knock-out was shown to have impaired hippocampus-dependent learning and impaired hippocampal synaptic plasticity (Silva *et al*., 1992a, 1992b). Subsequently, an overwhelming amount of data has highlighted the importance of CAMK2A and CAMK2B for many brain areas (Lisman *et al*., 2002; Lisman *et al*., 2012; Hell, 2014). The regulation of kinase

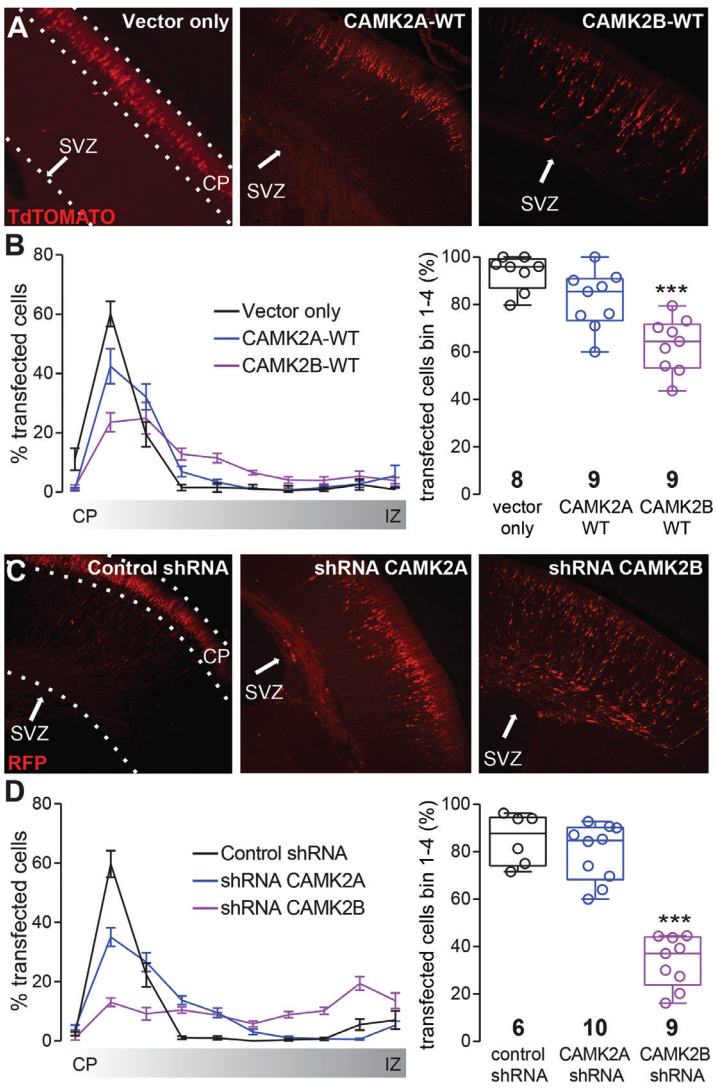

Figure 3. Increased or Decreased Levels of the CAMK2B but Not the CAMK2A Protein *In Vivo* Cause Deficits in Neuronal Migration in Mice
(A) Representative images of E14.5 *in utero* electroporated P0 brains (overexpression of CAMK2), with the cortical plate (CP, dashed lines) and the subventricular zone (SVZ, arrow) indicated. tdTomato-positive cells represent the successfully transfected neurons.
(B) Left: Quantification of the neuronal migration pattern observed in the different conditions. The cortex was divided into 10 bins of equal size and the percentage of tdTomato$^+$/RFP$^+$ cells per bin was counted. Right: Analysis of the percentage of targeted cells that reach the outer layers of the cortex measured as the sum of bin 1 to 4.
(C) Representative images of E14.5 *in utero* electroporated P0 brains (knockdown of endogenous CAMK2), with the cortical plate (CP, dashed lines) and the subventricular zone (SVZ, arrow) indicated. RFP-positive cells represent the successfully transfected neurons.
(D) Left: Quantification of the neuronal migration pattern observed in the different conditions. The cortex was divided into 10 bins of equal size and the percentage of tdTomato$^+$/RFP$^+$ cells per bin was counted. Right: Analysis of the percentage of targeted cells that reach the outer layers of the cortex measured as the sum of bin 1 to 4. Number in the box and whisker plot graphs indicates the number of pictures analyzed per construct. Error bars indicate the minimum and maximum of all data. Individual data points are shown in the box and whisker plots.

activity by auto-phosphorylation has been demonstrated to be essential for the role of CAMK2 in murine neuronal function (Mayford *et al*., 1995; Giese *et al*., 1998; Lisman *et al*., 2012). We now provide evidence that proper CAMK2A and CAMK2B functioning is also important for the human brain. We report 24 individuals with a neurodevelopmental disorder who carry a rare heterozygous nonsense, missense, or splice site variant in *CAMK2A* or *CAMK2B*—the majority (23/24) were proven *de novo*. The core clinical findings in affected heterozygous individuals are neurological and consistent with the knockout mouse models for *Camk2a* and *Camk2b* (the majority of which are homozygous knock-out) (Silva *et al*., 1992b; van Woerden *et al*., 2009; Achterberg *et al*., 2014; Bachstetter *et al*., 2014). Variants in *CAMK2A* or *CAMK2B* result in a non-dysmorphic neurodevelopmental phenotype characterized by a variable degree of ID. Language development is particularly impaired and behavioral problems are

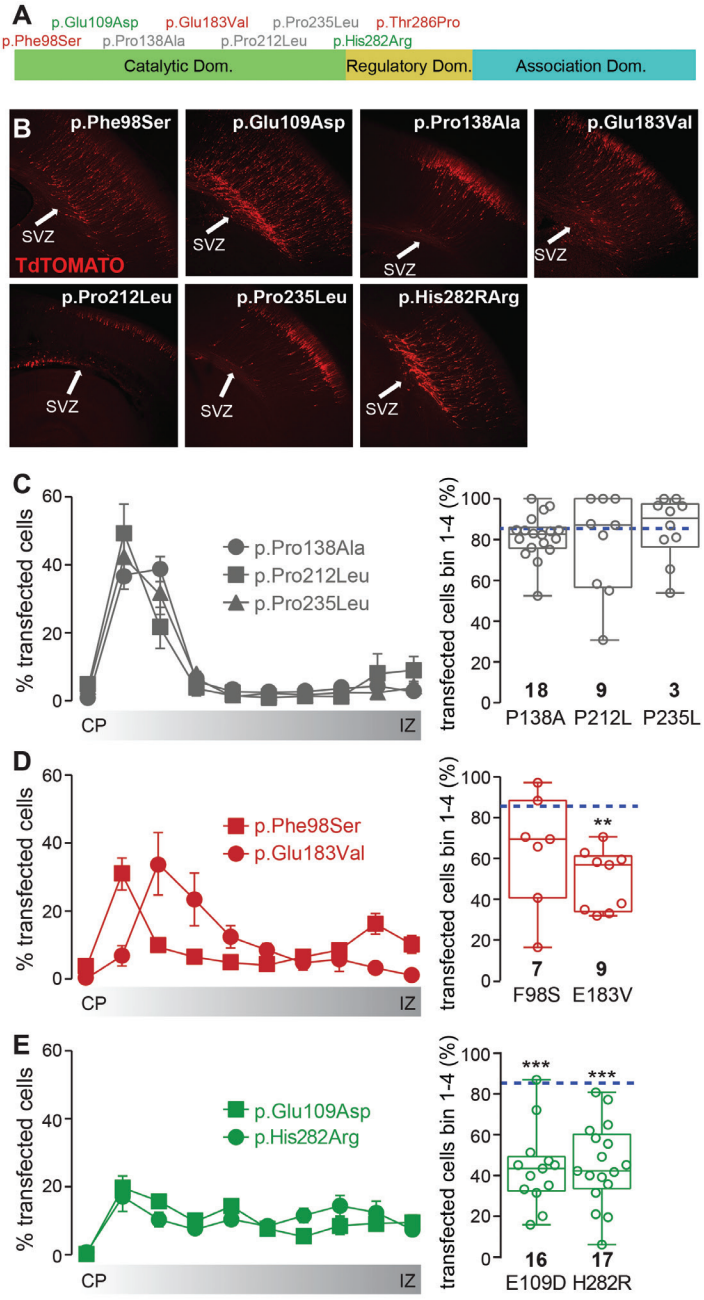

Figure 4. Transfection of CAMK2A Mutations with Changes in Thr286 Phosphorylation *In Vivo* Induces Migration Deficits (A) Schematic overview of CAMK2A with the location of the variants with increased (green), decreased (red), or unchanged (gray) Thr286 phosphorylation.
(B) Representative images of E14.5 *in utero* electroporated P0 brains. tdTomato-positive cells represent the successfully transfected neurons.
(C–E) Left: Quantification of the neuronal migration pattern observed in the variants with unchanged (C), decreased (D), or increased (E) Thr286 auto-phosphorylation. Right: Analysis of the percentage of targeted cells of the different constructs that reach the outer layers of the cortex measured as the sum of bin 1 to 4. Dotted line indicates the WT level. Number in the box and whisker plot graphs indicates the number of pictures analyzed per construct. Error bars indicate the minimum and maximum of all data. Individual data points are shown in the box and whisker plots.

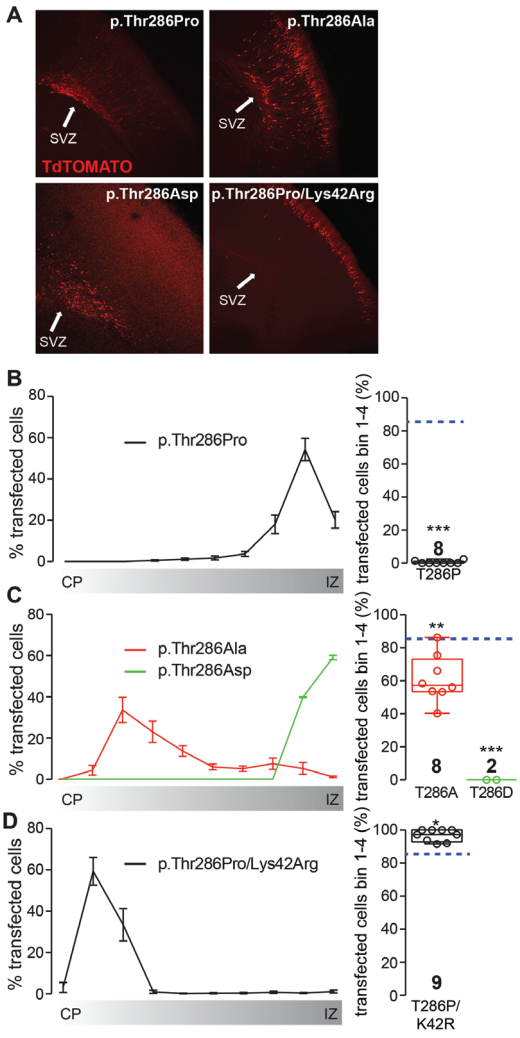

Figure 5. Transfection of the CAMK2A$^{p.(Thr286Pro)}$ Mutation *In Vivo* Reveals a Constitutive Active Phenotype (A) Representative images of E14.5 *in utero* electroporated P0 brains. tdTomato-positive cells represent the successfully transfected neurons.
(B) Left: Quantification of the neuronal migration pattern observed when overexpressing CAMK2A$^{p.(Thr286Pro)}$. Right: Analysis of the percentage of targeted cells of the different constructs that reach the outer layers of the cortex measured as the sum of bin 1 to 4.
(C) Left: Quantification of the neuronal migration pattern observed when overexpressing CAMK2A$^{p.(Thr286Ala)}$ or CAMK2A$^{p.(Thr286Pro)}$. Right: Analysis of the percentage of targeted cells of the different constructs that reach the outer layers of the cortex measured as the sum of bin 1 to 4.
(D) Left: Quantification of the neuronal migration pattern observed when overexpressing CAMK2A$^{p.(Thr286Pro)/p.(Lys42Arg)}$. Right: Analysis of the percentage of targeted cells of the different constructs that reach the outer layers of the cortex measured as the sum of bin 1 to 4. Dotted line indicates the WT level. Number in the box and whisker plot graphs indicates the number of pictures analyzed per construct. Error bars indicate the minimum and maximum of all data. Individual data points are shown in the box and whisker plots.

frequent. In our cohort, motor delay was more pronounced in the subgroup of individuals with *CAMK2A* variants, while ID appeared to be more severe and more frequently accompanied by hypotonia with *CAMK2B* variants. The differential diagnosis of the CAMK2A/B-associated disorder includes many individually rare neurodevelopmental disorders and is virtually impossible to diagnose without molecular testing.

A number of molecular arguments helped us to draw an outline of the clinical entity caused by *CAMK2A* or *CAMK2B* variants. The 23 proven *de novo* events reported here occur in two genes bioinformatically predicted to be intolerant to functional variations (Table S4). They are the only such events in the *CAMK2* genes noted in 19,980 trios. The extremely rare variants were identified in individuals who shared the same main clinical phenotype, making it unlikely that they represent incidental findings. The probability of observing 13 or more *CAMK2A* and 10 or more *CAMK2B* non-synonymous *de novo* variants by chance among 19,980 trios is extremely low (*CAMK2A* $p = 1.7 \times 10^{-11}$ and *CAMK2B* $p = 3.9 \times 10^{-8}$), implicating *CAMK2A* and *CAMK2B* as genome-wide significant developmental delay associated genes (exome-wide multiplicity adjusted $p < 2.6 \times 10^{-6}$).

In order to test this assumption further, we employed a number of functional assays to investigate the pathogenicity of the *CAMK2A/B* missense variants. We analyzed their effect on protein stability, Thr286/Thr287 (auto) phosphorylation, and neuronal function by using a neuronal migration assay. Whereas overexpression or knockdown of CAMK2A does not lead to aberrant migration, we found that five out of eight tested missense variants (CAMK2A$^{p.(Phe98Ser)}$, CAMK2A$^{p.(Glu109Asp)}$, CAMK2A$^{p.(Glu183Val)}$, CAMK2A$^{p.(His282Arg)}$, and CAMK2A$^{p.(Thr286Pro)}$)

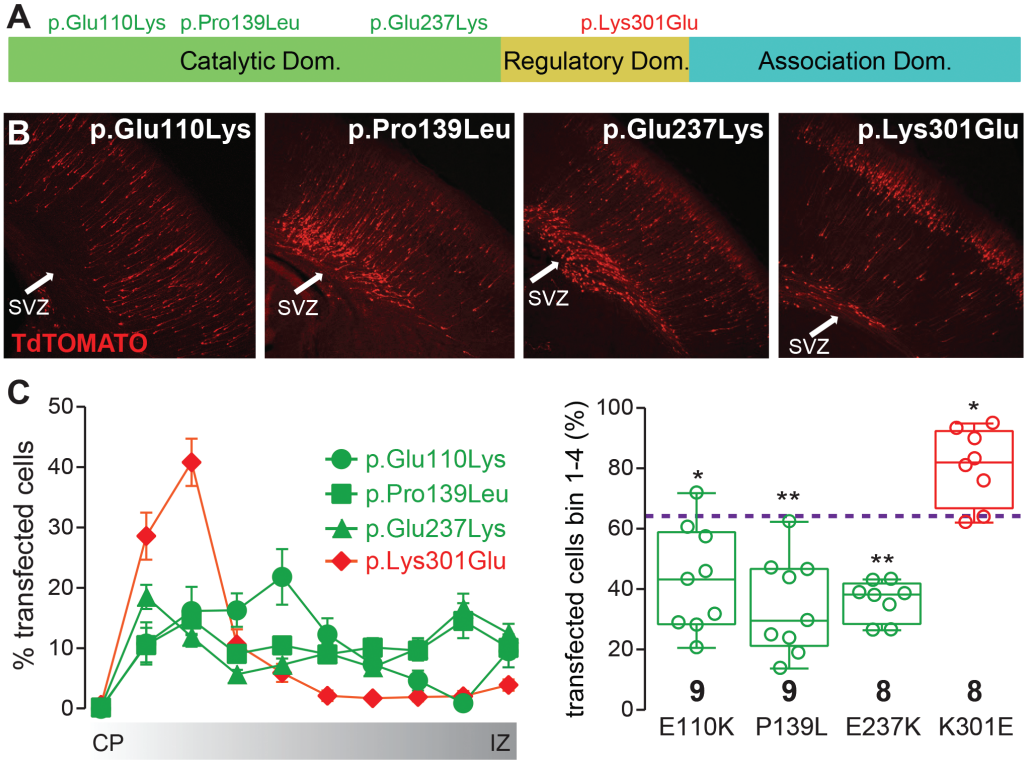

Figure 6. Transfection of CAMK2B Mutations *In Vivo* Causes Changes in the Migration Pattern of the Targeted Neurons (A) Schematic overview of CAMK2B with the location of the mutations with increased (green), decreased (red), or unchanged (gray) Thr286 phosphorylation. (B) Representative images of E14.5 *in utero* electroporated P0 brains. tdTomato-positive cells represent the successfully transfected neurons. (C) Left: Quantification of the neuronal migration pattern observed when overexpressing the mutations. Right: Analysis of the percentage of targeted cells of the different constructs that reach the outer layers of the cortex measured as the sum of bin 1 to 4. Dotted line indicates the WT level. Number in the box and whisker plot graph indicates the number of pictures analyzed per construct. Error bars indicate the minimum and maximum of all data. Individual data points are shown in the box and whisker plots.

affect neuronal migration when expressed *in vivo*. Notably, all these mutants showed either increased or decreased Thr286 phosphorylation in our cellular assays. Auto-phosphorylation of the Thr286 residue has been shown to be essential for CAMK2A function: it renders the protein autonomously active and facilitates interaction with the carboxy-terminal region of GRIN2B (GluN2B) NMDAR subunit (Lisman *et al*., 2012; Fan *et al*., 2014; Barcomb *et al*., 2016). Based on our results we further conclude that the CAMK2A$^{p.(Phe98Ser)}$ and CAMK2A$^{p.(Glu183Val)}$ variants result in a dominant acting loss of function (LoF) of the protein, whereas CAMK2A$^{p.(Glu109Asp)}$ and CAMK2A$^{p.(His282Arg)}$ induce a dominant acting gain of function (GoF). Surprisingly, the CAMK2A$^{p.(Thr286Pro)}$ variant, which cannot be auto-phosphorylated at Thr286, behaves as a dominant acting GoF mutation. For CAMK2A$^{p.(Pro138Ala)}$, CAMK2A$^{p.(Pro212Leu)}$, or CAMK2A$^{p.(Pro235Leu)}$, we found minimal effect on stability, autophosphorylation, and neuronal migration; thus, the pathogenicity of these variants by functional assay cannot be definitively confirmed. However, they likely affect other aspects of CAMK2 and neuronal function that were not examined in this study. For instance, the CAMK2A$^{p.(Pro212Leu)}$ variant recurs in three individuals with similar phenotypes, is located in the most missense depleted sequence of CAMK2A (Figure S10), and does not appear in large variant databases like ExAC or gnomAD, which is consistent with pathogenicity. This example underscores the necessity of designing additional tests to assess

Table 3. Overview of the Statistical Analysis on the Western Blot Experiments for Stability and Thr286/7 Phosphorylation

	Stability			Thr286/7 Phosphorylation		
	p value	df	t-value	p value	df	t-value
CAMK2A						
WT versus p.(Phe98Ser)	0.19	14	1.36	0.01*	14	2.98
WT versus p.(Glu109Asp)	0.06	13	2.02	0.01*	14	2.87
WT versus p.(Pro138Ala)	0.12	14	1.63	0.13	14	1.62
WT versus p.(Glu183Val)	<0.0001*	14	6.56	0.0006*	14	3.23
WT versus p.(Pro212Leu)	0.29	14	1.11	0.06	14	2.03
WT versus p.(Pro235Leu)	0.53	14	0.64	0.23	14	1.27
WT versus p.(His282Arg)	0.01*	13	2.99	0.004*	14	3.35
WT versus p.(Thr286Pro)	0.07	14	1.98	<0.0001*	14	39.23
CAMK2B						
WT versus p.(Glu110Lys)	<0.0001*	14	52.11	0.006*	15	3.21
WT versus p.(Pro139Leu)	0.0002*	16	4.78	0.03*	16	2.32
WT versus p.(Glu237Lys)	0.18	16	1.39	0.02*	16	2.66

Statistical test performed is the two-tailed unpaired t test. Asterisks (*) indicate statistical significant difference.

the effects of variants that could not be confidently classified by our screening.

We found that increased as well as decreased levels of CAMK2B during neuronal development caused migration defects, indicating that cortical development requires an optimal amount of CAMK2B protein. Of the four tested missense variants in CAMK2B, we found that CAMK2B$^{p.(Lys301Glu)}$ acts as a LoF mutation, showing reduced phosphorylation of Thr287 with less impaired migration compared to increased levels of CAMK2B^{WT}. In contrast, increased Thr287 phosphorylation severely affected neuronal migration (compared to CAMK2B^{WT}), suggesting that CAMK2B$^{p.(Glu110Lys)}$, CAMK2B$^{p.(Pro139Leu)}$, and CAMK2B$^{p.(Glu237Lys)}$ act as GoF mutations. Taken together, these results indicate that not only LoF but also GoF mutations in *CAMK2B* can disturb neurodevelopment, consistent with the notion that cortical development is highly sensitive to dosage of CAMK2B protein.

Considering that three of the variants, p.His282Arg, p.Thr286Pro, and p.Lys301Glu, are positioned in the regulatory domain, their effect on CAMK2 function could have potentially been predicted *a priori*. The CAMK2A His residue at 282 has been shown to be one of the important amino acid residues for potent inhibition of CAMK2A. Indeed, substitution of the histidine with an alanine at this position reduced the inhibitory potency about 25-fold (Smith *et al*., 1992). This is consistent with our findings of increased Thr286 autophosphorylation found in the CAMK2A$^{p.(His282Arg)}$ mutant. Similarly, the CAMK2A p.Thr286Pro variant blocks the critical Thr286 auto-phosphorylation of CAMK2A and hence is likely to be highly pathogenic. Surprisingly, however, we found that instead of acting as a LoF mutant, the variant renders the CAMK2A protein constitutively active and that silencing the kinase activity of this mutant form of CAMK2A normalizes migration. This is a rather unexpected finding, but one possible explanation could be that the change from a threonine into a proline causes a conformational change that is similar to undergoing phosphorylation at this site or to introducing a negatively charged amino acid (Mayford *et al*., 1995, 1996). Whether this is indeed the case will be subject of future research. Lastly, the CAMK2B p.Lys301Glu variant is located in the Ca^{2+}/CaM binding domain of CAMK2B and is therefore likely to interfere with Ca^{2+}/CaM binding and hence its activity. Indeed, our *in vitro* data show that phosphorylation of CAMK2B at Thr287 is largely absent. A knock-in mutation in CAMK2A (CAMK2$^{p.(Thr305Asp)}$) that interferes with Ca^{2+}/

Table 4. Overview of the Statistical Analysis on the In Utero Electroporation Experiments: Sum Percentage Targeted Cells Bin 1– 4 (One-way ANOVA)

	p value	F
shRNA	<0.0001*	(2,22) 53.58
CAMK2 WT	<0.0001*	(2,23) 17.70
CAMK2A	<0.0001*	(3,24) 51.07
CAMK2B	<0.0001*	(4,38) 17.54
CAMK2A controls mutants	<0.0001*	(3,24) 51.07

Asterisks (*) indicate statistical significant difference.

CaM binding has a dramatic effect on synaptic plasticity and learning (Elgersma *et al*., 2002). However, the *Camk2b*$^{p.(Ala303Arg)}$ mouse mutant, in which CaM can no longer bind to Camk2b (Shen and Mayer, 1999), has severe motor deficits (Kool *et al*., 2016) but no clear spatial learning or plasticity phenotype (Borgesius *et al*., 2011). Individual 23, in whom the CAMK2B$^{p.(Lys301Gly)}$ variant was identified, also presents the hemizygous variant *NLGN3* (GenBank: NM_018977; c.214dupG; p.Val72Glyfs*17), inherited from his mother who has microcephaly but no other cognitive or developmental impairments. Hence, it is still possible that the combination of both variants resulted in the clinical features.

The remainder of the missense variants found in our cohort all lie in the catalytic domain of the kinase and their effect is harder to predict *a priori*. The CAMK2A p.Glu183Val (CAMK2A$^{p.(Glu183Val)}$) variant was recently published by the Simons Simplex Collection as part of a large cohort study on autism spectrum disorders (Iossifov *et al*., 2014) and studied in a mouse model (Stephenson *et al*., 2017). In this study, the authors show that the CAMK2A$^{p.(Glu183Val)}$ variant results in reduced expression and activity of CAMK2A and causes behavioral deficits (Stephenson *et al*., 2017). These results are in line with our finding that the variant CAMK2A$^{p.(Glu183Val)}$ renders the protein unstable, reduces autonomous activity, and affects neuronal migration. The parallel findings emphasize the usefulness of the assays we employed to assess pathogenicity.

We observed that some variants resulted in increased and others in decreased CAMK2 activity and that all such variants also affected neuronal migration. However, the precise underlying pathogenic mechanisms may nevertheless be more complex and require further functional studies. An unresolved issue is whether haploinsufficiency could also lead to the same phenotype, as suggested by frameshift *CAMK2A* c.65del (p.Gly22Glufs*10) and nonsense *CAMK2B* c.85C>T (p.Arg29*) variants and by *CAMK2A* c.1204+1G>A which leads to out-of-frame skipping of exon 17. According to variant databases, *CAMK2A* and *CAMK2B* are predicted to be haploinsufficient (Table S4). Indeed, loss-of-function variants are exceedingly rare, in particular for the most abundant transcripts in brain, which are GenBank: NM_171825.2 for *CAMK2A* and GenBank: NM_172079.2 for *CAMK2B* (Figures S7 and S8). For these two transcripts combined, only three LoF variants were identified in 62,000 exomes sequenced by ExAC, and three in more than 69,500 exomes sequenced by centers participating in the study. A small deletion in 5q32 encompassing *CAMK2A* and four other genes was reported in two case subjects with Treacher Collins syndrome in which ID was suspected to be due to the deletion of *CAMK2A* (Vincent *et al*. 2014). The haploinsufficiency hypothesis is consistent with our knockdown experiments that showed that reduced CAMK2B disrupts migration. Yet, given that the amount of protein was reduced to 20%, this experiment may not be an appropriate test for haploinsufficiency. Our migration assay was insensitive to reducing CAMK2A levels, but this is not surprising given that CAMK2A is hardly expressed at this time point. Even if haploinsufficiency accounts for some of the case subjects, it is noteworthy that, *CAMK2A* and *CAMK2B* taken together, the ID seen in individuals included in our study seems more severe when associated with GoF variants (4/5) than when associated with LoF variants (1/6) (Table S2). This is consistent with the rather weak phenotypes of heterozygous *Camk2a* and *Camk2b* knock-out mice (Elgersma

Table 5. Post-hoc Analysis of the In Utero Electroporation Experiments: Sum Percentage Targeted Cells Bins 1–4 (Bonferroni's Multiple Comparison Test)

	p Value
shRNA	
ctr versus CAMK2A	0.7
ctr versus CAMK2B	<0.0001*
CAMK2 WT	
ctr versus CAMK2A	0.07
ctr versus CAMK2B	<0.0001*
CAMK2A	
WT versus p.Phe98Ser	0.36
WT versus p.Glu109Asp	<0.0001*
WT versus p.Pro138Ala	0.99
WT versus p.Glu183Val	0.002*
WT versus p.Pro212Leu	0.99
WT versus p.Pro235Leu	0.99
WT versus p.His282Arg	<0.0001*
WT versus p.Thr286Pro	<0.0001*
CAMK2B	
WT versus p.Glu110Lys	0.008*
WT versus p.Pro139Leu	0.0007*
WT versus p.Glu237Lys	0.005*
WT versus p.Lys301Glu	0.019*
shRNA	
WT versus p.Thr286Ala	0.002*
WT versus p.Thr286Asp	<0.0001*
WT versus p.Thr286Pro/p.Lys42Arg	0.02*

Asterisks (*) indicate statistical significant difference.

et al., 2002; Giese *et al*., 1998; Silva *et al*., 1992a, 1992b; Bachstetter *et al*., 2014; Chen *et al*., 1994), in contrast with the more severe phenotypes of mice with variants affecting auto-phosphorylation.

Of note, the case of variant *CAMK2A* c.1204+1G>A contrasts with the other variants in the series, as this is the only variant to interrupt the association domain. A similar observation was made in a recessive form of ID (B. Reversade, personal communication).

Our functional studies highlight the variety of mechanisms leading to ID related to CAMK2A/B mutations. Most certainly, this variety reflects the multiple ways CAMK2 acts on synaptic plasticity (Kim *et al*., 2016). We can therefore postulate that the spectrum of neurological disorders associated with *CAMK2A/B* variants could extend to other rare or common neurological or psychiatric disorders, as already suggested by others (Takemoto-Kimura *et al*., 2017). In our series, we stressed the frequency of abnormal behaviors, which is in line with a previous study suggesting a relationship between CAMK2A mutations and autism spectrum disorder (Stephenson *et al*., 2017). *CAMK2A* involvement was also recently shown in bipolar disorders (Ament *et al*., 2015). Given their tight link in NMDA-dependent LTP process, it is very tempting to draw a comparison between *CAMK2* and *GRIN2B* or *GRIN2A*. Variants in the latter genes may cause ID (Endele *et al*., 2010; O'Roak *et al*., 2012a; de Ligt *et al*., 2012) and infantile epileptic encephalopathy (Lemke *et al*., 2014), epileptic aphasia (Lesca *et al*., 2013), or be associated with Tourette syndrome (Che *et al*., 2015), schizophrenia (Yang *et al*., 2015), or autism (Pan *et al*., 2015).

In conclusion, our observations highlight a rare genetic cause of developmental delay/ID due to alterations in genes encoding subunits of CAMK2, a key holoenzyme in learning and memory processes in the AMPAR- and NMDAR-dependent signaling pathways. Our findings expand the phenotypic spectrum of the disorders caused by variants in other key actors of this pathway. We have identified mutations in two *CAMK2* paralogous genes as the cause of a neurodevelopmental phenotype characterized by ID. Functional studies performed in this study suggest that *CAMK2A* and *CAMK2B* may be involved in a broad range of neurologic and psychiatric disorders.

SUPPLEMENTAL DATA

De Novo Mutations in Protein Kinase Genes CAMK2A and CAMK2B Cause Intellectual Disability

Sébastien Küry, Geeske M. van Woerden, Thomas Besnard, Martina Proietti Onori, Xénia Latypova, Meghan C. Towne, Megan T. Cho, Trine E. Prescott, Melissa A. Ploeg, Stephan Sanders, Holly A.F. Stessman, Aurora Pujol, Ben Distel, Laurie A. Robak, Jonathan A. Bernstein, Anne-Sophie Denommé-Pichon, Gaëtan Lesca, Elizabeth A. Sellars, Jonathan Berg, Wilfrid Carré, Øyvind Løvold Busk, Bregje W.M. van Bon, Jeff L. Waugh, Matthew Deardorff, George E. Hoganson, Katherine B. Bosanko, Diana S. Johnson, Tabib Dabir, Øystein Lunde Holla, Ajoy Sarkar, Kristian Tveten, Julitta de Bellescize, Geir J. Braathen, Paulien A. Terhal, Dorothy K. Grange, Arie van Haeringen, Christina Lam, Ghayda Mirzaa, Jennifer Burton, Elizabeth J. Bhoj, Jessica Douglas, Avni B. Santani, Addie I. Nesbitt, Katherine L. Helbig, Marisa V. Andrews, Amber Begtrup, Sha Tang, Koen L.I. van Gassen, Jane Juusola, Kimberly Foss, Gregory M. Enns, Ute Moog, Katrin Hinderhofer, Nagarajan Paramasivam, Sharyn Lincoln, Brandon H. Kusako, Pierre Lindenbaum, Eric Charpentier, Catherine B. Nowak, Elouan Cherot, Thomas Simonet, Claudia A.L. Ruivenkamp, Sihoun Hahn, Catherine A. Brownstein, Fan Xia, Sébastien Schmitt, Wallid Deb, Dominique Bonneau, Mathilde Nizon, Delphine Quinquis, Jamel Chelly, Gabrielle Rudolf, Damien Sanlaville, Philippe Parent, Brigitte Gilbert-Dussardier, Annick Toutain, Vernon R. Sutton, Jenny Thies, Lisenka E.L.M. Peart-Vissers, Pierre Boisseau, Marie Vincent, Andreas M. Grabrucker, Christèle Dubourg, Undiagnosed Diseases Network, Wen-Hann Tan, Nienke E. Verbeek, Martin Granzow, Gijs W.E. Santen, Jay Shendure, Bertrand Isidor, Laurent Pasquier, Richard Redon, Yaping Yang, Matthew W. State, Tjitske Kleefstra, Benjamin Cogné, GEM HUGO, Deciphering Developmental Disorders Study, Slavé Petrovski, Kyle Retterer, Evan E. Eichler, Jill A. Rosenfeld, Pankaj B. Agrawal, Stéphane Bézieau, Sylvie Odent, Ype Elgersma, and Sandra Mercier

Supplemental note: case reports

Individual 1 is the child of non-consanguineous parents. Regarding family history, it is noteworthy that his mother and older maternal half-sister both attended special education classes, albeit having normal development and no behavioral issues. He also has two healthy maternal half-sisters. His younger brother was diagnosed with attention deficit hyperactivity disorder (ADHD) but showed no other behavioral anomalies, and he has been receiving a normal school education. Pregnancy was uncomplicated with normal screening. The individual rolled over at 6 months. Other motor milestones were delayed as he sat at 2 years and walked at 18 months. He does not have hypotonia. He spoke his first word at age 3 years, was able to use two-word phrases at 4 years and sentences at 5 years of age. He carries a diagnosis of ADHD and also has aggressive and self-injurious behavior. Intellectual disability was moderate but not formally assessed by an IQ test. Physical examination showed mild dysmorphic features with epicanthal folds. Growth parameters are all normal (Frontal-Occipital Circumference 49 percentile, height 24 percentile and weight 92 percentile). MRI has not been performed. Initial investigations, including chromosomal microarray, *FMR1* trinucleotide repeat analysis, plasma amino acids, and urine organic acids were within normal limits. Clinical WES revealed a heterozygous variant of unknown significance in *EP300*, which was also carried by the mother.

Individual 2 is the only child of non-consanguineous parents (French father and Mexican mother). Family history was unremarkable. Pregnancy was uncomplicated with normal screening ultrasounds. She had a normal birth weight and occipitofrontal circumference (OFC) and a birth length at the 90th percentile. She had developmental delay as she was able to sit independently after 9 months and to walk at 31 months. She was able to use two-word phrases at age 3 ½ years. Physical examination showed very mild dysmorphic features such as hypotelorism, a large mongolian spot, mild joint hyperlaxity and axial hypotonia. Brain magnetic resonance imaging (MRI) and serum creatine kinase (SCK) were normal. *FMR1* gene sequencing was negative.

Individual 3 is the first child of unrelated Irish parents with two unaffected siblings. He was born by a normal delivery with birth weight of 3.2 kg. He was noted to be floppy with poor muscle tone and had significant developmental delay at nine months. His brain MRI was normal. He was also investigated for Prader Willi syndrome. At five years of age he had severe developmental delay and was predominantly wheelchair-bound, although mother mentioned that he walks at home with a wide and unsteady gait. He had mild dysmorphic features such as straight eyebrows, almond shaped eyes and small ears. He was thought to have absence seizures, but EEG was reported normal. Array CGH was normal.

Individual 4 is the second child of non-consanguineous parents. Her sister and brother are healthy and family history is unremarkable. Pregnancy and delivery were uneventful. She has a delayed development since infancy: roll over at age 9-10 months, sitting at 12 months and walking at 24 months. At age 24 months she had a developmental delay of 12 months. Her speech development was also delayed. She uses short sentences to communicate. She has had sleeping problems (frequent awakenings during the night) since she was an infant. Melatonin patterns were normal. According to her parents she has autistic features, but she has not been officially evaluated for an autistic disorder. At age 7 years and 6 months a multidisciplinary evaluation for her intellectual disability was performed: her SON-IQ was <55; neurological exam was normal, except for a somewhat decreased tonus; mild hypermobility of the joints; no dysmorphic features, except for sandal gaps at both feet; normal ophthalmic evaluation. Brain MRI scan, standard metabolic screening and array CGH were normal. At age 10 years her IQ was <35.

Individual 5 is a boy with a diagnosis of autism who was enrolled in the Simons Simplex Collection (SSC) at the age of 5.25 years. He has one unaffected sister who has no recorded medical issues. No *de novo* CNVs were identified with a SNP genotyping array and a single *de novo* missense variant was observed in the gene *CAM2KA* (E183V). He was born by normal vaginal delivery at 41 weeks and 1 day gestation with normal Apgar scores. He said his first words at 18 months, followed by his first phrase at 3.3 years of age. He took his first unaided steps at 22 months. At the age of 5.25 years the SSC recorded a non-verbal IQ of 60 and a verbal IQ of 81, fluent speech with expressive language equivalent to 4.3 years of age, receptive language equivalent to 6.5 years of age and writing language equivalent to 2.8 years of age. These results suggest mild delays in expressive language use. In addition, the parents report concerns in the area of externalizing behaviors (e.g., attention problems and aggressive behaviors). There was no history of seizures, and cranial imagining was normal. No formal assessment of dysmorphology was recorded.

Individual 6 is a boy with a diagnosis of autism who was enrolled in the SSC at the age of 11 years. He has no brothers or sisters. No *de novo* CNVs were identified with a SNP genotyping array. Three *de novo* variants were predicted using whole exome sequencing: a missense variant in the gene *SLC26A7* (p.Ile638Val; predicted benign by PolyPhen-2), a synonymous variant in the gene *MAML2* (p.Gln605Gln), and an intronic variant adjacent to the splice donor site in *CAMK2A*. He was born by normal vaginal delivery at 38 weeks and 3 days gestation with normal Apgar scores. Initially, language was not delayed, as he said his first words at 12 months and his first phrase at 2 years of age. He took his first unaided steps at 3 years. At the age of 11 years the SSC recorded a non-verbal IQ of 38 and a verbal IQ of 35, phrased speech with expressive language equivalent to 5 years of age, receptive language equivalent to 4.5 years of age and writing language equivalent to 8.8 years of age. These results are consistent with expressive language delay. In addition, the parents reported concerns with internalizing (reflecting anxious, withdrawn/depressed, and/or somatic complaints) and externalizing behaviors (rule-breaking and aggressive behaviors), as well as elevated activity levels (relative to other children in SSC). There was no history of seizures, and cranial imagining/EEG were both normal. No formal assessment of dysmorphology was recorded.

Individual 7 is the first child of non-consanguineous French parents (with two healthy sisters). Family history was unremarkable, and pregnancy was uncomplicated. He had normal birth parameters but in the first year, he developed an overgrowth (weight +3SD, height +2.5 SD, head circumference +2 SD) that persisted through adolescence. He was also hypotonic. He was able to sit independently at 15 months and walked at 33 months. He was able to use two-word phrases at 4 ½ years old. At the age of 18 years, his language was underdeveloped, and he had not learned to read and write. Physical examination showed mild dysmorphic features with frontal cowlick, brachycephaly, and large mouth. He was still hypotonic with a severe scoliosis requiring arthrodesis and genu valgum. Brain MRI, serum creatine kinase, bone age, and array-CGH were normal. *FMR1* trinucleotide repeat analysis was negative.

Individual 8 is the third child of non-consanguineous parents. His sisters are healthy and family history is unremarkable. Pregnancy and delivery were uneventful and biological parameters at birth were normal. Neurological exam was marked by hypotonia, slowly regressive after several years. Walking was achieved at 27 months. Speech delay was prominent. He associated two words at age 5.5 years and sentences containing three words were noticed at the age of 8 years. His agitation diminished after age 6 years but hyperactivity and attention deficit disorder remained and grapho-motor skills are still impaired at age 10 years. Social competences increased progressively and the initial diagnosis of autistic behavior has been revised. He is attending a special school. His neurological exam is normal and he has no dysmorphic features except a micropenis. Epilepsy started at age 7 years with focal motor seizures of oropharyngeal type with salivation. He presented also rare secondary generalized seizures. EEGs showed bilateral independent biphasic rolandic spikes, becoming sub continuous in sleep. Background rhythm was normal. Seizures and EEG paroxysms diminished with aging consistent with benign childhood epilepsy with centro-temporal spikes. Brain MRI and standard metabolic screening were normal. *GRIN2A* mutation was suspected based on the cognitive profile (Vineland at age of 5 years and 9 months: communications skills 48; motor skills 71; social competences 68) and the significant activation of paroxysmal focal activity in sleep EEG, but it was ruled out by genetic analyses.

Individual 9 is the only child of healthy consanguineous parents from Turkey. Pregnancy was uneventful. Delivery was without complications, and head circumference was not measured at birth. Developmental delay was detected at the age of 6-8 months. Her motor development is slightly delayed. At the age of 3 years she uses some words. On physical examination, no dysmorphic features were noted. MRI and CT scan were normal.

Individual 10 is a boy born at 38 weeks gestation after a pregnancy complicated by polyhydramnios and concern for short femurs. He first presented to clinical genetics at 8 months of age due to mild speech delay, delayed growth, relative macrocephaly and large fontanelle. He had normal thyroid and growth hormone studies and normal skeletal films. He sat at 6 months, walked at 20 months and began to develop speech at 20 months. He received speech services for several months, but subsequently tested out of the need. At 35 months, he had three-word sentences. Family history is notable for a 13-year-old maternal half-brother with expressive and receptive language apraxia. His physical exam was notable for head circumference at the 95th percentile with height and weight at 50th and 25th percentiles, respectively. He had a nevus flammeus on his forehead and downslanted palpebral fissures. His fontanelle had closed by 23 months, when he was noted to have a prominent metopic suture, telecanthus, a mildly flat chest, diastasis recti, intermittent periods of staring at the room lights, mild ulnar deviation of the proximal interphalangeal joint of the second finger and mild prominence of the heels. Testing included a normal Illumina CRC 850K BeadChip

chromosome microarray, normal Russell-Silver testing (11p methylation, UPD7 testing and *CDKN1C* sequencing). Noonan syndrome genes were analyzed with the exome sequencing and were normal. Exome sequencing noted a *de novo CAMK2A* c.704C>T; p.(Pro235Leu) variant not seen in his parents or maternal half-brother.

Individual 11 is the second daughter of unrelated German parents, born after an uneventful pregnancy by CS because of breech presentation. She showed psycho-motor delay and hypotonia from the beginning. At age one year, mild microcephaly was noted and she showed an irritable behavior with stereotypies. At 15 months, she started to have complex focal seizures. On examination at age 3 years 10 months, she was still hypotonic, showed breathing irregularities, hyperkinetic-dystonic movements, drop feet and mild microcephaly (-2.1 SD). She could roll over but was unable to sit, crawl or stand up and had no speech. Under therapy with valproate she suffered from seizures once in 3 to 4 weeks. Her behavior was characterized by hyperkinesia, unrest and autistic traits. At the age of 6 years, she was reported to be still unable to walk and to pronounce words. Investigations prior to exome sequencing included chromosome analysis, SNP-array, MECP2 analysis, extensive metabolic investigations and analysis by next generation sequencing of targeted gene panels for epileptic encephalopathies and for intellectual disability, all with normal results. Repeated cranial MRI showed an unspecific deficiency of white matter and periventricular FLAIR hyperintense signals.

Individual 12 is the only child of non-consanguineous parents. Mother has a daughter with another partner. Family history was unremarkable except a cousin of the grandmother who had psychomotor retardation and autism. The affected individual was born after an uncomplicated pregnancy of 41 weeks. He was a quiet baby with a delayed development since birth. He was able to sit independently after the age of 15 months and walk after the age of 36 months. He is uttering sounds from the age of 3 years. He is not able to speak at the age of 7 years and 10 months except some simple words. He shows severe behavior problems: he is easily distracted by stimuli, hyperactive, anxious, with stereotypical movements, and he has been diagnosed with having a pervasive developmental disorder. Physical examination at the age of 6 years and 10 months showed a head circumference of 51.3 cm (-0.4 SD), height of 116 cm (-1.72 SD), mild full lips, mild valgus and flexion of the knees and bilateral pes planovalgus. Male genitalia are normal. Brain MRI showed a relative thick corpus callosum but no other specific abnormalities. Metabolic investigations, ophthalmological examination and SNP array analysis (Illumina® CytoSNP-850K SNP-array) are normal.

Individual 13 is the second child to non-consanguineous American parents. Family history is unremarkable. Pregnancy was complicated by preterm labor at 35 weeks gestation. After a period of bed rest, the individual was born at 38 weeks gestation with normal growth parameters. Initially, she had hypotonia and poor head and trunk control. Physical therapy started at 6 months of age. This individual is currently 20 months of age, and there are no additional health concerns. She does not track objects consistently. She has poor use of her hands and often has non-purposeful hand movements. Physical examination showed a profoundly hypotonic nondysmorphic child in constant motion, who repeatedly brings hands to mouth. Brain MRI, SNP microarray, *SNRPN* methylation, very long chain fatty acids, and metabolic studies were all normal. An 18-gene Rett/Angelman sequencing panel was also done, and a variant of unknown significance identified in the *ZEB2* gene (Next Generation Sequencing technology at Fulgent Diagnostics). This variant was later confirmed by whole exome sequencing to be paternally inherited and ruled out as the cause.

Individual 14 is a 3-year and 9-month-old female who was referred to genetics for behavioral issues. She had sleeping difficulties due to nightmares, and showed anxiety and aggressiveness manifesting by temper tantrums. Her developmental delay was mild, as she reached most developmental milestones at expected times. She sat at 8 months and first walked at 15 months. She spoke 100 words at 21 months. At last examination, her intellectual disability was mild. In addition, she had duodenal atresia, ventricular septal defect, and hypoplastic thumb and radius. Exome sequencing revealed a *de novo* splice site variant c.1204+1G>A p.? in *CAMK2A*.

Individual 15 is a 6-year-old female who was referred to genetics at 2 years of age for possible ectodermal dysplasia. She was born at full term via vaginal delivery and had normal growth and development as an infant and toddler. She was essentially bald until around 2 years of age when some scalp hair started growing in. She has no body hair. Her fingernails and toenails grow but they are thin and tear easily. She had no teeth until 22 months of age. She does not sweat normally. When she is overheated, she turns red and becomes fatigued. She never sweats with fevers, and her fevers can get quite high (104-105) without relief from antipyretics. She has required IV hydration with viral illnesses due to her high fevers. She has eczema and dry skin. She was diagnosed with Mycobacterium avium intracellulare (MAI) at 18 months of age and had a mediastinal mass that was resected. Given her history of an unusual infection plus sparse hair growth and delayed tooth eruption, she was sent to genetics for evaluation for ectodermal dysplasia, specifically an ectodermal dysplasia associated with immune dysfunction. She has had intermittent neutropenia. No specific form of immunodeficiency has been identified through extensive testing by immunology. Aside from her MAI infection, she has never has any other unusual or atypical infections. She had a recurrent laryngeal nerve injury from the surgery and has a persistent left vocal cord paralysis with aspiration requiring thickened liquids. She has a history of speech delays, primarily in speech enunciation, unrelated to her vocal cord paralysis. She has normal fine and gross motor development. With regard to her development, she had a kindergarten screen done and tested at the 7th percentile. She has an IEP and an aide in the classroom. With regard her verbal skills, she has gained a lot of language skills between ages 2 and 4. Mother feels that she is very intelligent and has good receptive language skills. She is able to speak in full sentences but pauses frequently due to her vocal cord paralysis. She had her

first tonic-clonic seizure with loss of consciousness at 3½ years. Since then she has multiple seizures including "drop seizures" and cluster seizures. The tonic-clonic seizures are focal with right facial twitching and right upper and lower extremities jerking. Her small clusters also only involve right side of body. She has been on various anticonvulsants, and seizures have been under better control on Keppra. *EDA1*, *EDAR*, *EDARADD*, *WNT10A*, and *NEMO* sequencing results were all normal. She underwent whole exome sequencing through GeneDx Laboratory. The lab reported several variants which were possibly associated with the reported phenotype. She was heterozygous for a maternally inherited p.Q31H variant of unknown significance in the *ALOXE3* gene. This gene encodes a lipid processing enzyme which is crucial for formation of the epidermal lipid barrier. Loss-of-function mutations in this gene are associated with autosomal recessive congenital ichthyosis. She was found to be heterozygous for a maternally inherited p.Q242R variant in the *RAG1* gene. This gene is associated with severe combined immune deficiency and Omenn syndrome which are both autosomal recessive forms of immunodeficiency. Mother was also heterozygous for the same change. Her immunological testing is not consistent with severe combined immune deficiency, and she only had one sequence variant in this gene; affected individuals would be expected to have mutations in both alleles. She was also found to be heterozygous for a paternally inherited p.W616R variant in the *TLR1* gene. This gene encodes the toll-like receptor 1, and the laboratory thought that it was a candidate gene with a potential relationship to the phenotype. To date, no mutations in *TLR1* have been reported in association with a specific human disease. This protein may play a role in susceptibility to mycobacterial infections. Subsequently, her exome was reanalyzed, and she was found to have a *de novo* heterozygous variant in the *CAMK2B*, c.85C>T p.(R29*). This variant has not been reported previously as a pathogenic variant or as a benign variant. It is predicted to cause loss of normal protein function, either through protein truncation or nonsense-mediated mRNA decay. She was last seen at 5 years of age. She got her first tooth at 22 months of age, and subsequently all of her deciduous teeth have come in. She does not have any missing teeth. She has had no dental cavities. Her teeth are crowded together. Her hair growth has improved. She has had 2 trims of her hair total, and her hair is getting thicker over time. Her nails are thin, but they do not tear as much as they used to. She trims the nails once a week. She has never had sweat production to date. She uses an umbrella when she is outside as well as a misting fan. She gets tired easily in the heat. On physical exam at 5 years of age, she was a well-nourished, white female. Height was 84th centile, and weight was 64th centile for age. Head shape was normal. She had more scalp hair than when she was younger, and it was thicker than before. Facial features were non-dysmorphic. Pupils were equal and round. Extraocular movements were intact. Eyebrows and eyelashes were present. Nose and mouth were normal. Examination of the oropharynx showed that she had normal deciduous dentition for her age. Palate was intact. Ears were normally formed. Neck was normal. Lungs were clear. She had a right thoracotomy scar. Cardiac exam showed a regular rate and rhythm, with no murmur. The abdomen was soft with no organomegaly or masses. GU exam was normal female. The limbs were normal. She had very little to no body hair. She had sweating on the soles of her feet and the palms of her hands but nowhere else on the body. Nails were present on all digits but were relatively thin and soft.

Individual 16 is a 10-year-old girl with a history of developmental delay, hypotonia and periodic behavior disturbances. She was born by spontaneous vaginal delivery at 37+1 weeks gestation to a 33-year-old G1P0 mother and a 33-year-old father. Pregnancy was complicated by preterm labor at 20 weeks treated with terbutaline and bed rest. Apgar scores were 4 and 8. Individual 16 was floppy at birth and required positive pressure ventilation for two minutes. At 20 hours of age the individual had an episode of redness and stiffening lasting 15-30 seconds. Evaluation for sepsis was negative, and no further episodes were observed. The individual first walked at 18 months and spoke her first word at approximately 30 months. She has had a history of constipation since one year of age. She was diagnosed with esotropia at age 2 years 10 months and underwent strabismus surgery at age 5. Her gait has always been slightly unsteady. MRI of the head has been unremarkable at ages 3, 8 and 10. Magnetic resonance spectroscopy was included in the first two studies. Since the age of 7 she has had recurrent episodes of atypical behavior featuring irritability, decreased appetite, aggression, and sometimes urinary retention or incontinence. Initially these episodes occurred roughly monthly and lasted approximately one week. She is reported to have always returned to her baseline between episodes. An EEG performed at the time of an early episode showed mild slowing. Subsequent studies have not redemonstrated this finding. Over time the episodes have decreased in severity, frequency and duration concurrent with the administration of lithium and verapamil. Previous trials of olanzapine, risperidone, quetiapine, nortriptyline, cyproheptadine, gabapentin, levetiracetam, selective serotonin reuptake inhibitors and benzodiazepines were not associated with symptomatic improvement. Individual 16 additionally has a history of eczema and food allergies. Her growth parameters have been typical for age. Prior laboratory evaluations have included DNA microarray, mitochondrial genome sequencing, muscle biopsy with electron transport chain studies, fragile X testing, cerebrospinal fluid (CSF) amino acids, CSF neurotransmitters, plasma and urine creatine studies, lysosomal enzyme panel, carbohydrate deficient transferrin screen, urine organic acids, plasma amino acids, plasma ammonia, plasma lactate, acylcarnitine profile and urine purines and pyrimidines.

Individual 17 is the second child to non-consanguineous American parents. She was born by caesarean section due to breech position after an uncomplicated pregnancy. At age 3 months, she was diagnosed with reflux and was noted to be "fussy" despite treatment of her reflux symptoms. She was evaluated at age 4 months for continued irritability and poor visual interaction in terms of eye contact and smiling responsiveness. Ophthalmology noted visual inattentiveness with possible delayed visual development, but she had an otherwise normal eye examination. At 5 months, she was diagnosed with developmental delay with head lag, lack of any verbalizations and delayed ability to step, walk or bear weight. Early intervention therapies, including physical, occupational and visual therapies were started. Brain MRI at 9 months was normal with no structural abnormalities or acute anomalies seen, and a

repeat MRI at 2 years was unchanged. EEG at 19 months was normal, with no history of seizure activity reported. A thorough genetic evaluation was inconclusive and included a normal karyotype, chromosomal microarray, *CDKL5, MECP2, UBE3A* sequencing and methylation and deletion and duplication studies for Angelman/Prader-Willi locus on chromosome 15. Other normal evaluations included thyroid hormone levels, urine organic acids and plasma amino acids. She was 3 years, 10 months at her last evaluation and was noted to have gastrointestinal dysmotility, a movement disorder, microcephaly with bitemporal narrowing, growth delay, and mild dysmorphic features (Figure S1) in addition to the findings noted above.

Individual 18 is the first child born to non-consanguineous parents. She has a younger unaffected sister. She was born at 41 weeks by caesarean section due to an abnormal cardiotocography trace. It was noted later that she had poor visual fixation and was diagnosed with delayed visual maturation. At four months she was found to have significant hypotonia. She was also noted to have irritability, gastroeosophageal reflux and constipation. Although head circumference was normal at birth, it was apparent that as she grew older she developed microcephaly. In addition to significant global developmental delay, Teeth grinding and abnormal breathing pattern consisting of hyperventilation and apneas led to investigations for Rett syndrome and then Pitt-Hopkins syndrome. MRI and EEG were normal, as were metabolic investigations and a microarray. She has sleep abnormalities, disturbed behaviour consisting of episodes of screaming, aggression to self and others and head nodding and autistic traits. Walking was attained between 4 and 5 years of age, but no speech developed. Mild dysmorphic features were also present.

Individual 19 is a 9-year and 7-month-old girl with a complex neurodevelopmental syndrome characterized by hypotonia, postnatal microcephaly, abnormal movements, autistic features, and constipation. She was born to her 43-year-old gravida 2, para 0-1 SAB 1 mother and unrelated 38-year-old father after a pregnancy complicated by preterm labor at 5 months requiring cerclage. There were no exposures reported during the pregnancy and her mother was given some betamethasone prior to delivery. Prenatal ultrasounds were within normal limits. She was born at 34 weeks of gestation by urgent caesarean section for fetal distress. She was noted to be small for gestational age with a birth weight of 1.93 kg, approximately the 10th percentile for gestational age. Birth length was 17.5 inches, and OFC was 31 cm, at the 50th percentile for gestational age. Some abnormalities were reported in the placenta, but pathology results are unknown. She remained in the Neonatal Intensive Care Unit for the first 11 days and had one small apneic event but did not require respiratory support. Feeding difficulties were treated with nasogastric feeds, but she progressed to breast feeding during her first 2 months of life. She had significant problems with spitting up, reflux, and poor feeding abilities in the first 6 months of life. There were concerns about her development starting at about 6-9 months of age. She stopped rolling over after a short while, and her head OFC was noted to be small at 1 year of age, so concern for microcephaly was raised. During her first formal evaluation at that time, she was noted to have microcephaly with progressive ataxia, developmental delays and visual inattention. On last assessment at 9 years and 7 months, she was noted to have the following medical issues: severe intellectual delays, postnatal microcephaly, hypotonia, severe gastrointestinal problems, including severe gastroesophageal reflux status post G-tube feeds, history of epilepsy, autistic features, abnormal movements and intermittent dysautonomia. Her seizures consisted of alteration of consciousness without any generalized tonic-clonic activity. She has not been started on any antiepileptic medications. She has undergone an extensive array of genetic and imaging studies including the following:

- metabolic workup that includes urine organic acids, serum amino acids, and acylcarnitine profile.
- CSF (cerebrospinal fluid) studies.
- normal enzyme testing for GM1 gangliosidosis, beta mannosidosis, and beta hexosaminidase A, Tay-Sachs, arylsulfatase-A for metachromatic leukodystrophy, and galactocerebrosidase for Krabbe's disease.
- Chromosomal microarray that revealed a duplication of 6q27.
- Angelman syndrome testing, including FISH for 15q11-q13, and *UBE3A* sequencing.
- *MECP2* sequencing and deletion/duplication analysis.
- Prader-Willi methylation testing.
- *CDKL5* sequencing.
- IGF-1 and IGFBP-3 testing and TTG level as well.

She previously had a brain MRI scan that revealed a low sloping forehead consistent with postnatal microcephaly, with mild cerebral and cerebellar atrophy. She did not have any cortical brain malformations or ventriculomegaly. The basal ganglia and thalami were normal.

Individual 20 is a 4-year-old girl who was evaluated in the NIH-funded Undiagnosed Diseases Network at the Harvard Clinical Site (Boston Children's Hospital). She had severe global developmental delay, hypotonia, feeding intolerance, short stature, hyperkinesia with some dyskinesia, and high pain threshold. She was born at 38 weeks' gestation following an unremarkable pregnancy with no known exposures to any teratogens, weighing 3.06 kg (25^{th}–50^{th} centile) and measuring 43.2 cm (less than 3^{rd} centile) in length. She had meconium aspiration at birth, and prior to discharge suffered an apneic episode requiring intubation for 16 hours. She has severe global developmental delay, but has not had any developmental regression. At 3 years old, she was functioning at a 6-7 month-old level. She was able to sit with support but was unstable. She was able to move her limbs symmetrically and against gravity, but she had mild diffuse hypotonia. Her expressive language consisted of non-specific babbling with no definite words. Socially, she had poor eye contact (attributed to inattention and perhaps difficulty with visual processing);

she does not typically respond to her name. Since infancy, she had had involuntary movements of the limbs, primarily hyperkinesia with occasional dyskinesia, and occasional arching of her back. These movements would resolve during sleep, raising the possibility of basal ganglia pathology, but her brain MRIs had been normal. There was no history of seizures. She has had sleep disturbances, characterized by long sleep latency and multiple nocturnal awakenings, since early infancy. She has also had extensive gastrointestinal issues, including poor weight gain, constipation, and feeding intolerance, and was dependent on her gastrostomy tube. She had short stature and her bone age was delayed, but there was no biochemical evidence for growth hormone deficiency, suggesting her short stature was related to her underlying diagnosis. Family history was unremarkable apart from a paternal first cousin with epilepsy. On physical examination, her height was at approximately -2.4 SD, weight was at approximately -2.9 SD, and head circumference was at approximately -3.4 SD. The height and weight were plotted on the United States Centers for Diseases Control and Prevention Growth Charts, while the head circumference was plotted on the United States head circumference charts published by Rollins JD, *et al*. (J Pediatr. 2010 Jun;156(6):907-13). She had mild dysmorphic facial features, including a slightly prominent forehead, midface retrusion and slightly deeply-set eyes with prominent lashes, short chin, and widely spaced teeth. Prior genetic and metabolic testing, including methylation studies for Prader-Willi/Angelman syndromes, chromosomal microarray, fragile X molecular analyses, and metabolomics studies on plasma, urine, and cerebrospinal fluid, was all negative. Muscle biopsy with electron transport chain analysis was also normal. Brain, spin, and abdominal MRIs were normal. Whole exome sequencing on individual 16 and both unaffected parents performed at Baylor Genetics Laboratories (Houston, TX) identified a *de novo* heterozygous *CAMK2B* variant: c.416C>T (p.P139L).

Individual 20 was born at term. The only notable feature of the pregnancy was marked maternal nausea during the pregnancy. She had normal growth parameters at birth, although weight was on a lower centile than head circumference. She was hypotonic with frequent apneas from birth. Originally an EEG was said to show Otahara burst suppression, but the diagnosis of epilepsy is uncertain as subsequent EEGs have been normal. She has persistent poor growth, hypotonia, a need for gastrostomy feeding and no speech development. She has never walked. Extensive metabolic and reasonably up-to-date genetic investigation was normal until inclusion in the DDD study and identification of a *de-novo CAM2KB* variant. There were no convincing abnormalities on MRI scan.

Individual 21 was born at term. The only notable feature of the pregnancy was marked maternal nausea during the pregnancy. She had normal growth parameters at birth, although weight was on a lower centile than head circumference. She was hypotonic with frequent apneas from birth. Originally an EEG was said to show Otahara burst suppression, but the diagnosis of epilepsy is uncertain as subsequent EEGs have been normal. She has persistent poor growth, hypotonia, a need for gastrostomy feeding and no speech development. She has never walked. Extensive metabolic and reasonably up-to-date genetic investigation was normal until inclusion in the DDD study and identification of a *de-novo CAM2KB* variant. There were no convincing abnormalities on MRI scan.

Individual 22 is the only child of non-consanguineous parents of mixed Scandinavian, Russian, and Irish ancestry. Pregnancy, delivery and birth parameters were normal. The individual was normal until one month of life when the parents noticed abnormal eye movements and body posturing with arm extension and jerking, head tilting and back arching. At two months of age, she was tracking 180 degrees, lifting her shoulders and head off the bed in prone position, cooing and vocalizing, and was attentive to auditory stimuli. At four months of age the individual was noted to be hypotonic, have poor neck control, and was diagnosed with nystagmus and esotropia with poor eye contact and tracking. Brain MRI and electroencephalogram at four months were normal and she was treated for clinical reflux. At eight months of age, the individual still was significantly hypotonic with head lag but was able to hold onto toys placed at her chest. She underwent surgery for strabismus at 13 months of age, which improved her ability to fix and follow. At 14 months of age, she was able to sit with significant support but not independently, was able to hold her bottle, but was not able recognize her parents, point, or communicate. Loud noises and crowded areas cause distress for the individual 22. Growth parameters have been normal throughout, and the individual has been able to eat pureed and soft foods without aspiration. No developmental regression has been noted. Prior laboratory evaluations were unremarkable and included thyroid function tests, morning cortisol and ACTH, creatine kinase, ammonia, lactate, pyruvate, uric acid, plasma amino acids, plasma acylcarnitine profile, urine organic acids, plasma and urine creatine studies, very long chain fatty acids, plasma oxysterols, carbohydrate deficient transferrin screen, chromosomal oligo microarray with SNP analysis, and Prader-Willi and Angelman Syndrome methylation analysis. AST and ALT were each 1-2 points above the upper limit of normal, and carbohydrate deficient transferrin analysis was essentially normal with slight elevation in mono-oligo/di-oligo, and Apo CIII0/Apo CIII2 ratios. The only variant of interest detected by exome trio sequencing was a de novo *CAMK2B* splice site variant.

Individual 23 is an 8-year-old boy who has been followed due to microcephaly, epilepsy and global developmental delays and intellectual disability. Pregnancy and birth history were unremarkable. Since early childhood, his growth parameters have shown height and weight above the 95th percentiles but head circumference below the 3rd percentile. Family history is significant for microcephaly in mother, but she has no cognitive deficiencies or history of seizures. There are 2 maternal male relatives with autism spectrum disorder. Previous genetic and metabolic testing had been non-diagnostic. Whole exome sequencing was performed in 2015 through Ambry Genetics Lab. He has a maternally inherited pathogenic mutation in the *NLGN3* gene. Mutations in this gene are associated with X-linked autism and intellectual disabilities. With this individual history of microcephaly, seizures and severe

intellectual disability, the *NLGN3* mutation did not appear to explain all of his findings. He was then also identified to have a *de novo* variant in the *CAMK2B* gene.

Individual 24, an 11-year-old boy with a static encephalopathy, is the first child of non-consanguineous Norwegian parents. His younger sister is healthy, and family history is unremarkable. High maternal titers of irregular anti-D and anti-C antibodies were noted antenatally, and delivery was induced at 38 weeks. Measurements at birth were: weight 2495 g (4th centile), length 46 cm (6th centile), occipitofrontal head circumference 33 cm (10th centile). An uncomplicated exchange transfusion was performed during the first day of life, and his neonatal course was otherwise unremarkable. The child was hospitalized in early infancy because of poor weight gain and developmental concerns. Global developmental delay and frequent involuntary movements, the latter beginning between age one and two years, resulted in an initial diagnosis of dyskinetic cerebral palsy. The movements are not epileptic in nature, not present during sleep and lessen when he is tired. At age 11 years he lacks speech but communicates by gestures and can write by pointing at letters. He is able to read. His cognitive level is difficult to judge. He still cannot sit without support and has never walked. He is able to swallow puréed food. He continues to receive liquids via a gastrostomy that was placed at age nine years. Recurrent serous otitis was an issue previously, but he hears well now. He was thought to be cortically blind until age six years but now sees reasonably well at close range and uses glasses to correct for mild nearsightness and astigmatism. However, his involuntary movements also interfere with his ability to sustain gaze and to track objects visually. A major parental concern is unexplained monthly bouts of irritability and apparent discomfort, possibly due to abdominal pain. The duration and severity of these episodes has decreased somewhat over time. Current medical issues include gastroesophageal reflux which is treated medically and brief complex partial seizures for which he is not medicated. On examination he is microcephalic but not dysmorphic. He has frequent, non-rhythmic, large amplitude, non-purposeful movements of limbs and head as well as poor head control. Truncal hypotonia is still present while spasticity of the lower limbs has developed. Cranial MR findings are non-specific. A 400k oligo array CGH was normal. Two *de novo* variants were detected by exome trio sequencing, a canonical splice site variant in *CAMK2B* and a substitution in intron 10 of *PSMD12* (Chr17 (GRCh37): g.65337173A>C NM_002816.3(*PSMD12*):c.1162-5T>G, p.?). Although the latter variant is not present in gnomAD or ExAC, we have classified it as likely benign based on prediction programs (predicted change at acceptor site 5 bps downstream -9.3%, MaxEnt -22.6%, NNSPLICE -1.4%, HSF -3.8%). Of note is the absence of features (other than ID) described in individuals with *PSMD12* mutations (eg. dysmorphic facial features, structural thumb abnormalities, structural renal abnormalities, anomalous shape and positioning of the outer ears, micro- or retrognathia) (Küry *et al*., 2017a). Although we cannot rule out a blended phenotype to which both *de novo* variants contribute, the clinical features in the child we report here are in consistent with the findings in individuals with *CAMK2A/B* mutations as described in this report.

Supplemental figures and legends

Figure S1. Photographs of individuals with *CAMK2A* or *CAMK2B* variants.
Individual numbers in bold and ages at the time of the photographs are indicated at the left of and below the pictures respectively.

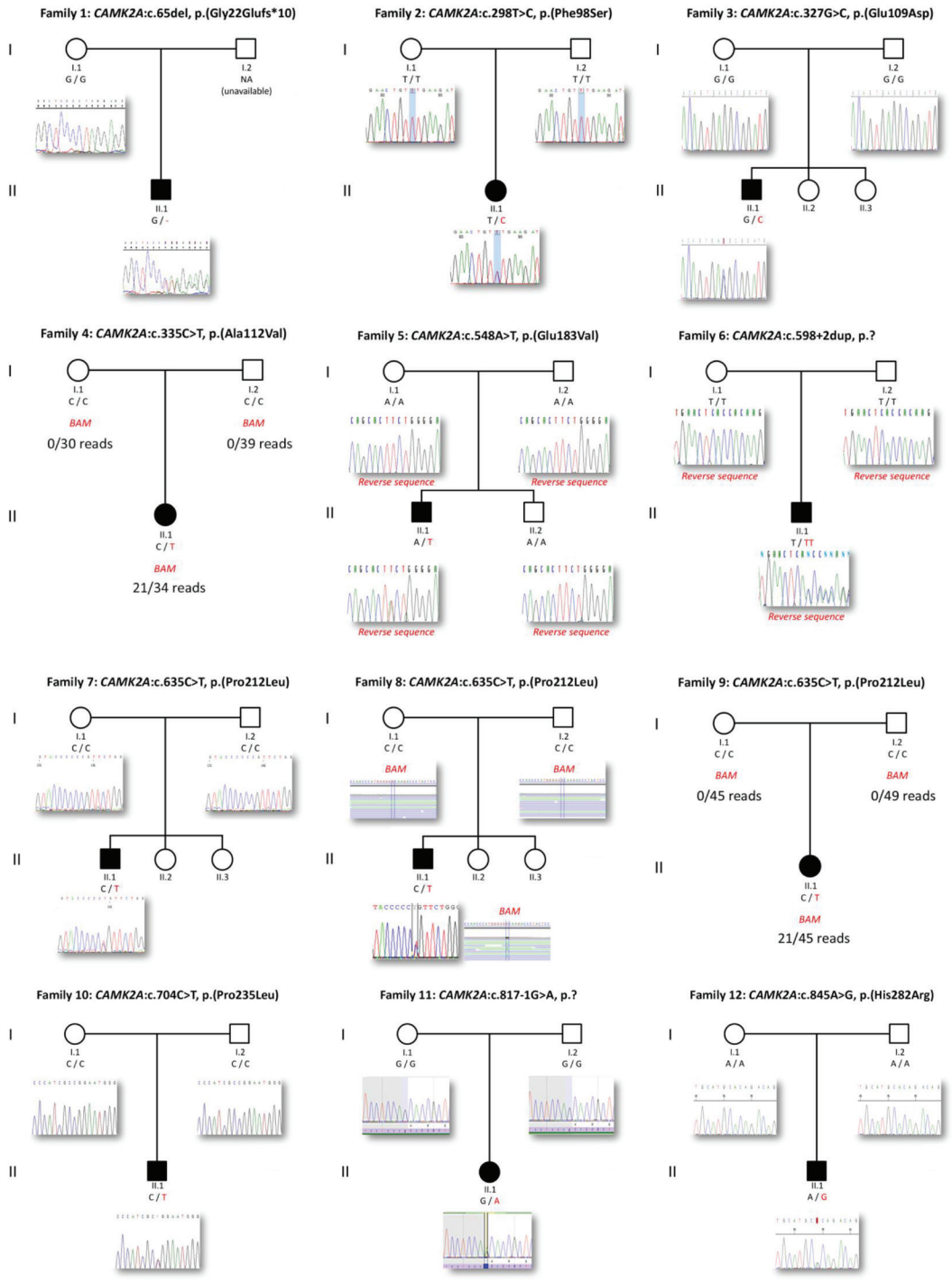

Figure S2. Segregation analysis of *CAMK2A* and *CAMK2B* variants (1/2).
This figure shows genealogical trees of families presented in the study for which genotypes identified by whole exome sequencing data were validated by Sanger sequencing. Electropherograms related to mutations found in Families by Sanger sequencing figure below each individual of the trios whenever traces were available (except for families 4, 9, 18 and 21).

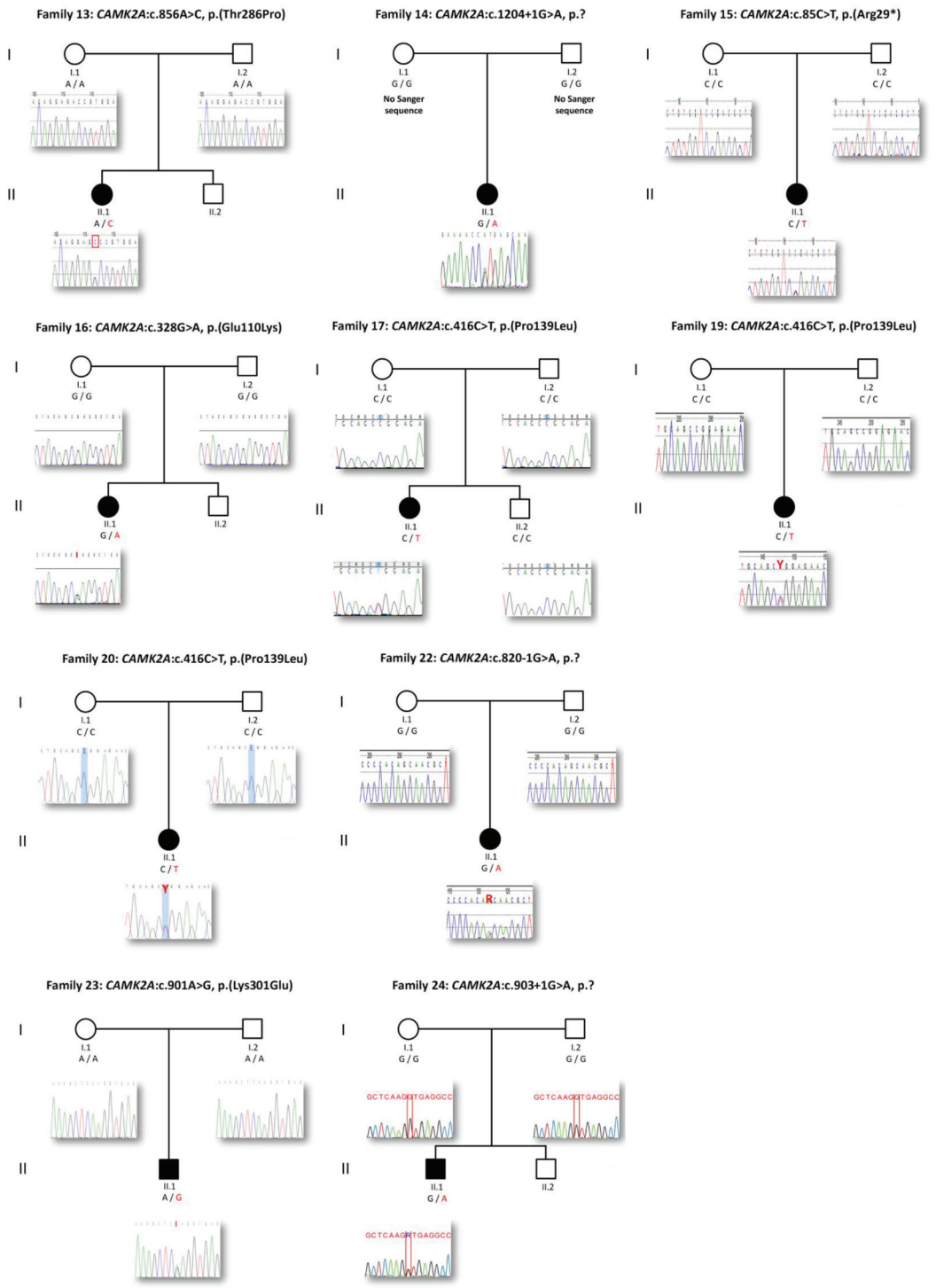

Figure S2 (continued 2/2).

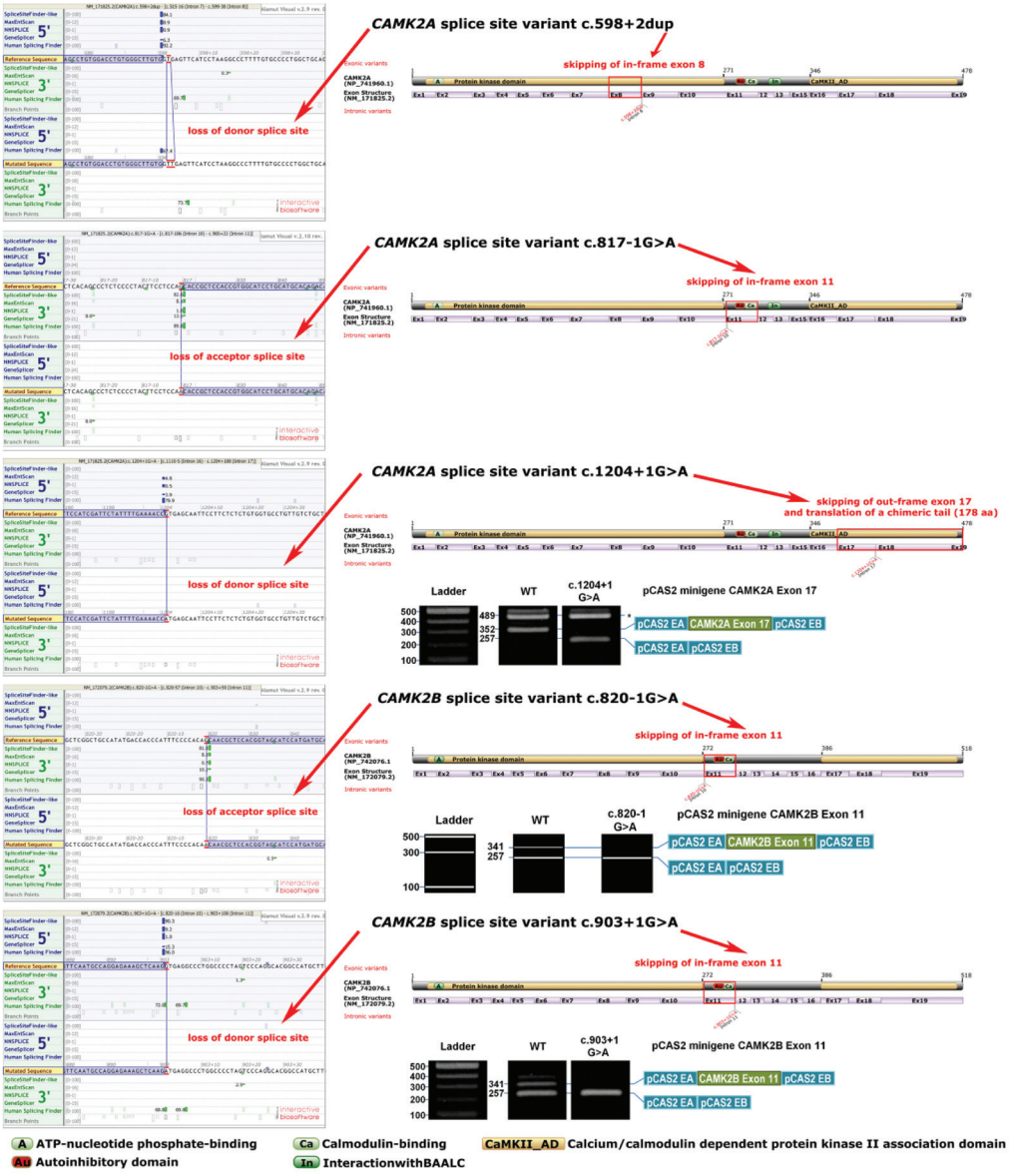

Figure S3. Predicted effect of splice site variants. According to prediction programs Splice Site Finder-like, MaxEntScan, NNSplice, Gene Splicer, and Human Splicing Finder compiled by Alamut Visual v2.9 rev. 0 (Interactive Biosoftware, Rouen, France), the five variants *CAMK2A* c.598+2dup, c.-817G>A and c.1204+1G>A, and *CAMK2B* c.820-1G>A and c.903+1G>A induce a loss of canonical acceptor and donor splice sites (see panels on the left). The most likely consequence is a skipping of in-frame *CAMK2A* exon 8 for c.598+2dup, in-frame *CAMK2A* exon 11 for c.-817G>A, out-frame *CAMK2A* exon 17 for c.1204+1G>A, and in-frame *CAMK2B* exon 11 for c.820-1G>A and c.903+1G>A. Predictions about the effects of variants *CAMK2A* c.1204+1G>A and *CAMK2B* c.903+1G>A were confirmed *in vitro* by used of a mini-gene system (see lower panels); PCR products were visualized on 1.% agarose gel for variants *CAMK2A* c.1204+1G>A and *CAMK2B* c.903+1G>A, and with a LabChip GX (PerkinElmer,Inc(USA); Software Version 4.2.1745.0) for variant *CAMK2B* exon 11 for c.820-1G>A. Asterisk indicates a non-physiological splicing artifact for c.1204+1G>A. At the protein level, *CAMK2A* variants would therefore result in a partial loss of the kinase domain of CAMK2A as concerns c.598+2dup, and of a replacement of most of the association domain of CAMK2A by a 178 amino acids long tail as regards c.1204+1G>A. On the other hand, *CAMK2A* c.-817G>A and the two *CAMK2B* variants would cause the loss of the autoinhibitory domain in CAMK2A and CAMK2B –which contains respectively phosphorylation sites T286 and T287- and of the calmodulin-binding site. DNA variants are described according to the nomenclature established by the Human Genome Variation Society. Nomenclature HGVS V2.0 is defined according to mRNA reference sequence NM_171825.2 for *CAMK2A* and NM_172079.2 for *CAMK2B*. Nucleotide numbering uses +1 as the A of the ATG translation initiation codon in the reference sequence, with the initiation codon as codon 1.

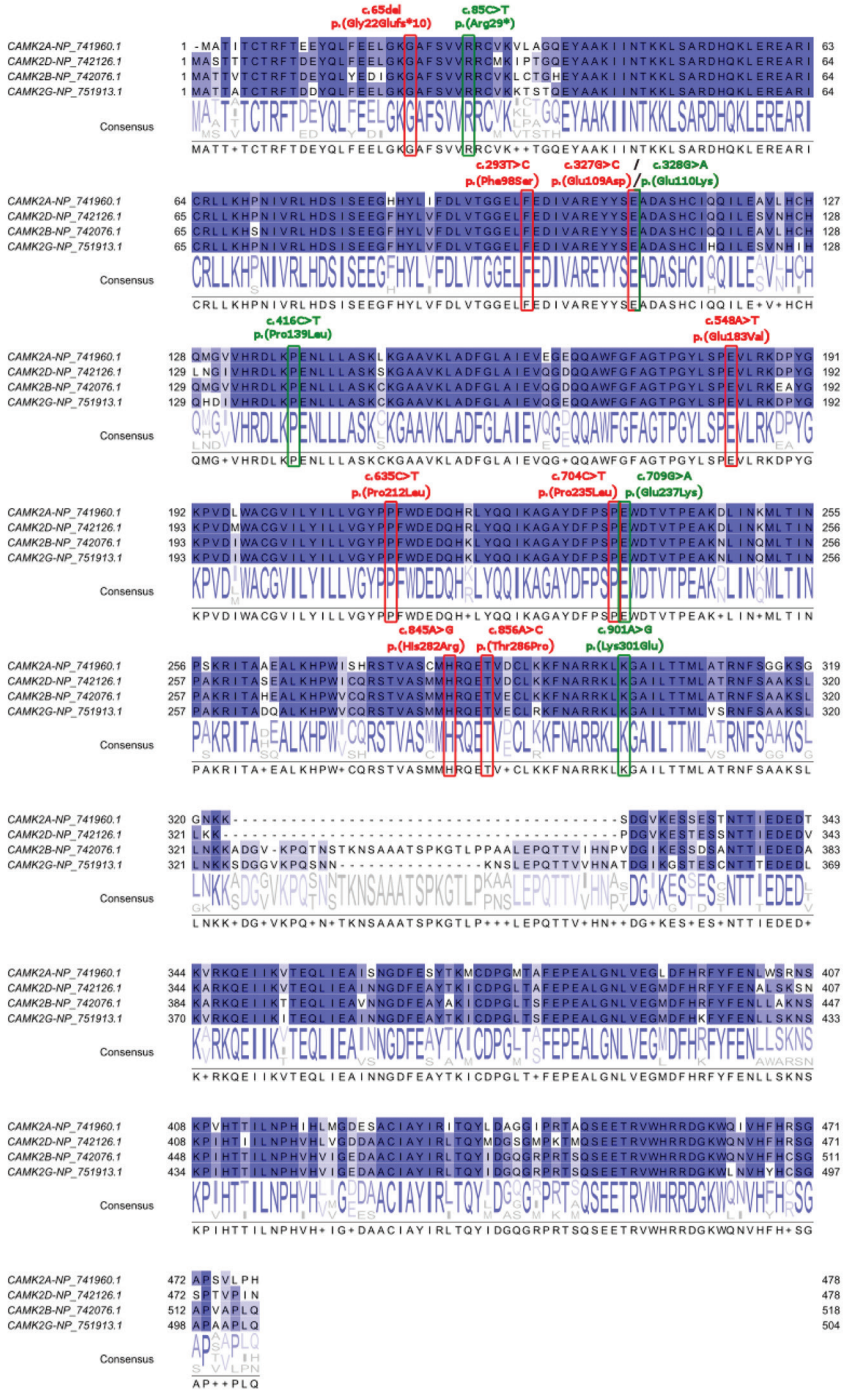

Figure S4. High conservation across CAMK2 paralogues of amino acid residues affected by CAMK2A and CAMK2B variants. Alignment by Clustal Omega program of the four homo sapiens CAMK2 protein sequences (Alpha, Beta, Gamma and Delta) released by UniProt and formatted using the Jalview program (Waterhouse *et al.*, 2009; Sievers *et al.*, 2011; UniProt, 2015) Red and green text boxes indicate coding variant positions found respectively in CAMK2A and CAMK2B.

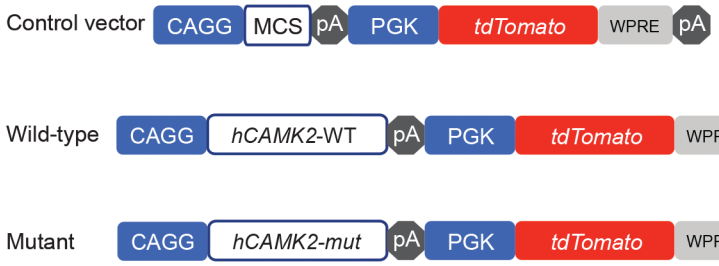

Figure S5. Transfection constructs. Schematic representation of the control vector consisting of a *CAGG* promoter followed by a multiple cloning site (MCS) to insert genes of interest. The presence of specific restriction sites (AscI and PacI in this case) allows the insertion of both the wild-type (WT) and mutated CAMK2A and CAMK2B genes. The *tdTomato* gene is expressed under the *PGK* promoter, to allow for independent expression of the two genes of interest and *tdTomato*.

III

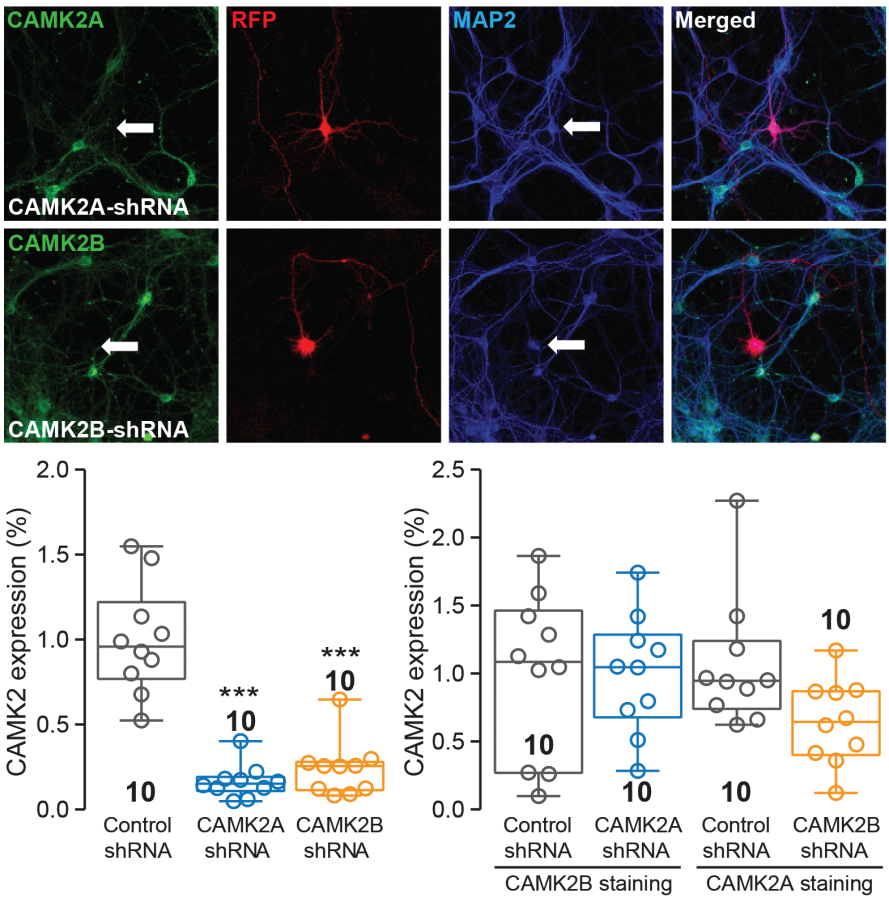

Figure S6. Efficiency and specificity of shRNAs. (A) Representative confocal images of hippocampal neurons cotransfected with shRNAs directed against either CAMK2B or CAMK2A and an RFP plasmid. Transfected neurons (indicated by the white arrow) are identified by the RFP plasmid (red). Neurons were stained with an antibody directed against the microtubules (MAP2) (blue) and with an antibody directed against CAMK2B or CAMK2A respectively (green). (B) shRNA knock-down of either CAMK2A or CAMK2B induces a reduction of around 80% of the protein levels for both CAMK2s ($p<0.0001$, $F[2,27]=45.18$, one-way ANOVA; CAMK2A versus control: $p<0.0001$; CAMK2B versus control: $p<0.0001$, Bonferroni's multiple comparison test), and the pool of shRNAs directed against CAMK2A does not affect the protein level of CAMK2B and vice versa, as shown in the right bar graph ($p=0.46$, $F[3,36]=0.87$, one-way ANOVA). Number in the box and whisker plot graphs indicates the n per construct. Individual datapoints are shown in the box and whisker plots.

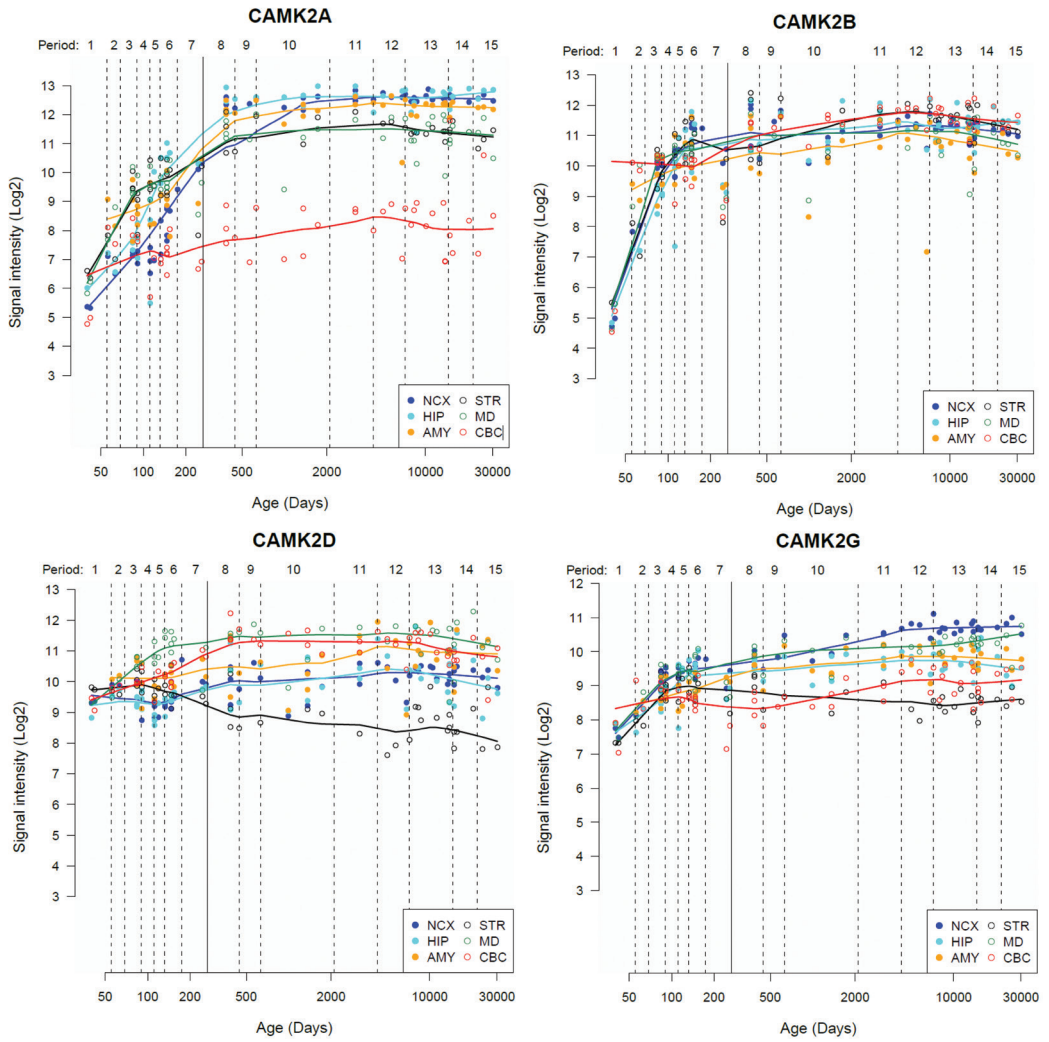

Figure S7. Expression of *CAMK2A*, *CAMK2B*, *CAMK2D* and *CAMK2G* in brain.
Dynamic gene expression along entire development and adulthood in the cerebellar cortex (CBC), mediodorsal nucleus of the thalamus (MD), striatum (STR), amygdale (AMY), hippocampus (HIP) and 11 areas of neocortex (NCX). The data were extracted from the Human Brain Transcriptome database (http://hbatlas.org/).

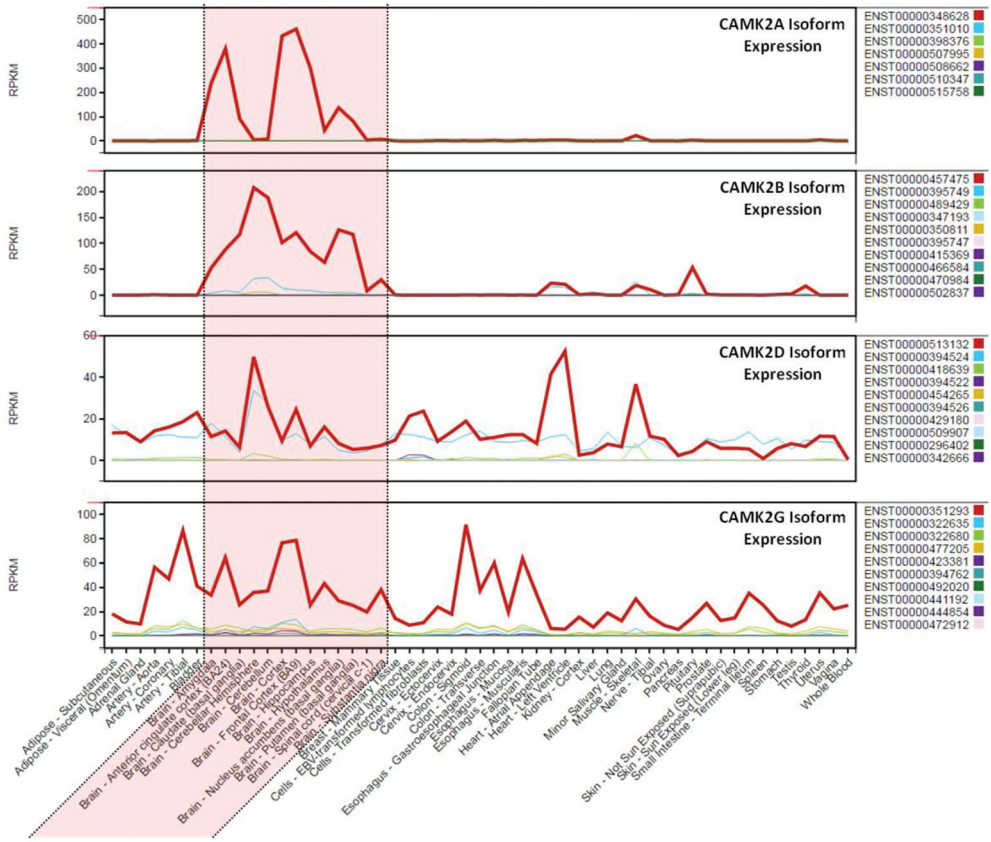

Figure S8. Overview of the gene expression of *CAMK2A*, *CAMK2B*, *CAMK2D* and *CAMK2G* in human tissues. The data used for the analyses described here were obtained from the Genotype-Tissue Expression (GTEx) Portal on 03/06/17. The figure shows the comparative expression of the different isoforms related to the four genes according to transcriptome data. Expression in brain tissues is highlighted in pink. The brain-specific expression of *CAMK2A* and *CAMK2B* contrasts with the wider throughout various tissues. The most abundant transcripts in brain are ENST000045475 (NM_171825.2) for *CAMK2A* and ENST00000513132 (NM_172079.2) for *CAMK2B*. RPKM : Reads Per Kilobase per Million mapped reads.

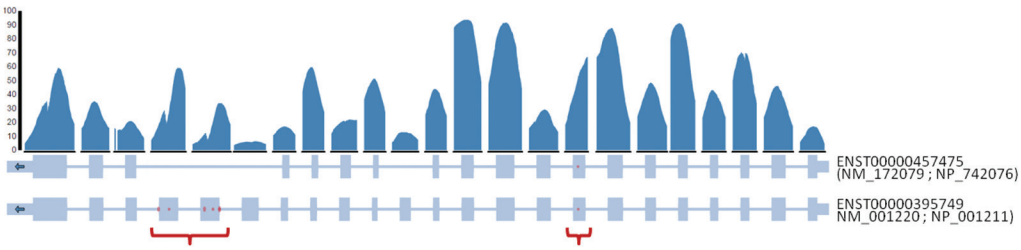

Consequence	Annotation	Allele Count
c.1597+2T>C	splice donor	4
p.Glu510Ter	stop gained	1
p.Ala472GlyfsTer15	frameshift	2
p.Ser461Ter	stop gained	1
c.1340-1G>A	splice acceptor	1
c.1340-2A>T	splice acceptor	16
		25

Consequence	Annotation	Allele Count
p.Glu189Ter	stop gained	1

Figure S9. Distribution across *CAMK2B* isoforms of the loss-of-function variants reported by ExAC (Lek *et al.*, 2016). Six out of the seven loss-of-function (LOF) variants recorded in ExAC database are absent in the most abundant transcript in brain, NM_172079.2 (ENST00000457475). They are present in minor transcript NM_001220 (ENST00000395749). In the context of a neurodevelopmental disorder, where the most important transcript is NM_172079.2, this changes the status of CAMK2B from 'rather tolerant' to 'intolerant' to LOF variants. Indeed, the number of LOF variants observed would therefore be lower than accounted by ExAC, which would increase the probability of LOF intolerance for *CAMK2B* to pLI=1 (one variant observed versus 27.4 variants expected) compared to the one calculated by ExAC (pLI = 0.47; six variants observed versus 27.4 variants expected).

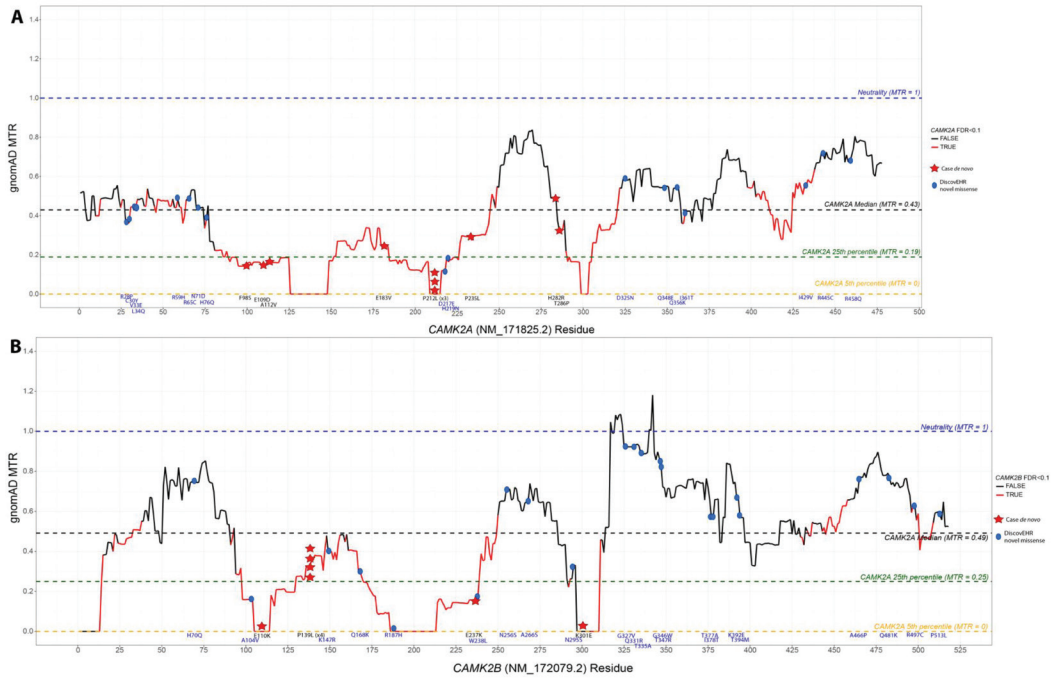

Figure S10. gnomAD Missense Tolerance Ratio (MTR) plots.
gnomAD MTR plots are provided for *CAMK2A* (A) and *CAMK2B* (B). MTR is one estimate of the extent of purifying selection acting specifically on missense variants in a given protein-coding window, entirely independent of known functional boundaries within a gene. It is estimated across 31 codon sliding windows (default) using exome-sequencing standing variation data in the gnomAD database, version 2.0. An MTR = 1 (blue dashed line) represents neutrality (i.e., observe the same proportion of missense variants in the window as expected based on the underlying sequence context). Red segments of MTR plot achieved exome-wide FDR < 0.10 for a significance test of a window's deviation from MTR = 1. Black dashed line (gene-specific median MTR), brown dashed line (gene-specific 25th percentile MTR) and orange dashed line (gene- specific 5th percentile MTR). Data available at http://mtr-viewer.mdhs.unimelb.edu.au/. The location of our 17 case-ascertained *de novo* missense variants is denoted by red stars and the location of 39 DiscovEHR novel control missense variants is denoted by blue circles along the MTR plot. Novel control missense variants were defined as missense variants reported among the DiscovEHR cohort that are not reported in the gnomAD database.
For *CAMK2A*, 9/10 (90%) case variants resided below the gene-specific median MTR compared to 6/17 (35%) novel control variants (Fisher's Exact test p = 0.01). For *CAMK2B*, 7/7 (100%) case variants resided below the gene-specific median MTR compared to 6/22 (27%) novel control variants (Fisher's Exact test p = 0.001). Collectively, 16/17 (94%) case variants and 12/39 (31%) novel control variants resided below their gene-specific median MTR (Fisher's Exact test p = 0.000018).
Correspondence between the nomenclatures of amino acid changes: F98S: p.(Phe98Ser); G109D: p.(Glu109Asp); A112V: p.(Ala112Val); P138A:p.(Pro138Ala); E183V: p.(Glu183Val); P212L: p.(Pro212Leu); P235L: p.(Pro235Leu); H282R: p.(His282Arg); T286P: p.(Thr286Pro); E110K: p.(Glu110Lys); P139L: p.(Pro139Leu); E237K: p.(Glu237Lys); K301E: p.(Lys301Glu).

Supplemental Tables

Tables S1-S2-S4 can be found at:
https://www.cell.com/ajhg/fulltext/S0002-9297(17)30423-8#supplementaryMaterial

Table S3. Candidates genes inferred from trio-based whole-exome sequencing data.

Individual	Putative *de novo* mutations	Newly Hemizygous genotype	New Heterozygous inherited variants	Newly Homozygous genotype	Compound Heterozygous genotype
1	*CAMK2A*	0	*EP300*	0	0
2	*CAMK2A SH2D3C*	0	0	0	*SSPO*
3	*CAMK2A*	ND	ND	ND	ND
4	*CAMK2A*	ND	ND	ND	ND
5	*CAMK2A TUSC1 TERF2*	0	0	0	0
6	*CAMK2A SLC26A7 RAB43 **	0	0	0	0
7	*CAMK2A MAN2C1 ADCY9 NAE1 SDK2*	0	0	0	*FAT4*
8	*CAMK2A*	0	0	0	0
9	*CAMK2A*	0	0	0	ND
10	*CAMK2A*	0	0	0	0
11	*CAMK2A PLCH2 RIPK4*	0	*0*	0	*RANBP2*
12	*CAMK2A LUZP1*	0	*ALOXE3 RAG1 TLR1*	0	0
13	*CAMK2A FUS*	0	*ZEB2*	0	0
14	*CAMK2A*	ND	ND	ND	ND
15	*CAMK2B*				
16	*CAMK2B*	0	*MED12*	0	0
17	*CAMK2B AK4*	0	0	0	0
18	*CAMK2B*	ND	ND	ND	ND
19	*CAMK2B*	0	0	0	0
20	*CAMK2B*	0	0	0	0
21	*CAMK2B*	ND	ND	ND	ND
22	*CAMK2B*	0	0	0	0
23	*CAMK2B DPP3*	*NLGN3 (PLXNA3)*	0	0	*ROBO3*
24	*CAMK2B PSMD12*	0	0	0	0

* Inferred from a SSC re-analysis by Krumm *et al.* 2015

Chapter IV

The intellectual disability-associated CAMK2G p.Arg292Pro mutation acts as a pathogenic gain-of-function

Martina Proietti Onori, Balwina Koopal, David B. Everman, Jessica D.Worthington, Julie R. Jones, Melissa A. Ploeg, Edwin Mientjes, Bregje W. van Bon, Tjitske Kleefstra, Howard Schulman, Steven A. Kushner, Sébastien Küry, Ype Elgersma, Geeske M. van Woerden

Published in Hum Mutat. 2018 Dec;39(12):2008-2024

ABSTRACT

The abundantly expressed calcium/calmodulin-dependent protein kinase II (CAMK2), alpha (CAMK2A), and beta (CAMK2B) isoforms are essential for learning and memory formation. Recently, a *de novo* candidate mutation (p.Arg292Pro) in the gamma isoform of CAMK2 (CAMK2G) was identified in a patient with severe intellectual disability (ID), but the mechanism(s) by which this mutation causes ID is unknown. Here, we identified a second, unrelated individual, with a *de novo* CAMK2G p.Arg292Pro mutation, and used *in vivo* and *in vitro* assays to assess the impact of this mutation on CAMK2G and neuronal function. We found that knockdown of CAMK2G results in inappropriate precocious neuronal maturation. We further found that the CAMK2G p.Arg292Pro mutation acts as a highly pathogenic gain-of-function mutation, leading to increased phosphotransferase activity and impaired neuronal maturation as well as impaired targeting of the nuclear CAMK2G isoform. Silencing the catalytic site of the CAMK2G p.Arg292Pro protein reversed the pathogenic effect of the p.Arg292Pro mutation on neuronal maturation, without rescuing its nuclear targeting. Taken together, our results reveal an indispensable function of CAMK2G in neurodevelopment and indicate that the CAMK2G p.Arg292Pro protein acts as a pathogenic gain-of-function mutation, through constitutive activity toward cytosolic targets, rather than impaired targeting to the nucleus.

INTRODUCTION

Intellectual disability (ID), characterized by an IQ score of <70 and moderate to severe limitations in adaptive functioning, often has a genetic cause. Next generation sequencing (NGS) offers a powerful diagnostic modality for undiagnosed ID patients. Currently, despite the recent identification of more than 700 genes associated with ID, in approximately half of ID cases, the genetic pathogenicity cannot be established with certainty, since the mutation has not been identified before (Vissers *et al*., 2016).

Calcium/calmodulin-dependent protein kinase type II (CAMK2) is a Ser/Thr protein kinase family consisting of four isozymes (CAMK2A, CAMK2B, CAMK2G, and CAMK2D). CAMK2A and CAMK2B have a highly abundant and neuron-selective expression. Targeted deletion of CAMK2A or CAMK2B in mice has revealed their indispensable requirement for normal cognition (Borgesius *et al*., 2011; Silva *et al*., 1992a, 1992b; Giese *et al*., 1998; Elgersma *et al*., 2002; Lisman *et al*., 2002; Lisman *et al*., 2012; van Woerden *et al*., 2009; Hell, 2014;). Moreover, human CAMK2A and CAMK2B mutations have recently been established as a cause of ID (Küry *et al*., 2017b). In contrast to CAMK2A and CAMK2B, much less is known about the other CAMK2 isoforms, CAMK2G and CAMK2D. However, recently a *de novo* mutation in the *CAMK2G* gene (c.875G > C p.Arg292Pro, henceforth denoted as CAMK2G^{Arg292Pro}) was identified in a patient with severe ID (de Ligt *et al*., 2012). In addition, here, we describe a second, unrelated individual with ID carrying the c.875G > C p.Arg292Pro mutation, strongly suggesting a causative role for CAMK2G in ID.

Even though the expression of CAMK2G in the adult brain is relatively low compared to CAMK2A and CAMK2B (Tobimatsu & Fujisawa, 1989), CAMK2G is highly abundant in the developing nervous system in rats (Bayer *et al*., 1999) and in humans, where it is the dominant isoform in the first trimester in the hippocampus (Figure 1A). Other than a few studies, reporting associations of common variation in CAMK2G with reduced memory performance (de Quervain & Papassotiropoulos, 2006), depression (Li *et al*., 2013) and chronic inflammatory pain (Pan *et al*., 2014), and a recent study proposing that CAMK2G functions as a calcium/calmodulin (Ca^{2+}/CaM) shuttle (Ma *et al*., 2014), the mechanistic function of CAMK2G during

neurodevelopment has remained largely unknown.

Here, we describe the clinical features of both individuals carrying the CAMK2G p.Arg292Pro mutation, the contribution of CAMK2G to neuronal migration *in vivo* and neuronal maturation *in vitro* and how the CAMK2G^{Arg292Pro} mutation affects CAMK2G function. We found that reduced expression of CAMK2G leads to inappropriate precocious neuronal maturation. Moreover, we demonstrate that the p.Arg292Pro mutation is a pathogenic gain-of-function mutation, which renders the CAMK2G protein constitutively active, and causes a severe impairment of neuronal migration and maturation. Although the mutation also interferes with nuclear import, we found that the pathogenic effect we describe is not related to Ca^{2+}/CaM shuttling. Taken together, our findings establish CAMK2G as a critical regulator of neurodevelopment and propose a novel mechanism by which the ID mutation, CAMK2G^{Arg292Pro} exerts its pathogenic effect.

MATERIAL AND METHODS

Identification of the CAMK2G p.Arg292Pro patients

Patient 1 was part of a whole-exome sequencing study performed on patients with severe intellectual disability in Nijmegen, the Netherlands (de Ligt *et al*., 2012). Written consent for use of the patients' photos were obtained from the parents. Patient 2 was identified by clinical whole-exome sequencing done as part of a diagnostic evaluation through the Greenwood Genetic Center in South Carolina.

Constructs

The cDNA sequence from human *CAMK2G^{WT}* (NM_172171.2, variant without NLS) was obtained from a human brain cDNA library by PCR (Phusion high fidelity, Thermo Fisher) using the following primers: Fw 5′ ACATCTGGCGCGCCACCATGGCCACCACCGCCACCTG 3′ and Rev 5′ AAGTCCTTAATTAATTATCACTGCAGCGGTGCGGCAG 3′ and cloned into our dual promoter expression vector (Suppl. Fig. S1). The cDNA sequence from rat *CAMK2A^{WT}* and *CAMK2B^{WT}* were kindly provided by Tobias Meyer and was cloned into our expression vector. The NLS version of *CAMK2G^{WT}* was generated using the following primers: Fw 5′ CGAGTTCCAGCGTGCACCTAATGCCACAGAGCAACAACAAAAACAGTCTCG 3′ and Rev 5′ CATTAGGTGCACGCTGGAACTCGACTTCCTTTTCTTGACACCGCCATCCGAC 3′. The p.Thr287Ala point mutation cDNA was synthesized by and ordered from GeneCust. The different point mutations were introduced with site-directed mutagenesis (Invitrogen) using the following primers: *CAMK2G*–c.875G > C (p.Arg292Pro), Fw 5′ CTGTGGAGTGTTTGCCCAAGTTCAATGCCCG 3′ and Rev 5′ CGGGCATTGAACTTGGGCAAACACTCCACAG 3′; *CAMK2G*– c.128A > G (p.Lys43Arg), Fw 5′ ACGCAGGAGTACGCAGCAAGAATCATCAATACCAAGAAG 3′ and Rev 5′ GTATTGATGATTCTTGCTGCGTACTCCTGCGT 3′; *CAMK2G*–c.859-860AC > GA (p.Thr287Asp), Fw 5′ GCATCGTCAGGAGGATGTGGAGTGTTTG 3′ and Rev 5′ CAAACACTCCACATCCTCCTGACGATGC 3′; *CAMK2G*–c.916-919ACGA > GTGG (p.Thr306Val/Thr307Ala), Fw 5′ CTGAAGGGTGCCATCCTCGTGGCCATGCTTGTCTCCAGGA 3′ and Rev 5′ TCCTGGAGACAAGCATGGCCACGAGGATGGCACCCTTCAG 3′; *CAMK2G*–c.907-909GCC > AGA (p.Ala303Arg), Fw 5′ GAAAACTGAAGGGTAGAATCCTCACGACCAT 3′ and Rev 5′ ATGGTCGTGAGGATTCTACCCTTCAGTTTTC 3′. CAMK2G–c.1000T > G (p.Ser334Ala), Fw 5′ GGTGTCAAGAAAAGGAAGGCGAGTTCCAGCGTGCACCT 3′ and Rev 5′ AGGTGCACGCTGGAACTCGCCTTCCTTTTCTTGACACC 3′. *CAMK2A*–c.871-873 AAG > CCT (p.Lys291Pro), Fw 5′ GGAGACCGTGGACTGCCTGCCTAAGTTCAATGCCAGGAGGA 3′ and Rev

5′ TCCTCCTGGCATTGAACTTAGGCAGGCAGTCCACGGTCTCC 3′; *CAMK2B*–c.874-876AAG > CCT (p.Lys292Pro), Fw 5′ GGAGACTGTGGAATGTCTGCCTAAGTTCAATGCAAGGAGGA 3′ and Rev 5′ TCCTCCTTGCATTGAACTTAGGCAGACATTCCACAGTCTCC 3′. The dual promoter expression vector was generated from the pCMV–*tdTomato* vector (Clonetech), where the *CMV* promoter was replaced with a *CAGG* promoter followed by a multiple cloning site (MCS) and transcription terminator sequence. To assure expression of the tdTOMATO independent from the gene of interest, a PGK promoter was inserted in front of the *tdTomato* sequence. For all the *in vivo* and *in vitro* experiments, the vector without a gene inserted in the MCS was taken along as control (control vector). shRNA constructs were obtained from the MISSION shRNA library for mouse genomes of Sigma Life Sciences and The RNAi Consortium (TRC). For knockdown of CAMK2G, we used three different shRNA plasmids, each targeting a different sequence: (1) GCCCGAGATCATCAGAAACTA, (2) CCTGAGGTCTTGAGGAAAGAT, and (3) CTACGCAGGAATATGCTGCAA. The control shRNA plasmid is the MISSION non-target shRNA control vector: CAACAAGATGAAGAGCACCAA.

Mice

For the neuronal cultures, FvB/NHsD females were crossed with FvB/NHsD males (both ordered at 8–10 weeks old from Envigo). For the *in utero* electroporation, female FvB/NHsD (Envigo) were crossed with male C57Bl6/J (ordered at 8–10 weeks old from Charles River). All mice were kept group-housed in IVC cages (Sealsafe 1145T, Tecniplast) with bedding material (Lignocel BK 8/15 from Rettenmayer) on a 12/12 h light/dark cycle in 21°C (±1°C), humidity at 40–70% and with food pellets (801727CRM(P) from Special Dietary Service) and water available *ad libitum*. All animal experiments were approved by the Local Animal Experimentation Ethical Committee, in accordance with Institutional Animal Care and Use Committee guidelines.

HEK-293T cell transfections

To test the expression vector with the CAMK2 constructs, to measure the phosphorylation levels of CAMK2, and for immunoprecipitation (IP) experiments, we chose HEK-293T cells, a cell line that is easy to transfect and culture. These cells were mycoplasma-free but not authenticated. HEK-293T cells were cultured in DMEM/10% Fetal Calf Serum (FCS)/1% penicillin/streptomycin in 6-well plates (or 10 cm dishes for IP experiments) and transfected when 50% confluent with the following DNA constructs: control vector, $CAMK2G^{WT}$, $CAMK2G\text{-}NLS^{WT}$, $CAMK2G^{Arg292Pro}$, $CAMK2G\text{-}NLS^{Arg292Pro}$, $CAMK2G^{Ala303Arg}$, $CAMK2A^{WT}$, $CAMK2A^{Lys291Pro}$, $CAMK2B^{WT}$, and $CAMK2B^{Lys292Pro}$ (3 ug per 6-well and 18 ug per 10 cm dish). Transfection of the plasmids was done using polyethylenimine (PEI) according to the manufacturer instructions (Sigma). Six to twelve hours after transfection, the medium was changed to reduce toxicity. Transfected cells were then used for western blot and Immunoprecipitation experiments.

Western blot

Two to three days after transfection, HEK cells were harvested and homogenized in lysis buffer (10 mM Tris-HCl 6.8, 2.5% SDS, 2 mM EDTA), containing protease inhibitor cocktail (#P8340, Sigma), phosphatase inhibitor cocktail 2 (#P5726, Sigma) and phosphatase inhibitor cocktail 3 (#P0044, Sigma). Protein concentration in the samples was determined using the BCA protein assay kit (Pierce) and then lysate concentrations were adjusted to 1 mg/ml. Western blots were probed with primary antibodies against CAMK2G (C-18; raised against the 478–495 C-terminal peptide, 1:1000, sc-1541, Santa Cruz; validated in this study by overexpression experiments), CAMK2A (6G9, 1:40.000, Abcam; validated in Elgersma *et*

al. (2002)), CAMK2B (CB-β1, 1:10.000, Invitrogen; validated in van Woerden *et al*. (2009)), Actin (MAB1501R, 1:20.000, Chemicon; validated in Antibodypedia (https://Antibodypedia.com), Ph-Thr286/Thr287 (auto-phosphorylated CAMK2 antibody; #06-881; 1:1000; Upstate Cell Signaling Solutions; validated in Elgersma et al. (2002)) and RFP (#600401379, 1:2000, Rockland, validated in this study by overexpression experiments), and secondary antibodies (goat anti-mouse (#926-32210), goat anti-rabbit (#926-68021), and donkey anti-goat (#926-68074), all 1:15.000, LI-COR). Blots were quantified using LI-COR Odyssey Scanner and Odyssey 3.0 software.

Immunoprecipitation

Two to three days after HEK transfection in 10 cm dishes, cells were harvested in PBS and cell pellets were taken up in 500 µl of IP lysis buffer (20 mM Tris pH 8.0, 150 mM NaCl, 1% NP40) supplemented with protease inhibitor cocktail (#P8340, Sigma), phosphatase inhibitor cocktail 2 (#P5726, Sigma), and phosphatase inhibitor cocktail 3 (#P0044, Sigma). Protein concentration in the samples was determined using the BCA protein assay kit (Pierce) and 600 g of total protein adjusted to a volume of 800 µl was used for immunoprecipitation. 20 µl of the total volume was saved as "input." Cell lysates were incubated with 50 µl of prewashed 50 % slurry Protein A Sepharose CL- 4B beads (#17-0780-01, GE Healthcare) at 4°C for >1 hr. Beads were then isolated and discarded by spinning down samples at 1000 rpm for 1′. Lysates were placed in a new tube with 3 µl of mouse calmodulin antibody (C3545, Sigma) and allowed to mix overnight at 4°C. The next morning, lysates were incubated with 50 µl of prewashed 50% slurry Protein G Sepharose beads (#17-0618-01, GE Healthcare) at 4°C for > 1 hr. Beads were then washed 3× with cold lysis buffer and after final wash proteins were eluted adding 20 µl of 2× Laemmli sample buffer and boiling for 5′ at 95°C before processing by western blot.

Primary hippocampal cultures

Primary hippocampal and cortical neuronal cultures were prepared from FvB/NHsD wild-type mice according to the procedure described in Banker and Goslin (1991). Briefly, hippocampi were isolated from brains of E16.5 embryos and collected altogether in 10 ml of neurobasal medium (NB, Gibco) on ice. After two washings with NB, the samples were incubated in pre-warmed trypsin/EDTA solution (Invitrogen) at 37°C for 20 min. After 2× washing in pre-warmed NB, the cells were resuspended in 1.5 ml NB medium supplemented with 2% B27, 1% penicillin/streptomycin, and 1% glutamax (Invitrogen), and dissociated using a 5 ml pipette. Following dissociation, neurons were plated in a small drop on poly-d-lysine (25 mg/ml, Sigma) coated 15 mm glass coverslips at a density of 1×10^6 cells per coverslip in 12 well plates containing 1 ml of supplemented NB for each coverslip. The plates were stored at 37°/5% CO_2 until the day of the transfection.

Neuronal transfection and immunocytochemistry

Neurons were transfected after 7 days *in vitro* (DIV) with the following DNA constructs: control vector (1.8 µg per coverslip), *CAMK2G*^{WT}, *CAMK2G*^{Arg292Pro}, *CAMK2G*^{Lys43Arg}, *CAMK2G*$^{Lys43Arg/Arg292Pro}$, *CAMK2G*^{Thr287Ala}, *CAMK2G*$^{Thr287D/Thr306Val/Thr307Ala}$, *CAMK2G*^{Ala303Arg}, *CAMK2G-NLS*^{WT}, *CAMK2G-NLS*^{Arg292Pro}, *CAMK2G-NLS*^{Ser334Ala}, *CAMK2G-NLS*$^{Ser334Ala/Arg292Pro}$, *CAMK2G-NLS*$^{Lys43Arg/Arg292Pro}$, *CAMK2A*^{WT}, *CAMK2A*^{Lys291Pro}, *CAMK2B*^{WT}, and *CAMK2B*^{Lys292Pro} (all 2.5 µg per coverslip) or for knockdown experiments with a pool of the CAMK2G shRNAs with an RFP plasmid (Addgene) or the control shRNA with an RFP plasmid (all in total 4 µg per coverslip). Lipofectamine 2000 was used to transfect neurons, according to the manufacturer instructions (Invitrogen). For the neuronal morphology analysis, neurons were fixed 5 days post-transfection with

methanol and 4% paraformaldehyde (PFA)/4% sucrose, when stained for CAMK2G and 4% paraformaldehyde/4% sucrose, when stained for CAMK2A or CAMK2B and incubated overnight at 4°C with primary antibodies in GDB buffer (0.2% BSA, 0.8 M NaCl, 0.5% Triton X-100, 30 mM phosphate buffer (PB), pH 7.4). To measure level of knockdown of CAMK2G and protein localization, neurons were fixed 5 days post-transfection with methanol and 4% paraformaldehyde/4% sucrose and stained for CAMK2G, but for morphological analysis neurons were fixed with 4% paraformaldehyde/4% sucrose and processed without staining for CAMK2G. The following primary antibodies were used: MAP2 (1:500, #188004, Synaptic System, validation can be found on the manufacturers website: https://www.sysy.com/products/map2/ref.php), CAMK2G (C-18, 1:100, Santa Cruz), CAMK2A (6G9, 1:200, Abcam), CAMK2B (CB-β1, 1:100, Invitrogen). For secondary antibodies, anti-mouse-Alexa488 (#715-545-150), anti-goat-Alexa488 (#705-545-003), and anti-guinea-pig-Alexa647 (#706-605-148) conjugated antibodies (all 1:200, Jackson ImmunoResearch) were used. For the localization experiments, neurons were also stained with 4′,6-diamidino-2-phenylindole solution (DAPI, 1:10000, Invitrogen) for 15′ before being mounted on glass. Slides were mounted using Mowiol-DABCO (Sigma) mounting medium. Confocal images were acquired using a LSM700 confocal microscope (Zeiss).

For the analysis of the neuronal transfections, at least 10 confocal images (20× objective, 0.5 zoom, 1024 × 1024 pixels) of different transfected neurons (identified by the red staining) were taken from each coverslip for each experiment with at least two independent replications. For the analysis of the neuronal morphology, the NeuronJ plugin for ImageJ software was used to trace the dendrites with their branches. Total neurite length and arborization were measured and analyzed. All values were normalized against the mean value for each parameter of the control (control vector). Sholl analysis for the *in vitro* knockdown experiment was performed by counting the number of neurite intersections between the traced neurons and a series of concentric circumferences at an interval of 10 um from each other with the center on the soma. For the analysis of the protein levels upon shRNA transfection, the "Measure RGB" plugin from ImageJ software was used to measure the intensity of the fluorescent signal of the transfected cell, which was normalized against non-transfected cells on the same coverslip and then normalized against the mean value of control shRNA transfected cells. For the analysis of the protein localization experiments, the DAPI staining was used to identify the nucleus and define a region of interest (ROI). To measure the intensity of the fluorescent signal relative to the protein of interest of the ROI nucleus and the ROI cytoplasm of each transfected cell, we used the "Measure" plugin of Fiji software. The intensity signal (Integrated density) was corrected for the area of the ROI and the background signal by using the following formula: IntDen–(area of the ROI × mean fluorescence of background reading). The ratio of the nucleus/cytoplasm corrected intensity value for each construct was averaged and normalized against the averaged ratio of the WT of the same neuronal batch. Analysis was done by an experimenter blinded for the transfection conditions.

In utero electroporation

The procedure was performed in pregnant FvB/NHsD mice at E14.5 of gestation to target mainly the progenitor cells giving rise to pyramidal cells of the layer 2/3 (Saito, 2006; Taniguchi *et al*., 2012). The DNA construct (1.5–3 μg/μl) was diluted in fast green (0.05%) and injected in the lateral ventricle of the embryos while still *in uterus*, using a glass pipette controlled by a Picospritzer III device. To ensure the proper electroporation of the injected DNA constructs (1–2 μl) into the progenitor cells, five electrical square pulses of 45 V with a duration of 50 ms per pulse and 150 ms inter-pulse interval were delivered using tweezer-type electrodes

connected to a pulse generator (ECM 830, BTX Harvard Apparatus). The electrodes were placed in such a way that the positive pole was targeting the developing somatosensory cortex. The following plasmids were injected: control vector, *CAMK2G*^{WT}, *CAMK2G*^{Arg292Pro}, *CAMK2G*^{Lys43Arg}, *CAMK2G*$^{Lys43Arg/Arg292Pro}$, *CAMK2G*^{Thr287Ala}, *CAMK2G*$^{Thr287Asp/Thr306Val/Thr307Ala}$, *CAMK2G*^{Ala303Arg}, *CAMK2G-NLS*^{WT}, *CAMK2G-NLS*^{Arg292Pro}, *CAMK2G-NLS*$^{Lys43Arg/Arg292Pro}$, *CAMK2A*^{WT}, *CAMK2A*^{Lys291Pro}, *CAMK2B*^{WT}, and *CAMK2B*^{Lys292Pro} or for knockdown experiments: a pool of the CAMK2G shRNAs with an RFP plasmid (Addgene) or the control shRNA with an RFP plasmid. After birth, pups (M/F) were sacrificed at P18-P22 for histochemical processing.

Immunohistochemistry

Mice were deeply anesthetized with an overdose of Nembutal and transcardially perfused with 4% paraformaldehyde. Brains were extracted and post-fixed in 4% PFA. Brains were then embedded in gelatin and cryoprotected in 30% sucrose in 0.1 M phosphate buffer, frozen on dry ice, and sectioned using a freezing microtome (40–50 µm thick). Free-floating coronal sections were washed in 0.1 M PB and a few selected sections were counterstained with 4′,6-diamidino-2-phenylindole solution (DAPI, 1:10,000, Invitrogen) before being mounted with Mowiol on glass. Overview images of the coronal sections were acquired by tile scan imaging using a LSM700 confocal microscope (Zeiss) with a 10× objective. Zoom in images of the targeted area were taken using a 20× objective. For the migration analysis, confocal images (10× objective, 0.5 zoom, 1024 × 1024 pixels) were taken from 2 to 3 non-consecutive sections from at least three successfully targeted animals per plasmid. Images were rotated to correctly position the cortical layers, and the number of cells in different layers were counted using ImageJ (Analyze particles option), and the results were exported to a spreadsheet for further analysis. Cortical areas from the pia to the ventricle were divided in 10 equal-sized bins and the percentage of tdTOMATO-positive cells per bin was calculated.

Statistical analysis

All data was assumed to be normally distributed. Statistical difference between the conditions for the *in vitro* overexpression experiments was determined using one-way analysis of variance (ANOVA) followed by Bonferroni's post-hoc test for multiple comparisons and for the knockdown experiments using the two-tailed unpaired *t*-test (dual comparison). For the western blot analysis, one-tailed and two-tailed unpaired *t*-test was used (dual comparison). For the *in vivo* experiments on neuronal migration, the analysis was performed on the number of targeted cells, measured as sum of the first four bins, considered to correspond to the layers 2/3 of the somatosensory cortex. Statistical analysis was performed using one-way ANOVA, followed by Bonferroni's multiple comparison tests. Based on previous experiments performed in our lab, we considered that for the neuronal experiments *in vitro* at least two replicates, with 10 neurons each were necessary. For the western blot analysis, we considered at least three replicates, and for the IUE experiments, previous experiments in our laboratory showed that at least three targeted pups were necessary to draw any conclusion about the migration. *P*-values are indicated in the figures with "*": * indicates $P < 0.05$, ** indicates $P < 0.01$, *** indicates $P < 0.0001$.

RESULTS

CAMK2G p.Arg292Pro mutation causes severe intellectual disability

Patient 1 carrying the CAMK2Gp.Arg292Pro mutation has already briefly been described in

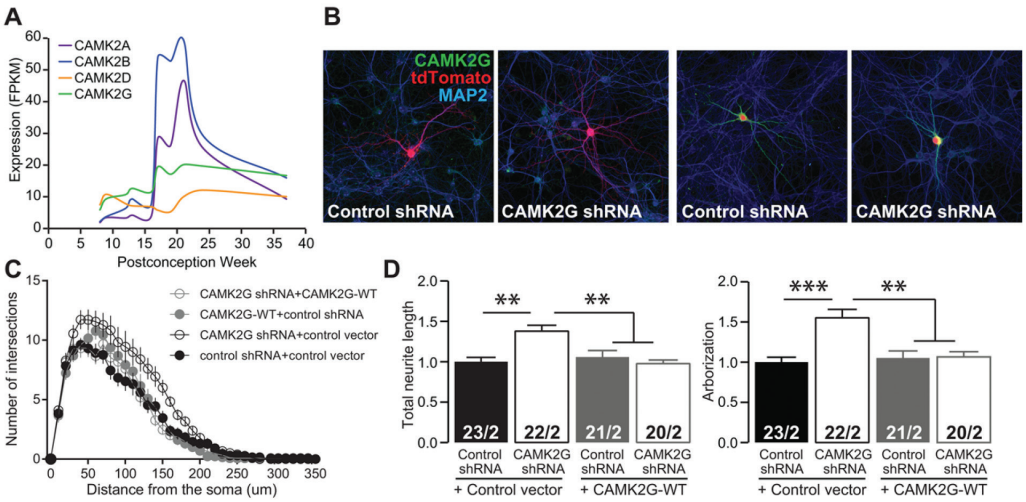

FIGURE 1 CAMK2G knockdown in primary hippocampal neurons results in increased arborization. (A) Expression levels of human CAMK2A, CAMK2B, CAMK2D, and CAMK2G in the hippocampus during gestation, showing that CAMK2G is the dominant isoform in the first trimester, and contributes substantially in the second and the third trimester. Data was extracted from the BrainSpan database (https://www.brainspan.org/). (B) Representative confocal images of hippocampal neurons co-transfected on DIV7 with combinations of control shRNA, with control vector or CAMK2G^{WT} and an RFP plasmid or shRNA against *Camk2g* with control vector or CAMK2G^{WT} and an RFP plasmid. Transfected neurons are identified by the RFP plasmid (red). See also Supplement 1 related to Figure 1. (C) Sholl analysis of neurite complexity. (D) Summary bar graphs of total neurite length and arborization measured for each condition and normalized to the control shRNA (total neurite length: one-way ANOVA, $F[3,82] = 8.42$, $P = 6.05E-05$; control vector+control shRNA vs. control vector+*Camk2g*-shRNA, $P = 0.0004$; CAMK2G^{WT}+control shRNA, $P = 0.99$; CAMK2G^{WT}+*Camk2g*-shRNA, $P = 0.99$; control vector+*Camk2g*-shRNA vs. CAMK2G^{WT}+control shRNA, $P = 0.005$; CAMK2G^{WT}+*Camk2g*-shRNA, $P = 0.0002$; CAMK2G^{WT}+control shRNA vs. CAMK2G^{WT}+*Camk2g*-shRNA, $P = 0.99$; arborization: one-way ANOVA, $F[3,82] = 10.08$, $P = 1.00E-05$; control vector+control shRNA vs. control vector+*Camk2g*-shRNA, $P = 0.0001$; CAMK2G^{WT}+control shRNA, $P = 0.99$; CAMK2G^{WT}+*Camk2g*-shRNA, $P = 0.99$; control vector+*Camk2g*-shRNA vs. CAMK2G^{WT}+control shRNA, $P = 0.0003$; CAMK2G^{WT}+*Camk2g*-shRNA, $P = 0.0005$; CAMK2G^{WT}+control shRNA vs. CAMK2G^{WT}+*Camk2g*-shRNA, $P = 0.99$)

a whole-exome sequencing study describing several individuals with severe ID (de Ligt *et al*., 2012). Here, we identified a second, unrelated carrier of the heterozygous *de novo* CAMK2Gp. Arg292Pro mutation (patient 2). He presented in infancy with generalized hypotonia and developmental delay and has remained hypotonic with markedly delayed gross motor and speech/language skills. He is currently diagnosed with severe ID and autism at 5 years of age. His physical exams have been notable for relative macrocephaly, prominent capillary vascular malformations on the forehead and glabella, minor dysmorphic facial features, and severe hypotonia. A detailed description of both patients is provided in Suppl. Fig. S2. Both patients suffer from severe ID and severe hypotonia. They both have some facial dysmorphisms (Suppl. Fig. S2), though not strikingly similar. By comparison, although individuals with mutations in CAMK2A or CAMK2B all suffer from ID and in most cases hypotonia, facial dysmorphisms are not commonly observed among individuals carrying mutations in CAMK2A or CAMK2B (Küry *et al*., 2017b).

Knockdown of CAMK2G causes increased neuronal arborization

Identifying two unrelated patients with a severe neurodevelopmental disorder carrying the same mutation in CAMK2G, strongly suggests that CAMK2G plays a role in neurodevelopment and neuronal functioning. However, whereas the indispensable roles of CAMK2A and CAMK2B for neuronal plasticity and cognitive function are well established, the neuronal function of CAMK2G remains poorly characterized. Considering the highly abundant expression of

CAMK2G in the first trimester during which the nervous system starts to develop and the stable expression during the rest of the prenatal period (Figure 1A), we set out to investigate the role of CAMK2G during neuronal maturation *in vitro*, using shRNAs to effect knockdown of the CAMK2G protein. We transfected mouse primary hippocampal neurons with shRNAs directed against *Camk2g* or a control plasmid, together with a red florescent protein (RFP) reporter plasmid to visualize transfected neurons. Despite the CAMK2G antibody cross-reactivity with CAMK2A and CAMK2B (Suppl. Fig. S3), we nevertheless observed a 35% reduction of immunofluorescent signal 5 days after transfection, without any change in CAMK2A or CAMK2B levels (Suppl. Fig. S3) consistent with a robust decrease specifically of CAMK2G. Transfection of *Camk2g* shRNA resulted in a substantial alteration of neuronal morphology, with a clear increase in the complexity of the neurite tree compared to the control condition, as measured by Sholl analysis (Figure 1C). Additional quantification of the neurite length and arborization revealed that neurons with reduced levels of CAMK2G exhibited a 38% increase in total neurite length and 55% increase of arborization compared to the control condition (Figure 1B and D, see figure legend for statistics). Mice express three CAMK2G isoforms, one of which contains a nuclear localization signal (NLS) (Suppl. Fig. S4A). This isoform is present in both cytosol and nucleus and was recently proposed to shuttle Ca^{2+}/CaM into the nucleus (Ma *et al*., 2014). In order to assess to what extent the observed effect on neurite length and arborization was specific for the down-regulation of CAMK2G and whether there is differential contribution of the CAMK2G isoforms, we co-transfected either the human CAMK2G isoform lacking the NLS (*CAMK2G*), the CAMK2G isoform containing the NLS (*CAMK2G-NLS)*, *CAMK2A* or *CAMK2B* together with the shRNA against mouse *Camk2g*. Whereas co-transfection of *CAMK2A* or *CAMK2B* with *Camk2g* shRNA had no effect on total neurite length (Suppl. Fig. S4B and C), co-transfection of *CAMK2G* or *CAMK2G-NLS* with *Camk2g* shRNA both resulted in a complete rescue of the neuronal morphology phenotype caused by the down-regulation of CAMK2G (Figure 1B–D and Suppl. Fig. S4B and C). These results indicate that CAMK2G is indispensable for regulating neuronal morphology, but that this function does not require its nuclear import.

The CAMK2G^{Arg292Pro} mutation is pathogenic both *in vitro* and *in vivo*

To study the effect of the ID-associated CAMK2G missense variant on neuronal function, we cloned the human *CAMK2G* gene with and without the c.875G > C mutation in a dual promoter expression vector (see Section "Material and Methods"). Transfection of HEK-293T cells with CAMK2G^{Arg292Pro} achieved a 10-fold lower CAMK2G protein signal compared to that achieved by transfection with CAMK2GWT, despite equal tdTomato levels, indicating that the p.Arg292Pro mutation affects protein stability (Figure 2A and B). Next, we investigated the effect of expression of CAMK2G^{WT} and CAMK2G^{Arg292Pro} in primary hippocampal neurons. Despite the reduced stability of CAMK2G^{Arg292Pro}, levels of CAMK2G were increased in neurons transfected (tdTomato-positive) with CAMK2G^{Arg292Pro} (Figure 2C). Whereas expression of CAMK2G^{WT} yielded no discernible morphological changes with respect to total neurite length or arborization, expression of CAMK2G^{Arg292Pro} strongly reduced total neurite length as well as arborization, which was notably in the opposite direction as observed following *Camk2g* knockdown (Figure 2D). These results suggest that the p.Arg292Pro mutation functions as a pathogenic gain-of-function.

To evaluate the effect of CAMK2G^{Arg292Pro} expression *in vivo*, we used *in utero* electroporation at E14.5. This assay measures the ability of targeted neural cells in the subventricular zone to successfully migrate to layer 2/3 of somatosensory cortex. This assay is very sensitive for changes that perturb normal neural cell function (Saito & Nakatsuji, 2001;

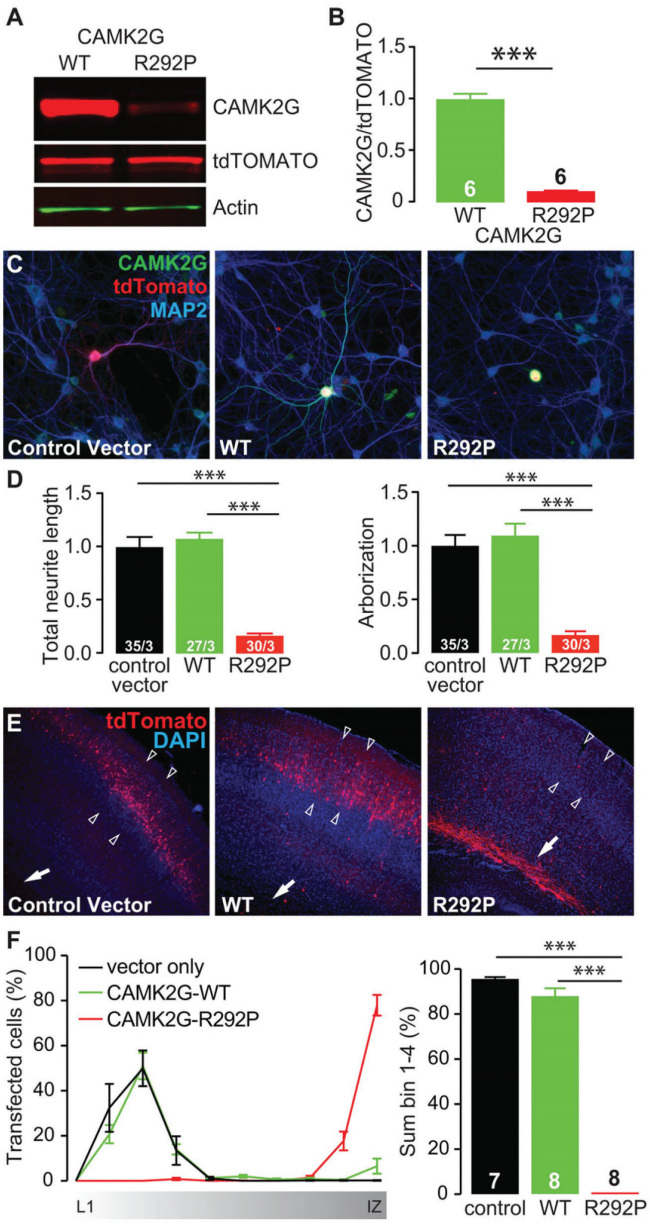

FIGURE 2 CAMK2G^{Arg292Pro} overexpression is severely disruptive for neurons *in vitro* and *in vivo*. *(A)* Representative western blot of CAMK2G^{WT} or CAMK2G^{Arg292Pro} (R292P) transfected HEK-293T cells. (B) Quantification of the levels of CAMK2G expression, normalized against tdTOMATO in the different conditions (CAMK2GWT vs. CAMK2G^{Arg292Pro}: $t[10] = 16.62$, $P = 1.30E-08$, two-tailed unpaired *t*-test). (C) Representative confocal images of hippocampal neurons transfected on DIV7 with control vector (lacking CAMK2G), CAMK2G^{WT} or CAMK2G^{Arg292Pro}. See also Supplement 1 related to Figure 2. Transfected neurons are identified by the tdTOMATO (red). *(D)* Summary bar graphs of total neurite length and arborization measured for each condition and normalized to the control vector (total neurite length: one-way ANOVA $F[2,89] = 49.35$, $P = 3.79E-15$; control vector vs. CAMK2G^{WT}, $P = 0.9$; CAMK2G^{Arg292Pro}, $P = 0.0001$; CAMK2G^{Arg292Pro} vs. CAMK2G^{WT}, $P = 0.0001$; arborization: one-way ANOVA $F[2,89] = 31.8$, $P = 3.80E-11$; control vector vs. CAMK2G^{WT}, $P = 0.9$; CAMK2G^{Arg292Pro}, $P = 0.0001$; CAMK2G^{Arg292Pro} vs. CAMK2G^{WT}, $P = 0.0001$). (E) Representative images of P20-P22 pups *in utero* electroporated at E14.5 with control vector, CAMK2G^{WT} or CAMK2G^{Arg292Pro} tdTOMATO positive cells indicate the successfully targeted neurons. DAPI (blue) counterstaining is used to identify general cortical structure. (F) Left: quantification of the neuronal migration pattern from the Layer 1 (L1) to the intermediate zone (IZ); Right: analysis of the percentage of targeted cells that reach the outer layers of the cortex measured as sum of bin 1–4 (one-way ANOVA, $F[2,20] = 58.88$, $P = 4.16E-09$; control vector vs. CAMK2G^{WT}, $P = 0.07$; CAMK2G^{Arg292Pro}, $P = 0.0001$; CAMK2G^{WT} vs. CAMK2G^{Arg292Pro}, $P = 0.0001$). Arrowheads indicate layer 2/3 of the somatosensory cortex, whereas the arrow indicates the subventricular zone (SVZ). Data in (B), (D), and (F) are presented as mean ± SEM. Numbers (*X*/*Y*) depicted in the bar graphs represent the number of samples (B), the total number of cells (*X*) and number of independent cultures (*Y*) (D) or the number of pictures (F) analyzed

Tabata & Nakajima, 2001; Taniguchi *et al*., 2012). Strikingly, cells expressing CAMK2G^{Arg292Pro} exhibited a complete block of migration from the subventricular zone, despite more than 80% of the cells expressing CAMK2G^{WT} having migrated normally to layer 2/3 of the somatosensory cortex (Figure 2E and F). These results further confirm the severe dominant effect of the p.Arg292Pro mutation on CAMK2G function.

Taken together these data suggest that although CAMK2G^{Arg292Pro} has reduced protein stability, this mutation does not lead to a loss of function of CAMK2G, but instead appears to result in a paradoxical gain-of-function.

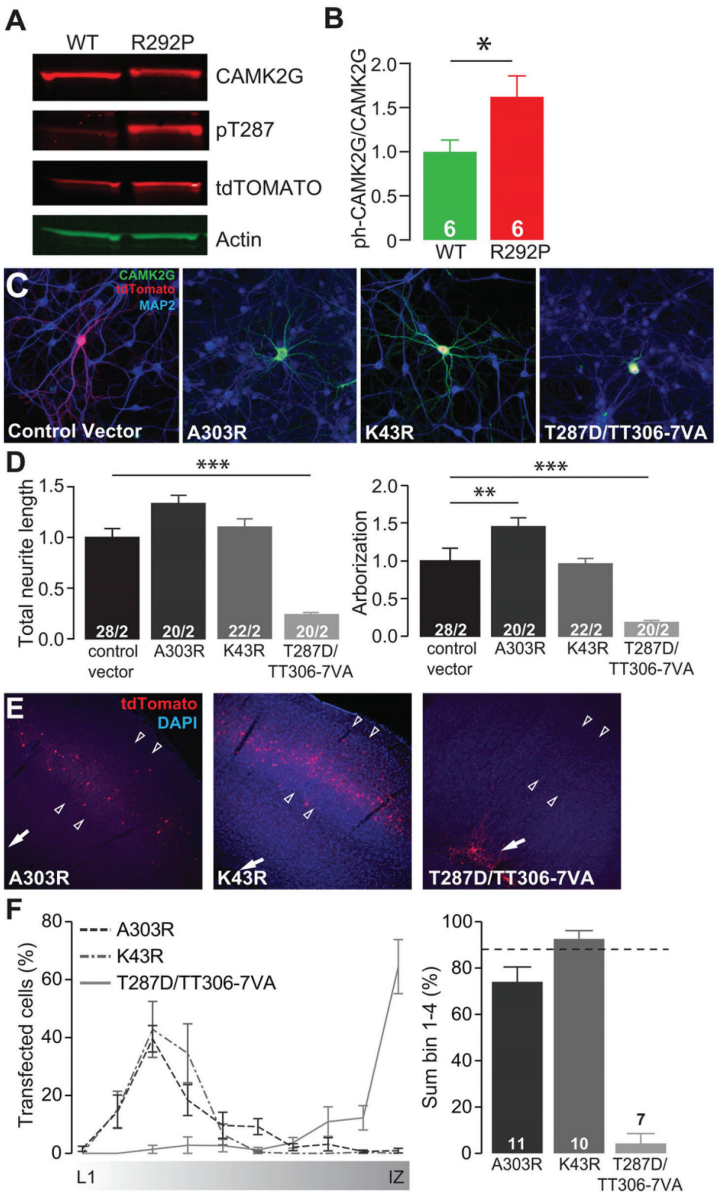

FIGURE 3 Overexpression of a dominant active form of CAMK2G is severely disruptive for neurons *in vitro* and *in vivo*. (A) Representative western blot of CAMK2G^{WT} or CAMK2G^{Arg292Pro} (R292P) transfected HEK-293T cells. (B) Quantification of the levels of CAMK2G–Thr287 phosphorylation, normalized against total CAMK2G in the different conditions (t[10] = 2.29, P = 0.05 two-tailed unpaired t-test). (C) Representative confocal images of hippocampal neurons transfected on DIV7 with control vector, CAMK2G^{Lys43Arg} (K43R), CAMK2G^{Ala303Arg} (A303R) or CAMK2G$^{Thr287Asp/Thr306Val/Thr307Ala}$ (T287D/TT306-7VA). Transfected neurons are identified by the tdTOMATO (red). (D) Summary bar graphs of total neurite length and arborization measured for each condition and normalized to the control vector (total neurite length: one-way ANOVA, F[3,86] = 24.75, P = 1.23E-11; control vector vs. CAMK2G^{Ala303Arg}, P = 0.03; CAMK2G^{Lys43Arg}, P = 0.99; CAMK2G$^{Thr287Asp/Thr306Val/Thr307Ala}$, P = 0.0001; arborization: one-way ANOVA, F[3,86] = 28.29, P = 8.03E-13; control vector vs. CAMK2G^{Ala303Arg}, P = 0.0003; CAMK2G^{Lys43Arg}, P = 0.99; CAMK2G$^{Thr287Asp/Thr306Val/Thr307Ala}$, P = 0.0001). (E) Representative images of P20-P22 pups *in utero* electroporated at E14.5 with control vector, CAMK2G^{Lys43Arg}, CAMK2G^{Ala303Arg} or CAMK2G$^{Thr287Asp/Thr306Val-Thr307Ala}$ tdTOMATO positive cells represent neurons successfully targeted. DAPI (blue) counterstaining is used to identify general cortical structure. (F) Left: quantification of the neuronal migration pattern from the Layer 1 (L1) to the intermediate zone (IZ); Right: analysis of the percentage of targeted cells that reach the outer layers of the cortex measured as sum of bin 1–4 (one-way ANOVA, F[3,32] = 56.92, P = 6.31E-13; CAMK2G^{WT} vs. CAMK2G^{Ala303Arg}, P = 0.15; CAMK2G^{Lys43Arg}, P = 0.99, CAMK2G$^{Thr287Asp/Thr306Val/Thr307Ala}$, P = 0.0001). The dotted line represents the level reached by the CAMK2G-WT (see Figure 2F for comparison). Arrowheads indicate layer 2/3 of the somatosensory cortex, whereas the arrow indicates the subventricular zone (SVZ). Data in (B), (D), and (F) are presented as mean ± SEM. Numbers (X/Y) depicted in the bar graphs represent the number of samples (B), the total number of cells (X) and number of independent cultures (Y) (D) or number of pictures (F) analyzed

IV

CAMK2G^{Arg292Pro} has increased phosphotransferase activity

Considering that a gain-of-function mediates the effects of CAMK2G^{Arg292Pro} and that the p.Arg292Pro mutation is located within the α-helical auto-regulatory domain of CAMK2G that maintains the kinase in an inactive state in the absence of Ca^{2+}/CaM (Hudmon & Schulman,

2002a; Rellos *et al*., 2010), we hypothesized that the mechanism for the gain-of-function elicited by CAMK2G^{Arg292Pro} might involve enhanced phosphotransferase or even constitutive activity. Therefore, we first assessed the level of Thr287 phosphorylation in HEK-293T cells as readout for the phosphotransferase activity by expressing either CAMK2G^{WT} or CAMK2G^{Arg292Pro}. To allow for a direct comparison of their relative phosphorylation, we obtained equal protein levels by titrating the amount of transfected DNA. We found a significant increase of Thr287 phosphorylation in cells expressing CAMK2G^{Arg292Pro} compared to CAMK2G^{WT} (Figure 3A and B), suggesting that the p.Arg292Pro mutation enhances phosphotransferase activity and acts as a gain-of-function mutation. To further test whether the p.Arg292Pro mutation affects neuronal function by acting as a gain of function mutation, we first analyzed the effect of two mechanistically well-established loss-of-function CAMK2 mutations on neuronal migration and morphology. The CAMK2G^{Ala303Arg} mutation prevents binding of Ca^{2+}/CaM, and therefore Ca^{2+}/CaM-dependent activation (Payne *et al*., 1988; Shen & Meyer, 1999 Fink *et al*., 2003). In contrast, the CAMK2G^{Lys43Arg} mutation impairs phosphotransferase activity (Shen & Meyer, 1999; Fink *et al*., 2003). Notably, neither CAMK2G^{Ala303Arg} nor CAMK2G^{Lys43Arg} altered neurite length when expressed in cultured primary hippocampal neurons. Moreover, although a small but statistically significant increase of arborization was observed in CAMK2G^{Ala303Arg} expressing neurons, no effect of arborization was found in neurons expressing CAMK2G^{Lys43Arg} (Figure 3C and D). Finally, *in vivo* neural cell migration was also unaffected by expression of CAMK2G^{Ala303Arg} or CAMK2G^{Lys43Arg} (Figure 3E and F). Taken together these results show that expression of these phosphotransferase loss-of-function variants does not phenocopy the severe effects of the ID-associated CAMK2G^{Arg292Pro}, indicating that the CAMK2G^{Arg292Pro} mutation is not a loss-of-function mutation.

We next tested the effect of the CAMK2G$^{Thr287Asp/Thr306Val/Thr307Ala}$ mutant, which has previously been shown to significantly enhance autonomous activity due to the combination of a Threonine 287 substitution by the phospho-mimetic aspartic amino acid (Waldmann *et al*., 1990; Mayford *et al*., 1995;) together with prevention of inhibitory phosphorylation at the Thr306 and 307 sites by substituting conserved but non-phosphorylatable amino acids (Elgersma *et al*., 2002; Pi *et al*., 2010a, 2010b). Interestingly, expression of this CAMK2G$^{Thr287Asp/Thr306Val/Thr307Ala}$ mutant in HEK-293T cells also achieved severe reduction of CAMK2G protein signal compared to cells transfected with CAMK2G^{WT} (data not shown). Consistent with the hypothesis that increased phosphor-transferase activity is a critical mediator of the gain-of-function mechanism underlying the p.Arg292Pro mutation, expression of the CAMK2G$^{Thr287Asp/Thr306Val/Thr307Ala}$ mutant phenocopied CAMK2G^{Arg292Pro} with similarly severe reductions of total neurite length (Figure 3C), arborization (Figure 3D), and neuronal migration (Figure 3E and F). These findings lend additional support to a model whereby the CAMK2G^{Arg292Pro} mutation acts as a gain-of-function mutation by rendering CAMK2G constitutively active.

CAMK2G-NLS^{Arg292Pro} has impaired nuclear translocation while permitting calmodulin binding

Recently, it was shown that CAMK2G functions as a shuttle for Ca^{2+}/CaM into the nucleus (Ma *et al*., 2014). Hence, we investigated if the p.Arg292Pro mutation impacts this shuttling function. Using the nuclear localization signal-containing isoform of CAMK2G, we first confirmed the functional impact of CAMK2G-NLS^{Arg292Pro} on neuronal maturation and migration, which yielded the similarly severe neurodevelopmental impairments as CAMK2G^{Arg292Pro} (Suppl. Fig. S5). We then investigated whether CAMK2G-NLS^{Arg292Pro} affects CaM binding by performing a CaM immunoprecipitation. Despite reduced expression levels, we found that more CAMK2G-NLS^{Arg292Pro} is pulled down using the CaM antibody compared to CAMK2G-NLS^{WT} (Figure 4),

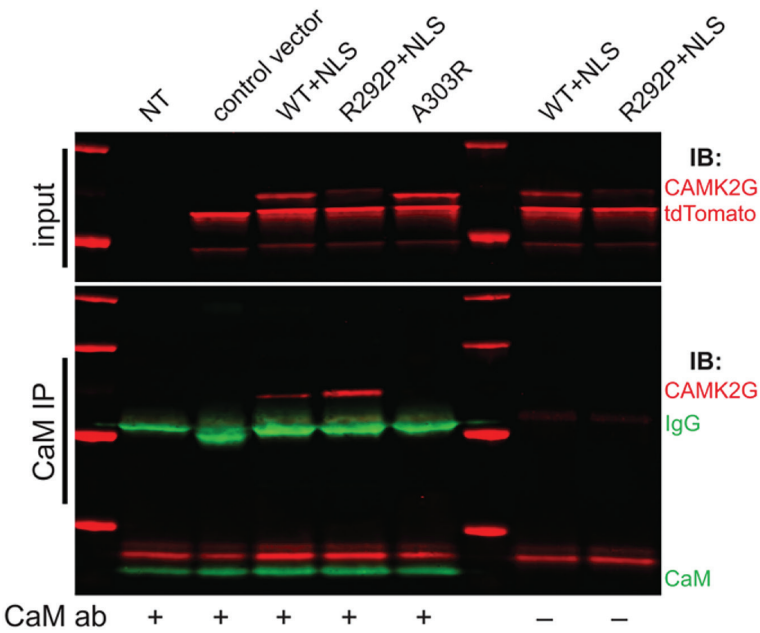

FIGURE 4 The CAMK2G-NLS^{Arg292Pro} does not disrupt calmodulin binding. Representative western blot of a calmodulin immunoprecipitation experiment performed in HEK-293T cells transfected with either control vector, CAMK2G-NLS^{WT}, CAMK2G-NLS^{Arg292Pro} (R292P), CAMK2G^{Ala303Arg} (A303R), or non-transfected (NT), probed with an antibody against CAMK2G, tdTOMATO, and calmodulin (CaM). Note the clear increase in CAMK2G pull-down (in the presence of CaM antibody, left blot) in the mutant CAMK2G-NLS^{Arg292Pro} lane compared to the WT, despite the reduced stability of the mutant (as observed in the input). As expected, no detectable CAMK2G is observed in the CAMK2G^{Ala303Arg} mutant lane. The "+" or "—" sign indicates the presence or absence, respectively of the calmodulin antibody

IV

suggesting that CaM binding is not disrupted, and even possibly that the affinity of CAMK2G-NLS^{Arg292Pro} for CaM is increased.

Next, we assessed whether CAMK2G-NLS^{Arg292Pro} has impaired nuclear translocation. Neurons were transfected with CAMK2G-NLS^{Arg292Pro} and CAMK2G-NLS^{WT} to determine their respective sub-cellular localization. As expected, we found that CAMK2G-NLS^{WT} was located in the nucleus as well as the cytoplasm. In contrast, CAMK2G-NLS^{Arg292Pro} was almost exclusively localized to the cytoplasm (Figure 5A and B), suggesting that the p.Arg292Pro mutation disrupts the nuclear localization of CAMK2G-NLS.

Nuclear translocation of NLS-containing CAMK2 isoforms requires a conformational change previously been shown to be dependent upon dephosphorylation of a Serine immediately adjacent to the NLS sequence (Ser334 in CAMK2G), resulting in exposure of the NLS domain (Heist *et al.*, 1998; Ma *et al.*, 2014; Shioda *et al.*, 2015). Given that the p.Arg292Pro mutation enhances the Serine/Threonine kinase activity of CAMK2G, we sought to investigate whether increased phosphorylation of the Ser334 residue is a critical mediator of the abnormal localization of CAMK2G-NLS^{Arg292Pro}. Therefore, we generated the CAMK2G-NLS^{Ser334Ala} mutant and the CAMK2G-NLS$^{Arg292Pro/Ser334Ala}$ double mutant constructs to assess their respective subcellular localization. Whereas CAMK2G-NLS^{Ser334Ala} was localized in both the nucleus and the cytoplasm, CAMK2G-NLS$^{Arg292Pro/Ser334Ala}$ remained exclusively cytoplasmic, indicating that the mislocalization resulting from the p.Arg292Pro mutation is not the result of excessive Ser334 phosphorylation (Figure 5C and D). Taken together, these data show that even though the p.Arg292Pro mutation does not reduce CaM affinity, it strongly impairs the nuclear localization of CAMK2G.

Pathogenicity of CAMK2G^{Arg292Pro} is not related to nuclear shuttling of Ca^{2+}/CaM

Our findings indicate that the p.Arg292Pro mutation has two major effects on CAMK2G: it renders the protein constitutively active and interferes with its nuclear targeting. Therefore, we next aimed to investigate whether the pathogenicity is caused by the constitutive activity or by the impairment of nuclear targeting.

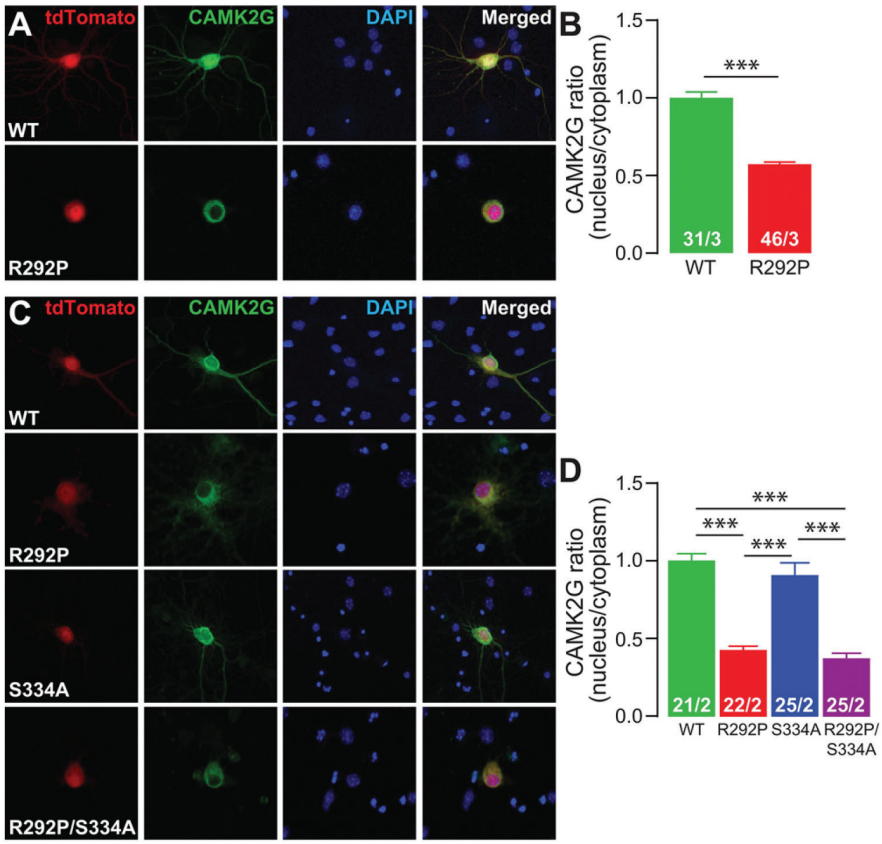

FIGURE 5 The CAMK2G-NLS^{Arg292Pro} mutation interferes with nuclear translocation of CAMK2G-NLS. (A and C) Representative confocal images of hippocampal (A) or cortical (C) neurons transfected on DIV7 with CAMK2G-NLS^{WT}, CAMK2G-NLS^{Arg292Pro} (R292P), CAMK2G-NLS^{Ser334Ala} (S224A), or CAMK2G-NLS$^{Arg292Pro/Ser334Ala}$ (R292P/S334A). Transfected neurons are identified by the tdTOMATO (red). (B and D) Summary bar graphs of CAMK2G expression level measured as a ratio nucleus vs. cytoplasm and normalized to the WT level. (B: CAMK2G^{WT} vs. CAMK2G^{Arg292Pro}, P = 6.81E-19, t(75) = 11.87, two-tailed unpaired t-test; D: one-way ANOVA, F[3,86] = 43.58, P = 3.19E-17; CAMK2G-NLS^{WT} vs. CAMK2G-NLS^{Arg292Pro}, P = 0.0001; CAMK2G-NLS^{Ser334Ala}, P = 0.99; CAMK2G-NLS$^{Arg292Pro/Ser334Ala}$, P = 0.0001; CAMK2G^{Arg292Pro} vs. CAMK2G-NLS^{Ser334Ala}, P = 0.0001; CAMK2G-NLS$^{Arg292Pro/Ser334Ala}$, P = 0.99; CAMK2G-NLS^{Ser334Ala} vs. CAMK2G-NLS$^{Arg292Pro/Ser334Ala}$, P = 0.0001). Data are presented as mean ± SEM. Numbers (X/Y) depicted in the bar graphs represent the total number of cells (X) and number of independent cultures (Y) analyzed

To examine whether the constitutive activity results from the observed increase of Thr287 auto-phosphorylation (Figure 3A and B), we mutated Threonine 287 to Alanine, a mutation that strongly reduces autonomous activity (Fong *et al*., 1989; Hanson *et al*., 1989; Waxham *et al*., 1990; Ohsako *et al*., 1991; Giese *et al*., 1998;). Expression of CAMK2G^{Thr287Ala} resulted in no discernible effects on morphology or neural cell migration (Figure 6). In contrast, expression of CAMK2G$^{Thr287Ala/Arg292Pro}$ was comparably disruptive as CAMK2G^{Arg292Pro} on neuronal morphology and migration (Figure 6). These results indicate that functional consequences of the CAMK2G^{Arg292Pro} mutation are independent of Thr287 phosphorylation.

We next examined whether the p.Arg292Pro mutation gain-of-function requires the catalytic function of the kinase by introducing a p.Lys43Arg mutation, known to severely disable CAMK2G catalytic function. Compared to the severe neurodevelopmental impairments resulting from expression of CAMK2G^{Arg292Pro}, CAMK2G$^{Arg292Pro/Lys43Arg}$ had a significantly milder impact on total neurite length and fully rescued arborization (Figure 7A). Moreover,

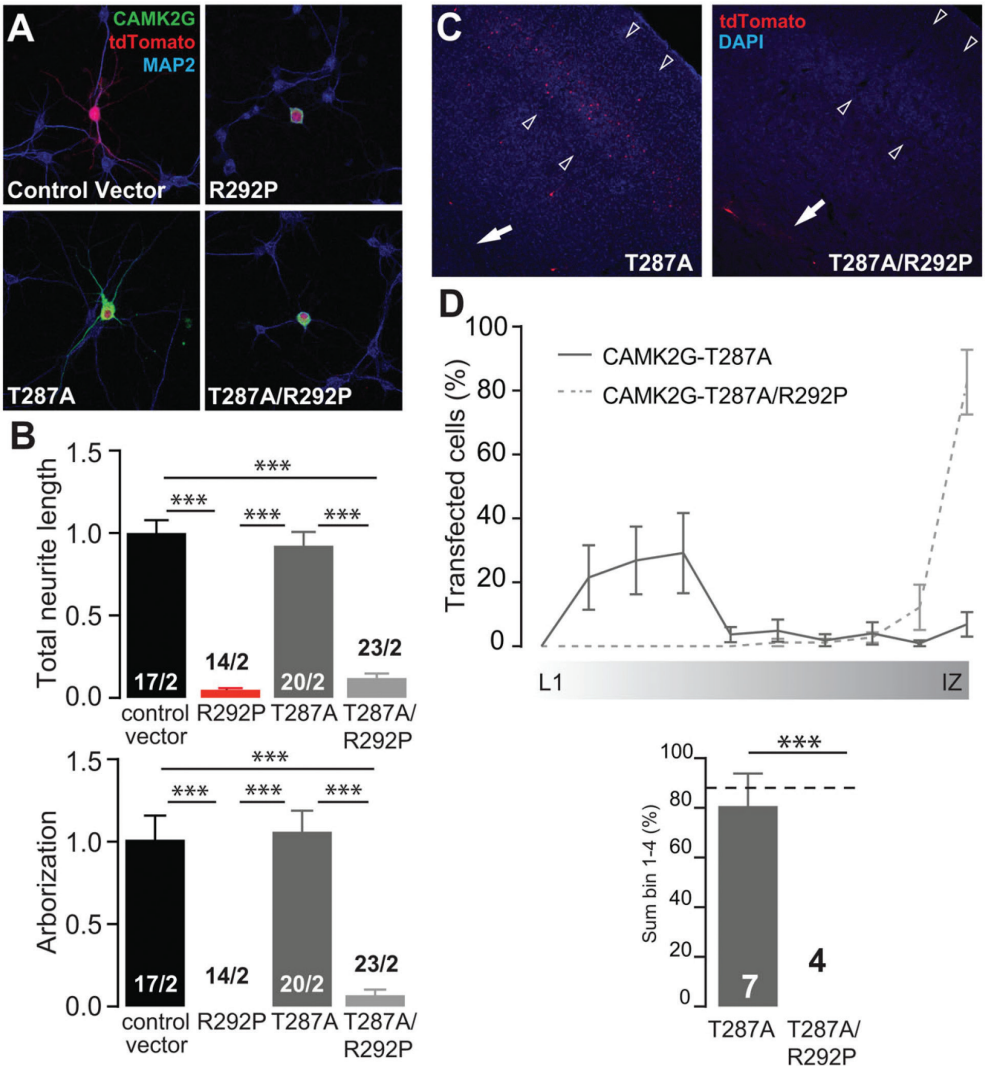

FIGURE 6 Auto-phosphorylation at the Thr287 site is dispensable for the phenotype caused by the p.Arg292Pro mutation. (A) Representative confocal images of hippocampal neurons transfected on DIV7 with control vector, CAMK2G^{Arg292Pro} (R292P), CAMK2G^{Thr287Ala} (T287A), CAMK2G$^{Thr287Ala/Arg292Pro}$ (T287A/R292P). Transfected neurons are identified by the tdTOMATO (red). (B) Summary bar graphs of total neurite length and arborization measured for each condition and normalized to the control vector (total neurite length: one-way ANOVA, F[3,70] = 69.33, P = 6.39E-21; control vector vs. CAMK2G^{Arg292Pro}, P = 0.0001; CAMK2G^{Thr287Ala}, P = 0.9; CAMK2G$^{Thr287Ala/Arg292Pro}$, P = 0.0001; CAMK2G^{Arg292Pro} vs. CAMK2G^{Thr287Ala}, P = 0.0001; CAMK2G$^{Thr287Ala/Arg292Pro}$, P = 0.99; CAMK2G^{Thr287Ala} vs. CAMK2G$^{Thr287Ala/Arg292Pro}$, P = 0.0001; arborization: one-way ANOVA, F[3,71] = 34.88, P = 5.74E-14; control vector vs. CAMK2G^{Arg292Pro}, P = 0.0001; CAMK2G^{Thr287Ala}, P = 0.9; CAMK2G$^{Thr287Ala/Arg292Pro}$, P = 0.0001; CAMK2G^{Arg292Pro} vs. CAMK2G^{Thr287Ala}, P = 0.0001; CAMK2G$^{Thr287Ala/Arg292Pro}$, P = 0.99; CAMK2G^{Thr287Ala} vs. CAMK2G$^{Thr287Ala/Arg292Pro}$, P = 0.0001). (C) Representative image of a P20 pup *in utero* electroporated at E14.5 with CAMK2G^{Thr287Ala} or CAMK2G$^{Thr287Ala/Arg292Pro}$. tdTOMATO positive cells represent neurons successfully targeted. DAPI (blue) counterstaining is used to identify general cortical structure. (D) Upper graph: quantification of the neuronal migration pattern from the Layer 1 (L1) to the intermediate zone (IZ); Lower graph: analysis of the percentage of targeted cells that reach the outer layers of the cortex measured as sum of bin 1–4 (one-way ANOVA, F[2,16] = 24.34, P = 1.40E-05; CAMK2G^{WT} vs. CAMK2G^{Thr287Ala}, P = 0.99; CAMK2G$^{Thr287Ala/Arg292Pro}$, P = 0.0001; CAMK2G^{Thr287Ala} vs. CAMK2G$^{Thr287Ala/Arg292Pro}$, P = 0.0001). The dotted line represents the level reached by the CAMK2G-WT (see Figure 2F for comparison). Arrowheads indicate layer 2/3 of the somatosensory cortex, whereas the arrow indicates the subventricular zone (SVZ). Data in (B) and (D) are presented as mean ± SEM. Numbers (X/Y) depicted in the bar graphs represent the total number of cells (X) and number of independent cultures (Y) (B) or number of pictures (D) analyzed

CAMK2G$^{Arg292Pro/Lys43Arg}$ expressing cells targeted at E14.5 by *in utero* electroporation revealed no discernible migration deficits compared to CAMK2G^{WT} (Figure 2F, Figure 7C and D), indicating that the pathogenicity of CAMK2G^{Arg292Pro} requires its kinase activity.

Since the introduction of the p.Lys43Arg mutation into the exclusively cytosolic CAMK2G^{Arg292Pro} isoform strongly attenuates the pathogenicity of the Arg292Pro mutation, we hypothesized that the pathogenicity of the p.Arg292Pro mutation is independent of its function as a nuclear Ca^{2+}/CaM shuttle. To investigate this, we introduced the p.Lys43Arg mutation into the CAMK2G that carries an NLS, resulting in CAMK2G-NLS^{Arg292Pro}. Analysis of the CAMK2G-NLS$^{Lys43Arg/Arg292Pro}$ double mutation showed that the Lys43Arg mutation did not alter the nuclear targeting deficit (Suppl. Fig. S6A and B). Nevertheless, both neuronal maturation and migration were again fully rescued by introducing the p.Lys43Arg mutation (Suppl. Fig. S6C–E).

Taken together these experiments suggest that the p.Arg292Pro mutation renders CAMK2G constitutively active and impairs neuronal maturation and migration independent of its role as a Ca^{2+}/CaM shuttle.

The CAMK2G^{Arg292Pro} analogous mutations in CAMK2A and CAMK2B exhibit similar neurodevelopmental pathogenicity as CAMK2G^{Arg292Pro}

Given that CAMK2G^{Arg292Pro} exerts the pathogenic phenotype we describe via a non-nuclear function, we hypothesized that the analogous mutations in CAMK2A or CAMK2B lacking an NLS might be similarly disruptive for neurodevelopment, given that they are almost exclusively localized to the cytoplasm. Therefore, we generated the analogous mutations of CAMK2G^{Arg292Pro} in CAMK2A and CAMK2B (Figure 8A). We first investigated the basal Thr286 and Thr287 phosphorylation levels of CAMK2A and CAMK2B, respectively. Whereas basal auto-phosphorylation in HEK-293T cells of CAMK2GWT was clearly evident, that of CAMK2A^{WT} or CAMK2B^{WT} was hardly detectible (Figure 8B). In contrast, both CAMK2A^{Lys291Pro} and CAMK2B^{Lys292Pro} exhibited robust basal Thr286/287 phosphorylation (Figure 8C), indicating that this Arg/Lys residue functions critically across multiple CAMK2 isoforms for constraining phospho-transferase activity.

We next tested whether the expression of CAMK2A^{Lys291Pro} and CAMK2B^{Lys292Pro} impacts the morphological development of cultured primary hippocampal neurons (Figure 8D). No changes in neuronal morphology were observed with expression of CAMK2A^{WT} (Figure 8E). Expression of CAMK2B^{WT} did result in a small but significant decrease in arborization, but without changes in total neurite length (Figure 8E). In contrast, expression of either CAMK2A^{Lys291Pro} or CAMK2B^{Lys292Pro} each resulted in substantial alterations of neuronal morphology (Figure 8D and E).

Lastly, we evaluated the impact of CAMK2A^{Lys291Pro} and CAMK2B^{Lys292Pro} on *in vivo* neural cell migration. The majority of cells expressing either CAMK2A^{WT} or CAMK2B^{WT} migrated normally to layer 2/3 of the somatosensory cortex (Figure 8F). However, expression of either CAMK2A^{Lys291Pro} or CAMK2B^{Lys292Pro} caused a severe disruption of migration, analogous to the effect of CAMK2G^{Arg292Pro} (Figure 8F).

Therefore, our findings suggest a strong functional conservation across the major brain-expressed CAMK2 isoforms of the ID-associated CAMK2Gp.Arg292Pro mutation for which neurodevelopmental pathogenicity is mediated by a gain-of-function through enhanced cytoplasmic phosphotransferase activity.

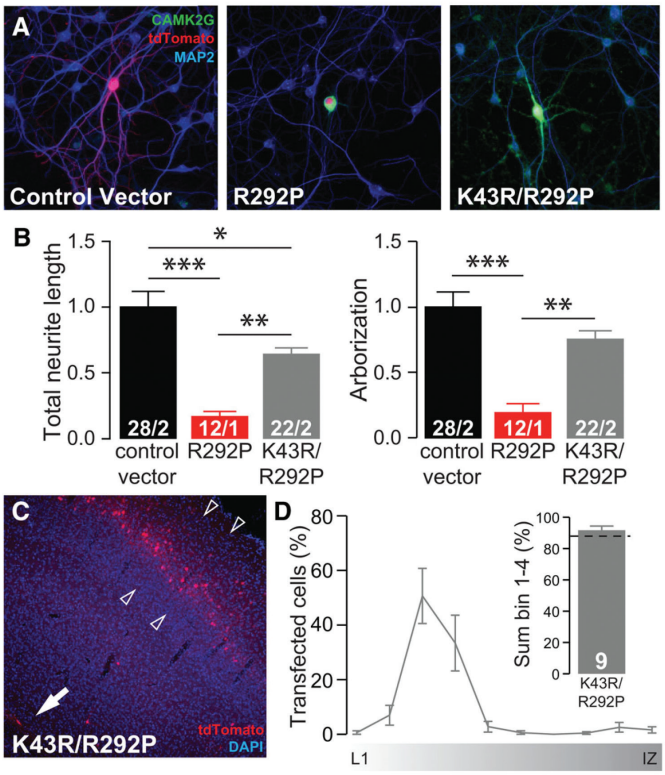

FIGURE 7 Silencing the catalytic activity of CAMK2G^{Arg292Pro} normalizes neuronal maturation and migration. (A) Representative confocal images of hippocampal neurons transfected on DIV7 with control vector or CAMK2G$^{Lys43Arg/Arg292Pro}$ (K43R/R292P). Transfected neurons are identified by the tdTOMATO (red). (B) Summary bar graphs of total neurite length and arborization measured for each condition and normalized to the control vector (total neurite length: one-way ANOVA, $F[2,61] = 18.50$, $P = 5.25E-07$; CAMK2G$^{Lys43Arg/Arg292Pro}$ vs. control vector: $P = 0.05$; CAMK2G^{Arg292Pro}: $P = 0.01$; arborization: one-way ANOVA, $F[2,61] = 15.02$, $P = 4.97E-06$; CAMK2G$^{Lys43Arg/Arg292Pro}$ vs. control vector, $P = 0.16$; CAMK2G^{Arg292Pro}, $P = 0.01$). (C) Representative image of a P20 pup *in utero* electroporated at E14.5 with CAMK2G$^{Lys43Arg/Arg292Pro}$. tdTOMATO positive cells represent neurons successfully targeted. DAPI (blue) counterstaining is used to identify general cortical structure. (D) Left: quantification of the neuronal migration pattern from the Layer 1 (L1) to the intermediate zone (IZ); Right: analysis of the percentage of targeted cells that reach the outer layers of the cortex measured as the sum of bin 1–4 (CAMK2G^{WT} vs. CAMK2G$^{Lys43Arg/Arg292Pro}$, $t[15] = 0.83$, $P = 0.42$, two-tailed unpaired t-test).The dotted line indicates the CAMK2G^{WT} level, see Figure 2F for comparison. Arrowheads indicate layer 2/3 of the somatosensory cortex, whereas the arrow indicates the subventricular zone (SVZ). Data in (B) and (D) are presented as mean±SEM. Numbers (X/Y) depicted in the bar graphs represent the total number of cells (X) and number of independent cultures (Y) (B) or number of pictures (D) analyzed

IV

DISCUSSION

In the present study, we describe two unrelated patients with severe ID, carrying a *de novo* CAMK2Gp.Arg292Pro mutation and made use of an *in vitro* morphology and *in vivo* migration assay to investigate the pathogenicity of this mutation.

Mutations in *CAMK2A* and *CAMK2B* have recently been shown to cause ID, severely delayed speech and behavioral issues (Küry *et al*., 2017b). Apart from these common features, there is much variability between the different CAMK2 patients. The two patients described here carrying a mutation in CAMK2G share similar features with *CAMK2A*/*CAMK2B*-mutated patients (e.g., ID and hypotonia), but also show clear differences such as facial dysmorphisms. The continuous identification of individuals with ID carrying mutations in the CAMK2 genes, may enable further characterization of specific characteristics for the CAMK2-dependent syndrome.

We have established several lines of mechanistic evidence indicating that the p.Arg292Pro mutation acts as a gain-of-function, with regard to catalytic activity of the kinase, but as a loss-of-function with regard to its nuclear localization. First, we showed that expression of CAMK2G mutants that reduce kinase activity by interfering with Ca^{2+}/CaM binding or rendering the protein kinase-dead, do not recapitulate the neurodevelopmental

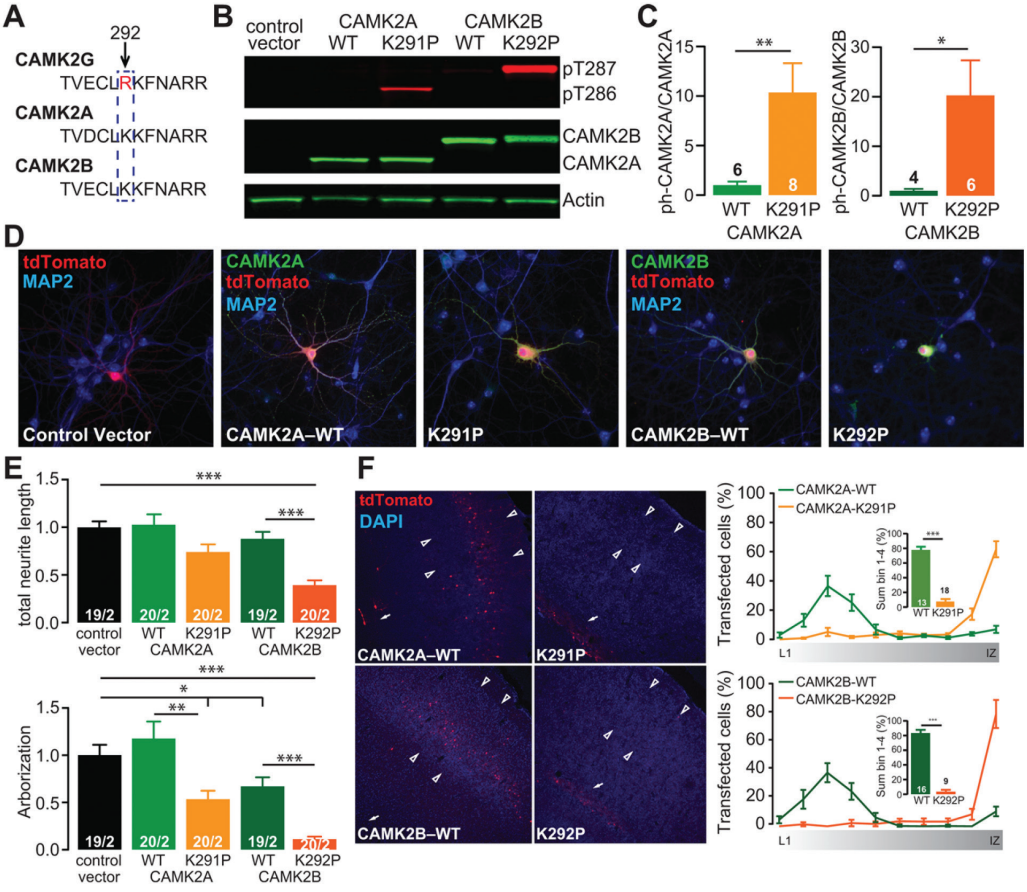

FIGURE 8 CAMK2A^{Lys291Pro} and CAMK2B^{Lys292Pro} exhibit similar neurodevelopmental pathogenicity as $^{CAMK2GArg292Pro.}$ (A) Alignment of the protein sequence of CAMK2A, CAMK2B, and CAMK2G showing that the Arginine (R) at 292 in CAMK2G is a Lysine (K) in CAMK2A and CAMK2B. (B) Representative western blot of HEK-293T cells transfected with control vector, CAMK2A^{WT}, CAMK2A^{Lys291Pro} (K291P), CAMK2B^{WT}, or CAMK2B^{Lys292Pro} (K292P). (C) Quantification of the levels of CAMK2–Thr286/Thr287 phosphorylation, normalized against total CAMK2 in the different conditions (CAMK2A^{WT} vs. CAMK2A^{Lys291Pro}, t[12] = 2.7, P = 0.01; CAMK2B^{WT} vs. CAMK2B^{Lys292Pro}, t(8) = 2.18, P = 0.03, one-tailed unpaired t-test). (D) Representative confocal images of hippocampal neurons transfected on DIV7 with control vector, CAMK2A^{WT}, CAMK2A^{Lys291Pro}, CAMK2B^{WT}, or CAMK2B^{Lys292Pro}. Transfected neurons are identified by the tdTOMATO (red). (E) Summary bar graphs of total neurite length and arborization measured for each condition and normalized to the control vector (CAMK2A total neurite length: one-way ANOVA, F[2,56] = 3.38, P = 0.04; control vector vs. CAMK2A^{WT}, P = 0.9; CAMK2A^{Lys291Pro}, P = 0.1, CAMK2A^{WT} vs. CAMK2A^{Lys291Pro}, P = 0.06; CAMK2A arborization: one-way ANOVA F[2,56] = 6.37, P = 0.003; control vector vs. CAMK2A^{WT}, P = 0.6; CAMK2A^{Lys291Pro}, P = 0.04, CAMK2A^{WT} vs. CAMK2A^{Lys291Pro}, P = 0.003; CAMK2B total neurite length: one-way ANOVA, F[2,55] = 27.26, P = 5,9E-09; control vector vs. CAMK2B^{WT}, P = 0.5; CAMK2B^{Lys292Pro}, P = 0.0001, CAMK2B^{WT} vs. CAMK2B^{Lys292Pro}, P = 0.0001; CAMK2B arborization: one-way ANOVA F[2,55] = 29.07, P = 2.4E-09; control vector vs. CAMK2B^{WT}, P = 0.02; CAMK2B^{Lys292Pro}, P = 0.0001, CAMK2B^{WT} vs. CAMK2B^{Lys292Pro}, P = 0.0001). (F) Representative images of P20–P22 pups *in utero* electroporated at E14.5 with control vector, CAMK2A^{WT}, CAMK2A^{Lys291Pro}, CAMK2B^{WT}, or CAMK2B^{Lys292Pro}. tdTOMATO positive cells represent neurons successfully targeted. Arrowheads indicate layer 2/3 of the somatosensory cortex, whereas the arrowhead indicates the subventricular zone (SVZ). Right: quantification of the neuronal migration pattern from the Layer 1 (L1) to the intermediate zone (IZ); insets represent the percentage of targeted cells that reach the outer layers of the cortex measured as the sum of bin 1–4 (CAMK2A^{WT} vs. CAMK2A^{Lys291Pro}, t(29) = 12.97, P = 1.34E-13, unpaired two-tailed t-test; CAMK2B^{WT} vs. CAMK2B^{Lys292Pro}, t(23) = 13.33, P = 2.64E-12, unpaired two-tailed t-test). Data in (C) and (E) are presented as mean ± SEM. Numbers (X/Y) depicted in the bar graphs represent the number of samples (C) or the total number of cells (X) and number of independent cultures (Y) (E) analyzed

phenotypes exhibited by expression of CAMK2G^{Arg292Pro}. Second, we showed that the CAMK2Gp.Arg292Pro mutation causes increased phosphotransferase activity as well as increased CaM affinity, resulting in increased Thr287 phosphorylation. Third, we showed that expression of the constitutively active mutant CAMK2G$^{Thr287Asp/Thr306Val/Thr307Ala}$ phenocopies the neurodevelopmental impairments seen with expression of CAMK2G^{Arg292Pro}. Finally, we showed that CAMK2G-NLS^{Arg292Pro} is deficient in nuclear localization. Taken together, we propose a model whereby the p.Arg292Pro mutation renders CAMK2G constitutively active albeit with a reduced protein half-life, either due to intrinsic instability or targeted degradation. Notably, expression of the constitutively active CAMK2G$^{Thr287Asp/Thr306Val/Thr307Ala}$ mutant in HEK-293T cells also resulted in lower CAMK2G protein expression but the higher activity of the expressed protein led to the gain-of-function phenotype. Additionally, mice expressing the CAMK2A$^{Thr305Val/Thr306Ala}$ protein, which lacks auto-inhibitory function, exhibits a two-fold reduction in CAMK2A protein but similarly produces a net gain-of-function phenotype (Elgersma *et al*., 2002). Since CAMK2 is highly dependent on a Ca^{2+} stimulus for activity, even low expression of a constitutively active form such as CAMK2G^{Arg292Pro} may elicit gain-of-function effects. Future studies using a targeted mouse mutant and genome-edited human pluripotent stem cells would provide further insights regarding the endogenous regulation of CAMK2G^{Arg292Pro} protein levels.

Although the effect of the CAMK2G^{Arg292Pro} mutation has not previously been studied, our finding that its pathogenicity derives from a gain-of-function is consistent with the rich knowledge of CAMK2 biochemistry (for reviews see, Hudmon and Schulman (2002b); Lisman *et al*. (2002)). In the basal state, the auto-regulatory domain functions to suppress catalytic activity by maintaining the kinase in an inactive conformation and blocking access of external substrates to the binding pocket. Binding of Ca^{2+}/CaM to the auto-regulatory domain displaces it to allow the active conformation and opening the substrate binding pocket. In the process, it exposes Thr286 (CAMK2A)/Thr287 (CAMK2B and CAMK2G) for auto-phosphorylation, which disables the inhibitory function of the auto-regulatory domain and results in Ca^{2+}/CaM independent (autonomous) activity. The auto-regulatory domain consists of several residues that participate in auto-inhibition, one of which is located at amino acid position 291 in CAMK2A (Smith *et al*., 1992). Indeed, for CAMK2A it has previously been shown that mutation of Lysine 291 (equivalent to Arginine 292 in CAMK2G) to Alanine increases the Ki for inhibitory peptides and reduced the inhibitory potency of the auto-regulatory domain (Smith *et al*., 1992). Notably, mutation of CAMK2A just three residues downstream, from Asparagine 294 to aspartic acid, generates an even greater enhancement of constitutive activity than the phosphomimetic p.Thr286Asp mutation. Therefore, it is possible that the disruptive nature of the Proline substitution in p.Arg292Pro reduces the contribution of the critical Asparagine for auto-inhibition resulting in enhanced constitutive activity (Yang & Schulman, 1999). Additionally, mutation of CAMK2A Lysine 291 to Glutamic acid reduced the relative K_{CaM} by 50%, thereby increasing CaM binding (Yang & Schulman, 1999). Hence, these structural and biochemical findings are entirely consistent with our finding that the p.Arg292Pro mutation would generates a constitutively active kinase that facilitates CaM binding and promotes Thr287 phosphorylation that delinks kinase activity from complete dependence on Ca^{2+} stimulus for activity.

Our finding that knockdown of CAMK2G affects neuronal arborization, which could be rescued by CAMK2G expression with or without an NLS, but not by heterologous CAMK2A or CAMK2B overexpression indicates that cytosolic CAMK2G plays a unique role in neuronal development, and that loss-of-function mutations or haploinsufficiency could potentially be disruptive. Indeed, according to ExAC, the probability of CAMK2G being LoF intolerant is high (pLI = 0.99). However, to our knowledge no patient with a neurodevelopmental disorder has

yet been found carrying an indel or a nonsense mutation in the *CAMK2G* gene. Interestingly, another CAMK2G candidate variant (CAMK2G c.1075G > A p.Val359Met) was found in a patient with a developmental disorder in the Deciphering Developmental Disorders Study (Deciphering Developmental Disorders Study, 2017). In contrast to the p.Arg292Pro mutation, this variant is located in the association domain of the protein, which makes it difficult to predict *a priori* if and how it affects CAMK2G protein function.

Very few studies have looked at the function of CAMK2G in neurons. Only recently, a first hint for CAMK2G having a unique function in spinal cord ganglion cells was published (Ma *et al*., 2014). This study indicated that CAMK2G functions as a shuttle to transport Ca^{2+}/CaM from the cell surface and cytoplasm to the nucleus, a function that does not require its catalytic activity but depends on phosphorylation of its Thr287 by a second CAMK2 holoenzyme, and on the integrity of its NLS to initiate changes in gene expression in response to specific Ca^{2+} signals. Our study further expands the mechanistic evidence underlying the function of CAMK2G in neurons by demonstrating that reduced levels of CAMK2G resulted in a significant elaboration of neuronal morphology. Notably, this effect could be reversed by expression of CAMK2G with or without an NLS, but not by expression of CAMK2A or CAMK2B. Therefore, we conclude that cytosolic CAMK2G functions to constrain dendritic arborization. In contrast, whereas CAMK2A knockdown does not affect dendritic arborization, CAMK2B knockdown has been shown to reduce dendritic arborization of primary hippocampal neurons (Fink *et al*., 2003), together suggesting distinct neurodevelopmental functions of the various CAMK2 isoforms.

Even though a subset of CAMK2G isoforms contains an NLS (Takeuchi *et al*., 2002), we did not observe differential effects on neuronal morphology or neural cell migration that were dependent on the presence of the NLS domain. However, we did find that CAMK2G-$NLS^{Arg292Pro}$ is localized predominantly to the cytosol, whereas CAMK2G-NLS^{WT} is located in both the nucleus and cytosol, indicating that the p.Arg292Pro mutation interferes with its nuclear localization. However, given that abrogation of the phospho-transferase activity (via the Lys43Arg mutation) fully rescued the pathogenic effect of the p.Arg292Pro mutation, independently of the presence or absence of the NLS domain, we conclude that the pathogenicity of the p.Arg292Pro mutation is most likely unrelated to its nuclear function.

Our results also demonstrate that the combination of *in vitro* and *in vivo* neurodevelopmental assays provide a robust platform for investigating the functional pathogenicity of candidate CAMK2 mutations for ID. Furthermore, by exploiting the wealth of previous data that has been gathered for the CAMK2 protein (Colbran, 1992; Hanson *et al*., 1994; Yang & Schulman, 1999; Hudmon & Schulman, 2002a; Colbran & Brown, 2004; Rellos *et al*., 2010;), we were subsequently able to carefully dissect the biochemical mechanism underlying the pathogenicity of the mutation.

In conclusion, we show that CAMK2G is indispensable for normally developing neurons. Moreover, we have demonstrated that the pathogenicity of the *de novo* CAMK2G p.Arg292Pro mutation is mediated by a gain-of-function through enhanced constitutive enzymatic activity.

SUPPLEMENTAL FIGURES

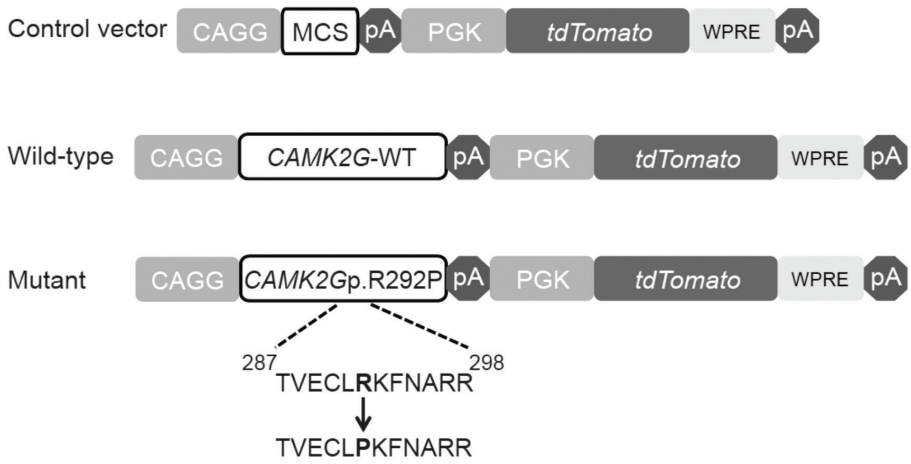

Suppl. Fig. S1. Schematic representation of the dual-promoter expression vector with the CAMK2G constructs. (Control Vector) Schematic representation of the control vector consisting of a *CAGG* promoter followed by a multiple cloning site (MCS) to insert genes of interest. The *tdTomato* gene is expressed under the *PGK* promoter, to have independent expression of both the gene of interest and *tdTomato*.

IV

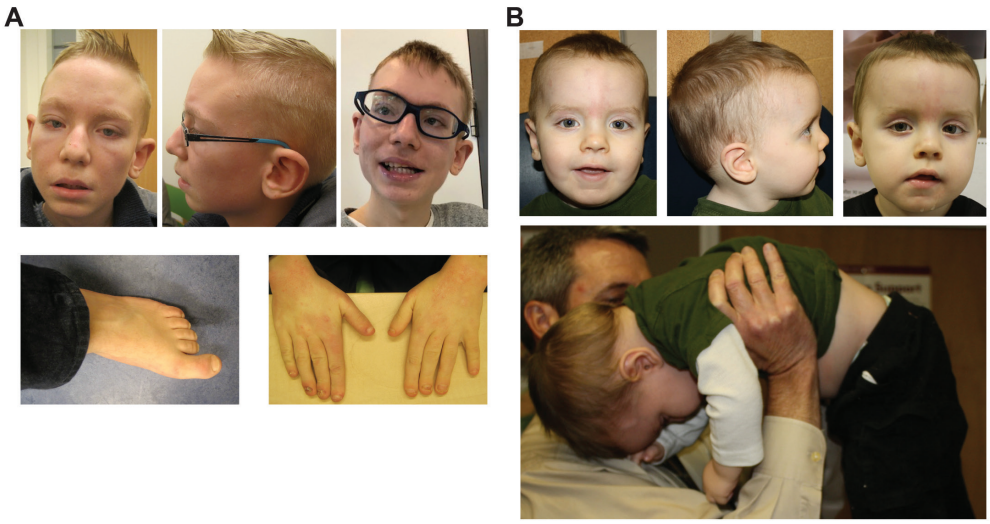

Suppl. Fig. S2. Clinical information on the two individuals carrying the *CAMK2G* c.875G>C p.Arg292Pro mutation. (A) Photographs of patient 1 in whom the p.Arg292Pro mutation was identified. This individual was already briefly described in a recent whole exome study (Trio 32 in De Ligt *et al*., 2012). At 16 and a half years old the boy shows severe ID (IQ<35), speaks only in short sentences, often repeating the same words, suffers from juvenile glaucoma, has short hands, brittle nails and prominent large first toes. His height was 160 cm (-2.7 SD). When he was younger he showed generalized hypotonia, which resolved with age. MRI/MRS imaging was done when he was 4 years old, which showed a mild increased signal of periventricular white matter and decreased amount of choline in the grey matter. There were no structural brain anomalies. The boy did not show any seizures. Facial characteristics show a narrow flat forehead, a small chin, long palpebral fissures, arched eyebrows, broad nose bridge and full nose tip, low-set prominent ears and long philtrum.
(B) Photographs of patient 2 in whom the p.Arg292Pro mutation was identified. He is currently 5 years 5 months of age and was first seen for genetic evaluation at 14 months of age for hypotonia and developmental delay. Over time, he has exhibited ongoing delays in gross motor and speech/language skills along with severe generalized hypotonia. He has a history of night terrors but no seizures. Brain and spine MRI scans were normal, and numerous metabolic and genetic studies done prior to whole exome sequencing were non-diagnostic. A psychological evaluation at 5 years of age showed severe intellectual disability and an autism spectrum disorder. Facial photos from ages 14 months (top left and top middle) and 25 months (top right) demonstrate prominent capillary vascular malformation on forehead and glabella, tall forehead, tubular nose with upturned tip, relatively large ears, rounded cheeks, and facial hypotonia. Photo from age 14 months (bottom) demonstrates severe truncal hypotonia with ventral suspension.

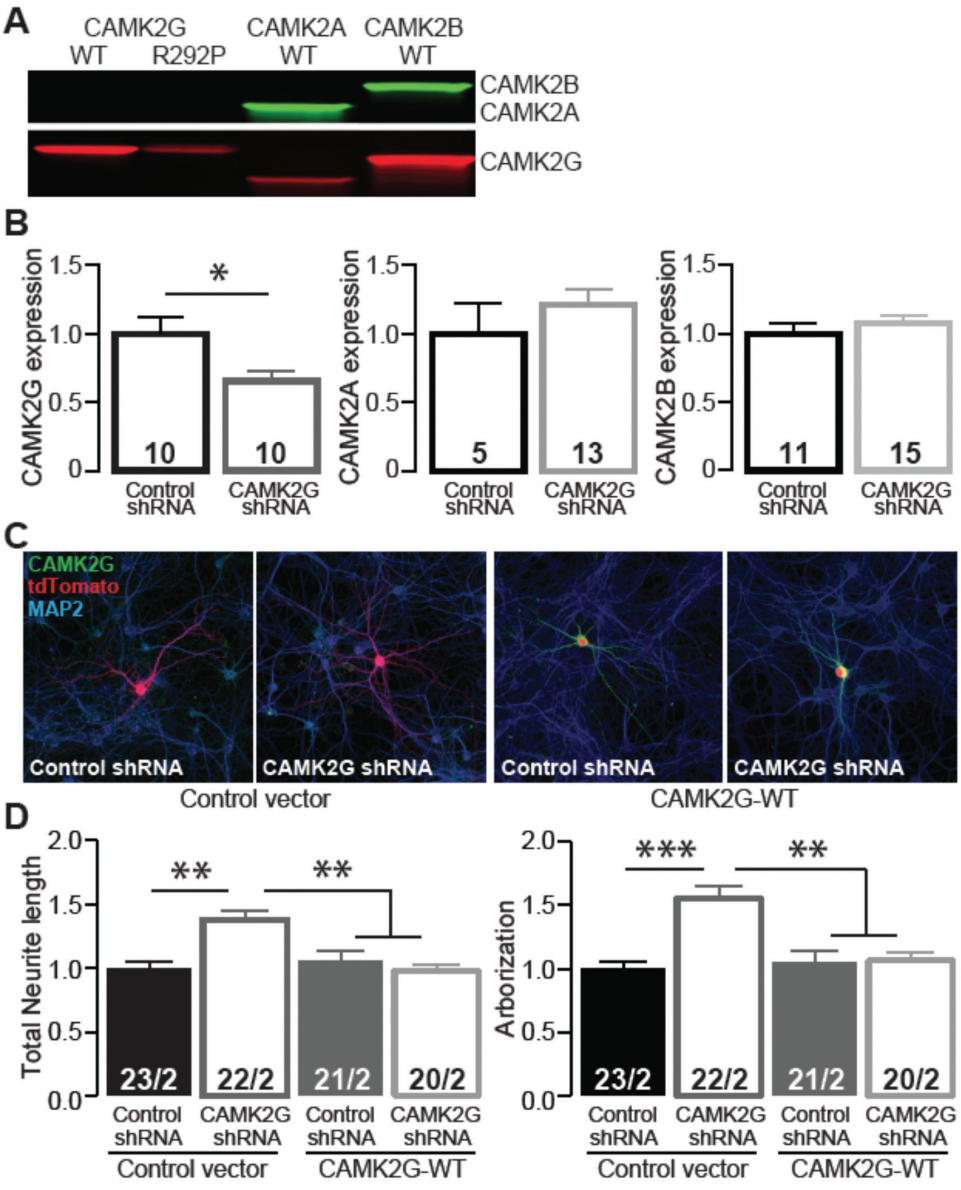

Suppl. Fig. S3. Specificity of the shRNA against CAMK2G. (A) Western blot showing cross-reaction of the CAMK2G antibody with CAMK2A and CAMK2B. Lysates of HEK cells transfected with CAMK2A, CAMK2B or CAMK2G constructs were used. (B) Quantification of the levels of CAMK2G (left), CAMK2A (middle) or CAMK2B (right) expression in neurons transfected with shRNA against CAMK2G, normalized against non-transfected neurons on the same coverslip and then normalized against neurons transfected with scrambled shRNA (CAMK2G: t[18]=2.4, p=0.03; CAMK2A: t[16]=0.9, p=0.38; CAMK2B: t[24]=0.81, p=0.43, two-tailed unpaired t-test). Data are presented as mean ± SEM. Numbers depicted in the bar graphs represent the number of neurons analyzed.

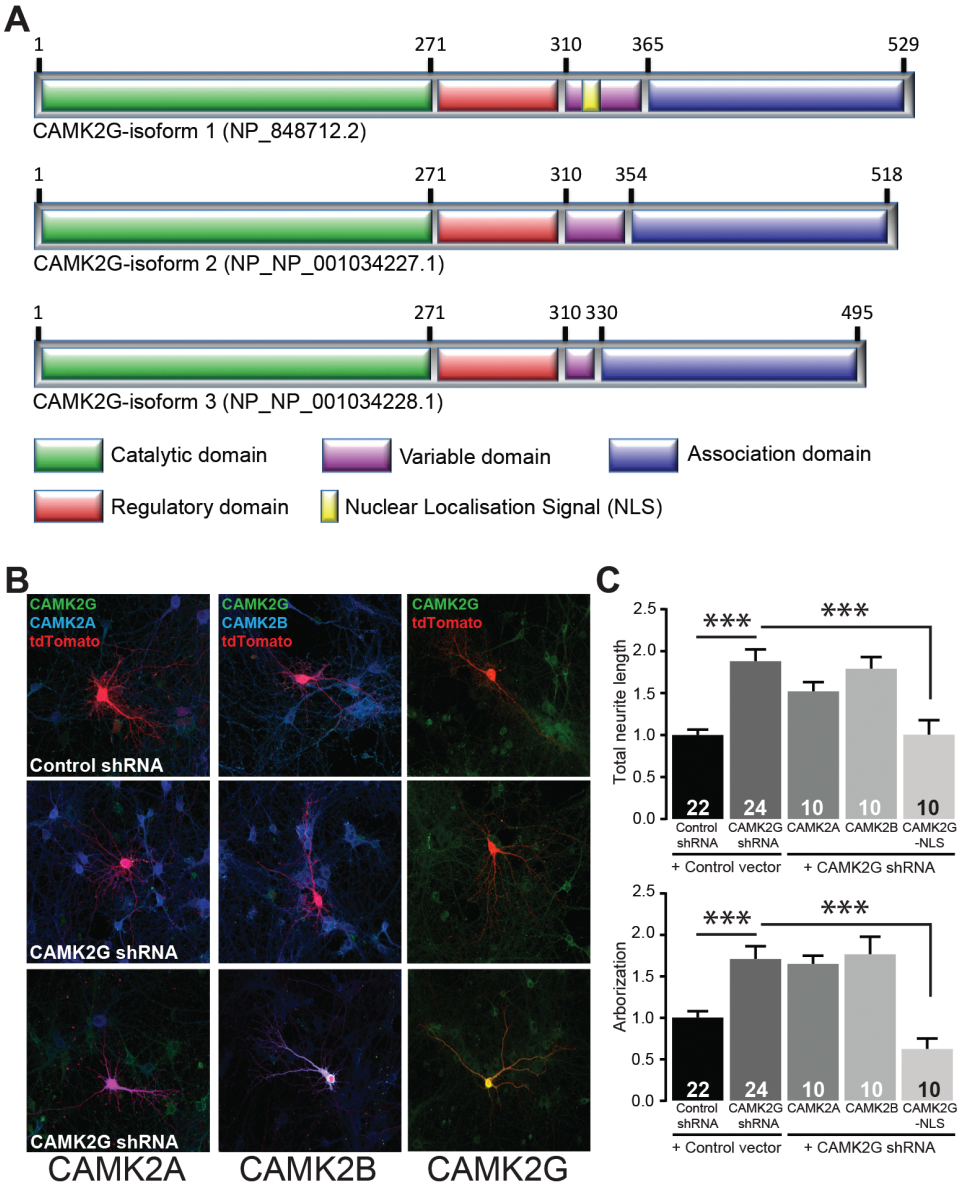

Suppl. Fig. S4. CAMK2G-NLS overexpression rescues the morphology phenotype caused by knockdown of CAMK2G. (A) Schematic overview of the three CAMK2G isoforms present in mice, showing that the three isoforms only differ in the variable region, with only isoform 1 containing the Nuclear Localization Signal (NLS). (B) Representative confocal images of hippocampal neurons co-transfected on DIV7 with combinations of control shRNA, with control vector and an RFP plasmid (first row) or shRNA against *Camk2g* with control vector and an RFP plasmid (second row) or shRNA against *Camk2g* with CAMK2A^{WT} or CAMK2B^{WT} or CAMK2G-NLS^{WT} and an RFP plasmid (third row). Transfected neurons are identified by the RFP plasmid (red). (C) Summary bar graphs of total neurite length and arborization measured for each condition and normalized to the control shRNA with control vector (total neurite length: one-way ANOVA, F[4,71]=11.48, p=3.05E-07; control vector+*Camk2g*-shRNA versus: control vector+control shRNA, p=0.0001; CAMK2A^{WT}+*Camk2g*-shRNA, p=0.27; CAMK2B^{WT}+*Camk2g*-shRNA, p=0.99; CAMK2G-NLS^{WT}+*Camk2g*-shRNA, p=0.0001; arborization: one-way ANOVA, F[4,71]=10.93, p=5.82E-07; control vector+*Camk2g*-shRNA versus: control vector+control shRNA, p=0.0002; CAMK2A^{WT}+*Camk2g*-shRNA, p=0.99; CAMK2B^{WT}+*Camk2g*-shRNA, p=0.99; CAMK2G-NLS^{WT}+*Camk2g*-shRNA, p=0.0001). Data are presented as mean ± SEM. Numbers depicted in the bar graphs represent the number of neurons analyzed.

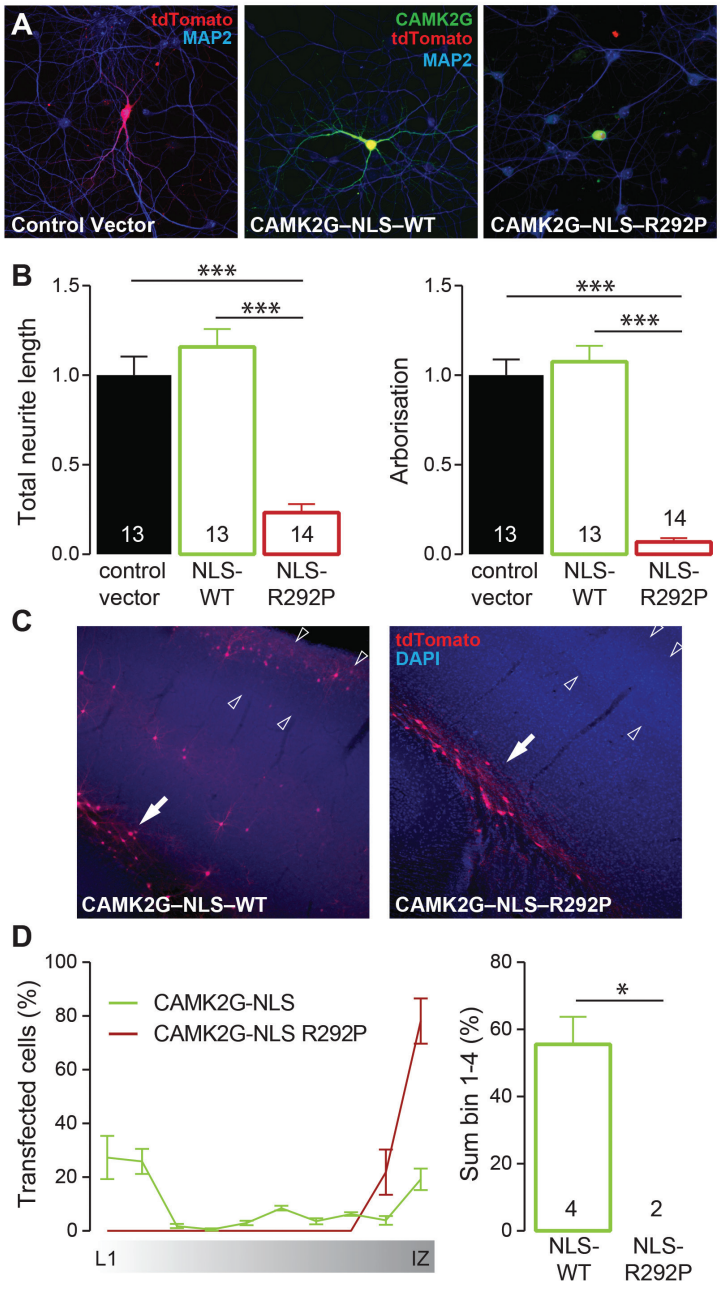

Suppl. Fig. S5. CAMK2G-NLS^{Arg292Pro} overexpression is severely disruptive for neurons *in vitro* and *in vivo*. (A) Representative confocal images of hippocampal neurons transfected on DIV7 with control vector (lacking CAMK2G), CAMK2G-NLS^{WT} or CAMK2G-NLS^{Arg292Pro}. Transfected neurons are identified by the tdTOMATO (red). (B) Summary bar graphs of total neurite length and arborization measured for each condition and normalized to the control vector (total neurite length: one-way ANOVA F[2,37]=33.75, p=4.55E-09; control vector versus: CAMK2G-NLS^{WT}, p=0.62; CAMK2G-NLS^{Arg292Pro}, p=0.0001; CAMK2G-NLS^{Arg292Pro} *vs.* CAMK2G-NLS^{WT}, p=0.0001; arborization: one-way ANOVA F[2,37]=62.5, p=1.37E-12; control vector versus: CAMK2G-NLS^{WT}, p=0.9; CAMK2G-NLS^{Arg292Pro}, p=0.0001; CAMK2G-NLS^{Arg292Pro} vs CAMK2G-NLS^{WT}, p=0.0001). (C) Representative images of P20-P22 pups *in utero* electroporated at E14.5 with control vector, CAMK2G-NLS^{WT} or CAMK2G-NLS^{Arg292Pro} tdTOMATO positive cells indicate the successfully targeted neurons. DAPI (blue) counterstaining is used to identify general cortical structure. (D) Left: quantification of the neuronal migration pattern from the Layer 1 (L1) to the intermediate zone (IZ); Right: analysis of the percentage of targeted cells that reach the outer layers of the cortex measured as sum of bin 1-4 (t[4]=4.52, p=0.0107, two-tailed unpaired t-test). Arrowheads indicate layer 2/3 of the somatosensory cortex, whereas the arrow indicates the subventricular zone (SVZ). Data in (B) and (D). Numbers depicted in the bar graphs represent the total number of cells (B) or the number of pictures (D) analyzed.

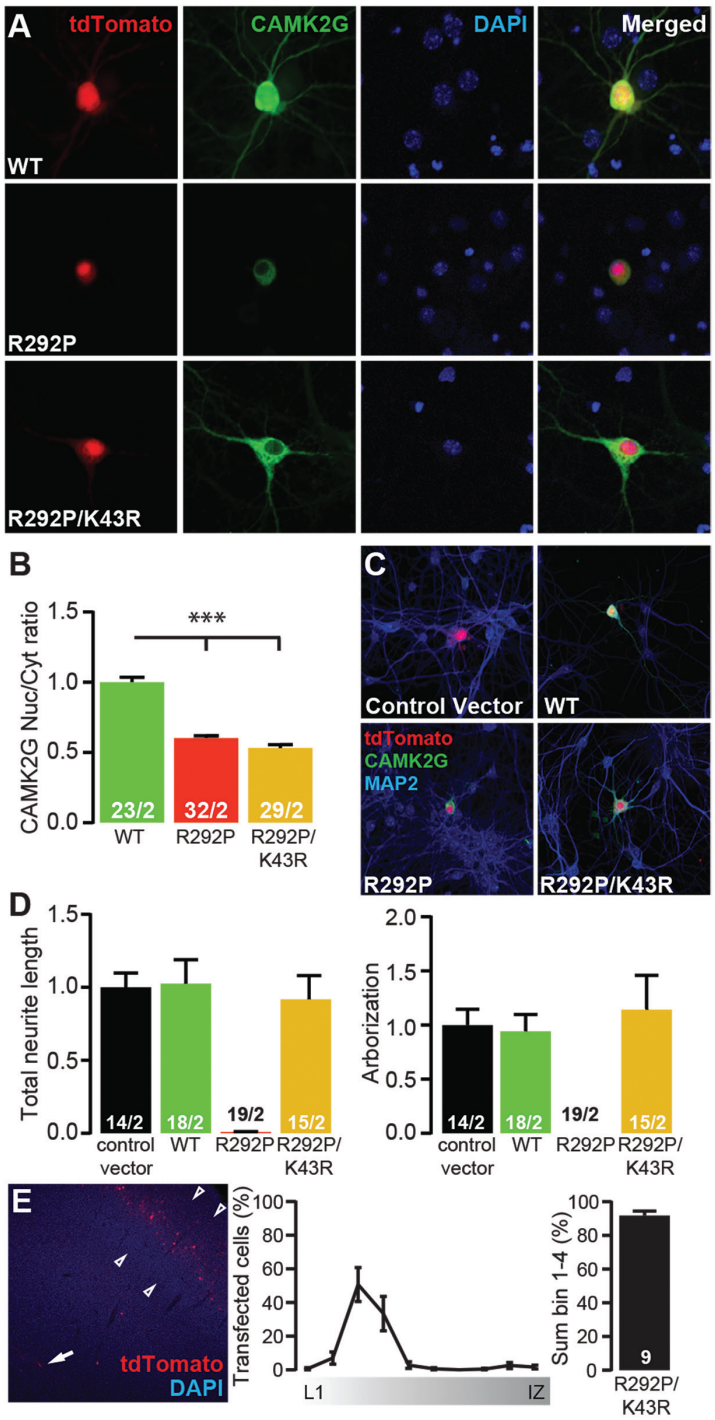

Suppl. Fig. S6. Silencing the catalytic activity of CAMK2G-NLS^{Arg292Pro} rescues the morphology and the *in vivo* phenotypes but not the localization. (A and C) Representative confocal images of hippocampal neurons transfected on DIV7 with CAMK2G-NLS^{WT}, CAMK2G-NLS^{Arg292Pro}, CAMK2G-NLS$^{Arg292Pro/Lys43Arg}$. Transfected neurons are identified by the tdTOMATO (red). (B) Summary bar graphs of CAMK2G expression level measured as a ratio nucleus *versus* cytoplasm and normalized to the WT level (one-way ANOVA, F[2,81]=99.36, p=1.59E-22; CAMK2G-NLS^{WT} versus: CAMK2G-NLS^{Arg292Pro}, p=0.0001; CAMK2G-NLS$^{Arg292Pro/Lys43Arg}$, p=0.0001; CAMK2G-NLS^{Arg292Pro} versus CAMK2G-NLS$^{Arg292Pro/Lys43Arg}$, p=0.10). (D) Summary bar graphs of total neurite length and arborization measured for each condition and normalized to the control vector (Total neurite length: one-way ANOVA, F[3,62]=17.25, p=2.95E-08; control vector versus: CAMK2G-NLS^{WT}, p=0.99; CAMK2G-NLS^{Arg292Pro}, p=0.0001; CAMK2G-NLS$^{Arg292Pro/Lys43Arg}$, p=0.99; CAMK2G-NLS^{WT} versus: CAMK2G-NLS^{Arg292Pro}, p=0.0001; CAMK2G-NLS$^{Arg292Pro/Lys43Arg}$, p=0.99; CAMK2G-NLS^{Arg292Pro} versus CAMK2G-NLS$^{Arg292Pro/Lys43Arg}$, p=0.0001; Arborization: one-way ANOVA, F[3,62]=9.30, p=3.64E-05; control vector versus: CAMK2G-NLS^{WT}, p=0.99; CAMK2G-NLS^{Arg292Pro}, p=0.0013; CAMK2G-NLS$^{Arg292Pro/Lys43Arg}$, p=0.99; CAMK2G-NLS^{WT} versus: CAMK2G-NLS^{Arg292Pro}, p=0.0011; CAMK2G-NLS$^{Arg292Pro/Lys43Arg}$, p=0.99; CAMK2G-NLS^{Arg292Pro} versus CAMK2G-NLS$^{Arg292Pro/Lys43Arg}$, p=0.0001). (E) Representative image of a P20 pup *in utero* electroporated at E14.5 with CAMK2G-NLS$^{Arg292Pro/Lys43Arg}$. tdTOMATO positive cells represent neurons successfully targeted. DAPI (blue) counterstaining is used to identify general cortical structure. Middle panel: quantification of the neuronal migration pattern from the Layer 1 (L1) to the intermediate zone (IZ); Right: analysis of the percentage of targeted cells that reach the outer layers of the cortex measured as the sum of bin 1–4 (one way ANOVA, F[2,12]=67.76, p=2.90E-07; CAMK2G-NLS^{Arg292Pro} versus CAMK2G-NLS$^{Arg292Pro/Lys43Arg}$, p=0.0001, see Figure 4-Supplement 1 for comparison). Arrowheads indicate layer 2/3 of the somatosensory cortex, whereas the arrow indicates the subventricular zone (SVZ). Data in (B) and (D) are presented as mean ± SEM. Numbers (X/Y) depicted in the bar graphs represent the total number of cells (X) and number of independent cultures (Y) (B and D) or number of pictures (E) analyzed.

Chapter V

Variation in a range of mTOR-related genes associates with intracranial volume and intellectual disability

M.R.F. Reijnders,* M. Kousi,* G.M. van Woerden,* M. Klein, J. Bralten, G.M.S. Mancini, T. van Essen, M. Proietti Onori, E.E.J. Smeets, M. van Gastel, A.P.A. Stegmann, S.J.C. Stevens, S.H. Lelieveld, C. Gilissen, R. Pfundt, P.L. Tan, T. Kleefstra, B. Franke, Y. Elgersma, N. Katsanis & H.G. Brunner

*These authors contributed equally

Published in Nat Commun. 2017 Oct 20;8(1):1052

ABSTRACT

De novo mutations in specific mTOR pathway genes cause brain overgrowth in the context of intellectual disability (ID). By analyzing 101 mTOR-related genes in a large ID patient cohort and two independent population cohorts, we show that these genes modulate brain growth in health and disease. We report the mTOR activator gene *RHEB* as an ID gene that is associated with megalencephaly when mutated. Functional testing of mutant *RHEB* in vertebrate animal models indicates pathway hyperactivation with a concomitant increase in cell and head size, aberrant neuronal migration, and induction of seizures, concordant with the human phenotype. This study reveals that tight control of brain volume is exerted through a large community of mTOR-related genes. Human brain volume can be altered, by either rare disruptive events causing hyperactivation of the pathway, or through the collective effects of common alleles.

INTRODUCTION

Many aspects of brain homeostasis, among which are measures of total brain volume, are highly heritable (Peper *et al*., 2007). Genome-wide association studies (GWAS) of brain volume have shown a polygenic architecture in the general population, with individual common genetic variants explaining <1% of phenotypic variance (Hibar *et al*., 2015). Neurodevelopmental disorders, such as intellectual disability (ID) and autism spectrum disorder (ASD), have been associated with significant brain overgrowth. In ID, up to 6% of the patients are macrocephalic (de Ligt *et al*., 2012). One of the key regulators of normal brain development is the evolutionarily conserved Ser/Thr protein kinase Mammalian Target Of Rapamycin (*MTOR*). The role of the mTOR pathway in brain development and function has been intensively studied both in vitro and in vivo using different mouse models. In these models, mutations in either the downstream effectors of mTOR, or the most important upstream regulators of mTOR, such as Ras homolog enriched in brain (Rheb), tuberous sclerosis 1 (Tsc1), and Tsc2, have been tested (Tee *et al*., 2003; Saxton and Sabatini, 2017). Collectively, all studies provide strong evidence that proper mTOR signaling is involved in key aspects of brain development, such as neuronal progenitor maintenance and differentiation (including regulation of neuronal polarity, soma size and neurite outgrowth) and neuronal migration (Tavazoie *et al*., 2005; Kwon *et al*., 2006; Li *et al*., 2008; Nie *et al*., 2010; Feliciano *et al*., 2011; Zhou *et al*., 2011; Urbanska *et al*., 2012; Hartman *et al*., 2013; Lafourcade *et al*., 2013; Baek *et al*., 2015; Moon *et al*., 2015; Lin *et al*., 2016). In the mature brain, mTOR is an important regulator of synapse formation and synaptic function (Bateup *et al*., 2011; Lozovaya *et al*., 2014; Tang *et al*., 2014; Sugiura *et al*., 2015), in particular through its role in regulating protein translation and elongation (Raab-Graham *et al*., 2006; Thoreen *et al*., 2012; Hoeffer *et al*., 2013; Santini *et al*., 2013). Not surprisingly, hyperactivity of the mTOR pathway in mice can lead to a myriad of phenotypes such as macrocephaly, seizures, and behavioral abnormalities (Kwon *et al*., 2006; Goorden *et al*., 2007; Zeng *et al*., 2011; Pun *et al*., 2012; Abs *et al*., 2013; Hsieh *et al*., 2016; Huang *et al*., 2016).

In contrast, sustained downregulation of the mTOR pathway appears to have little effect on neuronal function and behavior (Goorden *et al*., 2015). Findings that the epilepsy and behavioral deficits in mice can be rescued by mTOR inhibitors, offers a broad therapeutic window in which patients can potentially be treated. Indeed, recent studies indicated that mTOR inhibition is a promising treatment for epilepsy in tuberous sclerosis complex (TSC) patients (Franz *et al*., 2013; French *et al*., 2016; Overwater *et al*., 2016).

Given the large body of evidence implying mTOR function in key aspects of brain

development, it is not surprising that hyperactivating, somatic, and germline mutations in components of the PI3K-AKT3-mTOR pathway have been linked with rare ID syndromes associated with (hemi)megalencephaly, focal cortical dysplasia, and epilepsy (Lee *et al*., 2012; Riviere *et al*., 2012; Lim *et al*., 2015; Mirzaa *et al*., 2016). We were struck by the apparent recurrence of mTOR-related mutations in ID, the persistent co-morbid megalencephaly and the absence of studies investigating the overall contribution of the mTOR pathway to ID and brain growth. Considering this knowledge gap, we sought to identify deleterious germline mutations in mTOR-related genes, and assess their contribution to the development of ID and megalencephaly. Next, assuming that our findings are not only relevant to rare diseases such as ID, we hypothesized that the pathology of syndromic ID patients represents the extreme end of a more continuous contribution of the mTOR pathway to human brain development and neuroanatomical variance in the population. Our data indeed indicate that mTOR variation significantly contributes to megalencephaly in a large ID cohort and brain size in the population. Furthermore, we present that de novo mutations in a key regulator of mTOR, *RHEB*, causes severe ID, epilepsy and megalencephaly in humans. By functionally testing the *RHEB* mutations in vertebrate animal models, we show that the specific mutations cause hyperactivation of mTOR, with a concomitant increase in cell and head size, aberrant neuronal migration and induction of seizures, concordant with the human phenotype. The extent of mTOR activation likely affects brain volume in humans. In extreme cases, highly deleterious mutations can lead to profound pathology. For such patients, functional restoration of the pathway through treatment with selective mTOR inhibitors might be of direct clinical utility.

METHODS

Subjects and mutation analysis. We evaluated a cohort of 826 patients with ID, who had undergone diagnostic trio WES at Radboud University Medical Center (Radboudumc). We included 820 simplex patients described previously, as well as three sib pairs excluded from the earlier study (Lelieveld *et al*., 2016). Diagnostic WES was approved by the medical ethics committee of the Radboud University Medical Center (Commissie Mensgebonden Onderzoek), Nijmegen, The Netherlands (registration number 2011-188).Written informed consent was obtained from all individuals or their legal guardians. We collected all available clinical information and performed deep phenotyping of individuals with a de novo mutation in *RHEB*. Consent for publication of photographs was obtained. Brain images were re-evaluated where available.

Selection of mTOR-related genes. We focused on the two well-described, convergent pathways in which mTOR acts as key regulator: the PI3K-AKT-mTOR pathway and the RAS-MAPK-mTOR pathway. We defined a list of 101 mTOR-related genes based on three authoritative reviews on the mTOR regulators (Kolch, 2005; Laplante and Sabatini, 2012b; Shimobayashi and Hall, 2014;). Protein complexes were mapped to single proteins and genes based on information available in the literature. The final list contains 101 mTOR-related genes: 96 map on autosomes and five map on the X-chromosome.

Identification of mutations and collection of OFC data. From our cohort of 826 patients with ID, we selected all de novo mutations that affect mTOR-related genes. All mutations were confirmed by Sanger sequencing. mTOR-related genes were considered to be known ID genes, if present in our recently published list containing over 1500 known ID genes (Lelieveld *et*

al., 2016). We performed a literature search by querying Pubmed (https://www.ncbi.nlm.nih.gov/pubmed/? term=) to investigate which of the known mTOR-related ID genes have been associated with large or small head size. Within our cohort of 826 patients, individuals were classified as microcephalic (OFC < −2.5 SD), macrocephalic (OFC > +2.5 SD), normocephalic (OFC between −2.5 SD and +2.5 SD) or unknown. We used Fisher's Exact test to calculate enrichment of macrocephaly in mTOR-related mutation carriers. The significance threshold was set at $p < 0.05$.

Gene-based enrichment. To assess whether mTOR-related genes were significantly enriched for functional de novo mutations in our cohort, we tested each of the 101 genes using a statistical model as described previously (Lelieveld *et al*., 2016). For this statistical enrichment analysis, the RHEB p.(P37L) variant was considered as one single event. Multiple testing correction was performed by the Bonferroni procedure based on 101 tested genes. Additionally, we tested whether the mTOR pathway as a whole was enriched for functional de novo mutations in our cohort by combining the gene-specific mutation rates of all individual genes in the pathway.

Clustering analysis. Clustering analysis was performed by generating the full cDNA for the respective RefSeq genes. To increase the statistical power of the spatial clustering of the recurrently mutated genes, we added de novo missense variants from the denovo-db (Turner *et al*., 2017b) annotated by our in-house pipeline (Supplementary Data 5). The locations of observed de novo missense mutations were randomly sampled 100,000 times over the cDNA of the gene after which the distances (in base pairs) between the mutations were normalized for the total coding size of the respective gene. The geometric mean (the nth root of the product of n numbers) of all mutation distances between the mutations was taken as a measure of clustering. A pseudocount (adding 1 to all distances and 1 to the gene size) was applied to avoid a mean distance of 0 when there were identical mutations. To assess overall clustering of the set of genes, we used Fisher's combined probability test to combine the 5 *p*-values of individual genes. To avoid a possible bias introduced by highly significant *p*-values (e.g., gene *PPP2RD5*), we calculated the combined *p*-value on deflated *p*-values where all values smaller than 0.05 were set to 0.05.

ENIGMA and CHARGE study populations and data description. This study reports data on 25,974 subjects of Caucasian ancestry from 46 study sites that are part of the Enhancing NeuroImaging Genetics through Meta-Analysis (ENIGMA) (Thompson *et al*., 2014) consortium (13,171 subjects) and Cohorts for Heart and Aging Research in Genomic Epidemiology (CHARGE; 12,803 subjects) (Psaty *et al*., 2009). Briefly, the ENIGMA consortium (http://enigma.ini.usc.edu/download-enigma-gwas-results/) brings together numerous studies, mainly with case–control design, which performed neuroimaging in a range of neuropsychiatric or neurodegenerative diseases, as well as healthy normative populations. The CHARGE consortium is a collaboration of predominantly population-based cohort studies that investigate the genetic and molecular underpinnings of age-related complex diseases, including those of the brain. An overview of the demographics and type of contribution for each cohort is provided in Supplementary Table 8 (Table adapted from original publication by Adams *et al*., 2016). Written informed consent was obtained from all participants. The study was approved by the institutional review board of the University of Southern California and the local ethics board of Erasmus MC University Medical Center. Procedures of whole-genome genotyping, imputation, MRI, GWAS, and meta-analysis are summarized in Supplementary Methods (adapted from original publication Adams *et al*., 2016) The meta-analysis data from the recent ENIGMA2 and

CHARGE studies of ICV were available as genome-wide summary statistics, including genome-wide single-nucleotide polymorphism (SNP) data with corresponding *p*-values. The ENIGMA consortium has completed a meta-analysis of site-level GWAS in a discovery sample of 13,171 subjects of European ancestry (Hibar *et al*., 2015; Thompson *et al*., 2014). Access to the summary statistics of ENIGMA can be requested via their website (http://enigma.ini.usc.edu/download-enigma-gwas-results/). The CHARGE consortium has completed meta-analysis of site-level GWAS in a discovery sample of 12,803 subjects of European ancestry (Adams *et al*., 2016). Genome- wide summary statistics of the CHARGE consortium has been requested by the principal investigator of the study described by Adams *et al*., 2016. For both data sets, only SNPs with an imputation quality score of RSQ ≥ 0.5 and a minor allele frequency ≥0.005 within each site were included.

Procedures of whole-genome genotyping, imputation, magnetic resonance imaging (MRI), GWAS, and meta-analysis of the cohorts are summarized in the Supplementary Methods.

Gene-based and gene-set analyses. Gene-based and gene-set analyses were performed using the Multi-marker Analysis of GenoMic Annotation (MAGMA) software package (version 1.02) (de Leeuw *et al*., 2015). First, gene-based *p*-values were calculated using a symmetric 100 kb flanking region for each cohort separately for the 96 autosomal genes in the mTOR pathway. Genome-wide SNP data from a reference panel (1000 Genomes, v3 phase1) (Durbin *et al*., 2010) was annotated to NCBI Build 37.3 gene locations using a symmetric 100 kb flanking window, and both files were downloaded from http://ctglab.nl/software/magma. Next, the gene annotation file was used to map the genome-wide SNP data from the different studies (ENIGMA2 and CHARGE), to assign SNPs to genes and to calculate gene-based *p*-values for each cohort, separately. Since data from the genome-wide association analyses only included autosomal SNPs, five genes located on the X-chromosome were omitted from the analysis. For the gene-based analyses, single SNP *p*-values within a gene were transformed into a gene-statistic by taking the mean of the $\chi 2$-statistic among the SNPs in each gene. To account for linkage disequilibrium (LD), the 1000 Genomes Project European sample was used as a reference to estimate the LD between SNPs within (the vicinity of) the genes (http://ctglab.nl/software/MAGMA/ref_data/ g1000_ceu.zip). Gene-wide *p*-values were converted to *z*-values reflecting the strength of the association of each gene with the phenotype (ICV), with higher *z*-values corresponding to stronger associations. Subsequently, we tested, whether the genes in the mTOR gene-set were jointly associated with ICV in the ENIGMA2 data set, using self-contained and competitive testing (de Leeuw *et al*., 2016). For the gene-set analyses, we used an intercept-only linear regression model including a subvector corresponding to the genes in the gene-set. This self-contained analysis evaluating, whether the regression coefficient of this regression was larger than 0, tests whether the gene-set shows any association with ICV at all. Next, we tested whether genes in each gene-set were more strongly associated with ICV than all other genes in the genome. Therefore, the regression model was then expanded including all genes outside the gene-set. With this competitive test, the differences between the association of the mTOR gene-set to genes outside this gene-set is tested, accounting for the polygenic nature of a complex trait like ICV. To account for the potentially confounding factors of gene size and gene density, both variables as well as their logarithms were included as covariates in the competitive gene-set analysis. Since self-contained tests do not take into account the overall level of association across the genome, gene-size (number of principal components, or SNPs) and gene density, we were interested in the competitive test for the current analysis. The same procedure was followed for analysis of the CHARGE cohort. In addition to the gene-set analyses within the individual cohorts, we meta-analyzed data of both cohorts on the gene-

level followed by gene-set analysis. Post hoc, the potential effects of the two separate mTOR pathways in the gene-set (the PI3K-AKT-mTOR pathway (60 genes) and the RAS-MAPK-mTOR pathway (76 genes)) as well as the individual genes were investigated, by reviewing their gene test-statistics. Moreover, the Reactome_PI3K_AKT_activation gene-set, consisting of 38 genes, was tested for its association with ICV (downloaded from http://software.broadinstitute.org/gsea/msigdb/genesets.jsp). Genes were considered gene-wide significant, if they reached the Bonferroni correction threshold adjusted for the number of genes within the total gene-set ($N = 96$; $p < 0.000521$).

Generation of zebrafish rheb mutants. All animal experiments were carried out with the approval of the Institutional Animal Care and Use Committee (IACUC). Guide RNAs targeting the *Danio rerio* coding region of *rheb* were generated as described (Perles *et al*., 2015). Subsequently, *rheb* guide oligonucleotide sequences (rheb_ex3_g1F: 5′-TAGGGTCGTGGAACGCAGCGTTCA-3′ and rheb_ex3_g1R: 5′-AAACTGAACGCTGCGTTCCACGAC-3′) were ligated into the pT7Cas9sgRNA vector (Addgene) into *Bsm* BI sites. For the generation of gRNA, the template DNA was linearized with *Bam* HI, purified by phenol/chloroform extraction and in vitro transcribed using the MEGAshortscript T7 kit (Invitrogen). To generate F0 CRISPR mutants we injected 1 nl containing 100 pg *rheb* guide RNA and 200 ng Cas9 protein (PNA bio, CP01) to 1-cell stage embryos. To determine the efficiency of the guide RNA, embryos were allowed to grow to 5 days post fertilization (dfp), at which time they were killed and subjected to digestion with proteinase K (Life Technologies) to extract genomic DNA. The targeted locus was PCR amplified using the drrheb_g1test_1 F 5′-GAGTGATCAGCTGTGAAGAAGG-3′ and drrheb_g1test_1 R 5′-GAACAGCGACAGGAGCTACA-3′ primer pair. PCR amplicons were digested using T7 endonuclease I (New England Biolabs) at 37 °C for 1 h and were visualized on a 2% agarose gel. For Sanger sequencing of individual products from the *rheb* locus, PCR fragments from four embryos with a positive T7assay were cloned into the pCR4/TOPO TA cloning vector (Life Technologies), and 40 colonies from each cloned embryo were Sanger sequenced. We observed sequence aberrations in ~75% of the evaluated *rheb* clones.

In vivo modeling in zebrafish embryos. The human wild-type (Cawthon *et al*., 1990) mRNA of *RHEB* (NM_005614) was cloned into the pCS2+ vector and transcribed in vitro using the SP6 Message Machine kit (Ambion). The variants identified in *RHEB* in our patient cohort (RHEBp.P37L, RHEBp.S68P) were introduced using Phusion high-fidelity DNA polymerase (New England Biolabs) and custom-designed primers. We injected 50 pg of WT or mutant RNA into wild-type zebrafish embryos at the 1- to 4-cell stage. For the experiments with rapamycin treatment we added 2.7 nM of ready-made rapamycin solution in DMSO (R8781, Sigma-Aldrich) in each of the injection cocktails. For the headsize assay, the injected larvae were grown to 5 dpf and imaged live on dorsal view. The area of the head was traced excluding the eyes from the measurements and statistical significance was calculated using Student's *t*-test. All experiments were repeated three times and scored blind to injection cocktail.

Generation of constructs for mouse studies. The cDNA sequences from human *RHEB*-WT (NM_005614), and the variants found in the patient cohort (RHEBp.P37L and RHEBp.S68P) were synthesized by GeneCust, and cloned into our dual promoter expression vector. The dual promoter expression vector was generated from the pCMV-tdTomato vector (Clonetech), in which the CMV promoter was replaced with a CAGG promoter followed by a multiple cloning site (MCS) and transcription terminator sequence. To assure expression of the *tdTOMATO* independent from the gene of interest, a PGK promoter was inserted in front of the tdTomato

sequence (for a schematic overview of the expression vector see Supplementary Fig. 3). For all the in vivo and in vitro experiments, the vector without a gene inserted in the MCS was used as control (control vector).

Mice used for the in vitro and in vivo studies. For the neuronal cultures, FvB/ NHsD females were crossed with FvB/NHsD males (both ordered at 8–10 weeks old from Envigo). For the in utero electroporation female FvB/NHsD (Envigo) were crossed with male C57Bl6/J (ordered at 8–10 weeks old from Charles River). All mice were kept group-housed in IVC cages (Sealsafe 1145T, Tecniplast) with bedding material (Lignocel BK 8/15 from Rettenmayer) on a 12/12 h light/dark cycle in 21 °C (±1 °C), humidity at 40–70% and with food pellets (801727CRM(P) from Special Dietary Service) and water available ad libitum. All animal experiments were approved by the Erasmus MC institutional Animal Care and Ethical Committee, in accordance with European and Institutional Animal Care and Use Committee guidelines.

In vitro modeling in mouse primary hippocampal neurons. Primary hippocampal neuronal cultures were prepared from FvB/NHsD wild-type mice according to the procedure described in Banker and Goslin (Banker and Goslin, 1991). Briefly, hippocampi were isolated from brains of E16.5 embryos and collected altogether in 10 ml of neurobasal medium (NB, Gibco) on ice. After two washes with NB, the samples were incubated in pre-warmed trypsin/EDTA solution (Invitrogen) at 37 °C for 20 min. After two washes in pre-warmed NB, the cells were resuspended in 1.5 ml NB medium supplemented with 2% B27, 1% penicillin/streptomycin and 1% glutamax (Invitrogen), and dissociated using a 5 ml pipette. Following dissociation, neurons were plated on poly-D-lysine (25 mg/ml, Sigma) coated 15 mm glass coverslips at a density of 3×10^4 or 5×10^4 cells per coverslip for the axon length measurements and 1×10^6 cells per coverslip for all the other experiments. The plates were stored at 37 °C/5% CO_2 until the day of transfection. Neurons were transfected at 3 days in vitro (DIV3, DIV7, and DIV14) with the following DNA constructs: control vector (1.8 µg per coverslip), RHEB-WT, RHEBp.P37L, and RHEBp.S68P (all 2.5 µg per coverslip). Plasmids were transfected using Lipofectamine 2000 according to the manufacturer's instructions (Invitrogen). For the rescue experiments, 20 nM rapamycin (dissolved in 0.01% Ethanol) was applied to the culture 1 day post transfection for 3 days. Neurons were fixed 4 days (rapamycin experiment) or 5 days (for soma size) post transfection with 4% paraformaldehyde (PFA)/4% sucrose and incubated overnight at 4 °C with primary antibodies in GDB buffer (0.2% BSA, 0.8 M NaCl, 0.5% Triton X-100, 30 mM phosphate buffer, pH 7.4). The following primary antibodies were used: guinea-pig anti MAP2 (1:500, catalogue number: 188004, Synaptic System) to stain for dendrites, and rabbit anti-RHEB (1:100, catalogue number: 4935, Cell Signaling). Donkey anti-guinea-pig-Alexa647- and donkey anti-rabbit-Alexa488-conjugated were used as secondary antibodies (all 1:200, catalogue numbers: 706-605-148 and 711-545-152, respectively, Jackson ImmunoResearch). Slides were mounted using mowiol-DABCO mounting medium. Confocal images were acquired using a LSM700 confocal microscope (Zeiss). For the analysis of the neuronal transfections, at least ten distinct confocal images (×20 objective, 0.5 zoom, 1024 × 1024 pixels; neurons were identified by the red immunostaining signal) were taken from each coverslip for each experiment. ImageJ software was used for the analysis of the soma size, by drawing a line around the soma of the cell. For each coverslip, the area of the transfected cells was normalized against the area of the non-transfected cells (five cells per coverslips). These values were then normalized against the mean value of the control (control vector).

In vivo modeling in mice. The *in utero* electroporation was performed as described before (Saito and Nakatsuji, 2001). Pregnant FvB/NHsD mice at E14.5 of gestation were used to target the progenitor cells giving rise to pyramidal cells of the layer 2/3 (Taniguchi *et al*., 2012). The DNA construct (1.5–3 μg/μl) was diluted in fast green (0.05%) and injected in the lateral ventricle of the embryos while still in utero, using a glass pipette controlled by a Picospritzer ® III device. To ensure proper electroporation of the injected DNA constructs (1–2 μl) into the progenitor cells, five electrical square pulses of 45 V with a duration of 50 ms per pulse and 150 ms inter-pulse interval were delivered using tweezer-type electrodes connected to a pulse generator (ECM 830, BTX Harvard Appartus). The positive pole was targeting the developing somatosensory cortex. The following plasmids were injected: control vector, *RHEB*-WT, *RHEB*p. P37L and *RHEB*p.S68P. After birth, pups were sacrificed at P0 or P7 for histochemical processing (to investigate neuronal migration) or used to monitor seizure development.

For the migration analysis, confocal images (×10 objective, 0.5 zoom, 1024 × 1024 pixels) were taken from 2 to 3 non-consecutive sections from 2 and 3 electroporated animals per control and *RHEB*-containing plasmids, respectively. Images were rotated to correctly position the cortical layers, and the number of cells in different layers were counted using ImageJ using the analyze particles plugin. The results were exported to a spreadsheet for further analysis. Cortical areas from the pia to the ventricle were divided in 10 equal-sized bins and the percentage of tdTOMATO-positive cells per bin was calculated.

For immunofluorescence, mice were deeply anesthetized with an overdose of Nembutal and transcardially perfused with 4% PFA. Brains were extracted and post-fixed in 4% PFA. Brains were then embedded in gelatin and cryoprotected in 30% sucrose in 0.1 M phosphate buffer (PB), frozen on dry ice, and sectioned using a freezing microtome (40/50 μm thick). Free-floating coronal sections were washed in 0.1 M PB and a few selected sections were counterstained with 4′,6-diamidino-2- phenylindole solution (DAPI, 1:10,000, Invitrogen) before being mounted with mowiol® (Sigma-Aldrich) on glass. Overview images of the coronal sections were acquired by tile scan imaging using a LSM700 confocal microscope (Zeiss) with a ×10 objective. Zoom-in images of the targeted area were taken using a ×20 objective. For seizure observations, mice obtained after in utero electroporation were observed daily starting at P18. General behavior was observed by looking for abnormal behaviors such as hyperactivity, the presence of stereotypical behaviors and the presence of tonic–clonic seizures, either spontaneous or induced upon mild handling. Weaned mice were video-monitored for 24 h per day in the *Phenotyper* (Noldus), to assess seizure onset. Abnormal behaviors and onset of seizures were scored and analysed for each mouse by an expert experimentalist who had been blinded to the identity of samples (i.e., which plasmid had been transfected).

Statistical analysis used for the mouse studies. Statistical difference in soma size between the *RHEB* WT and mutants was determined using one-way analysis of variance (ANOVA) followed by Tukey's post hoc test for multiple comparisons. The effect of rapamycin treatment on soma size was determined using two-way analysis of variance (ANOVA) followed by Bonferroni's post hoc test for multiple comparisons. For the analysis of the in utero electroporation data, a two-way ANOVA repeated measure was performed, followed by the Bonferroni's multiple comparisons test. For the analysis of epilepsy onset, the log-rank Mantel–Cox test was used. The significance threshold was set at $p < 0.05$. Data are presented as mean ± standard error of the mean (SEM).

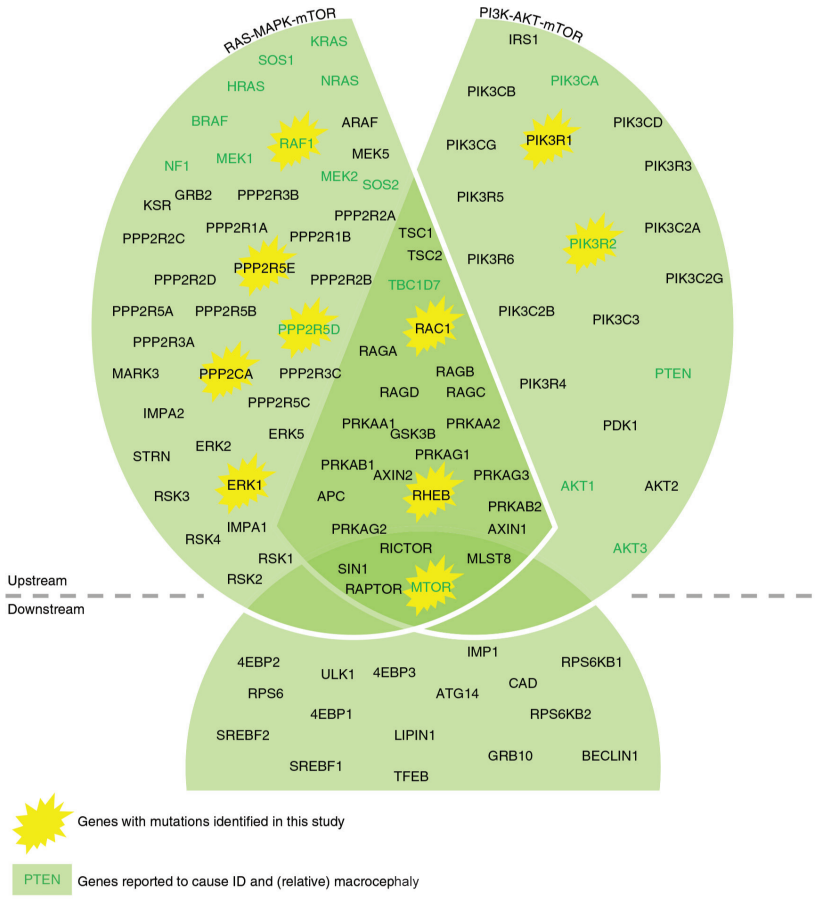

Fig. 1 Schematic overview of selected mTOR-related genes. Schematic representation of the genes (n = 101) included in our mTOR-related gene-set based on three different authoritative publications (Kolch, 2005; Thompson *et al.*, 2014; Turner *et al.*, 2017b;). Both proteins acting upstream of mTOR and proteins acting downstream of mTOR were included. Additionally, we subdivided the total set in two subsets: the RAS-MAPK-mTOR subset and the PI3K-AKT-mTOR subset. In both subsets, downstream genes are included as well. Genes in which we identified de novo mutations in this study were marked with a yellow star, and genes previously reported to cause ID and (relative) macrocephaly are shown in bold and dark green

RESULTS

mTOR-related mutations are associated with macrocephaly. To assess the overall burden of mTOR defects to ID, we performed whole-exome sequencing (WES) in a cohort of 826 patients with ID cataloguing de novo mutations (Supplementary Data 1) in a set of 101 mTOR-related genes (Supplementary Data 2, Fig. 1). We identified 17 de novo mutations affecting 10 different mTOR-related genes, providing a possible genetic diagnosis in 2.1% of our cohort. Five of the identified genes were known ID genes (*PIK3R1*, *PIK3R2*, *RAF1*, *PPP2R5D*, *MTOR*) and five (*RHEB*, *RAC1*, *PPP2R5E*, *PPP2CA*, *ERK1*) were not associated with ID previously (Fig. 1, Table 1, Supplementary Data 3). Three of the five novel genes (*RHEB*, *RAC1*, and *PPP2CA*) showed a significant enrichment for de novo mutations in our patient cohort (Table 1, Supplementary Table 1). Combining the gene-specific mutation rates of all individual mTOR-related genes, we found a significant enrichment for de novo mutations in mTOR-related genes (p = 3.50e−04) (Supplementary Table 1). Additionally, we found significant spatial clustering

Table 1 Identified mutations with bonferroni corrected *p*-value and occipital frontal circumference (OFC) of patients with de novo mutations in mTOR-related genes

Patient key	Gene	c.DNA	Protein change	Known ID gene	OFC	Bonferroni-corrected *p*-value
1	*RHEB*	c.202 T>C	p.(S68P)	No	>+2.5 SD	4.514e−03*
2	*RHEB*	c.110 C > T	p.(P37L)	No	>+2.5 SD	
3	*RHEB*	c.110 C > T	p.(P37L)	No	>+2.5 SD	
4	*RAC1*	c.53 G > A	p.(C18Y)	No	<−2.5 SD	7.657e−03
5	*RAC1*	c.116 A > G	p.(N39S)	No	<−2.5 SD	
6	*PPP2R5E*	c.605 T > G	p.(V202G)	No	No data	1
7	*PPP2CA*	c.882dup	p.(R295*)	No	No data	1.696e−02
8	*PPP2CA*	c.572 A > G	p.(H191R)	No	>+2.5 SD	
9	*ERK1*	c.569 T > C	p.(I190T)	No	<−2.5 SD	1
10	*PIK3R1*	c.1359 C > G	p.(N453K)	Yes	Normal	7.662e−02
11	*PIK3R1*	c.1692 C > G	p.(N564K)	Yes	>+2.5 SD	
12	*PIK3R2*	c.1117 G > A	p.(G373R)	Yes	>+2.5 SD	1
13	*RAF1*	c.1082 G > C	p.(G361A)	Yes	Normal	1
14	*PPP2R5D*	c.1258 G > A	p.(E420K)	Yes	No data	7.832e−04
15	*PPP2R5D*	c.598 G > A	p.(E200K)	Yes	>+2.5 SD	
16	*PPP2R5D*	c.592 G > A	p.(E198K)	Yes	>+2.5 SD	
17	*MTOR*	c.4555 G > A	p.(A1519T)	Yes	>+2.5 SD	1

OFC occipital frontal circumference; *SD* standard deviation
*In the statistical enrichment analysis, the *RHEB* p.(P37L) variant was considered as a single event

Table 2 Number of patients with macrocephaly, normal OFC, and microcephaly

	Macrocephaly	Normal OFC	Microcephaly
Patients with clinical data ($n = 732$)	47	580	105
Patients with de novo mutation(s) ($n = 553$)	35	442	76
Patients with de novo mutation in mTOR-related gene ($n = 14$)	9	2	3
Patients with de novo mutation in gene not related to mTOR ($n = 539$)	26	440	73

OFC occipital frontal circumference

of de novo missense variants for a single gene (PPP2R5D: $p < 1e{-}07$; permutation test) and a general pattern of spatial clustering across the five genes with recurrent de novo missense variants ($p = 0.0057$, Fisher's combined probability test; Supplementary Table 2).

To investigate the contribution of mTOR-related mutations on brain overgrowth, we performed a literature analysis of the 101 mTOR genes. This search showed that 23 genes had been previously reported to cause syndromic ID, with the majority (18/23; 78%) being associated with varying degrees of macrocephaly or relative macrocephaly (Supplementary Table 3). Motivated by this observation, we collected occipital frontal circumference (OFC) data from 732/826 patients (Supplementary Data 4). Macrocephaly was present in 6% of patients in our cohort (47/732 ID patients), a rate comparable to previous reports from an independent cohort (de Ligt *et al*., 2012). De novo mutations were identified in 76% of our cohort (553/732 patients; Table 2). Among the 35 patients presenting with ID, macrocephaly, and a de novo mutation, we found a significant enrichment ($p = 9.084e{-}09$) for de novo mutations within genes of the mTOR pathway (9/14) compared to genes that operate in mTOR independent pathways (26/539) (Table 2). In contrast, microcephaly was not enriched among patients with de novo mutations in mTOR-related genes ($p = 0.4228$).

mTOR pathway contributes to intracranial volume. Driven by the high frequency of brain overgrowth described in the literature and the strong enrichment of macrocephaly in patients with mutations in mTOR-related genes in our cohort, we tested our set of 101 mTOR pathway genes for an association with intracranial volume (ICV) in the general population (Fig. 1, Supplementary Table 2). The final data set contained 76,746 SNPs in 96 autosomal genes (data were unavailable for X-chromosomal *ARAF*, *RPS6KA3*, *RPS6KA6*, *RRAGB*, and *PPP2R3B*). Using the ENIGMA2 data set (n = 13,171) we found a significant association of

the entire mTOR gene set with ICV for the self-contained test ($p_{\text{self-contained}}$ = 0.0029088) and a suggestive association for the competitive test ($p_{\text{competitive}}$ = 0.054742). Data from the CHARGE consortium (n = 12,803) similarly revealed a significant association of the mTOR gene set with ICV for the self-contained test, but not for the competitive test ($p_{\text{self-contained}}$ = 0.00076589 and $p_{\text{competitive}}$ = 0.22105, respectively). Meta-analysis of the two data sets, confirmed the significant association of the mTOR gene set with ICV both for self-contained and competitive tests ($p_{\text{self-contained}}$ = 1.3895e−05, $p_{\text{competitive}}$ = 0.025764). Post hoc testing of the two major branches of the mTOR pathway separately (RAS-MAPK-mTOR, 76 genes; PI3K-AKT-mTOR, 60 genes; Fig. 1, Supplementary Table 4) showed stronger association of PI3K-AKT-mTOR than RAS-MAPK-mTOR with ICV (PI3K-AKT-mTOR: $p_{\text{self-contained}}$ = 0.00092471, $p_{\text{competitive}}$ = 0.0079133; RAS-MAPK-mTOR: $p_{\text{self-contained}}$ = 2.2885e−07, $p_{\text{competitive}}$ = 0.068983). The role of the PI3K-AKT-mTOR pathway in volumetric variation of the brain was further strengthened by testing the previously described Reactome_PI3K_AKT_activation gene-set (Adams *et al*., 2016) (35 genes; $p_{\text{self-contained}}$ = 3.8649e−13; $p_{\text{competitive}}$ = 0.00028957; Supplementary Table 5). Not all 96 genes in the gene-set analysis showed significant association with ICV individually. The most strongly associated individual gene was *AKT3* (P = 2.22E−05) and in total, 18 genes of the mTOR gene set including *APC* (P = 0.00042), and the new ID gene *RHEB* (P = 0.0041), showed nominally significant association with ICV (Supplementary Fig. 1; Supplementary Table 6).

RHEB mutations cause increased neuronal cell and head size. Two of the three individuals with de novo *RHEB* mutations were siblings and carried the same heterozygous p.(Pro37Leu) mutation, while a sporadic individual carried the p.(Ser68Pro) allele. The p.(Pro37Leu) mutation was not identified in either parent, suggesting parental gonadal mosaicism (Fig. 2a). The *RHEB* mutations are located in the RAS domain (Fig. 2b, c) and are absent from ExAC (query for *RHEB*: http://exac.broadinstitute.org/gene/ENSG00000106615), EVS (http://evs.gs.washington.edu/EVS/), or our internal clinical exome databases. All three individuals (Fig. 2d) with de novo *RHEB* mutations had short stature (−2 to −3 SD) and early brain overgrowth with pronounced macrocephaly during childhood (+2.5/+3 SD). They had severe to profound ID with hypotonia, as well as autism spectrum disorder. Two of three individuals were reported to have epilepsy. No epileptic episodes were noted for the third patient, but EEG recordings were suggestive of epileptic discharges (Supplementary Note, Supplementary Table 7). Brain magnetic resonance imaging (MRI) evaluation of the patient with the p.(Ser68Pro) allele, confirmed megalencephaly with broad frontal lobes and mild dilatation of the lateral ventricles. The MRI scan further showed a thickened rostrum of the corpus callosum and small splenium, and mild hypoplasia of the lower cerebellar vermis (Fig. 2e).

We selected the *RHEB* mutations to obtain experimental evidence for our hypothesis that de novo changes in mTOR- related genes are likely due to a gain-of-function mechanism, resulting in hyperactivation of mTOR, as previously shown for other syndromic neurodevelopmental cases associated with macrocephaly. We first tested in vitro whether the *RHEB* de novo changes have an impact on overall mTOR activity levels. Given that mTORC1 regulates cell size (Tavazoie *et al*., 2005; Takei *et al*., 2014), we used primary hippocampal neuron soma size as a readout to assess differences between RHEB-WT overexpressing vs. RHEBp.P37L and RHEBp.S68P overexpressing neurons. A significant increase in soma size was detected already in *RHEB*-WT transfected neurons, suggesting that *RHEB* is a highly dosage sensitive gene, likely causing hyperactivation of the mTOR pathway (Kassai *et al*., 2014). Overexpression of the RHEB mutant proteins caused an increase in soma size, confirming that these mutations do not cause a loss of function (Fig. 3a, b, one-way ANOVA, $p < 0.0001$, $F(3,260) = 50.35$; control vector vs. RHEB-WT: $p < 0.0001$; control vector vs. RHEBp.P37L: $p < 0.0001$;

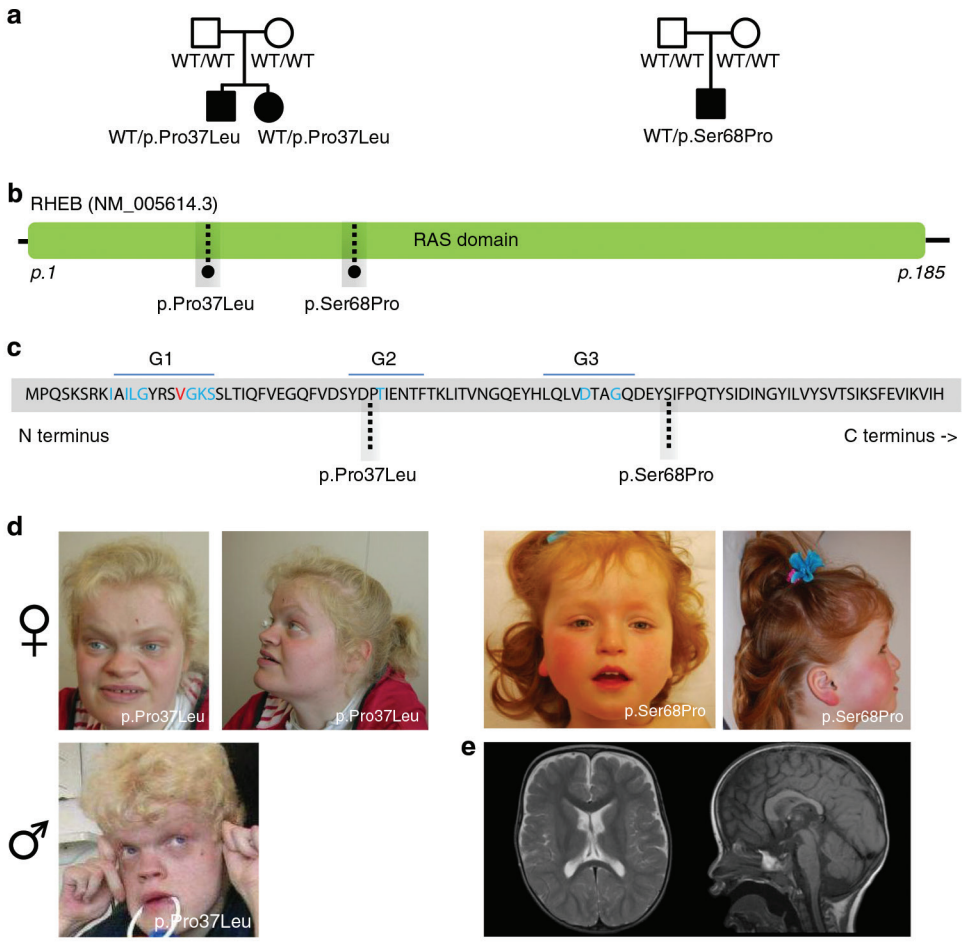

Fig. 2 De novo mutations in *RHEB* cause an ID syndrome associated with megalencephaly. **a** Pedigree structure, disease status and genotype information for patients with changes in *RHEB*. **b** Schematic of the RHEB protein and the RAS domain. **c** Schematic of the N-terminal portion of the human RHEB protein. G-box residues characteristic of RAS superfamily proteins' are shown in blue; highly conserved residue conserved in 90% of the RAS superfamily members are shown in red. Dotted lines are showing the amino-acid residues mutated in patients described in the context of this study. **d** Photographs of the probands carrying de novo variants in *RHEB*. **e** MRI images (left: axial, T2-weighted; right: sagittal midline, T1-weighted) of the proband (age 1 year, 9 months) carrying the de novo *RHEB*p.S68P variant, showing macrocephaly, megalencephaly, broad frontal lobes, mild dilatation of lateral ventricles, large rostrum of corpus callosum and mild hypoplasia of the lower cerebellar vermis. No cortical malformations have been observed

control vector vs. RHEBp.S68P: $p < 0.0001$ by Tukey's multiple comparisons test). Notably, overexpression of RHEBp.P37L had the strongest effect inducing a significantly pronounced increase in soma size compared to RHEB-WT ($p < 0.05$) and RHEBp.S68P ($p < 0.05$).

We next sought to evaluate the relevance of these variants in the development of neuroanatomical phenotypes in a developing zebrafish in vivo model. Toward this, we identified the sole zebrafish *rheb* ortholog (96% similarity, 91% identity). First, we corroborated that the variants identified are not acting through a loss of function mechanism by generating a CRISPR-Cas9 system to introduce deletions. Assessment of head size in mosaic F0 embryos injected with a guideRNA against exon 3 showed microcephaly in two biological replicates, which was opposite to the phenotype observed in the patients (Supplementary

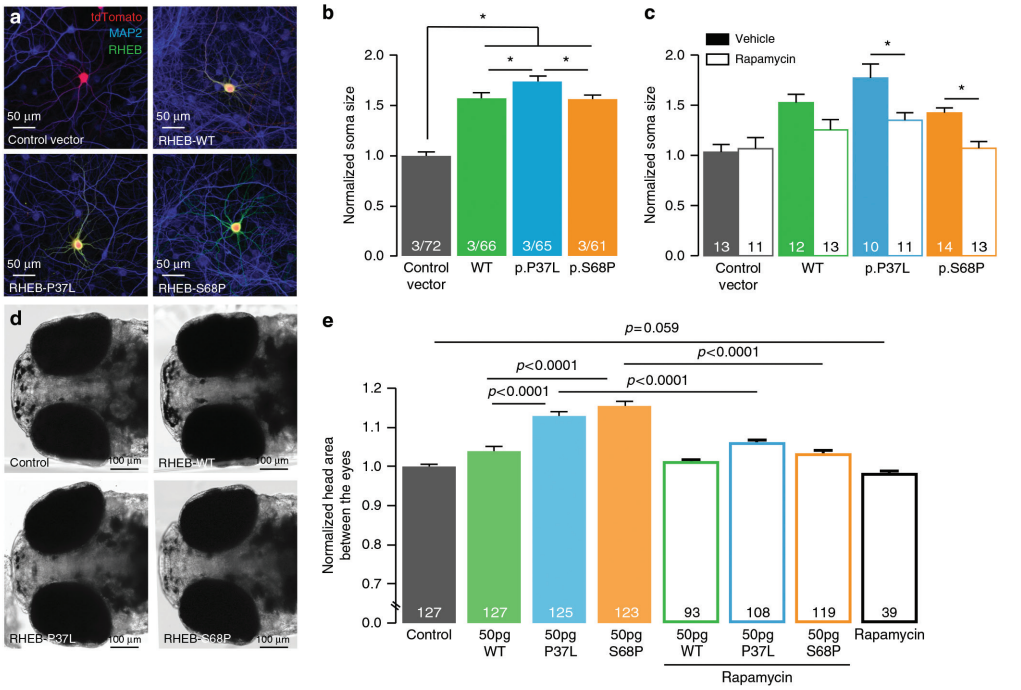

Fig. 3 De novo mutations in *RHEB* increase soma size and headsize, phenotypes that can be rescued by rapamycin. **a** Representative confocal images of hippocampal neurons transfected with control vector, RHEB-WT, RHEBp.P37L or RHEBp.S68P. **b** Summary bar graph of soma size measured for each condition and normalized to the control vector. **c** Summary bar graph of soma size measured with and without rapamycin. Data are presented as mean ± SEM. Numbers depicted in the bar graph in b represent the number of independent cultures/total number of cells analyzed and in c number of cells analysed. Statistical significance was assessed by one-way ANOVA followed by Tukey's post hoc test (*$p < 0.01$). **d** Dorsal view of 5 dpf control and overexpressant zebrafish larvae. For each experiment, embryos were injected with either WT or mutant *RHEB* human mRNA message. The area between the eyes was measured for every embryo, to produce a quantitative score. **e** Bar graph showing the quantification of the headsize phenotype in control embryos and embryos injected with either WT or mutant human *RHEB* with and without rapamycin. The graph represents cumulative plotted experiments across three biological replicas. Statistical analyses were performed by Student's *t*-test

Fig. 2). We next evaluated the effect of the *rheb* alleles on head size under a gain of function and mTOR hyperactivating paradigm, as suggested through our in vitro studies. To test this hypothesis, we injected human WT or mutant *RHEB* mRNA into 1- to 4-cell stage zebrafish embryos. Expression of WT human *RHEB* induced a significant increase in the headsize area of 5 dpf larvae ($p = 0.0013$). Overexpression of either *RHEB*p.P37L or p.S68P, also resulted in significantly increased headsize, reminiscent of the megalencephaly seen in our patients ($p < 0.0001$ for either mutant allele when compared to WT *RHEB*; Fig. 3d, e). This finding was reproducible across three independent biological replicates.

Rapamycin rescues neuronal soma and head size defects. Antagonists of the mTOR pathway, such as rapamycin, can ameliorate some of neurological deficits associated with mTOR hyperactivity (Talos *et al*., 2012; Franz *et al*., 2013; Wheless *et al*., 2015; French *et al*., 2016; Overwater *et al*., 2016). To evaluate whether this is true for the *RHEB* activating mutations described here, we treated the neurons with 20 nM rapamycin or vehicle 1 day after transfection for 3 days and assessed neuronal soma size. We found that while the soma size of RHEB-WT overexpressing neurons nominally decreased, a statistically significant reduction

of neuronal soma size was observed for both RHEBp.P37L and RHEBp.S68P and a trend in the same direction was seen for RHEB-WT (Fig. 3c, two- way ANOVA, effect of treatment $p < 0.0001$, $F(1,89) = 16.29$; RHEBp.P37L vehicle vs. RHEBp.P37L Rapamycin $p < 0.01$; RHEBp.S68P vehicle vs. RHEBp.S68P Rapamycin: $p < 0.05$; RHEB-WT vehicle vs. RHEB-WT Rapamycin: $p = 0.1$; by Bonferroni's multiple comparisons test). Taken together, these data show that overexpression of either wild-type or mutant *RHEB* induces an mTOR-dependent increase in soma size and that this phenotype can be rescued through the administration of the known mTOR antagonist rapamycin. Grounded on the in vitro observations, we next explored the possibility of rapamycin serving as a putative therapeutic agent in vivo. Toward this, we co-injected rapamycin together with WT or mutant *RHEB* mRNA in zebrafish embryos and we compared the embryos' head size at 5 dpf. Rapamycin alone did not induce any appreciable neuroanatomical pathologies, or indeed any other overt morphological phenotype(s) (Fig. 3e). In contrast, rapamycin sufficiently and reproducibly rescued the macrocephalic phenotype induced by both *RHEB*p.P37L and *RHEB*p.S68P, suggesting that suppression of mTOR hyperactivity might present a therapeutic target for disease ammelioration (Fig. 3e).

RHEB mutations affect neuronal migration and induce seizures. Previous studies have shown that mTOR signaling is not only involved in cell morphology and growth, but also plays a role in neuronal migration. Increased mTOR activity in vivo, induced either by overexpression of a constitutively active RHEB or by inactivating mutations in the *Tsc1* or *Tsc2* genes, two negative regulators of *RHEB*, causes neuronal migration defects (Feliciano *et al*., 2011; Zhou *et al*., 2011; Lafourcade *et al*., 2013; Baek *et al*., 2015; Moon *et al*., 2015; Lin *et al*., 2016). We performed *in utero* electroporation at E14.5 to induce the in vivo overexpression of RHEB-WT, RHEBp.P37L, and RHEBp.S68P, and tested the effect of the *RHEB* mutations on neuronal migration in the still developing somatosensory cortex of P0 pups (Dehay *et al*., 2007; Molyneaux *et al*., 2007). Although in neuronal cultures overexpression of RHEB-WT and RHEB mutants increased soma size equally, the results obtained in vivo showed notable differences between these proteins. We observed that while cells transfected with the control vector efficiently migrated to the cortical plate (CP), cells transfected with RHEB-WT could be found in all the layers of the cortex (Fig. 4a). Strikingly, the majority of cells transfected with either RHEBp.P37L or RHEBp.S68P remained in the subplate (SP), indicating more severe migration deficits compared to RHEB-WT overexpression (Fig. 4a). At P7, when the cortical layers are more defined, the difference between RHEB-WT and RHEBp.P37L or RHEBp.S68P was even more striking (Fig. 4b). Analysis of the number of tdTomato-positive cells present in the different cortical layers showed a significant difference between the four different conditions (two-way repeated measure ANOVA, effect of interaction: $F(27,180) = 13.73$, $p < 0.0001$), consistent with our previous in vitro and in vivo studies that the mutations in *RHEB* are gain-of-function hyperactivating mutations. Consistent with our findings in primary neuronal cultures, post hoc analysis revealed that the RHEBp.P37L mutation yielded the strongest effects among evaluated conditions (Fig. 4c).

Neuronal migration deficits are often linked with seizures and ID (Guerrini and Parrini, 2010). Additionally, the link between an epileptogenic phenotype and hyperactivity of the mTOR pathway has been established from studies in both human and mice (Cho, 2011; Abs *et al*., 2013; Hsieh *et al*., 2016). Interestingly, knockdown of the *TSC1* gene, a negative regulator of the mTOR pathway, in just a subset of cortical neurons reduces the threshold for seizure induction (Feliciano *et al*., 2011). Careful monitoring of the in utero electroporated mice, revealed that overexpression of RHEB-WT, RHEBp.P37L, and RHEBp.S68P resulted in spontaneous tonic–clonic seizures starting at P20 (Supplementary Movie 1). Seizures

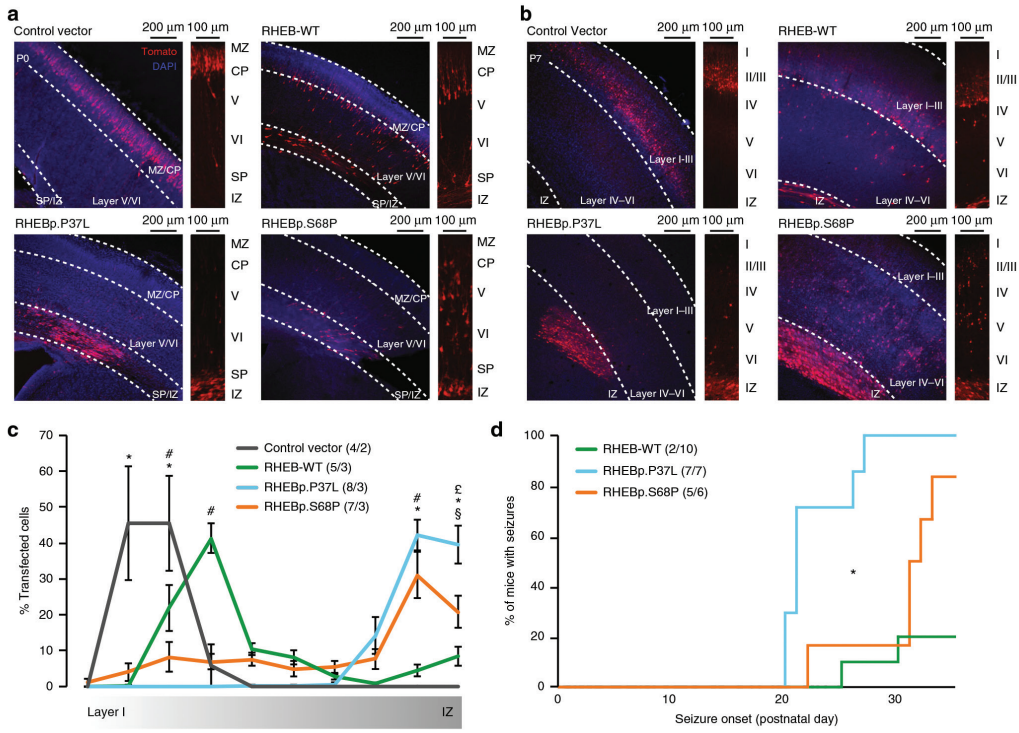

Fig. 4 Overexpression of RHEB mutants in vivo causes deficits in neuronal migration and seizures in mouse. **a, b** Representative images of E14.5 in utero electroporated P0 brains (a) or P7 brains (b), with an enlargement showing the migratory pathway of the transfected cells (tdTomato+) from the intermediate zone (IZ) and subplate (SP) to the more superficial layers of the cortex (CP = cortical plate and MZ = marginal zone). **c** Quantification of the neuronal migration pattern observed in different conditions. Data are presented as mean ± SEM. Statistical significance was assessed by two-way repeated measure ANOVA followed by Bonferroni's post hoc test (for bins 2–4: *indicates significant difference between control vector and the different RHEB conditions ($p < 0.0001$); #indicates significant difference between the RHEB-WT and all other conditions ($p < 0.0001$); for bins 9 and 10: *indicates significant difference between control vector and RHEBp.P37L and RHEBp.S68P; #indicates significant difference between RHEB-WT and RHEBp.P37L and RHEBp.S68P ($p < 0.0001$)); §indicates significant difference between RHEB-WT and RHEBp.P37L ($p < 0.0001$); £indicates significant difference between RHEBp.P37L and RHEBp.S68P ($p < 0.001$). **d** Kaplan–Meier graph representing onset of tonic–clonic seizures in successfully targeted mice. The insert legends of the graph show $N_{pictures}/N_{mice}$ (c) or $N_{seizure}/N_{total}$ (d)

were particularly common in mice expressing mutant RHEB: whereas 20% (2/10) of mice expressing RHEB-WT developed epilepsy, all (7/7) mice expressing RHEBp.P37L and 83% (5/6) of mice expressing RHEBp.S68P developed spontaneous seizures (Fig. 4d). Consistent with our findings from primary neuronal cultures and neuronal migration following in utero electroporation, the RHEBp.P37L allele was shown to have the strongest effect, as the mice expressing this allele also showed a significantly earlier onset of seizures (log-rank (Mantel–Cox) $p < 0.01$ compared to RHEBp.S68P; Fig. 4d). Taken together, our in vivo results further corroborate the conclusion that the missense mutations in *RHEB* act as dominant activating mutations.

DISCUSSION

Here we studied the contribution of mTOR-related genes to ID and brain overgrowth in 826 ID patients unselected for any other phenotypic features and found 17 germline de novo

mutations in genes related to mTOR, providing a possible genetic diagnosis for 2.1% of our cohort. We show that genes encoding components of the mTOR pathway, contribute to rare and common alleles that impact brain volume and provide insight into neurodevelopmental processes mediated through mTOR hyperactivity and outlook to potential treatment options for a subset of patients with ID.

A significant fraction of patients harboring a *de novo* mutation in mTOR-related genes was observed to be macrocephalic. The link between mTOR mutations and ID and/or head size differences has already been established through numerous studies that identified genes such as *AKT3*, *PIK3CA*, *PPP2R5D*, and recently *MTOR* itself (Lee *et al*., 2012; Riviere *et al*., 2012; Houge *et al*., 2015; Mirzaa *et al*., 2016). In fact, from the 23 genes previously reported to cause ID among our gene-set of 101 mTOR-related genes, most (18/23, 78%) have been associated in the literature with macrocephaly or relative macrocephaly. Our study significantly extends these findings: of the 35 patients with macrocephaly in the complete cohort, 9 patients (26%) harbored a de novo mutation in mTOR-related genes. As such, genes in this pathway should be carefully evaluated in patients with ID and macrocephaly.

Motivated by the high frequency of brain overgrowth in previous reports of mTOR-related syndromes, and in patients with mutations in mTOR-related genes in our cohort, we reasoned that the highly penetrant activating alleles that we identified de novo might represent only a fraction of alleles associated with severe neurocognitive disorders, and that more common and less penetrant alleles might be associated with head and brain growth in the general population. Indeed, a combined analysis of common variants of all 96 autosomal genes in the mTOR-related gene-set showed significant association with ICV in two large imaging genetics samples from the CHARGE and ENIGMA consortia, confirming our initial hypothesis. Interestingly, the PI3K-AKT-activation pathway (35 genes from the reactome gene-set) was recently shown to be among the most strongly associated pathways for ICV in an enrichment analysis testing 671 Reactome gene-sets using the same cohorts (Adams *et al*., 2016). Our analyses support and expand this conclusion by testing a different, carefully selected gene-set (only 15 out of 96 genes overlapping). Taken together, our data support a model by which mTOR-related genes, including the newly discovered ID gene *RHEB*, contribute to variation in brain growth, through common and rare genetic variants, in health and disease. Our observations corroborate, how rare disorders can inform biological mechanisms underlying common traits in the general population.

There is ongoing debate on the precise genetic composition of gene-sets. Gene-set databases, such as KEGG (query for *MTOR:* http://www.kegg.jp/kegg-bin/ highlight_pathway?scale=1.0&map=map04150&keyword=MTOR), Ingenuity (http://www.ingenuity.com/), and others, all differ in their coverage of specific biological pathways and their functional annotations. In line with this observation, the number of genes mapped to pathways may also vary greatly across the databases (Pers *et al*., 2016). For mTOR-related gene-sets, inclusion in databases is incomplete, with key proteins and protein complexes such as *RAC1*, *RAG*, *MEK*, and *PP2A* missing. For this reason, we used three authoritative reviews on mTOR signaling describing both upstream and downstream interactors of mTOR and then used additional evidence from the literature to subdivide various protein complexes into their constituent proteins and genes. Therefore, our selection of 101 mTOR-related genes might be incomplete and additional genes are likely to be involved in mTOR signaling. For this reason and because of limitation of our methods to detect reliably somatic mosaicism, a mechanism thought to be a significant contributor to mutation burden in this pathway (Lee *et al*., 2012; Riviere *et al*., 2012; Mirzaa *et al*., 2016), we postulate that the diagnostic rate within our cohort (2.1%) might represent the lower bound of the estimate.

In this study, we identified de novo mutations in both known ID genes (*PIK3R1*, *PIK3R2*, *RAF1*, *PPP2R5D*, *MTOR*) and novel candidate ID genes (*RHEB*, *RAC1*, *PPP2R5E*, *PPP2CA*, *ERK1*). For the most frequently mutated gene, *RHEB*, we show that hyperactivating mutations cause an ID syndrome with brain overgrowth and epilepsy. The finding that these mutations are hyperactivating, is in line with the observation that loss of RHEB activity does not result in overt neurological phenotypes in *Rheb* mutant mice (Goorden *et al*., 2015). Several mechanisms, such as increased proliferation, increased soma size and reduced apoptosis are known to have a role in the development of megalencephaly (Sun and Hevner, 2014). We observed a significant increase in soma size upon overexpressing WT and mutant RHEB alleles in vitro. Since RHEB is the canonical activator of mTOR, this finding is consistent with other reports that have highlighted mTOR as a main regulator of cell size (Tavazoie *et al*., 2005; Kwon *et al*., 2006; Meikle *et al*., 2008; Lin *et al*., 2016). In vivo, we postulate that the increased soma size might represent one of the mechanisms through which macrocephaly occurs, as the zebrafish embryos injected with mutant *RHEB* were phenotypically concordant with the human patients. Further dissecting the pathomechanism(s) underlying *RHEB*-associated ID, we showed severe neuronal migration defects in mouse embryos electroporated with mutant *RHEB* and an increased incidence of epileptogenic activity postnatally. These findings are reminiscent to what has been observed for mutations of *MTOR* itself. Constitutive activation of mTORC1 causes enlarged neuronal somata in rodent neurons, and focal cortical expression of *MTOR* mutations has been reported to disrupt neuronal migration and to cause spontaneous seizures by in utero electroporation in mice (Lim *et al*., 2015; Mirzaa *et al*., 2016; Hanai *et al*., 2017). This observation shows that activating mutations in different genes of the mTORC1 branch of the mTOR pathway act through convergent mechanisms and have similar phenotypic outcomes.

Based on these observations, we reasoned that patients with activating *RHEB* changes might be able to benefit from therapies that result in a reduction of mTOR activity, such as rapamycin. Indeed, we here showed that suppression of mTOR levels through the administration of the mTOR antagonist rapamycin can significantly and reproducibly prevent both the neuronal soma size phenotype in vitro and the macrocephalic phenotype in vivo. Recent studies have reported successful implementation of mTOR inhibitor treatment in individuals with TSC-associated epilepsy and brain tumors (Franz *et al*., 2013; French *et al*., 2016; Overwater *et al*., 2016). In a conceptually similar paradigm, fibroblasts from a patient with an mTOR activating *PIK3CA* change, were treated successfully with the PI3K inhibitors wortmannin or LY294002, which abrogated the overactivation of the pathway (Loconte *et al*., 2015). It is premature to advocate the use of rapamycin in patients with ID and mutations in all mTOR-related genes, not least because of the potentially adverse effects induced by prolonged exposure to this agent (Fang *et al*., 2013). However, we speculate that targeted administration of mTOR inhibitors (rapamycin, wortmannin, everolimus as well as currently emerging second-generation drugs), perhaps during critical postnatal neurodevelopmental windows, might be of significant benefit to patients. In that context, rapid molecular diagnosis in both known ID genes and candidate ID genes, would be a critical component of the treatment decision process.

In conclusion, our data show that a large number of mTOR-related genes together modulate human brain volume in the population. Severe disruption of such mTOR-related genes can cause intellectual disability and brain overgrowth, most likely through mTOR hyperactivation.

SUPPLEMENTARY INFORMATION

Supplementary Figures

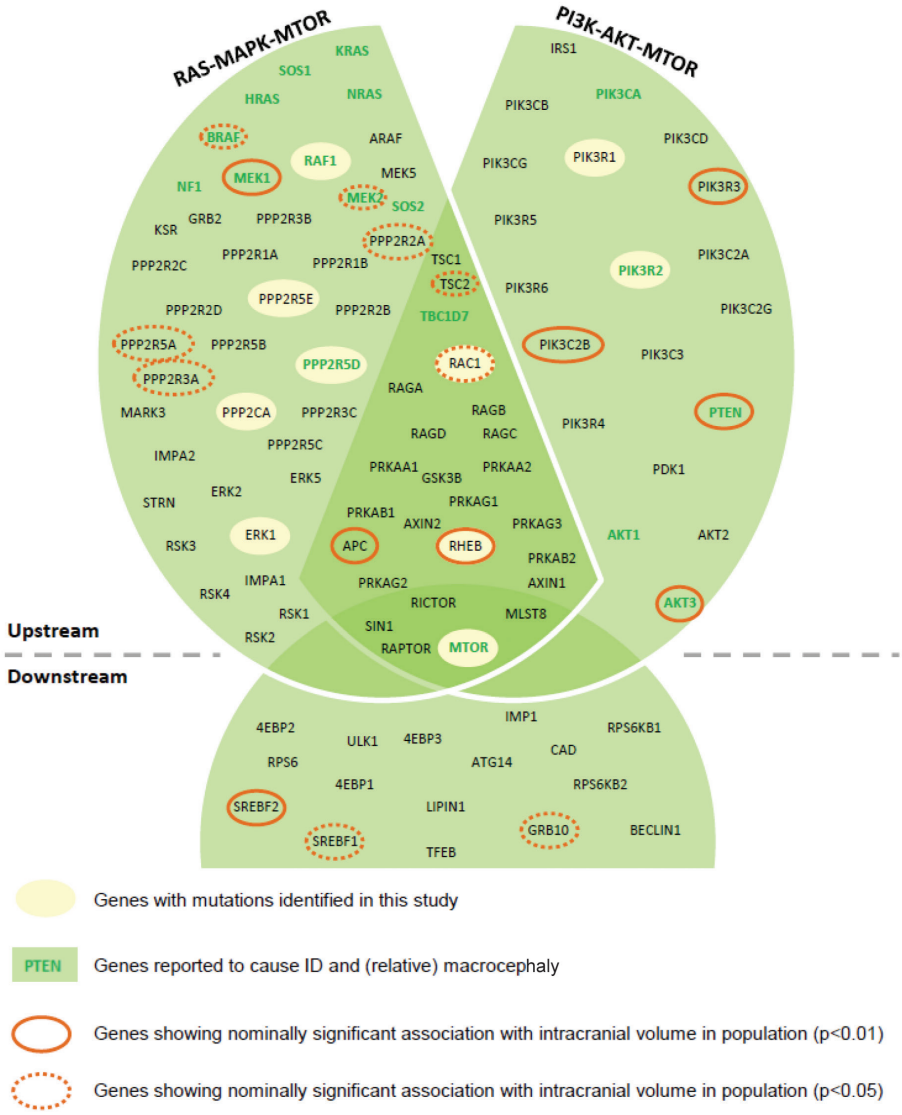

Supplementary Figure 1 Schematic overview of MTOR-related genes showing nominally significant association with intracranial volume in population. Genes (n=101) were included in our MTOR-related gene- set based on three different authoritative publications. Both proteins acting upstream of MTOR and proteins acting downstream of MTOR were included. Additionally, we subdivided the total set in two subsets: the RAS-MAPK- MTOR subset and the PI3K-AKT-MTOR subset. In both subsets, downstream genes are included as well. Genes in which we identified *de novo* mutation in this study are marked with a yellow ellipse and genes previously reported to cause ID and (relative) macrocephaly are shown in bolt and dark green. Genes with nominally significant association with ICV in population (n=18) are marked with a bold, orange eclipse (p<0.01) or striped, orange eclipse (p<0.05).

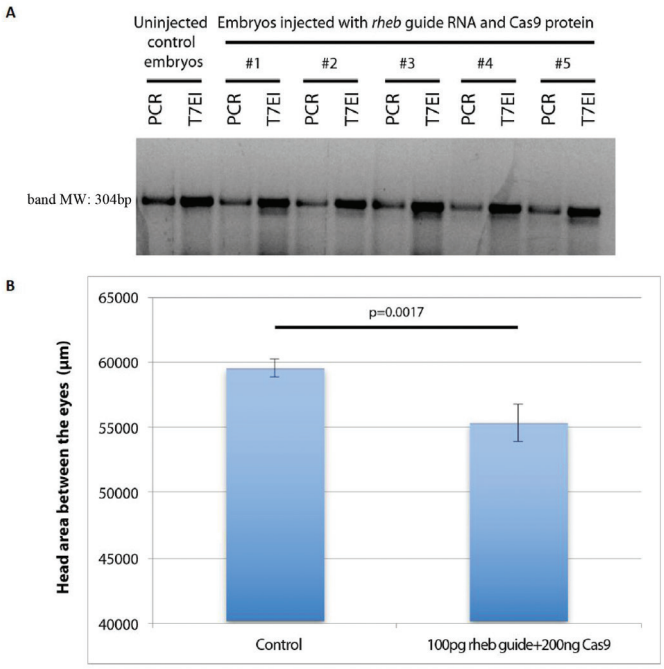

Supplementary Figure 2 Evidence for the efficiency of the CRISPR reagent used to suppress the endogenous expression of *rheb* in developing zebrafish embryos. (**A**) Gel image showing the efficiency of the *rheb* guide RNA following T7 endonuclease assay evaluation (band MW: 304bp). The first two lanes show control amplicons from the locus flanking the targeted sequence, with no aberrations observed. In the embryos injected with *rheb* guide RNA and Cas9 protein, aberrations are evident for embryos #1 - #5, showing that the guide is efficiently introducing sequence aberrations in all injected embryos. PCR fragments from 4 *rheb* embyos with a positive T7 assay were cloned into the pCR4/TOPO TA cloning vector (Life technologies), and 40 clonies from each cloned embryo were Sanger sequenced. Sequence aberrations were observed in ~75% of the evaluated *rheb* clones. (**B**) Bar graph showing the quantification of the headsize phenotype in control embryos and larvae injected with *rheb* guide RNA and Cas9. Statistical analyses were performed by Student`s t- test.

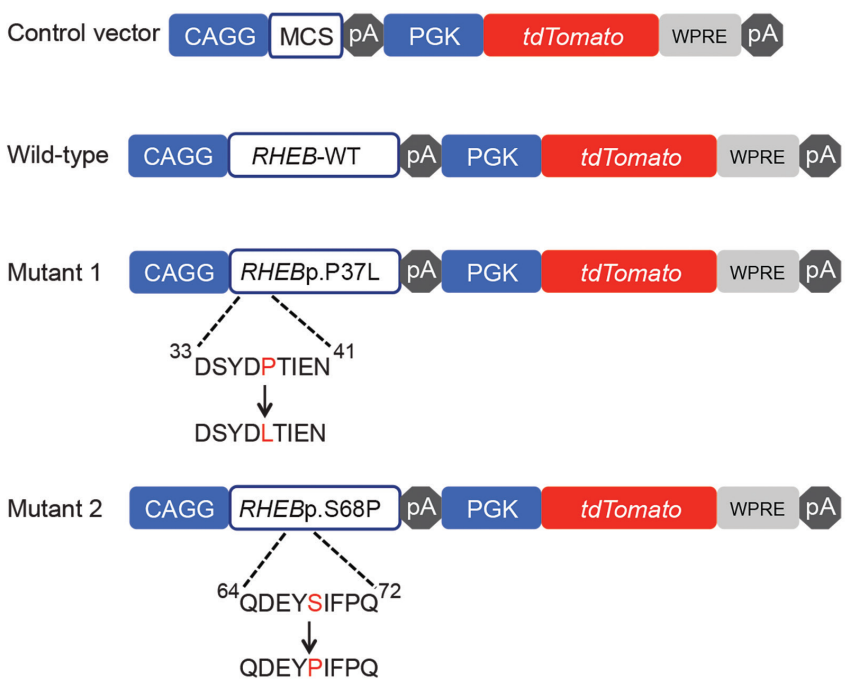

Supplementary Figure 3 Schematic representation of the dual-promotor expression vector with the different RHEB constructs. Schematic representation of the control vector consisting of a *CAGG* promoter followed by a multiple cloning site (MCS) to insert genes of interest. The *tdTomato* gene is expressed under the *PGK* promoter, to allow for independent expression of both the gene of interest and *tdTomato*.

Supplementary Tables

Supplementary Table 1: Statistical enrichment analysis of de novo mutations in MTOR-related genes

Gene name	Expected gene-specific mutation rat	Number functional DNMs	Functional p-value	Bonferroni corrected functional p-value
AKT1	2.21E-05	0	1	1
AKT2	2.09E-05	0	1	1
AKT3	1.46E-05	0	1	1
APC	8.18E-05	0	1	1
ARAF	2.51E-05	0	1	1
ATG14	1.91E-05	0	1	1
AXIN1	3.47E-05	0	1	1
AXIN2	3.35E-05	0	1	1
BECN1	1.52E-05	0	1	1
BRAF	2.31E-05	0	1	1
CAD	8.79E-05	0	1	1
EIF4EBP1	2.83E-06	0	1	1
EIF4EBP2	5.17E-06	0	1	1
EIF4EBP3	2.39E-06	0	1	1
GRB10	1.89E-05	0	1	1
GRB2	8.44E-06	0	1	1
GSK3B	1.48E-05	0	1	1
HRAS	7.87E-06	0	1	1
IMMP1L	5.23E-06	0	1	1
IMPA1	8.26E-06	0	1	1
IMPA2	1.12E-05	0	1	1
KRAS	5.20E-06	0	1	1
KSR1	3.09E-05	0	1	1
LPIN1	3.12E-05	0	1	1
MAP2K1	1.20E-05	0	1	1
MAP2K2	1.43E-05	0	1	1
MAP2K5	1.32E-05	0	1	1
MAPK1	9.81E-06	0	1	1
MAPK3	1.48E-05	1	0.024153414	1
MAPK7	3.01E-05	0	1	1
MAPKAP1	1.84E-05	0	1	1
MARK3	2.65E-05	0	1	1
MLST8	1.54E-05	0	1	1
MTOR	9.24E-05	1	0.141527932	1
NF1	8.54E-05	0	1	1
NRAS	5.78E-06	0	1	1
PDK1	1.40E-05	0	1	1

PIK3C2A	4.81E-05	0	1	1
PIK3C2B	6.00E-05	0	1	1
PIK3C2G	3.75E-05	0	1	1
PIK3C3	2.77E-05	0	1	1
PIK3CA	3.27E-05	0	1	1
PIK3CB	3.27E-05	0	1	1
PIK3CD	4.42E-05	0	1	1
PIK3CG	4.05E-05	0	1	1
PIK3R1	2.39E-05	2	0.000758647	0.076623383
PIK3R2	2.48E-05	1	0.040082839	1
PIK3R3	1.53E-05	0	1	1
PIK3R4	4.25E-05	0	1	1
PIK3R5	2.07E-05	0	1	1
PIK3R6	0.001017849	0	1	1
PPP2CA	1.12E-05	2	0.000167888	0.016956732
PPP2R1A	2.18E-05	0	1	1
PPP2R1B	2.03E-05	0	1	1
PPP2R2A	1.31E-05	0	1	1
PPP2R2B	1.65E-05	0	1	1
PPP2R2C	1.92E-05	0	1	1
PPP2R2D	1.58E-05	0	1	1
PPP2R3A	3.17E-05	0	1	1
PPP2R3B	2.22E-05	0	1	1
PPP2R3C	1.30E-05	0	1	1
PPP2R5A	1.49E-05	0	1	1
PPP2R5B	1.73E-05	0	1	1
PPP2R5C	1.67E-05	0	1	1
PPP2R5D	2.20E-05	3	7.75E-06	0.000783174
PPP2R5E	1.47E-05	1	0.023980694	1
PRKAA1	1.76E-05	0	1	1
PRKAA2	1.71E-05	0	1	1
PRKAB1	1.08E-05	0	1	1
PRKAB2	7.86E-06	0	1	1
PRKAG1	9.64E-06	0	1	1
PRKAG2	2.18E-05	0	1	1
PRKAG3	1.72E-05	0	1	1
PTEN	1.20E-05	0	1	1
RAC1	7.48E-06	2	7.58E-05	0.007657126
RAF1	2.27E-05	1	0.036735716	1
RHEB	5.74E-06	2	4.47E-05	0.004514218
RICTOR	5.23E-05	0	1	1

RPS6	1.03E-05	0	1	1
RPS6KA1	2.70E-05	0	1	1
RPS6KA2	3.07E-05	0	1	1
RPS6KA3	2.22E-05	0	1	1
RPS6KA6	2.23E-05	0	1	1
RPS6KB1	1.72E-05	0	1	1
RPS6KB2	2.08E-05	0	1	1
RPTOR	5.93E-05	0	1	1
RRAGA	1.36E-05	0	1	1
RRAGB	1.32E-05	0	1	1
RRAGC	9.12E-06	0	1	1
RRAGD	1.03E-05	0	1	1
SOS1	4.05E-05	0	1	1
SOS2	4.08E-05	0	1	1
SREBF1	4.06E-05	0	1	1
SREBF2	4.03E-05	0	1	1
STRN	2.22E-05	0	1	1
TBC1D7	1.05E-05	0	1	1
TFEB	1.70E-05	0	1	1
TSC1	3.88E-05	0	1	1
TSC2	7.36E-05	0	1	1
ULK1	4.89E-05	0	1	1
IRS1	5.31E-05	0	1	1
mTOR pathway	**3.51E-03**	**16**	**0.000350082**	

Supplementary Table 2: P-values of MTOR-related genes with recurrent *de novo* missense mutations

Gene name	Transcript	Coding size	Mutation location cDNA	P-value clustering analysis
MTOR	NM_004958	7650	4375, 4555, 5395	0.060619394
PPP2R5D	NM_006245	1809	157, 592, 592, 592, 592, 592, 592, 592, 592, 592, 592, 598, 602, 619, 752, 1258	1,00E-01
RHEB	NM_005614	555	110, 202	0.304626954
PIK3R1	NM_181523	2175	1359, 1614, 1692	0.0900091
RAC1	NM_018890	636	53, 116, 151, 190, 218	0.04898951

Supplementary Table 3: Known MTOR-related ID genes and association with aberrant brain size

Gene	Known ID gene?	Known aberrant brain size?	Reference
PIK3CA	Yes	(Hemi) megalencephaly	Riviere J.B., Mirzaa G.M., O'Roak B.J. et al (2012), Nature Genet. 44: 934-940
PIK3R1	Yes	Low-normal; Microcephaly	Thauvin-Robinet C., Auclair M., Duplomb L. et al (2013), Am. J. Hum. Genet. 93: 141-149
PIK3R2	Yes	Megalencephaly	Riviere J.B., Mirzaa G.M., O'Roak B.J. et al (2012), Nature Genet. 44: 934-940
PTEN	Yes	Megalencephaly	Liaw, D., Marsh, D. J., Li, J. et al (1997), Nature Genet. 16: 64-67
AKT1	Yes	Megalencephaly	Orloff M. S., He X., Peterson C. et al (2013), Am. J. Hum. Genet. 92: 76-80
AKT3	Yes	(Hemi) megalencephaly	Riviere J.B., Mirzaa G.M., O'Roak B.J. et al (2012), Nature Genet. 44: 934-940
TSC1	Yes	Normal	van Slegtenhorst M., de Hoogt R., Hermans C. et al (1997), Science 277: 805-808
TSC2	Yes	Normal	Kumar A., Wolpert C., Kandt R. S. et al (1995), Hum. Molec. Genet. 4: 1471-1472
TBC1D7	Yes	Megalencephaly	Capo-Chichi J.-M., Tcherkezian J., Hamdan F. F. (2013), J. Med. Genet. 50: 740-744
MTOR	Yes	Megalencephaly	Smith L. D., Saunders C. J., Dinwiddie D. L et al (2013), J. Genomes Exomes 2: 63-72
SOS1	Yes	Megalencephaly	Roberts A. E., Araki T., Swanson K. D. et al (2007), Nature Genet. 39: 70-74
SOS2	Yes	Relative macrocephaly	Yamamoto G. L., Aguena M., Gos M. et al (2015), J. Med. Genet. 52: 413-421
KRAS	Yes	Relative macrocephaly	Schubbert S., Zenker M., Rowe S. L. et al (2006), Nature Genet. 38: 331-336
HRAS	Yes	Megalencephaly	Aoki Y., Niihori T., Kawame H. et al (2005), Nature Genet. 37: 1038-1040
NRAS	Yes	Megalencephaly	Cirstea I. C., Kutsche K., Dvorsky R. et al (2010), Nature. Genet. 42: 27-29
B-RAF	Yes	Relative macrocephaly	Sarkozy A., Carta C., Moretti S. et al (2009), Hum. Mutat. 30: 695-702
RAF-1	Yes	Relative macrocephaly	Pandit B., Sarkozy A., Pennacchio L. A et al (2007), Nature Genet. 39: 1007-1012
NF1	Yes	Megalencephaly	Upadhyaya M., Shen M., Cherryson A. et al (1992), Hum. Molec. Genet. 1: 735-740
MEK-1 (MAP2K1/MKK1)	Yes	Relative macrocephaly	Rodriguez-Viciana P., Tetsu O., Tidyman W. E. et al (2006), Science 311: 1287-1290
MEK-2 (MAP2K2/MKK2)	Yes	Relative macrocephaly	Rodriguez-Viciana P., Tetsu O., Tidyman W. E. et al (2006), Science 311: 1287-1290
PPP2R1A (PR65a)	Yes	Microcephaly	Houge G., Haesen D., Vissers L. E. L. M. et al (2015), J. Clin. Invest. 125: 3051-3062
PPP2R5D (PR61D)	Yes	Megalencephaly; Microcephaly	Houge G., Haesen D., Vissers L. E. L. M. et al (2015), J. Clin. Invest. 125: 3051-3062
RSK-2 (RPS6KA3)	Yes	Microcephaly	Trivier E., De Cesare D., Jacquot S. et al (1996), Nature 384: 567-570

Supplementary Table 4: Subdivision of genes in two major branches of the MTOR pathway

RAS-MAPK-MTOR branch	PI3K-AKT-MTOR branch
3845	3667
3265	5290
4893	5291
369	5293
673	5294
5894	5295
4763	5296
5604	8503
5605	23533
5607	146850
8844	5286
5518	5287
5519	5288
5520	5289
5521	30849
5522	5728
55844	5163
5525	207
5526	208
5527	10000
5528	7248
5529	7249
5523	51256
28227	6009
55012	64223
6801	2475
5515	57521
4140	10670
3612	10325
3613	64121
5595	58528
5594	324
5598	8312
6195	8313
6197	2932
6196	5562
27330	5564
7248	5571
7249	5563
51256	5565
6009	51422
64223	53632
2475	5879
57521	79109
10670	253260
10325	8408
64121	6198
58528	6199
22863	1978
196294	1979
8312	8637
8313	2887
2932	6194

5562	23175
5564	6720
5571	6721
5563	790
5565	7942
51422	8678
53632	22863
5879	196294
79109	
253260	
8408	
6198	
6199	
1978	
1979	
8637	
2887	
6194	
23175	
6720	
6721	
790	
7942	
8678	
2885	
6654	
6655	
324	

Supplementary Table 5: Gene-based results of Reactome_PI3K_AKT_activation gene-set using the MAGMA software

GENE	Genename	CHR	START	STOP	NSNPS	EFF_SIZE	STAT	P
2309	FOXO3	6	108781026	1,09E+08	746	298	5,9392	1,43E-09
10000	AKT3	1	243551535	2,44E+08	861	320	4,0829	2,22E-05
387	RHOA	3	49296578	49549526	382	159	3,6811	0,000116
2931	GSK3A	19	42634338	42846736	243	87	2,7503	0,002977
5728	PTEN	10	89523195	89828532	681	320	2,7199	0,003265
5295	PIK3R1	5	67411584	67697649	1017	432	2,6298	0,004271
1147	CHUK	10	101848124	1,02E+08	621	219	2,6184	0,004417
3164	NR4A1	12	52316616	52553291	675	342	2,2467	0,012331
117145	THEM4	1	151743342	1,52E+08	620	216	2,1803	0,014617
7249	TSC2	16	1997990	2238713	604	319	1,7776	0,037731
2308	FOXO1	13	41029801	41340734	822	350	1,7677	0,038554
6199	RPS6KB2	11	67095935	67302879	309	139	1,5657	0,058706
1385	CREB1	2	208294616	2,09E+08	683	315	1,4066	0,07977
253260	RICTOR	5	38838022	39174501	878	301	1,4034	0,080253
64223	MLST8	16	2155178	2359418	343	193	1,3807	0,083687
1026	CDKN1A	6	36544237	36755116	893	366	1,3584	0,087167
4193	MDM2	12	69101971	69339212	657	313	1,2487	0,10589
79109	MAPKAP1	9	128099673	1,29E+08	1043	438	1,1962	0,11581
5291	PIK3CB	3	138274231	1,39E+08	468	167	1,0603	0,1445
4914	NTRK1	1	156685542	1,57E+08	606	238	1,045	0,14802
1027	CDKN1B	12	12770302	12975305	515	263	0,87281	0,19138
8660	IRS2	13	110306184	1,11E+08	857	410	0,72505	0,23421
207	AKT1	14	105135686	1,05E+08	676	306	0,70967	0,23895
5170	PDPK1	16	2487970	2753189	235	125	0,17362	0,43108
5296	PIK3R2	19	18164016	18381343	739	295	0,050073	0,48003
57761	TRIB3	20	261308	478203	729	417	0,043647	0,48259
4803	NGF	1	115728537	1,16E+08	977	370	-0,00436	0,50174

842	CASP9	1	15718769	15951285	753	242	-0,02734	0,51091
84335	AKT1S1	19	50272296	50480644	596	279	-0,03236	0,51291
3667	IRS1	2	227496033	2,28E+08	593	219	-0,17806	0,57066
23239	PHLPP1	18	60282672	60747666	1147	514	-0,23892	0,59442
2475	MTOR	1	11066588	11422608	776	172	-0,35988	0,64053
572	BAD	11	63937300	64152176	451	205	-0,42081	0,66305
208	AKT2	19	40636224	40891265	651	255	-0,88001	0,81057
5290	PIK3CA	3	178766311	1,79E+08	832	338	-1,5135	0,93492

Grey gene was also included in the expert-curated mTOR gene-set

Supplementary Table 6: Gene-based results of 96 genes belonging to the MTOR gene-set using the MAGMA software

GENE	GENE_NAME	CHR	START	STOP	NSNPS	EFF_SIZE	STAT	P
10000	AKT3	1	2,44E+08	2,44E+08	861	320	4,0829	2,22E-05
324	APC	5	1,12E+08	1,12E+08	1195	346	3,3416	0,000417
5594	MAPK1	22	22013946	22321970	911	385	3,157	0,000797
6721	SREBF2	22	42129106	42402375	732	291	2,9106	0,001804
8503	PIK3R3	1	46405812	46698708	537	169	2,7336	0,003132
5728	PTEN	10	89523195	89828532	681	320	2,7199	0,003265
6009	RHEB	7	1,51E+08	1,51E+08	770	362	2,6431	0,004107
5295	PIK3R1	5	67411584	67697649	1017	432	2,6298	0,004271
5287	PIK3C2B	1	2,04E+08	2,05E+08	727	277	2,5197	0,005872
673	BRAF	7	1,4E+08	1,41E+08	724	222	2,161	0,015346
2887	GRB10	7	50557760	50961159	1462	504	2,0816	0,018688
5879	RAC1	7	6314126	6543598	956	425	2,0013	0,022682
5523	PPP2R3A	3	1,36E+08	1,36E+08	681	294	1,9849	0,023575
5520	PPP2R2A	8	26049007	26330196	1052	490	1,8433	0,032643
5605	MAP2K2	19	3990319	4224126	642	313	1,7979	0,036094
7249	TSC2	16	1997990	2238713	604	319	1,7776	0,037731
5525	PPP2R5A	1	2,12E+08	2,13E+08	774	307	1,7725	0,038157
6720	SREBF1	17	17614663	17840325	338	162	1,6969	0,044858
23175	LPIN1	2	11786740	12067535	996	508	1,5968	0,05516
6199	RPS6KB2	11	67095935	67302879	309	139	1,5657	0,058706
4140	MARK3	14	1,04E+08	1,04E+08	884	295	1,4962	0,067301
253260	RICTOR	5	38838022	39174501	878	301	1,4034	0,080253
64223	MLST8	16	2155178	2359418	343	193	1,3807	0,083687
8312	AXIN1	16	237440	502676	882	482	1,3013	0,096576
79109	MAPKAP1	9	1,28E+08	1,29E+08	1043	438	1,1962	0,11581
58528	RRAGD	6	89974335	90221995	709	374	1,1949	0,11606
6198	RPS6KB1	17	57870443	58127787	308	121	1,0673	0,14291

5291	PIK3CB	3	1,38E+08	1,39E+08	468	167	1,0603	0,1445
8313	AXIN2	17	63424681	63657740	672	301	0,99861	0,15899
5526	PPP2R5B	11	64592143	64801950	462	199	0,99169	0,16067
51422	PRKAG2	7	1,51E+08	1,52E+08	1829	868	0,94281	0,17289
8408	ULK1	12	1,32E+08	1,33E+08	630	320	0,92147	0,1784
4763	NF1	17	29321945	29804695	698	259	0,92131	0,17844
30849	PIK3R4	3	1,3E+08	1,31E+08	536	167	0,84709	0,19847
57521	RPTOR	17	78418625	79040173	2580	1004	0,83039	0,20316
5518	PPP2R1A	19	52593055	52829678	963	361	0,7996	0,21197
1979	EIF4EBP2	10	72063861	72288374	736	335	0,76398	0,22244
6801	STRN	2	36964841	37293615	976	447	0,76315	0,22269
10670	RRAGA	9	18949372	19151023	906	322	0,74297	0,22875
207	AKT1	14	1,05E+08	1,05E+08	676	306	0,70967	0,23895
8637	EIF4EBP3	5	1,4E+08	1,4E+08	281	127	0,61756	0,26843
5522	PPP2R2C	4	6222305	6665327	1684	782	0,49929	0,30879
790	CAD	2	27340258	27566654	437	181	0,44216	0,32919
6194	RPS6	9	19276254	19480235	535	261	0,35128	0,36269
5163	PDK1	2	1,73E+08	1,74E+08	921	277	0,32056	0,37427
5293	PIK3CD	1	9611790	9889172	455	254	0,29966	0,38222
1978	EIF4EBP1	8	37788020	38017883	264	108	0,28672	0,38716
55012	PPP2R3C	14	35454678	35691519	851	286	0,27276	0,39252
4893	NRAS	1	1,15E+08	1,15E+08	504	225	0,26948	0,39378
5563	PRKAA2	1	57010990	57281008	927	332	0,24592	0,40287
5294	PIK3CG	7	1,06E+08	1,07E+08	732	338	0,24467	0,40336
6654	SOS1	2	39108690	39447604	727	296	0,23446	0,40731
7942	TFEB	6	41551716	41803997	745	379	0,2306	0,40881
3845	KRAS	12	25258180	25503854	818	253	0,20824	0,41752
64121	RRAGC	1	39205005	39425340	654	305	0,20159	0,42012
53632	PRKAG3	2	2,2E+08	2,2E+08	320	95	0,15254	0,43938
5515	PPP2CA	5	1,33E+08	1,34E+08	451	162	0,12783	0,44914

5564	PRKAB1	12	1,2E+08	1,2E+08	512	197	0,077046	0,46929
5286	PIK3C2A	11	17008122	17291354	705	240	0,070221	0,47201
5296	PIK3R2	19	18164016	18381343	739	295	0,050073	0,48003
5528	PPP2R5D	6	42852330	43080080	600	232	0,005518	0,4978
8844	KSR1	17	25699036	26050718	1006	363	0,002564	0,49898
5288	PIK3C2G	12	18314474	18901352	2012	675	-0,04873	0,51943
5595	MAPK3	16	30025426	30234630	236	120	-0,14791	0,55879
3667	IRS1	2	2,27E+08	2,28E+08	593	219	-0,17806	0,57066
5607	MAP2K5	15	67735021	68199455	1177	413	-0,20467	0,58109
7248	TSC1	9	1,36E+08	1,36E+08	915	456	-0,31862	0,62499
2475	MTOR	1	11066588	11422608	776	172	-0,35988	0,64053
55844	PPP2R2D	10	1,34E+08	1,34E+08	604	298	-0,41835	0,66215
3612	IMPA1	8	82469151	82698589	789	265	-0,47181	0,68147
2932	GSK3B	3	1,19E+08	1,2E+08	1055	424	-0,49086	0,68824
196294	IMMP1L	11	31353949	31631169	395	163	-0,49886	0,69106
6195	RPS6KA1	1	26756249	27001520	416	205	-0,54542	0,70727
5289	PIK3C3	18	39435199	39761448	718	240	-0,56914	0,71537
5565	PRKAB2	1	1,47E+08	1,47E+08	1027	263	-0,5724	0,71647
6655	SOS2	14	50483846	50798099	922	349	-0,67363	0,74973
8678	BECN1	17	40862150	41076310	218	130	-0,87324	0,80873
208	AKT2	19	40636224	40891265	651	255	-0,88001	0,81057
5562	PRKAA1	5	40659481	40898297	636	258	-0,92259	0,82189
5598	MAPK7	17	19181034	19386857	318	103	-0,95597	0,83046
5604	MAP2K1	15	66579211	66883882	1016	333	-0,96495	0,83271
3613	IMPA2	18	11881427	12130885	1123	425	-1,0587	0,85513
146850	PIK3R6	17	8606055	8870994	770	351	-1,0908	0,86232
23533	PIK3R5	17	8682233	8969024	773	400	-1,1182	0,86826
6196	RPS6KA2	6	1,67E+08	1,67E+08	2152	898	-1,1346	0,87173
5521	PPP2R2B	5	1,46E+08	1,47E+08	1705	598	-1,2241	0,88954
5527	PPP2R5C	14	1,02E+08	1,02E+08	1045	346	-1,2574	0,89569

5519	PPP2R1B	11	1,11E+08	1,12E+08	431	145	-1,3095	0,90482
22863	ATG14	14	55733109	55978576	958	238	-1,4038	0,91981
5529	PPP2R5E	14	63741355	64110079	945	332	-1,4202	0,92223
2885	GRB2	17	73214157	73501790	679	246	-1,5017	0,93342
5290	PIK3CA	3	1,79E+08	1,79E+08	832	338	-1,5135	0,93492
5571	PRKAG1	12	49296055	49512629	365	147	-1,5211	0,93588
51256	TBC1D7	6	13205183	13428787	777	205	-1,5707	0,94188
5894	RAF1	3	12525100	12805700	844	295	-1,5789	0,94282
3265	HRAS	11	432242	635550	857	448	-1,583	0,94329

Grey gene was also included in the Reactome_PI3K_AKT_activation gene-set

Supplementary Table 7: Clinical information of patients with de novo mutations in *RHEB*

Clinical details of individuals with *de novo RHEB* mutations			
	Family 1	*Family 2*	
	Individual 1	**Individual 2**	**Individual 3**
Gender	Female	Male	Female
Age of last visit	3.5 years	29 years	27 years
Ethnicity	Caucasian	Caucasian	Caucasian
Mutations			
cDNA change	c.202T>C	c.110C>T	c.110C>T
Amino acid change	p.Ser68Pro	p.Pro37Leu	p.Pro37Leu
Chromosome position (Hg 19)	Chr7:151174492	Chr7:151188043G>A	Chr7:151188043G>A
Growth			
Height	100.5 cm (-2 SD)	171cm (-2 SD)	151 cm (-3 SD)
Weight (-height)	NR	18 years: 47 kg (-1.5 SD)	17 years: 54 kg (+2 SD)
Head circumference	3.5 years: 53.4 cm (+2.5 SD)	5 years: 56.5 cm (+3 SD)	0.5 years: 50 cm (+3 SD)
		29 years: 60 cm (+1.5 SD)	23 years: 57 cm (+1 SD)
ICD	3,6 cm (+3 SD)	4 cm (+3.5 SD)	3.6 cm (+2 SD)
OCD	8.1 cm (+0.5 SD)	10 cm (+2 SD)	10 cm (+2 SD)
Development			
Intellectual disability	Severe-profound ID	Severe-profound ID	Severe ID
Neurologic			
Epilepsy	+	-	+
Hypotonia	+	+	+
Polyneuropathy		+	-
Spasticity	-	+	+
Behavior			
Autistic features	+	+	+
Sleep disturbances	-	+	-
Skeletal			
Scoliosis/kyphosis	-	+	+
Recurrent hipdislocation	-	+	+
Cardial			
Cardiac abnormality	-	+	-
Brain imaging	*MRI Re-evaluation*	*Ultrasound Report*	*CT*
Megalencephaly	+	+	NR
Dilatation lateral ventricles	+	+	+
Hypoplastic cerebellum	+	+	NR

Abbreviations: NR= Not Reported; SD = Standard Deviation

Supplementary Table 8: Information on sampling and demographics of study populations

			All Subjects					Patients Excluded (Healthy Only)			
Cohort	**Analysis**	**Study Design**	**Ancestry**	**Total N**	**N Females**	**Mean Age (SD)**	**Age Range**	**Total N**	**N Females**	**Mean Age (SD)**	**Age Range**
3C-Dijon (CHARGE)	CHARGE	Population-based	European	1403	882	72.2 (4.1)	65 - 82	-	-	-	-
AddNeuroMed	ENIGMA	Case-control (AD, MCI and health controls)	European	357	204	74.4 (6.4)	53 - 90	114	65	72.8 (6.8)	53 - 88
ADNI	ENIGMA	Case-Control (AD, MCI, healthy control)	European	747	302	75.4 (6.9)	55 - 91	204	93	76.1 (5.0)	60 - 89
ADNI2GO	ENIGMA	Case-Control (AD, MCI, healthy control)	European	362	203	72.8 (7.4)	55 - 91	337	186	72.6 (7.1)	55 - 91
AGES (CHARGE)	CHARGE	Population-based	European	2510	1506	75.95 (5.30)	66 - 95	-	-	-	-
ARIC	CHARGE	Population-based	European	413	253	72.71 (4.33)	62 - 82	-	-	-	-
ASPS (CHARGE)	CHARGE	Population-based	European	172	120	69.8 (6.7)	52 - 84	-	-	-	-
ASPSFam (CHARGE)	CHARGE	Population-based	European	339	205	65.2 (10.5)	38 - 86	-	-	-	-
Betula	ENIGMA	Population-based	European	353	185	62.3 (13.3)	25 - 95	-	-	-	-
BFS	ENIGMA	Population-based	European	220	115	24 (7.9)	15 - 60	-	-	-	-
BIG	ENIGMA	Population-based	European	1300	747	22.9 (3.8)	18 - 41	-	-	-	-
BrainSCALE	ENIGMA	Population-based Twin Study	European	277	147	10.0 (1.3)	9 - 15	-	-	-	-
BRCDECC	ENIGMA	Case-control (MDD and healthy controls)	European	169	105	49.9 (8.6)	26 - 71	79	44	51.3 (7.7)	26 - 66
CHS	CHARGE	Population-	European	648	398	78.89 (4.2)	73 - 95	-	-	-	-

(CHARGE)		based									
EPIGEN	ENIGMA	Epilepsy cases	European	233	138	38.5 (12.7)	14 - 85	Patients-only			
ERF (CHARGE)	CHARGE	Family-based study	European	118	60	64.3 (4.5)	55 - 76	-	-	-	-
FHS (CHARGE)	CHARGE	Population-based	European	938	534	58.47 (8.04)	34 - 85	-	-	-	-
GeneSTAR (CHARGE)	CHARGE	Family-based study	European	441	237	50.9 (10.6)	30 - 74	-	-	-	-
GIG	ENIGMA	Population-based	European	299	179	24.2 (2.4)	19 - 31	-	-	-	-
GSP	ENIGMA	Population-based	European	442	251	21.4 (3.2)	18 - 35	-	-	-	-
HUBIN	ENIGMA	Case-control (SCZ and healthy controls)	European	200	70	41.8 (8.1)	19 - 56	104	35	41.6 (8.9)	19 - 56
IMAGEN	ENIGMA	Population-based	European	1765	895	14.6 (0.4)	13 - 17	-	-	-	-
LBC1936	ENIGMA	Population-based	European	612	289	72.7 (0.7)	71 - 74	-	-	-	-
LLS	CHARGE	Family-based study	European	355	187	65.54 (6.65)	55-90	-	-	-	-
MCIC	ENIGMA	Case-control (SCZ and healthy controls)	European	170	58	34.0 (11.2)	18 - 60	97	40	32.9 (10.9)	18 - 58
MooDS	ENIGMA	Population-based	European	311	164	33.4 (9.8)	18 - 51	-	-	-	-
MPIP	ENIGMA	Case-control (MDD and healthy controls)	European	550	318	48.3 (13.3)	18 - 87	177	105	50.1 (12.3)	23 - 78
NCNG	ENIGMA	Population-based	European	327	223	51.8 (16.7)	19 - 79	327	223	51.8 (16.7)	19 - 79
NESDA	ENIGMA	Case-control (Depression, Anxiety, and healthy controls)	European	231	153	37.8 (10.1)	18 - 57	55	33	41.1 (9.7)	21 - 56
neuroIMAGE	ENIGMA	ADHD cases	European	154	23	17.0 (2.5)	11 - 24	Patients-only			
NTR - Adults	ENIGMA	Population-	European	400	238	29.7 (10.7)	12 - 56	-	-	-	-

		based Twin Study									
OATS	ENIGMA	Population-based Twin study	European	364	238	70.5 (5.1)	65 - 89	-	-	-	-
PAFIP	ENIGMA	Case-control (SCZ and healthy controls)	European	117	45	28.4 (8.1)	16 - 51	14	6	24.5 (6.3)	16 - 42
PROSPER	CHARGE	RCT/Population-based	European	315	150	74.90 (3.18)	70-82	-	-	-	-
QTIM	ENIGMA	Population-based Twin Study	European	845	527	22.5 (3.2)	16 - 30	-	-	-	-
RSI (CHARGE)	CHARGE	Population-based	European	939	544	78.9 (4.9)	69 - 96	-	-	-	-
RSII (CHARGE)	CHARGE	Population-based	European	1077	569	69.4 (6.0)	60 - 97	-	-	-	-
RSIII (CHARGE)	CHARGE	Population-based	European	2397	1333	57.0 (6.3)	45 - 89	-	-	-	-
RSIx (CHARGE)	CHARGE	Population-based	European	432	224	72.82 (7.90)	59-90	-	-	-	-
ROSMAP1	CHARGE	Population-based	European	184	138	83.19 (6.32)	67-98	-	-	-	-
ROSMAP2	CHARGE	Population-based	European	106	83	80.56 (6.88)	60-93	-	-	-	-
SHIP	ENIGMA	Population-based	European	966	507	56.4 (12.6)	31 - 90	-	-	-	-
SHIP-TREND	ENIGMA	Population-based	European	858	477	50.0 (13.5)	21 - 81	-	-	-	-
Sydney MAS	ENIGMA	Population-based	European	543	297	78.4 (4.7)	70 - 90	-	-	-	-
TOP	ENIGMA	Case-control (SCZ, BD, other psychoses, and healthy controls)	European	849	407	34.0 (10.4)	17 - 73	305	145	35.4 (9.9)	18 - 73
UMCU	ENIGMA	Case-control (SCZ and healthy controls)	European	279	73	31.9 (11.7)	17 - 68	117	44	32.8 (12.8)	17 - 65

CHAP	Replication	Population-based	European	261	159	81.02	65-98	-	-	-	-
LIBD	Replication	Case-Control (SCZ, healthy control)	European	481	215	33.2 (10.2)	18 - 61	311	175	32.2 (9.9)	18.7 - 61.2
NIMH-IRP	Replication	Population-based	European	327	213	34.5 (10.3)	18 - 61	90	66	35.1 (10.3)	19 - 59
NOMAS	Replication	Population-based	European	141	69	72.81 (9.11)	50-94	-	-	-	-
SYS	Replication	Family-based study	European Founder population	986	510	15.02 (1.84)	11 - 19	-	-	-	-
TASCOG	Replication	Replication	Cohort	European	340	142	71.9 (7)	-	-	-	-
UCLA_NL_BP	Replication	Case-control (BP and healthy controls)	European	284	150	45.9 (14,3)	19-80	91	49	43.9 (17.1)	19 - 80
WHICAP	Replication	Population-based	European	83	51	81 ± 5	70-92	-	-	-	-
ARIC-Black	Generalization	Population-based	African-American	389	237	71.6 (4.4)	61-83	-	-	-	-
CHAP-Black	Generalization	Population-based	African-American	321	194	78.57	65-97	-	-	-	-
EDIS-SCES	Generalization	Population-based	Chinese	210	107	69.88 (6.27)	60-86	-	-	-	-
EDIS-SiMES	Generalization	Population-based	Malay	201	106	70.56 (6.65)	60-85	-	-	-	-
GOBS	Generalization	Pedigree	Mexican-American	736	456	50.1 (13.3)	26 - 97	-	-	-	-
NOMAS-Black	Generalization	Population-based	African-American	168	104	73.55 (8.79)	50-94	-	-	-	-
NOMAS-Hispanic	Generalization	Population-based	Mexican-American	718	444	68.97 (8.22)	50-98	-	-	-	-
Osaka	Generalization	Case-control (SCZ and healthy controls)	Japanese	545	259	36.1 (12.5)	16 - 71	383	192	36.5 (12.7)	18 - 66
WHICAP-Black	Generalization	Case-control (SCZ and healthy controls)	African-American	60	46	81 ± 6	70-97	-	-	-	-

Supplementary methods

These three paragraphs have been adapted from Adams *et al*., 2016

ENIGMA and CHARGE

Genetics
Genotyping was performed using different commercial arrays across contributing sites. Both samples and variants underwent stringent quality control procedures based on genetic homogeneity, call rate (< 95%), minor allele frequency (MAF < 0.01), and Hardy-Weinberg Equilibrium (HWE $p<1\times10^{-6}$). Variants passing those thresholds were used as input for imputation to the 1000 Genomes reference panel (phase 1, version 3) using validated software packages (MaCH/minimac, IMPUTE2, BEAGLE, GenABLE). Variants that were poorly imputed (R2 < 0.5) or uncommon (MAF < 0.5%) were removed before meta-analysis. Full details on the site- specific genotyping and quality control can be found in Supplementary Table 2 of Adams *et al*., 2016.

Imaging
Magnetic resonance imaging (MRI) was obtained from different scanners with diverse manufacturers, field strengths, and acquisition protocols. Images were used to estimate milliliters of ICV from automated segmentations. Most sites measured ICV for each participant by multiplying the inverse of the determinant of the transformation matrix required to register the subject's MRI scan to a common template by the template volume (1,948,105 mm3), using the FreeSurfer software. Poorly segmented images were removed after visual inspection. Most sites generated histogram plots to identify any outliers, which were defined as individuals with a volume > 3 SD away from the mean. Statistical outliers were only excluded if the segmentations were deemed improper. More site-specific information related to the imaging is available in Supplementary Table 3 of Adams *et al*., 2016.

GWAS
GWAS of ICV were performed for each site separately, controlling for age, sex, and, when applicable, age2, population stratification variables (MDS / principal components), study site (for multi-site studies only), diagnosis (for case-control studies only). Studies of unrelated individuals performed a linear regression analyses whereas studies of related individuals (ASPSFam, BrainSCALE, ERF, GeneSTAR, GOBS, NeuroIMAGE, NTR-Adults, OATS, QTIM, SYS) used linear mixed models to account for familial relationships. Summary statistics, including effect estimates of the genetic variant with ICV under an additive model, were used to perform a fixed-effects sample size-weighted meta-analysis using METAL (Willer *et al*., 2010). After the final meta-analysis, variants were excluded if only available for fewer than 5,000 individuals. Meta-analyses were stratified by race and done separately for discovery, replication, and generalization samples. Site-specific quantile-quantile plots were generated to inspect presence of genomic inflation.

Supplementary Notes

Case reports
RHEB p.(Pro37Leu) (1) – This male is the first of two children of non-consanguineous parents. His younger sister is similarly affected and is described here as individual 3. Further anamnesis of family history of developmental delay was negative. He was born after 37 weeks of gestation with a birth weight of 3000 gram (0 SD) and APGAR scores of 7 and 8 after 1 and 5 minutes respectively. During his first year, severe hypotonia was present. Neurologic physical examination revealed balance problems, low stretch reflexes and polyneuropathy. An EEG showed diffuse hypofunctional abnormalities, mainly in the posterior brain regions.
His motor development was severely delayed. Ultrasound of the cerebrum showed megalencephaly, slightly enlarged ventricles and somewhat cerebellar hypoplasia. He could walk with support at the age of 20 months. Severe pedes plani valgi and a broad based gait were noticed. At the age of 4 years, he could walk unsupported, but this was lost at the age of 5 years due to the development of hip dislocation and kyphoscoliosis. Since that time, the use of a wheelchair is required. There is a lack of speech and there is only minimal non-verbal communication possible. He has a quiet behaviour, but mood changes are present. There are periods of hyperventilation noticed and his sleeping pattern is irregular. Cardiac screening revealed a ventricular tachycardia and ultrasound of the kidneys showed hydronephrosis of the right kidney, requiring surgery. He was diagnosed with gastro-oesophageal reflux, causing oesophagitis (degree II) and requiring medical treatment.
Physical examination at the age of 5 years showed macrocephaly with a head circumference of 56.5 cm (+3 SD). Upon evaluation at the age of 29 years, neurologic examination showed spastic tetraplegia, hypotonia and progressive loss of power of the extremities. The patient had severe ID, with absence of speech and used a wheelchair. Physical examination showed a normal head circumference of 60 cm (+1.5 SD) and low height of 171 cm (-2 SD). Telecanthus

with a ICD of 4 cm (+3.5 SD) and OCD of 10 cm (+2 SD) were measured. Facial dysmorphisms including frontal bossing, low nasal bridge, prominent nose and broad mouth were present.
White, curly hair were observed. Previous genetic testing, comprising karyotyping, analysis of subtelomeric regions, 250k SNP array and Angelman analysis were normal. Using whole exome sequencing, a heterozygous *de novo* mutation in *RHEB* was identified: Chr7 (GRch37); 9.1511880436>A; NM_005614.3:c 110c>T.(p(Pro37Leu)).

RHEB p.(Pro37Leu) (2) – This female is the second of two children of non-consanguineous parents. Her older brother is similarly affected and is described here as individual 2. Further anamnesis of family history of developmental delay was negative. She was born in breech position after 37 weeks of gestation with a birth weight of 2500 gram (-1 SD). Severe hypotonia was present since birth. She had macrocephaly with a head circumference of 50 cm (+3 SD). CT scan of the brain showed megalencephaly and wide ventricles. At the age of 3 years, epilepsy developed. She had tonic-clonic episodes, for which she was treated with Diazepam.
Medication was stopped several years later and after that, she developed absence seizures in a frequency of a few times per year. EEG showed diffuse abnormalities with right frontal more irritative focus. Both motor and language development were severely delayed. She could sit without support from the age of 18 months and walk without support from the age of 13 years. She is able to speak a few words. She was diagnosed with a kyphoscoliosis and congenital hipdislocation, the latter requiring surgery. During periods of anxiety or excitement, hyperventilation is present. Upon evaluation at the age of 23 years, regression of motor functions was reported and her behaviour became more aggressive. Physical examination showed short stature with a height of 151 cm (-3 SD) and normal head circumference of 57 cm (+1 SD). Telecanthus/hypertelorism with a ICD of 3.6 cm (+2 SD) and OCD of 2 cm (+2 SD) were measured. Facial dysmorphisms were similar as her older brother, comprising frontal bossing, low nasal bridge, prominent nose and broad mouth. White, curly hair were observed. Previous genetic testing, comprising karyotyping, analysis of subtelomeric regions, 250k SNP array and Angelman analysis were normal. Using whole exome sequencing, a heterozygous *de novo* mutation in *RHEB* was identified: Chr7 (GRch37); 9.1511880436>A; NM_005614.3:c 110c>T. (p(Pro37Leu)).

RHEB p.(Ser68Pro) - This female is the only child of nonconsanguineous parents. There was no family history of developmental delay. She was born after 36+4 weeks of gestation with a birth weight of 3140 gram (1 SD). At 20 weeks of gestation, a large head circumference was detected. At the end of the pregnancy, mother had protein urea. Delivery was in breech position without further complications. At the age of 1 month, her head circumference was 37.2 cm (+1.63 SD). Physical examination at the age of 3.5 years showed a height of 100.5 cm (0 SD) and a head circumference of 53.4 cm (+2.5 SD). She had severe developmental delay from the neonatal age. At the age of 4.5 years, she was not able to walk and could stand for a short while with support.
She was using a wheelchair. The patient had lack of speech and showed autistic features: she was fascinated by objects and there was an absence of eye contact. A brain MRI at the age of 1 year and 9 months showed megalencephaly, broad frontal lobes, mild dilatation of lateral ventricles, thick rostrum of the corpus callosum with relatively smaller splenium small hyperintense region left occipital region, large pons of the brainstem and multiple perivascular Virchow-Robin spaces. Several short periods with loss of consciousness have been reported but the patient has never been formally diagnosed with epilepsy. Upon EEG examination however, frequent abnormalities compatible with epileptiform activity were noted in the right temporal lobe. There were no feeding difficulties, except that fluids were made semi fluid, to prevent choking. She had frequent constipation. The patient was also reported to have facial dysmorphisms, including a large neurocranium, large fontanel, high broad forehead, low set, posteriorly rotated ears, hypotonic face with some drooping of the eyelids, telecanthus with a ICD of 3.6 cm (+3 SD) and OCD of 8.1 cm (+0.25 SD), slightly down slanting of the palpebral fissures, broad nasal bridge, open mouth appearance and a high narrow palate. Neurologic examination revealed axial hypotonia. She had hyperextensible elbows, hips and ankles. There was an obstruction of the right ductus nasolacrimalis and clinodactyly of digitus 5 of her right hand. Previous genetic testing, consisting of 180k array CGH, *FMR1* repeat expansion analysis, *PTEN* and NSD analysis were normal. Using whole exome sequencing, a heterozygous *de novo* mutation in *RHEB* was identified: Chr7(GRCh37):g.151174492A>G; NM_005614.3:c.202T>C (p.(Ser68Pro)).

"People think that epilepsy is divine simply because they don't have any idea what causes epilepsy.
But I believe that someday we will understand what causes epilepsy, and at that moment, we will cease to believe that it's divine.
And so it is with everything in the universe"
Hippocrates

Chapter VI

RHEB1-hyperactivity dependent cortical malformations cause spontaneous seizures due to aberrant connectivity

Martina Proietti Onori, Linda M.C. Koene, Carmen B. Schafer, Mark Nellist, Marcel de Brito van Velze, Zhenyu Gao, Ype Elgersma, Geeske M. van Woerden

Manuscript in preparation

ABSTRACT

Pathogenic mutations in *Ras Homolog Enriched in Brain 1* (*RHEB1*) have been shown to cause malformations of cortical development (MCD) and associated epilepsy. Exogenous expression in mouse brains of the dominant active RHEB1p.P37L mutant, identified in patients with intellectual disability, megalencephaly and epilepsy, strongly mimics a human MCD-like phenotype, with ectopic localization of new-born neurons, mTOR pathway hyperactivity and spontaneous tonic-clonic seizures. Making use of genetic tools and *in utero* electroporation, we show, similarly to other MCD-related and mTOR related mouse models, that the cortical malformation is not necessary to induce seizures. In addition, we provide evidence that having a cortical malformation *per se* is not sufficient to induce seizures. We identified the aberrant axonal connectivity caused by the RHEB1p.P37L mutant to be the primary cause for seizure development. We further found that distant cortical areas are functionally affected by the hyperactive cells through vesicular release. These experiments indicate that the cell-non autonomous effects caused by mTOR hyperactivity are not confined to cells surrounding the focal malformation, but extend to contralateral brain cells. These results provide new insights on the mechanisms of MCD-related epilepsy caused by mTOR hyperactivity and advance our understanding on how a local malformation can lead to generalized epilepsy.

INTRODUCTION

Malformations of cortical development (MCD) refers to a heterogenous group of micro- and macroscopic cortical abnormalities, such as Focal cortical dysplasia (FCD), megalencephaly, lissencephaly and paraventricular nodular heterotopia (PNH) (Barkovich *et al*., 2012), which arise from problems during the early embryological cortical development. MCD is often linked to epilepsy and intellectual disability (ID) (Leventer *et al*., 2008; Juric-Sekhar and Hevner, 2019; Represa, 2019). It is estimated that up to 40% of childhood seizures difficult to control medically or even intractable, are due to MCDs (Kuzniecky, 1994), and *vice versa*, at least 75% of the patients with MCD will develop seizures (Leventer *et al*., 1999).

Mammalian target of rapamycin (mTOR) is a kinase known to mediate many cellular processes, including neuronal proliferation and cell growth during development (Crino, 2011; Laplante and Sabatini, 2012a; Saxton and Sabatini, 2017). mTOR forms 2 distinct protein complexes, each regulated by different upstream pathways: 1) mTORC1 (Raptor binding to mTOR), regulated by the TSC1/TSC2 complex and the GTP binding protein Ras Homolog Enriched in Brain 1 (RHEB1), and 2) mTORC2 (Rictor binding to mTOR), regulated by PI3K and PTEN (Bhaskar and Hay, 2007; Meng *et al*., 2018). Over the recent years, hyperactivation of the mTOR pathway has been associated with different types of MCD, such as megalencephaly and FCD, as well as with epilepsy (Crino, 2007, 2011; Barkovich *et al*., 2015; Moffat *et al*., 2015; Majolo *et al*., 2018; Juric-Sekhar and Hevner, 2019; Represa, 2019). Indeed, mutations in many of the genes of the mTOR pathway (*AKT3*, *PIK3CA*, *DEPDC5*, *PTEN*, *RHEB1* and *MTOR* itself) have now been identified to cause MCD, potentially explaining the heterogeneity of MCD and the challenge in understanding the underlying mechanisms causing epilepsy to be able to identify new treatments (Backman *et al*., 2001; Baek *et al*., 2015; Mirzaa *et al*., 2016; Møller *et al*., 2016; D'Gama *et al*., 2017; Hanai *et al*., 2017; Lim *et al*., 2017; Reijnders *et al*., 2017; Salinas *et al*., 2019; Zhao *et al*., 2019; Pelorosso *et al*., 2019; Dawson *et al*., 2020).

The discovery of new genes potentially causing FCD or other types of cortical malformations, allowed the generation of animal models to study the development of cortical malformations and associated epilepsy (Chevassus-au-Louis *et al*., 1999; Schwartzkroin *et al*.,

2004; Wong, 2009; Wong and Roper, 2016). In particular, the use of *in utero* electroporation (IUE) made possible to spatially and temporally inactivate or express a specific gene or mutation during embryonic development to generate mouse models with focal malformations and epilepsy (Lafourcade *et al*., 2013; Baek *et al*., 2015; Lim *et al*., 2015, 2017; Hsieh *et al*., 2016; Hanai *et al*., 2017; Hu *et al*., 2018; Park *et al*., 2018; Ribierre *et al*., 2018). While most of these models are able to recapitulate the main cellular features typical of FCD, such as dysplastic and cytomegalic neurons sparsely diffused in the cortex, not all rodent MCD models develop reliably spontaneous seizures, which makes it difficult to study the relation between the cortical malformation and epileptogenesis (Wong, 2009; Wong and Roper, 2016).

RHEB, the direct activator of mTOR, is a member of the Ras family of small GTP-binding proteins and the conversion of the GTP bound RHEB to the GDP form is mediated by the TSC1:TSC2 complex. In response to nutrients, growth factors or amino acids RHEB is released from the TSC1:TSC2 complex inhibition and can activate mTORC1 (Bos, 1997; Manning and Cantley, 2003; Gebauer and Hentze, 2004; Han and Sahin, 2011; Jewell *et al*., 2013; Sabatini, 2017). One of the FCD mouse models generated using IUE, consists of overexpression of a constitutive active form of RHEB1 (RHEB1p.S16H) (Yan *et al*., 2006). Overexpression of this RHEB1p.S16H mutant results in mTOR hyperactivity, FCD and spontaneous seizures, but only when targeting the retrosplenial cortex, not the somatosensory cortex, suggesting that the somatosensory cortex is a non-epileptogenic region (Hsieh *et al*., 2016). However, this hyperactive mutant was identified based on biochemical experiments, but has not been found in patients with MCD and/or epilepsy. Recently two *de novo* mutations in RHEB1 (p.P37L and p.S68P) were identified in patients with ID, epilepsy and megalencephaly (Reijnders *et al*., 2017), causing hyperactivation of the mTOR pathway. *In utero* electroporation of the RHEB1p.P37L caused focal cortical lesions, resembling PNH, and diffuse cortical misplacement with dysplastic neurons. Furthermore, these mice reliably develop spontaneous seizures starting from three weeks of age (Reijnders *et al*., 2017). The anatomical and phenotypical features of this mouse model, fully recapitulating the most prominent characteristics of cortical malformations (focal lesions and epilepsy), make this a very powerful and preclinically relevant novel model to study mTOR and cortical malformations-related epilepsy. Here we make use of this novel mouse model to study the mechanism underlying the mTOR and MCD-related epilepsy and, confirming previous data (Hsieh *et al*., 2016), we show that the cortical malformation is not necessary for the development of seizures. Additionally, we provide evidence for the first time that the presence of heterotopia by itself is not sufficient to cause epilepsy but that aberrant connectivity between different brain areas, as well as vesicle release from the ectopic cells, is causative for the development of spontaneous seizures. Taken together our results provide novel insights on MCD-related epilepsy, which open new doors for the discovery of potential new treatments.

MATERIALS AND METHODS

Constructs. The cDNA sequence for the variant *RHEB1*p.P37L was synthesized by GeneCust and cloned in our dual promoter expression vector (Reijnders *et al*., 2017). For the *in vivo* and *in vitro* experiments, the empty vector used as control refers to the dual promoter expression vector without a gene inserted. The following DNA plasmids were obtained from Addgene: pGEMTEZ-TeTxLC (Addgene plasmid #32640; http://n2t.net/addgene:32640; RRID:Addgene_32640); RV-Cag-Dio-GFP (Addgene plasmid #87662; http://n2t.net/addgene:87662; RRID:Addgene_87662); pCAG-ERT2CreERT2 (Addgene plasmid # 13777; http://n2t.net/addgene:13777; RRID:Addgene_13777); pCAGGS-ChR2-Venus (Addgene plasmid #15753;

http://n2t.net/addgene:15753; RRID:Addgene_15753). The TeTxLC was isolated by PCR using the following primers: Fw 5' – TAAGCAGGCGCGCCaccATGccgatcaccatcaacaa – 3' and Rev 5' – gccatggcggccgcgggaattcgat – 3' inserted in our dual promoter expression vector. To generate the loxP-STOP-loxP constructs (loxP-STOP-loxP-*RHEB1*p.P37L and loxP-STOP-loxP-TeTxLC) the loxP-STOP-loxP sequence was obtained from the Ai6 CAG-Floxed ZsGreen in Rosa 26 targeting vector (Addgene plasmid #22798; http://n2t.net/addgene:22798; RRID:Addgene_22798) and inserted just after the CAGG promoter and before the beginning of the gene in our dual promoter expression vector containing either *RHEB1*p.P37L or TeTxLC. The floxed *RHEB1*p.P37L construct was generated by introducing one loxP site sequence before the CAGG promoter (Fw: 5'- cgcgtATAACTTCGTATAGCATACATTATACGAAGTTATg - 3', Rev: 5'- ctagcATAACTTCGTATAATGTATGCTATACGAAGTTATa - 3') and another loxP site sequence at the end of the *RHEB1*p.P37L gene (Fw: 5'- taaATAACTTCGTATAGCATACATTATACGAAGTTATg - 3', Rev: 5'- tcgacATAACTTCGTATAATGTATGCTATACGAAGTTATttaat - 3'), with the same orientation to ensure proper deletion.

Mice. For the neuronal cultures, FvB/NHsD females were crossed with FvB/NHsD males (both ordered at 8-10 weeks old from Envigo). For the *in utero* electroporation females FvB/NHsD (Envigo) were crossed with males C57Bl6/J (ordered at 8-10 weeks old from Charles River). Both female and male mice from the *in utero* electroporation litters were included in the experiments starting from 3 weeks of age. All mice were kept group-housed in IVC cages (Sealsafe 1145T, Tecniplast), unless mice underwent a surgical procedure, with bedding material (Lignocel BK 8/15 from Rettenmayer) on a 12/12 h light/dark cycle in 21°C (±1°C), humidity at 40-70% and with food pellets (801727CRM(P) from Special Dietary Service) and water available *ad libitum*. All animal experiments were conducted in accordance with the European Commission Council Directive 2010/63/EU (CCD approval AVD1010020172684).

Neuronal hippocampal cultures, transfection and immunocytochemistry. Primary hippocampal neuronal cultures were prepared from FvB/NHsD wild type mice according to the procedure described in Goslin and Banker, 1991. Briefly, hippocampi were isolated from brains of E16.5 embryos and collected altogether in 10 ml of neurobasal medium (NB, Gibco) on ice. After two washes with NB, the samples were incubated in pre-warmed trypsin/EDTA solution (Invitrogen) at 37° for 20 minutes. After 2 washes in pre-warmed NB, the cells were resuspended in 1.5 ml NB medium supplemented with 2% B27, 1% penicillin/streptomycin and 1% glutamax (Invitrogen), and dissociated. Following dissociation, neurons were plated on poly-D-lysine (25 mg per ml, Sigma) coated 15 mm glass coverslips at a density of $5*10^4$ cells per coverslip. The plates were stored at 37°C/5% CO_2 until the day of transfection. Neurons were transfected at 1 day *in vitro* (DIV1) with the following DNA constructs: control empty vector (1.8 µg per coverslip) and RHEB1p.P37L (2.5 µg per coverslip). Plasmids were transfected using Lipofectamine 2000 according to the manufacturer's instructions (Invitrogen). Neurons were fixed 3 days post-transfection with 4% paraformaldehyde (PFA)/4% sucrose and incubated overnight at 4°C with primary antibodies in GDB buffer (0.2% BSA, 0.8 M NaCl, 0.5% Triton X-100, 30mM phosphate buffer, pH7.4). Mouse pan anti-SMI312 (1:200, BioLegend) was used to stain for the axon and donkey anti-mouse-Alexa488 conjugated was used as secondary antibody (1:200, Jackson ImmunoResearch). Slides were mounted using mowiol-DABCO mounting medium. Confocal images were acquired using a LSM700 confocal microscope (Zeiss). For the analysis of the axon, at least ten distinct confocal images (20X objective, 0.5 zoom, 1024x1024 pixels; neurons were identified by the red immunostaining signal) from two different neuronal batches were taken from each coverslip for each experiment. The simple

neurite tracer plugin from the Fiji ImageJ software was used for the analysis of the axonal length and branches.

In utero electroporation. In utero electroporation was performed as described in (Saito and Nakatsuji, 2001). Pregnant FvB/NHsD mice at E14.5 of gestation were used to target the progenitor cells giving rise to pyramidal cells of the layer 2/3. Each *RHEB1* DNA construct (also in the LSL and floxed conditions) was diluted in all experiments to a final concentration of 0.5 µg per µl in fast green (0.05%) and PBS, while other plasmids were diluted to a final concentration of 1.5-2 µg per µl. The DNA solution was injected in the lateral ventricle of the embryos while still *in utero*, using a glass pipette controlled by a Picospritzer ® III device. When more than one DNA construct was injected, a mixture of plasmids was prepared to reach a final concentration of 1.5-2 µg per µl. To ensure proper electroporation of the injected DNA constructs (1-2 µl) into the progenitor cells, five electrical square pulses of 45V with a duration of 50 ms per pulse and 150 ms inter-pulse interval were delivered using tweezer-type electrodes connected to a pulse generator (ECM 830, BTX Harvard Apparatus). The positive pole was targeting the developing somatosensory cortex. After birth, animals starting from 3 weeks of age of both sexes were used to monitor seizure development, for *ex vivo* electrophysiology experiments or histological processing.

Immunohistochemistry and analysis. Mice were deeply anesthetized with an overdose of Nembutal and transcardially perfused with 4% PFA. Brains were extracted and post-fixed for 1 hr in 4% PFA. Brains were then embedded in gelatin and cryoprotected in 30% sucrose in 0.1 M Phosphate Buffer (PB) overnight, frozen on dry ice, and sectioned using a freezing microtome (40 µm thick). For immunofluorescence, free-floating 40-µm-thick sections were washed in PBS multiple times and afterwards primary antibodies were added diluted in PBS containing 2% NHS, 0.5% Triton X-100, and 150 mM bovine serum albumin (BSA) and shacking at room temperature overnight. The day after, sections were washed three times with PBS and secondary antibodies were added diluted in PBS containing 2% NHS, 0.5% Triton X-100, and 150 mM BSA. After washing in PBS and PB (0.05 M), sections were counterstained with 4′,6-diamidino-2-phenylindole solution (DAPI, 1:10000, Invitrogen) before being washed in PB 0.05 M and mounted on slides using chrome(3) potassium sulfatedodecahydrate and left to dry. Finally, sections were mounted on glass with mowiol® (Sigma-Aldrich). The primary antibodies used were: anti-rabbit pS6 (Ser 240/244), 1:1000; Cell signaling, catalog #5634; anti-rabbit pS6 (Ser 235/236), 1:1000; Cell signaling, catalog #2211; anti-rabbit RFP, 1:2000; Rockland, catalog 600-401-379; anti-rabbit RHEB1, 1:1000; Proteintech Group Inc., catalog 15924-1-AP; anti-rabbit CUX1, 1:1000; Proteintech Group Inc., catalog 11733-1-AP; anti-rat CTIP2, 1:200; Abcam, catalog ab18465; anti-rabbit NeuN, 1:2000; Millipore catalog ABN78 (RRID: AB_10807945); anti-mouse SATB2, 1:1000; Santa cruz, catalog sc-81376; Secondary antibodies used were: donkey anti rabbit 488, catalog #711-545-152; donkey anti rabbit 647,catalog #711-605-152; donkey anti rabbit Cy3, catalog #711-165-152; donkey anti mouse 488, catalog #715-545-150; donkey anti mouse 647, catalog #715-605-150; donkey anti rat Cy5, catalog #712-175-150; streptavidin 488, catalog #016-540-084; all from Jackson ImmunoResearch, 1:200. For Nissl stainings, a few selected free floating 40-µm-thick sections were mounted on glass using chrome(3) potassium sulfatedodecahydrate and left to dry overnight. Slides were stained in 0.1 % Cresyl Violet for 4-10 minutes, then rinsed briefly in tap water to remove excess staining, dehydrated in increasing percentages of alcohol, cleared with xylene and covered using Permount (Fisher Scientific). Overview images of the coronal sections were acquired by tile scan imaging using a LSM700 confocal microscope (Zeiss) with a 10X objective. Zoom in images of the targeted area (ipsilateral) and contralateral S1 were

taken using a 10X objective.

For the migration analysis, confocal images (10X objective, 0.5 zoom, 1024x1024 pixels) were taken from 2 – 3 non-consecutive sections from minimum 2/3 electroporated animals per control and *RHEB*-containing plasmids. Images were rotated to correctly position the cortical layers, and the number of cells in different layers were counted using the 'analyze particles' plugin of FIJI. The results were exported to a spreadsheet for further analysis. Cortical areas from the pia to the ventricle were divided in 10 equal-sized bins and the percentage of tdTomato-positive cells per bin was calculated.

For the soma size analysis, z-stacks images were taken using a 20X objective, 1 zoom, 1024x1024 pixels, of the targeted cells in both empty vector control and *RHEB1*p.P37L coronal sections. A ROI around each targeted cell in maximum intensity projection pictures was defined using the FIJI software and the area of the soma was measured using the 'Measure' option in ImageJ.

For the analysis of pS6 intensity levels, confocal images (10X objective, 0.5 zoom, 1024x1024 pixels) of the ipsilateral and contralateral S1 cortex were acquired with the same master gain from both control and RHEB1 groups previously stained together against pS6 (240/244). The overall intensity level of the staining for each picture was measured using the 'RGB measure' plugin of FIJI and the values of each ipsilateral side were normalized against the corresponding contralateral side and plotted.

For the analysis of the fluorescent intensity of the axonal branches over the contralateral cortical layers, 3 matched coronal sections from at least 2 different animals per group with comparable amount of targeting were selected. The amount of axonal arborization was measured selecting the S1/S2 border, drawing a straight segmented line with adjusted width and length and resized in 1000 bins, and using the 'plot profile' option of the analyze section of FIJI to measure the fluorescent intensity of the tdTomato signal over the different layers. The values obtained for each section were normalized against the mean background fluorescent intensity calculated on a non-targeted, fixed in size, cortical area.

For the analysis of the cell morphology of biocytin filled pyramidal cells and ectopic cells in the nodule labelled with streptavidin-488, z-stacks images were taken using a 20X objective, 0.5 zoom, 1024x1024 pixels, to include the dendritic tree. Maximum intensity projection pictures were analyzed to automatically detect the dendritic morphology and perform Sholl analysis using the SynD software for the MATLAB platform according to the procedure described in (Schmitz *et al*., 2011).

Stereotactic surgeries. Starting from 3 weeks of age surgeries were performed according to the following procedure. Mice were anaesthetized with a mixture of isoflurane and oxygen (5% for induction and <2% for maintenance) and body temperature was kept constant at 37 degrees during the entire surgical procedure. Temgesic (0.3 mg/ml) and lidocaine (Xylocaine, 100mg/ml) were used for general and local analgesia. After fixation in a custom-designed stereotaxic apparatus, the scalp was opened to expose the skull. The membranous tissue underneath was cleared and the bone was surgically prepared with Optibond prime and adhesive (Kerr, Bioggio, 584 Switzerland). For the electroencephalography (EEG) measurements, two EEG electrodes were placed on the left and right side of the somatosensory cortex while the reference electrode was placed on the cerebellar cortex. The placement of the bilateral recording electrodes in the somatosensory cortex layer II-III (Bear Lab Chronic Microelectrodes, #30070, FHC) for the local field potential (LFP) recordings, was determined using a digital xy manipulator according to the following coordinates: from the bregma AP -1.94 mm, DL - 3.00 mm, DV 0.6 mm. A reference silver wire electrode was placed on top of the *vermis* in the cerebellum and a small

brass pedestal was attached to the skull with Charisma (Heraeus Kulzer, 585 Armonk NY, USA) to allow the fixation of the mice to the head bar during LFP recordings.

EEG recordings and seizure assessment. After at least three days of recovery from the surgical procedure, mice were connected to a wireless EEG recorder (NewBehavior, Zurich, Switzerland) for 24 hours per day for at least two consecutive days (one session of recordings). EEG recordings were manually assessed by two different researchers to check for occurrence of seizures, defined as a pattern of repetitive spike discharges followed by a progressive evolution in spike amplitude with a distinct post-ictal depression phase, based on the criteria described in (Kane *et al*., 2017). If no seizures were detected during the first week *post*-surgery, mice were recorded for another session of 48-56 hr for a maximum of four sessions over four weeks *post*-surgery. During the days in which no EEG recordings were performed, mice were daily monitored to assess for the presence of behavioural seizures and discomfort.

LFP recordings and power spectrum analysis. Recordings were performed as described in Kool *et al*., 2019. Briefly, two days after the surgical procedure, mice were head-fixed to a brass bar suspended over a cylindrical treadmill to allow anaesthesia-free recording sessions and placed in a light-isolated Faraday cage. Mice were allowed to habituate to the set-up before proceeding to the recording. Local field potential measurements were acquired every day in sessions of 20-30' each for five consecutive days, using the Open Ephys platform with a sampling rate of 3 kS/s and a band pass filter between 0.1 and 200 Hz. For the power spectrum analysis, the average power density spectrum of 5 days of recording was obtained using MATLAB software (MathWorks; RRID:SCR_001622). The mean relative power was calculated over four frequency bands relative to the total power: delta (2–4 Hz), theta (4–8 Hz), beta (13–30 Hz), and gamma (30–50 Hz).

Ex vivo slice electrophysiology for excitability. P21-P25 mice of both sexes *in utero* electroporated with the DNA plasmids specified in the figure legends for each experiment were anaesthetized with isoflurane before decapitation. The brain was quickly removed and submerged in ice cold cutting solution containing (in mM): Choline Chloride 110, KCl 2.5, NaH_2PO_4 1.2, $NaHCO_3$ 26, D-Glucose 25, $CaCl_2$ 0.5, $MgSO_4$ 10. Acute 300 µm coronal slices were made of the somatosensory cortex using a vibratome (HM650V, Microm) while being saturated with 95% O_2/5% CO_2. The slices were immediately transferred to a submerged slice holding chamber and incubated at ±34°C for 5 min before being transferred to a second slice holding chamber also kept at ±34°C. The second holding chamber contained the same artificial cerebrospinal fluid (ACSF) as was used during all recordings and contained (in mM): NaCl 125, KCl 3, NaH_2PO_4 1.25, $NaHCO_3$ 26, Glucose 10, $CaCl_2$ 2, $MgSO_4$ 1. During the slicing procedure and experimental recordings, slices were saturated with 95% O_2/5% CO_2. Slices recovered for an hour on room temperature before starting the experiment. After the experiment, slices were put in 4% PFA overnight to fixate and were then transferred to PBS and kept in PBS until further processing. Whole-cell patch clamp recordings were obtained from the soma of visually identified L2/L3 pyramidal neurons from the S1 cortex with an upright microscope using IR-DIC optics (BX51WI, Olympus, Tokyo, Japan). Transfected cells in the ipsilateral side were identified by the presence of TdTomato elicited by an Olympus U-RFL-T burner. All recordings were done under physiological temperatures of 30± 1 °C. Patch clamp pipettes were pulled from standard wall with filament borosilicate glass with a tip resistance between 2-4 MΩ. All recordings were performed using a Multiclamp 700B (Molecular Devices, Sunnyvale, CA, USA) and digitized by a Digidata 1440A (Molecular Devices, Sunnyvale, CA, USA). For the current clamp recordings, pipets were filled with a K-gluconate internal solution containing (in mM): K-gluconate 125,

NaCl 10, HEPES 10, EGTA 0.2, MgATP 4.5, NaGTP 0.3 and Na-phosphocreatine 10. For analysis of cell morphology, biocytin (5%) was added to the intracellular solution. The final solution was adjusted to a pH of 7.2–7.4 using KOH and had a osmolarity of 280 ± 3. After getting a seal of at least 1 GΩ, whole cell configuration was obtained by applying brief negative pressure together with a short electric pulse. Prior to breaking in, cell capacitance was compensated. Series resistance was not corrected but monitored. Recordings with an unstable series resistance and higher than 20 MΩ were rejected. Membrane potentials were not corrected for liquid junction potential. Resting membrane potential was measured immediately after break in.

Excitability protocol and analysis. Each sweep started with a small and short hyperpolarizing step (-50 pA, 50 ms) to monitor access resistance. Action potentials were triggered by square step current injections into the patched neurons while holding them at -70 mV. Steps were 750 ms long and started at -300 pA with increments of 20 pA. The number of action potentials and action potential properties were analyzed using Clampfit 10.7.0.3 (Molecular Devices, LLC, USA). For each cell, the first action potential at rheobase was analyzed. The parameters considered were: maximum rise slope, maximum decay slope, peak amplitude, half-with and threshold. The threshold was calculated by plotting the first derivative of the trace. The threshold was defined when the first derivative was lower than 10 mV/ms. Furthermore, at the -300-hyperpolarization step, Ih current was calculated by measuring the amplitude of the deepest antipeak in the first 50 msec with the steady state level at the last 50 msec of the same current step subtracted. Series resistance was calculated offline for each cell by plotting the difference in voltages of the hyperpolarizing steps and baseline. A linear line was plotted to visualize passive current only. The tau was calculated by fitting a standard exponential on the end of the hyperpolarizing steps. From tau and series resistance, capacitance was calculated.

Ex vivo slice electrophysiology for optogenetics. P21-P25 mice of both sexes *in utero* electroporated either with the *RHEB1*p.P37L and pCAGGS-ChR2-Venus plasmids or the empty vector and pCAGGS-ChR2-Venus plasmids, were anaesthetized with isoflurane before decapitation. The brain was quickly removed and submerged in ice cold cutting solution containing (in mM): 93 NMDG, 93 HCl, 2.5 KCl, 1.2 $NaHPO_4$, 30 $NaHCO_3$, 25 Glucose, 20 HEPES, 5 Na-ascorbate, 3 Na-pyruvate, 2 Thiourea, 10 $MgSO_4$, 0.5 $CaCl_2$, 5 N-acetyl-L-Cysteine (osmolarity 310 ± 5; bubbled with 95% O_2 / 5% CO_2). Next, 250 μm thick coronal slices were cut using a Leica vibratome (VT1000S). For the recovery, brain slices were incubated for 5 min in slicing medium at 34 ± 1˚C and subsequently for ∼40 min in ACSF (containing in mM: 124 NaCl, 2.5 KCl, 1.25 Na_2HPO_4, 2 $MgSO_4$, 2 $CaCl_2$, 26 $NaHCO_3$, and 20 D–glucose, osmolarity 310 ± 5mOsm; bubbled with 95% O_2 / 5% CO_2) at 34 ± 1˚C. After recovery brain slices were stored at room temperature. For all recordings, slices were bathed in 34 ± 1˚C ACSF (bubbled with 95% O_2 and 5% CO_2). Whole-cell patch-clamp recordings were recorded with an EPC-10 amplifier (HEKA Electronics, Lambrecht, Germany) and sampled at 20 kHz. Resting membrane potential and input resistance were recorded after whole-cell configuration was reached. Recordings were excluded if the series resistance or input resistance (RS) varied by >25% over the course of the experiment. Voltage and current clamp recordings were performed using borosilicate glass pipettes with a resistance of 3-5 MΩ that was filled with K-Gluconate-based internal solution (in mM: 124 K-Gluconate, 9 KCl, 10 KOH, 4 NaCl, 10 HEPES, 28.5 Sucrose, 4 Na_2ATP, 0.4 Na_3GTP (pH 7.25-7.35; osmolarity 290 ± 5mOsm)). Recording pipettes were supplemented with 1 mg/ml biocytin to allow histological staining. Current clamp recordings were corrected offline for the calculated liquid junction potential of -10.2 mV.

Optogenetic stimulation. Full-field optogenetic stimulation (470 nm peak excitation) was

generated by the use of a TTL-pulse controlled pE2 light emitting diode (CoolLED, Andover, UK). Light intensities at 470 nm were recorded using a photometer (Newport 1830-C equipped with an 818-ST probe, Irvine, CA) at the level of the slice. To trigger neurotransmitter release from transfected axons we delivered a 1 ms light pulse with intensities ranging between 15 and 166.5 mW/mm^2 at a frequency of 0.1Hz. To ensure that we recorded action potential-driven neurotransmitter release most experiments were concluded by bath application of 10 *μM* tetrodotoxin (TTX), which blocked all post-synaptic responses in the recorded pyramidal neurons.

Drugs. For the experimental groups where Tamoxifen was used, mice from 7 days of age were intraperitoneally injected with Tamoxifen (Sigma-Aldrich, 0.1 mg/g of bodyweight) dissolved in sunflower oil (20 mg/ml) for 4 consecutive days. Rapamycin (10 mg/kg) was dissolved in dimethylsulfoxide (10 mg/ml, Sigma-Aldrich) and injected intraperitoneally.

Statistics. Normality of the distribution for the different experiments was determined using either the Wilk–Shapiro or the Kolmogorov-Smirnov test (specified in the results sections or in the figure legends). Statistical tests were performed using a one-way ANOVA (or non-parametric tests), two-way repeated-measures ANOVA (or mixed-effect analysis when missing data were present), Student's t test or correlation/association analyses (specified in the results sections or in the figure legends and in the Supplementary tables). For all statistical analyses α was set at 0.05. Values are represented as average ± SEM. Group sizes, number of cells or number of slices can be found in the figure legends. All statistical tests were performed either using GraphPad Prism 8.0 (RRID: SCR_002798) or SPSS Statistics v25.0 (RRID:SCR_002865).

RESULTS

Overexpression of RHEB1p.P37L *in vivo* causes aberrant cortical development

Using *in utero* electroporation, we have previously shown that overexpression of the ID-linked RHEB1p.P37L mutant, but not RHEB1-WT, results in the formation of a heterotopic nodule as well as spontaneous epilepsy in 100% of the targeted mice (Reijnders *et al*., 2017), giving us a valuable model to study the mechanisms behind mTOR-dependent and MCD-related epilepsy. To confirm previous results and further characterize the model, RHEB1p.P37L or an empty vector control was *in utero* electroporated at E14.5 to target progenitor cells giving rise to pyramidal neurons of layer 2/3 of the somatosensory cortex (Figure 1A). As previously shown, overexpression of RHEB1p.P37L resulted in a clear migration deficit, with only 20% of the targeted cells reaching the outer layers of the cortex compared to 97% in the empty vector condition ($t(19)=13.95$, $p<0.0001$; two-tailed unpaired t-test) (Figure 1B, inset). The non-migrated transfected neurons, mislocalized in the white matter to form a heterotopic nodule lining the ventricle in the adult brain (Figure 1B and Supplementary figure 1).

While the general cortical layer architecture remains intact (Supplementary figure 1), RHEB1p.P37L overexpressing cells, both in the heterotopic nodule and scattered through the cortex, showed cytological abnormalities, with dysmorphic appearance and enlarged soma size (empty vector targeted cells in layer 2/3 *vs* RHEB1p.P37L cells: $t(639)=41.37$, $p<0.0001$; two-tailed unpaired t-test) (Figure 2A and Supplementary figure 1). Sholl analysis of biocytin filled cells in layer 2/3 and in the nodule of mice *in utero* electroporated with RHEB1p.P37L revealed that the cells in the nodule present a more complex arborization while the overall morphology of cells that manage to migrate towards layer 2/3 does not differ from pyramidal cells transfected with the empty vector ($F(120, 2940)=10.15$, $p<0.0001$, Two-way repeated

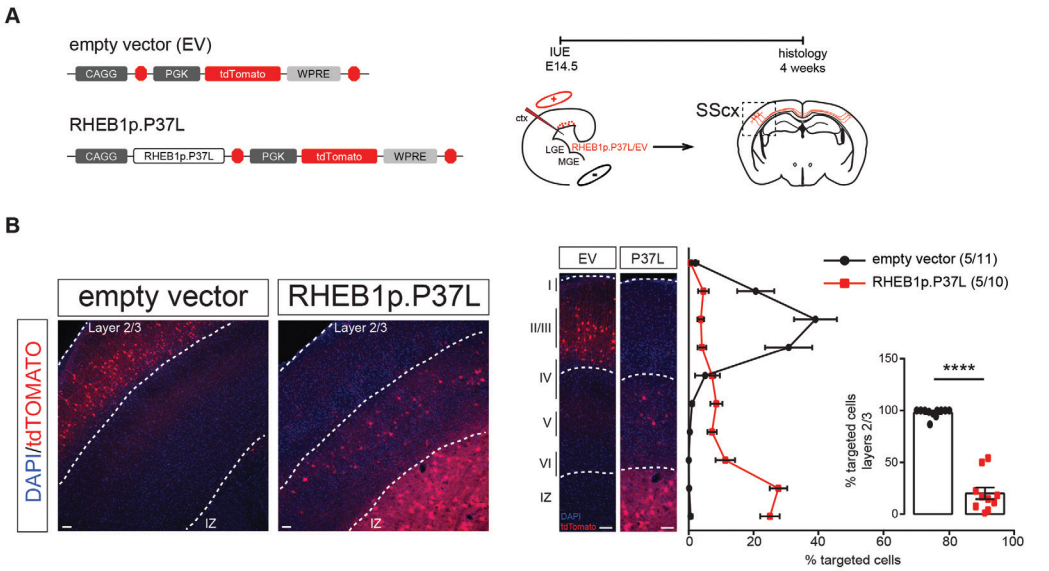

Figure 1. RHEB1p.P37L overexpression *in vivo* causes the formation of a heterotopic nodule. (A) *left:* Schematic representation of the constructs used throughout the experiments. The empty vector (EV) control consists of a *CAGG* promoter followed by a multiple cloning site to insert genes of interest (RHEB1p.P37L in this case). The *tdTomato* gene is expressed under the *PGK* promoter, to allow for independent expression of the gene of interest and tdTOMATO. *right:* schematic overview of the *in utero* electroporation (IUE) experiment, indicating the cortical area targeted (somatosensory cortex (SScx)) and timeline of the experiment. (B) *left:* Representative images of the SScx of mice targeted either with EV or the RHEB1p.P37L, showing the transfected cells (tdTomato+). Dotted lines indicate the borders of the intermediate zone (bottom) and layers 2/3. *right:* quantification of tdTomato+ cells across the different layers of the cortex; inset shows the percentage of targeted cells that managed to migrate out to layer 2/3; Numbers in the legend indicates number of mice/number of pictures analyzed; scale bars: 50 µm; values in the bar plot are represented as mean ± SEM; WPRE = Woodchuck Hepatitis Virus (WHP) Posttranscriptional Regulatory Element; ctx = cortex; LGE = lateral ganglion eminence; MGE = medial ganglion eminence; IZ = intermediate zone **** p<0.0001.

measure ANOVA; empty vector *vs* P37L layer 2/3: p=0.15; empty vector *vs* P37L nodule: p<0.0001; P37L layer 2/3 *vs* P37L nodule: p<0.0001; Bonferroni multiple comparisons) (Figure 2B). All the transfected ectopic neurons preserved the molecular identity of mature layer 2/3 pyramidal cells, being positive for the neuronal marker NeuN and the outer layer molecular marker CUX1 and negative for the deeper layer marker CTIP2 (Figure 2C and Supplementary figure 2A). Additionally, most of the neurons in the nodule are SATB2 positive, showing that, even when mislocalized, they maintain the callosal projection identity (Figure 2C and Supplementary figure 2A). Finally, confirming hyperactivation of the mTOR pathway *in vivo*, mice overexpressing RHEB1p.P37L show an overall increase in pS6 level in the transfected hemisphere, compared to the empty vector condition (t(19)=3.5, p=0.002; two-tailed unpaired t-test) (Figure 2D and Supplementary figure 2B).

Overexpression of RHEB1p.P37L *in vivo* causes mTORC1-dependent spontaneous tonic-clonic seizures and abnormal network activity

To assess the reliability of the development of spontaneous seizures, *in utero* electroporated mice were continuously EEG monitored from weaning (P21) (Figure 3A). Confirming previous data, spontaneous seizures started to occur in mice transfected with the RHEB1p.P37L construct from 3 weeks of age, with an average onset of 33 days (Supplementary figure 3A). The seizures are highly stereotyped, characterized by loss of upright posture followed by a tonic-clonic phase with presence of convulsions and twitching behavior (see video 1). Wireless

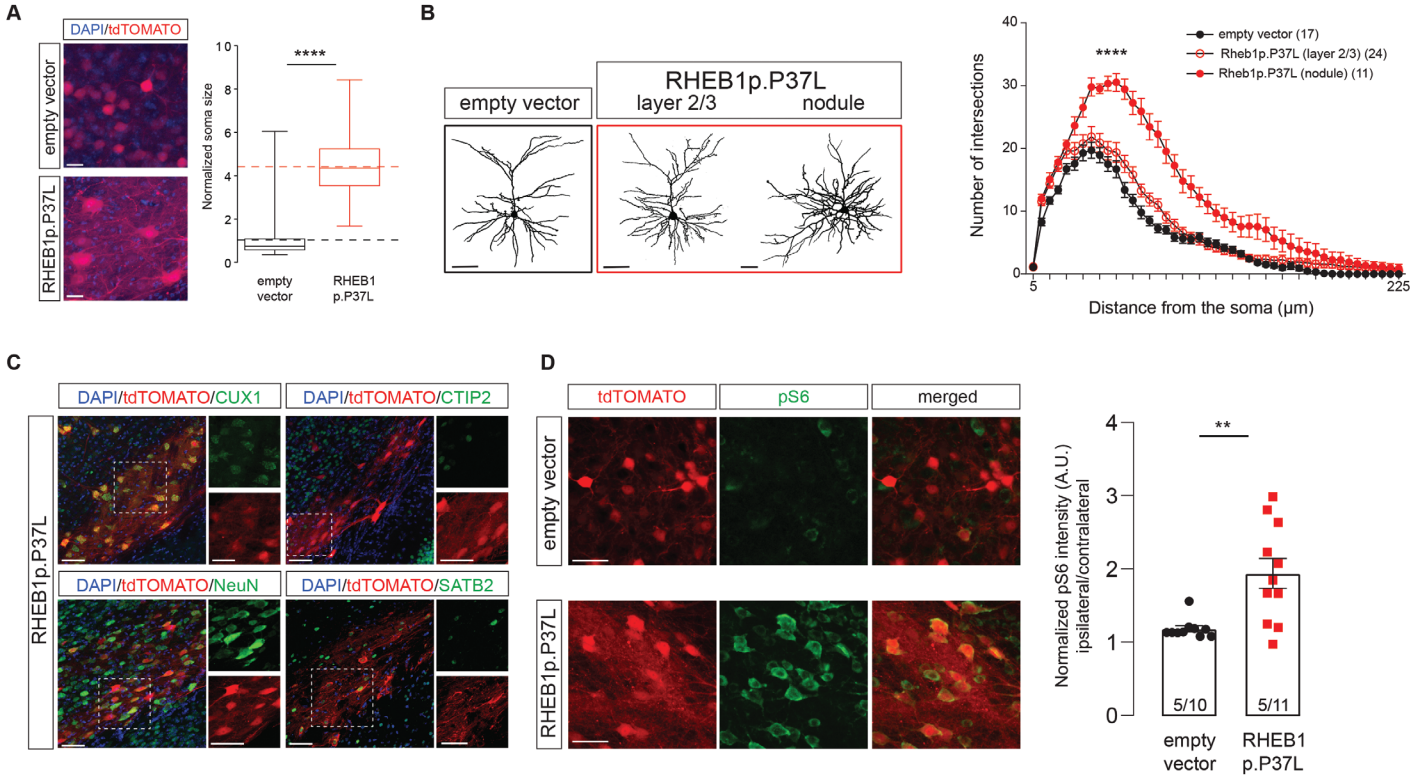

Figure 2. RHEB1p.P37L positive cells display aberrant morphology and show mTOR hyperactivity while still preserving the molecular identity of pyramidal cells layer 2/3. (A) representative images of layer 2 cells targeted with the empty vector (upper) and cells targeted with RHEB1p.P37L in the nodule (bottom) with relative soma size quantification of tdTomato+ cells showing that RHEB1p.P37L targeted cells (275 cells over 2 mice) have an enlarged cell body compared to empty vector control cells (366 cells over 3 mice); box plots represent minimum and maximum value with median, dashed lines represent the mean values for empty vector (black) and for RHEB1p.P37L (red); scale bars: 20 µm (B) reconstruction and Sholl analysis of dendritic morphology of biocytin filled cells in layer 2/3 of the SScx (for empty vector control and RHEB1p.P37L) and in the heterotopic nodule; numbers in the legend indicate the number of cells analyzed from a minimum of 2 mice for each group sacrificed between P20 and P25; scale bars: 50 µm (C) Representative images of the heterotopic nodule stained with common cortical layers markers (CUX1 for layer 2/3, CTIP2 for layer 5), cortical projection neurons marker (SATB2) and mature neurons marker (NeuN), scale bars: 50 µm (D) Representative images of the targeted layer 2 (SScx) of empty vector control and heterotopic nodule showing increased pS6-240 levels (readout of mTOR activity) for RHEB1p.P37L targeted mice (right bar graph) quantified as intensity of pS6 staining of the overall ipsilateral targeted area normalized against the corresponding contralateral non-targeted cortex for each mouse; scale bars: 50 µm; values in the bar plot are represented as mean ± SEM, numbers indicate number of mice/number of pictures analyzed ** p<0.01, **** *p*<0.0001.

EEG recordings showed that while control mice did not show any epileptic activity (N=6), all RHEB1p.P37L targeted mice (N=12) showed clear epileptic events (Figure 3B box 1 *vs* box 3 and Supplementary figure 3B), characterized and recognized by an increase in frequency and amplitude of the brain activity (Figure 3B, box 3) compared to baseline interictal activity (Figure 3B, box 2). The calculated average duration of an epileptic event was 40 seconds, followed by a post-ictal depression phase of variable length (Figure 3B, Box 4). The frequency of seizures per day differed between mice as well as within mice over the days (Supplementary figure 3C). Additionally, no correlation was found between the total number of seizures over three consecutive days of recording and the average number of transfected cells per mouse ($r(10)=-0.27$, $p=0.39$, two-tailed Pearson's correlation) (Supplementary figure 3D). To assess if the seizures are indeed mTORC1-dependent we treated a group of mice (N=6) for 7 days with rapamycin (10 mg/kg), a known inhibitor of mTORC1, after seizures were observed. Rapamycin treatment reduced and temporarily abolished the occurrence of seizures within one week after the last day of rapamycin administration. However, seizures reappeared again, starting 3 weeks after the last injection of rapamycin in 4 out of 6 mice (data not shown).

Electrographic frequency dynamics of the interictal phases, and especially *theta* oscillations, have been proven to be good predictors for epilepsy outcome, compared to epileptiform spikes or high-frequency oscillations (HFOs), in several epilepsy rodent models (Chauvière *et al*., 2009; Milikovsky *et al*., 2017). Therefore, using local field potential (LFP) recordings, we assessed the frequency dynamics of cortical brain activity in the interictal periods of RHEB1p.P37L *in utero* electroporated mice starting from 4 weeks of age (Figure 4A). The averaged power spectrum within the RHEB1p.P37L group did not reveal any difference between the targeted and non-targeted cortex (ipsilateral *vs* contralateral: $F(3, 33)=1.5$, $p=0.23$, Two-way repeated measure ANOVA; data not shown), therefore measurements from both sides were pooled. Whereas the total power across 5 days of recording did not differ between the RHEB1p.P37L (N=12) and the control group (N=8) ($t(38)=0.57$; two-tailed unpaired t-test, data not shown), a significant difference was seen in the RHEB1p.P37L group in the *delta* (2-4 Hz), *theta* (4-8 Hz) and *gamma* (30-50 Hz) frequency bands of the normalized power spectrum compared to the control group (Figure 4B and Supplementary figure 4, statistics in Supplementary table 1). The difference in the *theta* and *gamma* frequency bands, but not in the *delta*, could be reverted to the control condition by injecting the RHEB1 mice intraperitoneally for 3 consecutive days with 10 mg/kg rapamycin (Figure 4B and Supplementary figure 4, statistics in Supplementary table 1). Together with the finding that rapamycin abolished seizures, this result indicates that *theta* oscillations dynamic, which negatively correlate with *gamma* frequencies (Milikovsky *et al*., 2017), is a good predictor for epileptogenesis in the RHEB1p.P37L mouse model.

The cortical migration defect is neither necessary nor sufficient to induce spontaneous development of seizures

Cortical malformations occur during the early embryonic development and are generally associated with the development of epileptic activity (Represa, 2019). Therefore, early treatment that might prevent the formation of a cortical malformation could consequently reduce the chance to develop epilepsy. To assess if early transient downregulation of the mTOR pathway upon overexpression of RHEB1p.P37L could prevent the development of the heterotopic nodule, we injected pregnant female mice starting 1 day after *in utero* electroporation for two consecutive days with 1 mg/kg of rapamycin (Figure 5A). Prenatal downregulation of the mTOR pathway significantly improved, but did not completely normalize, the migration pattern of the transfected neurons, with 75% of the targeted cells successfully migrating out (% targeted

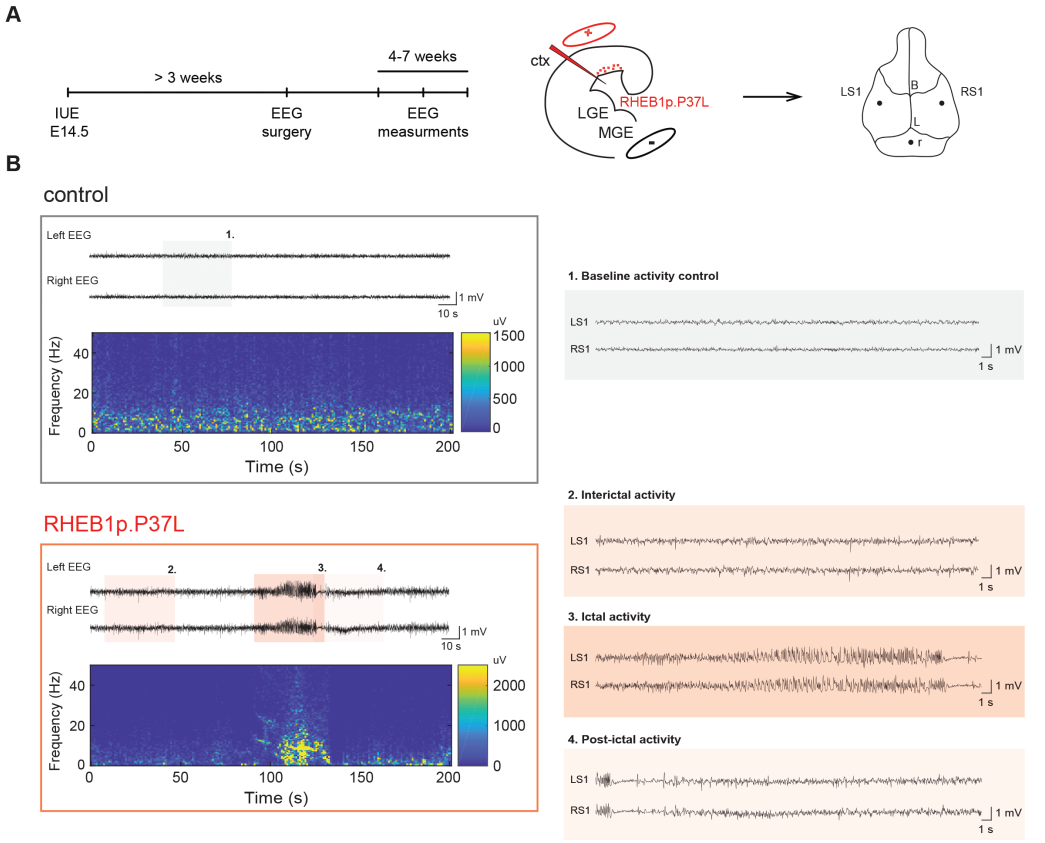

Figure 3. RHEB1p.P37L targeted mice develop spontaneous tonic-clonic seizures (A) Schematic representation of the timeline and *in utero* electroporation (IUE) experiment, indicating the cortical area targeted and position of the electrodes placed during the EEG surgery (B) *left*: example EEG traces and relative spectrogram from the left and right Somatosensory cortices of control mice (non-targeted mice from the same litters as the RHEB1p.P37L mice) and RHEB1p.P37L targeted mice; colored boxes are zoomed in on the *right*: box 1 represents the baseline activity of a control mouse and box 2 the interictal activity, box 3 the ictal (seizures) activity and box 4 the post-ictal phase of a RHEB1p.P37L targeted mouse. Ctx = cortex; LGE = lateral ganglion eminence; MGE = medial ganglion eminence; LS1 = left S1; RS1 = right S1; B = bregma; L= lambda; r = reference electrode.

cells in layer 2/3: $F(2, 39)=54.79$, $p<0.0001$, One-way ANOVA; empty vector *vs* RHEB1p.P37L-prenatal rapamycin, $p=0.005$; RHEB1p.P37L *vs* RHEB1p.P37L-prenatal rapamycin, $p<0.0001$; Tukey's multiple comparison) (Figure 5B). In addition, prenatal rapamycin treatment successfully prevented the formation of a cortical nodule in 9 out of 11 mice. However, 7 out of the 11 targeted mice (58%) still showed spontaneous seizures, including 5 mice that did not develop a heterotopic nodule (Figure 5C). Average onset of seizures was comparable to the non-treated RHEB1p.P37L mice (32.6 days ± 2.3; Chi square (1)=0.69, Log-rank test, data not shown). When separating the cortical migration patterns in mice with and without seizures, a clear correlation was seen between migration pattern and presence or absence of seizures: RHEB1p.P37L-prenatal treated mice with seizures showed overall a more severe migration deficit compared to RHEB1p.P37L-prenatal treated mice that did not show seizures ($\eta_p=0.821$, $\eta_p^2=0.674$, Eta measure of association) (Figure 5D). In fact, the percentage of cells that reached layer 2/3 in the somatosensory cortex of RHEB1p.P37L-prenatal treated mice with seizures (63%), was significantly lower than control mice (98%) and RHEB1p.P37L-prenatal treated

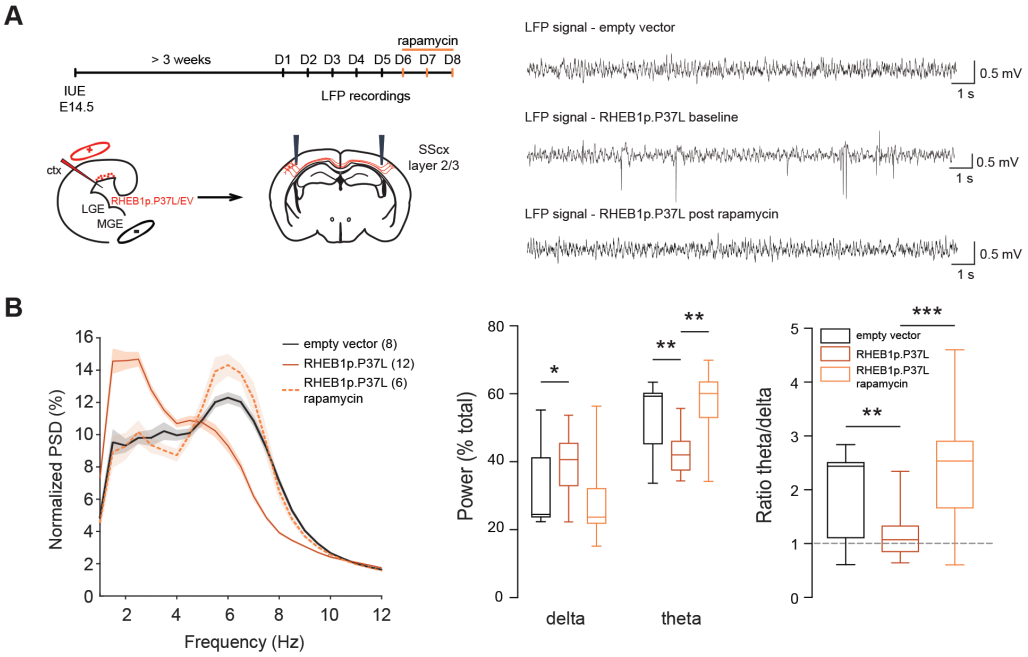

Figure 4. RHEB1p.P37L targeted mice show a decrease in the *theta* oscillations that can be reversed by rapamycin (A) *left:* Schematic representation of the timeline of the *in utero* electroporation (IUE), local field potential (LFP) recordings and rapamycin injections; *right:* example LFP traces for each condition. (B) Normalized Power spectrum density (PSD) of the different frequencies averaged bilaterally over 5 days of recordings and calculation of the *delta* (2-4 Hz) and *theta* (4-8 Hz) frequency bands over the total power, and relative ratio *theta*/*delta*; shadows in the PSD indicate the SEM and box plots represent minimum and maximum value with median; numbers within brackets indicate number of measured animals per group; ctx = cortex; LGE = lateral ganglion eminence; MGE = medial ganglion eminence; SScx = somatosensory cortex * p<0.05, ** p<0.01, *** p<0.001.

mice without seizures (93%) (F(2, 29)=29.21, p<0.0001, One-way ANOVA; empty vector *vs* Rheb1p.P37L-no seizures, p=0.66; empty vector *vs* Rheb1p.P37L-seizures, p<0.0001; Rheb1p.P37L-no seizures *vs* Rheb1p.P37L-seizures, p<0.0001; Tukey's multiple comparison) (Figure 5D).

The results obtained from the prenatal rapamycin treatment suggest a correlation between number of ectopic cells and the development of spontaneous seizures. However, previous *in utero* models of FCD showed that hyperactivation of mTOR, independently of the presence of ectopic cells, is sufficient to cause seizures (Hsieh *et al*., 2016). Whether the cortical malformation by itself -independent of continued mTOR signaling- is sufficient in causing the development of epilepsy has never been demonstrated. To verify this in our mouse model, we used a genetic approach, in combination with *in utero* electroporation, to either turn on (Lox-Stop-Lox(LSL)-RHEB1p.P37L vector) or off (floxed-RHEB1p.P37L vector) the expression of the RHEB1p.P37L gene upon tamoxifen administration during different stages of the cortical development (Figure 6A and Figure 7A, respectively). *In utero* electroporation of the LSL-RHEB1p.P37L gene in absence of tamoxifen, as expected, did not result in a migration deficit (Figure 6B). However, regardless of the developmental time point (P7 or P21) at which expression of RHEB1p.P37L was initiated (Figure 6A), a subset of the successfully transfected mice (38% of the P7 group and 50% of the P21 group) developed spontaneous seizures, albeit with a delayed onset (Chi square= 10.18, p=0.006; Log-rank test, data not shown), suggesting that also in our mouse model the presence of a cortical migration

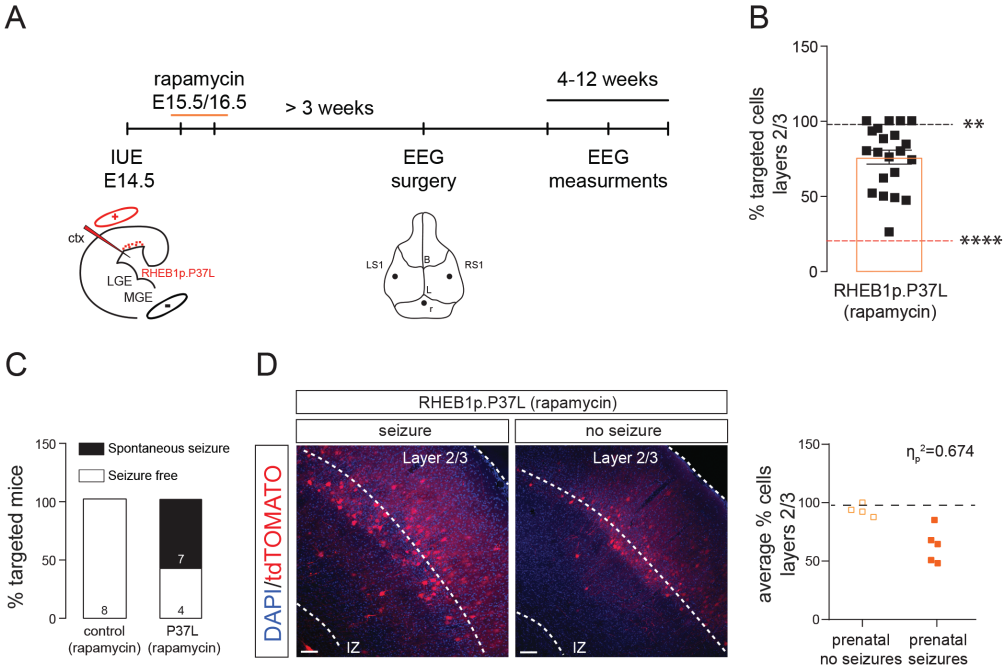

Figure 5. Prenatal rapamycin prevents the formation of a heterotopic nodule but does not fully prevent the epilepsy phenotype (A) Schematic representation of the timeline of the *in utero* electroporation (IUE), rapamycin injections, EEG surgery and measurements. (B) quantification of the percentage of tdTomato+ cells that managed to migrate out to layer 2/3 in mice prenatally exposed to rapamycin (2-3 pictures analyzed per mouse, with a total number of 11 mice); dashed lines indicate the mean value of cells reaching layers 2/3 in empty vector control mice (n=5, black dashed line) and in RHEB1p.P37L mice (n=5, red dashed line). (C) Percentage of targeted mice showing spontaneous seizures, control mice are non-targeted mice from the same litters as the RHEB1p.P37L mice prenatally exposed to rapamycin; numbers in the bar plots indicate the number of mice measured with EEG per group (note that out of the 7 mice that showed spontaneous seizures, 2 had an heterotopic nodule). (D) Representative images of RHEB1p.P37L mice prenatally exposed to rapamycin that showed or did not show seizures and degree of association (partial Eta squared) between the migration phenotype (mean values of % targeted cells in layers 2/3, dependent scale variable) and the presence (n=5, excluding the mice that showed heterotopia) or absence of seizure (n=4) (independent nominal variable) in RHEB1p.P37L mice, showing strong association between severity of the migration deficit and presence of seizure; scale bars: 100 µm; values in the bar plot in B are represented as mean ± SEM; ctx = cortex; LGE = lateral ganglion eminence; MGE = medial ganglion eminence; LS1 = left S1; RS1 = right S1; B = Bregma; L = Lambda; r = reference electrode; IZ = intermediate zone ** p<0.01, **** p<0.0001.

VI

defect is not required to cause development of seizures by RHEB1p.P37L expression (Figure 6B). *Vice versa*, overexpression of the floxed-RHEB1p.P37L in absence of tamoxifen resulted in the formation of a clear heterotopic nodule (Figure 7B). This time, reducing mTOR activity by inducing deletion of RHEB1p.P37L at P14 (a time point at which the heterotopic nodule is already formed) prevented the development of seizures in all (9/9) mice (Figure 7A and B, group 1). Furthermore, deletion of RHEB1p.P37L after epileptogenesis, completely stopped the seizures within one week from the last tamoxifen injection (N=4, last EEG measurements performed between day 85 and 90) (Figure 7A and B, group 2). Taken together, these results indicate that the MCD is neither necessary nor sufficient for the development of spontaneous seizures in our mouse model, and that early onset treatment alone might not be sufficient to fully prevent the development of seizures.

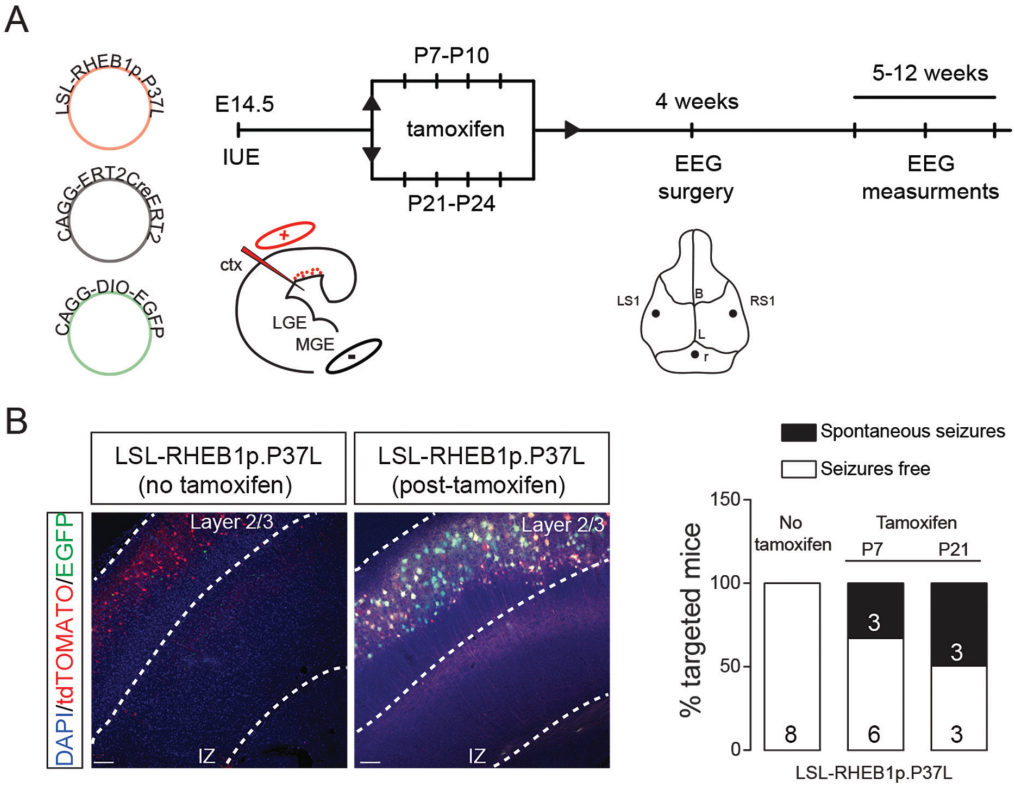

Figure 6. The cortical migration defect is not necessary to induce seizures (A) Simplified schematic of the DNA plasmids used in this experiment and timeline of the *in utero* electroporation (IUE), timepoints of Tamoxifen injections (4 days of injection starting at P7 or at P21), EEG surgery and measurements. The EGFP in the CAGG-DIO-EGFP construct will be expressed only upon efficient cre-dependent recombination induced by tamoxifen injection (B) representative images of adult mice injected *in utero* with the constructs shown in (A) without and with Tamoxifen injections, showing proper cortical migration and subsequent efficient activation of Cre by Tamoxifen injections. Bar graph indicates the percentage of targeted mice showing spontaneous seizures upon Tamoxifen injection, measured with EEG until 12 weeks of age; numbers in the bar plots indicate the number of mice; scale bars: 100 µm; LSL = loxP-STOP-loxP; ctx = cortex; LGE = lateral ganglion eminence; MGE = medial ganglion eminence; LS1 = left S1; RS1 = right S1; B = Bregma; L = Lambda; r = reference electrode; IZ = intermediate zone.

RHEB1p.P37L expressing neurons induce functional alterations in the contralateral hemisphere through aberrant axonal projections

The mTOR pathway was previously shown to play an important role in axonal outgrowth, with functional effects on neuronal network formation (Choi *et al*., 2008; Nie *et al*., 2010; Goto *et al*., 2011; Feliciano *et al*., 2012; Gong *et al*., 2015; Sokolov *et al*., 2018). Since transfection of a limited number of neurons in the brain with hyperactivation of the mTOR pathway is enough to cause seizures, independently from cell misplacement, we hypothesized that this could be due to aberrant network connectivity caused by RHEB1p.P37L overexpression. Therefore, we investigated the effect of RHEB1p.P37L on axonal length and branching. Overexpression of RHEB1p.P37L in primary hippocampal neurons *in vitro* caused a significant increase in axonal length and axonal branching, compared to the empty vector control (axonal length: Mann-Whitney U = 32, $p<0.0001$, Mann-Whitney test; axonal branches: Mann-Whitney U = 53, $p<0.0001$, Mann-Whitney test) (Figure 8A). *In vivo*, axons from the callosal projection neurons

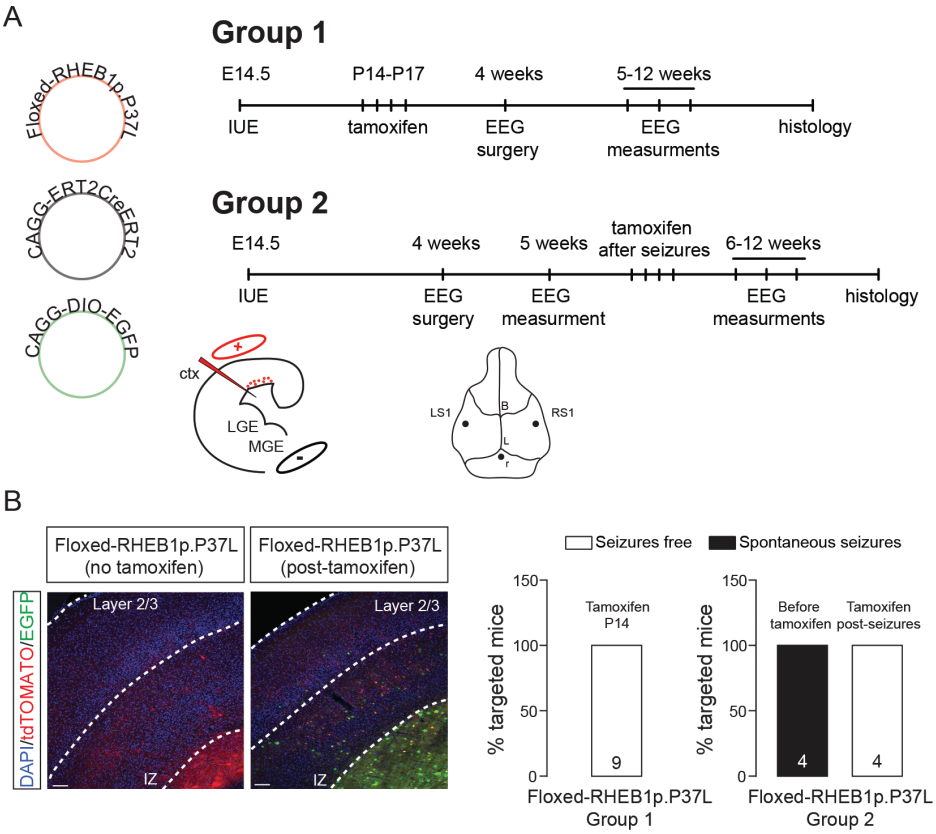

Figure 7. The cortical migration defect alone is not sufficient to induce seizures (A) Simplified schematic of the DNA plasmids used in this experiment and timelines of the *in utero* electroporation (IUE), timepoints of Tamoxifen injections (4 days of injection starting at P14 or after seizure onset), EEG surgery and measurements. (B) representative images of adult mice injected *in utero* with the constructs shown in (A) without and with Tamoxifen injections, showing cortical migration defect and efficient activation of Cre by Tamoxifen injections. Bar graphs indicate the percentage of seizure-free targeted mice upon Tamoxifen injection (group 1: P14 and group 2: post-seizures) measured with EEG until 12 weeks of age; numbers in the bar plots indicate the number of mice; scale bars: 100 µm; ctx = cortex; LGE = lateral ganglion eminence; MGE = medial ganglion eminence; LS1 = left S1; RS1 = right S1; B = Bregma; L = Lambda; r = reference electrode; IZ = intermediate zone.

originating from the somatosensory cortex layer 2/3 project to the contralateral hemisphere and innervate prevalently the border region between the primary (S1) and secondary (S2) somatosensory cortex (Fenlon *et al.*, 2017). Since RHEB1p.P37L overexpression affects axonal outgrowth and arborization *in vitro*, it is conceivable that *in vivo* overexpression of RHEB1p.P37L affects the callosal projections, thereby affecting not only the ipsilateral hemisphere, but also neurons in the non-transfected contralateral hemisphere. Analysis of the callosal axonal growth in matched equally targeted coronal sections revealed that in the RHEB1p.P37L overexpressing conditions, axonal terminals in the contralateral hemisphere, show a wider distribution compared to controls, reaching S1, S1/S2 border and S2 somatosensory cortices (Figure 8B). Furthermore, a significant difference was found in the distribution of the axonal terminals across the different layers in the contralateral hemisphere. While in the control condition most of the terminals were located in layer 2/3, with a lower abundance in layer 5, in the RHEB1 mouse model we found that most of the terminals were located in the deeper layers

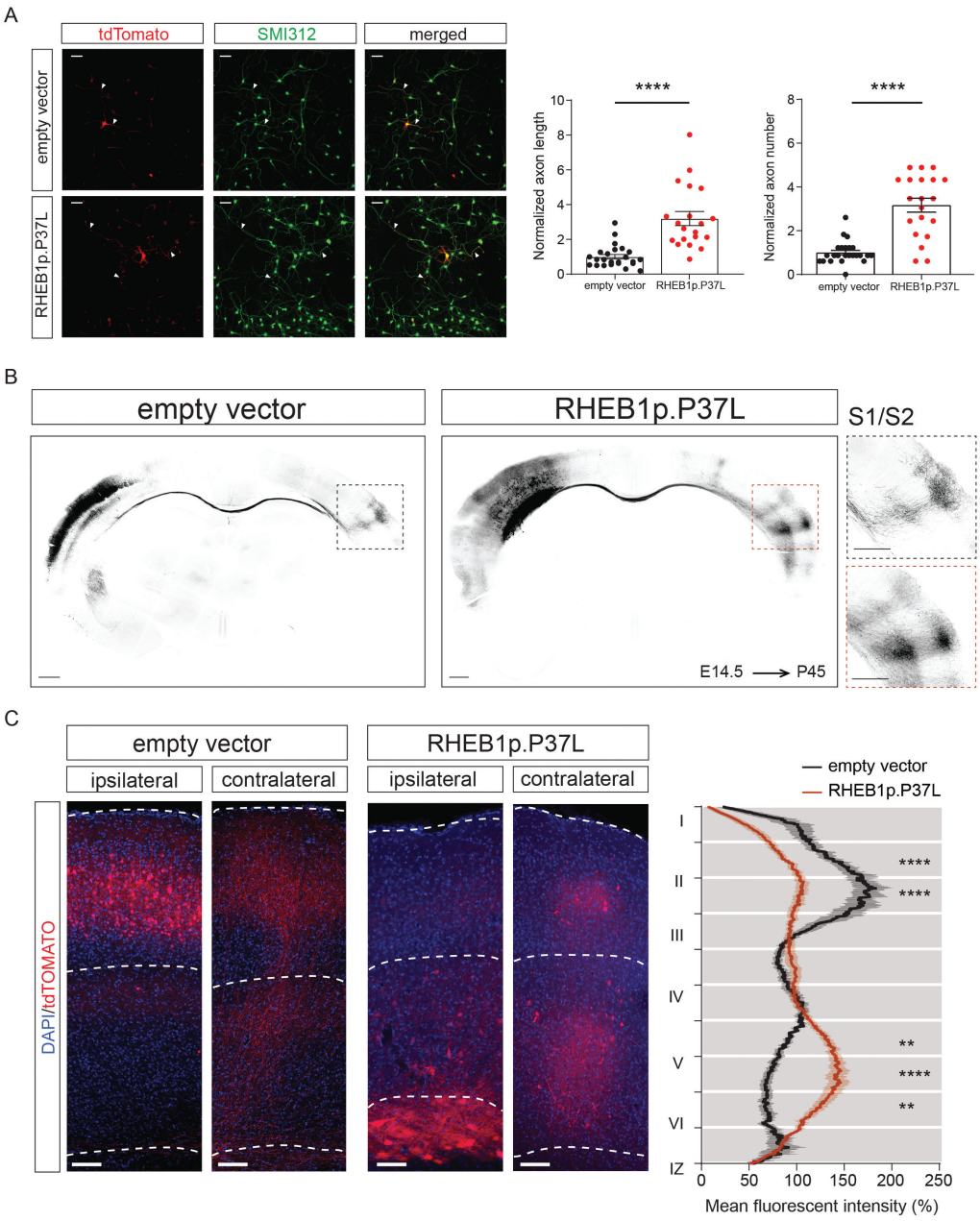

Figure 8. RHEB1p.P37L overexpression induces an increase in axon length and branching both *in vitro* and *in vivo* (A) representative images of primary hippocampal cultures transfected at day *in vitro* 1 (DIV1) with either empty vector control or RHEB1p.P37L constructs (tdTomato, in red) and fixed and stained at DIV4 with a pan axonal marker SMI312 (in green); bar plots show the quantification of total axonal length and branching; data in the plots are represented as mean ± SEM with the dots indicating the single value of each neuron analyzed (minimum 20 cells from 2 different neuronal batches were analyzed); arrowheads indicate the axons. (B) coronal sections in grey scale of an empty vector and a RHEB1p.P37L *in utero* electroporated mouse brain on the left S1 (ipsilateral) with a higher magnification of the axon terminals on the contralateral primary S1 (C) representative images of ipsilateral and contralateral S1 area of an empty vector and a RHEB1p.P37L mouse coronal section with quantification of the axonal projections across the different layers in the contralateral cortex (from 3 and 4 animals per group for a total of 10 and 23 pictures analyzed respectively); scale bars: (A) 50 µm (B) 500 µm (C) 100 µm ** p<0.01, **** p<0.0001.

of the cortex (F(9,279)=12.56, p<0.0001, Two-way repeated measure ANOVA; layer 2/3 (bin2-3 from the top): p<0.0001; layer 5: bin7, p=0.0074, bin8, p<0.0001, bin 9, p=0.002; Sidak's multiple comparisons test) (Figure 8C).

To investigate if the contralateral projections give rise to functional connections, we made use of optogenetics. We electroporated ChannelRhodopsin (ChR2) (Petreanu *et al*., 2007) together with either the empty vector control or the RHEB1p.P37L construct and recorded the postsynaptic response to widefield optogenetic stimulation after patch-clamping layer 2/3 (L2/3) and layer 5 (L5) neurons in the contralateral somatosensory cortex (S1) (Figure 9A). We found that the amplitude of evoked excitatory postsynaptic current (EPSC) following optogenetic stimulation in L2/3 of the contralateral somatosensory cortex is increased in the RHEB1p.P37L condition compared to the empty vector control condition (Mann-Whitney U = 3, p=0.006, Mann-Whitney test), while the input strength to L5 remains unchanged (Mann-Whitney U = 33, p=0.3562, Mann-Whitney test) (Figure 9B and Supplementary table 2 for statistics). When analysing the total charge of the compound postsynaptic response we observed similar response patterns (L2/3: Mann-Whitney U = 3, p=0.006, Mann-Whitney test; L5: Mann-Whitney U = 30, p=0.2428, Mann-Whitney test) (Figure 9B and Supplementary table 2 for statistics). The basic properties of L2/3 and L5 contralateral cells in empty vector control and RHEB1p.P37L conditions were unaffected (Supplementary figure 5 and Supplementary table 2 for statistical analysis). To control for bias of ChR2 expression level between empty vector control and RHEB1p.P37L groups, we recorded postsynaptic responses with light intensities ranging between 15.6 and 166.5mV and found that the EPSCs in L5 of both empty vector control and RHEB1p.P37L groups grade proportionally with increasing light intensity (Figure 9C), suggesting that the group differences we observed for L2/3 are not caused by differences in ChR expression levels. Bath application of TTX in the RHEB1p.P37L group decreased the post-synaptic responses evoked by photo-stimulating ChR2 expressing fibers to noise level, which is indicative of action potential driven neurotransmitter release (t(5)=4.8, p=0.005, two-tailed paired t-test) (Figure 9D). These data suggest increased synaptic strength to the contralateral somatosensory cortex upon overexpression of RHEB1p.P37L.

Blocking vesicle release of RHEB1p.P37L overexpressing neurons is sufficient to reverse the hyperexcitability phenotype on the contralateral side and stop the seizures

Having shown that the RHEB1p.P37L expressing neurons are anatomically and functionally connected to the contralateral hemisphere, we assessed whether also the intrinsic physiological properties in the contralateral hemisphere are affected. Whole cell patch clamp recordings were performed on RHEB1p.P37L transfected neurons that managed to migrate out to layer 2/3 of the somatosensory cortex (S1), surrounding non-transfected neurons (ipsilateral) and non-transfected neurons in S1 on the contralateral side (Figure 10A) in 3 weeks old mice. Measuring the basic properties of the neurons, overexpression of RHEB1p.P37L resulted in an increase in the capacitance (Cm) compared to empty vector control, which is consistent with the increase in soma size (F(3, 111)=6.53, p=0.0004, One-way ANOVA; control *vs* targeted RHEB1p.P37L cells: p=0.0003; Tukey's multiple comparisons test; for all the comparisons see Supplementary table 3) (Figure 10B). Additionally, the membrane resistance (*Rm*) was decreased, whereas the resting membrane potential (*Vm*) was unchanged compared to empty vector control (*Rm*: F(3, 111)=10.47, p<0.0001, One-way ANOVA; control *vs* targeted RHEB1p.P37L cells: p<0.0001; Tukey's multiple comparisons test; *Vm*: F(3, 111)=0.36, p=0.78, One-way ANOVA; control *vs* targeted cells: p=0.96; Tukey's multiple comparisons test; for all the comparisons see Supplementary table 3) (Figure 10B). Depolarizing the neurons with increasing current injections, revealed that RHEB1p.P37L expressing neurons are hypoexcitable compared

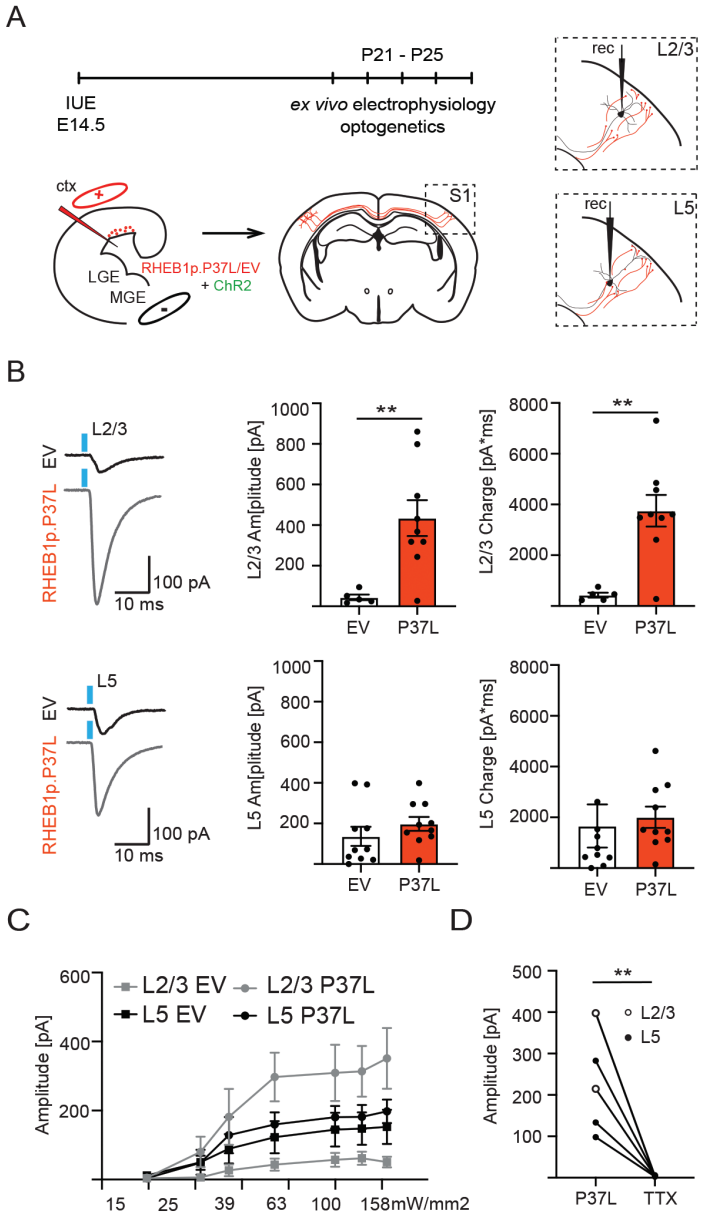

Figure 9. Overexpressing RHEB1p.P37L increases synaptic connectivity on the contralateral hemisphere. (A) Schematic representation of the timeline and experimental conditions of the *in utero* electroporation (IUE) and *ex vivo* whole-cell patch clamp recordings with wide-field optogenetic stimulation. (B) Example traces and analysis of the compound postsynaptic responses after photostimulation, showing that postsynaptic response amplitudes and total charge in L2/3 are increased in RHEB1p. P37L expressing mutants, while responses in L5 are unaffected. (C) The postsynaptic response at increasing light stimulation intensities are depicted for both L2/3 and L5 in empty vector control and RHEB1p. P37L mutant. (D) Wash-in of TTX proves the action potential dependence of photostimulation evoked responses in L2/3 and L5. ** p<0.01. Scale bar: 100 µm Standard errors show the SEM.

to non-transfected ipsilateral, contralateral and control neurons, without a change in the threshold *Vm* (Threshold: F(3, 94)=0.59, p=0.62 and see Supplementary table 4 for other statistics) (Figure 10C). Of note, overexpression of the empty vector did not affect neuronal excitability compared to non-transfected neurons in the same mice or compared to non-targeted mice (See Supplementary table 4 for statistics) (Figure 10C). Interestingly, the ipsilateral non-transfected surrounding neurons in RHEB1p.P37L mice did not show altered excitability compared to empty vector control, but the non-transfected neurons in layer 2/3 on the contralateral hemisphere showed a significant increase in excitability (See Supplementary table 4 for statistics) (Figure 10C).

Our findings that the targeted cells have increased connectivity but are hypoexcitable and that non-transfected cells in the contralateral side, but not in the ipsilateral side, are also affected suggest that there are cell non-autonomous mechanisms in place that are not confined to cells surrounding the cortical malformation itself. Targeted neurons

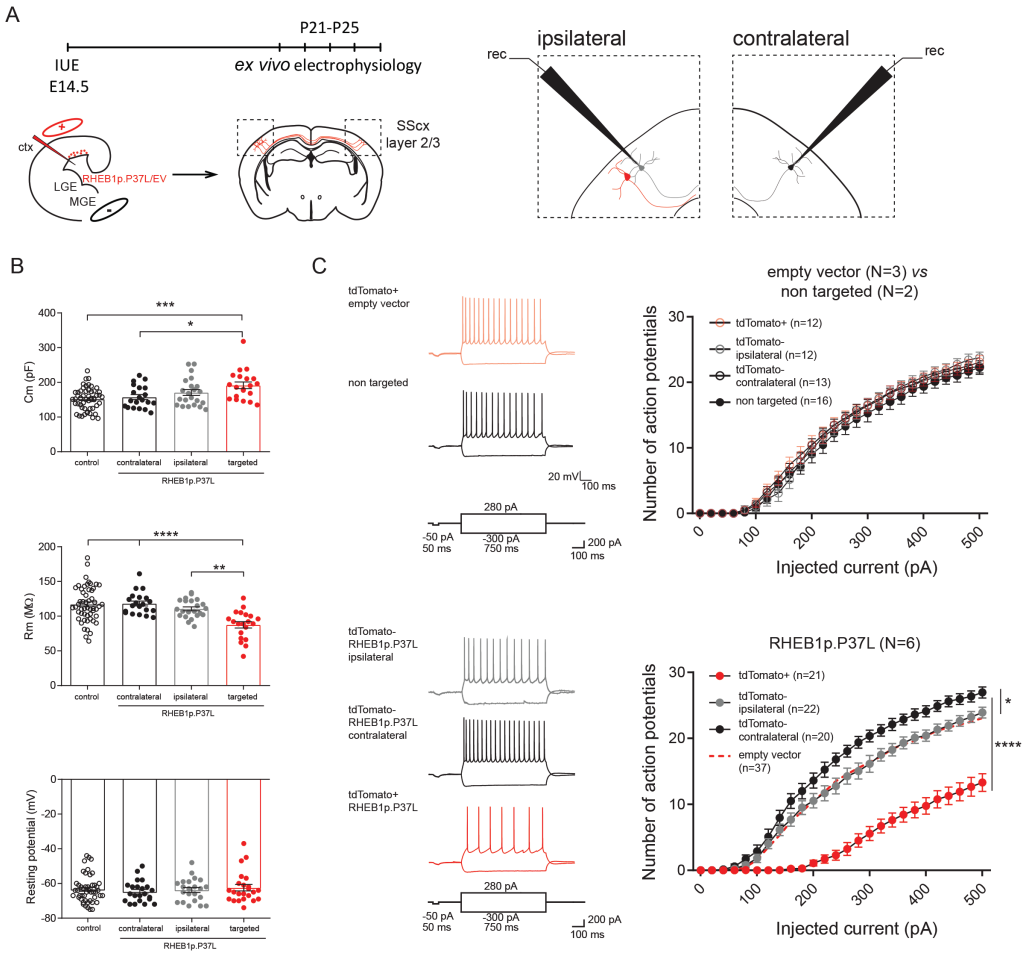

Figure 10. RHEB1p.P37L expressing neurons are hypoexcitable while non-transfected contralateral cells show increase in excitability (A) Schematic representation of the timeline and experimental conditions of the *in utero* electroporation (IUE) and *ex vivo* whole-cell patch clamp recordings showing the targeted cells patched in the ipsilateral side (targeted S1, layer 2) and non-targeted cells in the ipsilateral and contralateral sides. (B) Analysis of the passive membrane properties (capacitance, membrane resistance and resting membrane potential) of pyramidal cells in layer 2, S1 of mice targeted with an empty vector construct (control) and targeted and non-targeted pyramidal cells in layer 2, S1 of RHEB1p.P37L mice; data in the graphs are represented as mean ± SEM with the dots indicating the single value of each neuron analyzed. (C) Number of action potentials in response to increasing depolarizing currents and representative example traces, N numbers represent number of mice and n numbers within brackets represent number of cells analyzed; ctx = cortex; LGE = lateral ganglion eminence; MGE = medial ganglion eminence; EV = empty vector * p<0.05, ** p<0.01, *** p<0.001, **** p<0.0001.

could potentially alter the neighboring cells through the release of exosomes, small vesicles containing molecules that might mediate pathogenicity through an unknown mechanism, as was previously shown in an *in vitro* system (Patel *et al*., 2015). However, since we did not find physiological alterations in the surrounding ipsilateral non-targeted cells, we hypothesized that in our mouse model epilepsy is mainly mediated by the altered axonal connectivity, either through an increase in axonal branching, leading to more synaptic contacts or through an increase in synaptic strength of the existing connections.

Therefore, to test if the targeted RHEB1p.P37L positive cells can alter the

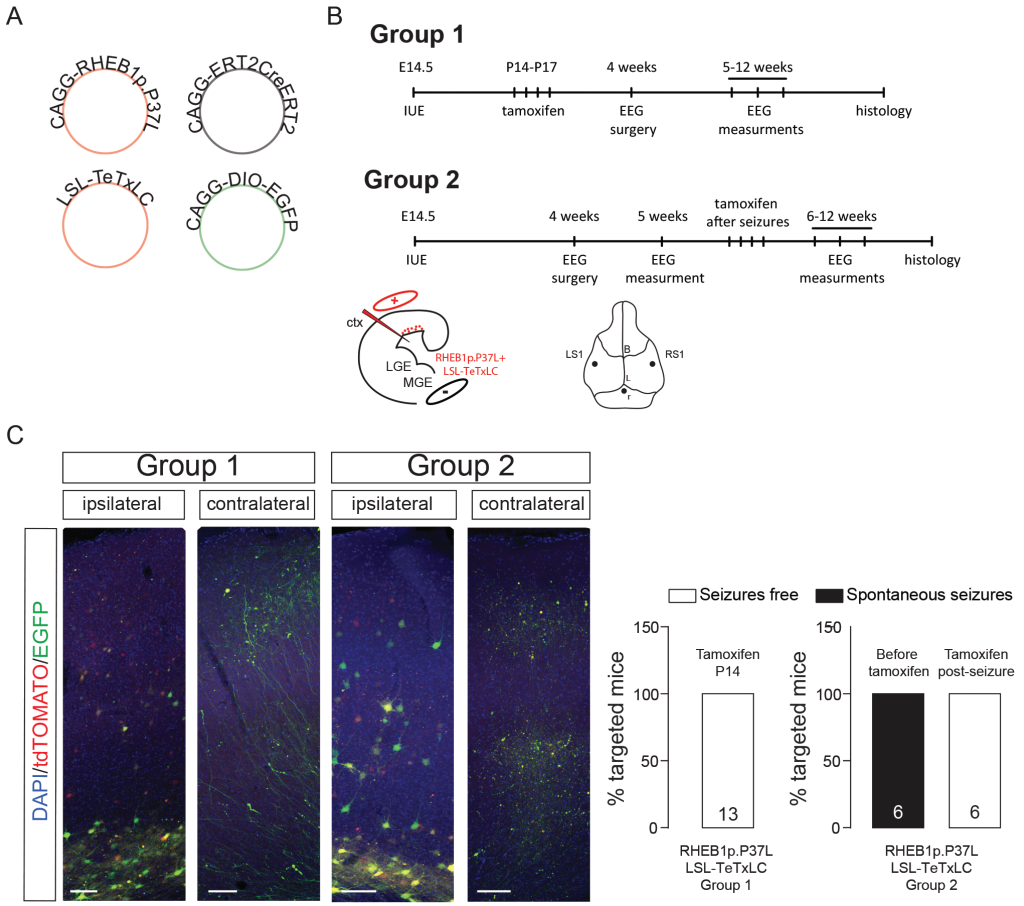

Figure 11. Inhibiting synaptic transmission by blocking vesicular release from the targeted cells is enough to prevent and abolish the occurrence of seizures. (A) Simplified schematic of the DNA plasmids used in this experiment. (B) timelines of the *in utero* electroporation (IUE), timepoints of Tamoxifen injections (Group 1: before seizures, Group 2: after seizures), EEG surgery and measurements. (C) representative image of ipsilateral and contralateral S1 area of mice targeted with the constructs shown in (A) and injected with tamoxifen starting at P14 (Group 1) or after seizures (Group 2). Bar graphs indicate the percentage of seizures-free targeted mice upon Tamoxifen injection (Group 1: P14, Group 2: post-seizures) measured with EEG until 12 weeks of age; numbers in the bar plots indicate the number of mice; scale bars: 100 µm; ctx = cortex; LGE = lateral ganglion eminence; MGE = medial ganglion eminence; LS1 = left S1; RS1 = right S1; B = Bregma; L = Lambda; r = reference electrode.

contralateral side through vesicular release, we made use of the Tetanus toxin light chain, known to specifically cleave the SNARE-complex protein Synaptobrevin/VAMP2 (Syb2) (Schiavo *et al.*, 1992; Sweeney *et al.*, 1995). VAMP2 is part of the SNARE complex that allows synaptic vesicles fusion and release of neurotransmitters (Gaisano *et al.*, 1994; Verderio *et al.*, 1999) and recently it has been shown to mediate also the vesicular release of BDNF from axon and dendrites, thereby regulating proper cortical connectivity (Shimojo *et al.*, 2015). We co-transfected using *in utero* electroporation the RHEB1p.P37L with a LSL-TeTxLC and a CAGG-ERT2-Cre-ERT2 vectors that would allow the activation of the Tetanus toxin light chain upon Tamoxifen injection (Yu *et al.*, 2004; Matsuda and Cepko, 2007) (Figure 11A). We first observed using whole-cell patch clamp recordings that activating the Tetanus toxin early during development (P14), did not change the intrinsic activity and basic properties

of targeted neurons co-transfected with the RHEB1p.P37L mutant and the Tetanus toxin compared to RHEB1p.P37L targeted neurons without the toxin (Supplementary figure 6A, see Supplementary table 5 for statistics). Interestingly, preliminary data reveals that the hyperexcitability phenotype of the contralateral non-targeted cells observed in the RHEB1p.P37L mice appeared to be normalized to control condition upon activation of Tetanus toxin (Supplementary figure 6B, see Supplementary table 5 for statistics). Additionally, activation of the Tetanus toxin early during development (P14), completely prevented the development of seizures (Figure 11B and C, group 1). However, as previously shown (Wang *et al*., 2007), intrinsic neuronal activity during early brain development is crucial for axonal growth and branching. In fact, it was shown that blocking synaptic transmission using Tetanus toxin interferes with proper cortical axonal formation resulting in a reduction and disappearance of axonal projections (Wang *et al*., 2007). Indeed, we also observed an overall reduction of axonal branching across the different layers in the contralateral side when activating the tetanus toxin at P14 and a complete block of axonal growth when co-transfecting the RHEB1p.P37L with a Tetanus toxin construct active during embryonic development which leads to no development of seizures (data not shown). Therefore, to assess if the effect we observed on the epilepsy is indeed through vesicular release and not only caused by reduced axonal projections, Tamoxifen was administered in 5 weeks old mice, when the cortical connectivity is complete and after the mice showed seizures (Figure 11B and C, group 2). After two days of Tamoxifen administration, 3 out of 6 mice (Supplementary table 6) stopped showing any seizures and 2 weeks after the last tamoxifen injection all mice appeared to be seizure free till the day of sacrifice (Supplementary table 6). These results indicate that inhibiting synaptic transmission by blocking vesicular release from the targeted cells is enough to stop the occurrence of seizures in our mouse model.

DISCUSSION

In this study, we investigated the mechanisms behind the spontaneous tonic-clonic seizures developed by a mouse model generated overexpressing *in utero* a mTOR-related ID mutation in the *RHEB1* gene (Reijnders *et al*., 2017). We showed that overexpression of the RHEB1p.P37L mutant causes the development *in vivo* of heterotopia with typical cellular features of human MCD such as enlarged dysplastic neurons with altered morphology and increase in mTOR activation. Furthermore, the presence of cortical malformations is accompanied by the development of spontaneous tonic-clonic seizures and alterations of the cortical brain dynamics that are rescued by administration of rapamycin, a known blocker of the mTOR pathway. Using a pharmacological and genetic approach we showed that the presence of the cortical malformation by itself is neither necessary nor sufficient to induce epilepsy, while rescuing the abnormal axonal connectivity is enough to both stop and prevent the development of seizures.

Similar to previously generated IUE mouse models of MCD, our model develops clear heterotopia, strikingly resembling focal human cortical malformations, associated with mTOR hyperactivity and reliable spontaneous seizures (Feliciano *et al*., 2011; Tsai *et al*., 2014; Kassai *et al*., 2014; Baek *et al*., 2015; Lim *et al*., 2015, 2017; Hsieh *et al*., 2016; Hanai *et al*., 2017; Hu *et al*., 2018; Park *et al*., 2018; Ribierre *et al*., 2018). The malformation seen in our mouse model is characterized by white matter heterotopia and neuronal misplacement across the different cortical layers, while maintaining the molecular fingerprint belonging to layer 2/3 neurons. However, it is difficult to categorize as a specific type of MCD since it includes characteristics of heterotopia, FCD type I and type IIa (with no Balloon cells observed) (Barkovich *et al*., 2012).

The targeted cells however do present common features of several types of mTOR dependent MCDs including enlarged and dysplastic cells with mTOR hyperactivation (Crino, 2011).

Recently, a constitutive active form of *RHEB1* (RHEB1p.S16H) was used to develop a IUE mouse model showing a migration deficit resembling FCD and spontaneous epilepsy (Lafourcade *et al*., 2013; Hsieh *et al*., 2016; Nguyen *et al*., 2019). Using this mouse model, it was shown that the presence of a cortical malformation is not necessary to induce seizures but the cause of epilepsy was not further investigated (Hsieh *et al*., 2016). Furthermore, it was suggested that the somatosensory cortex might be a non-epileptogenic area. This is in contrast with our mouse model using the human ID-related RHEB1p.P37L variant, where targeting the S1 area mice develop reliable seizures. One reason for these contradicting findings might be the severity of the mutation itself on RHEB1 function. Indeed, preliminary data from our lab reveals that RHEB1p.S16H can still be partially inhibited by the TSC1/2 complex, but RHEB1p.P37L cannot. This indicates that the human mutation results in a more active RHEB1 protein. Exploring the causes of epileptogenesis, we could observe physiological alterations in the contralateral cortex, anatomically connected to the ipsilateral S1 cortex, suggesting that there are cell non-autonomous effects caused by cells targeted with the RHEB1p.P37L construct which are not confined to the ipsilateral targeted area. Considering the abnormal axonal connectivity seen in our mouse model, this raises the possibility that also other cortical and sub-cortical areas not analyzed in this study might be affected, thereby providing an explanation how a small percentage of targeted cells, independently on their location, can lead to a generalized phenomenon such as epilepsy. Indeed, in line with previously generated mouse models of mTOR dependent epilepsy (Backman *et al*., 2001; Abs *et al*., 2013; Hsieh *et al*., 2016; Koene *et al*., 2019), we show that seizures can occur independently of the presence of a macroscopic cortical lesion, thereby suggesting that more subtle microscopic alterations and possibly abnormal neuronal connectivity are at the core of the epileptogenesis process.

Everolimus and rapamycin (Sirolimus) have been shown to be beneficial to treat TSC associated epilepsy, despite the immunosuppressant side-effects, (French *et al*., 2016; Overwater *et al*., 2016, 2019), but not for treating cognitive deficits (Krueger *et al*., 2017; Overwater *et al*., 2019). In this study we investigated the potential of a short prenatal rapamycin treatment in improving both malformation defects and epilepsy, but preventing the possible side effects (developmental delays and poor gain weight) (Anderl *et al*., 2011; Way *et al*., 2012; Fang *et al*., 2013; Tsai *et al*., 2013). We showed that short rapamycin treatments can cause a substantial improvement of the cortical malformation defects and can prevent the development of seizures in almost 50% of the cases. This result, in combination with the finding that a transient acute rapamycin treatment post-expression of seizures can temporarily stop the occurrence of seizures, is clinically promising because it shows that short and intermittent rapamycin treatments could potentially be beneficial also for treating epilepsy patients due to mTOR related MCD, similar to mTOR related epilepsy without MCD (Abs *et al*., 2013). Future studies will have to assess if a combination of prenatal and postnatal treatment with rapamycin can be sufficient to significantly reduce the epileptic events, as shown for brain malformations, without causing major side effects (Anderl *et al*., 2011; Way *et al*., 2012).

When rapamycin is not the preferred choice of treatment, alternative anti-epileptic drugs (AEDs) will have to be found for patients where the epilepsy is intractable with the existing AEDs. Our mouse model offers the perfect tool to test novel AEDs in an *in vivo* model. However, considering the variability in the number of seizures exhibited in our mouse model, it will be beneficial to focus on different parameters when assessing the potential therapeutic efficiency of anti-epileptic drugs. For this purpose, the *theta* frequency oscillation, which we have found to be affected and normalized upon rapamycin treatment, represents a good

biomarker for assessing the potential therapeutic value of treatments in our mouse model (Arabadzisz *et al*., 2005; Chauvière *et al*., 2009; Marcelin *et al*., 2009; Milikovsky *et al*., 2017).

When antiepileptic drugs are not a choice, surgery is often considered as an alternative treatment in MCD-related epilepsy. Human electrophysiological findings show that seizures can often have multiple starting points, besides the brain lesion itself (Chassoux *et al*., 2008; Major *et al*., 2009). Therefore, from a clinical point of view, it is important to evaluate if the seizures can also originate from the cells surrounding the cortical malformation itself. Even though EEG and LFP do not have the spatial resolution to assess the primary epileptogenic zone in our model (Herreras, 2016), we showed that mTOR hyperactivation caused by our dominant active mutant is the primary cause behind the epilepsy, since genetically removing the RHEB1p.P37L mutant, both before and after seizures occurred, is sufficient to stop the epilepsy. In addition, we observed altered intrinsic excitability in non-targeted cells in the contralateral cortex. This suggests that there are cell non-autonomous mechanisms in place that could potentially exacerbate the epilepsy phenotype, and these extend beyond the cells surrounding the cortical malformation. With the use of Tetanus toxin, we showed that these effects are directly driven by the abnormal enhanced axonal connectivity, since blocking vesicle release specifically from the cells targeted with the RHEB1p.P37L mutant completely rescues the epilepsy and normalizes the intrinsic firing properties of the non-targeted contralateral cortical neurons. Together, our results indicate that increased axonal connectivity, potentially through a higher number of axonal terminals, in combination with an increase in the single synaptic strength could explain the seizures observed in our mouse model. However, what the exact molecular content is of the vesicles released by the targeted cells is still unknown. Tetanus toxin is primarily used to block synaptic transmission due to its effect on neurotransmitter release, acting on the SNARE complex protein VAMP2 (Schiavo *et al*., 1992). Therefore we hypothesize a role for neurotransmitter mediated communication in causing the epilepsy phenotype. However, cells can also use a different form of communication that involves the local release of small vesicles, such as exosomes, containing various molecules (Budnik *et al*., 2016). While it has been proposed that specific tetanus insensitive VAMP proteins (such as VAMP7) are involved in the release of exosomes in the extracellular space (Fader *et al*., 2009), we cannot exclude the contribution of other types of vesicles to the observed phenotype. Recently it was shown that Tetanus toxin sensitive SNAREs also drive the release of BDNF (Shimojo *et al*., 2015). Some studies suggest that BDNF might contribute to epileptogenesis (Binder *et al*., 2001), leaving the option open that abnormal BDNF signaling could participate in the epileptic phenotype seen in our mouse model. Understanding the contribution of these different signaling pathways can potentially help for the development of new targeted therapeutic strategies to treat MCD associated epilepsy.

In conclusion, in this study we showed that hyperactivating *RHEB1* mutations identified in patients with intellectual disability, megalencephaly and epilepsy, strongly mimic in mice a human MCD-like phenotype, with mTOR pathway hyperactivity and seizures, giving us a tool to study the mechanisms of epileptogenesis in mTOR-dependent epilepsy with brain malformations. We provided the evidence that the cortical malformation *per se* is neither necessary nor sufficient to induce seizures. We showed that the only few neurons in the brain with increased mTOR activity are the driving force behind MCD-related epilepsy causing aberrant connectivity and cell non-autonomous effects that can be reversed by directly blocking vesicular release.

SUPPLEMENTARY INFORMATION

Supplementary Figures

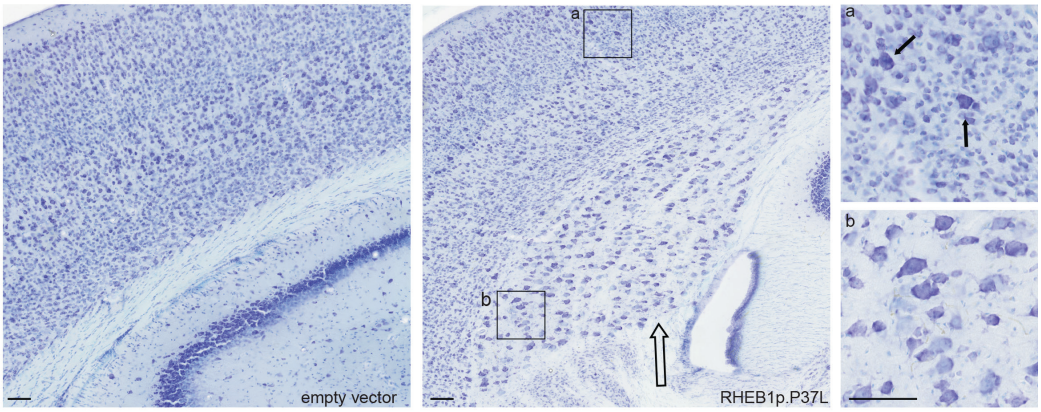

Supplementary figure 1. Presence of heterotopia in mice *in utero* electroporated with the RHEB1p.P37L construct. Nissl staining of coronal brain sections shows the presence of a clear heterotopia (indicated by the empty arrow) in the RHEB1p.P37L targeted somatosensory cortex compared to the empty vector control situation. Boxes *a* and *b* represent magnifications of layer 2 (*a*) and the heterotopia (*b*) highlighting the targeted dysplastic and enlarged cells (indicated by the arrows), scale bars:100 µm.

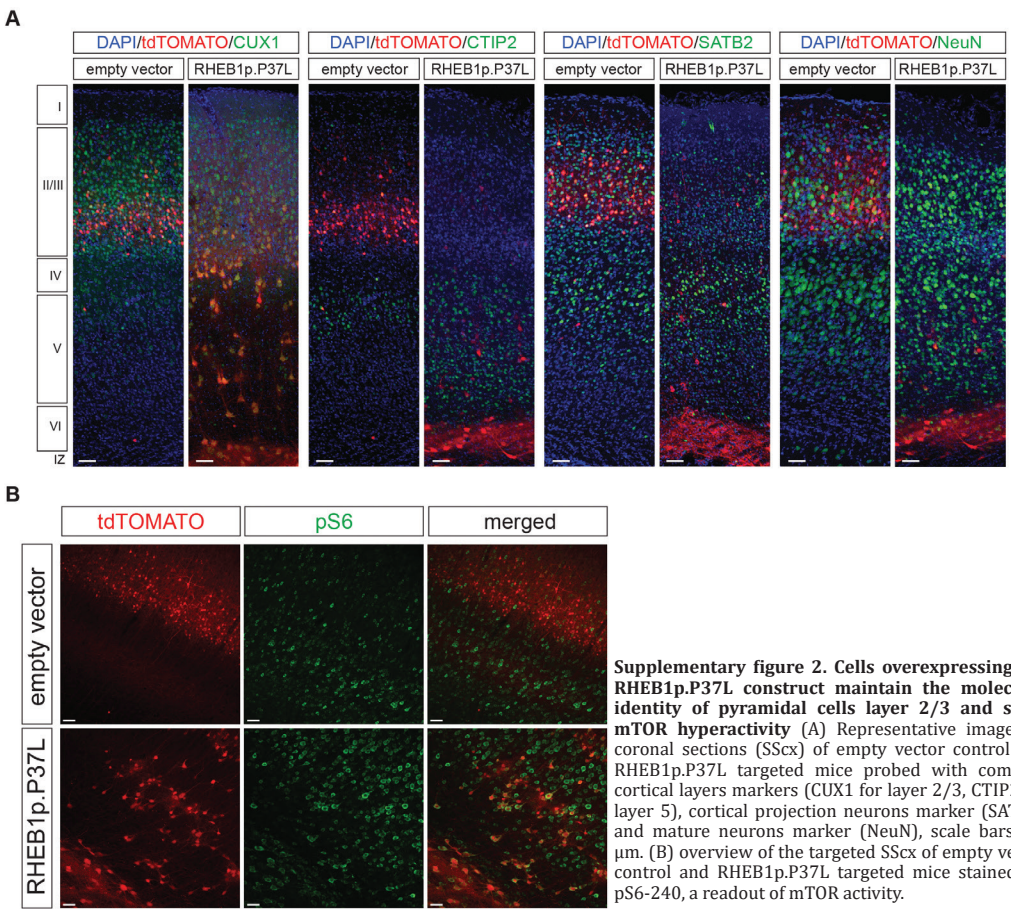

Supplementary figure 2. Cells overexpressing the RHEB1p.P37L construct maintain the molecular identity of pyramidal cells layer 2/3 and show mTOR hyperactivity (A) Representative images of coronal sections (SScx) of empty vector control and RHEB1p.P37L targeted mice probed with common cortical layers markers (CUX1 for layer 2/3, CTIP2 for layer 5), cortical projection neurons marker (SATB2) and mature neurons marker (NeuN), scale bars: 50 µm. (B) overview of the targeted SScx of empty vector control and RHEB1p.P37L targeted mice stained for pS6-240, a readout of mTOR activity.

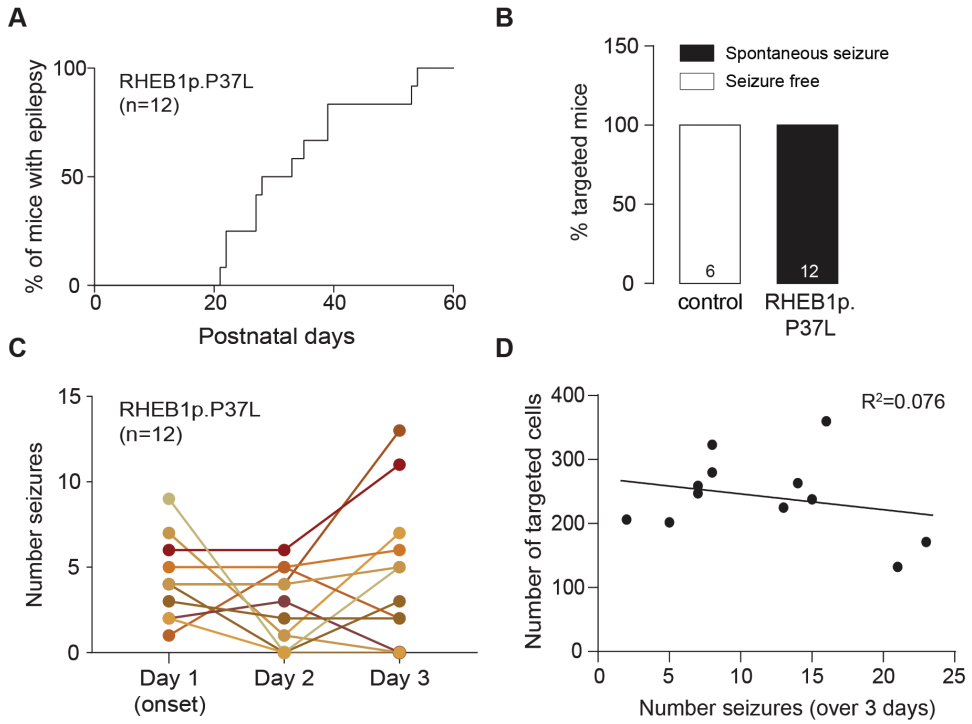

Supplementary figure 3. RHEB1p.P37L mice show reliable spontaneous seizures (A) Onset of seizure activity for the RHEB1p. P37L group (12 mice). (B) Percentage of targeted mice showing seizure activity measured with EEG, numbers in the bar columns indicate the number of mice per group. (C) Number of seizures per day for each mouse of the group in (A) and (B) across three consecutive days of recordings, with day 1 representing the onset of the very first seizure per mouse. (D) simple scatter correlation graph with best fit regression line (Y = -2,658*X + 272,9), showing no correlation between the number of targeted cells and the total number of seizures over three days per mouse.

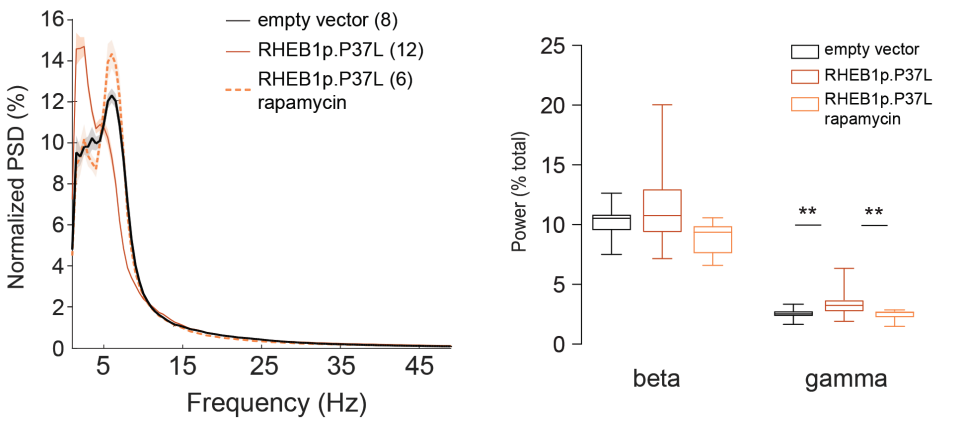

Supplementary figure 4. Power spectrum analysis in RHEB1p.P37L mice shows alterations in the *gamma* frequency band. Extended Normalized Power spectrum density (PSD) shown in Figure 4 to include the *beta* and *gamma* frequencies (till 50 Hz) with quantification of the *beta* (13-30 Hz) and *gamma* (30-50 Hz) frequency bands over the total power; shadows in the PSD indicate the SEM and box plots represent minimum and maximum value with median; numbers within brackets indicate number of measured animals per group ** $p<0.01$.

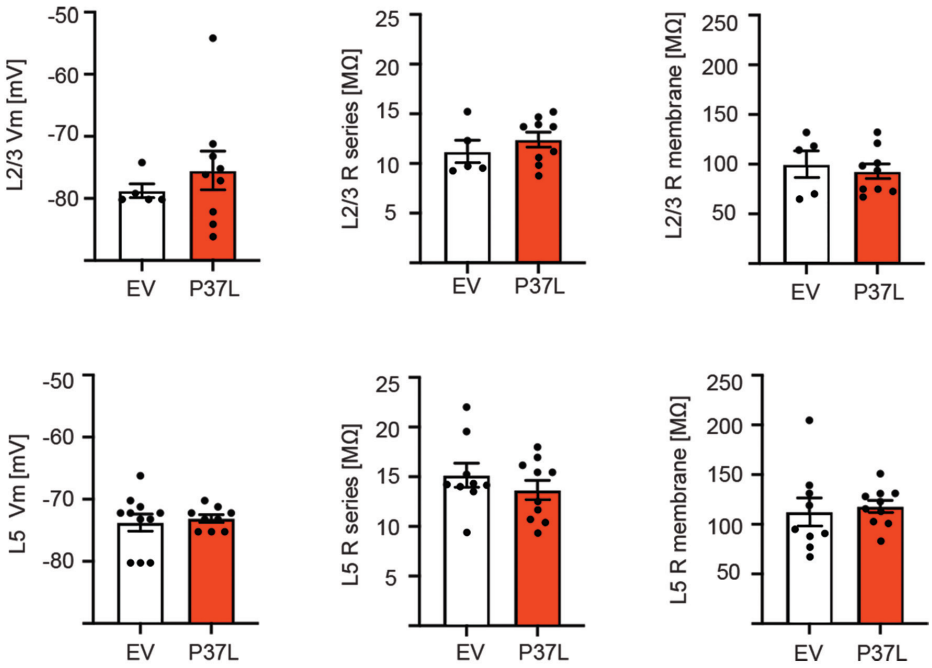

Supplementary figure 5. Basic properties of L2/3 and L5 cells in contralateral S1 cortex. For both the empty vector control and RHEB1p.P37L condition the membrane potential, series resistance and membrane resistance of patch-clamped neurons in contralateral S1 cortex are depicted. No differences were detected in any of the parameters. Data are represented as mean ± SEM.

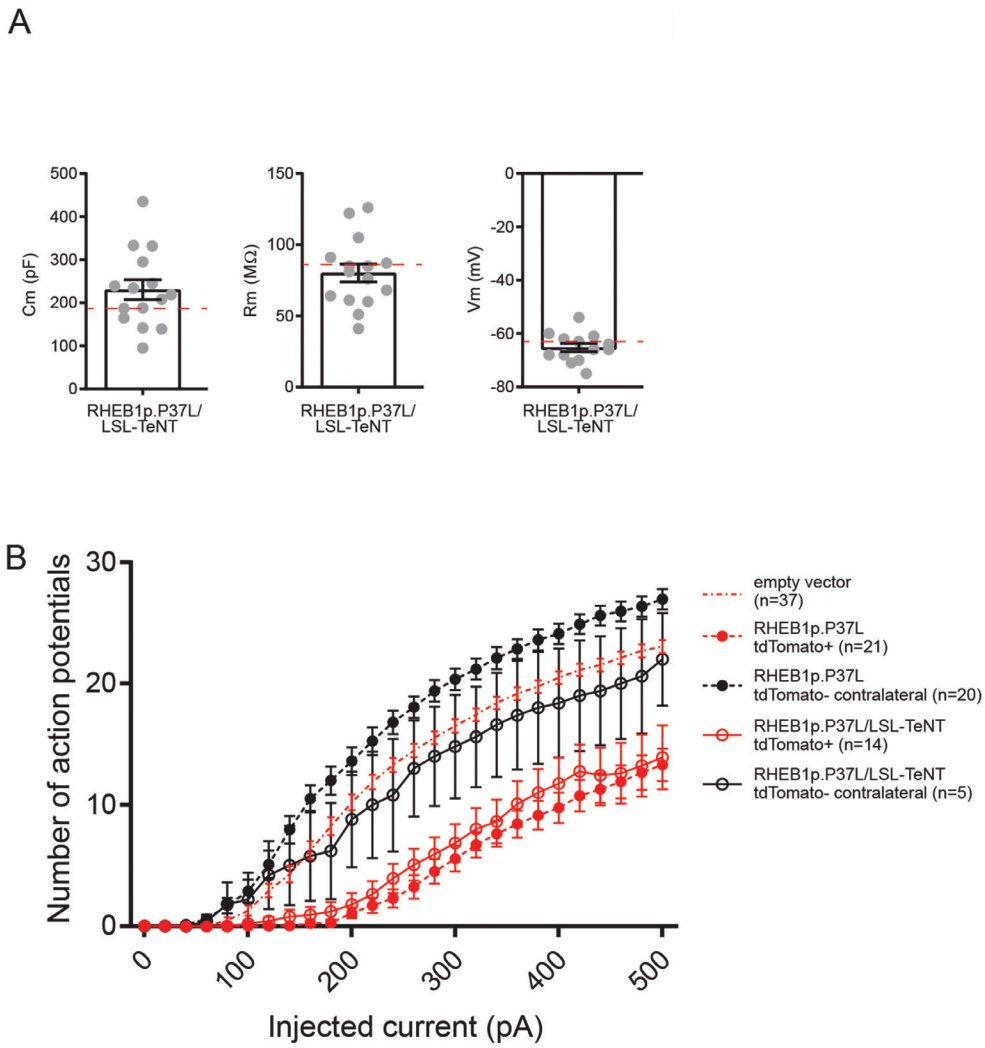

Supplementary figure 6. Basic properties and excitability phenotype in mice co-transfected with RHEB1p.P37L and Tetanus toxin (LSL-TeNT)(A) Analysis of the passive membrane properties (capacitance, membrane resistance and resting membrane potential) of pyramidal cells in layer 2 of ipsilateral S1 of mice targeted with RHEB1p.P37L and LSL-TeNT (4 mice).The red dashed lines indicate the mean value of capacitance, membrane resistance and resting membrane potential of RHEB1p.P37L targeted cells in layer 2 shown in Figure 10. (B) Number of action potentials in response to increasing depolarizing currents; dashed lines represent the values shown in Figure 10C, as comparison. Data in the plots are represented as mean ± SEM with the dots indicating the single value of each neuron analyzed; n = number of cells analyzed. For statistical analysis see Supplementary table 5.

Supplementary Tables

Supplementary table 1. statistical analysis for local field potential data (related to Figure 4 and Supplementary figure 4)

Two-way RM ANOVA table Band-frequencies	**F (DFn, DFd)**	**P value**
Control vs. RHEB1p.P37L	F (6, 147) = 7,456	P<0,0001
One-way ANOVA table Ratio theta/delta	**F (DFn, DFd)**	**P value**
Control vs. RHEB1p.P37L	F (2, 49) = 10,29	P=0,0002

Tukey's multiple comparisons test		**Summary**	**Adjusted P Value**
delta	empty vector control vs. RHEB1p.P37L	*	0,0479
	empty vector control vs. RHEB1p.P37L - rapamycin	ns	0,9614
	RHEB1p.P37L vs. RHEB1p.P37L - rapamycin	ns	0,0856
theta	empty vector control vs. RHEB1p.P37L	**	0,0024
	empty vector control vs. RHEB1p.P37L - rapamycin	ns	0,8288
	RHEB1p.P37L vs. RHEB1p.P37L - rapamycin	**	0,0053
beta	empty vector control vs. RHEB1p.P37L	ns	0,2043
	empty vector control vs. RHEB1p.P37L - rapamycin	ns	0,0637
	RHEB1p.P37L vs. RHEB1p.P37L - rapamycin	**	0,0071
gamma	empty vector control vs. RHEB1p.P37L	**	0,0039
	empty vector control vs. RHEB1p.P37L - rapamycin	ns	0,8465
	RHEB1p.P37L vs. RHEB1p.P37L - rapamycin	**	0,0016
ratio theta/delta	empty vector control vs. RHEB1p.P37L	**	0,0052
	empty vector control vs. RHEB1p.P37L - rapamycin	ns	0,5652
	RHEB1p.P37L vs. RHEB1p.P37L - rapamycin	***	0,0004

* $p<0.05$, ** $p<0.01$, *** $p<0.001$, ns: non significant.

Supplementary table 2. statistical analysis for optogenetics data (related to Figure 9 and Supplementary figure 5)

Parameter/Layer	Unit	Mean ± SEM	Test applied	Significance	N
Amplitude L2/3	pA	control: 44.16±13.76 RHEB1p.P37L: 434.4±88.16	Mann-Whitney test	p=0.006	5 9
Amplitude L5	pA	control: 151.84±49.79 RHEB1p.P37L: 197.9±34.13	Mann-Whitney test	p=0.3562	9 10
Charge L2/3	pA*ms	control: 429.0±96.27 RHEB1p.P37L: 3753.0±624.2	Mann-Whitney test	p=0.006	5 9
Charge L5	pA*ms	control: 1844.0±925.9 RHEB1p.P37L: 2001.0±419.0	Mann-Whitney test	p=0.2428	9 10
Vm L2/3	mV	control: -68.6±1.16 RHEB1p.P37L: -65.33±3.15	Mann-Whitney test	p=0.6044	5 9
Vm L5	mV	control: -62.89±0.61 RHEB1p.P37L: -62.9±1.34	Mann-Whitney test	p=0.9193	10 9
R series L2/3	MΩ	control: 11.18±1.15 RHEB1p.P37L: 12.38±0.78	Unpaired t-test	p=0.3930	5 9
R series L5	MΩ	control: 15.16±1.21 RHEB1p.P37L: 13.66±0.97	Unpaired t-test	p=0.3463	10 9
Rm L2/3	MΩ	control: 99.75±13.66 RHEB1p.P37L: 92.68±7.67	Unpaired t-test	p=0.6322	5 9
Rm L5	MΩ	control: 112.53±14.07 RHEB1p.P37L: 117.94±6.06	Unpaired t-test	p=0.7187	10 9

Significant values are indicated in grey

Supplementary table 3. statistical analysis for basic properties of whole-cell patch data (related to Figure 10)

ANOVA table	F (DFn, DFd)	P value
Cm	F (3, 111) = 6.525	P=0.0004
Rm	F (3, 111) = 10.47	P<0.0001
Vm	F (3, 111) = 0.3580	P=0.7834

Tukey's multiple comparisons test	Cm Summary	Cm Adjusted P Value	Rm Summary	Rm Adjusted P Value	Vm Summary	Vm Adjusted P Value
control vs. contralateral RHEB1p.P37L	ns	0.9218	ns	0.9970	ns	0.9028
control vs. ipsilateral RHEB1p.P37L	ns	0.1568	ns	0.6241	ns	0.9974
control vs. targeted RHEB1p.P37L	***	0.0003	****	<0.0001	ns	0.9585
contralateral RHEB1p.P37L vs. ipsilateral RHEB1p.P37L	ns	0.6314	ns	0.6506	ns	0.9751
contralateral RHEB1p.P37L vs. targeted RHEB1p.P37L	*	0.0171	****	<0.0001	ns	0.7394
ipsilateral RHEB1p.P37L vs. targeted RHEB1p.P37L	ns	0.2425	**	0.0033	ns	0.9337

* $p<0.05$, ** $p<0.01$, *** $p<0.001$, **** $p<0.0001$, ns: non significant.

Supplementary table 4. statistical analysis for excitability data (related to Figure 10)

Mixed effect analysis	**P value**	**P value summary**	**F (DFn, DFd)**
RHEB1p.P37L vs. control	<0.0001	****	F (75, 2397) = 29.02

Tukey's multiple comparisons test	Summary	Adjusted P Value
targeted RHEB1p.P37L vs. ipsilateral RHEB1p.P37L	****	<0.0001
targeted RHEB1p.P37L vs. contralateral RHEB1p.P37L	****	<0.0001
targeted RHEB1p.P37L vs. control	****	<0.0001
ipsilateral RHEB1p.P37L vs. contralateral RHEB1p.P37L	****	<0.0001
ipsilateral RHEB1p.P37L vs. control	ns	0.9447
contralateral RHEB1p.P37L vs. control	****	<0.0001

Two-way RM ANOVA table	**F (DFn, DFd)**	**P value**
Control vs. non targeted	F (75, 1225) = 0.7275	P=0.9603

Tukey's multiple comparisons test	**Summary**	**Adjusted P Value**
targeted empty vector vs. ipsilateral empty vector	ns	0.9940
targeted empty vector vs. contralateral empty vector	ns	0.9867
targeted empty vector vs. non targeted	ns	0.4892
ipsilateral empty vector vs. contralateral empty vector	ns	0.9999
ipsilateral empty vector vs. non targeted	ns	0.6817
contralateral empty vector vs. non targeted	ns	0.6938

**** $p<0.0001$, ns: non significant.

Supplementary table 5. statistical analysis for whole-cell patch data (related to Supplementary figure 6)

Unpaired t test two-tailed	t, df	p value	p summary
Cm	t=1.721, df=33	0.09	ns
Rm	t=0.9634, df=33	0.34	ns
Vm	t=1.019, df=34	0.3152	ns

Mixed effect analysis excitability	P value	P value summary	F (DFn, DFd)
RHEB1p.P37L vs RHEB1p.P37L/LSL-TeNT	<0.0001	****	F (100, 2292) = 19.44

Tukey's multiple comparisons test	Summary	Adjusted P Value
targeted empty vector vs. targeted RHEB1p.P37L/LSL-TeNT	****	<0.0001
targeted empty vector vs. controlateral RHEB1p.P37L/LSL-TeNT	ns	0.81
targeted RHEB1p.P37L vs. targeted RHEB1p.P37L/LSL-TeNT	ns	0.44
targeted RHEB1p.P37L vs. controlateral RHEB1p.P37L/LSL-TeNT	****	<0.0001
contralateral RHEB1p.P37L vs. targeted RHEB1p.P37L/LSL-TeNT	****	<0.0001
contralateral RHEB1p.P37L vs. controlateral RHEB1p.P37L/LSL-TeNT	**	0.001
targeted RHEB1p.P37L/LSL-TeNT vs. controlateral RHEB1p.P37L/LSL-TeNT	****	<0.0001

** $p<0.01$, **** $p<0.0001$, ns: non significant.

Supplementary table 6. Number of seizures per day monitored with EEG in RHEB1p.P37L/LSL-TeTxLC mice (6 mice) injected with Tamoxifen after seizures (related to Figure 11, group 2)

Number seizures/24hr	Mouse 1	Mouse 2	Mouse 3	Mouse 4	Mouse 5	Mouse 6
Day 0	5	5	7	6	6	5
Day 1	1	8	6	7	6	1
Day 2	0	6	3	0	3	2
Day 3	0	0	1	0	0	1
Day 4	0	0	2	0	0	0
Day 5	0	0	0	0	0	2
Day 6	0	0	0	0	0	0
Day 7	0	0	0	0	3	1
Day 8	-	0	0	0	0	0
Day 9	-	0	0	0	2	2
Day 10	-	-	-	-	0	-
Day 24	0	0	0	0	0	0
Day 25	0	0	0	0	0	0
Day 26	0	0	0	0	0	0
Day 44	0	0	0	0	0	0
Day 45	0	0	0	0	0	0

Mice *in utero* electroporated with the constructs indicated in Figure 11 were monitored from 5 weeks of age with EEG; Day 0 represents the first day of seizures onset (which differs between mice); days highlighted in **bold** indicate the days in which Tamoxifen was administered; numbers (and relative grey color-code) indicate the number of seizures per day.

Chapter VII

GENERAL DISCUSSION

In the New York Times bestseller book entitled "**Patient H.M.: A Story of Memory, Madness, and Family Secrets**" the author Luke Dittrich attempts to give a definition of science which I quote here: "*Each new generation takes the drafts created by the men and women who came before it and revises them, sometimes making small tweaks, adding commas or dropping clauses, sometimes making more drastic changes, discarding chapters altogether or writing entirely new ones. They're all editors, and all of them, the good ones at least, have to be passionate about altering someone else's draft if they're ever going to make any progress*." The story of patient H.M., Henry Molaison, described in this book, is emblematic of how scientific knowledge evolves over time with both groundbreaking discoveries and minor findings to alter or consolidate the existing believe. Henry Molaison was suffering from epilepsy since childhood and in 1953 the neurosurgeon William Beecher Scoville, in an attempt to cure his epilepsy, performed a surgical procedure that led to the removal of both *hippocampi* and adjacent cortical areas from his brain. At the time, the role that this anatomical structure plays in the brain was not known. After the surgery, Henry could not form any new long-lasting episodic memory (Scoville and Milner, 1957). This outcome was disastrous for Henry's life, however it contributed to revolutionize the scientific understanding of how learning and memory work.

Over the years, multiple experimental evidences contributed to consolidate the theory that the hippocampal formation is crucial to form different types of new memories [reviewed in (Martin and Clark, 2007; Moser *et al*., 2008; Moscovitch *et al*., 2016)]. But what are the cellular and molecular mechanisms that underlie memory formation? The experimental discovery of hippocampal LTP (Bliss and Lømo, 1973) reinforced the proposed hypothesis (Ramón Y, 1894; Hebb, 1949) that strengthening of neuronal connections at the level of the synapse is crucial for learning and memory processes. This led to a more general hypothesis that activity-dependent synaptic plasticity, in the forms of changes in presynaptic release and postsynaptic alterations such as insertion of new receptors, activation of signaling pathway and, ultimately, gene expression and new protein synthesis, constitutes the 'engram' or memory trace for memory formation and storage [reviewed in (Martin *et al*., 2000; Takeuchi *et al*., 2014; Tonegawa *et al*., 2018)]. Whether LTP, as a specific form of synaptic plasticity, can be considered strictly a model for learning and memory, or its equivalent, it is still a matter of investigation. In addition, probably the tentative to reduce a complex concept like memory, with its multiple forms, to a single unifying aspect such as LTP is too simplistic (Buzsáki, 1985; Lynch, 2004; Bliss *et al*., 2018).

However, it is without doubt that some prominent signaling pathways seem to underlie both expression of LTP and memory consolidation (Bliss *et al*., 2018). Evidence for an involvement of CAMK2, protein kinase C (PKC) and protein kinase A (PKA) in LTP came already in the late 80s (Malinow *et al*., 1989; Nayak *et al*., 1998) and subsequently the use of knock-out and mutant animals targeting specific pathways allowed to link LTP to learning *in vivo* [summarized in (Lynch, 2004)].

After more than 25 years from the generation of the first knock-out mouse for *Camk2a*

in 1992 (Silva *et al*., 1992a, 1992b), which shows impairments in both hippocampal LTP and learning tasks, CAMK2 still remains a 'hot' molecule in the field of learning and memory (Bayer and Schulman, 2019). Only recently John Lisman, before passing away, wrote a review (Lisman, 2017) to build a case in favor of CAMK2 as the best candidate to fulfill the role as a molecular substrate for memory formation against protein kinase Mζ (PKMζ), recently proposed to be a more suitable molecule for the storage of long-term memories (Sacktor, 2011; Sacktor and Fenton, 2018). But after 40 years of research, what is left to learn about CAMK2?

In the first part of this thesis (**chapters II**, **III** and **IV**) we showed that there are still fundamental questions that need to be answered about CAMK2. And, in this next-generation sequencing era, with the discovery of new variants in CAMK2 implicated in neurodevelopmental disorders, basic research demonstrates how crucial it is to understand the mechanisms of protein function and regulation to be able to translate these findings in a clinical context and potentially find therapeutic targets.

As summarized in the general introduction of this thesis, the unique roles of CAMK2A and CAMK2B in neuronal functions have been extensively investigated making use of either *Camk2a* or *Camk2b* knock-out mouse models and single point mutant mice that revealed unique roles for these isoforms in learning and plasticity phenotypes (Elgersma *et al*., 2004; Borgesius *et al*., 2011). However, the high structural homology between these two isoforms would support the hypothesis that CAMK2A and CAMK2B might have a certain degree of functional redundancy such that one isoform could compensate for the other when absent. In **chapter II** we explored this aspect by simultaneously deleting *Camk2a* and *Camk2b* to uncover previously unknown functions. We showed that germline as well as adult deletion of both *Camk2a* and *Camk2b* is lethal and that both calcium-dependent and calcium-independent functions are essential for survival. This means that CAMK2G and CAMK2D, despite the high structural homology, cannot compensate for the absence of CAMK2A and CAMK2B, which is probably due to the lower expression levels found in the brain (Bayer *et al*., 1999). Interestingly, we could observe in all cases that homozygous mutations in *Camk2b* are less tolerated than comparable mutations in *Camk2a*. We hypothesize that this is due to a developmental role for CAMK2B in the brain due to an earlier expression (starting from E12.5) compared to CAMK2A, or to a broader distribution for CAMK2B in different cell types in the brain (Brocke *et al*., 1995; Bayer *et al*., 1999; Waggener *et al*., 2013).

In addition to this newly identified role in survival, we could observe complete loss of hippocampal LTP in inducible double knock-out mice at the level of the CA3-CA1 synapse, explaining the residual LTP observed in single knock-out mice (Elgersma *et al*., 2002; Borgesius *et al*., 2011). This LTP deficit is completely dependent on loss of postsynaptic CAMK2 since restricted presynaptic deletion of both *Camk2a* and *Camk2b* from the CA3 area of the hippocampus did not cause any LTP impairment. Despite the LTP deficits, there were very little changes both at the biochemical and electrophysiological levels that could explain the lethality observed in these mice. Continuous EEG recordings did not reveal any epileptic activity in

the inducible double knock-out mice and the LFP analysis shows no decline in the general brain activity even when close to death. Additionally and maybe quite surprisingly, despite the proposed important role for CAMK2 in the organization and structure of the synapse (Hell, 2014), no significant changes were found in PSD composition in the double knock-out mice. This finding would raise the question, what exactly is the structural role of CAMK2 in the postsynaptic side? However, looking into the distribution of CAMK2 molecules at the level of the spines can shed some light on this matter. Within the dendritic spines, CAMK2 molecules are localized in different compartments: we have a cytoplasmic pool, with some molecules bound to F-actin to stabilize the cytoskeleton and other free in the cytosol, and a PSD pool, part of which is bound to the NMDA receptor that can lead to activation of the kinase. It has been estimated that the fraction of CAMK2 in the PSD pool is relatively small compared to the total number of molecules found in the total spine and that, under basal conditions, 1% of the spine pool of CAMK2 is bound to the NMDA receptors, only to double upon LTP induction (Feng *et al*., 2011). Considering that the total fraction of CAMK2 in the spine is very high compared to the dendritic shafts, and that CAMK2 has a crucial role in strengthening of the synapse, having only 1-2% of total CAMK2 in the PSD pool is quite surprising. But this might explain why we did not find severe changes in the composition of the PSD.

In the quest for the 'memory molecule', the low abundance of CAMK2 in the PSD raises the question whether CAMK2 can actually be considered the cellular correlate for memory and if it is indeed involved in LTP maintenance, as strongly supported by Lisman, and not only in LTP induction. Some recent studies using two-photon fluorescence lifetime imaging microscopy provide the evidence that activation of CAMK2 actually declines within one minute (Lee *et al*., 2009; Chang *et al*., 2017), thereby implying that CAMK2 is not involved in maintenance and keeping the debate on the 'memory molecule' still open.

Why deletion of CAMK2A and CAMK2B simultaneously results in lethality remains unclear. It is quite surprising that the deletion of two primarily brain specific kinases, one of which starts to be expressed post-natal, could lead to such a severe phenotype. Literature shows that knockout animals for the NR1 and NR2B subunits of the NMDA receptors die after birth due to respiratory failure and impaired suckling response, respectively (Forrest *et al*., 1994; Kutsuwada *et al*., 1996). However, we could rule out the contribution of both those aspects, since pups had food in there belly after birth and adult mice close to death did not show any alteration of respiratory rhythms. Since both isoforms have been proposed to play a crucial role in the structural organization of the synapse, in addition to their enzymatic function (Hojjati *et al*., 2007; Borgesius *et al*., 2011; Hell, 2014), it is not unlikely that deletion of a major protein such as CAMK2 could lead to substantial morphological alterations of the dendritic spines. Despite the fact that at the biochemical level we could not observe major alterations of synaptic proteins, this does not exclude that overall the morphology of the spines could be affected. Future studies should address this aspect by performing electron microscopy experiments on the inducible double knock out mice. If, on one hand, the

structural consequences could be interesting to further explore, they might not necessarily be an explanation for the lethality. However, the functional effects on the downstream targets upon removal of both CAMK2A and CAMK2B might shed light on the cause of the lethality for these mice. Thereby, performing a phosphoproteomic experiment could open new doors for the identification of crucial new targets of CAMK2.

With our findings we show that, despite so many years of research, there are still unknown functions for CAMK2 to be discovered. Understanding these functions, and the redundancy between the major CAMK2 brain isoforms, potentially has enormous therapeutic implications for patients. In fact, there is a whole new unexplored field in the CAMK2 research line that involves the role of CAMK2 in the human brain and in neurodevelopment, that we describe in **chapter III** and **IV**.

Over the years, we learnt from experimental studies *in vitro* and in rodents that CAMK2A mediates synaptic plasticity by regulating some of the main components of the PSD through sequential steps upon influx of calcium. These mechanisms involve: the rapid translocation of CAMK2A from the cytosol to the PSD where it binds the GluN2B subunit of the NMDA receptor (Shen and Meyer, 1999), which leads to further phosphorylation of the holoenzyme even in absence of calcium (Bayer *et al*., 2001); the enhancement of the conductance of the channel AMPA receptor, responsible for basal synaptic transmission (Barria *et al*., 1997; Derkach *et al*., 2002); and insertion of new AMPA receptors in the membrane (Hayashi *et al*., 2000). All of these steps and the molecules and channels involved, are crucial to regulate synaptic strength (Lisman *et al*., 2012). Indeed, both AMPA and NMDA receptor dysregulation has been linked to human neurological disorders (for reviews see (Lau and Zukin, 2007; Zhang and Abdullah, 2013; Yang *et al*., 2019)). Paradoxically, even though CAMK2 was indirectly associated with human disorders (Robison, 2014), patients with mutations in the major *CAMK2* brain isoforms had not been identified until a few years ago (described in **chapter III**). Why is that the case? First of all, given the primary role and high abundance of CAMK2 in neuronal function, one might think that germline mutations in the *CAMK2* gene would not be tolerated, therefore they would be eliminated and not transmitted to the progeny; second, only recently the technological advances in the sequencing methodologies have allowed the screening of the entire genome at a relatively low cost; third, from the clinical description of the 24 heterozygous patients that we identified in our study (**chapter III**), it appears evident that there is not a common distinctive set of clinical features that would allow the clear phenotypical recognition of individuals with *CAMK2* mutations, as it happens for monogenic disorders such as Angelman syndrome, Rett syndrome or fragile x syndrome, for example. Most of the individuals with mutations in *CAMK2A* and *CAMK2B* have as main clinical features mild to severe ID, language impairments and behavioral abnormalities. Additionally, when looking at the phenotypical variations between individuals bearing either *CAMK2A* (14) or *CAMK2B* (10) variants, it seems that cognitive impairments are more severe in individuals with *CAMK2B* mutations. However, the group is too small to make this comparison robust. Identification of new individuals with

CAMK2 variants would allow a more comprehensive categorization. Most of the 19 different variants identified, of which 18 were confirmed to be *de novo*, are rare missense variants, some result in the production of a premature stop codon or affect canonical splice sites. Since they are found in regions that are highly conserved across species, bioinformatics tools can predict their pathogenicity, but not how they can be pathogenic (e.g. gain-of-function or loss-of-function).

As described in the general introduction of this thesis, the use of functional assays is the required next step to be able to assess the pathogenicity of a given genetic variant in a certain disorder. In order to assess the pathogenicity of candidate variants, the **PR*i*SM** screen does not require any *a priori* knowledge of the biology of the gene under investigation. However, having basic knowledge of the genes and/or the molecular pathways involved generates the possibility to introduce additional, and more specific, assays to study not only the effect of the variant on the protein function but also to gain more knowledge on the protein itself. This was indeed the case for the *CAMK2* missense variants we investigated in **chapter III**. The missense variants we found are mainly localized in the catalytic domain and in the autoregulatory domain while none were identified in the association domain. Biochemical knowledge previously gained on CAMK2 (**Table 2** in the general introduction of this thesis), helps us to predict, *a priori*, for some of them, the potential effect on CAMK2 activity and regulation, thereby the pathogenicity of the variant. Overall, variants that affect the autoregulatory domain seem to correlate with more severe ID, as well as variants that we established to be gain-of-function (which are the majority). Compared to the relatively mild clinical phenotypes that we observed in some patients in our study, Chia and colleagues recently identified a homozygous loss-of-function mutation in *CAMK2A* that causes a range of symptoms such as growth delay, severe ID and epilepsy. Interestingly, this mutation (His477Tyr) is located in the association domain and causes partial disruption of self-oligomerization, affecting subcellular localization and spontaneous neuronal activity of iPSCs derived neurons plated on MEAs (Chia *et al*., 2018). Our findings, together with this study and another recent work reporting new *de novo* variants in *CAMK2A* and *CAMK2B* (Akita *et al*., 2018), clearly show that CAMK2 is involved in a broad range of neurological disorders that is only starting to be uncovered.

Understanding if a variant is pathogenic, and if so, whether it results in gain-of-function or loss-of-function of the protein, in combination with our basic knowledge on protein functioning, has strong implications for the clinical field. For example, recent experiments performed in the laboratory (not published) showed that CAMK2A does not have an important neurodevelopmental role since adult reinstatement of the *Camk2a* gene, in a mouse model where CAMK2A is absent from germline, rescues all the behavioral and plasticity phenotypes. These results indicate that patients with a haploinsufficiency phenotype could potentially benefit from a therapeutic approach where functional CAMK2A is reintroduced in the brain. Future experiments will have to investigate the mechanisms through which dysfunctions in CAMK2 exert their pathogenic roles in human brain disorders to identify possible therapeutic

targets. For example, the use of patient-derived iPSC neuronal lines in combination with the MEA technology will potentially enable us to develop an *in vitro* disease model with robust physiological relevance. This will constitute a preclinical platform on which we can assess the validity of mechanistic hypotheses that could explain a certain phenotype and screen the efficacy of specific drugs. Furthermore, genomic editing technologies, such as CRISPR-Cas, can be used to correct the mutation and create and isogenic control line to observe if the phenotypes are indeed specifically caused by the mutation. At the same time, the mutation can be introduced in a control iPSC line to evaluate the contribution of the patient genetic background to the phenotype.

Surprisingly, CAMK2A and CAMK2B were not the first isoforms of the CAMK2 family to be linked to human neurological disorders. Before the publication of the Iossifov study in 2014, a large-scale genomic study including children with severe ID, identified a *de novo* mutation in *CAMK2G* (de Ligt *et al*., 2012). Even though CAMK2G is less abundant in the adult brain compared to CAMK2A and CAMK2B, CAMK2G represents the major brain isoform in the developing system together with CAMK2D (Bayer *et al*., 1999). In **chapter IV** we describe a second individual suffering from ID and motor and speech delay, carrying the same mutation in *CAMK2G* (Arg292Pro) found in the individual described in the de Ligt study. The results presented in this chapter not only represent an example of the use of the basic **PR*i*SM** screen to assess pathogenicity of a variant but also show how extensive knowledge of the molecular characteristics of a protein can help to elucidate the mechanisms that can mediate pathogenicity. We show that *in vitro* the Arg292Pro is unstable but hyperactive and causes a striking reduction in neurite length and arborization upon overexpression in neuronal cultures, in contrast to the knock-down which causes an increase in neuronal morphology. Furthermore, *in vivo* overexpression induces a complete block of migration compared to the wild type protein. These results suggest that the mutation acts as a pathogenic gain-of-function. We further corroborate this by performing multiple mutagenesis experiments taking advantage of the existing knowledge (gained from 40 years of extensive fundamental research) on CAMK2 regulation and functioning.

The CAMK2G brain specific isoform (g_a) contains an NLS and only recently, it was proposed that CAMK2G in excitatory neurons, upon activation, may function as a shuttle for calcium/calmodulin to bring it into the nucleus, suggesting that the primary neuronal role for CAMK2G might be the control of gene expression instead of its kinase function (Ma *et al*., 2014). Testing the CAMK2Gp.Arg292Pro in the CAMK2G isoform that contains the NLS, we found that the mutation impaired the nuclear translocation of CAMK2G. This left us with two different functions that appear to be affected by the ID-related mutation: on one side the mutation has a gain-of-function effect, rendering the kinase constitutive active, on the other hand prohibiting the nuclear import, acting as a loss of function on gene expression. To understand which function can mediate the pathogenic effect seen in our assays, we introduced a second mutation that could block the catalytic function of the kinase (Arg292Pro/Lys43Arg). While

the nuclear import in this double mutant is still impaired, we could fully rescue the neuronal and migration phenotypes. This indicates that the increased kinase activity in the CAMK2Gp. Arg292Pro mutation but not the loss of nuclear shuttle function, is causing the phenotypes seen in our assays, most probably affecting specific targets in the cytosol.

In parallel with our study, a recent work from the Tsien lab also characterized the Arg292Pro mutant in the context of its role as a nuclear shuttle for calcium/calmodulin (Cohen *et al*., 2018). In this work the authors show that while the ID-related mutant is able to translocate to the nucleus upon depolarization, it is however unable to bring effectively calmodulin into the nucleus due to a higher dissociation rate compared to the wild type. They conclude that the mutant has a dominant negative effect in regulating nuclear calmodulin transport that could potentially explain the ID phenotype in the patient. The discrepancies in our studies can be mainly explained by methodological differences and by a different interpretation of the findings. The authors mainly focus on the nuclear function of CAMK2G and draw their conclusions without considering the non-nuclear role of CAMK2G in the brain. For example, when trying to rescue the spatial learning or the long-term LTP deficits seen in CAMK2G knock-out mice, they reintroduce CAMK2G wild type with NLS without considering the possibility that also a wild type protein without NLS might have rescued the phenotypes. Since the Arg292Pro fails to rescue these phenotypes and it is not able to efficiently transport calmodulin in the nucleus, they conclude that the absence of proper nuclear transport is the main pathogenic cause of the variant found in the individuals with ID. This is in contrast to what we concluded from our experiments. We showed that there actually appears to be a role for CAMK2G in the cytosol. In fact, we found that the neuronal arborization phenotype we observed upon knock-down of CAMK2G could be rescued by both isoforms, with or without NLS, but not by CAMK2A or CAMK2B, indicating that cytosolic CAMK2G can play a unique role in neuronal development. Not much is known regarding a possible neuronal function for CAMK2G as a kinase, rather than its role in the control of gene expression. In light of our results, it would be interesting to investigate if there are proteins that are specifically targeted by CAMK2G and not by other isoforms. For example, a phosphoproteomics experiment on the CAMK2G knock-out mouse model could show alterations in phosphorylation of targets that would indicate that the other isoforms cannot compensate for the absence of CAMK2G, highlighting a specific role for this isoform in a particular molecular pathway.

The different pathogenic effects of the Arg292Pro mutant show how crucial it is to screen variants using multiple experimental approaches that can address the several roles that a protein can have in the cell. Interestingly, our conclusion that the Arg292Pro acts as a constitutively active kinase that can explain pathogenicity, instead of a loss of function towards its nuclear function, is consistent with previous biochemical findings that show that mutation of the Lysine 291 in CAMK2A (equivalent to the Arg292 in CAMK2G) into Alanine reduces inhibition of the autoregulatory domain (Smith *et al*., 1992) and mutation into Glutamate increases calmodulin binding (**Table 2** in the general introduction).

With the results obtained in both **chapter III** and **chapter IV** we could not only show the efficacy of the **PR*i*SM** screen to assess pathogenicity of variants associated with neurodevelopmental disorders but we could start a promising new line of research in the CAMK2 field. Furthermore, in light of the recent discovery of new variants in CAMK2G and CAMK2D associated with ID, future studies should focus more and more on these less well-known isoforms. They both represent the main isoforms in the developing nervous system (Bayer *et al*., 1999), therefore it is likely that they might play an important function in shaping the early brain development. While so far most of the research on CAMK2G and CAMK2D focused on describing their general distribution in the nervous system at the transcript level, a more comprehensive anatomical and cellular characterization at the protein level could give new insights on specific neuronal roles played by these kinases. *In utero* electroporation will allow us to study the developmental role in a time- and cellular-specific fashion to evaluate the neuronal functional consequences of selectively deleting either CAMK2G or CAMK2D.

In contrast to the CAMK2 gene family, which has only been recently associated with neurodevelopmental disorders, the mTOR pathway has long been linked to several disorders presenting ID, epilepsy and cortical malformations as main clinical features (Crino, 2011; LaSarge and Danzer, 2014; Mirzaa *et al*., 2016). The *RHEB1* gene however, primary activator of the mTOR pathway, similar to *CAMK2*, was never directly linked to any neurodevelopmental disorder. We know, from mouse studies, that embryonic deletion of the *Rheb1* gene is lethal (Goorden *et al*., 2011), therefore we can hypothesize that germline homozygous loss-of-function mutations might also be lethal in humans. On the other hand, heterozygous gain-of-function mutations might be tolerated and cause an increase in the mTOR pathway activity in a similar way to loss-of-function mutations in the *TSC* genes. However, adult *Tsc1*$^{+/-}$ rodent models, despite learning and social deficits, do not show any brain morphological defects or seizures, indicating that both alleles have to be affected to cause hyperactivation of the mTOR pathway and epilepsy (Goorden *et al*., 2007). In **chapter V** we identified heterozygous *de novo* variants in several mTOR related genes associated with macrocephaly and ID, that expands the already vast number of genes associated with brain malformations (Moffat *et al*., 2015; Juric-Sekhar and Hevner, 2019). Within those, some were known ID genes while others were not. Two *RHEB1* variants were also identified as novel ID related genes, in patients with epilepsy or epileptic discharges observed in the EEG recordings. We performed the basic **PR*i*SM** screen assays to assess the pathogenicity of these variants, in combination with *in vivo* studies performed in zebrafish in collaboration with our colleagues. All these studies consistently showed that both variants were acting as hyperactivating mutations through the mTOR pathway and were likely to be pathogenic. Therefore, this suggests that patients with these mutations can potentially benefit from treatments acting on the mTOR pathway. One of the most interesting outcomes, was that by performing IUE with the *RHEB1* variants to assess cortical migration we could observe severe migration deficits causing heterotopia that

could mimic histopathological features observed in some types of MCDs (hyperactivation of the mTOR pathway, focal lesion and abnormally dysplastic neurons, described in **chapter VI**). How exactly mTOR hyperactivity can lead to migration deficits is not known. Interestingly, histopathological analysis of tubers from TSC patients and focal malformations from MCD cases reveals that there is a wide range of proteins (including Doublecortin, doublecortin-like and STAT3) observed to be aberrantly activated or expressed that are known to control cell proliferation, differentiation or migration (Qin *et al*., 2000; Mizuguchi *et al*., 2002; Baybis *et al*., 2004; Boer *et al*., 2009; Moffat *et al*., 2015). Follow up studies should address if these proteins are targets of mTOR regulation, thereby causing the migration disorder.

The majority of the mice targeted with the *RHEB1* constructs (with the most severe effect of the RHEB1p.Pro37Leu mutant) showed spontaneous tonic-clonic seizures starting from three weeks of age. This is quite surprising considering that the number of cells we target with IUE is quite low on an overall wild-type background. Since MCD disorders are highly associated with epilepsy, one of the open questions in the field is to what extent the malformations are responsible for the seizures (Represa, 2019). Animal models have been proven to be extremely valuable tools in trying to address this issue, with the final aim to develop efficient anti-epileptic therapies (Wong, 2009; Wong and Roper, 2016). One of the main challenges in studying complex disorders such as MCDs, is that the model should represent as reliably as possible the main characteristics of the pathology, which in this case include morphological abnormalities and epilepsy. To introduce a second level of complexity, despite the histopathological similarity of several disorders within the MCDs category, it has been widely recognized that the underlying cellular and circuit abnormalities can arise at different stages during development, thereby affecting proliferation, migration or final cortical organization, as categorized originally by Barkovich (Barkovich *et al*., 2012). Based on this classification, animal models have been developed using a variety of environmental insults (*e.g.* irradiation, exposure to teratogens or toxins, freeze lesions) or genetic manipulation to try to recapitulate specific aspects of MCDs (Chevassus-Au-Louis *et al*., 1999; Schwartzkroin *et al*., 2004; Najm *et al*., 2007). To study the genetic contribution of specific genes, a number of knock-out and conditional mouse models have been developed over the years that mimic some major histopathological features and, in some cases, epilepsy (summarized in (Wong, 2009; Wong and Roper, 2016)). Despite the fact that the underlying genetic causes of MCDs are the most diverse (Liu, 2011; Moffat *et al*., 2015; Parrini *et al*., 2016), the genetic involvement of the mTOR pathway in several types of MCDs (including FCD and hemimegalencephaly) is prominent and currently most of the animal models to study MCDs are models where the mTOR pathway is manipulated (Juric-Sekhar and Hevner, 2019). One example of the well-studied genes belonging to the mTOR pathway is *PTEN*. This gene has been linked to FCD and epilepsy, and cell-specific as well as global knock-out mouse models show abnormal cell proliferation with megalencephaly and epilepsy, providing a valuable tool to study the mechanisms of mTOR-dependent epilepsy in MCDs (Backman *et al*., 2001; Ljungberg *et al*., 2009; Pun *et al*.,

2012; Nguyen and Anderson, 2018). Another gene highly investigated is *TSC*: several mouse models have been generated with inactivation of either the *Tsc1* or *Tsc2* gene, some of which show brain morphological abnormalities and/or epilepsy (Kirschstein and Köhling, 2016). These models were extremely relevant in mimicking a specific genetic defect that can underlie human MCDs and, from the clinical point of view, to study potential therapeutic applications of mTOR inhibitors or anti-epileptic drugs. However, one of the main limitations is that they do not fully resemble the focal lesions observed in some patients, on the contrary, they show diffuse brain cytological abnormalities. The introduction of *in utero* electroporation techniques completely changed this aspect, making it possible to spatially and temporally control gene inactivation or overexpression (Saito and Nakatsuji, 2001). Using specific genetic manipulations (CRISPR-Cas9 techniques or gene overexpression), it was possible to introduce *in utero* variants in mTOR-related genes identified in patients with MCDs and generate mouse models with focal cortical malformations and, in some cases, spontaneous epilepsy (Baek *et al*., 2015; Lim *et al*., 2015, 2017; Hanai *et al*., 2017; Hu *et al*., 2018; Park *et al*., 2018; Ribierre *et al*., 2018). In **chapter VI** we also used IUE to develop a mouse model that represents a perfect tool, combining focal cortical malformation and mTOR hyperactivity, to underpin the mechanisms behind mTORopathies. However, like some of the previously generated mouse models, also this model has limitations. First of all, we have to consider that we are using overexpression to introduce the *RHEB1* variants, thereby not resembling the heterozygosity found in the patients. This, in combination with the spatially restricted technique we are using, is probably the reason why the morphological outcome (the cortical defect) does not mimic the patient's situation where megalencephaly was observed and not heterotopia. Second, we are targeting a subpopulation of cells by performing the IUE at a late time point during embryonic development, thereby confining our manipulation to a specific group of cells in a restricted brain area. However, despite the fact that a constitutive active form of *RHEB1* (Ser16His) was used before to develop a mouse model using IUE showing a cortical area dependent mild migration deficit and epilepsy (Lafourcade *et al*., 2013; Hsieh *et al*., 2016; Nguyen *et al*., 2019), our RHEB1p.P37L model represents the very first model where we could test *RHEB1* variants directly related to ID and MCDs. The advantages of this model over previous models generated using IUE are: 1) mice overexpressing RHEB1p.P37L show a severe migration deficit that highly resembles a localized heterotopic nodule of cells misplaced in the white matter with classical features of MCDs (enlarged dysplastic cells and with increased mTOR hyperactivity), which is not often observed in other mTOR-related models; 2) mice overexpressing RHEB1p.P37L show very consistently non-lethal spontaneous tonic-clonic seizures. This second aspect makes our mouse model a novel and powerful candidate to study epileptogenesis since not all the mouse models previously generated develop spontaneous seizures (Hanai *et al*., 2017) and, more importantly, if they do, there is often high variability in the onset of seizures, in the incidence of seizures and/or in causing lethality (Park *et al*., 2018; Ribierre *et al*., 2018).

From a clinical perspective, it is important to understand if the seizures in MCD

cases have focal starting points or whether they can also originate from surrounding cortical areas, especially when surgery is considered as a possible treatment. Therefore, our model will represent a valuable tool to define the critical regions involved in the development of seizures by using a combination of high-resolution recording techniques (Pittau *et al*., 2014). In **chapter VI** we investigated the role of the cortical malformation in epileptogenesis. In line with other mTOR-related mouse models (Backman *et al*., 2001; Abs *et al*., 2013; Hsieh *et al*., 2016), we showed that the presence of macroscopic focal cortical malformations is not necessary to cause epilepsy, since in our mouse model delayed developmental activation of the mTOR pathway, preventing the formation of cortical malformations, still results in the development of seizures. This also indicates that there is not a strict critical time window during development when hyperactivation of the mTOR pathway and downstream effects are crucial to induce epilepsy. We then used a genetic approach to turn off the mTOR hyperactivation once the cortical malformation is formed. Interestingly, the majority of the mice did not show any epilepsy upon inactivation of the mTOR pathway, indicating that the presence of a macroscopic cortical malformation, by itself, is not sufficient to induce seizures and that the mTOR pathway activation is the main source of the epileptic phenotype. However, it still remains unclear what the epileptogenic mechanisms (preceding the seizures) are, as well as the downstream effects caused by mTOR hyperactivation.

Histopathological analysis performed on brain tissues from patients suffering from TSC or other mTORopathies shows that not only the cells present in the tubers or in the malformations show morphological and molecular abnormalities but that also more or less distant brain areas are often affected, showing mTOR hyperactivity (Marcotte *et al*., 2012). Additionally, human electrophysiological studies show that often seizures can have multiple epileptogenic zones, besides the malformation itself, suggesting a cell non-autonomous effect on otherwise healthy areas of the brain (Chassoux *et al*., 2008; Major *et al*., 2009). This explains why for some patients, especially when the lesions are not focal (Lüders and Schuele, 2006), epilepsy surgery can be challenging, given that defining the border of the tubers and the truly epileptogenic areas is not always straightforward [see the commentary by (Gupta, 2017) on this topic]. What are then the mechanisms in place that are causing the epilepsy? Currently, one of the hypotheses that is being investigated in the field of seizures associated with brain malformations, is that abnormal neurons (with high levels of mTOR activity and located in the wrong position) can alter the surrounding cells by releasing small vesicles called exosomes that could alter the function of supposedly healthy cells in the surrounding, leading to a rewiring of cell circuits and lastly epilepsy (Karttunen *et al*., 2019; Upadhya and Shetty, 2019). Exosomes containing a variety of molecules (proteins, RNA) are being released by cells as a form of intercellular communication and could potentially mediate pathogenicity in different types of disorders (Budnik *et al*., 2016). A similar mechanism has been proposed for example in *Tsc1*$^{-/-}$ cell lines, where it has been shown that they can excrete vesicles containing *Rheb1* RNA, which affects the surrounding cells (Patel *et al*., 2015). However, the

mechanisms that mediate release, the content and the process through which these exosomes could favor epilepsy are not known. Furthermore, the cell non-autonomous effects seem to be not only restricted to the adjacent area to the malformations but can affect distant brain areas, as hypothesized from human studies and mouse models (Valton *et al*., 2008; Marcotte *et al*., 2012; Ishii *et al*., 2015). In line with this, in **chapter VI** we show that in our mouse model also distant, supposedly healthy, brain areas anatomically connected to our targeted area overexpressing the *RHEB1* construct show physiological alterations, even before epilepsy onset. This highlights the importance of not limiting the analysis of the cell non-autonomous effects to the cells immediately surrounding the targeted area, but to explore the effect of the genetic manipulations on more distant brain areas. Additionally, this warrants the use of non-affected cells in the same brain as control cells. In our study, we focused on the contralateral somatosensory cortex to characterize the effects of the abnormal axonal arborization. However, it is likely that the physiological alterations are not strictly confined to the areas directly connected to the targeted cortex but might extend to other cortical and subcortical areas. For example, it will be worthwhile to investigate the contribution of cortico-thalamic connections to the epilepsy phenotype, given the involvement of the Thalamus in other forms of epilepsy, to evaluate the extent of the physiological alterations caused by a local brain lesion (Blumenfeld, 2002). These experiments will be relevant to understand the generalized effects of seizures associated with focal malformations dependent on mTOR hyperactivity and could help to evaluate the choice of using a surgical strategy in patients with these disorders.

The results we obtained in **chapter VI** also reveal that in our model the transfected cells are the driving source behind the epilepsy since blocking vesicle release only from these cells is enough to stop the epilepsy, indicating that potential alterations to non-transfected cells are reversible. We can probably rule out a direct contribution of exosomes to this phenotype, since it has been proposed that specific tetanus insensitive VAMP proteins (such as VAMP7) are involved in the release of exosomes in the extracellular space (Fader *et al*., 2009), however, we cannot yet distinguish with our experimental set-up if this result is a direct effect of blocking synaptic transmission or whether BDNF signaling is also involved (Shimojo *et al*., 2015). The recent engineering of photoactivable neurotoxins could potentially overcome this aspect by selectively targeting neurotoxins to a certain vesicular pool thereby affecting only a specific secretory pathway (Liu *et al*., 2019).

The next step to understand the epileptogenic process will require to study how sparse single cell manipulations lead to changes at the circuit and network level before seizures even occur. Our mouse model proved to be a very effective tool to study this aspect *ex vivo* and will be of extreme value as a general model to further investigate how focal lesions caused by mTOR hyperactivity lead to a generalized phenomenon such as epilepsy. The use of optogenetics experiments and Designer Receptors Exclusively Activated by Designer Drugs (DREADD) tools will allow us to perform experiments *in vivo* to alter neuronal activity in a cell-type and/or area-specific fashion to study the mechanisms of epileptogenesis (Deisseroth,

2015; Roth, 2016; Cela and Sjöström, 2019). Understanding these mechanisms is important to develop new targeted therapeutic strategies to treat mTOR-dependent epilepsy with brain malformations.

In conclusion, the results presented in this thesis show that, in light of all the new genes being identified using NGS involved in neurodevelopmental disorders, the need of proper functional assays to assess the pathogenicity of all these variants is crucial. It becomes also clear how valuable the basic knowledge of the protein role and function in the neuronal context is in the interpretation of the results. Finally, given the heterogeneity of neurodevelopmental disorders, it is important not to limit the functional assays to a set of standardized experimental procedures but, based on the outcome, test specific functions to unravel the full mechanistic spectrum of the pathogenicity caused by a given variant.


VII

Appendix

LIST OF REFERENCES

Abs E, Goorden SMI, Schreiber J, Overwater IE, Hoogeveen-Westerveld M, Bruinsma CF, Aganović E, Borgesius NZ, Nellist M, Elgersma Y (2013) TORC1-dependent epilepsy caused by acute biallelic Tsc1 deletion in adult mice. Ann Neurol 74:569–579.

Achterberg KG, Buitendijk GHS, Kool MJ, Goorden SMI, Post L, Slump DE, Silva AJ, van Woerden GM, Kushner SA, Elgersma Y (2014) Temporal and region-specific requirements of *α*CaMKII in spatial and contextual learning. J Neurosci 34:11180–11187.

Adams HH, Hibar DP, Chouraki V, Stein JL, Nyquist PA, Renteria ME et al. (2016) Novel genetic loci underlying human intracranial volume identified through genome-wide association. Nat Neurosci 19: 1569–1582.

Ageta-Ishihara N, Takemoto-Kimura S, Nonaka M, Adachi-Morishima A, Suzuki K, Kamijo S, Fujii H, Mano T, Blaeser F, Chatila TA, Mizuno H, Hirano T, Tagawa Y, Okuno H, Bito H (2009) Control of Cortical Axon Elongation by a GABA-Driven Ca^{2+}/Calmodulin-Dependent Protein Kinase Cascade. J Neurosci 29:13720–13729.

Akita T, Aoto K, Kato M, Shiina M, Mutoh H, Nakashima M, Kuki I, Okazaki S, Magara S, Shiihara T, Yokochi K, Aiba K, Tohyama J, Ohba C, Miyatake S, Miyake N, Ogata K, Fukuda A, Matsumoto N, Saitsu H (2018) De novo variants in CAMK2A and CAMK2B cause neurodevelopmental disorders. Ann Clin Transl Neurol 5:280–296.

Alcamo EA, Chirivella L, Dautzenberg M, Dobreva G, Fariñas I, Grosschedl R, McConnell SK (2008) Satb2 Regulates Callosal Projection Neuron Identity in the Developing Cerebral Cortex. Neuron 57:364–377.

Ament SA, Szelinger S, Glusman G, Ashworth J, Hou L, Akula N, Shekhtman T, Badner JA, Brunkow ME, Mauldin DE, et al. (2015) Rare variants in neuronal excitability genes influence risk for bipolar disorder. Proc Natl Acad Sci USA 112: 3576– 3581.

American Psychiatric Association (2013) Diagnostic and Statistical Manual of Mental Disorders (5th edition).

Amiri A, Cho W, Zhou J, Birnbaum SG, Sinton CM, McKay RM, Parada LF (2012) Pten deletion in adult hippocampal neural stem/progenitor cells causes cellular abnormalities and alters neurogenesis. J Neurosci 32:5880–5890.

Anderl S, Freeland M, Kwiatkowski DJ, Goto J (2011) Therapeutic value of prenatal rapamycin treatment in a mouse brain model of tuberous sclerosis complex. Hum Mol Genet 20:4597–4604.

Angevine JB, Bodian D, Coulombre AJ, Edds M V., Hamburger V, Jacobson M, Lyser KM, Prestige MC, Sidman RL, Varon S, Weiss PA (1970) Embryonic vertebrate central nervous system: Revised terminology. Anat Rec 166:257–261.

Arabadzisz D, Antal K, Parpan F, Emri Z, Fritschy J-M (2005) Epileptogenesis and chronic seizures in a mouse model of temporal lobe epilepsy are associated with distinct EEG patterns and selective neurochemical alterations in the contralateral hippocampus. Exp Neurol 194:76–90.

Ardestani G, West MC, Maresca TJ, Fissore RA, Stratton MM (2019) FRET-based sensor for CaMKII activity (FRESCA): A useful tool for assessing CaMKII activity in response to Ca^{2+} oscillations in live cells. J Biol Chem 294:11876–11891.

Ardhanareeswaran K, Mariani J, Coppola G, Abyzov A, Vaccarino FM (2017) Human induced pluripotent stem cells for modelling neurodevelopmental disorders. Nat Rev Neurol 13:265–278.

Aspuria PJ, Tamanoi F (2004) The Rheb family of GTP-binding proteins. Cell Signal 16:1105–1112.

Bachstetter AD, Webster SJ, Tu T, Goulding DS, Haiech J, Watterson DM, Van Eldik LJ (2014) Generation and behavior characterization of CaMKIIβ knockout mice Skoulakis EMC, ed. PLoS One 9:e105191.

Backman SA, Stambolic V, Suzuki A, Haight J, Elia A, Pretorius J, Tsao MS, Shannon P, Bolon B, Ivy GO, Mak TW (2001) Deletion of Pten in mouse brain causes seizures, ataxia and defects in soma size resembling Lhermitte-Duclos disease. Nat Genet 29:396–403.

Backs J, Stein P, Backs T, Duncan FE, Grueter CE, McAnally J, Qi X, Schultz RM, Olson EN (2010) The isoform of CaM kinase II controls mouse egg activation by regulating cell cycle resumption. Proc Natl Acad Sci USA 107:81–86.

Bading H (2013) Nuclear calcium signalling in the regulation of brain function. Nat Rev Neurosci 14:593–608.

Baek ST, Copeland B, Yun EJ, Kwon SK, Guemez-Gamboa A, Schaffer AE, Kim S, Kang HC, Song S, Mathern GW, Gleeson JG (2015) An AKT3-FOXG1-reelin network underlies defective migration in human focal malformations of cortical development. Nat Med 21:1445–1454.

Bainbridge MN, Wang M, Wu Y, Newsham I, Muzny DM, Jefferies JL, Albert TJ, Burgess DL, Gibbs RA (2011) Targeted enrichment beyond the consensus coding DNA sequence exome reveals exons with higher variant densities. Genome Biol 12:R68

Bains JS, Longacher JM, Staley KJ (1999) Reciprocal interactions between CA3 network activity and strength of recurrent collateral synapses. Nat Neurosci 2:720 –726.

Banker G, Goslin K (1991) Culturing Nerve Cells. Cambridge, Mass: MIT Press.

Barber M, Pierani A (2016) Tangential migration of glutamatergic neurons and cortical patterning during development: Lessons from Cajal-Retzius cells. Dev Neurobiol 76:847–881.

Barcomb K, Hell JW, Benke TA, Bayer KU (2016) The CaMKII/GluN2B protein interaction maintains synaptic strength. J Biol Chem 291, 16082–16089.

Barkovich AJ, Chuang SH, Norman D (1987) MR of neuronal migration anomalies. Am J Roentgenol 150:179–187.

Barkovich AJ, Kuzniecky RI, Dobyns WB, Jackson GD, Becker LE, Evrard P (1996) A classification scheme for malformations of cortical development. Neuropediatrics 27:59–63.

Barkovich AJ, Guerrini R, Kuzniecky RI, Jackson GD, Dobyns WB (2012) A developmental and genetic classification for malformations of cortical development: Update 2012. Brain

135:1348–1369.

Barkovich AJ, Dobyns WB, Guerrini R (2015) Malformations of cortical development and epilepsy. Cold Spring Harb Perspect Med 5:a022392.

Barkus C, Sanderson DJ, Rawlins JN, Walton ME, Harrison PJ, Bannerman DM (2014) What causes aberrant salience in schizophrenia? A role for impaired short-term habituation and the GRIA1 (GluA1) AMPA receptor subunit. Mol Psychiatry 19, 1060–1070.

Barria A, Derkach V, Soderling T (1997) Identification of the Ca^{2+}/calmodulin-dependent protein kinase II regulatory phosphorylation site in the α-amino-3-hydroxyl-5-methyl-4-isoxazole-propionate-type glutamate receptor. J Biol Chem 272:32727–32730.

Bart Martens M, Frega M, Classen J, Epping L, Bijvank E, Benevento M, van Bokhoven H, Tiesinga P, Schubert D, Nadif Kasri N (2016) Euchromatin histone methyltransferase 1 regulates cortical neuronal network development. Sci Rep 6:35756.

Bast T, Ramantani G, Seitz A, Rating D (2006) Focal cortical dysplasia: Prevalence, clinical presentation and epilepsy in children and adults. Acta Neurol Scand 113:72–81.

Bateup HS, Takasaki KT, Saulnier JL, Denefrio CL, Sabatini BL (2011) Loss of Tsc1 in vivo impairs hippocampal mGluR-LTD and increases excitatory synaptic function. J Neurosci 31:8862–8869.

Baybis M, Yu J, Lee A, Golden JA, Weiner H, McKhann G, Aronica E, Crino PB (2004) mTOR cascade activation distinguishes tubers from focal cortical dysplasia. Ann Neurol 56:478–487.

Bayer KU, Löhler J, Schulman H, Harbers K (1999) Developmental expression of the CaM kinase II isoforms: ubiquitous gamma- and delta-CaM kinase II are the early isoforms and most abundant in the developing nervous system. Brain Res Mol Brain Res 70:147–154.

Bayer KU, De Koninck P, Leonard AS, Hell JW, Schulman H (2001) Interaction with the NMDA receptor locks CaMKII in an active conformation. Nature 411:801–805.

Bayer KU, de Koninck P, Schulman H (2002) Alternative splicing modulates the frequency-dependent response of CaMKII to Ca^{2+} oscillations. EMBO J 21:3590–3597.

Bayer KU, Schulman H (2019) CaM Kinase: Still Inspiring at 40. Neuron 103:380–394.

Bayés Á, Van De Lagemaat LN, Collins MO, Croning MDR, Whittle IR, Choudhary JS, Grant SGN (2011) Characterization of the proteome, diseases and evolution of the human postsynaptic density. Nat Neurosci 14:19–21.

Becker AJ, Urbach H, Scheffler B, Baden T, Normann S, Lahl R, Pannek HW, Tuxhorn I, Elger CE, Schramm J, Wiestler OD, Blümcke I (2002) Focal cortical dysplasia of Taylor's balloon cell type: Mutational analysis of the TSC1 gene indicates a pathogenic relationship to tuberous sclerosis. Ann Neurol 52:29–37.

Behjati S, Tarpey PS (2013) What is next generation sequencing? Arch Dis Child Educ Pract Ed 98:236–238.

Ben-Menachem E (2014) Medical management of refractory epilepsy-Practical treatment with novel antiepileptic drugs. Epilepsia 55:3–8.

Bennett MK, Erondu NE, Kennedy MB (1983) Purification and characterization of a calmodulin-dependent protein kinase that is highly concentrated in brain. J Biol Chem 258:12735–12744.

Bennett MK, Kennedy MB (1987) Deduced primary structure of the beta subunit of brain type II Ca^{2+}/calmodulin-dependent protein kinase determined by molecular cloning. Proc Natl Acad Sci USA 84:1794–1798.

Benson DL, Isackson PJ, Gall CM, Jones EG (1992) Contrasting patterns in the localization of glutamic acid decarboxylase and Ca^{2+}/calmodulin protein kinase gene expression in the rat central nervous system. Neuroscience 46:825–849.

Bessa C, Maciel P, Rodrigues AJ (2013) Using C. Elegans to decipher the cellular and molecular mechanisms underlying neurodevelopmental disorders. Mol Neurobiol 48:465–489.

Bhaskar PT, Hay N (2007) The Two TORCs and Akt. Dev Cell 12:487–502.

Bhattacharyya M, Stratton MM, Going CC, McSpadden ED, Huang Y, Susa AC, Elleman A, Cao YM, Pappireddi N, Burkhardt P, Gee CL, Barros T, Schulman H, Williams ER, Kuriyan J (2016) Molecular mechanism of activation-triggered subunit exchange in Ca^{2+}/calmodulin-dependent protein kinase II. Elife 5:1–32.

Binder DK, Croll SD, Gall CM, Scharfman HE (2001) BDNF and epilepsy: too much of a good thing? Trends Neurosci 24:47–53.

Bliss TVP, Lømo T (1973) Long-lasting potentiation of synaptic transmission in the dentate area of the anaesthetized rabbit following stimulation of the perforant path. J Physiol 232:331–356.

Bliss TVP, Collingridge GL, Morris RGM (2014) Synaptic plasticity in health and disease: Introduction and overview. Philos Trans R Soc B Biol Sci 369:20130129.

Bliss TVP, Collingridge GL, Morris RGM, Reymann KG (2018) Long-term potentiation in the hippocampus: Discovery, mechanisms and function. Neuroforum 24:A103–A120.

Blumenfeld H (2002) The thalamus and seizures. Arch Neurol 59:135–137.

Bockaert J, Marin P (2015) mTOR in Brain Physiology and Pathologies. Physiol Rev 95:1157–1187.

Boer K, Lucassen PJ, Spliet WGM, Vreugdenhil E, van Rijen PC, Troost D, Jansen FE, Aronica E (2009) Doublecortin-like (DCL) expression in focal cortical dysplasia and cortical tubers. Epilepsia 50:2629–2637.

Bomben VC, Aiba I, Qian J, Mark MD, Herlitze S, Noebels JL (2016) Isolated P/Q Calcium Channel Deletion in Layer VI Corticothalamic Neurons Generates Absence Epilepsy. J Neurosci 36:405–418.

Borgesius NZ, van Woerden GM, Buitendijk GHS, Keijzer N, Jaarsma D, Hoogenraad CC, Elgersma Y (2011) βCaMKII plays a nonenzymatic role in hippocampal synaptic plasticity and

learning by targeting αCaMKII to synapses. J Neurosci 31:10141–10148.

Borrie SC, Brems H, Legius E, Bagni C (2017) Cognitive Dysfunctions in Intellectual Disabilities: The Contributions of the Ras-MAPK and PI3K-AKT-mTOR Pathways. Annu Rev Genomics Hum Genet 18:115–142.

Bos JL (1997) Ras-like GTpases. Biochim Biophys Acta - Rev Cancer 1333:M19–M31.

Bourneville D (1880) Sclerose tubereuse circonvolutions cerebrales : idiotie et epilepsie hemiplegique. Arch Neurol (Paris) 1:81–91.

Bowley C, Kerr M (2000) Epilepsy and intellectual disability. J Intellect Disabil Res 44:529–543.

Bozzi Y, Casarosa S, Caleo M (2012) Epilepsy as a neurodevelopmental disorder. Front psychiatry 3:19.

Bradler JE, Barrionuevo G (1990) Heterosynaptic correlates of long-term potentiation induction in hippocampal CA3 neurons. Neuroscience 35: 265–271.

Braun AP, Schulman H (1995) The multifunctional calcium/calmodulin-dependent protein kinase: from form to function. Annu Rev Physiol 4:417–445.

Brocke L, Srinivasan M, Schulman H (1995) Developmental and regional expression of multifunctional Ca^{2+}/calmodulin-dependent protein kinase isoforms in rat brain. J Neurosci 15:6797–6808.

Brocke L, Chiang LW, Wagner PD, Schulman H (1999) Functional implications of the subunit composition of neuronal CaM kinase II. J Biol Chem 274:22713–22722.

Brown EJ, Albers MW, Bum Shin T, Ichikawa K, Keith CT, Lane WS, Schreiber SL (1994) A mammalian protein targeted by G1-arresting rapamycin-receptor complex. Nature 369:756–758.

Brownstein CA, Beggs AH, Rodan L, Shi J, Towne MC, Pelletier R, Cao S, Rosenberg PA, Urion DK, Picker J, Tan WH, Agrawal PB (2016) Clinical heterogeneity associated with KCNA1 mutations include cataplexy and nonataxic presentations. Neurogenetics 17:11–16

Budnik V, Ruiz-Cañada C, Wendler F (2016) Extracellular vesicles round off communication in the nervous system. Nat Rev Neurosci 17:160–172.

Buffington SA, Huang W, Costa-Mattioli M (2014) Translational Control in Synaptic Plasticity and Cognitive Dysfunction. Annu Rev Neurosci 37:17–38.

Bulleit RF, Bennett MK, Molloy SS, Hurley JB, Kennedy MB (1988) Conserved and variable regions in the subunits of brain type II Ca^{2+}/calmodulin-dependent protein kinase. Neuron 1:63–72.

Butler LS, Silva AJ, Abeliovich A, Watanabe Y, Tonegawa S, McNamara JO (1995) Limbic epilepsy in transgenic mice carrying a Ca^{2+}/calmodulin-dependent kinase II alpha-subunit mutation. Proc Natl Acad Sci USA 92:6852– 6855.

Buzsáki G (1985) What does the "LTP Model of Memory" Model? In, pp 157–166. Springer, Boston, MA.

Bystron I, Blakemore C, Rakic P (2008) Development of the human cerebral cortex: Boulder Committee revisited. Nat Rev Neurosci 9:110–122.

Caplan R, Austin JK (2000) Behavioral aspects of epilepsy in children with mental retardation. Ment Retard Dev Disabil Res Rev 6:293–299.

Carlin RK, Grab DJ, Cohen RS, Siekevitz P (1980) Isolation and characterization of postsynaptic densities from various brain regions: enrichment of different types of postsynaptic densities. J Cell Biol 86:831– 845.

Carvill GL, Regan BM, Yendle SC, et al. (2013) GRIN2A mutations cause epilepsy-aphasia spectrum disorders. Nat Genet 45:1073–1076.

Castro AF, Rebhun JF, Clark GJ, Quilliam LA (2003) Rheb binds tuberous sclerosis complex 2 (TSC2) and promotes S6 kinase activation in a rapamycin- and farnesylation-dependent manner. J Biol Chem 278:32493–32496.

Cavus¸ I, Teyler T (1996) Two forms of long-term potentiation in area CA1 activate different signal transduction cascades. J Neurophysiol 76:3038 – 3047.

Cawthon RM, O'Connell P, Buchberg AM, Viskochil D, Weiss RB, Culver M, Stevens J, Jenkins NA, Copeland NG, White R (1990) Identification and characterization of transcripts from the neurofibromatosis 1 region: The sequence and genomic structure of EVI2 and mapping of other transcripts. Genomics 7:555–565.

Cela E, Sjöström PJ (2019) Novel Optogenetic Approaches in Epilepsy Research. Front Neurosci 13:947.

Cesca F, Baldelli P, Valtorta F, Benfenati F (2010) The synapsins: Key actors of synapse function and plasticity. Prog Neurobiol 91:313–348.

Chang JY, Parra-Bueno P, Laviv T, Szatmari EM, Lee SJR, Yasuda R (2017) CaMKII Autophosphorylation Is Necessary for Optimal Integration of Ca^{2+} Signals during LTP Induction, but Not Maintenance. Neuron 94:800-808.e4.

Chapman PF, Frenguelli BG, Smith A, Chen CM, Silva AJ (1995) The alpha-Ca^{2+}/calmodulin kinase II: a bidirectional modulator of presynaptic plasticity. Neuron 14:591–597.

Chassoux F, Landre E, Rodrigo S, Beuvon F, Turak B, Semah F, Devaux B (2008) Intralesional recordings and epileptogenic zone in focal polymicrogyria. Epilepsia 49:51–64.

Chauvière L, Rafrafi N, Thinus-Blanc C, Bartolomei F, Esclapez M, Bernard C (2009) Early deficits in spatial memory and theta rhythm in experimental temporal lobe epilepsy. J Neurosci 29:5402–5410.

Che F, Zhang Y, Wang G, Heng X, Liu S, Du Y (2015) The role of GRIN2B in Tourette syndrome: Results from a transmission disequilibrium study. J Affect Disord 187: 62–65.

Chen C, Rainnie DG, Greene RW, Tonegawa S (1994) Abnormal fear response and aggressive behavior in mutant mice deficient

for alpha-calcium-calmodulin kinase II. Science 266: 291–294.

Chen Y, Chen H, Rhoad AE, Warner L, Caggiano TJ, Failli A, Zhang H, Hsiao CL, Nakanishi K, Molnar-Kimber KL (1994) A putative sirolimus (rapamycin) effector protein. Biochem Biophys Res Commun 203:1–7.

Chen B, Schaevitz LR, McConnell SK (2005a) Fezl regulates the differentiation and axon targeting of layer 5 subcortical projection neurons in cerebral cortex. Proc Natl Acad Sci USA 102:17184–17189.

Chen JG, Rasin MR, Kwan KY, Sestan N (2005b) Zfp312 is required for subcortical axonal projections and dendritic morphology of deep-layer pyramidal neurons of the cerebral cortex. Proc Natl Acad Sci USA 102:17792–17797.

Cheng D, Hoogenraad CC, Rush J, Ramm E, Schlager MA, Duong DM, Xu P, Wijayawardana SR, Hanfelt J, Nakagawa T, Sheng M, Peng J (2006) Relative and Absolute Quantification of Postsynaptic Density Proteome Isolated from Rat Forebrain and Cerebellum. Mol Cell Proteomics 5:1158–1170.

Chevassus-Au-Louis N, Baraban SC, Gaïarsa JL, Ben-Ari Y (1999) Cortical malformations and epilepsy: New insights from animal models. Epilepsia 40:811–821.

Chia PH, Zhong FL, Niwa S, Bonnard C, Utami KH, Zeng R, Lee H, Eskin A, Nelson SF, Xie WH, Al-Tawalbeh S, El-Khateeb M, Shboul M, Pouladi MA, Al-Raqad M, Reversade B (2018) A homozygous loss-of-function CAMK2A mutation causes growth delay, frequent seizures and severe intellectual disability. ELife 7: e32451.

Cho CH (2011) Frontier of epilepsy research - mTOR signaling pathway. Exp Mol Med 43: 231–274.

Choi YJ, Di Nardo A, Kramvis I, Meikle L, Kwiatkowski DJ, Sahin M, He X (2008) Tuberous sclerosis complex proteins control axon formation. Genes Dev 22:2485–2495.

Cloëtta D, Thomanetz V, Baranek C, Lustenberger RM, Lin S, Oliveri F, Atanasoski S, Rüegg M a (2013) Inactivation of mTORC1 in the developing brain causes microcephaly and affects gliogenesis. J Neurosci 33:7799–7810.

Coe BP, Stessman HAF, Sulovari A, Geisheker MR, Bakken TE, Lake AM, Dougherty JD, Lein ES, Hormozdiari F, Bernier RA, Eichler EE (2019) Neurodevelopmental disease genes implicated by de novo mutation and copy number variation morbidity. Nat Genet 51:106–116.

Cohen SM, Li B, Tsien RW, Ma H (2015) Evolutionary and functional perspectives on signaling from neuronal surface to nucleus. Biochem Biophys Res Commun 460:88–99.

Cohen SM, Ma H, Kuchibhotla K V., Watson BO, Buzsáki G, Froemke RC, Tsien RW (2016) Excitation-Transcription Coupling in Parvalbumin-Positive Interneurons Employs a Novel CaM Kinase-Dependent Pathway Distinct from Excitatory Neurons. Neuron 90:292–307.

Cohen SM, Suutari B, He X, Wang Y, Sanchez S, Tirko NN, Mandelberg NJ, Mullins C, Zhou G, Wang S, Kats I, Salah A, Tsien RW, Ma H (2018) Calmodulin shuttling mediates cytonuclear signaling to trigger experience-dependent transcription and memory. Nat Commun 9:2451.

Colbran RJ, Soderling TR (1990) Calcium/calmodulin-independent autophosphorylation sites of calcium/calmodulin-dependent protein kinase II: Studies on the effect of phosphorylation of threonine 305/306 and serine 314 on calmodulin binding using synthetic peptides. J Biol Chem 265:11213–11219.

Colbran RJ (1992) Regulation and role of brain calcium/calmodulin-dependent protein kinase II. Neurochem Int 21:469–497.

Colbran RJ (2004) Targeting of calcium/calmodulin-dependent protein kinase II. Biochem J 378: 1–16.

Colbran RJ, Brown AM (2004) Calcium/calmodulin-dependent protein kinase II and synaptic plasticity. Curr Opin Neurobiol 14:318–327.

Coll-Tané M, Krebbers A, Castells-Nobau A, Zweier C, Schenck A (2019) Intellectual disability and autism spectrum disorders 'on the fly': insights from Drosophila. Dis Model Mech 12:dmm039180.

Cooper JA (2008) A mechanism for inside-out lamination in the neocortex. Trends Neurosci 31:113–119.

Costa MR, Müller U (2015) Specification of excitatory neurons in the developing cerebral cortex: Progenitor diversity and environmental influences. Front Cell Neurosci 8:1–9

Coultrap SJ, Bayer KU (2012) CaMKII regulation in information processing and storage. Trends Neurosci 35:607–618.

Crino PB (2005) Molecular pathogenesis of focal cortical dysplasia and hemimegalencephaly. J Child Neurol 20:330–336.

Crino PB (2007) Focal brain malformations: a spectrum of disorders along the mTOR cascade. Novartis Found Symp 288:260–272; discussion 272-81.

Crino PB (2011) MTOR: A pathogenic signaling pathway in developmental brain malformations. Trends Mol Med 17:734–742.

Crino PB (2015) mTOR signaling in epilepsy: Insights from malformations of cortical development. Cold Spring Harb Perspect Med 5.

Curatolo P, Moavero R, Roberto D, Graziola F (2015) Genotype/Phenotype Correlations in Tuberous Sclerosis Complex. Semin Pediatr Neurol 22:259–273.

D'Gama, AM, Woodworth MB, Hossain AM, Bizzotto S, Hatem NE, LaCoursiere CM, Najm I, Ying Z, Yang E, Barkovich AJ, Kwiatkowski DJ, Vinters HV, Madsen JR, Mathern GW, Blümcke I, Poduri A, Walsh CA, (2017) Somatic Mutations Activating the mTOR Pathway in Dorsal Telencephalic Progenitors Cause a Continuum of Cortical Dysplasias. Cell Rep 21:3754–3766.

Dawson RE, Nieto Guil AF, Robertson LJ, Piltz SG, Hughes JN, Thomas PQ (2020) Functional screening of GATOR1 complex variants reveals a role for mTORC1 deregulation in FCD and focal epilepsy. Neurobiol Dis 134:104640.

de Leeuw CA, Mooij JM, Heskes T, Posthuma D (2015) MAGMA: Generalized Gene-Set Analysis of GWAS Data Tang H, PLoS

Comput Biol 11:e1004219.

de Leeuw CA, Neale BM, Heskes T, Posthuma D (2016) The statistical properties of gene-set analysis. Nat Rev Genet 17:353–364.

de Ligt J, Willemsen MH, van Bon BWM, Kleefstra T, Yntema HG, Kroes T, Vulto-van Silfhout AT, Koolen DA, de Vries P, Gilissen C, del Rosario M, Hoischen A, Scheffer H, de Vries BBA, Brunner HG, Veltman JA, Vissers LELM (2012) Diagnostic Exome Sequencing in Persons with Severe Intellectual Disability. N Engl J Med 367:1921–1929.

de Quervain DJ-F, Papassotiropoulos A (2006) Identification of a genetic cluster influencing memory performance and hippocampal activity in humans. Proc Natl Acad Sci USA 103:4270–4274.

Debanne D, Gähwiler BH, Thompson SM (1998) Long-term synaptic plasticity between pairs of individual CA3 pyramidal cells in rat hippocampal slice cultures. J Physiol 507:237–247.

Debanne D, Gähwiler BH, Thompson SM (1999) Heterogeneity of synaptic plasticity at unitary CA3–CA1 and CA3–CA3 connections in rat hippocampal slice cultures. J Neurosci 19:10664–10671.

Deciphering Developmental Disorders Study (2015). Large-scale discovery of novel genetic causes of developmental disorders. Nature 519, 223–228.

Deciphering Developmental Disorders Study (2017). Prevalence and architecture of de novo mutations in developmental disorders. Nature 542, 433–438.

Dehay C, Kennedy H (2007) Cell-cycle control and cortical development. Nat Rev Neurosci 8:438–450

Deisseroth K (2015) Optogenetics : 10 years of microbial opsins in neuroscience. Nature 18:1213–1225.

DeLorenzo RJ, Freedman SD, Yohe WB, Maurer SC (1979) Stimulation of Ca^{2+}-dependent neurotransmitter release and presynaptic nerve terminal protein phosphorylation by calmodulin and a calmodulin-like protein isolated from synaptic vesicles. Proc Natl Acad Sci USA 76:1838 –1842.

Demetriades C, Doumpas N, Teleman AA (2014) Regulation of TORC1 in response to amino acid starvation via lysosomal recruitment of TSC2. Cell 156:786–799.

Deng L, Chen L, Zhao L, Xu Y, Peng X, Wang X, Ding L, Jin J, Teng H, Wang Y, Pan W, Yu F, Liao L, Li L, Ge X, Wang P (2019) Ubiquitination of Rheb governs growth factor-induced mTORC1 activation. Cell Res 29:136–150.

Derkach V, Barria A, Soderling TR (2002) Ca^{2+}/calmodulin-kinase II enhances channel conductance of -amino-3-hydroxy-5-methyl-4-isoxazolepropionate type glutamate receptors. Proc Natl Acad Sci USA 96:3269–3274.

Desikan RS, Barkovich AJ (2016) Malformations of cortical development. Ann Neurol 80:797–810.

Devinsky O, Vezzani A, O'Brien TJ, Jette N, Scheffer IE, de Curtis M, Perucca P (2018) Epilepsy. Nat Rev Dis Prim 4:18024.

Di Lullo E, Kriegstein AR (2017) The use of brain organoids to investigate neural development and disease. Nat Rev Neurosci 18:573–584.

Dittrich L (2016) Patient H.M: A story of memory, madness and family secrets. Random House Publishing Group.

Durbin R, Altshuler D, Durbin R et al. (2010) A map of human genome variation from population-scale sequencing. Nature 467:1061–1073.

Easley CA, Faison MO, Kirsch TL, Lee JA, Seward ME, Tombes RM (2006) Laminin activates CaMK-II to stabilize nascent embryonic axons. Brain Res 1092:59–68.

Edman CF, Schulman H (1994) Identification and characterization of δB-CaM kinase and δC-CaM kinase from rat heart, two new multifunctional Ca^{2+}/calmodulin-dependent protein kinase isoforms. BBA - Mol Cell Res 1221:89–101.

Elgersma Y, Fedorov NB, Ikonen S, Choi ES, Elgersma M, Carvalho OM, Giese KP, Silva AJ (2002) Inhibitory autophosphorylation of CaMKII controls PSD association, plasticity, and learning. Neuron 36:493–505.

Elgersma Y, Sweatt JD, Giese KP (2004) Mouse genetic approaches to investigating calcium/calmodulin-dependent protein kinase II function in plasticity and cognition. J Neurosci 24:8410–8415.

Endele S, Rosenberger G, Geider K, Popp B, Tamer C, Stefanova I, Milh M, Kortum F, Fritsch A, Pientka FK, et al. (2010) Mutations in GRIN2A and GRIN2B encoding regulatory subunits of NMDA receptors cause variable neurodevelopmental phenotypes. Nat Genet 42:1021–1026.

Englot DJ, Chang EF, Vecht CJ (2016) Epilepsy and brain tumors. In: Handbook of Clinical Neurology, pp 267–285. NIH Public Access.

Erondu NE, Kennedy MB (1985) Regional distribution of type II Ca^{2+}/calmodulin-dependent protein kinase in rat brain. J Neurosci 5:3270–3277.

Evers C, Staufner C, Granzow M, Paramasivam N, Hinderhofer K, Kaufmann L, Fischer C, Thiel C, Opladen T, Kotzaeridou U, Wiemann S, Schlesner M, Eils R, Kölker S, Bartram CR, Hoffmann GF, Moog U (2017) Impact of clinical exomes in neurodevelopmental and neurometabolic disorders. Mol Genet Metab 121:297–307.

Fader CM, Sánchez DG, Mestre MB, Colombo MI (2009) TI-VAMP/VAMP7 and VAMP3/cellubrevin: two v-SNARE proteins involved in specific steps of the autophagy/multivesicular body pathways. Biochim Biophys Acta - Mol Cell Res 1793:1901–1916.

Fan X, Jin WY, Wang YT (2014) The NMDA receptor complex: a multifunctional machine at the glutamatergic synapse. Front Cell Neurosci 8: 160.

Fang Y, Westbrook R, Hill C, Boparai RK, Arum O, Spong A, Wang F, Javors MA, Chen J, Sun LY, Bartke A (2013) Duration of rapamycin treatment has differential effects on metabolism in mice. Cell Metab 17:456–462.

Farwell KD, Shahmirzadi L, El-Khechen D, Powis Z, Chao EC, Tippin Davis B, Baxter RM, Zeng W, Mroske C, Parra MC, et al.

(2015) Enhanced utility of family-centered diagnostic exome sequencing with inheritance model-based analysis: Results from 500 unselected families with undiagnosed genetic conditions. Genet Med 17:578–586.

Fassunke J, Blümcke I, Lahl R, Elger CE, Schramm J, Merkelbach-Bruse S, Mathiak M, Wiestler OD, Becker AJ (2004) Analysis of chromosomal instability in focal cortical dysplasia of Taylor's balloon cell type. Acta Neuropathol 108:129–134.

Feliciano DM, Su T, Lopez J, Platel J-C, Bordey A (2011) Single-cell Tsc1 knockout during corticogenesis generates tuber-like lesions and reduces seizure threshold in mice. J Clin Invest 121:1596–1607.

Feliciano DM, Quon JL, Su T, Taylor MM, Bordey A (2012) Postnatal neurogenesis generates heterotopias, olfactory micronodules and cortical infiltration following single-cell Tsc1 deletion. Hum Mol Genet 21:799–810.

Feng B, Raghavachari S, Lisman J (2011) Quantitative estimates of the cytoplasmic, PSD, and NMDAR-bound pools of CaMKII in dendritic spines. Brain Res 1419:46–52.

Fenlon LR, Suárez R, Richards LJ (2017) The anatomy, organisation and development of contralateral callosal projections of the mouse somatosensory cortex. Brain Neurosci Adv 1:239821281769488.

Filosa A, Paixao S, Honsek SD, Carmona MA, Becker L, Feddersen B, Gait- anos L, Rudhard Y, Schoepfer R, Klopstock T, Kullander K, Rose CR, Pasquale EB, Klein R (2009) Neuron-glia communication via EphA4/ ephrin-A3 modulates LTP through glial glutamate transport. Nat Neurosci 12:1285–1292.

Fink CC, Bayer KU, Myers JW, Ferrell JE, Schulman H, Meyer T (2003) Selective regulation of neurite extension and synapse formation by the β but not the α isoform of CaMKII. Neuron 39:283–297.

Firth HV, Richards SM, Bevan AP, Clayton S, Corpas M, Rajan D, Van Vooren S, Moreau Y, Pettett RM, Carter NP (2009) DECIPHER: Database of Chromosomal Imbalance and Phenotype in Humans Using Ensembl Resources. Am J Hum Genet 84: 524–533.

Fishwick KJ, Li RA, Halley P, Deng P, Storey KG (2010) Initiation of neuronal differentiation requires PI3-kinase/TOR signalling in the vertebrate neural tube. Dev Biol 338:215–225.

Fong YL, Taylor WL, Means AR, Soderling TR (1989) Studies of the regulatory mechanism of Ca^{2+}/calmodulin-dependent protein kinase II. Mutation of threonine 286 to alanine and aspartate. J Biol Chem 264:16759–16763.

Forrest D, Yuzaki M, Soares HD, Ng L, Luk DC, Sheng M, Stewart CL, Morgan JI, Connor JA, Curran T (1994) Targeted disruption of NMDA receptor 1 gene abolishes NMDA response and results in neonatal death. Neuron 13:325–338.

Franz DN, Belousova E, Sparagana S, Bebin EM, Frost M, Kuperman R et al. (2013) Efficacy and safety of everolimus for subependymal giant cell astrocytomas associated with tuberous sclerosis complex (EXIST-1): A multicentre, randomised, placebo-controlled phase 3 trial. Lancet 381:125–132.

Frega M, Linda K, Keller JM, Gümüş-Akay G, Mossink B, van Rhijn J-R, Negwer M, Klein Gunnewiek T, Foreman K, Kompier N, Schoenmaker C, van den Akker W, van der Werf I, Oudakker A, Zhou H, Kleefstra T, Schubert D, van Bokhoven H, Nadif Kasri N (2019) Neuronal network dysfunction in a model for Kleefstra syndrome mediated by enhanced NMDAR signaling. Nat Commun 10:4928.

Frega M, Selten M, Mossink B, Keller JM, Linda K, Moerschen R, Qu J, Koerner P, Jansen S, Oudakker A, Kleefstra T, van Bokhoven H, Zhou H, Schubert D, Nadif Kasri N (2020) Distinct Pathogenic Genes Causing Intellectual Disability and Autism Exhibit a Common Neuronal Network Hyperactivity Phenotype. Cell Rep 30:173-186.e6.

French JA, Lawson JA, Yapici Z, Ikeda H, Polster T, Nabbout R, Curatolo P, de Vries PJ, Dlugos DJ, Berkowitz N, Voi M, Peyrard S, Pelov D, Franz DN (2016) Adjunctive everolimus therapy for treatment-resistant focal-onset seizures associated with tuberous sclerosis (EXIST-3): a phase 3, randomised, double-blind, placebo-controlled study. Lancet 388:2153–2163.

Gaisano HY, Sheu L, Foskett JK, Trimble WS (1994) Tetanus toxin light chain cleaves a vesicle-associated membrane protein (VAMP) isoform 2 in rat pancreatic zymogen granules and inhibits enzyme secretion. J Biol Chem 269:17062–17066.

Garelick MG, Kennedy BK (2011) TOR on the brain. Exp Gerontol 46:155–163.

Garza-Lombó C, Gonsebatt ME (2016) Mammalian Target of Rapamycin: Its Role in Early Neural Development and in Adult and Aged Brain Function. Front Cell Neurosci 10:157.

Gatto CL, Broadie K (2011) Drosophila modeling of heritable neurodevelopmental disorders. Curr Opin Neurobiol 21:834–841.

Gebauer F, Hentze MW (2004) Molecular mechanisms of translational control. NatRevMolCell Biol 5:827–835.

Giese KP, Fedorov NB, Filipkowski RK, Silva AJ (1998) Autophosphorylation at Thr286 of the alpha calcium-calmodulin kinase II in LTP and learning. Science 279:870 – 873.

Gilissen C, Hoischen A, Brunner HG, Veltman JA (2011) Unlocking Mendelian disease using exome sequencing. Genome Biol 12:228.

Gilissen C, Hehir-Kwa JY, Thung DT, et al. (2014) Genome sequencing identifies major causes of severe intellectual disability. Nature 511:344–347.

Goldberg EM, Coulter DA (2013) Mechanisms of epileptogenesis: a convergence on neural circuit dysfunction. Nat Rev Neurosci 14:337–349.

Gómez MR (1995) History of the tuberous sclerosis complex. Brain Dev 17:55–57.

Gong X, Zhang L, Huang T, Lin T V., Miyares L, Wen J, Hsieh L, Bordey A (2015) Activating the translational repressor 4E-BP or reducing S6K-GSK3β activity prevents accelerated axon growth induced by hyperactive mTOR in vivo. Hum Mol Genet 24:5746–5758.

Goorden SMI, Van Woerden GM, Van Der Weerd L, Cheadle JP, Elgersma Y (2007) Cognitive deficits in Tsc1+/- mice in the absence of cerebral lesions and seizures. Ann Neurol 62:648–

655.

Goorden SMI, Hoogeveen-Westerveld M, Cheng C, Van Woerden GM, Mozaffari M, Post L, Duckers HJ, Nellist M, Elgersma Y (2011) Rheb Is Essential for Murine Development. Mol Cell Biol 31:1672–1678.

Goorden SMI, Abs E, Bruinsma CF, Riemslagh FW, van Woerden GM, Elgersma Y (2015) Intact neuronal function in Rheb1 mutant mice: implications for TORC1-based treatments. Hum Mol Genet 24:3390–3398.

Goto J, Talos DM, Klein P, Qin W, Chekaluk YI, Anderl S, Malinowska IA, Di Nardo A, Bronson RT, Chan JA, Vinters H V, Kernie SG, Jensen FE, Sahin M, Kwiatkowski DJ (2011) Regulable neural progenitor-specific Tsc1 loss yields giant cells with organellar dysfunction in a model of tuberous sclerosis complex. Proc Natl Acad Sci USA 108:E1070-9.

Grajkowska W, Kotulska K, Jurkiewicz E, Matyja E (2010) Brain lesions in tuberous sclerosis complex. Review. Folia Neuropathol 48:139–149.

Grant SG, Silva AJ (1994) Targeting learning. Trends Neurosci 17: 71–75.

Grant SGN (2012) Synaptopathies: Diseases of the synaptome. Curr Opin Neurobiol 22:522–529.

Gray CBB, Brown JH (2014) CaMKIIdelta subtypes: Localization and function. Front Pharmacol 5:1–8.

Greig LC, Woodworth MB, Galazo MJ, Padmanabhan H, Macklis JD (2013) Molecular logic of neocortical projection neuron specification, development and diversity. Nat Rev Neurosci 14:755–769.

Greig LC, Woodworth MB, Greppi C, Macklis JD (2016) Ctip1 Controls Acquisition of Sensory Area Identity and Establishment of Sensory Input Fields in the Developing Neocortex. Neuron 90:261–277.

Griffith LC (2004) Calcium/Calmodulin-Dependent Protein Kinase II: An Unforgettable Kinase. J Neurosci 24:8391–8393.

Groenewoud MJ, Zwartkruis FJTT (2013) Rheb and Rags come together at the lysosome to activate mTORC1. Biochem Soc Trans 41:951–955.

Grover LM, Teyler TJ (1990) Two components of long-term potentiation induced by different patterns of afferent activation. Nature 347:477– 479.

Guerrini R, Parrini E (2010) Neuronal migration disorders. Neurobiol Dis 38:154–166

Gullo F, Manfredi I, Lecchi M, Casari G, Wanke E, Becchetti A (2014) Multi-electrode array study of neuronal cultures expressing nicotinic β2-V287L subunits, linked to autosomal dominant nocturnal frontal lobe epilepsy. An in vitro model of spontaneous epilepsy. Front Neural Circuits 8:87.

Gupta A (2017) Epilepsy surgery in tuberous sclerosis complex: In pursuit of the epileptogenic center(s). Epilepsy Curr 17:150–152.

Hamdan FF, Gauthier J, Araki Y, et al. (2011) Excess of de novo deleterious mutations in genes associated with glutamatergic systems in nonsyndromic intellectual disability. Am J Hum Genet 88:306–316.

Han J, Wang B, Xiao Z, Gao Y, Zhao Y, Zhang J, Chen B, Wang X, Dai J (2008) Mammalian target of rapamycin (mTOR) is involved in the neuronal differentiation of neural progenitors induced by insulin. Mol Cell Neurosci 39:118–124.

Han JM, Sahin M (2011) TSC1/TSC2 signaling in the CNS. FEBS Lett 585:973–980.

Hanai S, Sukigara S, Dai H, Owa T, Horike S ichi, Otsuki T, Saito T, Nakagawa E, Ikegaya N, Kaido T, Sato N, Takahashi A, Sugai K, Saito Y, Sasaki M, Hoshino M, Goto Y ichi, Koizumi S, Itoh M (2017) Pathologic Active mTOR Mutation in Brain Malformation with Intractable Epilepsy Leads to Cell-Autonomous Migration Delay. Am J Pathol 187:1177–1185.

Hanker AB, Mitin N, Wilder RS, Henske EP, Tamanoi F, Cox AD, Der CJ (2010) Differential requirement of CAAX-mediated posttranslational processing for Rheb localization and signaling. Oncogene 29:380–391.

Hanley RM, Means AR, Ono T, Kemp BE, Burgin KE, Waxham N, Kelly PT (1987) Functional analysis of a complementary DNA for the 50-kilodalton subunit of calmodulin kinase II. Science 237:293–297.

Hannah JA, Brodie MJ (1998) Epilepsy and learning disabilities - a challenge for the next millennium? Seizure 7:3–13.

Hansel C, de Jeu M, Belmeguenai A, Houtman SH, Buitendijk GHS, Andreev D, De Zeeuw CI, Elgersma Y (2006) αCaMKII Is Essential for Cerebellar LTD and Motor Learning. Neuron 51:835–843.

Hanson PI, Kapiloff MS, Lou L, Rosenfeld MC, Schulman H (1989) Expression of a Multifunctional Protein Kinase and Mutational Analysis of Its Autoregulation. Cell 3:59–70.

Hanson PI, Meyer T, Stryer L, Schulman H (1994) Dual role of calmodulin in autophosphorylation of multifunctional CaM kinase may underlie decoding of calcium signals. Neuron 12:943–956.

Hanson PI, Schulman H (1992) Inhibitory autophosphorylation of multifunctional Ca^{2+}/calmodulin-dependent protein kinase analyzed by site-directed mutagenesis. J Biol Chem 267:17216–17224.

Harris TE, Lawrence JC (2003) TOR signaling. Sci STKE 2003:re15–re15

Hartlaub AM, McElroy CA, Maitre NL, Hester ME (2019) Modeling Human Brain Circuitry Using Pluripotent Stem Cell Platforms. Front Pediatr 7:57.

Hartman NW, Lin T V., Zhang L, Paquelet GE, Feliciano DM, Bordey A (2013) mTORC1 targets the translational repressor 4E-BP2, but not S6 kinase 1/2, to regulate neural stem cell self-renewal in vivo. Cell Rep 5:433–444.

Hay N, Sonenberg N (2004) Upstream and downstream of mTOR. Genes Dev 18:1926–1945.

Hayashi Y, Shi SH, Esteban JA, Piccini A, Poncer JC, Malinow R (2000) Driving AMPA receptors into synapses by LTP and CaMKII: Requirement for GluR1 and PDZ domain interaction. Science 287:2262–2267.

Heard JJ, Fong V, Bathaie SZ, Tamanoi F (2014) Recent progress in the study of the Rheb family GTPases. Cell Signal 26:1950–1957.

Heard JJ, Tamanoi F (2018) GTP-Binding Protein Rheb. In: Encyclopedia of Signaling Molecules, pp 2288–2293. Cham: Springer International Publishing.

Hebb DO (1949) The organization of behavior: a neuropsychological theory. New York, John Wiley.

Heist EK, Srinivasan M, Schulman H (1998) Phosphorylation at the nuclear localization signal of Ca^{2+}/calmodulin-dependent protein kinase II blocks its nuclear targeting. J Biol Chem 273:19763–19771.

Hell JW (2014) CaMKII: claiming center stage in postsynaptic function and organization. Neuron 81:249 –265.

Hempel M, Cremer K, Ockeloen CW, Lichtenbelt KD, Herkert JC, Denecke J, Haack TB, Zink AM, Becker J, Wohlleber E et al. (2015) De novo mutations in CHAMP1 cause intellectual disability with severe speech impairment. Am J Hum Genet 97: 493–500.

Hentges KE, Sirry B, Gingeras A-C, Sarbassov D, Sonenberg N, Sabatini D, Peterson AS (2001) FRAP/mTOR is required for proliferation and patterning during embryonic development in the mouse. Proc Natl Acad Sci USA 98:13796–13801.

Heyne HO, Singh T, Stamberger H, et al. (2018) De novo variants in neurodevelopmental disorders with epilepsy. Nat Genet 50:1048–1053.

Herreras O (2016) Local Field Potentials: Myths and Misunderstandings. Front Neural Circuits 10:101.

Hibar D, Stein J, Renteria M. et al. (2015) Common genetic variants influence human subcortical brain structures. Nature 520:224–229.

Hinds HL, Tonegawa S, Malinow R (1998) CA1 long-term potentiation is diminished but present in hippocampal slices from alpha-CaMKII mutant mice. Learn Mem 5:344 –354.

Hinds HL, Goussakov I, Nakazawa K, Tonegawa S, Bolshakov VY (2003) Essential function of calcium/calmodulin-dependent protein kinase II in neurotransmitter release at a glutamatergic central synapse. Proc Natl Acad Sci USA 100:4275– 4280.

Hirano T (2013) Long-term depression and other synaptic plasticity in the cerebellum. Proc Japan Acad Ser B Phys Biol Sci 89:183–195.

Hirota Y, Nakajima K (2017) Control of Neuronal Migration and Aggregation by Reelin Signaling in the Developing Cerebral Cortex. Front Cell Dev Biol 5:40.

Hoeffer CA, Santini E, Ma T, Arnold EC, Whelan AM, Arnold EC, Pierre P, Pelletier J, Klann E (2013) Multiple components of eIF4F are required for protein synthesis-dependent hippocampal long-term potentiation. J Neurophysiol 109:68–76.

Hoffman L, Farley MM, Waxham MN (2013) Calcium-calmodulin-dependent protein kinase II isoforms differentially impact the dynamics and structure of the actin cytoskeleton. Biochemistry 52:1198–1207.

Hojjati MR, van Woerden GM, Tyler WJ, Giese KP, Silva AJ, Pozzo-Miller L, Elgersma Y (2007) Kinase activity is not required for alphaCaMKII- dependent presynaptic plasticity at CA3–CA1 synapses. Nat Neurosci 10:1125–1127.

Holla OL, Busk OL, Tveten K, Hilmarsen HT, Strand L, Høyer H, Bakken A, Skjelbred CF, Braathen GJ (2015) Clinical exome sequencing – Norwegian findings. Tidsskr. Nor. Laegeforen. 135: 1833–1837.

Houge G, Haesen D, Vissers LELM, et al. (2015) B56δ-related protein phosphatase 2A dysfunction identified in patients with intellectual disability. J Clin Invest 125:3051–3062.

Hsieh LS, Wen JH, Claycomb K, Huang Y, Harrsch FA, Naegele JR, Hyder F, Buchanan GF, Bordey A (2016) Convulsive seizures from experimental focal cortical dysplasia occur independently of cell misplacement. Nat Commun 7:11753.

Hu S, Knowlton RC, Watson BO, Glanowska KM, Murphy GG, Parent JM, Wang Y (2018) Somatic Depdc5 deletion recapitulates electroclinical features of human focal cortical dysplasia type IIA. Ann Neurol 84:140–146.

Huang WC, Chen Y, Page DT (2016) Hyperconnectivity of prefrontal cortex to amygdala projections in a mouse model of macrocephaly/autism syndrome. Nat Commun 7:13421.

Hudmon A, Schulman H (2002a) Structure–function of the multifunctional Ca^{2+}/calmodulin-dependent protein kinase II. Biochem J 364:593–611.

Hudmon A, Schulman H (2002b) Neuronal Ca^{2+}/calmodulin-dependent protein kinase II: the role of structure and autoregulation in cellular function. Annu Rev Biochem 71:473–510.

Im E, Von Lintig FC, Chen J, Zhuang S, Qui W, Chowdhury S, Worley PF, Boss GR, Pilz RB (2002) Rheb is in a high activation state and inhibits B-Raf kinase in mammalian cells. Oncogene 21:6356–6365.

Incontro S, Díaz-Alonso J, Iafrati J, Vieira M, Asensio CS, Sohal VS, Roche KW, Bender KJ, Nicoll RA (2018) The CaMKII/NMDA receptor complex controls hippocampal synaptic transmission by kinase-dependent and independent mechanisms. Nat Commun 9:2069.

Iossifov, I., O'Roak, B.J., Sanders, S.J., Ronemus, M., Krumm, N., Levy, D., Stessman, H.A., Witherspoon, K.T., Vives, L., Patterson, K.E., et al. (2014). The contribution of de novo coding mutations to autism spectrum disorder. Nature 515:216–221.

Ishii K, Kubo KI, Endo T, Yoshida K, Benner S, Ito Y, Aizawa H, Aramaki M, Yamanaka A, Tanaka K, Takata N, Tanaka KF, Mimura M, Tohyama C, Kakeyama M, Nakajima K (2015) Neuronal heterotopias affect the activities of distant brain areas and lead to behavioral deficits. J Neurosci 35:12432–12445.

Isidor B, Küry S, Rosenfeld JA, et al. (2016) De novo truncating mutations in the kinetochore-microtubules attachment gene CHAMP1 cause syndromic intellectual disability. Hum Mutat

37:354–358.

Islam MP, Roach ES (2015) Tuberous sclerosis complex. Handb Clin Neurol 132:97–109.

Iwase S, Bérubé NG, Zhou Z, Kasri NN, Battaglioli E, Scandaglia M, Barco A (2017) Epigenetic etiology of intellectual disability. J Neurosci 37:10773–10782.

Izumi K (2016) Disorders of Transcriptional Regulation: An Emerging Category of Multiple Malformation Syndromes. Mol Syndromol 7:262–273.

Jabaudon D (2017) Fate and freedom in developing neocortical circuits. Nat Commun 8:16042.

Jacob HJ (2013) Next-generation sequencing for clinical diagnostics. N Engl J Med 369:1557–1558.

Jewell JL, Russell RC, Guan KL (2013) Amino acid signalling upstream of mTOR. Nat Rev Mol Cell Biol 14:133–139.

Jiang X, Lautermilch NJ, Watari H, Westenbroek RE, Scheuer T, Catterall WA (2008) Modulation of CaV2.1 channels by Ca^{2+}/calmodulin-dependent protein kinase II bound to the C-terminal domain. Proc Natl Acad Sci USA 105:341–346.

Johnson LD, Willoughby CA, Burke SH, Paik DS, Jenkins KJ, Tombes RM (2008) δ Ca^{2+}/Calmodulin-Dependent Protein Kinase II Isozyme-Specific Induction of Neurite Outgrowth in P19 Embryonal Carcinoma Cells. J Neurochem 75:2380–2391.

Jones EG, Huntley GW, Benson DL (1994) Alpha calcium/calmodulin-dependent protein kinase II selectively expressed in a subpopulation of excitatory neurons in monkey sensory-motor cortex: Comparison with GAD-67 expression. J Neurosci 14:611–629.

Juric-Sekhar G, Hevner RF (2019) Malformations of Cerebral Cortex Development: Molecules and Mechanisms. Annu Rev Pathol Mech Dis 14:293–318.

Ka M, Condorelli G, Woodgett JR, Kim W-Y (2014) mTOR regulates brain morphogenesis by mediating GSK3 signaling. Development 141:4076–4086.

Ka M, Smith AL, Kim WY (2017) MTOR controls genesis and autophagy of GABAergic interneurons during brain development. Autophagy 13:1348–1363.

Kaizuka T, Takumi T (2018) Postsynaptic density proteins and their involvement in neurodevelopmental disorders. J Biochem 163:447–455.

Kakegawa W, Tsuzuki K, Yoshida Y, Kameyama K, Ozawa S (2004) Input- and subunit-specific AMPA receptor trafficking underlying long-term potentiation at hippocampal CA3 synapses. Eur J Neurosci 20:101–110.

Kamata A, Takeuchi Y, Fukunaga K (2006) Identification of the isoforms of Ca^{2+}/calmodulin-dependent protein kinase II and expression of brain-derived neurotrophic factor mRNAs in the substantia nigra. J Neurochem 96:195–203.

Kanaseki T, Ikeuchi Y, Sugiura H, Yamauchi T (1991) Structural features of Ca^{2+}/calmodulin-dependent protein kinase II revealed by electron microscopy. J Cell Biol 115:1049–1060.

Kane N, Acharya J, Benickzy S, Caboclo L, Finnigan S, Kaplan PW, Shibasaki H, Pressler R, van Putten MJAM (2017) A revised glossary of terms most commonly used by clinical electroencephalographers and updated proposal for the report format of the EEG findings. Revision 2017. Clin Neurophysiol Pract 2:170–185.

Karls U, Müller U, Gilbert DJ, Copeland NG, Jenkins NA, Harbers K (1992) Structure, expression, and chromosome location of the gene for the beta subunit of brain-specific Ca^{2+}/calmodulin-dependent protein kinase II identified by transgene integration in an embryonic lethal mouse mutant. Mol Cell Biol 12:3644–3652.

Karttunen J, Heiskanen M, Lipponen A, Poulsen D, Pitkänen A (2019) Extracellular vesicles as diagnostics and therapeutics for structural epilepsies. Int J Mol Sci 20:1–22.

Kassai H, Sugaya Y, Noda S, Nakao K, Maeda T, Kano M, Aiba A (2014) Selective Activation of mTORC1 Signaling Recapitulates Microcephaly, Tuberous Sclerosis, and Neurodegenerative Diseases. Cell Rep 7:1626–1639.

Kelly PT, McGuinness TL, Greengard P (1984) Evidence that the major postsynaptic density protein is a component of a Ca^{2+}/calmodulin-dependent protein kinase. Proc Natl Acad Sci USA 81:945–949.

Kennedy MB, Greengard P (1981) Two calcium/calmodulin-dependent protein kinases, which are highly concentrated in brain, phosphorylate protein I at distinct sites. Proc Natl Acad Sci USA 78:1293–1297.

Kennedy MB, McGuinness T, Greengard P (1983a) A calcium/calmodulin-dependent protein kinase from mammalian brain that phosphorylates Synapsin I: partial purification and characterization. J Neurosci 3:818–831.

Kennedy MB, Bennett MK, Erondu NE (1983b) Biochemical and immunochemical evidence that the "major postsynaptic density protein" is a subunit of a calmodulin-dependent protein kinase. Proc Natl Acad Sci USA 80:7357–7361.

Kim DH, Sarbassov DD, Ali SM, King JE, Latek RR, Erdjument-Bromage H, Tempst P, Sabatini DM (2002) mTOR interacts with raptor to form a nutrient-sensitive complex that signals to the cell growth machinery. Cell 110:163–175.

Kim WY (2015) Brain size is controlled by the mammalian target of rapamycin (mTOR) in mice. Commun Integr Biol 8:e994377.

Kim K, Saneyoshi T, Hosokawa T, Okamoto K, Hayashi Y (2016) Interplay of enzymatic and structural functions of CaMKII in long-term potentiation. J Neurochem 139:959–972.

Kircher M, Witten DM, Jain P, O'Roak BJ, Cooper GM, Shendure J (2014) A general framework for estimating the relative pathogenicity of human genetic variants. Nat Genet 46:310–315.

Kirschstein T, Köhling R (2015) Animal models of tumour-associated epilepsy. J Neurosci Methods 260:109-117.

Kirschstein T, von der Brelie C, Steinhauser M, Vincon A, Beck H, Dietrich D (2004) L-CCG-I activates group III metabotropic

glutamate receptors in the hippocampal CA3 region. Neuropharmacology 47:157–162.

Kocerha J, Faghihi MA, Lopez-Toledano MA, Huang J, Ramsey AJ, Caron MG, Sales N, Willoughby D, Elmen J, Hansen HF, Orum H, Kauppinen S, Kenny PJ, Wahlestedt C (2009) MicroRNA-219 modulates NMDA receptor-mediated neurobehavioral dysfunction. Proc Natl Acad Sci USA 106:3507–3512.

Koene LMC, van Grondelle SE, Proietti Onori M, Wallaard I, Kooijman NHRM, van Oort A, Schreiber J, Elgersma Y (2019) Effects of antiepileptic drugs in a new TSC/mTOR-dependent epilepsy mouse model. Ann Clin Transl Neurol 6:1273–1291.

Kolch W. (2005) Coordinating ERK/MAPK signalling through scaffolds and inhibitors. Nat Rev Mol Cell Biol 6: 827–837.

Kolodziej SJ, Hudmon A, Waxham MN, Stoops JK (2000) Three-dimensional reconstructions of calcium/calmodulin-dependent (CaM) kinase IIα, and truncated CaM kinase IIα reveal a unique organization for its structural core and functional domains. J Biol Chem 275:14354–14359.

Kool MJ, van de Bree JE, Bodde HE, Elgersma Y, van Woerden GM (2016) The molecular, temporal and region-specific requirements of the beta isoform of calcium/calmodulin-dependent protein kinase type 2 (CAMK2B) in mouse locomotion. Sci Rep 6:26989.

Kool MJ, Proietti Onori M, Borgesius NZ, van de Bree JE, Elgersma-Hooisma M, Nio E, Bezstarosti K, Buitendijk GHS, Aghadavoud Jolfaei M, Demmers JAA, Elgersma Y, van Woerden GM (2019) CAMK2-dependent signaling in neurons is essential for survival. J Neurosci:1341–18.

Kremer EJ, Yu S, Pritchard M, Nagaraja R, Heitz D, Lynch M, Baker E, Hyland VJ, Little RD, Wada M (1991) Isolation of a human DNA sequence which spans the fragile X. Am J Hum Genet 49:656–661.

Krueger DA, Sadhwani A, Byars AW, de Vries PJ, Franz DN, Whittemore VH, Filip-Dhima R, Murray D, Kapur K, Sahin M (2017) Everolimus for treatment of tuberous sclerosis complex-associated neuropsychiatric disorders. Ann Clin Transl Neurol 4:877–887.

Krumm N, Turner TN, Baker C, Vives L, Mohajeri K, Witherspoon K, Raja A, Coe BP, Stessman, HA, He ZX, et al. (2015) Excess of rare, inherited truncating mutations in autism. Nature genetics 47:582-588.

Kuret J, Schulman H (1985) Mechanism of autophosphorylation of the multifunctional Ca^{2+}/calmodulin-dependent protein kinase. J Biol Chem 260:6427–6433.

Küry S, Besnard T, Ebstein F, Khan TN, Gambin T, Douglas J, Bacino CA, Craigen WJ, Sanders SJ, Lehmann A, et al. (2017a) De Novo Disruption of the Proteasome Regulatory Subunit PSMD12 Causes a Syndromic Neurodevelopmental Disorder. Am J Hum Genet 100:352-363.

Küry S, van Woerden GM, Besnard T, Proietti Onori M, Latypova X, Towne MC, Cho MT, Prescott TE, Ploeg MA, Sanders S, Stessman HAF, Pujol A, Distel B, Robak LA, Bernstein JA, Denommé-Pichon AS, Lesca G, Sellars EA, Berg J, Carré W, et al. (2017b) De novo mutations in protein kinase genes CAMK2A and CAMK2B cause intellectual disability. Am J Hum Genet 101:768 –788.

Kutsuwada T, Sakimura K, Manabe T, Takayama C, Katakura N, Kushiya E, Natsume R, Watanabe M, Inoue Y, Yagi T, Aizawa S, Arakawa M, Takahashi T, Nakamura Y, Mori H, Mishina M (1996) Impairment of suckling response, trigeminal neuronal pattern formation, and hippocampal LTD in NMDA receptor epsilon 2 subunit mutant mice. Neuron 16:333–344.

Kuzniecky RI (1994) Magnetic Resonance Imaging in Developmental Disorders of the Cerebral Cortex. Epilepsia 35:S44–S56.

Kwan KY, Šestan N, Anton ES (2012) Transcriptional co-regulation of neuronal migration and laminar identity in the neocortex. Development 139:1535–1546.

Kwon CH, Luikart BW, Powell CM, Zhou J, Matheny SA, Zhang W, Li Y, Baker SJ, Parada LF (2006) Pten Regulates Neuronal Arborization and Social Interaction in Mice. Neuron 50:377–388

Lafourcade CA, Lin T V., Feliciano DM, Zhang L, Hsieh LS, Bordey A (2013) Rheb Activation in Subventricular Zone Progenitors Leads to Heterotopia, Ectopic Neuronal Differentiation, and Rapamycin-Sensitive Olfactory Micronodules and Dendrite Hypertrophy of Newborn Neurons. J Neurosci 33:2419–2431.

Lai Y, Nairn AC, Greengard P (1986) Autophosphorylation reversibly regulates the Ca^{2+}/calmodulin-dependence of Ca^{2+}/calmodulin-dependent protein kinase II. Proc Natl Acad Sci USA 83:4253–4257.

Lamsa KP, Heeroma JH, Somogyi P, Rusakov DA, Kullmann DM (2007) Anti-hebbian long-term potentiation in the hippocampal feedback inhibitory circuit. Science 315:1262–1266.

Laplante M, Sabatini DM (2012a) mTOR Signaling. Cold Spring Harb Perspect Biol 4:a011593.

Laplante M, Sabatini, DM (2012b) mTOR signaling in growth control and disease. Cell 149:274–293.

LaSarge CL, Danzer SC (2014) Mechanisms regulating neuronal excitability and seizure development following mTOR pathway hyperactivation. Front Mol Neurosci 7:1–15.

Lau CG, Zukin, RS (2007) NMDA receptor trafficking in synaptic plasticity and neuropsychiatric disorders. Nat Rev Neurosci 8:413–426.

Laumonnier F, Cuthbert PC, Grant SGN (2007) The role of neuronal complexes in human X-linked brain diseases. Am J Hum Genet 80:205–220.

Lee SJ, Escobedo-Lozoya Y, Szatmari EM, Yasuda R (2009) Activation of CaMKII in single dendritic spines during long-term potentiation. Nature 458:299 –304.

Lee JH, Huynh M, Silhavy JL, Kim S, Dixon-Salazar T, Heiberg A, Scott E, Bafna V, Hill KJ, Collazo A, Funari V, Russ C, Gabriel SB, Mathern GW, Gleeson JG (2012) De novo somatic mutations in components of the PI3K-AKT3-mTOR pathway cause hemimegalencephaly. Nat Genet 44:941–945.

Lee DY (2015) Roles of mTOR Signaling in Brain Development. Exp Neurobiol 24:177.

Lee J (2017) Malformations of cortical development: Genetic mechanisms and diagnostic approach. Korean J Pediatr 60:1–9.

Lehman A, Thouta S, Mancini GMS, et al. Loss-of-Function and Gain-of-Function Mutations in KCNQ5 Cause Intellectual Disability or Epileptic Encephalopathy. Am J Hum Genet 101:65–74.

Lek M, Karczewski KJ, Minikel EV, Samocha KE, Banks E, Fennell T, O'Donnell-Luria AH, Ware JS, Hill AJ, Cummings BB, et al. (2016) Analysis of protein-coding genetic variation in 60,706 humans. Nature 536:285-291.

Lelieveld SH, Reijnders MRF, Pfundt R, et al. Meta-analysis of 2,104 trios provides support for 10 new genes for intellectual disability. Nat Neurosci 19:1194–1196.

Lemke JR, Lal D, Reinthaler EM, Steiner I, Nothnagel M, Alber M, Geider K, Laube B, Schwake M, Finsterwalder K, et al. (2013) Mutations in GRIN2A cause idiopathic focal epilepsy with rolandic spikes. Nat Genet 45:1067–1072.

Lemke JR, Hendrickx R, Geider K, Laube B, Schwake M, Harvey RJ, James VM, Pepler A, Steiner I, Hortnagel K, et al. (2014) GRIN2B mutations in west syndrome and intellectual disability with focal epilepsy. Ann Neurol 75:147–154.

Lerche H, Shah M, Beck H, Noebels J, Johnston D, Vincent A (2013) Ion channels in genetic and acquired forms of epilepsy. J Physiol 591:753–764.

Lesca G, Rudolf G, Bruneau N, Lozovaya N, Labalme A, Boutry-Kryza N, Salmi M, Tsintsadze T, Addis L, Motte J, et al. (2013) GRIN2A mutations in acquired epileptic aphasia and related childhood focal epilepsies and encephalopathies with speech and language dysfunction. Nat Genet 45:1061–1066.

Leventer RJ, Phelan EM, Coleman LT, Kean MJ, Jackson GD, Harvey AS (1999) Clinical and imaging features of cortical malformations in childhood. Neurology 53:715–722.

Leventer RJ, Guerrini R, Dobyns WB (2008) Malformations of cortical development and epilepsy. Dialogues Clin Neurosci 10:47–62.

Li Y, Inoki K, Guan K-L (2004) Biochemical and Functional Characterizations of Small GTPase Rheb and TSC2 GAP Activity. Mol Cell Biol 24:7965–7975.

Li YH, Werner H, Puschel AW (2008) Rheb and mTOR regulate neuronal polarity through Rap1B. J Bio Chem 283:33784–33792.

Li K, Zhou T, Liao L, Yang Z, Wong C, Henn F, Malinow R, Yates JR 3rd, Hu H (2013) βCaMKII in lateral habenula mediates core symptoms of depression. Science 341:1016 –1020.

Li D, Yuan H, Ortiz-Gonzalez XR, Marsh ED, Tian L, McCormick EM, Kosobucki GJ, Chen W, Schulien AJ, Chiavacci R, et al. (2016) GRIN2D Recurrent De Novo Dominant Mutation Causes a Severe Epileptic Encephalopathy Treatable with NMDA Receptor Channel Blockers. Am J Hum Genet 99:802–816.

Lim KC, Crino PB (2013) Focal malformations of cortical development: New vistas for molecular pathogenesis. Neuroscience 252:262–276.

Lim JS, Kim W, Kang H-C, Kim SH, Park AH, Park EK, Cho Y-W, Kim S, Kim HM, Kim JA, Kim J, Rhee H, Kang S-G, Kim HD, Kim D, Kim D-S, Lee JH (2015) Brain somatic mutations in MTOR cause focal cortical dysplasia type II leading to intractable epilepsy. Nat Med 21:395–400.

Lim JS, Gopalappa R, Kim SH, Ramakrishna S, Lee M, Kim W il, Kim J, Park SM, Lee J, Oh JH, Kim HD, Park CH, Lee JS, Kim S, Kim DS, Han JM, Kang HC, Kim H, Lee JH (2017) Somatic Mutations in TSC1 and TSC2 Cause Focal Cortical Dysplasia. Am J Hum Genet 100:454–472.

Lin CR, Kapiloff MS, Durgerian S, Tatemoto K, Russo AF, Hanson P, Schulman H, Rosenfeld MG (1987) Molecular cloning of a brain-specific calcium/calmodulin-dependent protein kinase. Proc Natl Acad Sci USA 84:5962–5966.

Lin JW, Sugimori M, Llinas RR, McGuinness TL, Greengard P (1990) Effects of synapsin I and calcium/calmodulin-dependent protein kinase II on spontaneous neurotransmitter release in the squid giant synapse. Proc Natl Acad Sci USA 87:8257–8261.

Lin YC, Redmond L (2008) CaMKIIβ binding to stable F-actin in vivo regulates F-actin filament stability. Proc Natl Acad Sci USA 105:15791–15796.

Lin TV, Hsieh L, Kimura T, Malone TJ, Bordey A (2016) Normalizing translation through 4E-BP prevents mTOR-driven cortical mislamination and ameliorates aberrant neuron integration. Proc Natl Acad Sci USA 113:11330–11335.

Lipton JO, Sahin M (2014) The Neurology of mTOR. Neuron 84:275–291.

Lisman J (1985) A mechanism for memory storage insensitive to molecular turnover. Proc Natl Acad Sci USA 82:3055–3057.

Lisman J (2017) Criteria for identifying the molecular basis of the engram (CaMKII, PKMzeta). Mol Brain 10:55.

Lisman J, McIntyre CC (2001) Synaptic plasticity: A molecular memory switch. Curr Biol 11:788–791.

Lisman J, Schulman H, Cline H (2002) The molecular basis of CaMKII function in synaptic and behavioural memory. Nat Rev Neurosci 3:175–190.

Lisman J, Yasuda R, Raghavachari S (2012) Mechanisms of CaMKII action in long-term potentiation. Nat Rev Neurosci 13:169–182.

Liu JS (2011) Molecular genetics of neuronal migration disorders. Curr Neurol Neurosci Rep 11:171–178.

Liu XB, Jones EG (1996) Localization of alpha type II calcium calmodulin-dependent protein kinase at glutamatergic but not γ-aminobutyric acid (GABAergic) synapses in thalamus and cerebral cortex. Proc Natl Acad Sci USA 93:7332–7336.

Liu Q, Sinnen BL, Boxer EE, Schneider MW, Grybko MJ, Buchta WC, Gibson ES, Wysoczynski CL, Ford CP, Gottschalk A, Aoto J, Tucker CL, Kennedy MJ (2019) A Photoactivatable Botulinum Neurotoxin for Inducible Control of Neurotransmission. Neuron 101:863-875.e6.

Ljungberg MC, Sunnen CN, Lugo JN, Anderson AE, D'Arcangelo G (2009) Rapamycin suppresses seizures and neuronal hypertrophy in a mouse model of cortical dysplasia. Dis Model Mech 2:389–398.

Llinás R, McGuinness TL, Leonard CS, Sugimori M, Greengard P (1985) Intraterminal injection of synapsin I or calcium/calmodulin-dependent protein kinase II alters neurotransmitter release at the squid giant synapse. Proc Natl Acad Sci USA 82:3035–3039.

Loconte DC, Grossi V, Bozzao C, Forte G, Bagnulo R, Stella A, Lastella P, Cutrone M, Benedicenti F, Susca FC, Patruno M, Varvara D, Germani A, Chessa L, Laforgia N, Tenconi R, Simone C, Resta N (2015) Molecular and functional characterization of three different postzygotic mutations in PIK3CA-related overgrowth spectrum (PROS) patients: Effects on PI3K/AKT/mTOR signaling and sensitivity to PIK3 inhibitors Phillips WA, ed. PLoS One 10:e0123092

Long X, Lin Y, Ortiz-Vega S, Yonezawa K, Avruch J (2005) Rheb binds and regulates the mTOR kinase. Curr Biol 15:702–713.

Long X, Lin Y, Ortiz-Vega S, Busch S, Avruch J (2007) The Rheb switch 2 segment is critical for signaling to target of rapamycin complex 1. J Biol Chem 282:18542–18551.

Lou LL, Lloyd SJ, Schulman H (1986) Activation of the multifunctional Ca^{2+}/calmodulin-dependent protein kinase by autophosphorylation: ATP modulates production of an autonomous enzyme. Proc Natl Acad Sci USA 83:9497–9501.

Lozovaya N, Gataullina S, Tsintsadze T, et al. (2014) Selective suppression of excessive GluN2C expression rescues early epilepsy in a tuberous sclerosis murine model. Nat Commun 5:4563.

Lu FM, Hawkins RD (2006) Presynaptic and postsynaptic Ca^{2+} and CaMKII contribute to long-term potentiation at synapses between individual CA3 neurons. Proc Natl Acad Sci USA 103:4264 – 4269.

Lucke-Wold BP, Nguyen L, Turner RC, Logsdon AF, Chen YW, Smith KE, Huber JD, Matsumoto R, Rosen CL, Tucker ES, Richter E (2015) Traumatic brain injury and epilepsy: Underlying mechanisms leading to seizure. Seizure 33:13–23.

Lüders H, Schuele SU (2006) Epilepsy surgery in patients with malformations of cortical development. Curr Opin Neurol 19:169–174.

Lukiw WJ (2007) Micro-RNA speciation in fetal, adult and Alzheimer's disease hippocampus. Neuroreport 18:297–300.

Lynch MA (2004) Long-Term Potentiation and Memory. Physiol Rev 84:87–136.

Ma XM, Blenis J (2009) Molecular mechanisms of mTOR-mediated translational control. Nat Rev Mol Cell Biol 10:307–318.

Ma H, Groth RD, Cohen SM, Emery JF, Li B, Hoedt E, Zhang G, Neubert TA, Tsien RW (2014) *γ*CaMKII shuttles Ca^{2+}/CaM to the nucleus to trigger CREB phosphorylation and gene expression. Cell 159:281–294.

MacArthur DG et al. (2014) Guidelines for investigating causality of sequence variants in human disease. Nature 508:469–476.

MacDonald JL, Fame RM, Azim E, Shnider SJ, Molyneaux BJ, Arlotta P, Macklis JD (2013) Specification of Cortical Projection Neurons: Transcriptional Mechanisms. Patterning Cell Type Specif Dev CNS PNS:475–502.

Majolo F, Marinowic DR, Machado DC, Da Costa JC (2018) MTOR pathway in focal cortical dysplasia type 2: What do we know? Epilepsy Behav 85:157–163.

Major P, Rakowski S, Simon M V., Cheng ML, Eskandar E, Baron J, Leeman BA, Frosch MP, Thiele EA (2009) Are cortical tubers epileptogenic? Evidence from electrocorticography. Epilepsia 50:147–154.

Malenka RC, Bear MF (2004) LTP and LTD: An embarrassment of riches. Neuron 44:5–21.

Malinow R, Schulman H, Tsien RW (1989) Inhibition of postsynaptic PKC or CaMKII blocks induction but not expression of LTP. Science 245:862–866.

Manning BD, Cantley LC (2003) Rheb fills a GAP between TSC and TOR. Trends Biochem Sci 28:573–576.

Marcelin B, Chauvière L, Becker A, Migliore M, Esclapez M, Bernard C (2009) h channel-dependent deficit of theta oscillation resonance and phase shift in temporal lobe epilepsy. Neurobiol Dis 33:436–447.

Marcotte L, Aronica E, Baybis M, Crino PB (2012) Cytoarchitectural alterations are widespread in cerebral cortex in tuberous sclerosis complex. Acta Neuropathol 123:685–693.

Marshall CB, Ho J, Buerger C, Plevin MJ, Li GY, Li Z, Ikura M, Stambolic V (2009) Characterization of the intrinsic and TSC2-GAP - Regulated GTPase activity of rheb by real-time nmr. Sci Signal 2:ra3–ra3.

Martin SJ, Clark RE (2007) The rodent hippocampus and spatial memory: From synapses to systems. Cell Mol Life Sci 64:401–431.

Martin SJ, Grimwood PD, Morris RGM (2000) Synaptic Plasticity and Memory: An Evaluation of the Hypothesis. Annu Rev Neurosci 23:649–711.

Matsuda T, Cepko CL (2007) Controlled expression of transgenes introduced by in vivo electroporation. Proc Natl Acad Sci USA 104:1027–1032.

Maulik PK, Mascarenhas MN, Mathers CD, Dua T, Saxena S (2011) Prevalence of intellectual disability: A meta-analysis of population-based studies. Res Dev Disabil 32:419–436.

Mayer P, Möhlig M, Schatz H, Pfeiffer A (1993) New isoforms of multifunctional calcium/calmodulin-dependent protein kinase II. FEBS Lett 333:315–318.

Mayer P, Möhlig M, Schatz H, Pfeiffer A (1994) Additional isoforms of multifunctional calcium/calmodulin-dependent protein kinase II in rat heart tissue. Biochem J 298:757–758.

Mayford M, Wang J, Kandel ER, O'Dell TJ (1995) CaMKII regulates the frequency-response function of hippocampal synapses for the production of both LTD and LTP. Cell 81:891–904.

Mayford M, Bach ME, Huang YY, Wang L, Hawkins RD, Kandel ER (1996) Control of memory formation through regulated

expression of a CaMKII transgene. Science 274:1678–1683.

Mazhab-Jafari MT, Marshall CB, Ishiyama N, Ho J, Di Palma V, Stambolic V, Ikura M (2012) An autoinhibited noncanonical mechanism of GTP hydrolysis by Rheb maintains mTORC1 homeostasis. Structure 20:1528–1539.

Mazhab-Jafari MT, Marshall CB, Ho J, Ishiyama N, Stambolic V, Ikura M (2014) Structure-guided mutation of the conserved G3-box glycine in Rheb generates a constitutively activated regulator of mammalian target of rapamycin (mTOR). J Biol Chem 289:12195–12201.

McKenzie K, Milton M, Smith G, Ouellette-Kuntz H (2016) Systematic Review of the Prevalence and Incidence of Intellectual Disabilities: Current Trends and Issues. Curr Dev Disord Reports 3:104–115.

McRae JF, Clayton S, Fitzgerald TW, et al. (2017) Prevalence and architecture of de novo mutations in developmental disorders. Nature 542:433–438.

Mefford HC, Batshaw ML, Hoffman EP (2012) Genomics, Intellectual Disability, and Autism Feero WG, Guttmacher AE, eds. N Engl J Med 366:733–743.

Meikle L, Pollizzi K, Egnor A, Kramvis I, Lane H, Sahin M, Kwiatkowski DJ (2008) Response of a neuronal model of tuberous sclerosis to mammalian target of rapamycin (mTOR) inhibitors: effects on mTORC1 and Akt signaling lead to improved survival and function. J Neurosci 28:5422–5432.

Mendoza MC, Er EE, Blenis J (2011) The Ras-ERK and PI3K-mTOR pathways: Cross-talk and compensation. Trends Biochem Sci 36:320–328.

Meng D, Frank AR, Jewell JL (2018) mTOR signaling in stem and progenitor cells. Dev 145.

Menon S, Dibble CC, Talbott G, Hoxhaj G, Valvezan AJ, Takahashi H, Cantley LC, Manning BD (2014) Spatial control of the TSC complex integrates insulin and nutrient regulation of mTORC1 at the lysosome. Cell 156:771–785.

Meyer T, Hanson PI, Stryer L, Schulman H, Soderling TR (1992) Calmodulin Trapping by Calcium-Calmodulin-Dependent Protein Kinase. Science 256:1199–1202.

Milikovsky DZ, Weissberg I, Kamintsky L, Lippmann K, Schefenbauer O, Frigerio F, Rizzi M, Sheintuch L, Zelig D, Ofer J, Vezzani A, Friedman A (2017) Electrocorticographic dynamics as a novel biomarker in five models of epileptogenesis. J Neurosci 37:4450–4461.

Miller SG, Kennedy MB (1985) Distinct forebrain and cerebellar isozymes of type II Ca^{2+}/calmodulin-dependent protein kinase associate differently with the postsynaptic density fraction. J Biol Chem 260:9039–9046.

Miller SG, Kennedy MB (1986) Regulation of brain type II Ca^{2+}/calmodulin-dependent protein kinase by autophosphorylation: a Ca^{2+}- triggered molecular switch. Cell 44:861– 870.

Miller SG, Patton BL, Kennedy MB (1988) Sequences of autophosphorylation sites in neuronal type II CaM kinase that control Ca^{2+}-independent activity. Neuron 1:593–604.

Mironov SL (2013) Calmodulin and calmodulin kinase II mediate emergent bursting activity in the brainstem respiratory network (preBotzinger complex). J Physiol 591:1613–1630.

Mirzaa GM, Campbell CD, Solovieff N, et al. (2016) Association of MTOR Mutations With Developmental Brain Disorders, Including Megalencephaly, Focal Cortical Dysplasia, and Pigmentary Mosaicism. JAMA Neurol 73:836–845.

Mizuguchi M, Yamanouchi H, Becker LE, Itoh M, Takashima S (2002) Doublecortin immunoreactivity in giant cells of tuberous sclerosis and focal cortical dysplasia. Acta Neuropathol 104:418–424.

Moffat JJ, Ka M, Jung EM, Kim WY (2015) Genes and brain malformations associated with abnormal neuron positioning. Mol Brain 8:1–12.

Møller RS et al. (2016) Germline and somatic mutations in the MTOR gene in focal cortical dysplasia and epilepsy. Neurol Genet 2:e118.

Molloy SS, Kennedy MB (1991) Autophosphorylation of type II Ca^{2+}/calmodulin-dependent protein kinase in cultures of postnatal rat hippocampal slices. Proc Natl Acad Sci USA 88:4756–4760.

Molyneaux BJ, Arlotta P, Hirata T, Hibi M, Macklis JD (2005) Fezl is required for the birth and specification of corticospinal motor neurons. Neuron 47:817–831.

Molyneaux BJ, Arlotta P, Menezes JRL, Macklis JD (2007) Neuronal subtype specification in the cerebral cortex. Nat Rev Neurosci 8:427–437.

Mony L, Kew JN, Gunthorpe MJ, Paoletti P (2009) Allosteric modulators of NR2B-containing NMDA receptors: molecular mechanisms and therapeutic potential. Br J Pharmacol 157:1301–1317.

Moon UY, Park JY, Park R, Cho JY, Hughes LJ, McKenna J, Goetzl L, Cho S-H, Crino PB, Gambello MJ, Kim S (2015) Impaired Reelin-Dab1 Signaling Contributes to Neuronal Migration Deficits of Tuberous Sclerosis Complex. Cell Rep 12:965–978.

Morris EP, Török K (2001) Oligomeric structure of α-calmodulin-dependent protein kinase II. J Mol Biol 308:1–8.

Moscovitch M, Cabeza R, Winocur G, Nadel L (2016) Episodic Memory and Beyond: The Hippocampus and Neocortex in Transformation. Annu Rev Psychol 67:105–134.

Moser EI, Kropff E, Moser M-B (2008) Place Cells, Grid Cells, and the Brain's Spatial Representation System. Annu Rev Neurosci 31:69–89.

Mukherji S, Soderling TR (1994) Regulation of Ca^{2+}/calmodulin-dependent protein kinase II by inter- and intrasubunit-catalyzed autophosphorylations. J Biol Chem 269:13744–13747.

Mula M (2015) Investigational new drugs for focal epilepsy. Expert Opin Investig Drugs 3784:1–5.

Mullin AP, Gokhale A, Moreno-De-Luca A, Sanyal S, Waddington JL, Faundez V (2013) Neurodevelopmental disorders: Mechanisms and boundary definitions from genomes, interactomes and

proteomes. Transl Psychiatry 3:e329.

Muotri AR (2016) The iPSC Technology to Study Neurodevelopmental Disorders. In: Neuronal and Synaptic Dysfunction in Autism Spectrum Disorder and Intellectual Disability, pp 295–300. Academic Press.

Murakami M, Ichisaka T, Maeda M, Oshiro N, Hara K, Edenhofer F, Kiyama H, Yonezawa K, Yamanaka S (2004) mTOR Is Essential for Growth and Proliferation in Early Mouse Embryos and Embryonic Stem Cells. Mol Cell Biol 24:6710–6718.

Myers JB, Zaegel V, Coultrap SJ, Miller AP, Bayer KU, Reichow SL (2017) The CaMKII holoenzyme structure in activation-competent conformations. Nat Commun 8:15742.

Nadarajah B (2003) Radial glia and somal translocation of radial neurons in the developing cerebral cortex. Glia 43:33–36.

Nadif Kasri N, Van Aelst L (2008) Rho-linked genes and neurological disorders. Pflugers Arch Eur J Physiol 455:787–797.

Najm IM, Tilelli CQ, Oghlakian R (2007) Pathophysiological mechanisms of focal cortical dysplasia: A critical review of human tissue studies and animal models. Epilepsia 48:21–32.

Nayak A, Zastrow DJ, Lickteig R, Zahniser NR, Browning MD (1998) Maintenance of late-phase LTP is accompanied by PKA-dependent increase in AMPA receptors synthesis. Nature 394:680–683.

Neal SE, Eccleston JF, Hall A, Webb MR (1988) Kinetic analysis of the hydrolysis of GTP by p21N-ras. The basal GTPase mechanism. J Biol Chem 263:19718–19722.

Neal Waxham M, Aronowski J, Westgate SA, Kelly PT (1990) Mutagenesis of Thr-286 in monomeric Ca^{2+}/calmodulin-dependent protein kinase II eliminates Ca^{2+}/calmodulin-independent activity. Proc Natl Acad Sci USA 87:1273–1277.

Nesbitt A, Bhoj EJ, McDonald Gibson K, Yu Z, Denenberg E, Sarmady M, Tischler T, Cao K, Dubbs H, Zackai EH, Santani A (2015) Exome sequencing expands the mechanism of SOX5-associated intellectual disability: A case presentation with review of sox-related disorders. Am J Med Genet Part A 167:2548–2554

Nghiem P, Saati SM, Martens L, Gardner P, Schulman H (1993) Cloning and Analysis of Two New Isoforms of Multifunctional Protein Kinase. 268:5471–5479.

Nguyen LH, Anderson AE (2018) MTOR-dependent alterations of Kv1.1 subunit expression in the neuronal subset-specific Pten knockout mouse model of cortical dysplasia with epilepsy. Sci Rep 8:3568.

Nguyen LH, Mahadeo T, Bordey A (2019) mTOR Hyperactivity Levels Influence the Severity of Epilepsy and Associated Neuropathology in an Experimental Model of Tuberous Sclerosis Complex and Focal Cortical Dysplasia. J Neurosci 39:2762–2773.

Nichols RA, Sihra TS, Czernik AJ, Nairn AC, Greengard P (1990) Calcium/calmodulin-dependent protein kinase II increases glutamate and noradrenaline release from synaptosomes. Nature 343:647–651.

Nickels KC, Zaccariello MJ, Hamiwka LD, Wirrell EC (2016) Cognitive and neurodevelopmental comorbidities in paediatric epilepsy. Nat Rev Neurol 12:465–476.

Nicoll RA (2017) A Brief History of Long-Term Potentiation. Neuron 93:281–290.

Nie D, Di Nardo A, Han JM, Baharanyi H, Kramvis I, Huynh T, Dabora S, Codeluppi S, Pandolfi PP, Pasquale EB, Sahin M (2010) Tsc2-Rheb signaling regulates EphA-mediated axon guidance. Nat Neurosci 13:163–172.

Ninan I, Arancio O (2004) Presynaptic CaMKII is necessary for synaptic plasticity in cultured hippocampal neurons. Neuron 42:129 –141.

O'Leary DDM, Nakagawa Y (2002) Patterning centers, regulatory genes and extrinsic mechanisms controlling arealization of the neocortex. Curr Opin Neurobiol 12:14–25.

O'Leary H, Lasda E, Bayer KU (2006) CaMKIIβ association with the actin cytoskeleton is regulated by alternative splicing Forscher P, ed. Mol Biol Cell 17:4656–4665.

O'Roak BJ, Deriziotis P, Lee C, Vives L, Schwartz JJ, Girirajan S, Karakoc E, MacKenzie AP, Ng SB, Baker C, Rieder MJ, Nickerson DA, Bernier R, Fisher SE, Shendure J, Eichler EE (2011) Exome sequencing in sporadic autism spectrum disorders identifies severe de novo mutations. Nat Genet 43:585–589.

O'Roak BJ, Vives L, Girirajan S, et al. (2012a) Sporadic autism exomes reveal a highly interconnected protein network of de novo mutations. Nature 485:246–250.

O'Roak BJ, Vives L, Fu W, Egertson JD, Stanaway IB, Phelps IG, Carvill G, Kumar A, Lee C, Ankenman K, et al. (2012b). Multiplex targeted sequencing identifies recurrently mutated genes in autism spectrum disorders. Science 338:1619–1622.

Ohsako S, Nakazawa H, Sekihara S, Ikai A, Yamauchi T (1991) Role of threonine-286 as autophosphorylation site for appearance of Ca^{2+}- independent activity of calmodulin-dependent protein kinase II alpha subunit. J Biochem 109:137–143.

Ohtaka-Maruyama C, Okado H (2015) Molecular Pathways Underlying Projection Neuron Production and Migration during Cerebral Cortical Development. Front Neurosci 9:447.

Okamoto KI, Narayanan R, Lee SH, Murata K, Hayashi Y (2007) The role of CaMKII as an F-actin-bundling protein crucial for maintenance of dendritic spine structure. Proc Natl Acad Sci USA 104:6418–6423.

Omar Faison M, Perozzi EF, Caran N, Stewart JK, Tombes RM (2002) Axonal localization of delta Ca^{2+}/calmodulin-dependent protein kinase II in developing P19 neurons. Int J Dev Neurosci 20:585–592.

Oshiro N, Yoshino KI, Hidayat S, Tokunaga C, Hara K, Eguchi S, Avruch J, Yonezawa K (2004) Dissociation of raptor from mTOR is a mechanism of rapamycin-induced inhibition of mTOR function. Genes to Cells 9:359–366.

Ostrem B, Di Lullo E, Kriegstein A (2017) oRGs and mitotic somal translocation — a role in development and disease. Curr Opin Neurobiol 42:61–67.

Otmakhov N, Khibnik L, Otmakhova N, Carpenter S, Riahi S, Asrican B, Lisman J (2004) Forskolin-induced LTP in the CA1 hippocampal region is NMDA receptor dependent. J Neurophysiol 91:1955–1962.

Overwater IE, Rietman AB, Bindels-De Heus K, Looman CWN, Rizopoulos D, Sibindi TM, Cherian PJ, Jansen FE, Moll HA, Elgersma Y, De Wit MCY (2016) Sirolimus for epilepsy in children with tuberous sclerosis complex. Neurology 87:1011–1018.

Overwater IE, Rietman AB, van Eeghen AM, de Wit MCY (2019) Everolimus for the treatment of refractory seizures associated with tuberous sclerosis complex (TSC): current perspectives. Ther Clin Risk Manag 15:951–955.

Paliouras GN, Hamilton LK, Aumont A, Joppe SE, Barnabe-Heider F, Fernandes KJL (2012) Mammalian Target of Rapamycin Signaling Is a Key Regulator of the Transit-Amplifying Progenitor Pool in the Adult and Aging Forebrain. J Neurosci 32:15012–15026.

Palmini A, Andermann F, Olivier A, Tampieri D, Robitaille Y, Melanson D, Ethier R (1991) Neuronal migration disorders: a contribution of modern neuroimaging to the etiologic diagnosis of epilepsy. Can J Neurol Sci 18:580–587.

Pan Z, Zhu L-J, Li Y-Q, Hao L-Y, Yin C, Yang J-X, Guo Y, Zhang S, Hua L, Xue Z-Y, Zhang H, Cao J-L (2014) Epigenetic Modification of Spinal miR-219 Expression Regulates Chronic Inflammation Pain by Targeting CaMKII. J Neurosci 34:9476–9483.

Pan Y, Chen J, Guo H, Ou J, Peng Y, Liu Q, Shen Y, Shi L, Liu Y, Xiong Z, et al. (2015) Association of genetic variants of GRIN2B with autism. Sci Rep 5:8296.

Pang T, Atefy R, Sheen V (2008) Malformations of cortical development. Neurologist 14:181–191.

Pang ZP, Cao P, Xu W, Sudhof TC (2010) Calmodulin controls synaptic strength via presynaptic activation of calmodulin kinase II. J Neurosci 30:4132– 4142.

Paoletti P, Bellone C, Zhou Q (2013) NMDA receptor subunit diversity: impact on receptor properties, synaptic plasticity and disease. Nat Rev Neurosci 14:383–400.

Paridaen JT, Huttner WB (2014) Neurogenesis during development of the vertebrate central nervous system. EMBO Rep 15:351–364.

Park SM, Lim JS, Ramakrishina S, Kim SH, Kim WK, Lee JHJ, Kang H-C, Reiter JF, Kim DS, Kim H (Henry), Lee JHJ (2018) Brain somatic mutations in MTOR disrupt neuronal ciliogenesis, leading to focal cortical dyslamination. Neuron 99:1–15.

Parmar N, Tamanoi F (2010) Rheb G-proteins and the activation of mTORC1. In: The Enzymes, pp 39–56. Academic Press.

Parrini E, Conti V, Dobyns WB, Guerrini R (2016) Genetic basis of brain malformations. Mol Syndromol 7:220–233.

Patel PH, Thapar N, Guo L, Martinez M, Maris J, Gau C-L, Lengyel JA, Tamanoi F (2003) Drosophila Rheb GTPase is required for cell cycle progression and cell growth. J Cell Sci 116:3601–3610.

Patel B, Patel J, Cho J-H, Manne S, Bonala S, Henske E, Roegiers F, Markiewski M, Karbowniczek M (2015) Exosomes mediate the acquisition of the disease phenotypes by cells with normal genome in tuberous sclerosis complex. Oncogene:1–10.

Patil V V., Guzman M, Carter AN, Rathore G, Yoshor D, Curry D, Wilfong A, Agadi S, Swann JW, Adesina AM, Bhattacharjee MB, Anderson AE (2016) Activation of extracellular regulated kinase and mechanistic target of rapamycin pathway in focal cortical dysplasia. Neuropathology 36:146–156.

Patton BL, Miller G, Kennedy MB (1990) Activation of type II calcium/calmodulin-dependent protein kinase by Ca^{2+}/calmodulin is inhibited by autophosphorylation of threonine within the calmodulin-binding domain. J Biol Chem 265:11204–11212.

Pavlidis P, Montgomery J, Madison DV (2000) Presynaptic protein kinase activity supports long-term potentiation at synapses between individual hippocampal neurons. J Neurosci 20:4497– 4505.

Payne ME, Fong YL, Ono T, Colbran RJ, Kemp BE, Soderling TR, Means AR (1988) Calcium/calmodulin-dependent protein kinase II. Characterization of distinct calmodulin binding and inhibitory domains. J Biol Chem 263:7190–7195.

Pelorosso C, Watrin F, Conti V, Buhler E, Gelot A, Yang X, Mei D, McEvoy-Venneri J, Manent J-B, Cetica V, Ball LL, Buccoliero AM, Vinck A, Barba C, Gleeson JG, Guerrini R, Represa A (2019) Somatic double-hit in MTOR and RPS6 in hemimegalencephaly with intractable epilepsy. Hum Mol Genet 28:3755–3765.

Peper JS, Brouwer RM, Boomsma DI, Kahn RS, Hulshoff Pol HE (2007) Genetic influences on human brain structure: a review of brain imaging studies in twins. Hum Brain Mapp 28: 464–473.

Perles Z, Moon S, Ta-Shma A, Yaacov B, Francescatto L, Edvardson S, Rein AJ, Elpeleg O, Katsanis N (2015) A human laterality disorder caused by a homozygous deleterious mutation in MMP21. J Med Genet 52:840–847.

Pers TH (2016) Gene set analysis for interpreting genetic studies. Hum Mol Genet 25:R133–R140.

Petreanu L, Huber D, Sobczyk A, Svoboda K (2007) Channelrhodopsin-2-assisted circuit mapping of long-range callosal projections. Nat Neurosci 10:663–668.

Philips AK, Sirén A, Avela K, Somer M, Peippo M, Ahvenainen M, Doagu F, Arvio M, Kääriäinen H, Van Esch H, Froyen G, Haas SA, Hu H, Kalscheuer VM, Järvelä I (2014) X-exome sequencing in Finnish families with Intellectual Disability - Four novel mutations and two novel syndromic phenotypes. Orphanet J Rare Dis 9:49.

Pi HJ, Otmakhov N, El Gaamouch F, Lemelin D, De Koninck P, Lisman J (2010a) CaMKII control of spine size and synaptic strength: Role of phosphorylation states and nonenzymatic action. Proc Natl Acad Sci USA 107:14437–14442

Pi HJ, Otmakhov N, Lemelin D, De Koninck P, Lisman J (2010b) Autonomous CaMKII can promote either long-term potentiation or long-term depression, depending on the state of T305/T306 phosphorylation. J Neurosci 30:8704–8709

Pitkänen A, Lukasiuk K (2011) Mechanisms of epileptogenesis and potential treatment targets. Lancet Neurol 10:173–186.

Pitkänen A, Lukasiuk K, Edward Dudek F, Staley KJ (2015) Epileptogenesis. Cold Spring Harb Perspect Med 5.

Pittau F, Mégevand P, Sheybani L, Abela E, Grouiller F, Spinelli L, Michel CM, Seeck M, Vulliemoz S (2014) Mapping epileptic activity: Sources or networks for the clinicians? Front Neurol 5:218.

Pizzo F, Roehri N, Catenoix H, Medina S, McGonigal A, Giusiano B, Carron R, Scavarda D, Ostrowsky K, Lepine A, Boulogne S, Scholly J, Hirsch E, Rheims S, Bénar CG, Bartolomei F (2017) Epileptogenic networks in nodular heterotopia: A stereoelectroencephalography study. Epilepsia 58:2112–2123.

Plummer JT, Gordon AJ, Levitt P (2016) The genetic intersection of neurodevelopmental disorders and shared medical comorbidities - relations that translate from bench to bedside. Front Psychiatry 7:1–8.

Pollen AA, Bhaduri A, Andrews MG, et al. (2019) Establishing Cerebral Organoids as Models of Human-Specific Brain Evolution. Cell 176:743-756.

Pratt KG, Khakhalin AS (2013) Modeling human neurodevelopmental disorders in the Xenopus tadpole: from mechanisms to therapeutic targets. Dis Model Mech 6:1057–1065.

Proietti Onori M, Koopal B, Everman DB, Worthington JD, Jones JR, Ploeg MA, Mientjes E, van Bon BW, Kleefstra T, Schulman H, Kushner SA, Kury S, Elgersma Y, van Woerden GM (2018) The intellectual disability-associated CAMK2G p.Arg292Pro mutation acts as a pathogenic gain-of- function. Hum Mutat 39:2008 –2024.

Psaty BM, O'Donnell CJ, Gudnason V, Lunetta KL, Folsom AR, Rotter JI, Uitterlinden AG, Harris TB, Witteman JCM, Boerwinkle E (2009) Cohorts for Heart and Aging Research in Genomic Epidemiology (CHARGE) Consortium design of prospective meta-analyses of genome-wide association studies from 5 Cohorts. Circ Cardiovasc Genet 2:73–80.

Pun RYK, Rolle IJ, LaSarge CL, Hosford BE, Rosen JM, Uhl JD, Schmeltzer SN, Faulkner C, Bronson SL, Murphy BL, Richards DA, Holland KD, Danzer SC (2012) Excessive Activation of mTOR in Postnatally Generated Granule Cells Is Sufficient to Cause Epilepsy. Neuron 75:1022–1034.

Qin J, Mizuguchi M, Itoh M, Takashima S (2000) Immunohistochemical expression of doublecortin in the human cerebrum: Comparison of normal development and neuronal migration disorders. Brain Res 863:225–232.

Raab-Graham KF, Haddick PC, Jan YN, Jan LY (2006) Activity- and mTOR-dependent suppression of Kv1.1 channel mRNA translation in dendrites. Science 314:144–148.

Rakic P (1990) Principles of neural cell migration. Experientia 46:882–891.

Rakic P (2009) Evolution of the neocortex: A perspective from developmental biology. Nat Rev Neurosci 10:724–735.

Ramón Y CS La (1894) The Croonian lecture.—La fine structure des centres nerveux. Proc R Soc London 55:444–468.

Rauch A, Wieczorek D, Graf E, et al. (2012) Range of genetic mutations associated with severe non-syndromic sporadic intellectual disability: An exome sequencing study. Lancet 380:1674–1682.

Raymond CR, Redman SJ (2002) Different calcium sources are narrowly tuned to the induction of different forms of LTP. J Neurophysiol 88:249 – 255.

Reilly C, Atkinson P, Das KB, Chin RFMC, Aylett SE, Burch V, Gillberg C, Scott RC, Neville BGR (2014) Neurobehavioral comorbidities in children with active epilepsy: A population-based study. Pediatrics 133:e1586–e1593.

Reijnders MRFRF et al. (2017) Variation in a range of mTOR-related genes associates with intracranial volume and intellectual disability. Nat Commun 8:1052.

Rellos P, Pike ACW, Niesen FH, Salah E, Lee WH, von Delft F, Knapp S (2010) Structure of the CaMKIIδ/calmodulin complex reveals the molecular mechanism of CamKII kinase activation Taylor SS, ed. PLoS Biol 8:e1000426.

Represa A (2019) Why Malformations of Cortical Development Cause Epilepsy. Front Neurosci 13:250.

Retterer K, Juusola J, Cho MT, Vitazka P, Millan F, Gibellini F, Vertino-Bell A, Smaoui N, Neidich J, Monaghan KG, et al. (2016) Clinical application of whole- exome sequencing across clinical indications. Genet Med 18:696–704.

Ribierre T, Deleuze C, Bacq A, Baldassari S, Marsan E, Chipaux M, Muraca G, Roussel D, Navarro V, Leguern E, Miles R, Baulac S (2018) Second-hit mosaic mutation in mTORC1 repressor DEPDC5 causes focal cortical dysplasia–associated epilepsy. J Clin Invest 128:2452–2458.

Rivière JB et al. (2012) De novo germline and postzygotic mutations in AKT3, PIK3R2 and PIK3CA cause a spectrum of related megalencephaly syndromes. Nat Genet 44:934–940.

Robison AJ (2014) Emerging role of CaMKII in neuropsychiatric disease. Trends Neurosci 37:653–662.

Rollins JD, Collins JS, Holden KR (2010) United States head circumference growth reference charts: birth to 21 years. J Pediatr 156:907-913.e2.

Roth BL (2016) DREADDs for Neuroscientists. Neuron 89:683–694.

Roy M, Sorokina O, McLean C, Tapia-González S, DeFelipe J, Armstrong J, Grant S (2018) Regional Diversity in the Postsynaptic Proteome of the Mouse Brain. Proteomes 6:31.

Ryan TJ, Grant SG (2009) The origin and evolution of synapses. Nat Rev Neurosci 10:701–712.

Sabatini DM (2017) Twenty-five years of mTOR: Uncovering the link from nutrients to growth. Proc Natl Acad Sci USA 114:11818–11825.

Sabatini DM, Erdjument-Bromage H, Lui M, Tempst P, Snyder SH (1994) RAFT1: A mammalian protein that binds to FKBP12 in a rapamycin-dependent fashion and is homologous to yeast TORs. Cell 78:35–43.

Sabers CJ, Martin MM, Brunn GJ, Williams JM, Dumont FJ, Wiederrecht G, Abraham RT (1995) Isolation of a protein target of the FKBP12-rapamycin complex in mammalian cells. J Biol Chem 270:815–822.

Sacktor TC (2011) How does PKMζ maintain long-term memory? Nat Rev Neurosci 12:9–15.

Sacktor TC, Fenton AA (2018) What does LTP tell us about the roles of CaMKII and PKMζ in memory? Mol Brain 11:77.

Saito T (2006) In vivo electroporation in the embryonic mouse central nervous system. Nature Protocols 1:1552–1558.

Saito T, Nakatsuji N (2001) Efficient gene transfer into the embryonic mouse brain using in vivo electroporation. Dev Biol 240:237–246.

Sakagami H, Kondo H (1993) Differential expression of mRNAs encoding γ and δ subunits of Ca^{2+}/calmodulin-dependent protein kinase type II (CaM kinase II) in the mature and postnatally developing rat brain. Mol Brain Res 20:51–63.

Sakai C, Ijaz S, Hoffman EJ (2018) Zebrafish Models of Neurodevelopmental Disorders: Past, Present, and Future. Front Mol Neurosci 11:294.

Sakakibara A, Hatanaka Y (2015) Neuronal polarization in the developing cerebral cortex. Front Neurosci 9:116.

Salinas V, Vega P, Piccirilli MV, Chicco C, Ciraolo C, Christiansen S, Consalvo D, Perez-Maturo J, Medina N, González-Morón D, Novaro V, Perrone C, García M del C, Agosta G, Silva W, Kauffman M (2019) Identification of a somatic mutation in the RHEB gene through high depth and ultra-high depth next generation sequencing in a patient with Hemimegalencephaly and drug resistant Epilepsy. Eur J Med Genet 62:103571.

Sanders SJ, Murtha MT, Gupta AR, et al. (2012) De novo mutations revealed by whole-exome sequencing are strongly associated with autism. Nature 485:237–241.

Sando R, Bushong E, Zhu Y, Huang M, Considine C, Phan S, Ju S, Uytiepo M, Ellisman M, Maximov A (2017) Assembly of excitatory synapses in the absence of glutamatergic neurotransmission. Neuron 94:312–321.e3.

Santen GW, Aten E, Sun Y, Almomani R, Gilissen C, Nielsen M, Kant SG, Snoeck IN, Peeters EA, Hilhorst- Hofstee Y, et al. (2012) Mutations in SWI/SNF chromatin remodeling complex gene ARID1B cause Coffin-Siris syndrome. Nat Genet 44:379–380.

Santini E, Huynh TN, MacAskill AF, Carter AG, Pierre P, Ruggero D, Kaphzan H, Klann E (2013) Exaggerated translation causes synaptic and behavioural aberrations associated with autism. Nature 493:411–415.

Sato T, Umetsu A, Tamanoi F (2008) Characterization of the Rheb-mTOR Signaling Pathway in Mammalian Cells: Constitutive Active Mutants of Rheb and mTOR. Methods Enzymol 438:307–320.

Sato T, Nakashima A, Guo L, Tamanoi F (2009) Specific activation of mTORC1 by Rheb G-protein in vitro involves enhanced recruitment of its substrate protein. J Biol Chem 284:12783–12791.

Sato A, Sunayama J, Matsuda K ichiro, Tachibana K, Sakurada K, Tomiyama A, Kayama T, Kitanaka C (2010) Regulation of neural stem/progenitor cell maintenance by PI3K and mTOR. Neurosci Lett 470:115–120.

Saucedo LJ, Gao X, Chiarelli DA, Li L, Pan D, Edgar BA (2003) Rheb promotes cell growth as a component of the insulin/TOR signalling network. Nat Cell Biol 5:566–571.

Saus E, Soria V, Escaramís G, Vivarelli F, Crespo JM, Kagerbauer B, Menchòn JM, Urretavizcaya M, Gratacòs M, Estivill X (2010) Genetic variants and abnormal processing of pre-miR-182, a circadian clock modulator, in major depression patients with late insomnia. Hum Mol Genet 19:4017–4025.

Saxton RA, Sabatini DM (2017) mTOR Signaling in Growth, Metabolism, and Disease. Cell 168:960–976.

Scanziani M, Salin PA, Vogt KE, Malenka RC, Nicoll RA (1997) Use-dependent increases in glutamate concentration activate presynaptic metabotropic glutamate receptors. Nature 385:630 – 634.

Schiavo GG, Benfenati F, Poulain B, Rossetto O, De Laureto PP, Dasgupta BR, Montecucco C (1992) Tetanus and botulinum-B neurotoxins block neurotransmitter release by proteolytic cleavage of synaptobrevin. Nature 359:832–835.

Schmitz SK, Hjorth JJJJ, Joemai RMS, Wijntjes R, Eijgenraam S, de Bruijn P, Georgiou C, de Jong APH, van Ooyen A, Verhage M, Cornelisse LN, Toonen RF, Veldkamp W (2011) Automated analysis of neuronal morphology, synapse number and synaptic recruitment. J Neurosci Methods 195:185–193.

Schöpel M, Potheraveedu VN, Al-Harthy T, Abdel-Jalil R, Heumann R, Stoll R (2017) The small GTPases Ras and Rheb studied by multidimensional NMR spectroscopy: Structure and function. Biol Chem 398:577–588.

Schulman H, Greengard P (1978a) Stimulation of brain membrane protein phosphorylation by calcium and an endogenous heat-stable protein. Nature 271:478–479.

Schulman H, Greengard P (1978b) Ca^{2+}-dependent protein phosphorylation system in membranes from various tissues, and its activation by "calcium-dependent regulator". Proc Natl Acad Sci USA 75:5432–5436.

Schwartzkroin PA, Roper SN, Wenzel HJ (2004) Cortical dysplasia and epilepsy: Animal models. Adv Exp Med Biol 548:145–174.

Schworer CM, Colbran RJ, Soderling TR (1986) Reversible generation of a Ca^{2+}-independent form of Ca^{2+}(calmodulin)-dependent protein kinase II by an autophosphorylation mechanism. J Biol Chem 261:8581–8584.

Schworer CM, Rothblum LI, Thekkumkara TJ, Singer HA (1993) Identification of novel isoforms of the δ subunit of Ca^{2+}/calmodulin- dependent protein kinase II. Differential expression in rat brain and aorta. J Biol Chem 268:14443–14449.

Shimojo M, Courchet J, Pieraut S, Torabi-Rander N, Sando R, Polleux F, Maximov A (2015) SNAREs Controlling Vesicular Release of BDNF and Development of Callosal Axons. Cell Rep 11:1054–1066.

Scoville WB, Milner B (1957) Loss of recent memory after bilateral hippocampal lesions. J Neurol Neurosurg Psychiatry 20:11–21.

Sengupta S, Peterson TR, Sabatini DM (2010) Regulation of the mTOR Complex 1 Pathway by Nutrients, Growth Factors, and Stress. Mol Cell 40:310–322.

Shafi MM, Vernet M, Klooster D, Chu CJ, Boric K, Barnard ME, Romatoski K, Westover MB, Christodoulou JA, Gabrieli JDE, Whitfield-Gabrieli S, Pascual-Leone A, Chang BS (2015) Physiological consequences of abnormal connectivity in a developmental epilepsy. Ann Neurol 77:487–503.

Shen K, Meyer T (1999) Dynamic control of CaMKII translocation and localization in hippocampal neurons by NMDA receptor stimulation. Science 284:162–166.

Shen K, Teruel MN, Subramanian K, Meyer T (1998) CaMKIIβ functions as an F-actin targeting module that localizes CaMKIIα/β heterooligomers to dendritic spines. Neuron 21:593–606.

Shen K, Teruel MN, Connor JH, Shenolikar S, Meyer T (2000) Molecular memory by reversible translocation of calcium/calmodulin-dependent protein kinase II. Nat Neurosci 3:881–886.

Shen X, Yeung HT, Lai KO (2019) Application of Human-Induced Pluripotent Stem Cells (hiPSCs) to Study Synaptopathy of Neurodevelopmental Disorders. Dev Neurobiol 79:20–35.

Shendure J, Balasubramanian S, Church GM, Gilbert W, Rogers J, Schloss JA, Waterston RH (2017) DNA sequencing at 40: Past, present and future. Nature 550:345–353.

Sheng M, Kim E (2011) The postsynaptic organization of synapses. Cold Spring Harb Perspect Biol 3:a005678.

Sherr EH (2016) Neurodevelopmental Disorders, Causes, and Consequences. Elsevier Inc.

Shields S, Ingebritsen T, Kelly P (1985) Identification of protein phosphatase 1 in synaptic junctions: dephosphorylation of endogenous calmodulin-dependent kinase II and synapse-enriched phosphoproteins. J Neurosci 5:3414–3422.

Shimobayashi M, Hall MN (2014) Making new contacts: the mTOR network in metabolism and signalling crosstalk. Nat Rev Mol Cell Biol 15:155–162.

Shimojo M, Courchet J, Pieraut S, Torabi-Rander N, Sando R, Polleux F, Maximov A (2015) SNAREs Controlling Vesicular Release of BDNF and Development of Callosal Axons. Cell Rep 11:1054–1066.

Shioda N, Fukunaga K (2018) Physiological and pathological roles of CaMKII-PP1 signaling in the brain. Int J Mol Sci 19:20.

Shioda N, Sawai M, Ishizuka Y, Shirao T, Fukunaga K (2015) Nuclear translocation of calcium/calmodulin-dependent protein kinase IIδ3 promoted by protein phosphatase-1 enhances brain-derived neurotrophic factor expression in dopaminergic neurons. J Biol Chem 290:21663–21675.

Shiota C, Woo JT, Lindner J, Shelton KD, Magnuson MA (2006) Multiallelic Disruption of the rictor Gene in Mice Reveals that mTOR Complex 2 Is Essential for Fetal Growth and Viability. Dev Cell 11:583–589.

Shorvon SD (2011) The causes of epilepsy: Changing concepts of etiology of epilepsy over the past 150 years. Epilepsia 52:1033–1044.

Sievers F, Wilm A, Dineen D, Gibson TJ, Karplus K, Li W, Lopez R, McWilliam H, Remmert M, Söding J, Thompson JD, Higgins DG (2011) Fast, scalable generation of high-quality protein multiple sequence alignments using Clustal Omega. Mol Syst Biol 7:539.

Sigler A, Oh WC, Imig C, Altas B, Kawabe H, Cooper BH, Kwon HB, Rhee JS, Brose N (2017) Formation and maintenance of functional spines in the absence of presynaptic glutamate release. Neuron 94:304 –311.e4.

Sík A, Hájos N, Gulácsi A, Mody I, Freund TF (1998) The absence of a major Ca^{2+} signaling pathway in GABAergic neurons of the hippocampus. Proc Natl Acad Sci USA 95:3245–3250.

Silva AJ, Stevens CF, Tonegawa S, Wang Y (1992a) Deficient hippocampal long-term potentiation in alpha-calcium-calmodulin kinase II mutant mice. Science 257:201–206.

Silva AJ, Paylor R, Wehner JM, Tonegawa S (1992b) Impaired spatial learning in alpha-calcium-calmodulin kinase II mutant mice. Science 257:206 –211.

Sims J (1835) On Hypertrophy and Atrophy of the Brain. Med Chir Trans 19:315–380.

Singh D, Bhalla US (2018) Subunit exchange enhances information retention by CaMKII in dendritic spines. Elife 7:1–22.

Sisodiya SM (2000) Surgery for malformations of cortical development causing epilepsy. Brain 123:1075–1091.

Sisodiya SM (2004) Malformations of cortical development: burdens and insights from important causes of human epilepsy. Lancet Neurol 3:29–38.

Smith KL, Swann JW (1999) Long-term depression of perforant path excitatory postsynaptic potentials following synchronous network bursting in area CA3 of immature hippocampus. Neuroscience 89:625– 630.

Smith MK, Colbran RJ, Brickey DA, Soderling TR (1992) Functional determinants in the autoinhibitory domain of calcium/calmodulin-dependent protein kinase II. Role of His282 and multiple basic residues. J Biol Chem 267:1761–1768.

Sobreira N, Schiettecatte F, Valle D, Hamosh A (2015) GeneMatcher: a matching tool for connecting investigators with an interest in the same gene. Hum Mutat 36:928–930.

Soderling TR (1999) The Ca^{2+}–calmodulin-dependent protein kinase cascade. Trends Biochem Sci 24:232–236.

Sokolova IV, Lester HA, Davidson N (2006) Postsynaptic mechanisms are essential for forskolin-induced potentiation of synaptic transmission. J Neurophysiol 95:2570–2579.

Sokolov AM, Seluzicki CM, Morton MC, Feliciano DM (2018) Dendrite growth and the effect of ectopic Rheb expression on

cortical neurons. Neurosci Lett 671:140–147.

Srinivasan M, Edman CF, Schulman H (1994) Alternative splicing introduces a nuclear localization signal that targets multifunctional CaM kinase to the nucleus. J Cell Biol 126:839–852.

Srivastava AK, Schwartz CE (2014) Intellectual disability and autism spectrum disorders: Causal genes and molecular mechanisms. Neurosci Biobehav Rev 46:161–174.

Starita LM, Ahituv N, Dunham MJ, Kitzman JO, Roth FP, Seelig G, Shendure J, Fowler DM (2017) Variant Interpretation: Functional Assays to the Rescue. Am J Hum Genet 101:315–325.

Steffenburg U, Hagberg G, Viggedal G, Kyllerman M (1995) Active epilepsy in mentally retarded children. I. Prevalence and additional neuroimpairments. Acta Pædiatrica 84:1147–1152.

Steinlein OK (2001) Ion channels and epilepsy. Am J Med Genet - Semin Med Genet 106:146–159.

Stephenson JR, Wang X, Perfitt TL, Parrish WP, Shonesy BC, Marks CR, Mortlock DP, Nakagawa T, Sutcliffe JS, Colbran RJ (2017) A Novel Human CAMK2A Mutation Disrupts Dendritic Morphology and Synaptic Transmission, and Causes ASD-Related Behaviors. J Neurosci 37:2216–2233.

Stocker H, Radimerski T, Schindelholz B, Wittwer F, Belawat P, Daram P, Breuer S, Thomas G, Hafen E (2003) Rheb is an essential regulator of S6K in controlling cell growth in Drosophila. Nat Cell Biol 5:559–565.

Stouffer MA, Golden JA, Francis F (2015) Neuronal migration disorders: Focus on the cytoskeleton and epilepsy. Neurobiol Dis 92:18–45.

Stratton M, Chao LH, Schulman H, Kuriyan J (2013) Structural studies on the regulation of Ca^{2+}/calmodulin dependent protein kinase II. Curr Opin Struct Biol 23:292–301.

Stratton M, Lee I-H, Bhattacharyya M, Christensen SM, Chao LH, Schulman H, Groves JT, Kuriyan J (2014) Activation-triggered subunit exchange between CaMKII holoenzymes facilitates the spread of kinase activity. Elife 3:1–28.

Sugiura H, Yasuda S, Katsurabayashi S, Kawano H, Endo K, Takasaki K, Iwasaki K, Ichikawa M, Kobayashi T, Hino O, Yamagata K (2015) Rheb activation disrupts spine synapse formation through accumulation of syntenin in tuberous sclerosis complex. Nat Commun 6:6842:1–15.

Sun T, Hevner RF (2014) Growth and folding of the mammalian cerebral cortex: from molecules to malformations. Nat Rev Neurosci 15:217–232.

Sweeney ST, Broadie K, Keane J, Niemann H, O'Kane CJ (1995) Targeted expression of tetanus toxin light chain in Drosophila specifically eliminates synaptic transmission and causes behavioral defects. Neuron 14:341–351.

Swiech L, Perycz M, Malik A, Jaworski J (2008) Role of mTOR in physiology and pathology of the nervous system. Biochim Biophys Acta - Proteins Proteomics 1784:116–132.

Switon K, Kotulska K, Janusz-Kaminska A, Zmorzynska J, Jaworski J (2017) Molecular neurobiology of mTOR. Neuroscience 341:112–153.

Tabata H, Nakajima K (2001) Efficient in utero gene transfer system to the developing mouse brain using electroporation: visualization of neuronal migration in the developing cortex. Neuroscience 103:865–872.

Takano T, Xu C, Funahashi Y, Namba T, Kaibuchi K (2015) Neuronal polarization. Development 142:2088–2093.

Takei N, Nawa H (2014) mTOR signaling and its roles in normal and abnormal brain development. Front Mol Neurosci 7:28.

Takemoto-Kimura S, Suzuki K, Horigane SI, Kamijo S, Inoue M, Sakamoto M, Fujii H, Bito H (2017) Calmodulin kinases: essential regulators in health and disease. J Neurochem 141:808–818.

Takeuchi Y, Kimura T, Katsuragi S, Miyakawa T, Yamamoto H, Matsumoto K, Miyamoto E (1999) Nuclear localization of the δ subunit of Ca^{2+}/calmodulin-dependent protein kinase II in rat cerebellar granule cells. J Neurochem 72:815–825.

Takeuchi Y, Yamamoto H, Miyakawa T, Miyamoto E (2000) Increase of brain-derived neurotrophic factor gene expression in NG108- 15 cells by the nuclear isoforms of Ca^{2+}/calmodulin-dependent protein kinase II. J Neurochem 74:1913–1922.

Takeuchi Y, Fukunaga K, Miyamoto E (2002) Activation of nuclear Ca^{2+}/calmodulin-dependent protein kinase II and brain-derived neurotrophic factor gene expression by stimulation of dopamine D2 receptor in transfected NG108-15 cells. J Neurochem 82:316–328.

Takeuchi T, Duszkiewicz AJ, Morris RGM (2014) The synaptic plasticity and memory hypothesis: Encoding, storage and persistence. Philos Trans R Soc B Biol Sci 369:20130288.

Talos DM, Sun H, Zhou X, Fitzgerald EC, Jackson MC, Klein PM, Lan VJ, Joseph A, Jensen FE (2012) The interaction between early life epilepsy and autistic-like behavioral consequences: A role for the mammalian target of rapamycin (mTOR) pathway Bonkowsky JL, ed. PLoS One 7:e35885.

Tam V, Patel N, Turcotte M, Bossé Y, Paré G, Meyre D (2019) Benefits and limitations of genome-wide association studies. Nat Rev Genet 20:467–484.

Tang G, Gudsnuk K, Kuo S-HH, Cotrina MLL, Rosoklija G, Sosunov A, Sonders MSS, Kanter E, Castagna C, Yamamoto A, Yue Z, Arancio O, Peterson BSS, Champagne F, Dwork AJJ, Goldman J, Sulzer D (2014) Loss of mTOR-Dependent Macroautophagy Causes Autistic-like Synaptic Pruning Deficits. Neuron 83:1131–1143.

Taniguchi Y, Young-Pearse T, Sawa A, Kamiya A (2012) In utero electroporation as a tool for genetic manipulation in vivo to study psychiatric disorders: from genes to circuits and behaviors. Neuroscientist 18:169–179.

Taoufik E, Kouroupi G, Zygogianni O, Matsas R (2018) Synaptic dysfunction in neurodegenerative and neurodevelopmental diseases: An overview of induced pluripotent stem-cell-based disease models. Open Biol 8.

Tavazoie SF, Alvarez VA, Ridenour DA, Kwiatkowski DJ, Sabatini

BL (2005) Regulation of neuronal morphology and function by the tumor suppressors Tsc1 and Tsc2. Nat Neurosci 8:1727–1734.

Tee AR, Manning BD, Roux PP, Cantley LC, Blenis J (2003) Tuberous Sclerosis Complex gene products, Tuberin and Hamartin, control mTOR signaling by acting as a GTPase-activating protein complex toward Rheb. Curr Biol 13:1259–1268.

Telias M, Ben-Yosef D (2014) Modeling Neurodevelopmental Disorders Using Human Pluripotent Stem Cells. Stem Cell Rev Reports 10:494–511.

Thapar A, Cooper M, Rutter M (2017) Neurodevelopmental disorders. The Lancet Psychiatry 4:339–346.

Thiagarajan TC, Piedras-Renteria ES, Tsien RW (2002) α- and βCaMKII inverse regulation by neuronal activity and opposing effects on synaptic strength. Neuron 36:1103–1114.

Thomas PD, Campbell MJ, Kejariwal A, Mi H, Karlak B, Daverman R, Diemer K, Muruganujan A, Narechania A (2003) PANTHER: a library of protein families and subfamilies indexed by function. Genome Res 13: 2129 –2141.

Thompson PM et al. (2014) The ENIGMA Consortium: large-scale collaborative analyses of neuroimaging and genetic data. Brain Imaging Behav. 8:153–182.

Thoreen CC, Chantranupong L, Keys HR, Wang T, Gray NS, Sabatini DM (2012) A unifying model for mTORC1-mediated regulation of mRNA translation. Nature 485:109–113.

Tian Q, Smart JL, Clement JH, Wang Y, Derkatch A, Schubert H, Danilchik M V., Marks DL, Fedorov LM (2016) RHEB1 expression in embryonic and postnatal mouse. Histochem Cell Biol 145:561–572.

Tighilet B, Hashikawa T, Jones EG (1998) Cell- and lamina-specific expression and activity-dependent regulation of type II calcium/calmodulin-dependent protein kinase isoforms in monkey visual cortex. J Neurosci 18:2129–2146.

Ting JT, Peça J, Feng G (2012) Functional Consequences of Mutations in Postsynaptic Scaffolding Proteins and Relevance to Psychiatric Disorders. Annu Rev Neurosci 35:49–71.

Tobimatsu T, Fujisawa H (1989) Tissue-specific expression of four types of rat calmodulin-dependent protein kinase II mRNAs. J Biol Chem 264:17907–17912.

Tombes RM, Faison MO, Turbeville J (2003) Organization and evolution of multifunctional Ca^{2+}/CaM-dependent protein kinase genes. Gene 322:17–31.

Tonegawa S, Morrissey MD, Kitamura T (2018) The role of engram cells in the systems consolidation of memory. Nat Rev Neurosci 19:485–498.

Traynelis SF, Wollmuth LP, McBain CJ, Menniti FS, Vance KM, Ogden KK, Hansen KB, Yuan H, Myers SJ, Dingledine R (2010) Glutamate receptor ion channels: Structure, regulation, and function Sibley D, ed. Pharmacol Rev 62:405–496.

Traynelis J, Silk M, Wang Q, Berkovic SF, Liu L, Ascher DB, Balding DJ, Petrovski S (2017) Optimizing genomic medicine in epilepsy through a gene-customized approach to missense variant interpretation. Genome Res 27:1715–1729.

Trinidad JC, Thalhammer A, Specht CG, Lynn AJ, Baker PR, Schoepfer R, Burlingame AL (2008) Quantitative Analysis of Synaptic Phosphorylation and Protein Expression. Mol Cell Proteomics 7:684–696.

Tsai PT, Greene-Colozzi E, Goto J, Anderl S, Kwiatkowski DJ, Sahin M (2013) Prenatal rapamycin results in early and late behavioral abnormalities in wildtype C57BL/6 mice. Behav Genet 43:51–59.

Tsai V, Parker WE, Orlova KA, Baybis M, Chi AWSS, Berg BD, Birnbaum JF, Estevez J, Okochi K, Sarnat HB, Flores-Sarnat L, Aronica E, Crino PB (2014) Fetal brain mTOR signaling activation in tuberous sclerosis complex. Cereb Cortex 24:315–327.

Turner TN, Eichler EE (2019) The Role of De Novo Noncoding Regulatory Mutations in Neurodevelopmental Disorders. Trends Neurosci 42:115–127.

Turner TN, Coe BP, Dickel DE, Hoekzema K, Nelson BJ, Zody MC, Kronenberg ZN, Hormozdiari F, Raja A, Pennacchio LA, Darnell RB, Eichler EE (2017a) Genomic Patterns of De Novo Mutation in Simplex Autism. Cell 171:710-722.e12.

Turner TN, Yi Q, Krumm N, Huddleston J, Hoekzema K, Stessman HAF, Doebley AL, Bernier RA, Nickerson DA, Eichler EE (2017b) denovo-db: A compendium of human de novo variants. Nucleic Acids Res 45:D804–D811.

Tyvaert L, Hawco C, Kobayashi E, LeVan P, Dubeau F, Gotman J (2008) Different structures involved during ictal and interictal epileptic activity in malformations of cortical development: An EEG-fMRI study. Brain 131:2042–2060.

UniProt C (2015) UniProt: a hub for protein information. Nucleic acids res 43:D204-212.

Upadhya D, Shetty AK (2019) Promise of extracellular vesicles for diagnosis and treatment of epilepsy. Epilepsy Behav 0:106499.

Urano J, Comiso MJ, Guo L, Aspuria PJ, Deniskin R, Tabancay AP, Kato-Stankiewicz J, Tamanoi F (2005) Identification of novel single amino acid changes that result in hyperactivation of the unique GTPase, Rheb, in fission yeast. Mol Microbiol 58:1074–1086.

Urbanska M, Gozdz A, Swiech LJ, Jaworski J (2012) Mammalian target of rapamycin complex 1 (mTORC1) and 2 (mTORC2) control the dendritic arbor morphology of hippocampal neurons. J Biol Chem 287:30240–30256.

Vallano M Lou (1989) Separation of isozymic forms of type II calcium/calmodulin-dependent protein kinase using cation-exchange chromatography. J Neurosci Methods 30:1–9.

Vallano M Lou, Beaman-Hall CM, Mathur A, Chen Q (2000) Astrocytes express specific variants of CaM KII δ and γ, but not α and β, that determine their cellular localizations. Glia 30:154–164.

Valton L, Guye M, McGonigal A, Marquis P, Wendling F, Régis J, Chauvel P, Bartolomei F (2008) Functional interactions in brain networks underlying epileptic seizures in bilateral diffuse periventricular heterotopia. Clin Neurophysiol 119:212–223.

van Loo K, Martens G (2009) Genetic and Environmental Factors in Complex Neurodevelopmental Disorders. Curr Genomics 8:429–444.

van Slegtenhorst M, Nellist M, Nagelkerken B, Cheadle J, Snell R, van den Ouweland A, Reuser A, Sampson J, Halley D, van der Sluijs P (1998) Interaction Between Hamartin and Tuberin, the TSC1 and TSC2 Gene Products. Hum Mol Genet 7:1053–1057.

van Woerden GM, Harris KD, Hojjati MR, Gustin RM, Qiu S, De Avila Freire R, Jiang YH, Elgersma Y, Weeber EJ (2007) Rescue of neurological deficits in a mouse model for Angelman syndrome by reduction of αCaMKII inhibitory phosphorylation. Nat Neurosci 10:280–282.

van Woerden GM, Hoebeek FE, Gao Z, Nagaraja RY, Hoogenraad CC, Kushner SA, Hansel C, De Zeeuw CI, Elgersma Y (2009) betaCaMKII controls the direction of plasticity at parallel fiber-purkinje cell synapses. Nat Neurosci 12:823– 825.

Vaz R, Hofmeister W, Lindstrand A (2019) Zebrafish models of neurodevelopmental disorders: Limitations and benefits of current tools and techniques. Int J Mol Sci 20.

Verderio C, Coco S, Bacci A, Rossetto O, De Camilli P, Montecucco C, Matteoli M (1999) Tetanus toxin blocks the exocytosis of synaptic vesicles clustered at synapses but not of synaptic vesicles in isolated axons. J Neurosci 19:6723–6732.

Verpelli C, Montani C, Vicidomini C, Heise C, Sala C (2013) Mutations of the synapse genes and intellectual disability syndromes. Eur J Pharmacol 719:112–116.

Vincent M, Collet C, Verloes A, Lambert L, Herlin C, Blanchet C, Sanchez E, Drunat S, Vigneron J, Laplanche JL, Puechberty J, Sarda P, Geneviève D (2014) Large deletions encompassing the TCOF1 and CAMK2A genes are responsible for treacher collins syndrome with intellectual disability. Eur J Hum Genet 22:52–56.

Vissers LELM, De Ligt J, Gilissen C, Janssen I, Steehouwer M, De Vries P, Van Lier B, Arts P, Wieskamp N, Del Rosario M, Van Bon BWM, Hoischen A, De Vries BBA, Brunner HG, Veltman JA (2010) A de novo paradigm for mental retardation. Nat Genet 42:1109–1112.

Vissers LELM, Gilissen C, Veltman JA (2016) Genetic studies in intellectual disability and related disorders. Nat Rev Genet 17:9–18.

Vitrac A, Cloëz-Tayarani I (2018) Induced pluripotent stem cells as a tool to study brain circuits in autism-related disorders. Stem Cell Res Ther 9:226.

Vogt MA, Chourbaji S, Brandwein C, Dormann C, Sprengel R, Gass P (2008) Suitability of tamoxifen-induced mutagenesis for behavioral phenotyping. Exp Neurol 211:25–33.

Waggener CT, Dupree JL, Elgersma Y, Fuss B (2013) CaMKIIβ regulates oligodendrocyte maturation and CNS myelination. J Neurosci 33:10453–10458.

Wahane SD, Hellbach N, Prentzell MT, Weise SC, Vezzali R, Kreutz C, Timmer J, Krieglstein K, Thedieck K, Vogel T (2014) PI3K-p110-alpha-subtype signalling mediates survival, proliferation and neurogenesis of cortical progenitor cells via activation of mTORC2. J Neurochem 130:255–267.

Waldmann R, Hanson PI, Schulman H (1990) Multifunctional Ca2+/Calmodulin-Dependent Protein Kinase Made Ca2+ Independent for Functional Studies. Biochemistry 29:1679–1684.

Wang C-L, Zhang L, Zhou Y, Zhou J, Yang X-J, Duan S, Xiong Z-Q, Ding Y-Q (2007) Activity-dependent development of callosal projections in the somatosensory cortex. J Neurosci 27:11334–11342.

Wang ZW (2008) Regulation of synaptic transmission by presynaptic CAMKII and BK channels. Mol Neurobiol 38:153–166.

Wang X, Zhang C, Szábo G, Sun QQ (2013) Distribution of CaMKIIα expression in the brain in vivo, studied by CaMKIIα-GFP mice. Brain Res 1518:9–25.

Wang X, Marks CR, Perfitt TL, Nakagawa T, Lee A, Jacobson DA, Colbran RJ (2017) A novel mechanism for Ca^{2+}/calmodulin-dependent protein kinase II targeting to L-type Ca^{2+}channels that initiates long range signaling to the nucleus. J Biol Chem 292:17324–17336.

Wang W, Corominas R, Lin GN (2019) De novo mutations from whole exome sequencing in neurodevelopmental and psychiatric disorders: From discovery to application. Front Genet 10:258.

Ware JS, Samocha KE, Homsy J, Daly MJ (2015) Interpreting de novo variation in human disease using denovolyzeR. Current Prot Human Genet 87:21–15.

Waterhouse AM, Procter JB, Martin DMA, Clamp M, Barton GJ (2009) Jalview Version 2-A multiple sequence alignment editor and analysis workbench. Bioinformatics 25:1189–1191.

Waxham MN, Aronowski J, Westgate SA, Kelly PT (1990) Mutagenesis of Thr-286 in monomeric Ca2+/calmodulin-dependent protein kinase II eliminates Ca^{2+}/calmodulin-independent activity. Proc Natl Acad Sci USA 87:1273–1277.

Way SW, Rozas NS, Wu HC, Mckenna J, Reith RM, Hashmi SS, Dash PK, Gambello MJ (2012) The differential effects of prenatal and/or postnatal rapamycin on neurodevelopmental defects and cognition in a neuroglial mouse model of tuberous sclerosis complex. Hum Mol Genet 21:3226–3236.

Wayman GA (2004) Regulation of Axonal Extension and Growth Cone Motility by Calmodulin-Dependent Protein Kinase I. J Neurosci 24:3786–3794.

Wennerberg K, Rossman KL, Der CJ (2005) The Ras superfamily at a glance. J Cell Sci 118:843–846.

West AE, Greenberg ME (2011) Neuronal activity-regulated gene transcription in synapse development and cognitive function. Cold Spring Harb Perspect Biol 3:1–21.

Wheeler DG, Barrett CF, Groth RD, Safa P, Tsien RW (2008) CaMKII locally encodes L-type channel activity to signal to nuclear CREB in excitation - transcription coupling. J Cell Biol 183:849–863.

Wheeler DG, Groth RD, Ma H, Barrett CF, Owen SF, Safa P, Tsien RW (2012) CaV1 and CaV2 channels engage distinct modes of Ca^{2+} signaling to control CREB-dependent gene expression. Cell 149:1112–1124.

Wheless JW (2015) Use of the mTOR inhibitor everolimus in a patient with multiple manifestations of tuberous sclerosis complex including epilepsy. Epilepsy Behav Case Rep 4:63–66.

Wilfert AB, Sulovari A, Turner TN, Coe BP, Eichler EE (2017) Recurrent de novo mutations in neurodevelopmental disorders: Properties and clinical implications. Genome Med 9:101.

Willer CJ, Li Y, Abecasis GR. (2010) METAL: fast and efficient meta-analysis of genome wide association scans. Bioinformatics 26: 2190-2191.

Willsey AJ et al. (2018) The Psychiatric Cell Map Initiative: A Convergent Systems Biological Approach to Illuminating Key Molecular Pathways in Neuropsychiatric Disorders. Cell 174:505–520.

Wong M (2009) Animal models of focal cortical dysplasia and tuberous sclerosis complex: Recent progress toward clinical applications. Epilepsia 50:34–44.

Wong M, Crino PB (2010) MTOR and epileptogenesis in developmental brain malformations. Epilepsia 51:72.

Wong M, Roper SN (2016) Genetic animal models of malformations of cortical development and epilepsy. J Neurosci Methods 260:73–82.

Woodworth MB, Greig LC, Liu KX, Ippolito GC, Tucker HO, Macklis JD (2016) Ctip1 Regulates the Balance between Specification of Distinct Projection Neuron Subtypes in Deep Cortical Layers. Cell Rep 15:999–1012.

Wu Y et al. (2007) Mutations in ionotropic AMPA receptor 3 alter channel properties and are associated with moderate cognitive impairment in humans. Proc Natl Acad Sci USA 104:18163–18168.

Yamagata K, Sanders LK, Kaufmann WE, Yee W, Barnes CA, Nathans D, Worley PF (1994) Rheb, a Growth Factor- and Synaptic Activity-Regulated Gene, Encodes a Novel Ras-Related Protein. J Biol Chem 269:16333–16339.

Yamagata Y, Kobayashi S, Umeda T, Inoue A, Sakagami H, Fukaya M, Watanabe M, Hatanaka N, Totsuka M, Yagi T, Obata K, Imoto K, Yanagawa Y, Manabe T, Okabe S (2009) Kinase-Dead Knock-In Mouse Reveals an Essential Role of Kinase Activity of Ca^{2+}/Calmodulin-Dependent Protein Kinase II in Dendritic Spine Enlargement, Long-Term Potentiation, and Learning. J Neurosci 29:7607–7618.

Yan L, Findlay GM, Jones R, Procter J, Cao Y, Lamb RF (2006) Hyperactivation of mammalian target of rapamycin (mTOR) signaling by a gain-of-function mutant of the Rheb GTPase. J Biol Chem 281:19793–19797.

Yang E, Schulman H (1999) Structural Examination of Autoregulation of Multifunctional Calcium / Calmodulin-dependent Protein Kinase II. J Biol Chem 274:26199–26208.

Yang Q, Inoki K, Kim E, Guan KL (2006) TSC1/TSC2 and Rheb have different effects on TORC1 and TORC2 activity. Proc Natl Acad Sci USA 103:6811–6816.

Yang H, Jiang X, Li B, Yang HJ, Miller M, Yang A, Dhar A, Pavletich NP (2017) Mechanisms of mTORC1 activation by RHEB and inhibition by PRAS40. Nature 552:368–373.

Yang Y, Muzny DM, Reid JG, Bainbridge MN, Willis A, Ward PA, Braxton A, Beuten J, Xia F, Niu Z, et al. (2013). Clinical whole-exome sequencing for the diagnosis of mendelian disorders. N Engl J Med 369:1502–1511.

Yang Y, Li W, Zhang H, Yang G, Wang X, Ding M, Jiang T, Lv L (2015) Association study of N-methyl-D-aspartate receptor subunit 2B (GRIN2B) polymorphisms and schizophrenia symptoms in the Han Chinese population. PLoS ONE 10: e0125925.

Yang Y, Lu J, Zuo Y (2018) Changes of Synaptic Structures Associated with Learning, Memory and Diseases: Brain Sci Adv 4:99–117.

Yao Y, Jones E, Inoki K (2017) Lysosomal regulation of mTORC1 by amino acids in mammalian cells. Biomolecules 7:51.

Yasuda H, Barth AL, Stellwagen D, Malenka RC (2003) A developmental switch in the signaling cascades for LTP induction. Nat Neurosci 6:15–16.

Ye J, Das S, Roy A, Wei W, Huang H, Lorenz-Guertin JM, Xu Q, Jacob TC, Wang B, Sun D, Wang QJ (2019) Ischemic Injury-Induced CaMKIIδ and CaMKIIγ Confer Neuroprotection Through the NF-κB Signaling Pathway. Mol Neurobiol 56:2123–2136.

Yu CR, Power J, Barnea G, O'Donnell S, Brown HEV, Osborne J, Axel R, Gogos JA (2004) Spontaneous neural activity is required for the establishment and maintenance of the olfactory sensory map. Neuron 42:553–566.

Yu Y, Li S, Xu X, Li Y, Guan K, Arnold E, Ding J (2005) Structural basis for the unique biological function of small GTPase RHEB. J Biol Chem 280:17093–17100.

Zalcman G, Federman N, Fiszbein A, de la Fuente V, Ameneiro L, Schor I, Romano A (2019) Sustained CaMKII Delta Gene Expression Is Specifically Required for Long-Lasting Memories in Mice. Mol Neurobiol 56:1437–1450.

Zalutsky RA, Nicoll RA (1990) Comparison of two forms of long-term potentiation in single hippocampal neurons. Science 248:1619 –1624.

Zamboni V, Jones R, Umbach A, Ammoni A, Passafaro M, Hirsch E, Merlo GR (2018) Rho GTPases in intellectual disability: From genetics to therapeutic opportunities. Int J Mol Sci 19:1821.

Zeng LH, Rensing NR, Zhang B, Gutmann DH, Gambello MJ, Wong M (2011) Tsc2 gene inactivation causes a more severe epilepsy phenotype than Tsc1 inactivation in a mouse model of Tuberous Sclerosis Complex. Hum Mol Genet 20:445–454.

Zhang J, Abdullah JM (2013) The role of GluA1 in central nervous system disorders. Rev Neurosci 24:499–505.

Zhang Y (2008) I-TASSER server for protein 3D structure prediction. BMC Bioinformatics 9: 40.

Zhang Y, Fan M, Wang Q, He G, Fu Y, Li H, Yu S (2015) Polymorphisms in MicroRNA Genes and Genes Involving in NMDAR Signaling and Schizophrenia: A Case-Control Study in Chinese Han Population. Sci Rep 5:12984.

Zhang Y, Gao X, Saucedo LJ, Ru B, Edgar B a, Pan D (2003) Rheb is a direct target of the tuberous sclerosis tumour suppressor proteins. Nat Cell Biol 5:578–581.

Zhao S, Li Z, Zhang M, Zhang L, Zheng H, Ning J, Wang Y, Wang F, Zhang X, Gan H, Wang Y, Zhang X, Luo H, Bu G, Xu H, Yao Y, Zhang Y (2019) A brain somatic RHEB doublet mutation causes focal cortical dysplasia type II. Exp Mol Med 51:84.

Zhou J, Shrikhande G, Xu J, McKay RM, Burns DK, Johnson JE, Parada LF (2011) Tsc1 mutant neural stem/progenitor cells exhibit migration deficits and give rise to subependymal lesions in the lateral ventricle. Genes Dev 25:1595–1600.

Zhu F, Cizeron M, Qiu Z, Benavides-Piccione R, Kopanitsa M V., Skene NG, Koniaris B, DeFelipe J, Fransén E, Komiyama NH, Grant SGN (2018) Architecture of the Mouse Brain Synaptome. Neuron 99:781-799.

Ziff EB (1997) Enlightening the postsynaptic density. Neuron 19:1163–1174.

Zou J et al. (2011) Rheb1 Is Required for mTORC1 and Myelination in Postnatal Brain Development. Dev Cell 20:97–108.

Zou Y, Jiang W, Wang J, Li Z, Zhang J, Bu J, Zou J, Zhou L, Yu S, Cui Y, Yang W, Luo L, Lu QR, Liu Y, Chen M, Worley PF, Xiao B (2014) Oligodendrocyte precursor cell-intrinsic effect of Rheb1 controls differentiation and mediates mTORC1-dependent myelination in brain. J Neurosci 34:15764–15778.


A

SUMMARY

Neurodevelopmental disorders are a complex and heterogeneous group of neurological disorders characterized by their early-onset, and estimated to affect more than 3% of children worldwide. Hence, they represent a major health problem. The rapid advancement in sequencing technologies of the past years allowed the identification of hundreds of variants in several different genes involved in neurodevelopmental disorders. One of the main challenges for the development of efficient therapeutic interventions is understanding how the genetic risk factors, in combination with individual environmental factors, can lead to the disorder. The functional biological validation of the contribution of the candidate variants to the pathogenesis of the disorder represents a very first step in this endeavor. This thesis shows the results obtained from a series of functional assays to validate the contribution of *de novo* missense variants identified in *CAMK2* and *RHEB1* to the pathogenesis of intellectual disability (ID) and epilepsy.

CAMK2 is one of the most abundant proteins in the mammalian brain and 40 years of research established its fundamental role in learning and memory. Despite the vast knowledge acquired over the years, we uncovered in **chapter II** hitherto unknown roles for the major brain isoforms, CAMK2A and CAMK2B, that were previously masked due to their redundancy. Using an inducible knock-out approach deleting both mouse isoforms simultaneously, we showed that CAMK2 is crucial for survival. Surprisingly, there are very little biochemical changes at the synaptic level, where CAMK2 is thought to play a major structural role.

Understanding the unique and specific functions of CAMK2A and CAMK2B has crucial therapeutic implications for the newly identified patients suffering from neurodevelopmental disorders with variants in *CAMK2A* and *CAMK2B*. Biochemical knowledge on CAMK2 activity and regulation, helped us to predict *a priori* the potential effect of some of the missense variants identified in *CAMK2A* and *CAMK2B* and to refine the assays used to assess their pathogenicity. In **chapter III** we showed that, despite the lack of clear common clinical features (ID being the only true commonality for all children carrying a variant in one of the *CAMK2* genes), variants that affect the autoregulatory domain and variants that we established to be gain-of-function (which are the majority) seem to correlate with a more severe neurological clinical phenotype. Our findings show that CAMK2 is involved in a broad range of neurological disorders that are only starting to be uncovered. In **chapter IV** we showed that not only the major brain isoforms of the CAMK2 family are associated with human neurodevelopmental disorders, but that also one of the less well-known isoforms, CAMK2G, is associated with ID. Despite the low abundance in the adult brain compared to the other major isoforms, we showed using functional assays that the variant Arg292Pro acts as a pathogenic dominant gain-of-function, revealing that also CAMK2G can play an indispensable previously unknown function in neurodevelopment.

In the second part of this thesis, we focused on the *RHEB1* gene, the direct activator of mTOR, whose role in brain development, neuronal differentiation and synaptic organization has been previously shown. mTOR dysfunction has been associated with several neurological disorders such as epilepsy, ID, autism and brain malformations, however, *RHEB1* itself was never directly linked to neurodevelopmental disorders. In **chapter V** we report a number of *de novo* mutations in both known and novel mTOR-related genes associated with brain growth and ID, and highlight the contribution of *RHEB1* as a causative gene for ID with megalencephaly and epilepsy. In **chapter VI** we explored how the hyperactive mutant RHEB1p.Pro37Leu contributes to the mechanisms of epileptogenesis. We showed that, while the presence of macroscopic focal cortical malformations is not necessary to cause epilepsy, the alterations caused at the circuit level through abnormal connectivity can explain the seizures caused by hyperactivation of the mTOR pathway.

Although the number of genes involved in neurodevelopmental disorders is steadily

increasing, the identification of variants in genes belonging to shared molecular pathways can offer an invaluable tool in understanding the etiology of neurodevelopmental disorders. Using functional assays, the results presented in this thesis highlight a novel role for *CAMK2* as a disease-causing gene and expand the current knowledge on mTOR-related epilepsy. This knowledge can potentially lead to novel therapeutic interventions.

SAMENVATTING

Neurologische ontwikkelingsstoornissen (NOS) vormen een groep van complexe en heterogene neurologische aandoeningen met een vroege aanvang die naar schatting meer dan 3% van de kinderen over de hele wereld treft, waardoor ze een groot gezondheidsprobleem. De snelle vooruitgang in genetische diagnose technologieën van de afgelopen jaren maakte de identificatie mogelijk van honderden varianten in verschillende genen die betrokken zijn bij NOS. Dit variëreert van veranderingen van een enkele nucleotide tot veranderingen van hele stukken van het DNA, met variabele frequenties in de populatie, van veel voorkomend tot zeldzaam. Een van de belangrijkste uitdagingen voor de ontwikkeling van efficiënte therapeutische interventies is begrijpen hoe de genetische risicofactoren, in combinatie met individuele omgevingsfactoren, tot de aandoening kunnen leiden. De functionele biologische validatie van de bijdrage van de kandidaat varianten aan de pathogenese van de aandoening vormt een eerste stap. Dit proefschrift toont de resultaten verkregen uit een reeks functionele testen om de bijdrage van *de novo* missense varianten, geïdentificeerd in *CAMK2* en *RHEB1*, aan de pathogenese van verstandelijke beperking en epilepsie te valideren.

CAMK2 is een van de meest voorkomende eiwitten in de hersenen van zoogdieren en 40 jaar onderzoek vestigde zijn fundamentele rol in leren en geheugen. Ondanks de enorme kennis die we in de loop der jaren hebben opgedaan, hebben we in **hoofdstuk II** nieuwe onbekende rollen ontdekt voor de belangrijkste CAMK2 eiwitten in de hersenen, CAMK2A en CAMK2B, die eerder werden gemaskeerd doordat de een kan compenseren voor de ander, indien afwezig. Met behulp van een induceerbare knock-out techniek bij muizen, waarbij beide CAMK2 eiwitten tegelijkertijd zijn verwijderd, hebben we aangetoond dat ze cruciaal zijn om te kunnen overleven. Verrassend genoeg zijn er nauwelijks veranderingen gevonden in de biochemische kenmerken op synaps niveau, waar CAMK2 een belangrijke (structurele) rol speelt.

Inzicht in de unieke en specifieke functies van CAMK2A en CAMK2B heeft cruciale therapeutische implicaties voor de nieuw geïdentificeerde patiënten die lijden aan neurologische aandoeningen met varianten in *CAMK2A* en *CAMK2B*. Biochemische kennis over CAMK2-activiteit en -regulatie hielp ons *a priori* het potentiële effect van enkele van de *CAMK2A* en *CAMK2B* missense-varianten, te voorspellen en de testen te verfijnen die werden gebruikt om hun pathogeniteit te beoordelen. In **hoofdstuk III** hebben we laten zien dat ondanks dat er weinig klinische overeenkomsten zijn tussen de kinderen die een variant in een van de *CAMK2* genen dragen (het enige kenmerk wat ieder kind deelt is verstandelijke beperking). Varianten die invloed hebben op het autoregulatoire domein en varianten waarvan we hebben vastgesteld dat ze het eiwit activeren (wat de meerderheid van de varianten betreft) lijken te correleren met een ernstiger neurologisch fenotype. Onze bevindingen tonen aan dat CAMK2 betrokken is bij een breed scala aan neurologische aandoeningen die we pas beginnen te ontdekken. In **hoofdstuk IV** hebben we aangetoond dat niet alleen de meest voorkomende CAMK2 eiwitten in het brein geassocieerd zijn met NOS, maar dat ook een van de minder voorkomende CAMK2 eiwitten, CAMK2G, geassocieerd is met een verstandelijke beperking. Ondanks de lage abundantie in de hersenen van volwassenen in vergelijking met CAMK2A en CAMK2B, toonden we met behulp van functionele testen aan dat de CAMK2G variant Arg292Pro een pathogene dominant-actieve mutatie is, en laten we zien dat ook CAMK2G een onmisbare rol speelt in normale neurologische ontwikkeling.

In het tweede deel van dit proefschrift hebben we ons gericht op het *RHEB1*-gen, directe activator van mTOR, waarvan de rol in hersenontwikkeling, neuronale differentiatie en synaptische organisatie eerder is aangetoond. mTOR-disfunctie is in verband gebracht met verschillende neurologische aandoeningen zoals epilepsie, mentale retardatie, autisme en hersenafwijkingen, maar RHEB1 zelf was nooit rechtstreeks gekoppeld aan NOS. In **hoofdstuk**

V beschrijven we een hele reeks *de novo*-mutaties in zowel bekende als nieuwe mTOR-gerelateerde genen, geassocieerd met hersengroei en NOS en benadrukken we de bijdrage van *RHEB1* als een oorzakelijk gen voor NOS met megalencefalie en epilepsie. In **hoofdstuk VI** hebben we de mechanismen van epileptogenese onderzocht die worden veroorzaakt door de hyperactieve mutant RHEB1p.Pro37Leu. We hebben aangetoond dat de aanwezigheid van macroscopische focale corticale misvormingen niet nodig zijn om epilepsie te veroorzaken, maar dat juist de abnormale connectiviteit die veroorzaakt wordt door hyperactivatie van mTOR, bijdraagt aan de epilepsie.

Hoewel het aantal genen dat betrokken is bij neurologische aandoeningen gestaag toeneemt, kan de identificatie van varianten in genen die behoren tot gedeelde moleculaire paden een waardevol hulpmiddel zijn bij het begrijpen van de etiologie van neurologische aandoeningen. Al met al benadrukken de resultaten in dit proefschrift een nieuwe rol voor *CAMK2* als een NOS-veroorzakend gen en breiden ze de huidige kennis over mTOR-gerelateerde epilepsie uit. Deze kennis kan mogelijk leiden tot nieuwe therapeutische interventies.

CURRICULUM VITAE

PERSONAL INFORMATION

Martina Proietti Onori
Born in Subiaco (Rome), Italy on 11th of December 1989
email: martina.proiettionori@gmail.com
linkedin: https:/www.linkedin.com/in/martina-proietti-onori-95bbb47b/

EDUCATION

Bachelor's degree | Biological sciences, "Sapienza" University of Rome, Italy
2008 – 2011
Obtained *summa cum laude*

Master's degree | Neurobiology, "Sapienza" University of Rome, Italy
2011 – 2013
Obtained *summa cum laude*, with thesis title: "Development and behavioural validation of an immune-mediated mouse model of Tourette syndrome" supervised by Prof. Andrea Mele ("Sapienza" University of Rome) and Dr. Giovanni Laviola (Istituto Superiore di Sanità, Rome)

RESEARCH EXPERIENCE

Master's degree internship | Istituto Superiore di Sanità, Rome, Italy
2011 – 2013
During this internship period at the Department of Cell Biology and Neuroscience, Section of Behavioral Neuroscience, Istituto Superiore di Sanità, (supervised by Dr. Giovanni Laviola and Dr. Simone Macrí) I developed an autoimmune mouse model for Tourette Syndrome and tested it on several behavioural paradigms

Postgraduate research| Erasmus MC, Rotterdam, The Netherlands
2014 – 2015
During my postgraduate lab experience at the Department of Neuroscience of the Erasmus MC in Rotterdam, under the supervision of Prof. Dr. Chris de Zeeuw and Dr. Zhenyu Gao, I focused on understanding the cerebellar electrophysiological mechanisms underlying the learning of eye-blink conditioning in mice

PhD| Erasmus MC, Rotterdam, The Netherlands
2016 – 2020
At the Department of Neuroscience of the Erasmus MC in Rotterdam, under the supervision of Prof. Dr. Ype Elgersma, director of ENCORE (Erfelijke Neuro-Cognitieve Ontwikkelingsstoornissen Rotterdam Erasmus MC) expertise centre, and Dr. Geeske van Woerden, I started my PhD project on the identification of molecular and cellular mechanisms underlying the development of mTOR dependent epilepsy and the characterization of novel CAMK2 mutations related to intellectual disability


A

LIST OF PUBLICATIONS

In this thesis

Reijnders MRF*, Kousi M*, van Woerden GM*, Klein M, Bralten J, Mancini GMS, van Essen T, **Proietti Onori M**, Smeets EEJ, van Gastel M, Stegmann APA, Stevens SJC, Lelieveld SH, Gilissen C, Pfundt R, Tan PL, Kleefstra T, Franke B, Elgersma Y, Katsanis N, Brunner HG. Variation in a range of mTOR-related genes associates with intracranial volume and intellectual disability. *Nat Commun*, 2017, 8(1):1052.

Küry S*, van Woerden GM*, Besnard T*, **Proietti Onori M**, … , Bézieau S, Odent S, Elgersma Y, Mercier S. De Novo Mutations in Protein Kinase Genes CAMK2A and CAMK2B Cause Intellectual Disability. *Am J Hum Genet*, 2017, 101(5):768-788.

Proietti Onori M, Koopal B, Everman DB, Worthington JD, Jones JR, Ploeg MA, Mientjes E, van Bon BW, Kleefstra T, Schulman H, Kushner SA, Küry S, Elgersma Y, van Woerden GM. The intellectual disability-associated CAMK2G p.Arg292Pro mutation acts as a pathogenic gain-of-function. *Hum Mutat*, 2018, 39(12):2008-2024.

Kool MJ*, **Proietti Onori M***, Borgesius NZ, van de Bree JE, Elgersma-Hooisma M, Nio E, Bezstarosti K, Buitendijk GHS, Aghadavoud Jolfaei M, Demmers JAA, Elgersma Y, van Woerden GM. CAMK2-dependent signaling in neurons is essential for survival. *J Neurosci*, 2019, 39(28):5424-5439.

Proietti Onori M, Koene LMC*, Schafer CB*, Nellist M, de Brito van Velze M, Gao Z, Elgersma Y, van Woerden GM. RHEB1-hyperactivity dependent cortical malformations cause spontaneous seizures due to aberrant connectivity. *Manuscript in preparation.*

Others

Macrì S, **Proietti Onori M**, Laviola G. Theoretical and practical considerations behind the use of laboratory animals for the study of Tourette syndrome. *Neurosci Biobehav Rev*, 2013, 37(6): 1085-100.

Macrì S*, **Proietti Onori M***, Roessner V, Laviola G. Animal models recapitulating the multifactorial origin of Tourette syndrome. *Int Rev Neurobiol,* 2013, 112:211-37.

Proietti Onori M, Ceci C, Laviola G, Macrì S. A behavioural test battery to investigate tic-like symptoms, stereotypies, attentional capabilities, and spontaneous locomotion in different mouse strains. *Behav Brain Res*, 2014, 267:95-105.

Ceci C, **Proietti Onori M**, Macrì S, Laviola G. Interaction between the endocannabinoid and serotonergic system in the exhibition of head twitch response in four mouse strains. *Neurotox Res,* 2015, 27(3):275-83.

Macrì S, Ceci C, **Proietti Onori M**, Invernizzi RW, Bartolini E, Altabella L, Canese R, Imperi M, Orefici G, Creti R, Margarit I, Magliozzi R, Laviola G. Mice repeatedly exposed to Group-A β-Haemolytic Streptococcus show perseverative behaviors, impaired sensorimotor gating, and immune activation in rostral diencephalon. *Sci Rep*, 2015, 25;5:13257.

Gao Z, **Proietti Onori M**, Lin Z, Ten Brinke MM, Boele HJ, Potters JW, Ruigrok TJ, Hoebeek FE, De Zeeuw CI. Excitatory Cerebellar Nucleocortical Circuit Provides Internal Amplification during Associative Conditioning. *Neuron,* 2016, 89(3):645-57.

Ten Brinke MM*, Heiney SA*, Wang X*, **Proietti Onori M**, Boele HJ, Bakermans J, Medina JF, Gao Z, De Zeeuw CI. Dynamic modulation of activity in cerebellar nuclei neurons during pavlovian eyeblink conditioning in mice. *Elife*, 2017, 6. pii: e28132.

Koene LMC*, van Grondelle SE*, **Proietti Onori M**, Wallaard I, Kooijman NHRM, van Oort A, Schreiber J, Elgersma Y (2019) Effects of antiepileptic drugs in a new TSC/mTOR-dependent epilepsy mouse model. *Ann Clin Transl Neurol*, 2019, 6:1273-1291.

**these authors contributed equally*

PHD PORTFOLIO

Name:	Martina Proietti Onori
PhD period:	January 2016 - April 2020
Erasmus MC Department:	Neuroscience
Promotor:	Prof. Dr. Ype Elgersma
Co-promotor:	Dr. Geeske van Woerden
Research School:	Graduate School Neurosciences Amsterdam Rotterdam (ONWAR)

SUMMARY OF PHD TRAINING AND TEACHING

PHD TRAINING

Courses and workshops

Article 9 – Course on laboratory animal science	31 March-11 April 2014
Stereology and morphometry in Neurosciences	20-23 June 2016
Basic course on R	18-24 May 2017
Workshop on Innovative Mouse Models	15-16 June 2017
Functional Imaging and Super resolution	30 Oct-3 Nov 2017
Scientific Integrity	06 August 2019

National and international conferences

Dutch Neuroscience Meeting Lunteren, The Netherlands (*poster presentation*)	9-10 June 2016
Annual PhD-meeting ONWAR Woudschoten, The Netherlands	24-25 November 2016
The brain conferences – Cortex evolution and development Copenhagen, Denmark (*poster presentation*)	24-27 September 2017
11th International Meeting on Substrate-Integrated Mircoelectrode Arrays Reutlingen, Germany	4-6 July 2018
11th FENS Forum of European Neurosciences Berlin, Germany (*poster presentation*)	7-11 July 2018
Spontaneous Activity in Brain Development Leiden, The Netherlands	8-10 October 2018

Dutch Neuroscience Meeting
Lunteren, The Netherlands (*oral presentation*) 20 June 2019

SFN Society for Neuroscience meeting 2019
Chicago, USA (*poster presentation*) 19-23 October 2019

TEACHING AND SUPERVISION

Teaching activities

Lecture in the module "plasticity and behavior" for the neuroscience master course in March 2017

Lecture on "learning and memory" for the Computing Brain minor in October 2019

Students supervision

Sandra van Iwaarden, Hogeschool Rotterdam
May 2016 – February 2017

Annabel van Oort, Hogeschool Rotterdam
November 2016 – June 2017

Hang Le Ha, MSc Biomedical Sciences, UvA Amsterdam
April 2018 – November 2018

Eva Hordijk, Avans University of Applied Sciences, Breda
October 2018 – May 2019

Anne Polman, BSc University of Applied Sciences Leiden
September 2018 – June 2019

Jeffrey de Hoogen, MSc Nanobiology, TU Delft
September 2018 – June 2019

Chi Yeung, Hogeschool Rotterdam
September 2019 – June 2020

ACKNOWLEDGEMENTS

"The value of things is not the time they last,
but the intensity with which they occur.
That is why there are unforgettable moments
and unique people"

Fernando Pessoa

I could not start any acknowledgements without thanking first, above all, **Geeske**. Most of the things I learnt during this journey were possible because of your patience, enthusiasm, mentorship and teaching skills as a supervisor. You believed in me and I could not be most grateful! You gave me all the freedom and chances to always try new things, and fail and try again and succeed, you proposed new experiments and listened to all the new dumb suggestions that could pop-up in my mind. This approach gives me enough hope and boldness to believe in Science and Research. I enjoyed all the scientific conversations we had, the not so scientific ones and I appreciated so much that I could always express my opinion in my own most true Italian spirit without ever feeling I was stepping on toes. Most of all, it's your *humanitas*, friendship and listening skills that not only gave me the chance to be myself as a person in the lab, but most importantly gave me the tools to endure the most difficult moments of this PhD, especially during the past few months. Having contributed to start the van Woerden lab and later to belong to it was a great honor! Nel frattempo, ho deciso di aggiungere qualche frase in italiano per assicurarmi che tu non perda le capacita' di leggere in italiano anche se, considerando tutte le volte che aggiungo parole in italiano nelle mie frasi in inglese, non credo ci sia troppo da preoccuparsi!

Ype, I will always be grateful for giving me the possibility to join the lab and for the scientific freedom you allowed during my PhD, it renewed my scientific enthusiasm and contributed to help me finding my own path in Science.

Carmen, after losing touch for a while, I was so glad we ended up crossing our paths again and even collaborate on a project! These past few months were quite difficult and you have been there to support me! I enjoyed all our chats, the walks and bicycle rides through Rotterdam. I'm extremely lucky to have you as a paranymph! I hope we'll stay in touch to keep on sharing the Science, the frustration and the fun!!
Dear **Selina**, your sweetness and kindness are so comforting that I cannot express how important it was to have you in the lab, first as a student and then as a member of the van Woerden lab. Having you as a paranymph means really a lot to me!

Charlie, I still cannot believe that I could find within the Dutch world somebody so amazingly Italian! I was so glad that we could share all the frustration, the joy and the laughs that came along during this journey. Finally, somebody with whom I could complain without thinking I was overdoing it or exaggerating, I will surly miss you!
Edwin, I cannot remember all the weird topics of conversations we had in the lab nor how they started, but I truly enjoyed them all!
Marcel, you were definitely the best buddy I had in the lab, it was great we could share experiments, that I could learn all I could about wires and cables, but most of all that we could talk about Science, Life, Philosophy and all the rest with some true enthusiasm!

Minetta, thank you for all your support in the lab and for always having a smile on your face. **Ilse**, I still remember teaching you the very first perfusion as a student, you have come a long way since then! **Linda**, thank you for all the time you spent patching my Rheb mice, we got some very cool results out of it! **Pomme**, as a new PhD student of the van Woerden lab, I wish you the best PhD ever and lots of fun. **Stijn**, if there's somebody I really missed when I moved to the van Woerden molecular lab, that was definitely you, thank you for all your awesome weirdness! **Enzo**, thank you for all the patience you had in helping me with Matlab, I learnt a lot from you! **Martijn**, thank you for initiating me to the CAMK2 world and for being one of the first to try to teach me some Dutch! Dear **Mehrnoush**, thank you for always being available to help.
To all the **Elgersma lab members**, past and present, a special thanks for all the time spent laughing and eating birthday cakes and a truly sincere thanks goes to all the **students** that I had the chance to supervise during the past years, they thought me so much about how to become more patient and understanding.

Dear **Marielle**, your support during the past few years and especially in the last months was truly invaluable, thank you for always making some time to help!

Erika, **Elize** and **Mandy** you were the most amazing and supporting figures that one could possibly hope to find during a PhD abroad! **Vincenzo**, sei tra le prime persone che ho incontrato all'inizio di questo percorso e che ancora (r)esistono in dipartimento, continua a mantenere sempre il tuo entusiasmo, è contagioso e fa bene allo spirito (quando non iniziamo a parlare di politica, altrimenti mi prende lo sconforto). **Francois**, I remember some very interesting conversations we had in the histology lab but especially, thanks to you, I will always remember the very famous bin cells and think twice before pronouncing "*cerebellum*". **Zhanmin**, I was glad I could share with you my first steps in the department and thank you for initiating me to the molecular biology! Negah, Jochen, Sander, Simona, Oscar, Bas, Martijn, Aaron, Farnaz, Bin, Elisabetta, Marco, Maurizio and all the many others I met along this journey it was a pleasure to share moments with all of you!

Gao, thank you for everything you taught me, I truly appreciated.
Devika, thank you so much for the time you spent brainstorming with me and for inspiring confidence.
Steven, thank you for your invaluable advices on the Rheb project.
Dick, thank you for sharing all your wisdom. **Freek**, thank you for always being available.
Martijn, thank you for always having a kind word and a smile!
Chris, thank you for giving me the chance to join the Neuroscience department, it was a precious experience for my scientific career.

Mark Nellist, thank you for collaborating with us on the Rheb story and for the proofreading of the paper.
Monica Frega, grazie mille per tutto l'aiuto con i MEAs e con l'analisi, senza di te non sarebbe stato possibile!
A special thanks goes to all the countless **collaborators** we had over the years on both the CAMK2 and the RHEB projects and the patients' families that made this thesis possible.

To all the **members of the committee**, I would like to thank you all for reading my thesis, giving suggestions and for accepting to be part of the committee.

For all the ones that were not mentioned by name, I did not forget you! There are always reasons to be thankful: a simple smile, a pleasant memory or a kind word can be enough to turn a bad day around and give you the strength to keep on going.

Non sarei arrivata fin qui senza il contributo e l'appoggio di tutti quei maestri e professori incontrati lungo il mio percorso formativo che hanno incoraggiato la mia crescita intellettuale. Le figure che hanno modellato ed indirizzato le mie scelte senza alcuna costrizione, dando spazio e linfa allo sviluppo di quelle capacita' individuali che formano la Persona, contrastando la mediocrita', favorendo l'originalita' e la liberta' di pensiero. Grazie per essere stati una fonte di ispirazione. La strada meno battuta potra' fare piu' paura ma e' anche quella che da piu' soddisfazioni, sempre *In direzione ostinata e contraria*.
Un sentito grazie a Maria Vittoria Lollobrigida, Alda Lollobrigida, Maria Grazia Spila, Egle de Stefano, Fabrizio Rufo.

Nicco, finalmente e' fatta!! Grazie per aver condiviso con me le gioie e i dolori di questi lunghi anni, chi meglio avrebbe potuto capire la frustrazione di un PhD in terra straniera dopo gli anni passati a Roma...

Marti, che dire, la copertina è bellissima…fatta in fretta ma e' venuta comunque benissimo! un pezzo di Italia da mostrare con orgoglio…! Grazie per esserci sempre stata e per avermi ascoltata tutte le volte che qualcosa andava storto...

Ed infine, cari **mamma** e **papà**, questi ultimi mesi sono stati molto incerti, difficili, dopo settimane di lockdown la mia speranza e' di riuscire a trovarci tutti insieme alla fine di questo lungo percorso. Nonostante le distanze e le ansie, a voi dedico il frutto di questo lavoro durato ben sei anni. E' grazie a voi principalmente che tutto ciò è stato reso possibile: dal momento in cui avete iniziato a spronarmi a studiare, leggere ed informarmi ho raggiunto la consapevolezza che il duro lavoro prima o poi paga. Ma non sarebbe stato possibile senza i vostri sacrifici e la volontà di credere nelle mie capacità, e per questo vi ringrazio!

A nonna Emma, che avrebbe detto "*ma Martina e' brava*" e a nonno Romolo, che avrebbe sicuramente fatto mettere la notizia del mio Dottorato sul giornale!


A

"You only grow by coming to the end of something
and by beginning something else."

The World According to Garp, John Irving